TEMPUS: A METHODOLOGY FOR MODEL-BASED ROBUST-OPTIMAL DESIGN OF TIME-DYNAMIC SYSTEM IDENTIFICATION EXPERIMENTS USING VARIATIONAL ASYMPTOTIC EXPANSIONS

A Thesis
Presented to
The Academic Faculty

by

John W. Dykes

In Partial Fulfillment
of the Requirements for the Degree
Doctor of Philosophy in the
School of Aerospace Engineering

Georgia Institute of Technology
December 2016

TEMPUS: A METHODOLOGY FOR MODEL-BASED ROBUST-OPTIMAL DESIGN OF TIME-DYNAMIC SYSTEM IDENTIFICATION EXPERIMENTS USING VARIATIONAL ASYMPTOTIC EXPANSIONS

Approved by:

Professor Dimitri Mavris,
Committee Chair
Regents Professor/Boeing Professor of Advanced Aerospace Systems Analysis
Georgia Institute of Technology

Dr. Jon Zumberge
Aerospace Systems Directorate
The Air Force Research Laboratory

Professor Rafael de la Llave
School of Mathematics
Georgia Institute of Technology

Professor Daniel Schrage
School of Aerospace Engineering
Georgia Institute of Technology

Dr. Jean Charles Domerçant
Defense Open Systems Division
Georgie Tech Research Institute

Professor Lakshmi Sankar
School of Aerospace Engineering
Georgia Institute of Technology

Date Approved: August 8, 2016

To my late grandfather,

Osborne Jefferson Dykes,

It took me a while, but I've finally come around to seeing things your way, and now I wished we would have had more time to talk about all things engineering.

PREFACE

This work has certainly proven to be my greatest challenge yet. I think, in part, due to a creative mindset which has indeed driven a fun but difficult road through this process. Some of the following quotes capture this aspect of my research.

"Two roads diverged in a wood, and I-
I took the one less traveled by,
And that has made all the difference."
-Robert Frost, The Road Not Taken

"Imagination is more important than knowledge. Knowledge is limited. Imagination encircles the world."
-Albert Einstein

"Ask, and it shall be given you; seek, and ye shall find; knock, and it shall be opened unto you."
-Matthew 7:7 (KJV)

"The reward of understanding the universe may be a glimpse of 'the mind of God.'"
-Stephen Hawking

"If we knew what it was we were doing, it would not be called research, would it?"
-Albert Einstein

"If I have seen further it is by standing on the shoulders of giants."

-Isaac Newton, letter to Robert Hooke, 1676

"No man is an island,

Entire to itself.

Each is a piece of the continent,

A part of the main.

.... Therefore, send not to know

For whom the bell tolls,

It tolls for thee."

- For Whom the Bell Tolls by John Donne

"Nullius in verbal. (Take nobody's word for it.)"

-Motto of the Royal Society of London

"I want to help turn the wheel of progress."

-young Wernher von Braun

"Scientists discover the world that exists; engineers create the world that never was."

-Theodore von Karman

"Knowledge is of no value unless you put it into practice."

-Anton Chekhov

"Real knowledge is to know the extent of one's ignorance."

-Confucius

"There comes a time when the mind takes a higher plane of knowledge but can never prove how it got there."

-Albert Einstein

"Beware of false knowledge; it is more dangerous than ignorance."

-George Bernard Shaw

"Knowing others is wisdom; knowing yourself is enlightenment."

-Lao Tzu

"Knowledge is a process of piling up facts; wisdom lies in their simplification."

-Martin H. Fischer

"A doctor can bury his mistakes, but an architect can only advise his clients to plant vines."

-Frank Lloyd Wright

"Make everything as simple as possible, but not simpler."

-Alber Einstein

"Perfection is not attainable, but if we chase perfection we can catch excellence."

-Vince Lomdardi

ACKNOWLEDGEMENTS

I would like to first start off by thanking, my advisor, Dr. Mavris. His guidance, patience, care, and support has truly shaped me into the person that I am today and has made this work possible. I would also like to thank him for teaching inspirational classes, such as advanced design methods and fixed wing aircraft design I and II. He has always tried to instill in his students a higher level of critical thinking, and I think this his greatest gift to us.

I am grateful to my committee, Dr. Mavris, Dr. de la Llave, Dr. Domerçant, Dr. Zumberge, and Dr. Schrage, for their guidance and feedback through this process. I appreciate all the time and effort that they have put into me and this dissertation. Notably, to Dr. Domerçant for taking a big part in helping me formulate my research early on in proposal phase, and to Dr. de la Llave for the encouragement, inspiration, and advisement to further pursue this work, which simply started out as a term project for his class.

I would also like to express my thanks to my fellow students and colleagues for their feedback, encouragement, and critique. Without this collaboration, the quality of my work would be significantly less. I can only hope that I have helped some of you with your own work, as you certainly have done so for me. Also, there are many instances were people have loaned me their time and resources, during critical times, I can't thank them enough. Specifically to Ed Scheuermann and Jeff Kornuta, who are both colleagues and life-long friends to me. You both have challenged me to always push harder towards the pursuit of excellence and self-improvement. They both know that the impact that they have had on this work.

There are many fantastic teachers that I have had along the way that have made an immeasurable impact on shaping my future, and they feel deserve a large amount of credit for my accomplishments. Starting in high school, I would like to thank Mr. Meekins, my AP physics and chemistry II teacher, for planting the seeds of interest in math and science within me – even though I seemed disinterested at the time. Thanks to many many of my college instructors during my time at LSU pursuing my mechanical engineering undergraduate degree, including: Dr. Gonthier, Dr. al Rub, Dr. Sinclair, and Dr. Nikitopoulos. It was under their guidance, motivation, and inspiration that I matured into the person that I am today. They have instilled a fire and a passion within me that will never be quenched.

There is one very special person who has had a profound impact on my life, my friend, my piano teacher, Mrs. Bilie Leach. Her passion and enthusiasm has had a lasting effect on me, beyond my love for classical music, as she taught me that no goal is impossible if I set my mind to it and put in the hard work to obtain it. I certainly would not have made it through this dissertation without learning this lesson.

To my family and friends, thank you for your love and support. Thank you for believing in me and always being there for me. To my mom and dad, I hope this makes you proud of me. To my wife Amy, thank you for standing by me through this process, and for encouraging me and supporting me when the path forward felt insurmountable. I could not have asked for a better partner in life!

TABLE OF CONTENTS

PART IV: RESEARCH FORMULATION

PART V: EXPERIMENTAL RESULTS

LIST OF TABLES

LIST OF FIGURES

NOMENCLATURE

α, β	=	Aerodynamic angles of attack and sideslip
$\boldsymbol{\gamma}$	=	Vector of overall objective criterion weighting factors
$\boldsymbol{\delta}$	=	Vector of additive perturbative effects
$\boldsymbol{\lambda}$	=	Vector of dynamic system co-states
$\boldsymbol{\xi}$	=	Vector of sources of statistical error
$\boldsymbol{\varphi}$	=	Dynamic experiment design vector
$\boldsymbol{\theta}$	=	Vector of "true" system parameters
$\hat{\boldsymbol{\theta}}$	=	Vector of "estimated" system parameters
$\boldsymbol{\Theta}$	=	Admissible region of parameters
ϕ_k	=	The phase angle for the k^{th} sinusoidal component
ϕ, θ, ψ	=	Euler roll, pitch, yaw angles
τ	=	Duration of dynamic experiment
ω_k	=	The frequency for the k^{th} sinusoidal component
$\boldsymbol{\nu}(t)$	=	Vector of random measurement noise
Δc	=	Vector of operational/environmental uncertainty
Δm	=	Vector of measurement uncertainty
Δp	=	Vector of model parameter uncertainty
Δx	=	Vector of input uncertainty
$\partial \mathbf{x} / \partial \theta_j$	=	Vector of state sensitivity to changes in parameter j
$\partial \dot{\mathbf{x}} / \partial \theta_j$	=	Vector of state time-derivative sensitivity to changes in parameter j
$\partial \mathbf{y} / \partial \theta_j$	=	Vector of output sensitivity to changes in parameter j
n_p	=	Number of parameters to be estimated by a dynamic experiment
$\mathbf{u}(t)$	=	Vector of time-varying input controls
i, j, k	=	Index variables
t	=	Scalar time variable

t_0	=	Initial time
$\mathbf{t}_{sp}$	=	Vector of N sampling times
$\bar{\mathbf{w}}$	=	Vector of time-invariant (constant) input controls
$\mathbf{x}(t)$	=	Vector of dynamic system states
$\mathbf{x}_0$	=	Vector of initial state conditions
$\dot{\mathbf{x}}(t)$	=	Vector of dynamic system state time-derivatives
$\mathbf{y}\,(t)$	=	Vector of dynamic system outputs
$\mathbf{z}\,(t)$	=	Vector of dynamic system output measurements
A_k	=	The amplitude for the k^{th} sinusoidal component
$\mathbf{C}$	=	Covariance matrix
H	=	The Hamiltonian of an optimal control problem
$\mathbf{H}$	=	Hessian matrix
$J[u]$	=	Optimal control problem cost function
M	=	Number of sinusoids comprising of a multi-sine input maneuver
N	=	Number of output measurements
S	=	Flight dynamic aerospace vehicle system
T	=	The time length of the multi-sine excitation
$T_k(x)$	=	The k^{th}-order Chebyshev basis function
$\mathscr{I}_x$	=	Scalar Fisher information-based objective criterion
$\mathscr{M}$	=	The Fisher information matrix
Ma	=	Mach number
$P_k(x)$	=	The k^{th}-order Legendre basis function
$\mathbf{R^{-1}}$	=	Inverse of the measurement (sensor) covariance matrix
$S_k(x)$	=	The k^{th}-order Taylor basis function
$\mathcal{U}_{\text{adm}}$	=	Admissible region of control inputs
$\mathcal{X}_{\text{adm}}$	=	Admissible region of states

ABBREVIATIONS

ABHV	Air-breathing hypersonic vehicle
ADIFOR	Automatic DIfferentiation of FORtran
ADOL-C	Automatic Differentiation by OverLoading in C++
ADIMAT	Automatisches DIfferenzieren für MATlab
AE	Asymptotic Expansion / *Aerospace Engineering*
AFRL	Air Force Research Laboratories
AIAA	American Institute of Aeronautics and Astronautics
ANOVA	ANalysis Of VAriance
ASDL	Aerospace Systems Design Lab
BVP	Boundary Value Problem
CADAC	Computer Aided Design of Aerospace Concepts
CAS	Computer Algebra System
CDF	Cumulative Density Function
CFD	Computational Fluid Dynamics
DAE	Differential Algebraic Equations
DOE	Design Of Experiments
DSTO	(Australian) Defense Science and Technology Organization
FEA	Finite Element Analysis
FFT	Fast Fourier Transform
GA	Genetic Algorithm
GHV	Generic Hypersonic Vehicle model
GMP	GNU Multiple Precision arithmetic library
GT	Georgia Tech
HALRAAM	High-Speed Advanced Long Range Air-to-Air Missile
HFT	Hypersonic Flight Testing

HIFiRE	Hypersonic International Flight Research and Experimentation
H.O.T	Higher Order Terms
HRE	Hypersonic Research Engine
HVD	Hypersonic Vehicle Design
HVT	Hypersonic Vehicle Testing
ICBM	InterContinental Ballistic Missile
IPPD	Integrated Product/Process Development
IVP	Initial Value Problem
MC	Monte Carlo
MPFR	Multi-Precision Floating-Point arithmetic library
M&S	Modeling & Simulation computational environment
NAI	National Aerospace Initiative
NASA	National Aeronautics and Space Administration
OCP	Optimal Control Problem
ODE	Ordinary Differential Equation(s)
OED	Optimal Experiment Design
PDE	Partial Differential Equation
PDF	Probability Density Function
PIE	Parametric Integrated Environment
PMP	Pontryagin's Maximization Principle
RDO	Robust Design Optimization
RDS	Robust Design Simulation
RK4	Runge-Kutta 4th-order numerical integration algorithm
RKF56	Runge-Kutta-Fieldburg 5th/6th-order numerical integration algorithm
ROED	Robust-Optimal Experiment Design
RPF	Relative Peak Factor
RSE	Response Surface Equations

RSM	Response Surface Methodology
SAS	Stability Augmentation System
SCRAMjet	Supersonic Combustion RAMjet
SMD	Spring Mass Damper model
SIDPAC	System IDentificaiton Programs for AirCraft
STS	Space "shuttle" Transportation System
SysID	System Identification
SWM	Stepwise Regression Models
TEMPUS	Time-dynamic Experiment design using a Model-based approach to Propagate Uncertainty for System Identification
VAE	Variational Asymptotic Expansion
VX	Virtual eXperimentation
USAF	United States Air Force
WWII	World War II

SUMMARY

The development of appropriate flight tests has proven to be a critical element in the development process of many revolutionary next-generation aerospace vehicles. For example, in the case of hypersonic vehicles with air-breathing SCRAMjet engines, sophisticated computational analyses have been developed which require extensive validation and calibration with physical test data. The current state of hypersonic ground testing facilities has not yet been able to accommodate these demands due to the inability to replicate hypersonic flow conditions with sufficient accuracy. These deficiencies have put increased demand and pressure on hypersonic flight testing experiments which have historically proven to produce the highest quality results but at the potential price of extreme complexity and expense. In the case of hypersonic flight testing for SCRAMjet vehicles, the combination of high expense, high complexity, and high modeling uncertainties has led to conservative, risk-averse experiments. These efforts have historically yielded little gain in knowledge, observing only marginal improvements to prediction confidence in the computational models.

There is an entire discipline devoted to the process of design and information extraction from aerospace-type experiments known as aircraft system identification (SysID) which combines three interdependent topics: (i) computational modeling and simulation, (ii) experimental design methods, and (iii) statistical estimation techniques. Essentially, SysID attempts to develop time-dynamic experiments so that statistical estimation techniques can most effectively be used to identify high-confidence physics-based models. An implicit limitation to this process lies within the topic of dynamic experiment design, often posed as a mixed parameter optimization/optimal

control problem for the concurrent design of aircraft maneuver inputs, instrumentation system parameters, flight conditions, test duration, etc. Here, Fisher information-based optimality criterion are sought to be used for the quantification of information quality; however, these metrics can only be accurately computed if the true values of the unknown model parameters (*e.g.* SCRAMjet aero-propulsive-elastic stability and control coefficients, vehicle mass/inertia parameters, etc.) are known prior to conducting an actual experiment, which is often not the case. This is commonly referred to as *the circulatory problem* in statistics literature, suggesting that dynamic optimal experiment design (DOED) requires an augmented robust-optimization approach (DROED) to account for modeling uncertainties.

This research focuses on the design of flight-dynamic experiments from the perspective of an integrated system for the concurrent design of information-dense flight experiments which are robust with respect to model parameter uncertainties. The proposed methodology is called TEMPUS, which stands for Time-dynamic Experiment design using a Model-based approach to Propagate Uncertainty for System identification. By using the top-down design decision support process within the Georgia Tech Integrated Product/Process Development methodology (GT-IPPD), TEMPUS fuses elements from two existing experiment design methodologies to enable a systems engineering approach to the design of large-scale robust-optimal dynamic system identification experiments (such as the design of SCRAMjet-powered flight tests). Within this method the generation of feasible design alternatives is achieved via a sizing and synthesis method, providing for the concurrent design of measurement system parameters, control system architecture and parameters, probabilistic uncertainty models, aero-thermal-fluids models, design constraints, and even vehicle geometry and mission-level parameters. To assess the performance of a given experiment design, a variety of different information quality metrics are able to be calculated from a dynamic high-order sensitivity analysis, providing for an *a priori* estimate of expected

goodness-of-fit quality in the *a posteriori* parameter estimators. To evaluate feasible alternatives, a virtual experimentation strategy is utilized to assess information performance metrics of a given alternative via nondeterministic techniques (*e.g.* Monte Carlo methods).

Implementation of TEMPUS depends on the capability to perform a high-order dynamic sensitivity analysis on nonlinear industrial-sized aerospace flight-dynamic models (including guidance, navigation, and control logic) in a fashion that is both automatable and easily implementable by flight test designers and control systems engineers, all the while without introducing computational uncertainties. To address this challenge, an automatic differentiation tool specialized for use in dynamic experiment design was developed, providing for the ability to automatically compute robust-optimal Fisher information performance metrics by constructing variational asymptotic expansions (*i.e.* time-dynamic arrays of multivariate Taylor series expansions, parameterized by design and uncertainty perturbation variables). In general, these variational asymptotic expansions (VAEs) allow for a number of desirable capabilities for SysID applications, because they can essentially be considered as asymptotically accurate surrogate models to solutions of dynamic systems, including: (i) the construction of nominal Fisher information metrics (requiring at least 1st-order output-to-parameter sensitivity trajectories to be computed); (ii) the construction of arbitrarily high-order robust-optimal Fisher information metrics using both (deterministic and nondeterministic approaches to calculate robustness); (iii) rapid exploration of neighboring solutions to optimal control problems; and (iv) the implementation of arbitrarily high-order optimization algorithms (*e.g.* high-accuracy nonlinear parameter estimators in SysID) (not considered in this work).

High-order VAEs can suffer from many of the same complications that often hinder high-order multivariate response surface equations (RSEs), such as: (i) poor numerical conditioning, (ii) diminishing returns on accuracy (e.g. slow rates of convergence,

finite radii of convergence, etc.), and (iii) the curse of dimensionality (*e.g.* large computational times and memory requirements). Therefore prior to using VAEs for dynamic experiment design problems within TEMPUS, four developmental experiments were designed to study the adverse effects of diminishing returns on accuracy, the curse of dimensionality, and application of VAEs to create surrogates of optimal control problems on simple dynamic systems. These include: (i) investigating the potential improvements of using alternative sets of basis functions on problems where diminishing returns on accuracy are observed for the standard Taylor (monomial) basis; (ii) investigating the effects of diminishing returns on accuracy in dynamic uncertainty propagation using high-order VAEs and various probabilistic uncertainty models; (iii) investigating the computational time and memory complexities of high-order, high-dimensional VAEs for use in dynamic experiment design; and (iv) investigating how automatic differentiation can be used to generate high-order VAEs to solutions of optimal control problems. The objective of the fourth experiment is to overcome the limitations that many indirect numerical optimization methods possess, namely, being cumbersome, nonautomatable analyses which hinder the ability to perform design space exploration and uncertainty propagation analyses due to a human-in-the-loop dependency. The results of the first experiment suggest that the use of Chebyshev basis functions can alleviate problems where the diminishing returns on accuracy are observed when Taylor basis functions are used. In the second experiment, it was observed that even for uncertainty propagation with high-order VAEs that slow/poor convergence characteristics can result in adverse effects, such as artificial multi-modality in propagated uncertainty distributions. The results of the third experiment suggest that high-dimensional problems (such as experiment design problems) scale exponentially with increasing order, and therefore high-performance computing capabilities will be necessary to practically obtain robust-optimal dynamic

experiment designs for large industrial-sized aerospace problems. In the final experiment, two high-order optimal control formulations were developed for computing VAE surrogates. Promising results were observed for a simple optimal control problem where VAE surrogates were successfully computed; however, more effort is needed before these formulations can be applied to larger dynamic experiment design problems.

In light of the results of the aforementioned experiments, the TEMPUS methodology was applied to two design problems: (i) a simple mass-spring-damper problem under sinusoidal forcing, and (ii) the Generic Hypersonic Vehicle (GHV) model to design information-dense SCRAMjet-powered flight tests at steady-level flight under multi-sine forcing. In the first study, the small problem size allowed for investigation of high-order VAEs without experiencing the adverse effects due to the curse of dimensionality. Here, it was observed that robust-optimal experiment designs did produce probabilistic information metric distributions with better robustness with respect to parameter uncertainties than designs using the traditional nominal information metrics, and all experiment designs were found to produce intuitive results, serving as a form of validation (*e.g.* the sinusoidal forcing frequency was designed to excite the system near the expected natural frequency to maximize output-to-parameter sensitivities). For the flight test design problems, a nonlinear robust-adaptive flight controller is required to ensure safe operation throughout flight, because the GHV open-loop dynamics possess unstable, non-minimum phase behavior in the aero-propulsive-elastic modes in addition to the parametric uncertainties within the aero-propulsive-elastic stability and control coefficients. As a result, the complexity of the overall closed-loop model is greatly increased; however, computation of high-order VAEs for this system does not require any special attention in regards to practical implementation, but a substantial increase in computation time and memory was observed. The objective of experiment designs for the SCRAMjet-powered flight tests was to generate

data for the system identification of eight thrust force stability and control coefficients: $C_T^{\Phi\alpha^3}$, $C_T^{\Phi\alpha^2}$, $C_T^{\Phi\alpha}$, C_T^{Φ}, $C_T^{\alpha^3}$, $C_T^{\alpha^2}$, C_T^{α}, C_T^{0}. For the combination of the adaptive control architecture and multi-sine excitation maneuvers implemented here, this experimental objective proved difficult to obtain where adaptation is known to have a canceling effect on the open-loop dynamics, therefore, making it difficult to excite the system enough to generate sufficient amounts of the high angle of attack data for improving the information content of the high-order coefficients $C_T^{\Phi\alpha^3}$ and $C_T^{\alpha^3}$. It is hypothesized that alternative control strategies, employing machine learning for real-time estimation of open-loop natural frequencies, may improve the information quality, but implementation of this is beyond the scope of this work. Nevertheless, TEMPUS does allow for the robust-optimal assessment of information quality for alternative flight test designs (by using the computation of variational asymptotic expansions to overcome the deficiencies of the circulatory problem), implying that trade-offs between alternative controls architectures, measurement systems, etc. is now an available capability to the flight test designer and controls system engineer.

PART I

Introduction and Motivation

In the following chapters, the introduction and motivation for designing flight dynamic experiments will be presented. To aid in this, a certain aerospace design problem will be considered as a case study which is the development of SCRAMjet-powered hypersonic vehicles. Throughout this discussion, relevant gaps in the state-of-the-art will be identified. Following this gap analysis, the formal research objective will be stated, providing a clear description of the goal of this work.

CHAPTER 1

MOTIVATION: DESIGNING THE REVOLUTIONARY

Often times in history, something new comes along that causes a paradigm shift in the way things are conducted in everyday life. Perhaps the most significant example of this is the emergence of the Industrial Revolution, which at the time changed almost every aspect of daily life [154]. Defined as a transition towards new automated manufacturing processes, this revolution is believed to have occurred somewhere in the period between 1760 and 1840 and marks a major turning point in history, where for the first time average income and population began to exhibit unprecedented and sustained growth [184].

Since the time of the industrial revolution, there have been other paradigm shifts that have radically changed the landscape of how things are done. For example, in the area of transportation, the automobile first emerged in 1886 which replaced animal-drawn carriages and carts in much of western culture around the turn of the 20th century [93, 157]. Shortly thereafter, the airplane was invented and flown by the Wright brothers in 1903, which again changed the landscape, enabling transportation over long distances in a reliable fashion over relatively short periods of time [8, 9, 10].

This chapter focuses on the topic of designing revolutionary aerospace vehicles. To this end, it is briefly elaborated upon as to how these vehicles are designed and tested in such a way so as to identify and obtain the required knowledge to be used for developing vehicles with high performance and reliability.

1.1 Revolutionary-Type Aerospace Vehicles

In aerospace, pushing the boundaries of capability, reliability, affordability, and performance often results in the design of revolutionary-type concepts, which are anticipated to cause paradigm shifts. For example, the advent of the ballistic missile in WWII enabled strikes against enemy targets at much longer ranges and considerably less risk as opposed to the more traditional approach of aircraft bombing raids [31]. Figure 1 shows some current examples that fit the description of being revolutionary concepts.

Figure 1: Examples of revolutionary vehicles and concepts that represent the current state-of-the-art.

The Sierra Nevada Dream Chaser is a concept to provide rapid and affordable access to space. The Boeing blended wing-body subsonic transport is a long-range, fuel-efficient passenger transport concept. The Lockheed Martin SR-72 is a high-speed, high-altitude, and long-range unmanned vehicle concept which could enable prompt global strike and surveillance capabilities. The Israeli Arrow 3 is a ballistic missile interceptor [2], which is capable of terminal-phase endo-atmospheric kinetic kill intercepts with

a high degree of reliability. The Boeing 6th generation fighter jet concept is a high-maneuver, potentially unmanned vehicle platform, which is being considered as a potential platform for directed energy weapons. The Bell/Boeing V-22 Osprey is a vertical take-off and landing aircraft, capable of transporting heavy cargo quickly over long distances. Finally, the USAF X-51A Waverider is an air-breathing hypersonic vehicle, which is capable of reaching speed up to Mach 9 using hydrocarbon-based fuels enabling prompt global military strikes.

By definition, revolutionary vehicles are new concepts, and therefore, it is difficult if not impossible to predict their performance solely based on historical data. Due to this, as well as the fact that these vehicles are inherently complex, large physics-based computational analyses must be used to assess performance which can require much time and effort. This observation is formally stated below.

Observation: *The design of next generation, revolutionary vehicles is a time-consuming, complex task that requires an extensive physics-based analysis due to the lack of historical data.*

To physically model aerospace vehicles, a multidisciplinary analysis of sufficient fidelity and accuracy is required, which is capable of fully describing the vehicle at the system, subsystem, and component levels. This is manifested as an integrated computational environment, which incorporates common physical disciplines used to model aerospace vehicles (*e.g.* aerodynamics, propulsion, structures, flight dynamics, stability and control, thermodynamics, etc.). Once it has been established that an integrated environment physically describes the operation of a given vehicle with suitable accuracy, it can be used to conduct virtual experiments via computational simulation to evaluate and assess vehicle concepts in terms of performance, reliability,

etc. Over the last 25 years, computational design has become increasingly popular to the point of being heavily relied upon for the design of aerospace vehicles [148, 256, 280], because it is often expensive and time-consuming to design, build, test, and fly concepts in an iterative fashion to reach a state of technological maturity. As an alternative to the traditional point-design philosophy (which is often a manual, expert-driven process), computational design has enabled a parametric design approach to explore and optimize the entire vehicle architecture with respect to performance at the system, subsystem, and discipline levels. Computational design emphasizes the following:

- Disciplinary breadth and depth while accounting for uncertainty and risk
- Multidisciplinary analysis, optimization and design
- Reduction of analysis and design process cycle time
- Physics-based analysis and design of unconventional vehicles
- System of systems, architecture-based system engineering
- Interdisciplinary research through collaboration between academia, industry, and government

In recent times, computational design has been extended to incorporate a probabilistic design approach, which has proven necessary to enforce quality control [194, 266]. Here, a large number of computational cases can be generated to quantify the effects of various sources of uncertainty that have been identified (*e.g.* operational uncertainties, manufacturing uncertainties, performance uncertainties, etc.). When a design has been found that possesses satisfactory performance characteristics (*e.g.* an optimal design), and yet is suitably insensitive to various sources of uncertainty (*i.e.* a robust design), then a solution of suitable "quality" has been found.

Observation: *To achieve the goal of robust design, probabilistic methods must be applied to the design of all vehicle components and subsystems, and to the integrated vehicle system itself.*

1.2 Revolutionary-Type Testing Facilities

Because revolutionary designs are often complex, the development of a computational modeling and simulation (M&S) environment to characterize these vehicles also becomes increasingly complex, requiring higher fidelity physics-based models [25, 87, 241]. Before use in computational design, however, a level of confidence in the accuracy and reliability of the model outputs must be established. For example, in the case of hypersonic vehicles with air-breathing scramjet engines, sophisticated computational analyses have been developed, requiring extensive validation and calibration [241]. This is done through a verification and validation exercise, which compares and calibrates the M&S environment with actual experiments and tests.

It is of no surprise that testing is often an expensive, high-effort endeavor that can also be highly complex in terms of both design and operation [183]. Figure 2 shows some examples of testing facilities that were developed in response to the need to support the development of next generation technologies.

In certain cases, facilities required to test/validate these tools have limited capabilities, which can inhibit proper validation of the M&S tools necessary for design. For example, the Apollo program required +20 separate ground test facilities to fully test the flow conditions in order to verify that components like the heat shield design was sufficient and reliable enough for planetary reentry [25]. This was indeed a substantially large effort, requiring a significant amount of time and man-power.

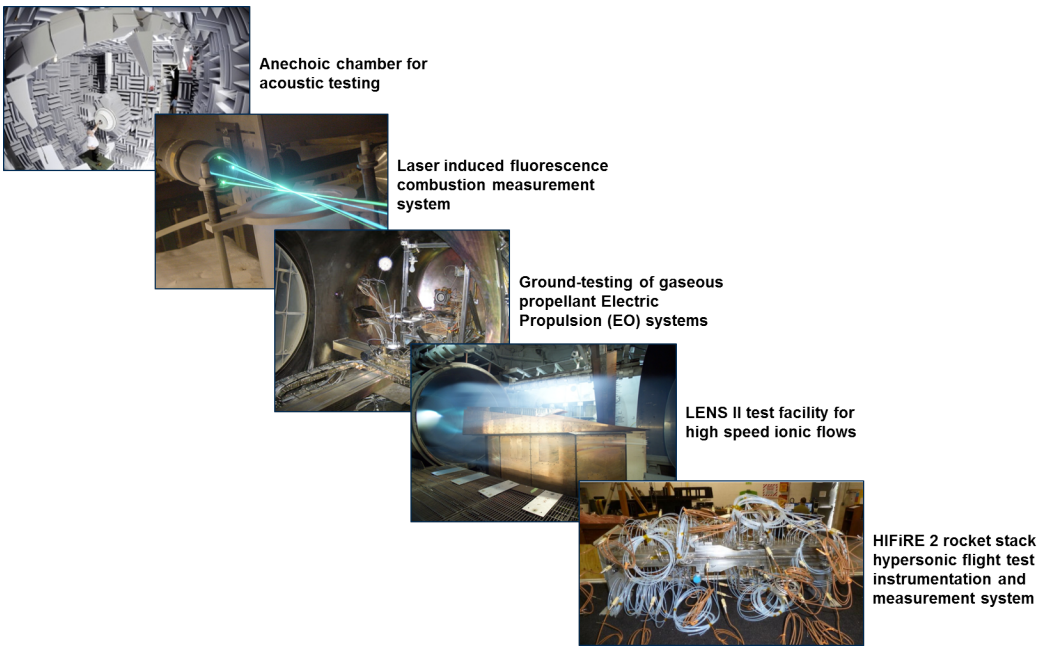

Figure 2: New generation of facilities are required to accommodate the demand for new computational tools which require validation and calibration with physical data.

In another example, hypersonic wind tunnels simply cannot fully replicate the rarefied gas, non-equilibrium conditions required to sufficiently test the operation of air-breathing hypersonic scramjet engines. To overcome this, an alternate strategy is to use flight testing to obtain the appropriate flight testing data to be used for model validation; however, there are inhibiting factors which make flight testing difficult, such as high cost, long development times, and a high degree of programmatic and operational risk [87]. As a result, the following observation holds true in many cases.

Observation: *Limitations in testing facilities inhibit proper validation of tools that are necessary to design revolutionary-type vehicles.*

Keeping in mind that the end goal is to design revolutionary-type vehicles, there

is clearly a need to efficiently develop M&S tools and testing capabilities, simultaneously. Then, these assets can be incorporated into an effort towards the development of revolutionary vehicles. In modern history, successful examples of this approach have been documented in past programs such as the Apollo program, the Space Transportation System (STS), and the X-15 [229, 230]. Again, referring back to the case of hypersonic scramjet engines, a substantial amount of effort has been invested in the development of hypersonic facilities for testing of scramjets since the mid-1950s [25, 183].

Observation: *Significant effort is required to develop proper test facilities before vehicle design can be undertaken, due to the need to calibrate physics-based models.*

1.3 Hypersonics – The Confluence of Air and Space

A certain class of revolutionary-type vehicles operates at or near the overlap of what constitutes aerodynamics and astrodynamics – the hypersonic regime. The hypersonic regime is typically classified as flight above Mach 5; however, perhaps a better categorization is the regime where a number of the following flow attributes emerge [25, 26]: strong flow phenomena (*e.g.* turbulence, pressure, temperature, density, vorticity, and energy), thin shock layers, viscous interactions, entropy layers, changes in vehicle stability and control, and strong high-enthalpy real-gas effects (*e.g.* ionization, dissociation, equilibrium effects, and other molecular phenomena). In addition, the hypersonic designer must remain aware of the other flow regimes since a hypersonic vehicle will have to transition from rest to the designed hypersonic flight Mach number and transition throughout the various layers of the atmosphere.

Reflecting back on historical examples, there are indeed a large number of vehicles and concepts that fit this description, which can be commonly identified as aspiring

to satisfy at least one of the three following motivations for pursuit: (i) affordable access to space, (ii) faster global transportation, and (iii) prompt global strikes and surveillance. Figure 3 illustrates "the confluence of air and space" concerning these motivations of pursuit, providing historical examples. Here, the "hypersonic revolution" can be seen with origins dating as far back as the end of WWII [128]. Many people perceive hypersonics as the last unknown frontier and the only inherent, true integrator of the streams of air and space development into "genuine aerospace" [10, 129].

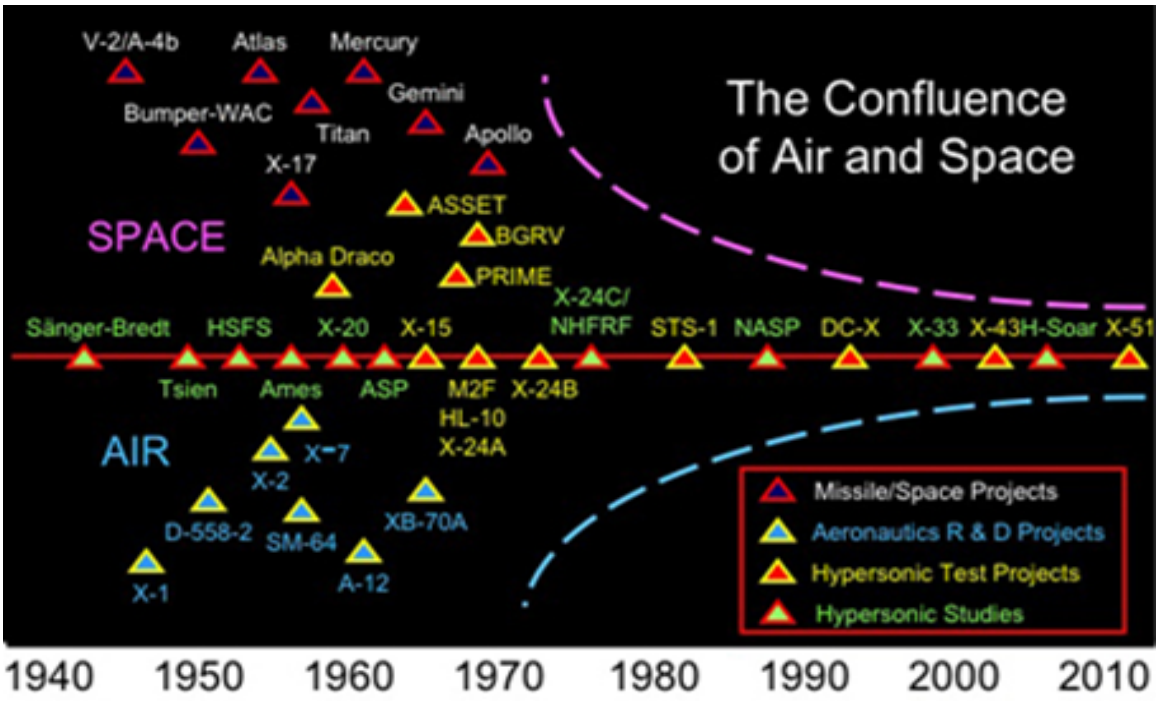

Figure 3: The confluence of air and space: 75 years of effort [128, 129].

As time has progressed, the development of this classification of revolutionary-type vehicles has become an increasingly complex and difficult task, resulting in highly-integrated designs which are intended to push the envelop of what is currently possible. A current example of this is the scramjet-powered air-breathing hypersonic vehicle (ABHV), which has repeatedly fallen short of expectations over the last 40 to 50 years due to high uncertainties in performance and economics [47, 229, 230].

Development of ABHVs stress every aspect of developing revolutionary aerospace technologies, including computational modeling and design of vehicles, as well as required supporting facilities. For example, Figure 4 illustrates the highly-integrated and complex systems design of the Hyper-X (X-43A) vehicle, which relied on physics-based models to achieved sustained hypersonic flight using an air-breathing SCRAMjet engine. Development of ABHV technology is still considered one of the most challenging problems to solve of the current time; however, it is speculated that if a breakthrough is achieved, then an abundance of new applications and capabilities will be possible – truly causing a revolutionary paradigm shift. In Figure 5, the potential performance gains of utilizing SCRAMjets for sustained hypersonic flight is illustrated. In the next chapter, ABHVs will be considered in more detail from the perspective of a case study, so as to clearly identify limiting problems that currently inhibit this technological breakthrough.

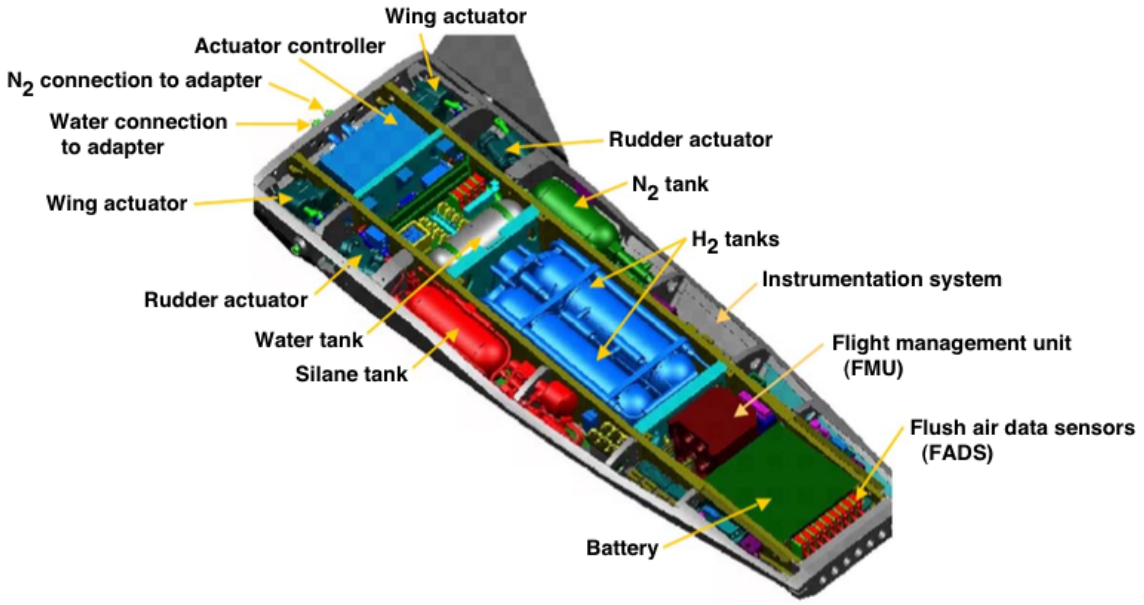

Figure 4: Air-breathing hypersonic vehicles, such as the X-43A, are highly-integrated and complex systems designed to push the physical limits of performance [188, 196].

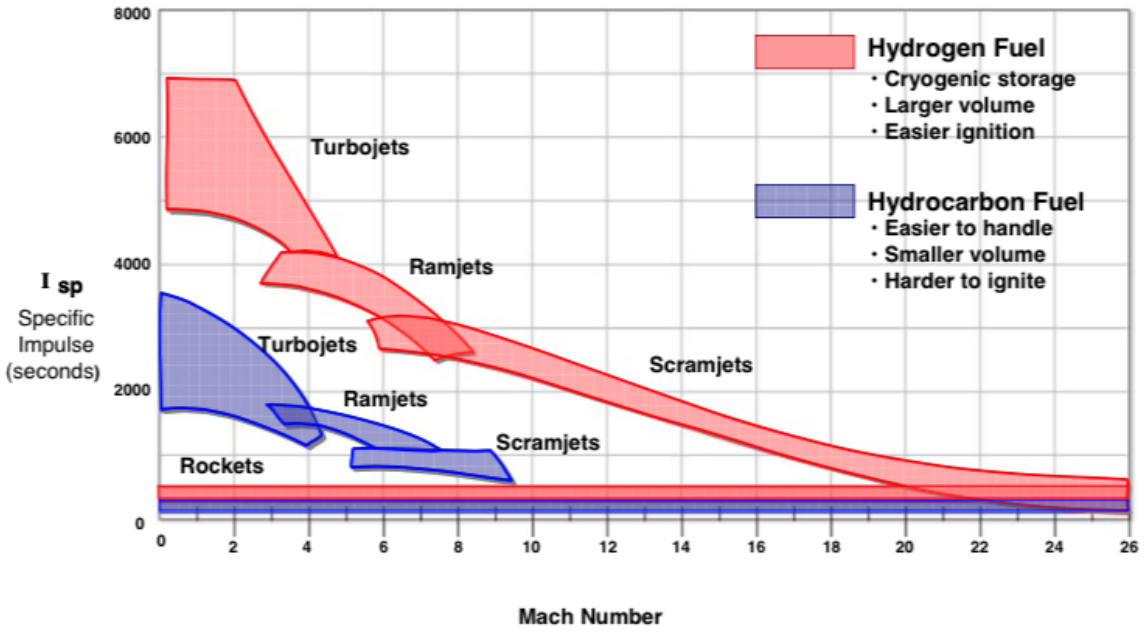

Figure 5: Comparison of engine and fuel performances to highlight the advantages of hypersonic scramjet propulsion [7, 268].

CHAPTER 2

CASE STUDY: AIR-BREATHING HYPERSONIC VEHICLES

2.1 Introduction

Since the 1960s, the United States has possessed operational hypersonic systems in the form of intercontinental ballistic missiles (ICBMs), launch vehicles, and reentry vehicles [1]. This chapter addresses another type of hypersonic system: the sustained-flight of hypersonic systems characterized by air-breathing hypersonic propulsion systems. The primary focus here is to identify what are the current limiting factors through a survey of the current state of the art.

2.2 Current Gaps, Limitations, and Obstacles in Hypersonics

Over the years, there has been much confusion in ascertaining what are the true barriers impeding the development of hypersonic technologies, and some of these issues remain as relevant today as they were nearly five decades ago. Periodically, initiatives have been established to identify the critical barriers that confront engineers in industry, academia, and government. The idea here is that, once issues are identified, effective strategies can then be proposed to help to overcome these challenges in a systematic fashion. Examples include the National Aerospace Initiative (NAI) Technology Development Approach [238] and the USAF Hypersonic Scientific Advisory Boards [1] and NASA Hypersonic Vehicle Roadmaps and Activities [176, 190, 265].

Gaps, obstacles, and technological challenges in hypersonic analysis are numerous and an abundant amount of literature exists, which can broadly be categorized as follows:

1. **Theoretical**

   - **Aerodynamics** $\sim$ the need to operate in several flight regimes can lead to unforeseen aerodynamic conditions
   - **Propulsion** $\sim$ similar to aerodynamics, the disparities among ABHV flight regimes have no easy propulsion solutions (*e.g.* SR-72 dual turbojet-ram/scramjet engine concept [223, 189])
   - **Materials & Structures** $\sim$ the need for strong, light-weight, heat resistant, and cost effective materials has long been considered one of the most critical in high speed propulsion applications

2. **Modeling and Testing**

   - **Analytical Modeling** $\sim$ interpreting data from experiments or numerical solutions is difficult without an analytical framework [25]
   - **Computational Testing & Numerical Modeling** $\sim$ produce quicker results, but the simulation time can rapidly increase with the complexity at hand
   - **Ground Testing** $\sim$ limitations in flow conditions, scaling, and test durations but sometimes allow verifications in the absence of full scale vehicles
   - **Flight Testing** $\sim$ require the most effort due to complexity and expense but prove to be the most rewarding and validating

3. **Education**

   - A great source of concern today is the attrition in the workforce in addition to a lack of emphasis on high speed aerodynamic in the college classroom.
   - Due to the pressing competition to produce more engineers in less time, numerous graduates are finding themselves ill-prepared to confront the challenges of hypersonic research.

Within these categories, it may be argued that deficiencies in propulsion, configurations, and materials are chiefly responsible for restricting the viability of full-scale hypersonic vehicles [25, 26]. As a result of barriers in propulsion technology, designers are compelled to reduce payloads to a point where new concepts offer no advantages over current or past designs [129]. The most pressing need seems to concern the current state of engineering tools for development and testing of hypersonic technologies – specifically scramjet propulsion [185]. The remainder of this chapter will be devoted to the discussion of the current state of these engineering tools, which involves elaborating on the second classification of the above list: modeling and testing.

Observation: *As a result of limitations in current state of tools for modeling and testing of hypersonic scramjet propulsion technologies, designers are compelled to develop vehicles which offer little to no advantages over current or past designs [34].*

2.3 The State-of-The-Art in Modeling and Testing

Modeling and testing share a unique integrated relationship which provides opportunity for the mutual development of both (see Figures 6 and 7). In the modeling and testing of new aerospace vehicle concepts, this is often an iterative, cyclic process known as spiral development. First, computational models use data gathered from ground and flight testing to calibrate and validate the model. Next, computational testing can be used to verify or disprove an incremental change in the attendant theoretical model. This can then be again implemented in ground test facilities, such as wind tunnels, requiring changes to physical models multiple times. Also, flight data can be used to find trends in parameters, characteristics, and/or data to assist future ground tests and vice-versa. Often times, this is a process that can become both expensive and time consuming.

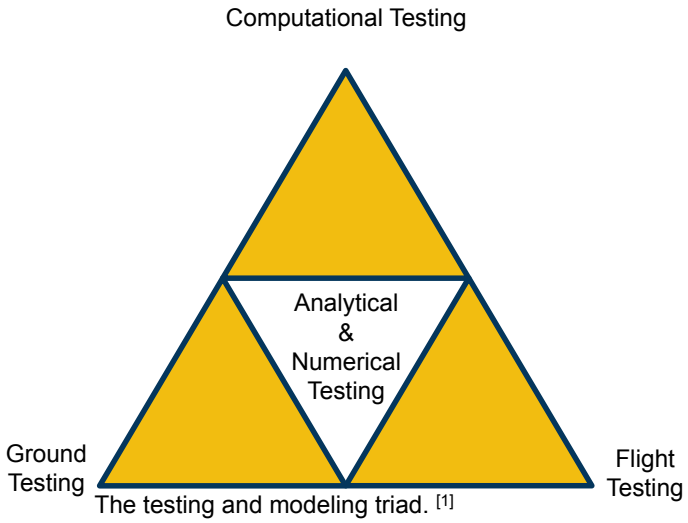

Figure 6: The testing and modeling triad, showing the integrated and coupled relationship that the three forms of testing share with modeling [25].

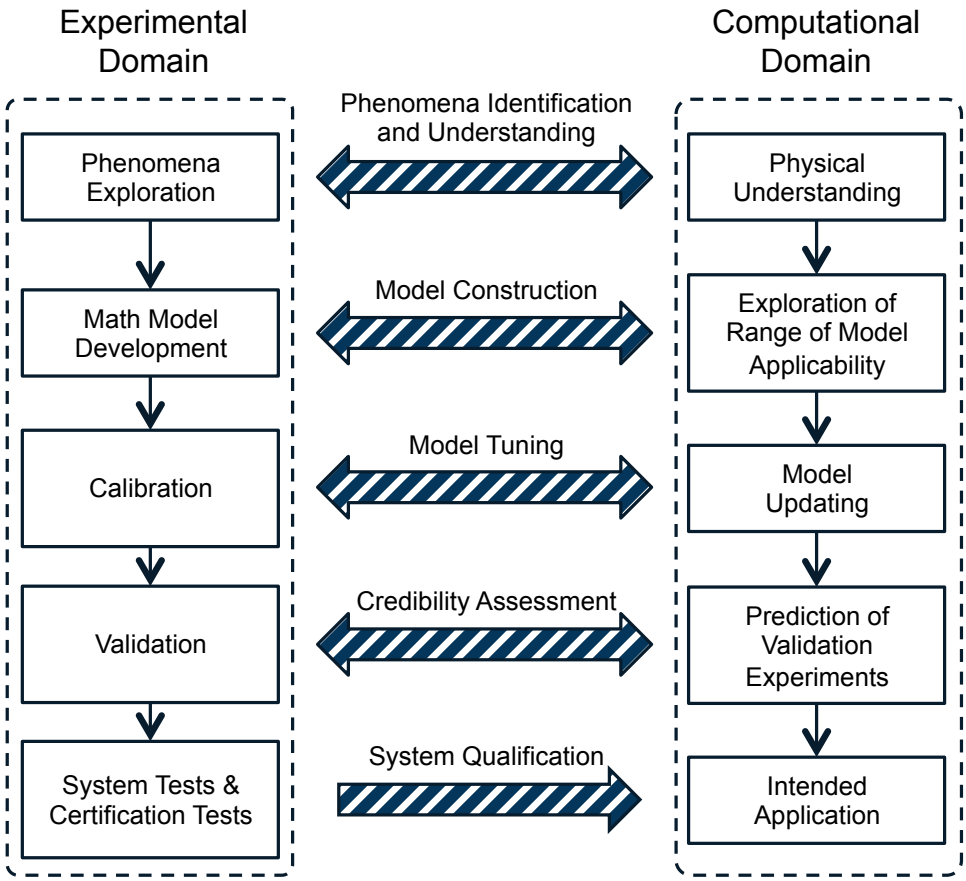

Figure 7: Interaction of Various Experimental and Computational Activities [26].

2.3.1 Computational Analysis and Design

Computational modeling of hypersonic phenomena is a formidable challenge and an active area of research. These models are often extremely complicated and require formidable efforts by subject matter experts with detailed knowledge of hypersonic flow conditions. To properly model hypersonic flows, the level of required fidelity is dictated by the influence that a particular phenomenon has on the overall vehicle performance, which is often significant. As an example, Figure 8 shows the results of one of the largest computational fluid dynamics simulations ever conducted, requiring over 190,000 parallel processors and four consecutive days of computation time.

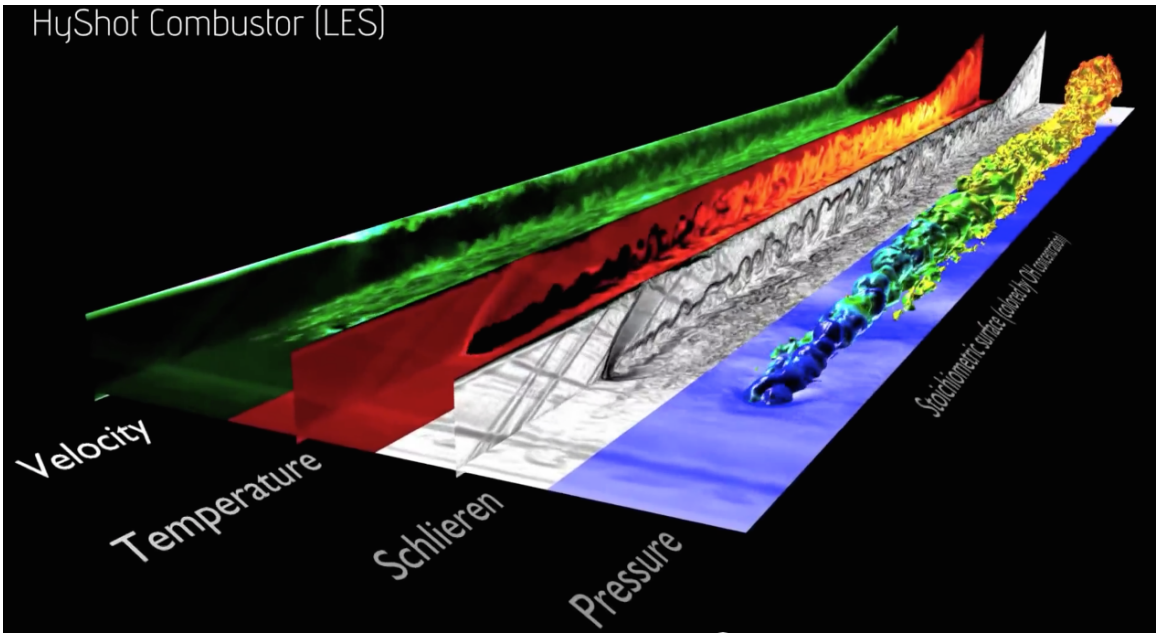

Figure 8: Example of optimized ABHV geometry using CFD to model flow physics [47].

Hypersonic vehicles are, by necessity, highly integrated flying machines, which are subject to inherently high uncertainties in both performance and economics [47]. Combined, these characteristics render conventional practices (*e.g.* employing a single-discipline, point-design approach) to be inadequate for developing hypersonic

vehicles. As advanced physics-based analysis algorithms enable increasingly sophisticated design tools and computational speed continues to grow exponentially, systems will continue to be designed in an ever more integrated fashion to wring the most out of robustness, performance, and economics [47]. As an illustration of the required capability that a physics environment must model, Figure 9 shows results of a CFD analysis, where key phenomena in propulsion-airframe integration are highlighted.

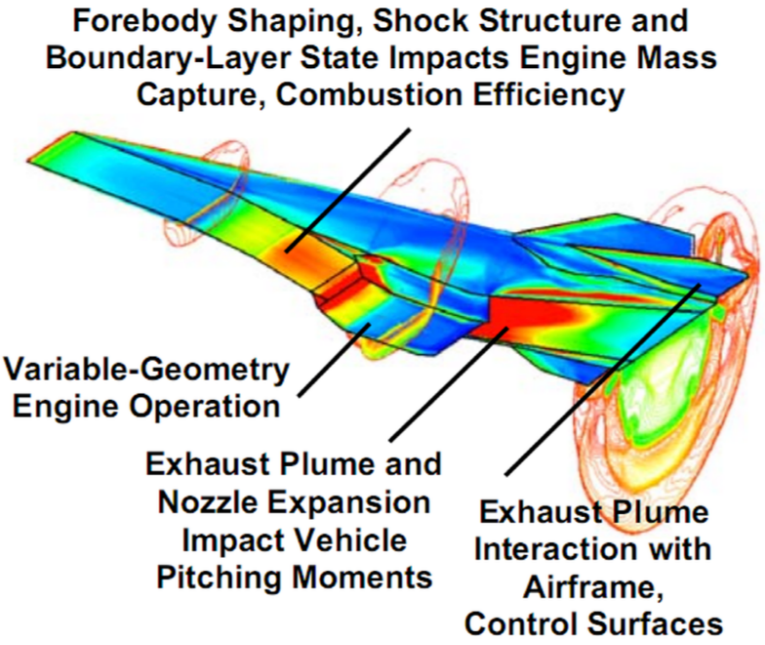

Figure 9: Example of optimized ABHV geometry using CFD to model flow physics [47].

For hypersonic systems in particular, adequate performance and economic viability is unlikely without first developing and using improved **integrated design methods**, which can efficiently leverage the physics-based environment to perform parametric design. In fact, hypersonic vehicles are representative of systems that require this integrated design approach to overcome the large set of design requirements that are demanding and sometimes competing. To this effect, several enabling integrated design system technologies have been identified as necessary [47, 48, 194]:

1. A parametric geometry generation system

2. Automation in data transfer between analysis tools and execution of high-fidelity computational analysis

3. Multidisciplinary design optimization techniques

4. Probabilistic tools enabling system level risk assessment and mitigation, and uncertainty-based optimization

5. Collaborative/distributed/grid computing

6. Development, manufacturing, operations, and campaign modeling and simulation to quantify system effectiveness

7. Response surface methodology and other surrogate modeling construction techniques

8. Design of Experiments to enable the construction of surrogate models

As opposed to conventional aircraft design, the optimization of air-breathing hypersonic vehicles for performance relies upon multidisciplinary physics-based models where fidelity and complexity are extreme. This results in intricate disciplinary coupling within the physics-based environment. Figure 11 illustrates the difference between computational, physics-based environments for both conventional and highly integrated vehicles, where the highly integrated environment, by definition, implies that the inputs and outputs of every discipline depend on each other.

To make matters even more taxing for the physics environment, these vehicles are expected to model an expansive region of operating conditions. Figures 12-14 delineate the various types of hypersonic vehicles at mission specific altitudes and speeds and the various aerodynamic phenomena that occur at the corresponding altitude and flight speeds.

In summary, these various sources of complexity (*e.g.* performance and economic uncertainty, highly integrated systems, multidisciplinary coupling, expansive region

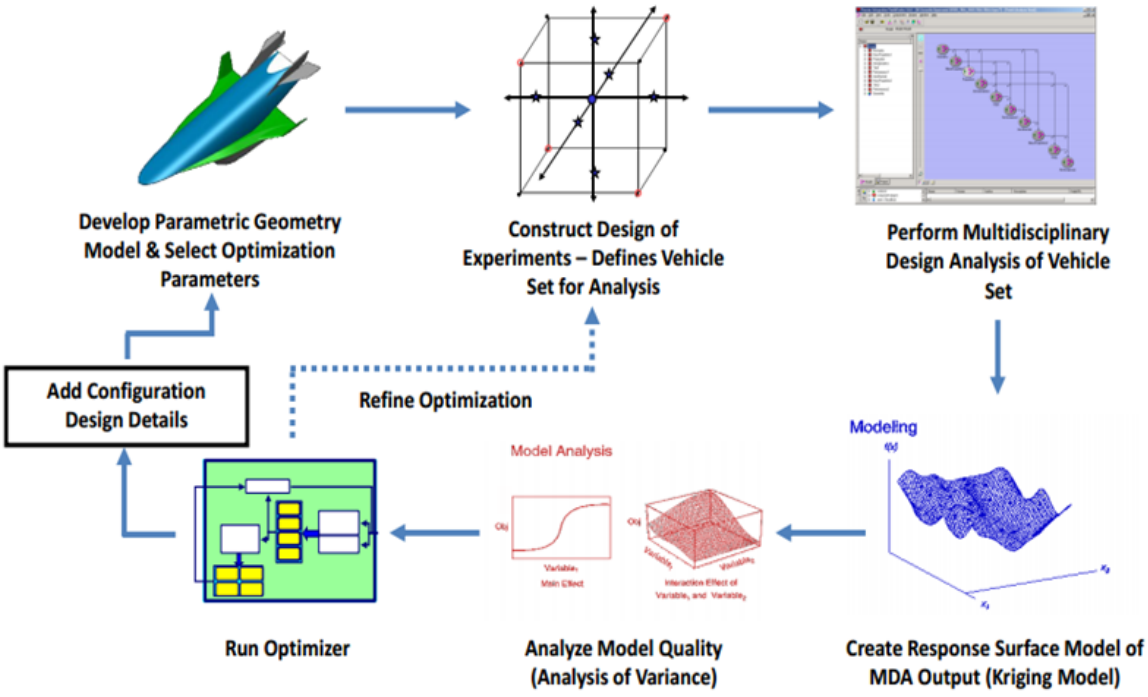

Figure 10: An example of a parametric integrated design environment for computational design of air-breathing hypersonic vehicles [47].

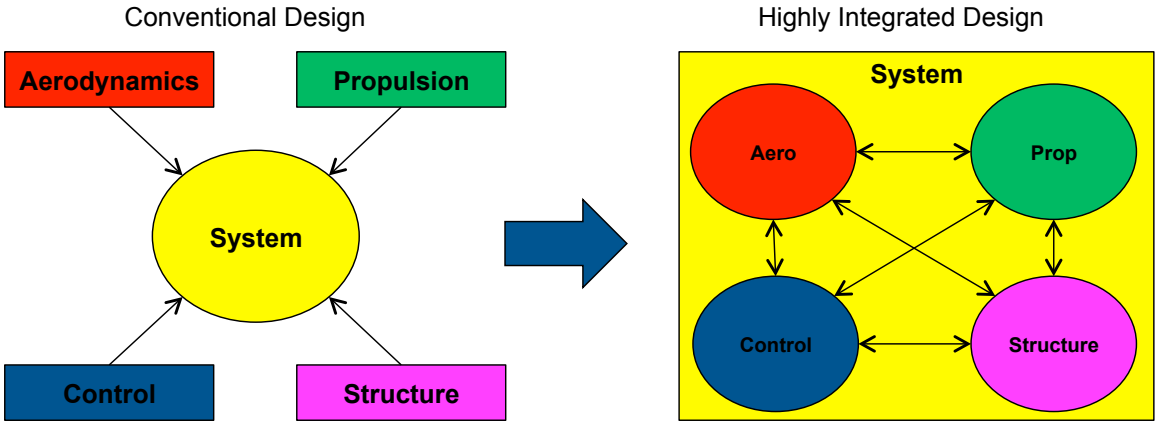

Figure 11: Complexity of hypersonic physics due to an extreme level of disciplinary coupling.

of operation, and integrated design methods) suggest that a potentially large team of subject matter experts are required to assemble a complex code, which will require a significant amount of time and effort to construct, test, and validate. The observation below formally states this fact.

Observation: *Development of a physics-based PIE for HVD that incorporates probabilistic analysis is necessary, but it is a difficult and time consuming task that relies on subject matter experts and requires extensive verification and validation [47, 48].*

2.3.2 Hypersonic Ground Testing

Currently the ability to understand hypersonic phenomenon using computational modeling is limited, due to the inability of physical testing to establish a suitable level of confidence through model validation and calibration exercises. Despite visible progress that has been made in ground facilities and flight testing strategies, many difficulties still linger today. Thus, to speak of limitations in HVD is currently synonymous with limitations in HVT. The following observation summarizes this fact, which is a primary inhibitor to developing operational ABHVs.

Observation: *Before a physics-based M&S environment can be used for HVD, an extensive verification and validation exercise must be conducted to establish confidence in the predictive ability of the environments to accurately mimic physical reality.*

The ability to test lab-scale models in a controlled environment is a standard approach to how verification and validation of aerospace vehicles has been historically conducted [25], where properly designed ground tests significantly contribute

Speed Regimes	Flow Properties
Subsonic (M < 0.8)	Ideal Gas
Transonic (0.8 < M < 1.2)	Weak Shock Waves Ideal Gas
Supersonic (1.2 < M < 5.0)	Shock Waves Calorically Imperfect Gas
Hypersonic (M > 5.0)	Thin, Hot Shock Layers Thermally Imperfect Gas Chemically Reacting Flow

Flow Regimes (Knudsen Number, K_n)

- Continuum Flow ($\sqrt{Re/M}>100$ and $K_n<0.01$)
- Slip Flow ($1<\sqrt{Re/M}<100$ and $0.01<K_n<0.1$)
- Transitional Flow ($0.1<\sqrt{Re/M}<1$ and $1<K_n<10$)
- Free Molecular Flow ($\sqrt{Re/M}<0.1$ and $K_n>10$)

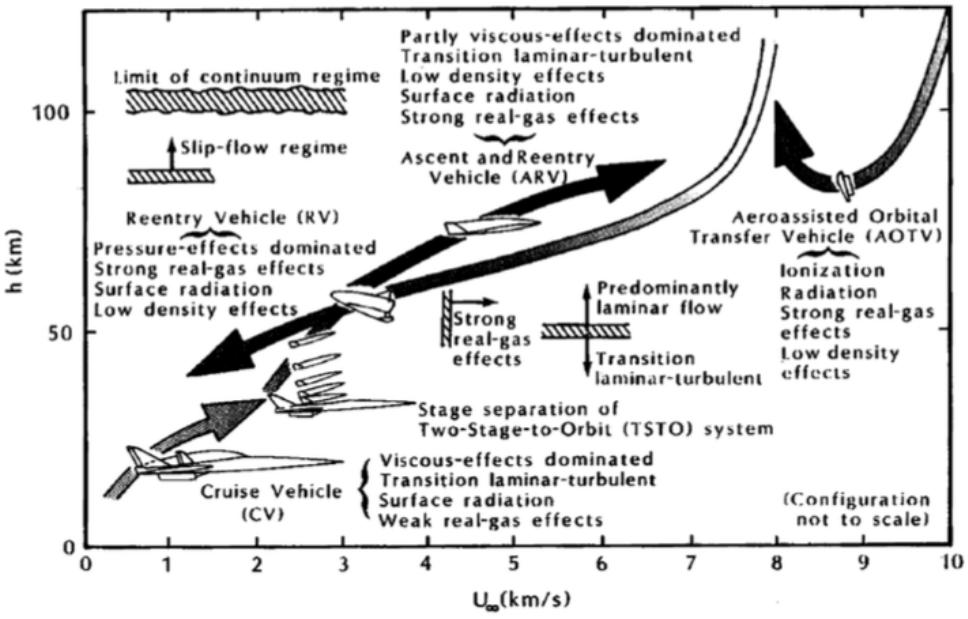

Figure 12: Complexity of hypersonic physics due to an extreme range of gas dynamic operating conditions in flight [47].

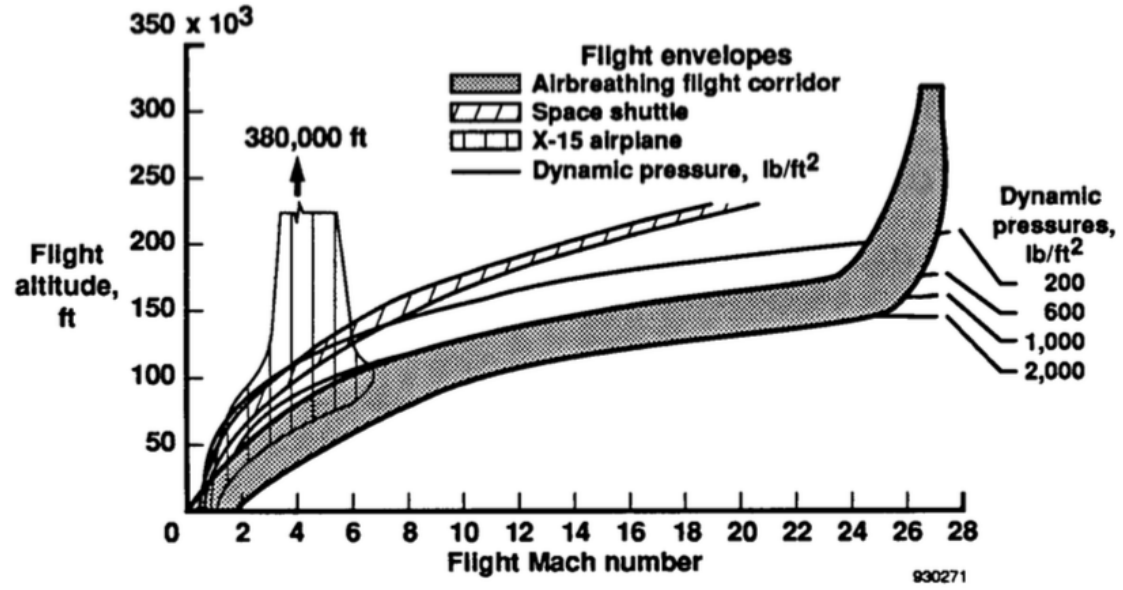

Figure 13: Comparison of air-breathing and non-air-breathing hypersonic corridors [137].

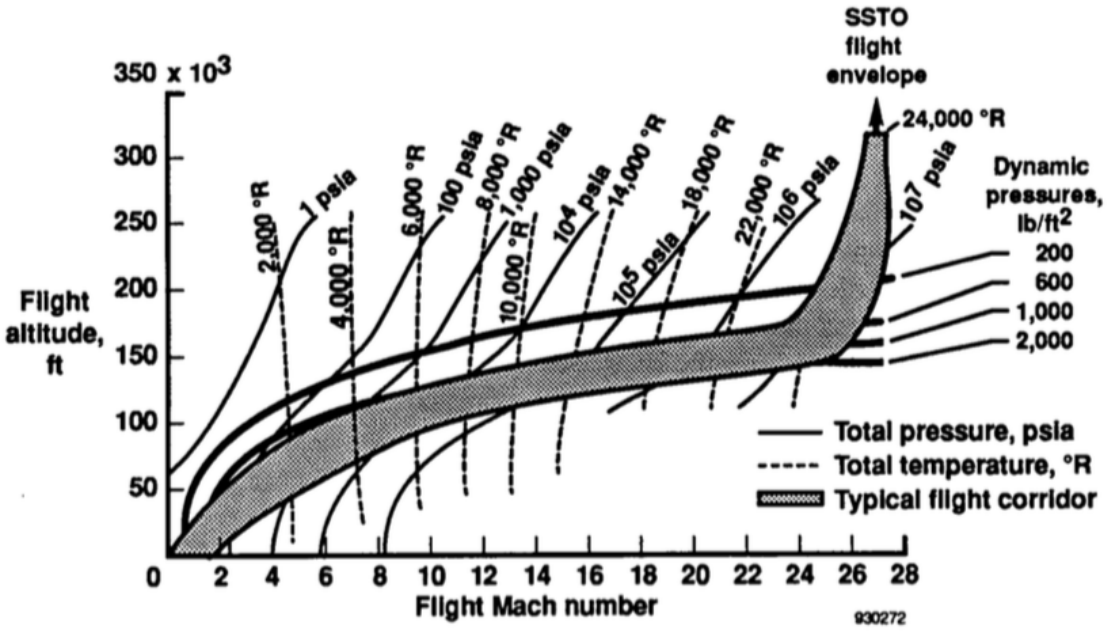

Figure 14: Typical air-breathing hypersonic corridor [137].

to successful vehicle design and development. Often, these tests provide the most dependable means of isolating and addressing technical problems or issues in a design through component tests or controlled experimental conditions. The results usually form the genesis of (i) databases and design tools, (ii) measurement and analysis techniques, and (iii) system design validations which lead to developing the integrated flight vehicle. Ground testing therefore remains a high priority for HVT, especially in the case of ABHVs.

The current state of hypersonic ground test facilities, however, have not been able to accommodate these demands, due to the inability to sufficiently replicate hypersonic flow conditions. Here, the term *replication* has a specific meaning in context to qualitatively describing the quality of the test environment, along with the terms *simulation* and *duplication* which are described below [183].

1. **Def.** (*Simulation*) $\sim$ only recreates a few important physical phenomena
2. **Def.** (*Replication*) $\sim$ recreates temperature, pressure, velocity, and chemical composition
3. **Def.** (*Duplication*) $\sim$ fully mimics all aspects of actual flight

Generally speaking ground testing has been used to assist numerical and flight test development by using *partial-simulation* as a stepping stone to reach the ultimate goal of fully operational vehicle testing, where *duplication* of flight conditions can then be considered [183]. In traditional applications, such as aerodynamic body testing for subsonic, supersonic, and even some hypersonic vehicles, ground testing has an established track record of being a cornerstone in the development of both computational models and large-scale flight testing; however, in the case of hypersonic scramjet technology a *partial simulation* is not satisfactory and *replication* to near *duplication* of flight conditions is required over an expansive range of operating

conditions. Figure 15 shows some examples of limited scramjet testing to the degree of *simulation* and *partial-replication* of the actual operating conditions, where sustained, power-on scramjet testing has not yet been acquired. Until this capability is acquired, computational models cannot be used to understand key hypersonic phenomenon with a high degree of confidence.

Observation: *Due to limitations in hypersonic testing, the ability to model and understand key hypersonic phenomena is also limited.*

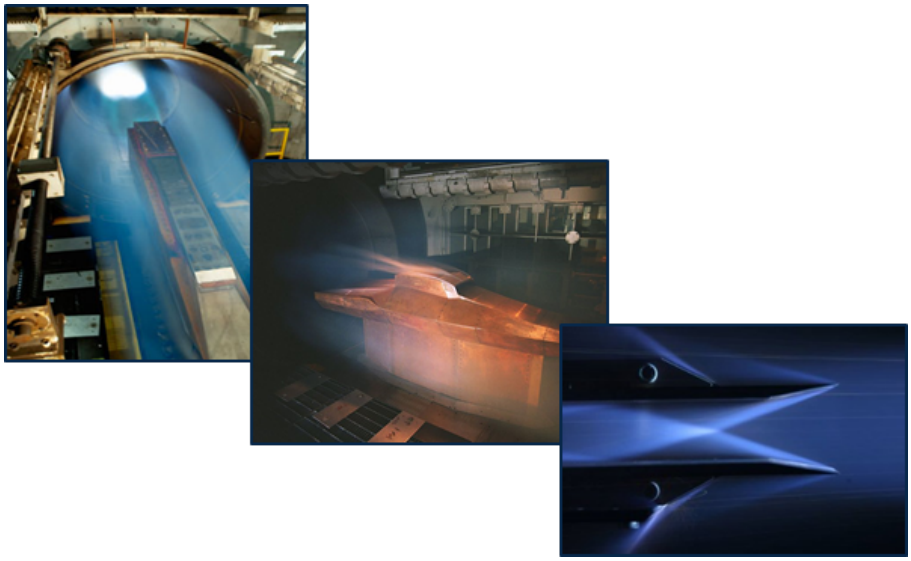

Figure 15: Examples of scramjet testing using ground test facilities: (*left*)–X-51 scramjet testing; (*middle*)–X-43A scramjet testing; (*right*)–arc-heated hypersonic inlet flow test at Mach 6.

The fundamental challenge that hypersonic ground facilities must overcome is the ability to accommodate testing over the expansive region of operating conditions that are experience in flight. To cover the expansive region of operation and represent the

various flow phenomenon and their features, many ground test facilities are needed, where no one facility can duplicate, replicate, or simulate the vast range of gas dynamics, as was the case in the Mercury, Apollo and Space Shuttle programs. To accomplish this, many different types of facilities have been developed, including: arc tunnels, shock tunnels, gun tunnels, and wind tunnels, all of which posses different strengths and span different regions of the hypersonic operating conditions. Figure 16 delineates the various types of hypersonic ground test facilities by comparing their respective coverage of the mission specific altitudes and speeds. It is clear from this figure that the ABHV flight corridor is not well spanned by existing ground testing capabilities, as most of these facilities were originally designed applications such as stable hypersonic reentry.

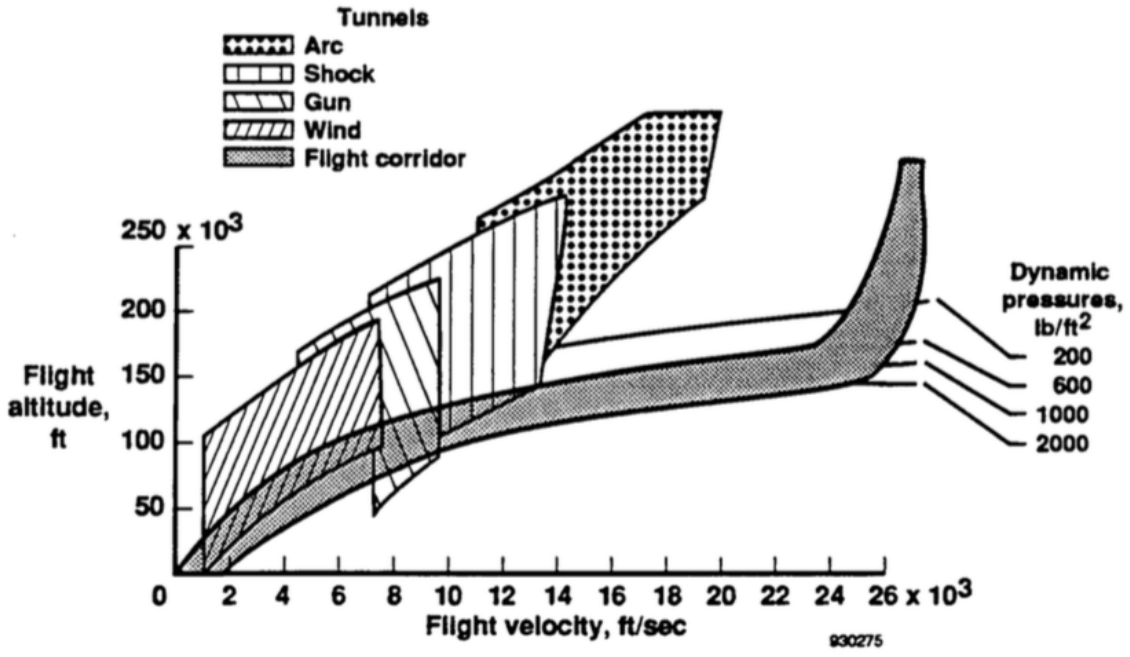

Figure 16: Existing ground test capabilities for hypersonic development [137].

Some of major inhibitors towards the advancement of hypersonic scramjets include the inability to test the following physical phenomena: rarefied flows, non-equilibrium flows, and boundary layer transition effects [183, 241, 247]. This can be attributed

to practical hardware problems, such as: (i) inaccurate instrumentation to measure subscale models, (ii) the lack of incorporating or simulating critical systems, and (iii) the lack of properly represented system integration, which arise because of facility volume and other operational limitations. Other facility limitations also arise, for example, brief test duration (milliseconds in shock tunnels when seconds are needed), as shown in Figure 17, and limited Mach number and altitude ranges (a maximum of Mach 8 for long-duration wind tunnels), as shown in Figure 16. Often real air cannot be simulated because of the need to test with other gases or to combustion-heat air for enthalpy simulation. Heating, in turn, results in vitiated air (*i.e.* air containing combustion products or contaminating particulates), or the chemical composition is otherwise changed because of oxygen depletion and chemical make-up. Other test problems include accurate Reynolds number simulation; pressure and temperature, or both, (enthalpy) simulation at high Mach number and dynamic pressure conditions; tunnel interference problems; and engine exhaust effects simulation.

In light of the current situation, it has been concluded that ground testing facilities cannot be fully relied upon as the dependable work-horse for technology development that it has historically proven to be. As a result, both computational models and ground testing facilities are reliant on hypersonic flight testing data for validation and calibration [25, 137, 241].

Observation: *In the light of current limitations, hypersonic ground testing facilities cannot be used as a work-horse for development of a hypersonic database but are instead reliant on hypersonic flight testing data for validation and calibration.*

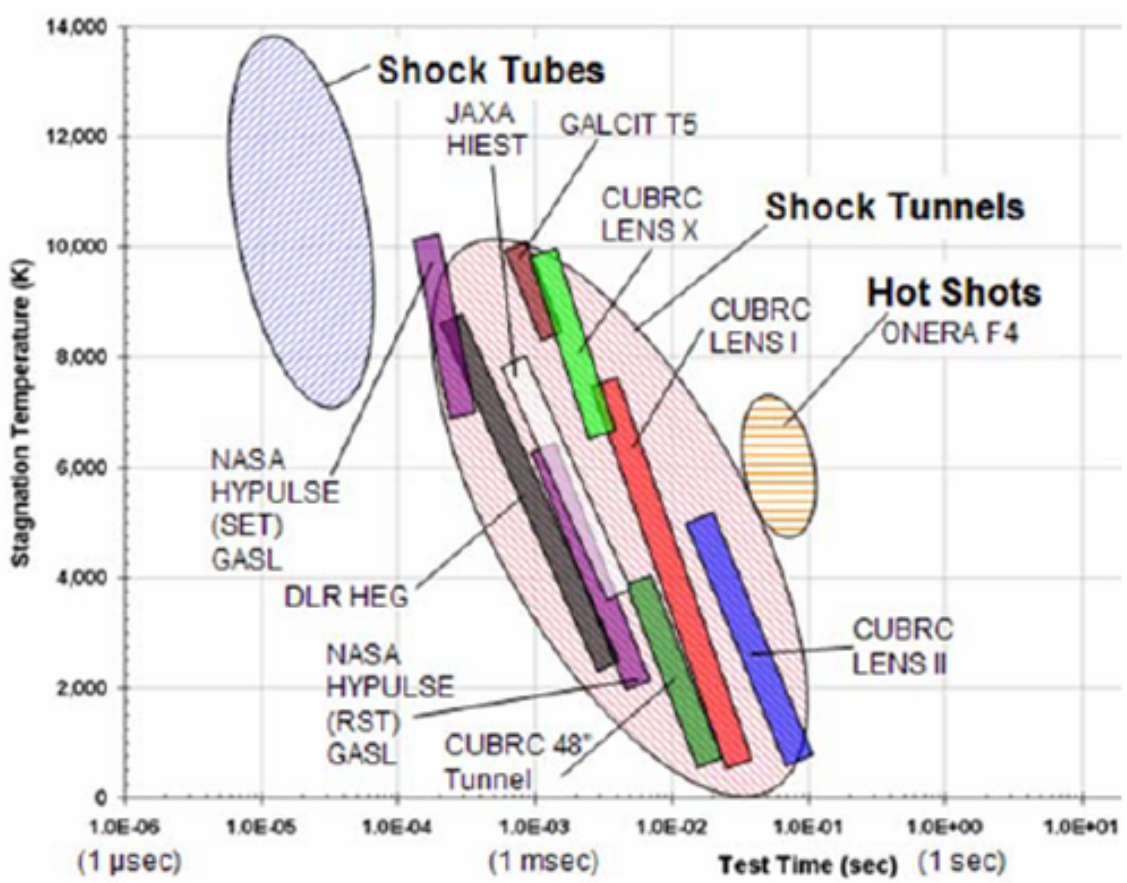

Figure 17: The transient performance of hypersonic facilities for high-enthalpy scramjet engine testing purposes is very limiting, often on the order of milliseconds [183].

2.3.3 Hypersonic Flight Testing

The current deficiencies of computational modeling and ground testing facilities place increasing demand and pressure on flight experiments to advance the hypersonic database and support technological development [25, 47, 87, 275]. Historically speaking, flight testing has proven to be the ultimate validation of a design or technology development process, providing the highest possible fidelity data for a potentially unlimited range of flight conditions (since the vehicle is tested in its intended operational environment) [25, 137]. Because flight testing and evaluation often requires the most effort, it is traditionally undertaken during the final stages of a programmatic

RDT&E timeline, which is shown below in Figure 18 [46, 144, 160]. For fixed-winged aircraft, flight testing has a well established role, which Kimberlin [163] categorizes into the following types of tests.

- **Research Tests** – intended to push the frontiers of knowledge
- **Product Development Tests** – intended to determine characteristics of the new product and solve problems with the product
- **Mission Assessment and Reliability Tests** – intended to determine if the new vehicle will accomplish its intended missions
- **Certification Tests** – intended to demonstrate compliance with established requirement and regulation for safety of flight

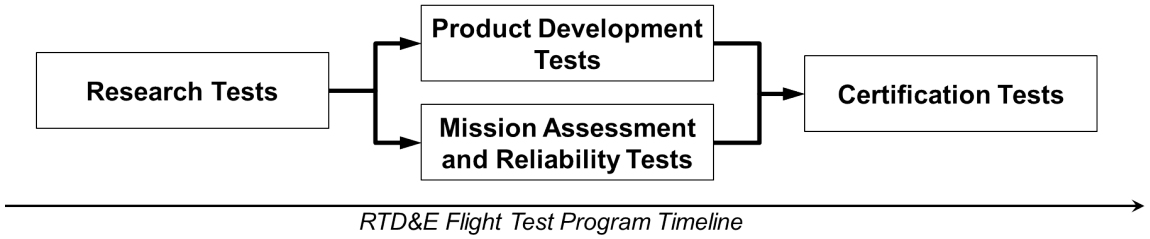

Figure 18: An illustration of the RDT&E sequential timeline for various types of flight testing that are conducted near the end of a vehicle development program.

Applying the classification of Kimberlin to the case of HFT, there has been significant focus on a combination of research, mission assessment, and reliability tests. The first, and perhaps the most successful, example of this is the X-15 program [25]. The X-15 was a rocket propelled hypersonic testbed, which flew 199 missions by 12 pilots between 1959 and 1968. In 1967 the first scramjet engine concept was tested on the X-15, called the Hypersonic Research Engine (HRE); however, due to unexpected heating problems caused by shock waves, the engine was badly damaged during testing and very little data was recovered. Two recent examples which conducted flight

testing of operational hypersonic scramjet vehicles include the X-43A and X-51A programs [229, 230]. Both of these programs focused on operational demonstration of an airframe-integrated, scramjet-powered vehicle at selected test conditions. The X-43A falls closer to the category of a mission assessment test, as the focus was mainly on scramjet proof-of-concept. To date, the X-43A is the fastest air-breathing aircraft on record at approximately 7,000 miles per hour (11,000 km/h or Mach 9.68) [270].

Figure 19: Images of three of the most successful hypersonic flight test programs in history: (*left*) the North American X-15; (*middle*) – the NASA Hyper-X Plane (X-43A); (*right*) – the USAF Waverider (X-51).

Following the success of the X-43A, the X-51A (Waverider) program focused on scramjet reliability issues and the use of hydrocarbon fuels for sustained scramjet-powered flight [133]. On its fourth and final attempt, the X-51 finally performed its first fully successful flight test, setting the current standing record for the longest sustained scramjet powered flight with 210 seconds of powered flight [222]. Many of the difficulties and failures encountered in this program were attributed to a hypersonic phenomenon known as combustion unstarting. While these two programs were able to successfully prove the viability of scramjets for sustained hypersonic flight, only a handful of successful flight tests were produced.

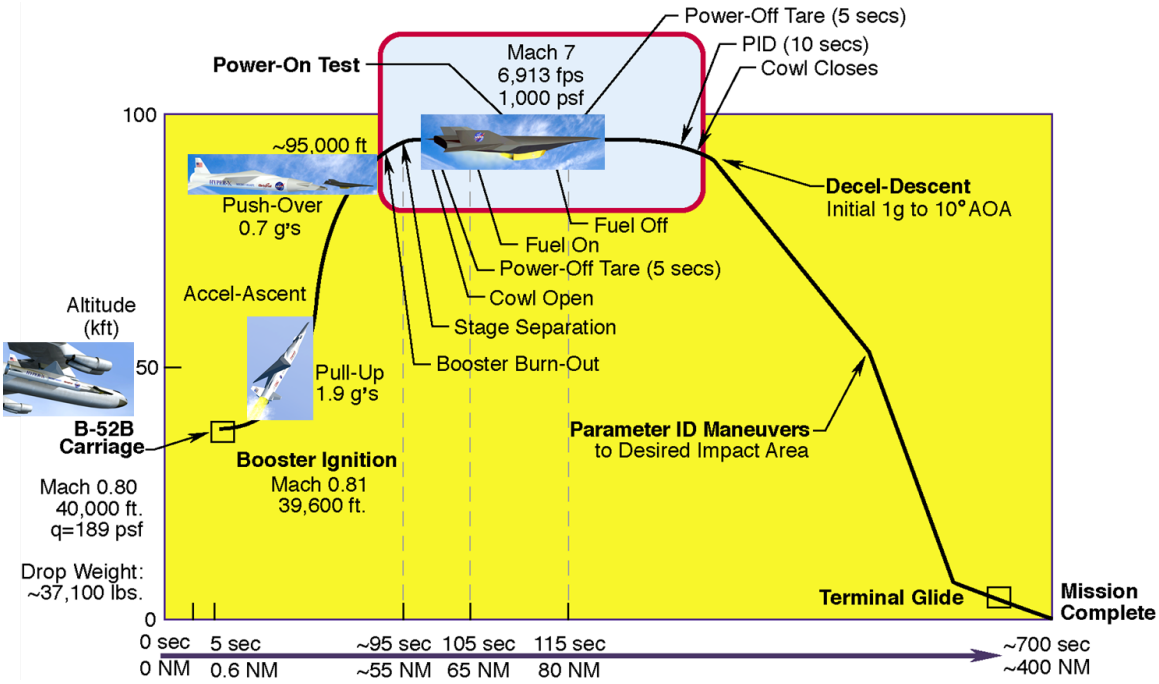

Figure 20: A notional X-43A mission profile to test scramjet operation at +Mach 7 for approximately 10 seconds [188].

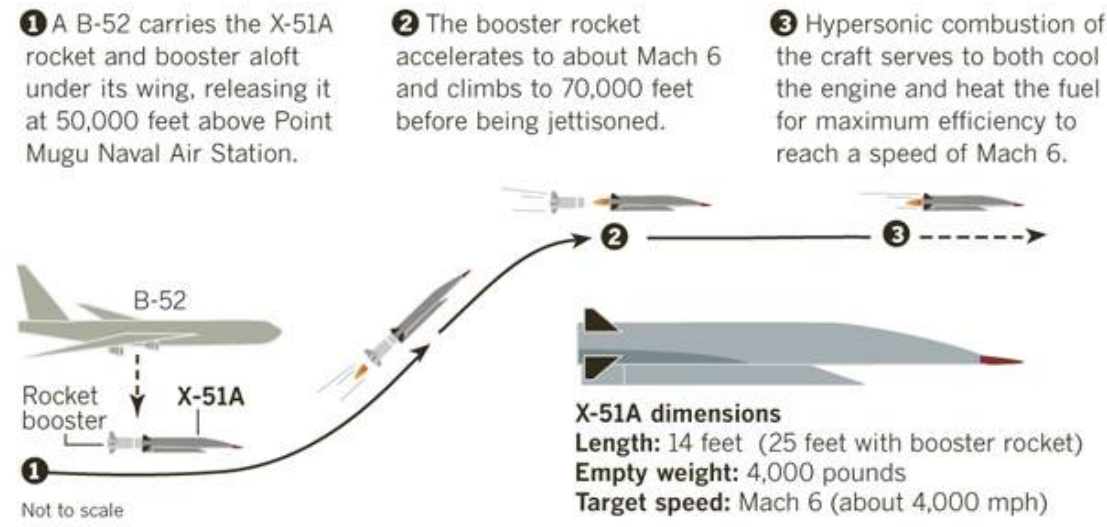

Figure 21: A simple description of the X-51A mission to test scramjet operation at near Mach 6 for approximately 4 minutes [136].

In contrast to ground testing, which is performed in a controlled setting, flight testing is performed in an environment where physical understanding of the operating conditions is still significantly limited and littered with uncertainty. This is the fundamental challenge currently facing hypersonic flight testing: to fill the role of traditional ground testing by providing a means to generate data towards the advancement of the hypersonic database and the maturation of relevant hypersonic technologies. This is indeed a difficult challenge, as HFT programs are often characterized as large-scale efforts with extreme complexity, substantial costs, and significant uncertainty. These types of programs are often focused on the reduction of programmatic risk, often resulting in highly conservative, risk-averse flight experiments which provide limited opportunity for scientific advancement [87, 179].

Observation: *Due to excessive complexity, high costs, and long development times, hypersonic flight experiments are often conservative and risk-averse endeavors, which yield little gain in knowledge and do not significantly contribute to the expansion of the hypersonic database [87, 109].*

In an attempt to mitigate these issues, the Hypersonic International Flight Research and Experimentation (HIFiRE) program has recently emerged [87, 179]. HIFiRE is a joint effort between the United States ARFL and the Australian Defense Science and Technology Organization (DSTO) with the overall objective of gathering fundamental scientific and engineering data on the physics and technologies critical enabling to future operational hypersonic flight. Using relatively low cost sounding rockets to conduct a diverse array of hypersonic flight experiments, the HIFiRE program is attempting to reduce the programmatic risk, and therefore allowing for more

aggressive, risk-tolerant experimental approaches, such as performing as many experiments on a single fight test as possible. Figure 22 and Table 1 summarize key details of the HIFiRE program, which has employed a diverse variety of approaches including both ballistic and suppressed trajectories; captive carry and free flight research vehicles; and unpowered and air-breathing scramjet powered research vehicles [87].

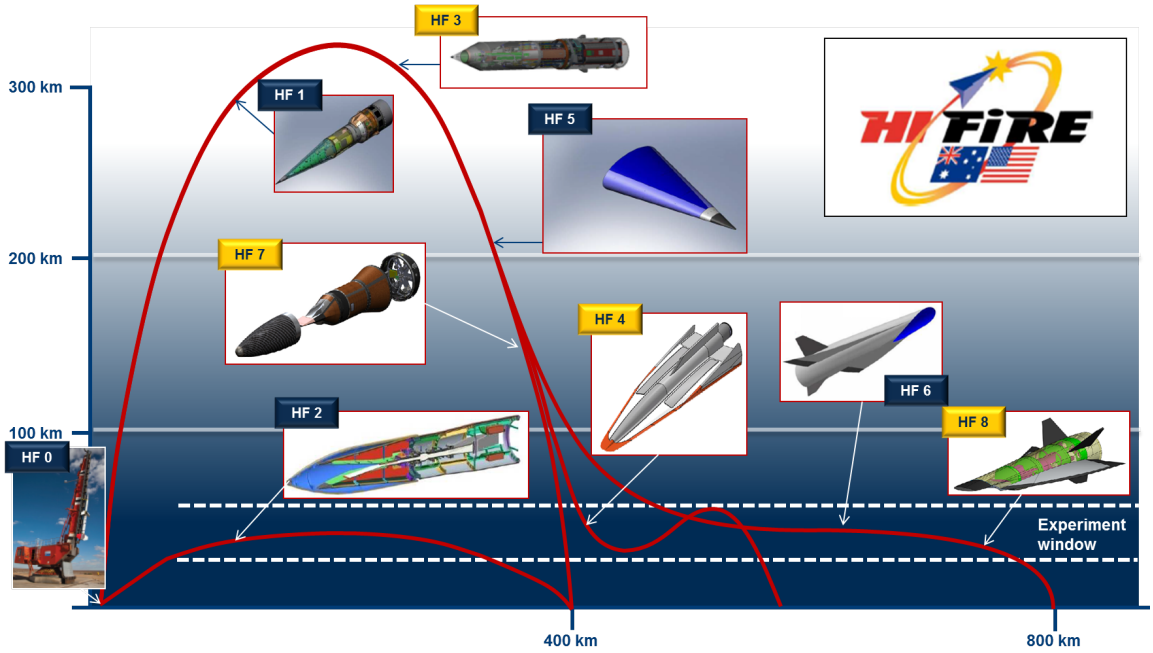

Figure 22: The HIFiRE represents a paradigm shift in hypersonic flight testing, where diverse vehicles, key technologies, and various trajectories are employed to grow the hypersonic database.

The HIFiRE program has made significant strides toward enabling a more practical, cost-effective approach to HFT. As seen in Table 2, the total program cost is approximately one-fifth of the cost of the Hyper-X and Waverider programs while still conducting two-to-three times as many flight tests. Indeed, the HIFiRE program has made sizeable contributions towards the expansion of the hypersonic database, which can readily be seen in the literature [102, 151, 155, 179, 255]; however, this program is not immune to setbacks, as it is currently +3 years behind schedule.

As efforts focus more on database expansion and research-oriented flight tests,

Table 1: Summary of the HIFiRE flight test manifest, focusing on multi-experiment, research-focused tests over a diverse array of key disciplinary phenomenon and technologies [87].

TECHNOLOGY DISCIPLINE	Flight Project								
	HF 0^{AUS}	HF 1^{US}	HF 2^{US}	HF 3^{AUS}	HF 4^{AUS}	HF 5^{US}	HF 6^{US}	HF 7^{AUS}	HF 8^{AUS}
AEROSCIENCES		BLT, SBLI			Flight Mechanics	BLT	Aerodynamic Uncertainties		Sustained Level Flight
PROPULSION			MCSJ Operation @ Ma 8	SJ Fueling / Combustion				SJ Thrust Measurement	SJ Thrust Measurement
STABILITY AND CONTROL			Controlled Depressed Flight		Controlled Suppressed Flight		IAG&C		Controlled Flight
MATERIALS AND STRUCTURES		Materials Survivability	Materials Survivability		Materials Survivability	Materials Survivability	Materials Survivability		
SENSORS		GPS/AO/MC				GPS/AO/MC			
Flight Dynamics & Trajectories	Evaluate ACS and Subsystems				Re-entry + pull out				
INSTRUMENTATION & MEASUREMENTS		TDLAS	OMC	OMC					
PAYLOAD CONFIGURATION	Ogive	Cone Cylinder	2D HC Scramjet	Cruiser H2 Scramjet	Lifting Body	Elliptical Cone	Waverider Cruiser	Inward Turngin CH4 Scramjet Engine	TBD
TRAJECTORY	Ballistic / Captive Carry	Ballistic / Captive Carry	Suppressed / Captive Carry	Ballistic / Captive Carry	Ballistic / Semi-suppressed / Re-entry / Free Flight	Ballistic / Captive Carry	Suppressed / Free Flight	Ballistic / Semi-suppressed / Re-entry / Free Flight	Ballistic / Semi-suppressed / Re-entry / Free Flight

Table 2: Comparisons of the Hyper-X, Waverider, and HIFiRE programs [13, 91, 231].

Program	Total Program Cost	Number of Tests	Program Length
Hyper-X	\$230M	3	2001 – 2004
Waverider	\$250M-\$300M	4	2010 – 2013
HIFiRE	\$54M	9	2009 – current

demand has increased for ways to squeeze every last drop of useful information out of a single experiment. This has led to efforts, such as: (i) the design of more sensitive and robust instrumentation packages, (ii) advanced experimental design methods with uncertainty quantification, (iii) strategies to further reduce developmental costs and effort, and (iv) identification of future key validation cases for modeling hypersonic configurations and technologies, just to name a few. In the case of instrumentation systems and data acquisition, significant improvements are still needed due to increasing demands being placed on hypersonic flight instrumentation packages to be compact, sensitive, yet capable of operating in an environment that has extreme pressures, severe temperatures, and is highly-vibrational [43, 137]. For example, the survivability of transducers in thermochemical environments often requires the use of thermal coolant systems. As a result, instrumentation packages have become increasingly sophisticated, where the integration of systems with hundreds of sensors into test vehicles further exacerbates the problem of vehicle complexity. For example, strategies for the optimal placement of sensor arrays are being increasingly considered for detailed 3-D flow field reconstruction using experimental data [92, 151]. Figures 23 and 24, show a portion of the HIFiRE 2 flight test vehicle instrumentation suite which was used to measure flow field properties within the isolator/combustor portion of the scramjet engine.

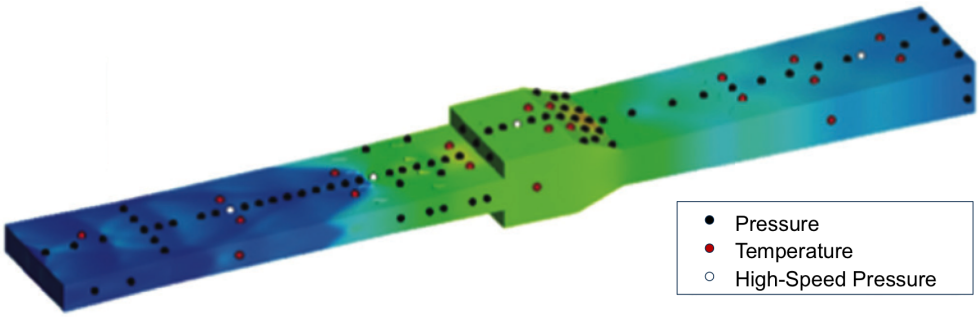

Figure 23: Results of CFD sensitivity analysis for determination of optimal sensor placement within the isolator/combustor of the HIFiRE 2 scramjet engine [151].

Figure 24: A portion of the HIFiRE 2 prototype instrumentation system for the isolator/combustor [151].

2.4 Summary and Conclusions

In summary, there are still lingering issues within the area of hypersonics testing due to the needs of computational models for validation and the currents limitations of ground testing. Table 3 provides a summary of the current state of hypersonic modeling and testing, highlighting strengths and weaknesses of each. In light of the current situation, hypersonic flight testing has assumed a dominant role in growing the hypersonic database and jumpstarting the capabilities of the other two. To this end, there is currently a high demand to conduct research-focused flight experiments which yield high amounts of information in an uncertain environment. These are conflicting requirements, as conservative experiments often provide little information and aggressive information experiments often result in failure. This is formally stated in the observation below, which will be addressed further in the next chapter.

Observation: *As flight testing assumes a more dominant role in the expansion of hypersonic database, there is a need to develop experiments that are highly efficient at extracting information, while accounting for the effects of uncertainty and risk [87].*

Table 3: Summary of current strengths and weaknesses of hypersonic modeling and testing capabilities.

Enablers	Pros	Cons
Computational Testing 	▪*Low risk* ▪*Variable fidelity* ▪*Can be used to perform virtual experiments*	▪*Requires testing for validation/calibration* ▪*Can require long development times* ▪*Unforeseen phenomena might not be captured*
Ground Testing 	▪*Less required cost and effort than flight testing* ▪*Less risk than flight testing*	▪*Sparse availability of hypersonic facilities* ▪*Does not sufficiently capture flight conditions (e.g. +M7 scramjet testing)* ▪*Often limited to only transient testing*
Flight Testing 	▪*Highest fidelity data* ▪*Unlimited number of flight conditions*	▪*High uncertainty and risk* ▪*High cost and operational effort*

CHAPTER 3

RESEARCH FOCUS

In the previous chapter, a particular classification of revolutionary-type aerospace vehicles, air-breathing hypersonic SCRAMjets, were discussed. In this case, advancements in knowledge and technology have become increasingly dependent on novel flight testing approaches, due to both the highly-integrated nature of these vehicles and the expansive region of operating conditions. As a result, flight testing has assumed a more dominant role in the expansion of hypersonic database and there is a recognized need to develop flight tests that are highly efficient at extracting information, while still accounting for the effects of uncertainty and risk. This chapter will formally state the intent of this research: to utilize a computational design approach.

3.1 Current Approaches to Flight Test Development

The process of flight test development is usually begun using computational analysis to predict expected experimental outcomes. This pre-test analysis is performed using the very computational tools which are sought to be validated by the experiment itself and ultimately be used for integrated vehicle design. Using these tools various parameters and sub-models are identified, which are suspected of contributing to model inaccuracies and uncertainties. Then testing strategies are developed that are expected to generate experimental data which can be used to refine these models by eliminating sources of uncertainty. The extent to which these sources of uncertainty are eliminated or reduced depends on the information content within the experimental data. Since models only serve as an approximation of physical reality, there is always some level of uncertainty present within a model regardless of the quality and quantity of available experimental data; however, high information experiments enable for the

refinement of models which are more capable of generating predictions both more accurately and over a wider range of operating conditions.

Often times, regardless of the level of up-front effort put forth to identify and mitigate uncertainties in the flight test development process, significant surprises are encountered during testing which were not anticipated. In hypersonics, this has historically been quite a common occurrence. The STS program had mispredicted several aero-thermo-dynamic heating phenomena during early flights. Some of these mispredictions were advantageous, while others where not. Examples include reaction control system jet interaction effects on higher than predicted angles of sideslip during reentry, flow impingement angle-of-attack effects on orbital maneuvering system pod heating, wing leading-edge heating from boundary-layer and shock interactions, and predictions of thermal protection system surface catalysis heating effects on the lower side of the vehicle [137, 147].

The Hyper-X project is a prime example of an involved pre-flight test development effort to test an operational ABHV. The objectives of the Hyper-X flight tests were two-fold: (i) to demonstrate the capability of SCRAMjet technology, and (ii) to estimate stability and control derivatives (*i.e.* aerodynamic coefficients). In essence, objective (ii) is effectively an external wind-tunnel test of an unpowered ABHV. Using the notional mission profile form Figure 20 as a reference, Figures 25-26 show comparisons of the actual measured experimental data to the pre-test analysis predictions during the SCRAMjet operation portion of flight. In addition to the nominal prediction and the measured data, Monte Carlo cases were run prior to the test to quantify the effects of uncertain parameters on the transient response. Figure 25 shows that the uncertainty in the expected performance of the SCRAMjet to generate positive axial acceleration for a sustained period of time was accounted for; however, in Figure 26 it is observed that several portions of the measured inertial angle of attack response drift outside of the expected envelope, representing unexpected behavior.

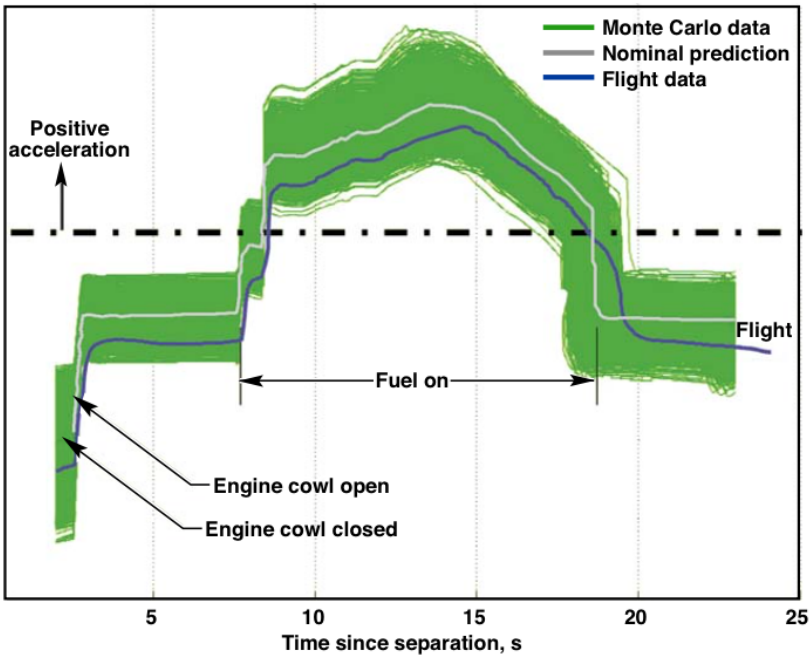

Figure 25: SCRAMjet operation: observation of positive axial acceleration.

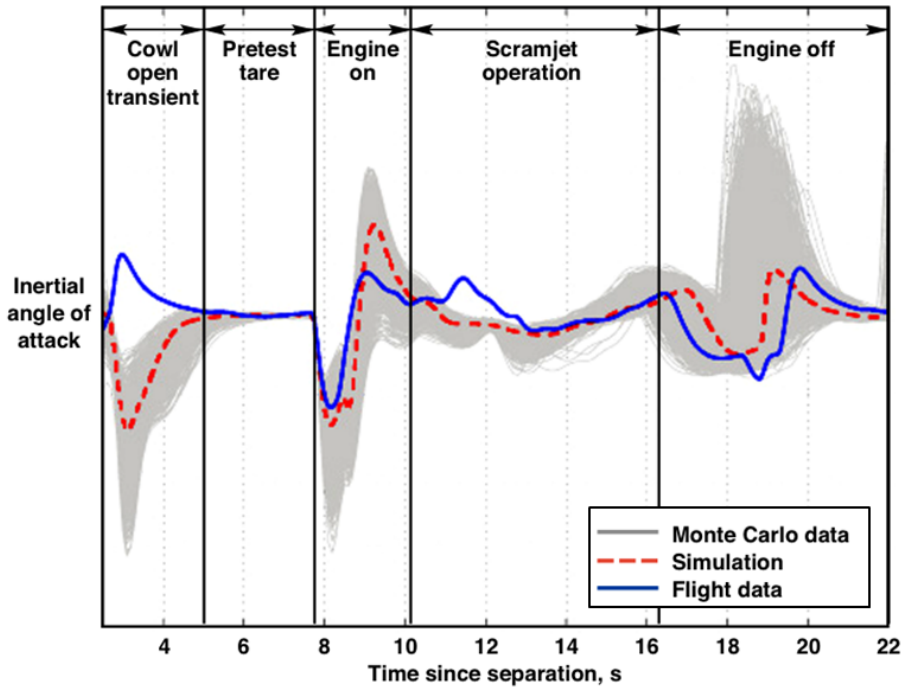

Figure 26: Inertial angle of attack transient response during engine test.

The Hyper-X experiment shown above was deemed an operational success, demonstrating that sustained SCRAMjet-powered flight is achievable; however, the ensuing experiment data was not very useful from the perspective of developing high-confidence computational modeling capabilities. This is because the data content only provided information for a small portion of the expansive range of potential operating conditions (*e.g.* Mach number, altitude, dynamic pressure, and aerodynamic angles) and even that information is limited due to the short duration of operation. As a result, the predictive capabilities of the X-43A SCRAMjet computational models were not enhanced significantly.

Ironically, a good example of a flight experiment where high information content was obtained can be observed from the same X-43A flight test. Following this powered flight portion of the flight, a series of maneuvers were conducted for parameter identification as the vehicle descended unpowered back towards Earth. In contrast to the powered portion of flight, this data content was able to be collected over a significantly wider range of Mach numbers, altitudes, dynamic pressures, and aerodynamic angles, resulting in the refinement of the computational models to simulate the unpowered X-43A more accurately and over a larger range of flight conditions.

3.2 Gap Analysis: A Need for an Integrated Design Approach

In the context of high-risk, research-focused flight experiments, a paradigm shift has recently begun. In Chapter 3, it was discussed that programs such as the HIFiRE program have led this initiative by focusing on (i) conducting lower cost experiments, (ii) reducing experimental development times, and (iii) accepting larger amounts of risk caused by uncertainty. The idea is that by accepting larger amounts of risk a more aggressive approach can be taken towards the development of flight tests aimed at high information yield. A primary goal of the HIFiRE program was aimed at generating a canonical set of data to help boost the hypersonic database and assist in the efforts of

ground testing and computational modeling to enhance their respective capabilities. To this end, the program has yielded mixed results, as higher risk experiments do not always translate directly into higher information yield experiments in every case.

While there has been an observed relationship between sources of uncertainty/risk and the expected amount of information yield, this relationship has proven to be a complex one, potentially requiring an in-depth computational analysis to evaluate and compare alternative flight testing strategies. Generating these alternatives implies consideration of an integrated flight test design space, consisting of parameters which can be broadly classified as follows:

- *Testing Apparatus* – vehicle geometry, sensor suites, control systems, input actuators, etc.
- *Testing Plan* – test duration, operating conditions, maneuver alternatives, excitation (perturbation) signals, etc.
- *Physics-based Models* – aero-propulsive-elastic stability and control parameters, mass/inertia parameters, aeroelastic modes, aero-servo-elastic modes, etc.

Indeed, such an analysis would utilize many of the same physics-based computational models, which will ultimately be used for integrated vehicle systems design. Further, many elements of integrated systems design are also applicable, due to the integrated and multi-disciplinary nature of this problem. Decision making based on this type of analysis would enable the development of "efficient" experimental approaches to flight testing, ultimately allowing for the design of high information flight testing while also being robust with respect to sources of uncertainty.

This analysis relies on the ability to quantify the complex relationship between uncertainty and the expected information content within the experimental data. Further, due to the time-dynamic aspect of this problem additional complications in flight test design are anticipated, due to the functional nature of a portion of the design

vector (*i.e.* design variables (such as vehicle parameters) vs. design functions (such as input maneuvers)). As a result, the following two research questions must be addressed if such an analysis is to be effective.

Research Question #3.1: *How to quantify a relationship between uncertainty/risk and expected data information content?*

Research Question #3.2: *How to design flight test experiments, which yield data with high information content yet are robust to the various sources of uncertainty?*

3.3 Research Objective

In the previous section, it was discussed that using elements of systems engineering analysis, which are traditionally used to design complex systems, are also applicable to the design of high information yield flight testing strategies that are robust with respect to uncertainty/risk. These types of flight tests are intended for the refinement of the physics-based computational models that will ultimately be used for vehicle design purposes once a suitable level of confidence has been established in them. The objective of this research is to enable the integrated systems design of information dense, robust flight tests. This research objective is formally stated below, and is intended to provide the flight test designer (*i.e.* flight dynamics and control systems design experts) with the ability to evaluate simulated flight tests alternatives (*e.g.* controls systems architectures, maneuver/perturbation excitation signals, sensor measurement systems, vehicle geometry, testing plans, etc.) for the anticipated information quality in flight test data, prior to conducting a physical flight test.

Research Objective: From the consideration that a flight test is an integrated system, the research objective of this thesis is to develop a methodology to enable intelligent design of these time-dynamic experiments, which can efficiently and accurately extract information in the presence of uncertainties in current modeling capabilities.

The extent to which the said methodology can be effective at enabling flight testing of revolutionary vehicles and support developmental efforts, the following criteria should be addressed:

1. Bring as much design knowledge up front in the design process prior to the actual flight test for reduction of uncertainty/risk toward information poor experiments [195].

2. Minimize the amount of required testing for satisfying model-to-reality acceptance, effectively minimizing the level of required effort and expense [87].

3. Allow for collaboration with ground & computational testing in order to leverage existing capabilities, allowing for maximized knowledge database growth [87].

4. Identify quantitative performance metrics for the determination of information rich experiments

5. Assess the nondeterministic relationships between sources of uncertainty/risk and expected knowledge yield by enabling a probabilistic design approach

6. Enable a transparent and traceable means for validation and discrimination between several competing candidate models [100].

PART II

Problem Formulation

As discussed in the previous chapters, even for more traditional programs, flight testing can be very expensive endeavor, stretching over long periods of development time. Consequently, the development of techniques leading to more efficient measurement of these characteristics is of great practical interest [215].

Given the research objective discussed in the previous chapter, the next set of chapters will discuss useful concepts and current practices in designing flight tests with the intent of identifying (i) the current state-of-the-art and (ii) gaps, limitations, and shortcomings. To this end, a suitable starting place is to discuss the methods of aircraft system identification, which has been extensively used for flight vehicle modeling over the last 75 years [131].

CHAPTER 4

SYSTEM IDENTIFICATION

4.1 What is System Identification?

System identification, as it is termed today, is an applied scientific and engineering discipline that provides answers to the age-old inverse problem of obtaining a description for a system in some suitable form, given its behavior as a set of observations [269]. Indeed this interest is one of the oldest and most fundamental of all human scientific pursuits and can be more descriptively stated as: the development of mathematical models for physical systems based on imperfect observations or measurements [170]. In the broadest sense, inverse problems and, hence, system identification have been a fundamental part of obtaining knowledge about any physical system that can be observed and measured. System identification covers applications in all possible areas of the sciences where experimental data can be acquired, including biology, medicine, chemical processes, economics, geology, material science, civil and mechanical engineering, automobiles, and, of course, flight vehicles, just to name a few.

The term system identification is one that has caught on over the last century within certain engineering communities. A formal definition is provided by Zadeh [282]:

Def. (*System Identification*): the determination on the bases of observation of input and output, of a system within a specified class of systems to which the system under test is equivalent.

To elaborate on this definition, system identification attempts to develop experiments for dynamic systems so that statistical estimation techniques can most effectively be used to identify a high-confidence mathematical model of an actual physical system. Implicit in the preceding definition is the practical fact that the mathematical representation of a physical system is not unique and that often several different models of varying complexity can adequately describe a given system of interest. In general, the guiding principle for model selection is the parsimony principle, also known as Ockham's Razor, which needs to be applied to determine the "best" model [42]. Translated from Latin, in essence, it implies:

"The number of entities should not be increased beyond what is necessary to explain anything."

Here, the term "entities" refers to the assumptions or parameters appearing in the mathematical model. This implies that the model needs to be *as simple as possible, but as complex as necessary.* Zadeh's definition also mentions that system identification is based on observations of input and output for the system under test. In practice, these observations are corrupted by measurement noise. This requires the use of statistical theory and estimation methods, which are discussed in Section 4.3.5. Finally, the meaning of the word "equivalent" in the preceding definition must be clarified. There is more than one way in which a model can be considered equivalent to a system under test, which alludes to the various approaches for model validation.

4.2 System Identification Applied to Aircraft

When system identification is applied for the development of modeling aircraft, it can be categorized as one of three general problems found in aircraft flight dynamics and control, which are described with the aid of Figure 27. The three problems are as follows [170]:

1. **Simulation**: given input $\mathbf{u}(t)$ and system $\mathbf{S}$, find $\mathbf{y}(t)$ (*e.g.* performance assessment)

2. **Control**: given $\mathbf{S}$ and $\mathbf{y}(t)$, find $\mathbf{u}(t)$ (*e.g.* design of SAS controllers)

3. **System Identification**: given $\mathbf{u}(t)$ and $\mathbf{y}(t)$, find $\mathbf{S}$ (*e.g.* verification and validation of aerodynamic coefficients)

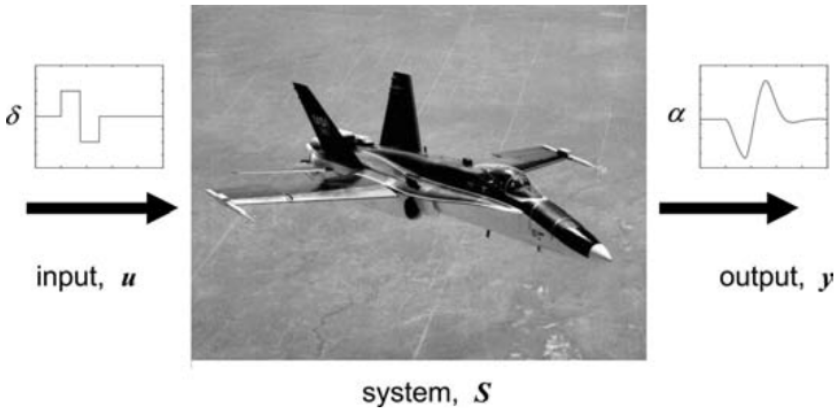

Figure 27: Aircraft dynamics and control [170].

All three of these problem types require an input, output, and a system. For the simulation and control problems, the aircraft system is represented by the governing equations of motion and is assumed to be known. A suitable model for these pursuits can be developed in several different ways, including theoretical modeling and empirical modeling; however, prior to using the model for any significant task (*i.e.* aircraft design), there must be some benchmarking exercise or analysis to establish a suitable level of confidence in the model. Without benchmarking, the results of simulation and control problems cannot be trusted and hence provide meaningless information. As a result, in the context of aircraft model development, system identification is the enabler for the development of high-confidence models and therefore the enabler for useful simulation and control problems that yield trusted and meaningful results.

Modern computational methods and wind-tunnel testing can often provide comprehensive data about the aerodynamic characteristics of an aircraft. However, there are still several motivations for identifying aircraft models from flight data, including:

1. Verifying and interpreting theoretical predictions and wind-tunnel test results (flight results can also be used to help improve ground-based predictive methods);

2. Obtaining more accurate and comprehensive mathematical models of aircraft dynamics, for use in designing stability augmentation and flight control systems;

3. Developing flight simulators, which require accurate representation of the aircraft in all flight regimes (many aircraft motions and flight conditions simply cannot be duplicated in the wind tunnel or computed analytically with sufficient accuracy or computational efficiency);

4. Expanding the flight envelope for new aircraft, which can include quantifying stability and control impact of aircraft modifications, configuration changes, or special flight conditions;

5. Verifying aircraft specification compliance.

Over the years, these motivations have driven the development of system identification techniques, resulting in a rich and diverse track record of practical experiences and successful flight vehicle applications [119, 203, 282]. Most of these dramatic improvements came in the late 1960s and early 1970s, when digital computers became more available. Some of the more significant achievements during this time were by Taylor et al. [146] Mehra, [198], Stepner and Mehra [262], and Gerlach [114]. These contributions were mainly in the development and application of various estimation techniques. In the mid-1980s new challenges to aircraft system identification and parameter estimation were presented by the introduction of highly maneuverable and

unstable aircraft. Some of these challenges were addressed by Klein [169] and Klein and Murphy [171]. An extensive bibliography for aircraft parameter estimation was compiled by Iliff and Maine [145] in 1986. Excellent theoretical and practical material on aircraft system identification is given by Maine and Iliff [187, 220], with emphasis on the output-error method. Mulder [215] addressed methods for experiment design, measured data compatibility, and parameter estimation. Broad overviews of aircraft system identification methods can be found in the works by Klein [167, 168], Hamel and Jategaonkar [130], and the authors of two special issues of the *Journal of Aircraft* on applications of system identification to aircraft [3, 4].

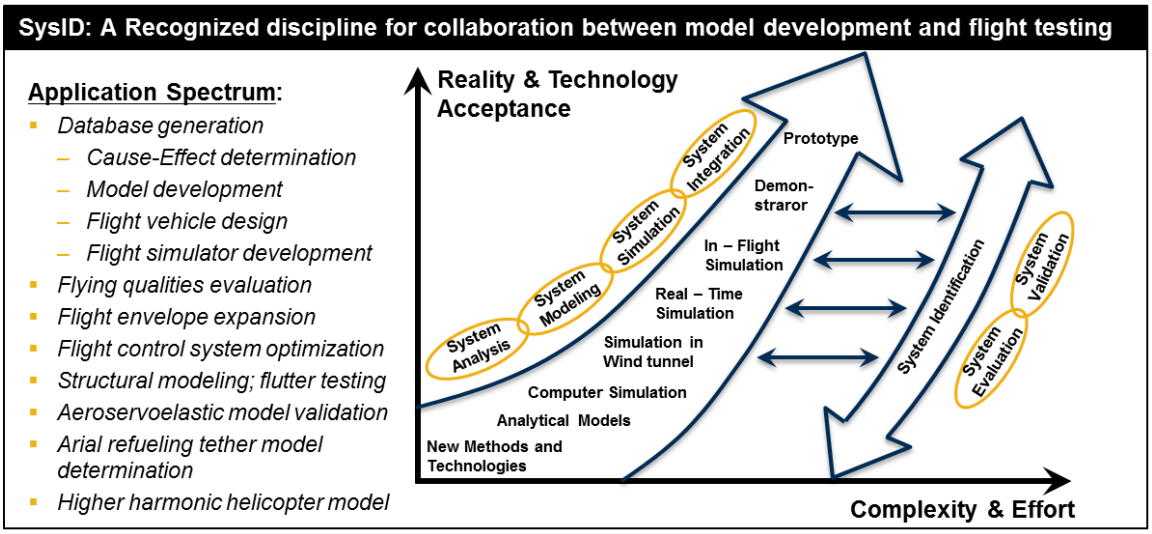

Figure 28: The key role of system identification in the development of aircraft models [131].

Today, the scope of applications ranges from the classical purpose of data correlation for increasing the confidence in flight mechanical prediction techniques to generating high-fidelity aerodynamic databases, flight envelope expansion, high-performance unstable aircraft, and high-bandwidth rotorcraft modeling [152]. As shown in Figure 28, the scope of these applications is diverse, and system identification methods have proven to be flexible in terms of variation in complexity and effort versus the level

of reality and technology acceptance. A few noteworthy examples of system identification applications include: development of an aerial refueling dynamic model for simulation of a C-141B receiver and a KC-135R tanker [243], development of a stability augmentation for the F-18 Hugh Alpha Research Vehicle (HARV) [210], database development of longitudinal aerodynamics models for the X-43A hypersonic research vehicle [213], and the inclusion of higher-order rotor dynamics for improved modeling of a BRC Bell 412 HP helicopter in hover [143].

Based on the development of system identification methodologies, it is now possible to determine the structure of aerodynamic model equations and estimate the model parameters involved, along with their confidence intervals, using data from a single flight-test maneuver. If necessary, measurement noise in the output variables can be distinguished from external disturbances to the system caused by wind gusts or modeling errors. The analysis can also include prior knowledge of aircraft aerodynamic model parameters obtained from wind-tunnel measurements and/or previous flight measurements. There are tools for estimating aircraft flying quality parameters from measured pilot inputs and aircraft responses, and for obtaining more accurate measured data by reconstructing output variables and estimating systematic instrumentation errors, such as biases and scale factor errors. System identification techniques can also be used for experiment design to maximize information content in the measured data, which leads to more accurate models.

4.3 Methodology for Aircraft System Identification

When formulating a system identification problem (for aircraft or any physical system), some general questions must be addressed:

1. What are the inputs and outputs?

2. How should the data be collected?

3. What is a reasonable form for the model to take, given the data and prior knowledge?

4. How can the unknown parameters in the model be accurately estimated based on the measured data?

5. How good is the identified model?

6. How will the results be used?

Over time, aircraft system identification has gradually evolved into a coordinated approach based on flight test techniques, flight test instrumentation, and data analysis methods. These strongly interdependent topics are summarized here [152]:

1. *Instrumentation and Measurement Systems* – the entire flight data acquisition process, including adequate instrumentation and airborne or ground-based recording equipment.

2. *Experimental Design* – related to the selected flight vehicle's maneuvering procedures; the input signals have to be optimized in such a way as to excite all response modes from which parameters are to be estimated.

3. *Statistical Estimation* – includes the mathematical model of the flight vehicle and an estimation criterion, which devises some suitable computational algorithm which iterates based on starting values or a priori estimates of the unknown parameters. This result is a set of best parameter estimates, which minimize error between the model response and the measured response.

From these three strongly interdependent topics stem four important aspects of system identification. The engineer must treat these carefully to sufficiently design an effective experiment. These four aspects are referred to as the "Quad-M" requirements by Jategaonkar [152]:

1. *Maneuvers* – design of control input shape to excite different modes of the vehicle dynamic motion.

2. *Measurements* – selection of instrumentation and filters for high accuracy measurements.

3. *Methods* – selection of the most suitable parameter estimation method to ensure quality of data analysis.

4. *Models* – selection of candidate trajectory and vehicle models under consideration to define the structure of a possible mathematical model.

Aircraft system identification includes model postulation, experiment design, data compatibility analysis, model structure determination, parameter and state estimation, collinearity diagnostics, and model validation. These steps are necessary to identify a mathematical description of the functional dependence of the applied aerodynamic forces and moments on aircraft motion and control variables. The control variables, or design vector, all stem from the Quad-M requirements discussed above. A block diagram depicting the general approach to aircraft system identification is shown in Figure 29. Each of the steps in the procedure are discussed subsequently.

4.3.1 Step 1: Model Postulation

Usually the starting point for the methodology, the equations governing the aircraft dynamic motion are postulated prior to being used in a model-based experiment design. Based on *a priori* knowledge about the aircraft dynamics, aerodynamics, propulsion, etc., candidate models are usually constructed from some combination of theoretical derivation, computational physics analyses (*i.e.* CFD, FEA, etc.), wind-tunnel experiments, propulsion ground tests, and existing flight test data. In the process of developing an aircraft flight dynamic model, some sort of taxonomy is created to provide traceability and manage complexity, which can become considerable.

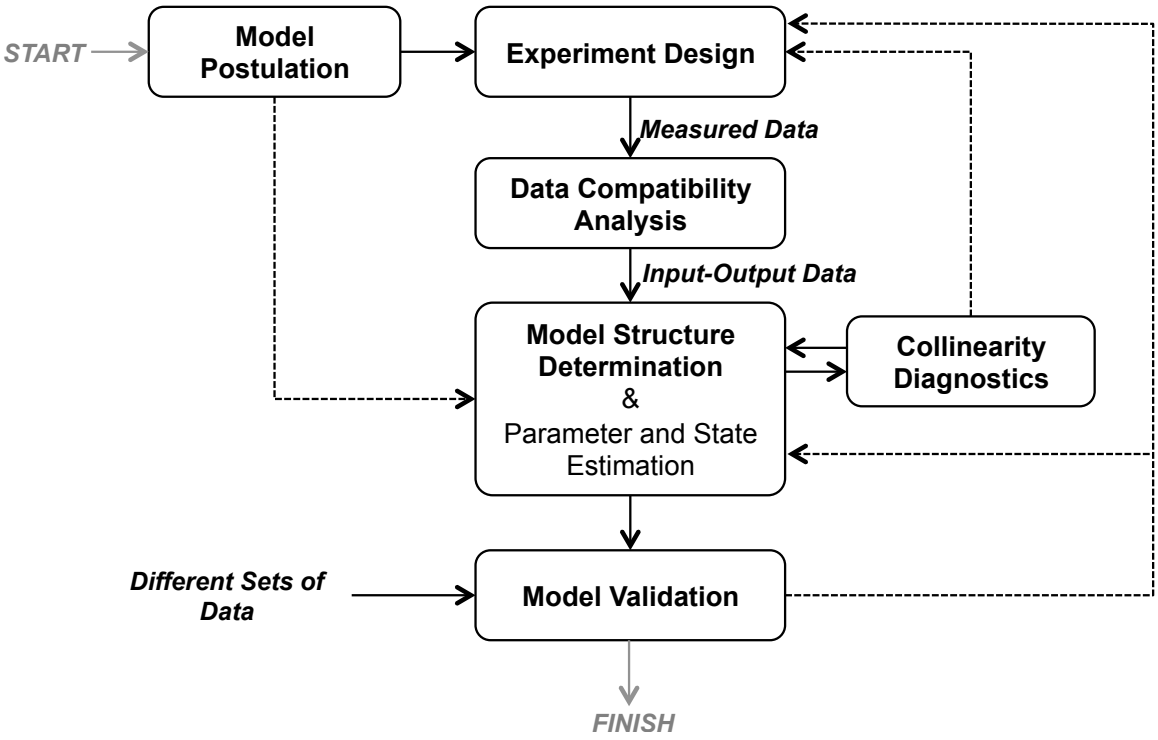

Figure 29: Methodology for aircraft system identification [170].

For this reason a useful classification for the models is as follows: [152]

- **White-box models** – *model structure is derived from first principles of physics; model parameters are physically meaningful*
- **Black-box models** – *no physics used; a general model structure is defined; model parameters are physically meaningless*
- **Grey-box models** – *between white/black box models; a combination of the two*

For example, the aircraft dynamics model is typically derived from the first principles, such as Newtonian mechanics, and as such is considered to be a white-box model. The sub-disciplinary models for the aerodynamic and propulsion forces and moments are usually gray-box models because while the models are not necessarily derived from first principles, the parameters can be somewhat physically meaningful.

It is common and useful for aircraft flight dynamic systems to be compactly expressed in a state-space representation, as follows [83, 170]:

$$\dot{\mathbf{x}}(t) = \mathbf{f}\left(\mathbf{x}(t), \mathbf{u}(t), \boldsymbol{\theta}; t\right) \quad (1)$$

$$\mathbf{y}(t) = \mathbf{g}(\mathbf{x}(t), \mathbf{u}(t), \boldsymbol{\theta}; t) \quad (2)$$

$$\mathbf{z}(i) = \mathbf{y}(i) + \boldsymbol{\nu}(i), \quad i = 1, 2, ..., N. \quad (3)$$

Here $\mathbf{x}(t)$ is the state vector of the system and provides complete information necessary to describe the motion of the aircraft over time. In general, $\mathbf{x}(t)$ includes the aircraft position, orientation, and translational and rotational velocity components. The quantity $\boldsymbol{\theta}$ is a vector of parameters that are used in the aerodynamics and propulsion grey-box models. These values are usually assumed or empirically estimated. The control vector $\mathbf{u}(t)$ is generally composed of throttle position and control surface deflections. Elements of the output vector $\mathbf{y}(t)$ are aircraft response variables, which usually include state variables. Discrete measured outputs $\mathbf{z}(i)$ are sampled N times throughout an experiment at some sampling frequency T and are corrupted by the random measurement noise $\boldsymbol{\nu}(i)$ of the instrumentation and measurement system. It is common to refer to (1) as the state equations, (2) as the output equations, and (3) as the measurement equations.

4.3.2 Step 2: Experiment Design

The goal of experiment design is to maximize the information content in the experimental data so that high-accuracy parameter estimates can be obtained, subject to practical constraints. Examples of these constraints are:

- limits on input and/or output amplitudes, *e.g.*, to ensure that a linear model structure can be used to estimate parameters from the measured data;
- limited resolution or range for the sensors or data acquisition system;

- hardware or telemetry limitations restricting the rate at which data can be measured or the number of physical quantities that can be measured at an acceptable rate;
- limited time available for each maneuver and/or for the overall experimental investigation;
- sensor limitations, characteristics, or availability; and
- limitations on how the aircraft can be excited (*e.g.* control surface rate or position limits) or a requirement for a continuously operating feedback control system when the aircraft is open-loop unstable.

Operating on a postulated model of the structure from Equations (1)-(3), experiment design results in the selection of an appropriate design vector according to the Quad-M requirements previously discussed. These requirements imply that the design of a single flight test is an integrated system, including: (i) specification of an instrumentation and data acquisition system, (ii) selection of the aircraft configurations and flight conditions, and (iii) the optimization of inputs for maneuvers.

The primary role of the instrumentation system is to measure input and output variables at regular sampling intervals. In this context, inputs are throttle setting and control surface deflections for open-loop or bare-airframe modeling. The output variables include quantities specifying the magnitude and direction of the air-relative velocity (airspeed, angle of attack, and sideslip angle), angular velocities, translational and angular accelerations, and Euler attitude angles. The ability of the instrumentation system to accurately measure these quantities relies on design parameters such as sensor placement on the aircraft, measurement bias(es), measurement variance(s), and sampling rates.

In addition to these variables, quantities defining flight conditions and configuration are needed. Most often these variables are closely linked to specified requirements

that have been derived from the needs of ground testing and computational analysis for validation and calibration purposes.

An important aspect of experiment design is the selection of input forms for the flight maneuvers. The input influences the aircraft response, which in turn influences the accuracy of the system identification from the measured flight data. Attempts to obtain parameter estimates with high accuracy in the most efficient manner has led to development of optimized inputs for aircraft parameter estimation [170]. This is how the postulated model influences the type of flight-test maneuver used for system identification. It must be noted that nominal values of the parameters to be estimated must be assumed at this point.

4.3.3 Step 3: Data Compatibility Analysis

Once an experimental plan and procedure have been developed, executed, and measured data has been recovered, an analysis known as data compatibility is usually performed. In practice it has been observed that measured aircraft response data can contain some systematic and random errors. This is always the case, even when care has been taken in the experimental and instrumentation procedure. Common sources of aircraft instrumentation errors are calibration, sensor alignment and position errors, and sensor dynamics. Data compatibility methods are used to verify data accuracy and eliminate the systematic and random errors by enforcing that the data be kinematically consistent so that the rigid-body flight dynamic equations can subsequently be for model determination and parameter estimation [112, 170]. These error analyses involve implementation of state-estimation methods, such as Kalman filtering [23] and the output-error method [161, 165] and are based on the known rigid-body kinematic relationships and available sensor measurements. Once the data set has been made to be kinematically consistent and accurate, the model structure and parameter estimation stages can be undertaken.

4.3.4 Step 4: Model Structure Determination

Model structure determination in aircraft system identification implies selecting a specific model from a class of models by utilizing measured data and *a priori* knowledge. This process is closely tied with parameter estimation methods, which typically employ regression techniques. In the context of regression, model structure refers to the number and form of the model terms used to generate a regression equation.

As an example, this might involve the selection of an appropriate polynomial expansion in the aircraft motion and control variables to sufficiently describe the aerodynamic lift force acting on the aircraft. In general, this expansion could be truncated at any arbitrary order, resulting in a different and unique lift force model. Equations (4) and (5) illustrate two different model candidates for the lift force coefficient in the case of air-breathing hypersonic SCRAMjet flight dynamic modeling. The lift force coefficient is commonly parameterized as a function of Mach number, angle of attack, and elevator control surface deflection.

- **Model Structure # 1**: Lift force varies linearly with angle of attack.

$$C_L^1(M,\alpha,\delta) = C_{L_0}^1(M) + C_{L_\alpha}^1(M)\cdot\alpha + C_{L_\delta}^1(M)\cdot\delta + H.O.T. \tag{4}$$

- **Model Structure # 2**: Lift force varies nonlinearly with angle of attack.

$$C_L^2(M,\alpha,\delta) = C_{L_0}^2(M,\alpha) + C_{L_\alpha}^2(M,\alpha)\cdot\alpha + C_{L_\delta}^2(M,\alpha)\cdot\delta + H.O.T. \tag{5}$$

For steady level flight, these models have been recognized as acceptable model structures for hypersonic aircrafts [99, 285], which assume that the lift coefficient is nearly linearly proportional to angle of attack and control surface deflection. The variation on Mach number is typically more complex, but the model structures, such as $C_{L_0}^1(M)$, $C_{L_\alpha}^1(M)$, and $C_{L_\delta}^1(M)$, can be readily considered with the use additional polynomial expansion or interpolation techniques. In the case of the $C_L^2(M,\alpha,\delta)$ model structure, 2D polynomial expansions have effectively been used [285].

A key goal with model structure identification is that the determined model should be parsimonious to retain good prediction capability, while still adequately representing the physical phenomena. An adequate model refers to a model that fits the measured data well, has good prediction capabilities, and facilitates the effective estimation of the unknown parameters associated with model terms whose existence can be substantiated. In determining model structure, there are two conflicting objectives:

1. **Use as many regressors as possible** – The model can approximate a wide region of variation in the dependent variables.

2. **Use as few regressors as possible** – The variance in the prediction increases as the number of regressors increases and it becomes more difficult to accurately fit models with higher and higher numbers of regressors.

These conflicting objectives suggest that there is a balance to be struck between over-parameterized models and excessively simplified models. This balance is where the adequate model structure can be found.

Several techniques have been developed for determination of adequate model structures, such as forward selection, backward elimination, and stepwise regression [90, 94, 219]. Stepwise regression has been used extensively in practice and proceeds in three steps: (i) postulation of terms that might enter the model, (ii) selection of an adequate model based on statistical metrics, and (iii) validation of the selected model. Often different methods will select different subsets of candidate regressors as the best model and there is no guarantee that any selected procedure will give the one best model. Additional discussion on model structure determination, refer to [90, 218, 207, 141].

4.3.5 Step 5: Parameter and State Estimation

The goal of parameter estimation is to use the measured input(s) and output(s) from a dynamic experiment (*i.e.* $\boldsymbol{u}(t)$ and $\boldsymbol{y}(t)$) to estimate the system parameters of interest, $\boldsymbol{\theta}$, with as high of a degree of confidence as statistically possible. In general estimation theory, statistical accuracy is defined with the aid of the following statistical metrics and means that the expected values of the parameters $\hat{\boldsymbol{\theta}}$ are determined using unbiased, minimum variance estimators.

- expected value: $E(\hat{\boldsymbol{\theta}}|\mathbf{z})$
- covariance: $\text{Cov}(\hat{\boldsymbol{\theta}}) = E\left\{[\hat{\boldsymbol{\theta}} - E(\hat{\boldsymbol{\theta}}|\mathbf{z})][\hat{\boldsymbol{\theta}} - E(\hat{\boldsymbol{\theta}}|\mathbf{z})]^T\right\}$
- bias: $E(\hat{\boldsymbol{\theta}}|\mathbf{z}) - E(\boldsymbol{\theta}|\mathbf{z})$

These so-called optimum estimators result in the best, tightest fits for parameter estimation (*i.e.* the uncertainty in parameter estimation is minimized). The term "unbiased" means that on average the expected value tends to the actual parameter, and the term "variance" means that estimates are clustered together to some degree. This clustering represents the efficiency of the estimator to determine the expected value, which is theoretically lower bounded. The *Cramer-Ráo Lower Bound* (CRLB) proves a formula that established the minimum possible variance of an estimator, and hence can be used as a measure of efficiency for estimation algorithms. An estimation algorithm that achieves an estimate variance equal to the CRLB is said to be efficient.

$$\text{Cov}\left(\hat{\boldsymbol{\theta}}\right) \geq \mathscr{M}^{-1} \tag{6}$$

The matrix $\mathscr{M}^{-1}$ is known as the CRLB, and the expression is the Cramer-Rao (information) inequality for an unbiased estimator $\hat{\boldsymbol{\theta}}$. This equality indicates that any unbiased estimator can have a covariance matrix no smaller than $\mathscr{M}^{-1}$. From maximum likelihood statistical theory, the matrix $\mathscr{M}$ is called the Fisher information matrix and is generally dependent on the unknown parameters $\boldsymbol{\theta}$ and the measurement

Table 4: Three statistical estimation theories for the uncertainties in the parameters and the measurements [249].

Model	**Parameter Vector**	**Noise Vector**
Bayesian Model	$\boldsymbol{\theta}$ is a vector of random variables with probability density $p(\boldsymbol{\theta})$	$\boldsymbol{\nu}$ is a random vector with probability density $p(\boldsymbol{\nu})$
Fisher Model	$\boldsymbol{\theta}$ is a vector of unknown constant parameters	$\boldsymbol{\nu}$ is a random vector with probability density $p(\boldsymbol{\nu})$
Least-Squares Model	$\boldsymbol{\theta}$ is a vector of unknown constant parameters	$\boldsymbol{\nu}$ is a random vector of measurement noise

data $\mathbf{z}$. The information equality is a well known results and can be found in many places in the literature [170, 257, 74, 236, 237].

Within the area of dynamic system identification, there are a variety of parameter estimation methods which come in a variety of formulations, such as time domain methods and frequency domain methods. Another useful classification is to categorize methods according the different statical estimation theories. Table 4 outlines the three most common statical estimation theories and how they consider model parameters and model noise.

Sometimes during flight testing, the aircraft is subjected to random external disturbances (*e.g.* turbulence, wind gusts, etc.). In this case, the model becomes stochastic, and the states must be estimated, in addition to model parameters. For this problem, the Kalman filter is the predominant state estimation technique used, which comes in a variety of formulations [24]. For example, for a nonlinear dynamic model, the extended Kalman filter can be used to estimate the states. The extended Kalman filter can also serve as a technique for obtaining simultaneous estimates of states and parameters, regardless of whether the flight dynamic model is linear or nonlinear.

4.3.6 Step 6: Collinearity Diagnostics

In almost all practical applications of linear regression, the model terms are correlated to some extent. Usually this is not problematic, because the levels of correlation are low; however, in some situations model terms can become nearly linearly related. When this happens, problems concerned with data collinearity exists, and any inferences made from this type of model can be misleading or even completely wrong. Because of this, the ability to diagnose when data collinearity is present within a model is of importance. Typically, this diagnosis process consists of three basics steps:

1. detecting the presence of collinearity among the model terms,
2. assessing the extent to which these relationships have adversely impacted the estimated parameters, and
3. deciding what corrective actions are necessary and worthwhile.

Many different techniques for detection of data collinearity exist, including: (i) examination of the regressor correlation matrix and its inverse, (ii) eigensystem analysis or singular value decomposition, and (iii) parameter variance decomposition. For more information on these techniques, refer to [207, 29].

4.3.7 Step 7: Model Validation

Model validation is the last step in the identification process. The purpose of model validation is to establish confidence in the results of the system identification process. This is accomplished through demonstration of the following:

- **Parameter Comparison** – parameters have physically reasonable values and acceptable accuracy
- **Trajectory Reconstruction** – the model has good prediction capability on comparable maneuvers.

It is convenient that the flight-determined parameter estimates obtained from the system identification process can be compared to other sources of information. In the case where system identification is used to estimate aircraft aerodynamics, the results can be compared to theoretical predictions, wind-tunnel experiments, CFD analyses, and other flight tests using different maneuvers and/or different estimation techniques. During these comparisons, the limitations and accuracy of the other sources of information can be taken into consideration and improvements to these sources can be imposed. For example, validation of a CFD analysis for a hypersonic vehicle aerodynamics can be validated and even calibrated using results from a hypersonic database, which was constructed from the flight-determined parameters of a system identification exercise.

To demonstrate predictive capability, parameter estimation is usually performed on a subset of the original flight data. The measured input for the fit portion of the flight data is applied to the identified model to computed predicted responses. The difference between the computed response and the measured output data is called the model fit error. If this error is suitably small and random in nature, then the identified model is be said to be "verified". Next, the the remaining measured input data can to be applied to the identified model to again computed predicted responses. In this case, the difference between the computed response and the measure output data is called the model representation error. It represents how well the identified model can be used for prediction purposes, and if this error is small, the identified model is said to be "validated".

4.4 Observations

As seen in Figure 29 aircraft system identification methodology provides a link between the statistical estimation of parameters and experiment design. It was observed that what constitutes a good experiment is one that allows for the most efficient and

accurate estimation of model parameters. In the parameter estimation phase, this goal is achieved by using an unbiased, minimum variance estimation method to operate on an assumed model structure and the measured flight-test data. The result is a set of numerical values for the parameters of interest and an associated covariance matrix, which quantifies the *a posteriori* uncertainty in the estimated parameters.

It was mentioned that the extent to which the parameter uncertainty can be minimized is bounded by the information inequality, which is related to the quality of the experimental data. As a result, the ability of SysID to successfully refine an existing model is not theoretically dependent on the quality of the estimation algorithm but rather on the quality of the experiment design. To this end, the following observation is stated.

Observation: *Within the aircraft system identification methodology, experiment design is the most significantly limiting factor towards the development of high-accuracy, high-confidence models, because performance of statistical estimators is theoretically bounded by the quality of the data information content, the Cramer-Rao lower bound.*

Due to the above observation, it is deduced that any further improvements in model development through system identification will be in the area of experiment design of flight tests that result in measured data that has high information density. To this end, the next section is focused on exploring the area of experiment design with the predisposition of identifying any existing gaps and limitations.

CHAPTER 5

EXPERIMENT DESIGN FOR MODEL IDENTIFICATION

5.1 What is Experiment Design?

For a long time, the attention of mathematical statistics was focused on the perfection of methods of model reduction when the method of conducting the experiment was pre-established [100]. The choice of the experiment itself, that is, when and where to take measurements, was determined mainly by the intuition of the experimenter. When problems are comparatively simple and do not require significant expenditures (*i.e.* financial means, time, limited material resources), then this approach has proven to be satisfactory. Over the years, the development of science and technology led to natural complications in the interpretation of the results obtained, and in the methods of carrying out necessary experimental investigations. More complicated experimental situations have led to sharply increased cost of experimental investigations. As discussed in Chapter 3, the development of canonical air-breathing hypersonic vehicle data using flight testing is a current example of this, reflecting the fact that the problem of extracting an increased quantity of data from processes under study with finite resources is very real.

Poorly planned experiments can cause a waste of time and resources, yielding little useful information. Therefore there is a need to develop models, such as models governing flight vehicle dynamics, in a systematic way in order to maximize the information obtained from each experiment and to minimize the number of analyses, cost of materials, and required test time [109]. The set of techniques to do this are called experiment design, or design of experiments (DOE) and represent an important link between the experimental and the modeling world.

Def. (*Experiment Design*): a systematic process involving (i) the identification of experimental objectives, (ii) the selection of factors, and (iii) the laying out of a detailed experimental plan prior to performing any actual experiment.

The goal of experiment design is to adjust the experimental conditions so that maximal information is gained from the experiment [240]. This information can be used in building high-quality, validated models which can describe physical systems, such as model-based process design, control, and optimization. Experiment design begins with determining the objectives of an experiment and selecting the input variables, or factors, for the study. A designed experiment is the laying out of a detailed experimental plan in advance of doing the experiment. This includes deciding how the system will be perturbed (*e.g.* initial conditions, which input variables will be modified, when and how, etc.) and where, how and when the experimenter will observe the phenomena under investigation (*e.g.* which variables are measured, type and location of sensors, sampling schedules, etc.) [276].

Well chosen experimental designs maximize the amount of "information" that can be obtained for a given amount of experimental effort. This greatly alleviates the efforts of post-experiment data analysis, which are frequently performed to measure the effects of one or more important factors on a response. For example, experimental data with high information density enables regression methods to estimate model parameters with a high degree of confidence and accuracy. For this purpose, a good experiment design is essential, as badly designed experiments quickly require more sophisticated data analysis techniques which can often still fail to extract useful information from collected data. Because of this, there has been a significant amount of interest in developing methods for optimal experiment design (OED).

The first ideas of OED were introduced by Fisher [105], who described the basic problem of deciding what pattern of factors combination (the design points) will best reveal the properties of the response and how this response is influenced by the factors. Over time OED has evolved, as different disciplines have found different applications. From Franceschini [109], experiment design methods can be broadly classified as follows:

- **Factorial methods** – *also referred to as "black-box experiment design", this type of DOE views an experiment as simply connecting inputs (factors) and outputs (responses) and is focused on selecting combinations of factors that can provide the most information on the input-output relationship in the presence of variation.*

- **Model-based methods** – *this type of DOE explicitly uses model equations and current parameters to predict the "information content" of the next experiment, and applies an optimization framework to solve the resulting numerical problem.*

Factorial methods have been found useful for many applications in science and engineering disciplines, which are desirable because such designs are straightforward to implement and their results can be very easily interpreted [109, 219]. These methods measure both the additive effects and the effects of interactions between factors on a response; however, in the case of a large number of factors, the experimental cost is very high since all possible combinations of factor values must be taken into consideration. Usually in this case, fractional factorial designs can be used to reduce the size of the design matrix [52]. Unlike factorial methods, model-based experiment design methods take explicit advantage of some (usually incomplete) knowledge of the structure of the underlying system, as represented by a mathematical model. The goal of these methods is typically to assist in the rapid development, refinement, and statistical validation of deterministic process models.

5.2 Experiment Design Applied to Dynamic Systems

Early development in experiment design considered mainly steady-state models (both linear and non-linear model forms) and the application reporting in literature are very broad: from engineering and science to social disciplines [53, 51, 49]. The extension of experiment design concepts to dynamic experiments/models has been a slow process although the potential benefits of these techniques for dynamic studies were amply recognized as early as 1977 [117, 199]. Within engineering literature, the emphasis has been on experiment design for dynamic system identification, including chemical processes, biological systems, and aerospace systems [152, 170, 215]. Within the statistics literature, dynamic experiment design has been much more broadly developed within the *theory of optimal experiments* but is often less practical [18, 100, 162, 232].

Most approaches to dynamic experiment design incorporate a model-based design approach due to the limitations of factorial methods to be implemented on transient experiments, where factors and responses are often a mixture of both variables and functions. In some cases factorial methods can be applied to dynamic experiment design but typically require an extra step in the design process, known as *transcription*, where design functions are parameterized as a finite vector of variables. Often times this parameterization is not straight forward, as capturing the degrees of freedom of a single design function can result in a substantial growth in the dimensionality of the design vector. This observation is formally stated below.

Observation: *In general, factorial methods for experiment design are not well suited to handle dynamic experiments, where both "factors" and "responses" may not be single values (say a constant temperature, a conversion) but rather complicated time profiles of the same variables [109].*

A core concept within the theory of dynamic OED is that model-based approaches explicitly leverage the current state of existing models (*i.e.* model structure and parameters) to predict the "information content" of a potential experiment. Shirt et al. [251] noted that the issue of optimal input signal selection to identify dynamic models was treated for the first time in the case of differential equation models by Espie and Macchietto [97], where these authors formulated the design of transient experiments as an optimal control problem determine the best input $\mathbf{u}^*(t)$ to maximize metrics that quantify information content $\mathscr{I}_x$ [109, 140, 215, 232].

$$\mathbf{u}^*(t) = \max_{\mathbf{u}} \mathscr{I}_x = \min_{\mathbf{u}} \mathscr{I}_x^{-1} \tag{7}$$

Most objective metrics use the Fisher information matrix $\mathscr{M}$ as the basis for OED [18, 100, 109, 162, 215], due to the Cramer-Ráo lower bound inequality, previously discussed in Section 4.3.5. Therefore, prior to conducting any experiment, the Fisher information matrix provides the experimenter the ability to quantify the potential limits of post-experiment parameter estimation techniques to minimize parameter uncertainty. Shown below in Equation (8) and referencing Equations (1)-(3), it can be seen that the Fisher information content is quantified by the sensitivity of the model output to changes in the parameters, called the output sensitivity and that the best choice of input for a parameter estimation experiment is the input that maximizes the squared output sensitivity over the duration of the test. Note, that this also includes the effective performance of the instrumentation and measurement system, as it discretely samples time-continuous signals and is weighted by $\mathbf{R}^{-1}$, which is the inverse of the sensor covariance matrix (assuming a gaussian sampling distribution) and represents the degree of measurement uncertainty.

$$\mathscr{M}(\boldsymbol{\theta}, \boldsymbol{\varphi}) = \sum_{i=1}^{N} \left[\frac{\partial \mathbf{y}(i)}{\partial \boldsymbol{\theta}} \right]^T \mathbf{R}^{-1} \left[\frac{\partial \mathbf{y}(i)}{\partial \boldsymbol{\theta}} \right] \tag{8}$$

In practical applications, the optimization problem of Equation (7) is often subject to numerous constraints, including:

$$\dot{\mathbf{x}}(t) = f(\mathbf{x}(t), \mathbf{u}(t), \boldsymbol{\theta}; t), \ \mathbf{x}(t_0) = \mathbf{x_0} \tag{9}$$

$$\mathbf{x}(t) \in \mathcal{X}_{\text{adm}} \tag{10}$$

$$\mathbf{u}(t) \in \mathcal{U}_{\text{adm}} \tag{11}$$

In essence, Equation (9) requires that the laws of physics must be obeyed, Equation (10) requires that the states remain in some admissible region $\mathcal{X}_{\text{adm}}$, and Equation (11) requires that the input signals remain in some admissible region $\mathcal{U}_{\text{adm}}$. In practical applications of optimal dynamic experiment design, some physical examples of these types of constraints are:

1. limits on input and/or output amplitudes, e.g. to ensure that a linear model structure can be used to estimate parameters from the measure data;

2. limited resolution or range for the sensors or data acquisition system;

3. hardware or telemetry limitations restricting the rate at which data can be measured or the number of physical quantities that can be measured at an acceptable rate;

4. limited time available for each input signal and/or for the overall experimental investigation;

5. sensor limitations, characteristics, or availability; and

6. limitations on how the system can be excited, e.g., control surface rate or position limits, or the requirement for a continuously operating feedback control system when the plant or process is open-loop unstable.

Recent efforts have tried to improve experiment design methods by developing new objective functions and/or novel and more efficient algorithms for the numerical solution of the underlying optimization problem. Most objective functions use the Fisher information matrix [240] as the basis for experiment design; however, this matrix depends inter alia on the true system parameters. Since only *a priori* knowledge of these system parameters is known, this implies a circulatory dependence on parameters, meaning that the nominal optimal experiment cannot be known prior to performing the actual experiment.

Def. (*The Circulatory Problem*): uncertainty in assumed *a priori* models and parameters causes inaccuracy in Fisher optimality criteria, which leads to sub-optimal experiments [18, 109, 215, 240].

This issue has been recognized in the statistics literature [240], where several approaches have been proposed to address this, including:

- **Sequential design** – *iterates between parameter estimation and experiment design using current parameter estimates; requires a potentially large number of experiments to "converge" on an accurate model [68, 106, 107, 216, 276]*
- **Bayesian design** – *characterized by the minimization of the expected value (over the prior parameter distribution) of a local optimality criterion related to the information matrix [20, 19, 63, 64, 95, 250]*
- **Min-max design** – *characterized by the minimization of the worst case scenario (over the entire parameter space) of a local optimality criterion related to the information matrix [75, 84, 85, 101, 178, 202, 233]*

5.3 Methodology for Designing Dynamic Model Identification Experiments

In an attempt to address and mitigate the circulatory problem on parameters, discussed in the previous section, Asprey and Macchietto [18] have proposed a flexible methodology for the model-based design of dynamic model-identification experiments, which can be generally used for sequential, Bayesian, and min-max approaches. This methodology is essentially an inversion of the SySID methodology outlined in Section 4.3, as it still captures the cyclic nature of designing experiments, performing experiments, refining models, and again designing experiments. As seen in Figure 30, the outer-loop reflects this cyclic nature. The inner feedback loop is a sizing loop for the design vector and is dependent on which experiment design approach is employed. Additional important aspects of this methodology will be highlighted in the discussion below.

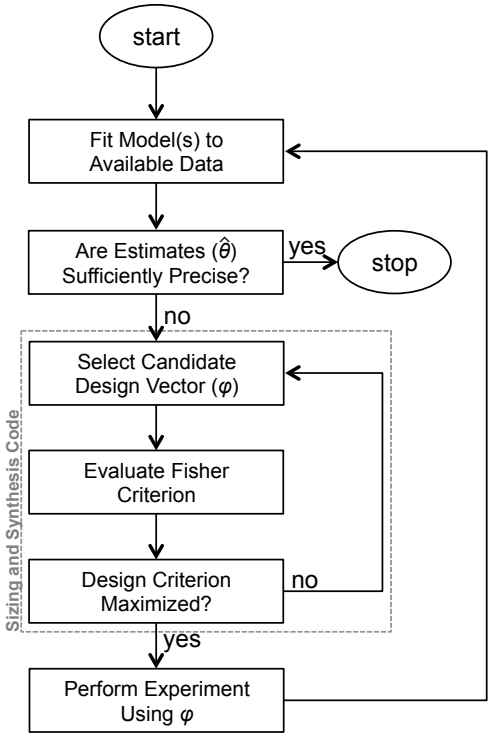

Figure 30: A simplified diagram of the robust-optimal dynamic experiment design methodology [18].

5.3.1 Step 1: Fit Models to Available Data

As discussed in Section 4.3, fitting models to available data includes using statistical methods for state and parameter estimation. This is essentially the same analysis that is used within the SysID methodology to refine models after experimental data has been generated; however, here this analysis is considered up-front, prior to performing an experiment. This is to emphasize the fact that, regardless of what the current state of knowledge is, there are always means of gathering proposed models and accumulating available data. These models can be produced from theoretical (derived) models, existing empirical (fitted) models, computational (numerical) models, or some combination thereof.

5.3.2 Step 2: Are Estimates Sufficiently Precise?

Once a specified level of confidence has been sufficiently established in the accuracy of model prediction, then there is no longer a need to further refine a said model using experiments, and the model is now ready for use in engineering analyses, such as design, control, optimization, etc. Pulling again from elements of the SysID methodology, this is the step where verification and validation between models and experimental results is analyzed. In the case of aerospace vehicles, this is done on several levels, such as comparison of model predictions and flight test data; or comparison of calculated aerodynamic parameters and wind tunnel data.

This step is also where the performance of the statistical estimation methods to determine the parameters is considered. This includes elements of statistical measurement theory to account for sources of measurement uncertainties, including things like: goodness of fit metrics, confidences intervals, and hypothesis testing. These measurement uncertainties are typically categorized as systematic errors (*i.e.* a reproducible inaccuracy which is introduced by equipment, calibration, or experimental

technique) and random errors (*i.e.* fluctuation in observations due to things like instrumentation uncertainty and statistical fluctuation). From these sources of errors provide a way of defining the performance of an estimator through estimation accuracy and precision.

- **Accuracy** – *the ability to indicate the true value exactly; minimization of systematic errors*
- **Precision** – *the ability to indicate a particular value upon repeated but independent applications; minimization of random errors*

More accurate parameter estimations result in smaller $\%\alpha$ joint confidence regions which means smaller variance in the expected value of the parameter. In practice, there are many cases where there have been observed large discrepancies between the accuracy of these predicted confidence regions due to factors such as nonlinear dependence on parameters and non-gaussian measurement noise. Indeed, this occurrences are quite common in aerospace flight testing [166, 186, 214]. As a result, techniques for determining the accuracy of a general parameter estimator have been developed, based on higher-order sensitivity analysis of an estimator for a general dynamic system [125]. The higher-order sensitivity analysis provides a very general tool that can, in theory, be used for error analysis for any estimator, including the effects of any misspecification of the postulated model. Unfortunately, the complexity of the analysis makes this approach impractical for multidimensional dynamic systems.

5.3.3 Step 3: Select Candidate Design Vector

When confronted with a physical system whose dynamics are sought to be identified, there are a number of questions to be answered, such as:

1. Where and what to measure? – *Which signals are to be considered as outputs and which are to be considered as inputs? This question is really two separate*

questions concerning where to place sensors and the identification of what signals should be manipulated so as to "excite" the system of interest.

2. When to measure? – *Most often the signals are sampled using a constant sampling interval, and then this quantity has to be chosen; however, dynamically changing sampling rates is something to consider.*

3. What is an appropriate choice of inputs? – *The choice of input signals has a very substantial influence on the observed data. The input signals determine the operating point of the system and which parts and modes of the system are excited during the experiment. The user's freedom in choosing the input characteristics may vary considerable with the application.*

4. How many measurements need to be collected? – *As a final choice for the identification experiment, the number of input-output measurement to be collected is related to the test duration and sampling rates.*

The process of answering these questions helps the experimenter identify the quantities that are useful in designing an appropriate experiment. The experimental conditions which define an experiment include quantities that can be controlled and quantities that cannot be controlled. When an optimal experiment is designed, the values of the control variables characterizing the experiment are determined so as to optimize the predicted information content of the experiment or analogous requirements. Simultaneously, the effects of the quantities that cannot be controlled, such as systematic and random errors, must be minimized. For the generic dynamic system defined from Equations (1)-(3), a generalized design vector is outlined as follows:

Design Vector: $\boldsymbol{\varphi} = \{\mathbf{u}(t), \bar{\mathbf{w}}, \mathbf{x}_0, \mathbf{t}_{sp}, \tau\}$

- time-varying controls, $\mathbf{u}(t)$
- time-invariant (constant) controls, $\bar{\mathbf{w}}$
- sampling times, $\mathbf{t}_{sp}$
- measured responses, $\mathbf{z}(i)$, $i = 1, 2, \ldots, N$
- initial conditions, $\mathbf{x}_0$
- duration of the experiment τ

5.3.4 Step 4: Evaluate Fisher Information Criterion

Once a suitable design vector has been selected, the Fisher information-based performance criterion can be evaluated. This generally involves a process that incorporates elements of: (i) dynamic simulation, (ii) dynamic output sensitivity analysis, and (iii) Fisher information matrix construction. Recall, that the Fisher information matrix is typically used as the basis for experiment design because it can be used to determine the Cramer-Ráo lower bound; however, this matrix depends, inter alia, on the true system parameters (*i.e.* the circulatory problem of Section 5.2). Therefore, if an optimal experiment design is desired that is robust with respect to parameter uncertainties, then evaluating information criteria over the parameter space would require a large amount of computational effort, since dynamic simulation and sensitivity analyses must be repeated.

While it is the Fisher information *matrix* that represents the Cramer-Ráo lower bound of the parameter covariance matrix of an unbiased and minimum-variance estimator, much effort has been on reducing the complex information contained in this matrix to a *scalar* number so that numerical optimization schemes can be utilized.

The most commonly used criteria are D-optimality, A-optimality, and E-optimality, which are described in Table 5. All of these criteria have a geometrical interpretation as illustrated for the two-parameter case in Figure 31. The uncertainty associated with the estimates of the parameters can be represented by joint parameter confidence regions (typically, $\alpha = 90\%$ or $\alpha = 95\%$ confidence level) and, as can be seen, the D-optimal criterion aims at minimizing the volume of this joint confidence region, the E-optimal the size of its major axis, and the A-optimal the dimension of the enclosing box around the joint confidence region.

Table 5: Examples of Fisher information-based criteria which can be used for optimal and robust model-based design of dynamic system identification experiments.

Optimality Criteria	**Expression**	**Description**
D-optimality	$\mathscr{I}_d = \max_{u \epsilon U} det(\mathscr{M})$	*maximize the determinant of the information matrix*
E-optimality	$\mathscr{I}_e = \max_{u \epsilon U} \lambda_{min}(\mathscr{M})$	*maximize the smallest eigenvalue of the information matrix*
A-optimality	$\mathscr{I}_d = \max_{u \epsilon U} tr(\mathscr{M})$	*maximize the trace of the information matrix*
ED-optimality	$\mathscr{I}_{ed} = \max_{u \epsilon U} \underset{\theta \epsilon \Theta}{\mathbf{E}} \{det(\mathscr{M})\}$	*maximize the expected-value of the determinant of the information matrix*
R-optimality	$\mathscr{I}_r = \max_{u \epsilon U} \min_{\theta \epsilon \Theta} det(\mathscr{M})$	*maximize the worst-case determinant of the information matrix*

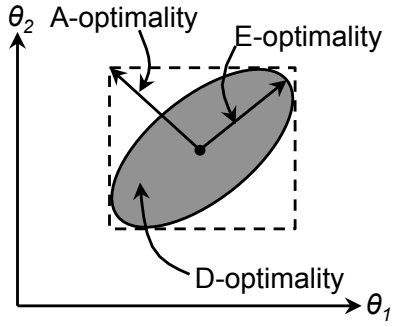

Figure 31: Joint Parameter Confidence Region – post experiment; post estimation

D-optimality is the most commonly used of the three standard criteria due to some appealing properties of the criterion: simple geometrical interpretation [27, 53], theoretical invariance with respect to any non-degenerated transformation (*e.g.* rescaling of model parameters)[100, 199]; and yielding of optimal experiments which correspond to replications of a small number of different experimental conditions [273].

While these three criteria are the most common, they are not devoid of drawbacks. The D-optimal design tends to give excessive importance to the parameters for which the model is most sensitive. Thus, although the confidence region volume can be reduced, the uncertainties of all other parameters may remain large. The A-optimal criterion is considered to be unreliable in the particular case of high correlations between parameters. This is because the matrix trace operator does not include the off-diagonal elements, and thus, causes appreciable loss of information in the case when there is high cross-correlation between parameters. The so-called E-optimal criterion minimizes the condition number of the information matrix, leading to spherical joint confidence regions; however, it is often discontinuous and can therefore cause convergence problems when used within gradient-based optimization routines.

In light of the current limitations in optimality criteria, there has been a recent effort to formulate criteria that account for parameter variations caused by the circulatory problem. To this effect, D-optimality was augmented to ED-optimality and R-optimality, as shown Table 5, which account for uncertainty using Bayesian and worst-case scenarios, respectively. The drawbacks of these metrics is that they can be very expensive to compute over the entire parameter space.

As shown in Equation (8), computation of the Fisher information matrix first requires computation of the output sensitivities. There are two approaches that can be used to compute the sensitivities $\partial \mathbf{y}/\partial \theta_j,\ j = 1, 2, ..., n_p$, where n_p is the

number of parameters: the analytical approach and the numerical approach. In the analytical approach, equations for the output sensitivities are generated by taking partial derivatives of the original dynamic system of equations, which can then be numerically integrated along-side the original system. These equations are collectively referred to as the sensitivity equations and note that it is necessary to have *a priori* values for the model parameters to solve both the dynamic and sensitivity equations, respectively. For the dynamic system of Equations (1)-(3), the output sensitivity equations take the following form:

$$\frac{\partial \dot{\mathbf{x}}(t)}{\partial \boldsymbol{\theta}} = \left[\frac{\partial \mathbf{f}}{\partial \mathbf{x}}\right] \cdot \frac{\partial \mathbf{x}(t)}{\partial \boldsymbol{\theta}} + \left[\frac{\partial \mathbf{f}}{\partial \boldsymbol{\theta}}\right], \quad \frac{\partial \mathbf{x}(0)}{\partial \boldsymbol{\theta}_j} = \mathbf{0}_{n \times m} \tag{12}$$

$$\frac{\partial \mathbf{y}(t)}{\partial \boldsymbol{\theta}} = \left[\frac{\partial \mathbf{g}}{\partial \boldsymbol{x}}\right] \cdot \frac{\partial \mathbf{x}(t)}{\partial \boldsymbol{\theta}} + \left[\frac{\partial \mathbf{g}}{\partial \boldsymbol{\theta}}\right], \quad j = 1, 2, ..., n_p \tag{13}$$

Typically a numerical approach is used more often, because the analytic derivatives of general dynamic systems can become quite complicated to differentiate by hand. The numerical approach to computing output sensitivities uses an approximation to the definition of numerical partial derivatives, which can be calculated using forward or center differencing approaches.

$$\frac{\partial \mathbf{y}}{\partial \theta_j} = \frac{\mathbf{y}(\boldsymbol{\theta}_0 + \delta\boldsymbol{\theta}_j) - \mathbf{y}(\boldsymbol{\theta}_0)}{|\delta \boldsymbol{\theta_j}|} \quad j = 1, 2, ..., n_p \tag{14}$$

$$\frac{\partial \mathbf{y}}{\partial \theta_j} = \frac{\mathbf{y}(\boldsymbol{\theta}_0 + \delta\boldsymbol{\theta}_j) - \mathbf{y}(\boldsymbol{\theta}_0 + \delta\boldsymbol{\theta}_j)}{|\delta \boldsymbol{\theta_j}|} \quad j = 1, 2, ..., n_p \tag{15}$$

Here $\delta\boldsymbol{\theta}_j$ denotes a perturbation vector with all zero elements excepts for the nth element. The appropriate selection of the magnitude of the perturbation parameter is both an art and a science, as it must be selected suitably small to provide an accurate estimate of the sensitivity but not too small so as to excite singular behavior.

5.3.5 Step 5: Design Criterion Maximized?

There have been many approaches to optimal input design for aircraft parameter estimation, including: optimal control formulations using variational calculus [199,

200, 199, 262]; a multidimensional optimization approach using multisite input forms [210, 215]; a suboptimal solution for minimum time to achieve specified parameter error bounds using Walsh functions [67]; and a globally optimal square-wave solutions using dynamic programming [208, 210, 209]. Also, optimal input design methods in the frequency domain have been developed by Mehra [199], Mehra and Gupta [200], and Gupta and Hall [124]; however, these methods are often not practical, due to the relative complexity of required calculations, dependence on *a priori* models, practical implementation issues, etc.

Table 6 summarizes numerical approaches to solve an optimal control problem (OCP), such as the generic formulation of Equation (7). These approaches can be broadly categorized as direct methods and indirect methods [30]. Direct methods operate by transcribing an input signal into a vector of variables, enabling the use of traditional optimization techniques. These methods do not directly satisfy the necessary conditions for optimality, resulting in concerns about the optimality of the solution [164]. In contrast to direct methods, solutions found using indirect methods are assured to satisfy the necessary conditions for optimality [59]; however, these methods suffer form convergence issues, as they are often highly sensitive to initial guesses. Therefore, these methods are difficult to automate, which limits application in large scale engineering-type problems.

Observation: *Due to current limitations in computational optimal control methods, the ability of optimal information dynamic experiment design methods to solve engineering problems is limited.*

Table 6: Survey of implemented numerical optimal control problem solution techniques [30, 59, 164].

	OCP Approaches	
	Direct	**Indirect**
Strengths	• *Finite dimensional* • *Less suceptible to convergence issues* • *Automatable process*	• *High solution accuracy* • *Assured satisfaction of optimality criteria*
Weaknesses	• *Accuracy issues* • *Parametric optimization*	• *Sensitive fo convergence issues* • *Not automatable solution process*
Existing Methods	• *Parametric optimization* • *Collocation methods* • *Pseudospectral methods*	• *Shooting/multiple-shooting methods* • *Forward-backward integration* • *Function space gradient methods*

5.4 Observations

Currently, significant issues hinder the applicability of experiment design for dynamic system identification to solve engineering-type, industrial-sized problems. These include: limitations in figures of merit for robust-optimal experiments; limitations of computational approaches to solve optimal control problems; the dependence of experiment designs on *a priori* parameter values; and large requirements on computation expense. Also, there is a need for a sensitivity analysis tool that can automatically generate the output sensitivities to construct the Fisher information matrix of an arbitrary dynamic system.

While the use of Fisher information metrics do provide the experiment designer with the ability to predict *a posteriori* parameter estimation accuracy, this prediction accuracy is severely hampered by a circular dependence of the information criteria on the true values of the system parameters. In an attempt to address this,

techniques have been developed to account for *a priori* parameter uncertainty and generate robust experiment designs. These techniques require a large number of optimal control problems to be solved so that estimates on the expected (Bayesian) and worst-case (minimax) performance of the information criteria can account for the entire parameter space. In addition, scalar information criteria are typically used within optimization problems; however, these metrics do not fully capture the information content of the entire Fisher information matrix, which leads to unbalanced, suboptimal experiment designs.

In light of these deficiencies, it is observed that there is a need to develop optimal information experiment designs that are robust to parameter uncertainty in a manner that is less computationally intensive and does not depend on advancements in computational optimal control. To this end, the following research question is posed.

RQ #6: *Is there a way to design dynamic system identification experiments that are robust to uncertainty in system parameters without requiring a large number of computationally expensive optimal control problems to be solved?*

The implications of this question suggest that the design of robust-optimal dynamic system identification experiments does not require an automatable OCP solver; however, accuracy of the joint parameter confidence regions must be preserved. The next chapter is focused on an alternate approach to robust design, which has been developed by the systems engineering community.

CHAPTER 6

ROBUST DESIGN OPTIMIZATION

6.1 What is Robust Design Optimization?

In the last chapter it was concluded that there is a need to design robust-optimal dynamic system identification experiments with respect to uncertainties in model parameters. Because the Fisher information matrix is dependent, inter alia, on the true values of the parameters, the use of *a priori* information to calculate this matrix results in erroneous, inaccurate predictions. In addition to parameter uncertainty, variation in experimental conditions must also be considered, as realistic modeling and simulation of complex systems must include the nondeterministic features of both the system and the environment [224]. As a result, design algorithms are sought that can (i) leverage as much of the current knowledge as possible, (ii) address robustness to uncertainty, and (iii) still produce dynamic experiments with high enough information density to satisfy experimental requirements [81].

The field of *robust design optimization* (RDO) is devoted to the design of such techniques. Scattered across the literature [35], there are numerous efforts that are aimed at designing quality into products or processes by minimizing and managing sources of uncertainty. To apply these techniques, sources of uncertainty must first be identified and whether or not it is possible to reduce these uncertainties must be determined [224]. For complex, multidisciplinary systems, this task, known as *uncertainty quantification*, can quickly become a large and tedious endeavor, often yielding bad designs. The focus of this chapter is to discuss both uncertainty quantification and current approaches to RDO. Useful attributes which could aid robust-optimal

dynamic experiment design will be highlighted. Finally, a systems engineering approach to determine robust-optimal solutions to complex, multidisciplinary systems, such has the design of flight test strategies will be discussed.

6.1.1 Uncertainty Analysis

Uncertainty analysis investigates the uncertainty of variables that are used in decision-making problems in which observations and models represent the knowledge base [81]. As seen in Table 7, definitions for uncertainty vary in the literature. They are important, since there is a delicate balance between accuracy and conservatism when constructing effective uncertainty models. Conservative uncertainty bounds are seen as inefficient akin to the "safety factors" approach of structural design. However, in attempting to maximize the "preciseness of an uncertainty model", one must guard against missing the full range of likely behavior. Achieving this balance is uniquely connected to a comprehensive understanding of the analysis limitations, baseline models employed, and sensitivity of system outputs to the uncertainty itself.

Table 7: The diverse definitions of uncertainty found in engineering literature [81].

Source/Perspective	Definition	Classification/Sources
(Zhao, 1995) *Controls Perspective*	Uncertainty refers to the differences or errors between models and reality.	• Unstructured, representing that which is un-modeled or not possible to model (e.g. high frequency dynamics) • Structured, representing that for which information on the likely behavior is available (e.g. model parameters)
(Hazelrigg, 1996) *Systems Design Perspective*	In an experiment, when the sample space contatins more than one element with non-zero probability, there is uncertainty.	• Insufficient knowledge of the laws of nature • Inability to assess or measure a phenomenon • Inability to measure initial or boundary conditions • Inherent ransomness of a physical process
(Wershing, 1996) *Structural Design Perspective*	(no formal definition)	• Inherent (variability in nature of phenomena) • Statistical (results from incompleteness of statistical data, e.g. too small smaple size) • Modeling (use of simplified analysis models) • Human error (in calculations, fabrication, judgment, etc.)
(Oberkampf, et al., 1999) *Engineering Design Perspective*	Uncertainty is a potential deficiency in any phase or activity of the modeling process that is due to a lack of knowledge.	• Predicting dependent variables from measured quantities • Whether and when an event may occur • Validity of a performance prediction hypothesis
(Tung/Yen, 1993) *Complex Systems Design Perspective*	Uncertainties attributed mainly to the lack of perfect understanding with regard to phenonema or processes.	• Natural (inherent to physical process) • Model (inability to perfectly model nature via mathematics) • Input (stochastic inputs) • Measurement/data transfer manipulation • Operational/environmental

In the context of dynamic experiment design, the definitions provided by Zhao [284] and Oberkampf [224] are the most useful. From this, a simple, consistent general definition if uncertainty is desired that is useful for high information dynamic experiment design settings.

Def. (*Uncertainty*): the incompleteness in knowledge (either in information or context), that causes model-based predictions to differ from reality in a manner described by some distribution function [81].

Uncertainty analysis is the science of quantitative characterization and reduction of uncertainties. This usually consists of the following elements: (i) identification of what are the sources of uncertainty; (ii) characterization of what form the sources are in (*e.g* interval, distribution, etc.); (iii) propagation of how the sources of uncertainty affect metrics of interest; (iv) analysis to determine what are the implications of certain sources of uncertainty; and (v) reduction of the influence of important sources. To help in this process, it is commonly assumed that uncertainty can be classified into two categories [82, 192], which is often useful in determining which sources of uncertainty to target for minimization:

- **Aleatory uncertainty** – also known as statistical uncertainty, it is the inherent, irreducible uncertainty; natural variability (*e.g.* atmospheric conditions).
- **Epistemic uncertainty** – also known as systematic uncertainty, it represents a lack of knowledge about the quantity in question; reducible, subjective, or state-of-knowledge uncertainty (*e.g.* low confidence in the values of model parameters).

Another classification that is more specific to the dynamic experiment design process can be inferred from analogies with *robust control theory* [284]. This can be seen in Figure 32, where a treatment of uncertainty has been achieved through a formal mathematical construct using Equations (1)-(3). Using this figure as a guide, the following design uncertainty sources are proposed as analogs to the control model: input Δx, operational/environmental Δc, model parameter Δp, and measurement Δm. These are organized in the figure, with parenthetical references to aircraft control system "analogies", with respect to the true system.

- **Input uncertainty** (Δx) – due to an imprecise definition in the requirements that define a design problem which trickle down variability in to the design/input variables.
- **Model parameter uncertainty** (Δp)– refers to error present in all mathematical models that attempt to represent a physical system (*i.e.* "insufficient knowledge of the laws of nature").
- **Measurement uncertainty** (Δm) – present when the response of interest is not directly accessible from the math model (*i.e.* it must be inferred, for example, state estimation using Kalman filters).
- **Operational/environmental uncertainty** (Δc) – due to the unknown or known uncontrollable external disturbances (*e.g.* wind gusts).

Each of these types of uncertainty can cause the "model-based predictions to differ from reality" as described in the definition for uncertainty

There are multiple ways to mathematically represent different uncertainties. Some of which are deterministically, probabilistically, or possibilistically.

1. **Deterministic type** – define parameter domains in which the uncertainties can vary; mathematically represented by crisp sets.

2. **Probabilistic type** – define probability measures describing the likelihood by which a certain event occurs; mathematically represented by probability distributions.

3. **Possibilistic type** – define fuzzy measures describing the possibility or membership grade by which a certain event can be plausible or believable; mathematically modeled by fuzzy sets.

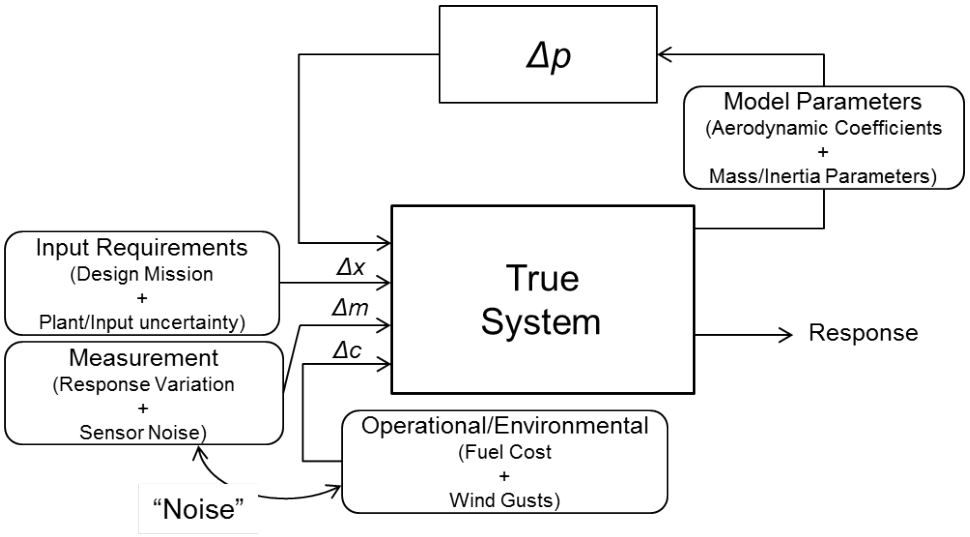

Figure 32: Uncertainty types within a dynamic system, using a robust control analogy [284].

6.1.2 Robust Design Optimization

There are principle problems in solving optimization problems, such as NP-hardness in discrete search spaces or multi-modality in continuous search spaces [35]. As a result, solving optimization problems often requires an involved effort. Thus, the question frequently arises as to whether it is desirable to locate isolated, singular design points with any significant amount of precision: (i) high accuracy solutions are limited by a model's ability to approximate the real world, (ii) required precision in manufacturing might be too costly, (iii) optimized systems can be very sensitive

to small changes, and (iv) an optimal solution is inherently static (*e.g.* variations in lifecycle costs and fuel costs). As a result, a better design target is one that provides a high degree of robustness, meaning that it is insensitive with respect to changes in uncertainty. Here, the search is again for optimality but also for robustness. The process of finding such solutions is referred to as *robust design optimization*. In these types of problems a robust design solution has stochastic connotation, as defined below.

Def. (*Robust Design Solution*): A robust design solution that maximizes the likelihood of success while satisfying constraints in a way that is insensitive to sources of uncertainty [17, 81].

A plethora of techniques for robust design and optimization have been developed to model and manage uncertainty, most of which can be categorized into two approaches: deterministically and nondeterministically (*i.e.* randomly).

- **Deterministic Approach** – Methods which calculate the desired robustness measures $F(x)$ and the related robust constraints explicitly using numerical techniques. Thus, the resulting optimization problem is an ordinary one, to be solved using local or global optimization algorithms.

- **Nondeterministic Approach** – Treating the (probabilistic) uncertainties directly by optimizing noisy functions and constraints. This is sometimes referred to as Monte-Carlo techniques. Since the noisy information is usually obtained by simulation programs, this kind of optimization is also referred to as simulation optimization [11].

6.1.2.1 Deterministic Approach

Deterministic methods focus on how to transform the robust-optimization problem into an ordinary optimization problem, which allows for standard optimization techniques to be used. These optimization techniques rely on a strong assumption that higher-order gradient information exists (*i.e.* at least the 1st or 2nd-order derivatives). For example, consider the objective function to be minimized where there is uncertainty in the parameter vector $\boldsymbol{\theta} \in \mathbb{R}^M$.

$$\min_{\mathbf{x}\in\mathbb{R}^N} f(\mathbf{x}, \boldsymbol{\theta}) \tag{16}$$

Assuming that the parameter uncertainty perturbations are normally distributed $\delta\boldsymbol{\theta} \sim \mathcal{N}(0, \mathbf{C})$, the deterministic methods utilize the mean and the variance of f as robustness measures, resulting the multi-objective optimization problem.

$$\min_{\mathbf{x}\in\mathbb{R}^N} \mathbf{F}_R(\mathbf{x}, \boldsymbol{\theta}) = \big(\mathrm{E}\big[f(\mathbf{x})|\boldsymbol{\theta}\big],\ \mathrm{Var}\big[f(\mathbf{x})|\boldsymbol{\theta}\big]\big) \tag{17}$$

The search for optimal robust designs using multiple criteria is called *robust multi-objective optimization* [35], where one can consider the set of *Pareto-optimal* solutions [134, 272]. As an alternative to this approach, these two objectives can be aggregated into a single function using a weighted sum as follows.

$$\min_{x\in\mathbb{R}^N} (1-\beta)\,\mathrm{E}\big[f(\mathbf{x})|\boldsymbol{\theta}\big] + \beta\mathrm{Var}\big[f(\mathbf{x})|\boldsymbol{\theta}\big] \tag{18}$$

Here $\beta \in [0, 1]$ is a weight factor, chosen by the designer.

The applicability of using deterministic methods for robust design optimization is nearly always limited by the ability of a sensitivity analysis to calculate higher-order gradient information, where calculation of these measures analytically is almost always intractable [35]. Therefore, approximation techniques must be used, which require the use of Taylor series expansions. To illustrate this, consider the example of a Taylor expansion of objective function $f(\mathbf{x}, \boldsymbol{\theta})$ with respect to some guessed

nominal values of the uncertainty vector $\boldsymbol{\theta}_o$, including 2^{nd}-order gradient terms, which is perturbed by the vector $\delta\boldsymbol{\theta}$.

$$f(\mathbf{x}, \boldsymbol{\theta}_o + \delta\boldsymbol{\theta}) = f(\mathbf{x}, \boldsymbol{\theta}_o) + \sum_{i=1}^{M} \frac{\partial f}{\partial \theta_i}\delta\theta_i + \frac{1}{2}\sum_{i=1}^{M}\sum_{j=1}^{M} \frac{\partial^2 f}{\partial \theta_i \partial \theta_j}\delta\theta_i\delta\theta_j + \ldots \text{H.O.T} \quad (19)$$

Assuming that $\delta\boldsymbol{\theta} \sim N(0, \mathbf{C})$, the expected value $\mathrm{E}\big[f(\mathbf{x})|\boldsymbol{\theta}_o\big]$ and the variance $\mathrm{Var}[f(\mathbf{x})|\boldsymbol{\theta}_o]$ can be calculated. Equations (20)-(21) below show these parameters considering only the linear approximation of Equation (19) (*i.e.* the higher-order terms, including 2^{nd}-order, are neglected).

$$\mathrm{E}\big[f(\mathbf{x})|\boldsymbol{\theta}_o\big]_1 = f(\mathbf{x}, \boldsymbol{\theta}_o) \quad (20)$$

$$\begin{aligned}
\mathrm{Var}[f(\mathbf{x})|\boldsymbol{\theta}_o]_1 &= \mathrm{E}\left[\left(f(\mathbf{x}, \boldsymbol{\theta}_o) + \sum_{i=1}^{M}\frac{\partial f}{\partial \theta_i}\delta\theta_i - \mathrm{E}\big[f(\mathbf{x})|\boldsymbol{\theta}_o\big]_1\right)^2\right] \\
&= \mathrm{E}\left[\sum_{i=1}^{M}\sum_{j=1}^{M}\frac{\partial f}{\partial \theta_i}\frac{\partial f}{\partial \theta_j}\delta\theta_i\delta\theta_j\right] \\
&= \sum_{i=1}^{M}\sum_{j=1}^{M}\frac{\partial f}{\partial \theta_i}\frac{\partial f}{\partial \theta_j}\mathbf{C} \quad (21)
\end{aligned}$$

Thus, provided that there is a way to calculate the 1^{st}-order derivatives of f analytically or numerically, these equations may be used to estimate the variance. If these equations are inserted into either Equation (17) or Equation (18), then the resulting approach is the so-called *sensitivity robustness approach* [76]. The sensitivity robustness approach assumes the mean value to be equal to f at the nominal parameter values, $\boldsymbol{\theta}_o$; however, in certain applications, such as objective functions with noise induced multi-modality, this assumption may not be appropriate.

While not being a final solution to this problem, considering high-order approximation can improve the situation. To this end, consider the calculation of $\mathrm{E}\big[f(\mathbf{x})|\boldsymbol{\theta}_o\big]$ and $\mathrm{Var}[f(\mathbf{x})|\boldsymbol{\theta}_o]$ taking the quadratic terms in Equation (19) into account. As seen in Equations (22)-(23), the inclusion of the quadratic terms yields different results for

both the expected value and the variance of f.

$$\begin{aligned}\mathrm{E}\big[f(\mathbf{x})|\boldsymbol{\theta}_o\big]_2 &= f(\mathbf{x},\boldsymbol{\theta}_o) + \frac{1}{2}\sum_{i=1}^{M}\sum_{j=1}^{M}\frac{\partial^2 f}{\partial\theta_i\partial\theta_j}\mathbf{C} \\ &= f(\mathbf{x},\boldsymbol{\theta}_o) + \frac{1}{2}\mathrm{Tr}\big[\mathbf{HC}\big] \end{aligned} \tag{22}$$

Here $\mathbf{H}$ is the Hessian of f, (*i.e.* $H_{ij} := \frac{\partial^2 f}{\partial\theta_i\partial\theta_j}$).

$$\begin{aligned}\mathrm{Var}[f(\mathbf{x})|\boldsymbol{\theta}_o]_2 &= \mathrm{E}\left[\left(f(\mathbf{x},\boldsymbol{\theta}_o) + \sum_{i=1}^{M}\frac{\partial f}{\partial\theta_i}\delta_i + \frac{1}{2}\sum_{i=1}^{M}\sum_{j=1}^{M}\frac{\partial^2 f}{\partial\theta_i\partial\theta_j}\delta\theta_i\delta\theta_j - \mathrm{E}\big[f(\mathbf{x})|\boldsymbol{\theta}_o\big]_2\right)^2\right] \\ &= \mathrm{E}\left[\left(\sum_{i=1}^{M}\frac{\partial f}{\partial\theta_i}\delta\theta_i + \frac{1}{2}\sum_{i=1}^{M}\sum_{j=1}^{M}\frac{\partial^2 f}{\partial\theta_i\partial\theta_j}\left(\delta\theta_i\delta\theta_j - \mathrm{E}\big[\delta\theta_i\delta\theta_j\big]\right)\right)^2\right] \\ &= \sum_{i=1}^{M}\sum_{j=1}^{M}\frac{\partial f}{\partial\theta_i}\frac{\partial f}{\partial\theta_j}\mathbf{C} + \frac{1}{2}\mathrm{Tr}\big[\,(\mathbf{HC})^2\,\big] \end{aligned} \tag{23}$$

If these equations can be inserted into either Equation (17) or Equation (18), then the resulting approach is the so-called *mean-variance robustness approach* [76]. Applications using this approach can be found throughout literature, including: robust-optimal aircraft design [118], robust shape optimization of an airfoil using a weighted sum of performance values [227], etc.

As discussed in Section 5.3.4, the Fisher information metrics to dynamic system identification experiments are already constructed form first-order output sensitivities. Therefore the construction of the mean-variance robustness metrics of Equations (22)-(23) will require $3^t extrd$-order output sensitivities to be calculated, which could prove to be a tedious, if not an intractable, task for complex dynamic systems.

Observation: *The use of deterministic methods for accurate robust design optimization of large, integrated systems requires an automated higher-order sensitivity analysis, which in the case of dynamic systems means higher-order sensitivity time-profiles.*

6.1.2.2 Nondeterministic Approach

Randomized methods may be regarded as direct approaches to robust optimization in that they directly incorporate the uncertainties into a generic optimization problem. According to this formulation, each particular uncertainty source is represented by a random variable with a probability density function. When a system is desired to be optimized, these probability distributions can be sampled many times, and variability in performance and constraints can be observed as probability density functions. Figure 33 illustrates the generic implementation of randomized methods given a modeling and simulation environment that can be evaluated many times.

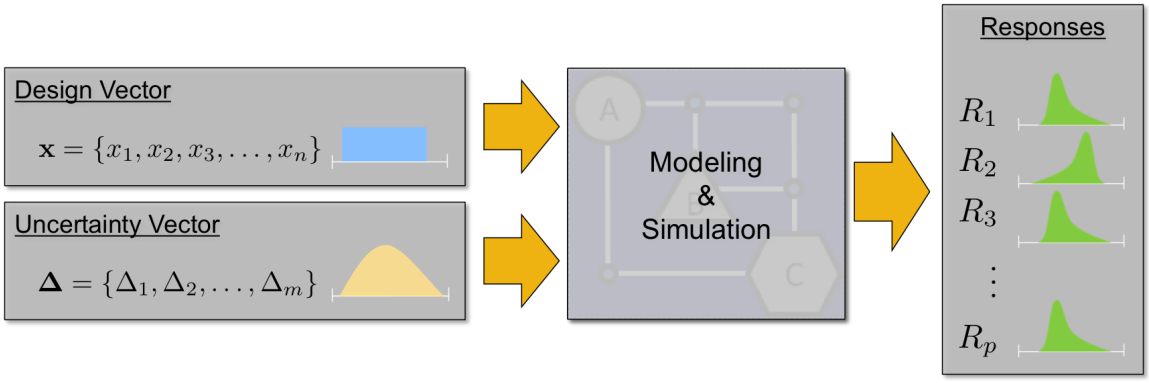

Figure 33: Probabilistic approach to robust optimization.

There are three basic categories for randomized methods: Monte-Carlo strategies, Meta-model approaches, and evolutionary algorithms. These methods enable the ability to directly evaluate the expectancy robustness measures by averaging over a fixed number of samples of uncertainty distributions for fixed design variables. While this approach is very simple to implement, it is often computationally expensive, and with respect to optimization it remains an open issue as to how the degree of accuracy in evaluating robustness is controlled by the number of simulation cases. To alleviate computational expense, response surface methods has become popular, enabling rapid evaluation of optimization metrics and constraints for complex systems.

6.2 Methodology for Robust Design Simulation

Excellent examples of well established RDO techniques applied to complex models can be observed within the field of aerospace systems engineering[1-3]. The methodology considered here is known as robust design simulation (RDS) and has been extensively applied to aircraft systems design and incorporates a nondeterministic approach [194]. The ultimate goal of RDS is to aid the aircraft designer in improving system affordability, over a range of possible operating conditions, by choosing designs from within a set of feasible alternatives. At the core of RDS consists of a sizing and synthesis combined with an environment to simulate its operation [81]. A *sizing and synthesis* is, by definition, multidisciplinary and hierarchical. The implementation of this methodology is illustrated in Figure 34 and is decomposed into five separate steps.

6.2.1 Step 1: Screening Test

Often times for large, complex systems, it is important to minimize the number of design variables before attempting to determine robust-optimal solutions. A technique known as *screening* can be used to reduce dimensionality, which is a particular instance of a sampling-based method for sensitivity analysis [108]. The objective of screening is to identify which input variables are contributing significantly to the output response or uncertainty in high-dimensionality models. If an objective function $f(\mathbf{x})$ is at least once differentiable over the design domain D with respect to each x, $\partial f/\partial x_i|_x$ is a useful criterion for establishing a taxonomy of design variables. Namely:

- if $\partial f/\partial x_i|_{\mathbf{x}} = 0$, $\forall\ x \in D$, the variable x_i can safely be neglected
- if $\partial f/\partial x_i|_{\mathbf{x}} = \text{constant} \neq 0$, $\forall\ x \in D$, the effect of the variable x_i is linear
- if $\partial f/\partial x_i|_{\mathbf{x}} = g(x_i)$, $\forall\ x \in D$, where $g(x_i) \neq constant$, f is nonlinear in x_i
- if $\partial f/\partial x_i|_{\mathbf{x}} = g(x_i)$, $\forall\ x \in D$, where $g(x_i, x_j, ...) \neq \text{constant}$, f is nonlinear in x_i and involved in interactions with other variables

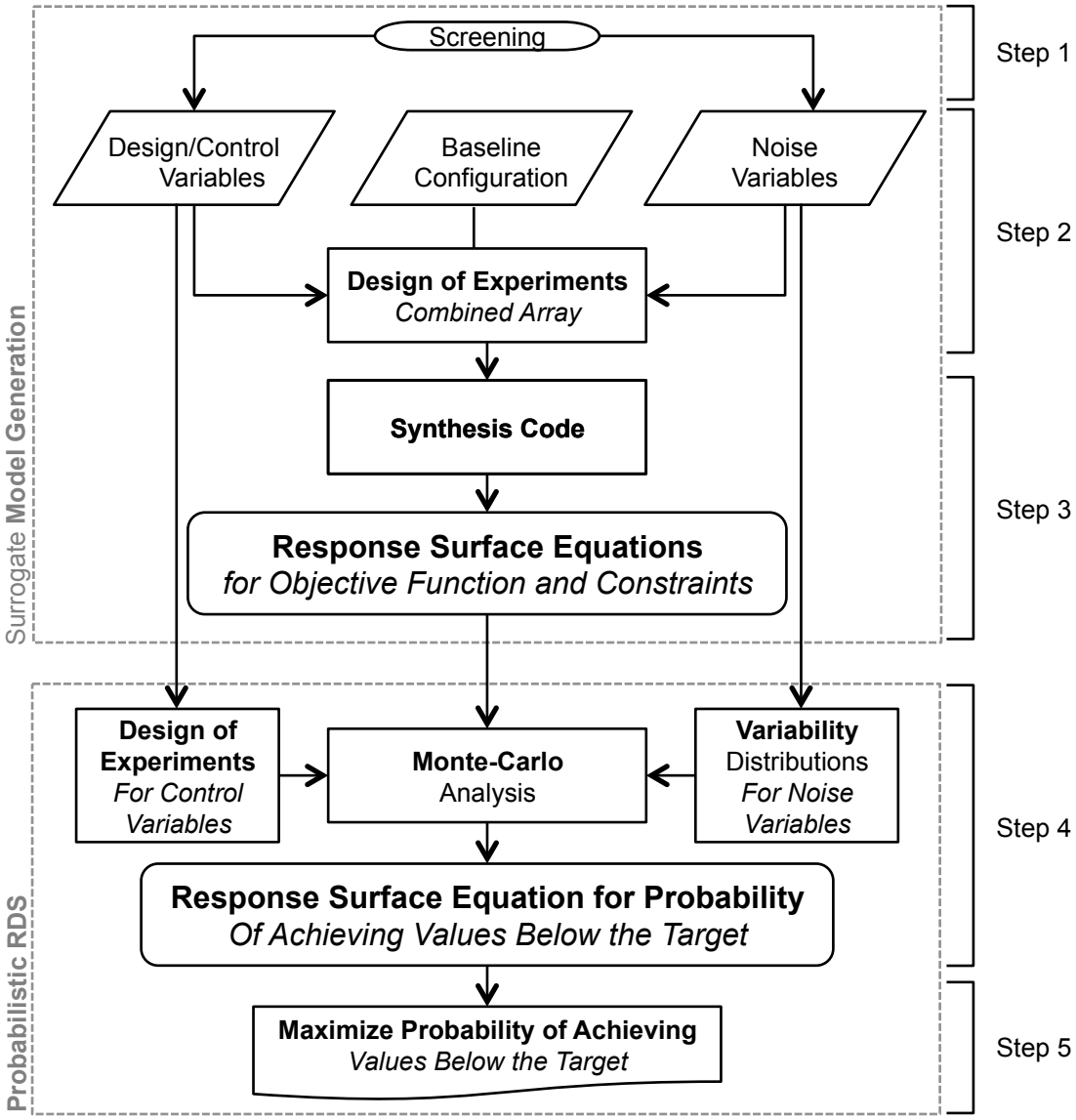

Figure 34: RDS Methodology flowchart [194].

The above classification is merely a statement of terminology, as in practice it is difficult to measure $\partial f/\partial x_i|_{\mathbf{x}}$ across the entire design space. Even a reasonable estimate is a tall order considering that the budget available for the screening study is generally very limited. Rather than exactly quantifying sensitivity, RDS uses factorial experiments to generate sampling plans (*i.e.* factorial DOEs) and an analysis known as *analysis of variance* (ANOVA) to approximate the expected value and influence in the variance in the response for changes in the design variables [158, 219]. This analysis can be used to isolate which factors contribute the most to the variance in the response, where the others are set to constant, nominal values, thus reducing the dimensionality of the design space. This analysis operates on the principle known as the *Pareto Principle*, which states that 20% of the variables in a given system control 80% of the variability in the dependent. Figure 35 shows results of a notional screening test in a form known as a Pareto plot.

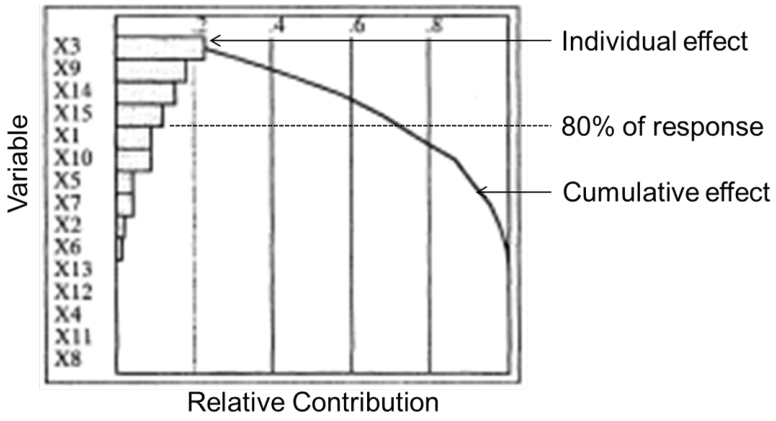

Figure 35: Notional Pareto plot for visual inspection of analysis of variance.

6.2.2 Steps 2 and 3: Response Surface Methodology

The goal of this portion of the RDS methodology is to enable the rapid evaluation of system level objectives and constraints as a function of both control (design) factors and noise variables. The collection of techniques to do this are collectively referred to as *response surface methodology*, which is a methodology for the generation of

multivariate regressions using factorial DOEs [219].

RSM begins by identification of a "true system" (*i.e.* a computational model, a measurable physical process, etc.), which is desired to be approximated. In RDS the system under consideration is a multi-disciplinary, integrated design environment for aircraft sizing and synthesis. The true system can be formulated as shown below for a response y that depends on the controllable input variables $\mathbf{x}$ and sources of statistical error $\boldsymbol{\xi}$ (*i.e.* uncertainty sources, numerical error, etc.).

$$y = f(\mathbf{x}, \boldsymbol{\xi}) \tag{24}$$

RSM is enabled by factorial DOEs to perform an economic number of computational experiments. Using the selected set of variables from the screening test, this DOE should be designed to allow for the estimation of main effects, interactions, and quadratic effects. Examples of factorial DOEs include Taguchi orthogonal arrays, full factorial designs, Latin hypercube designs, and Box-Behnken designs [219]. Figure 36 shows two examples of DOE sampling plans.

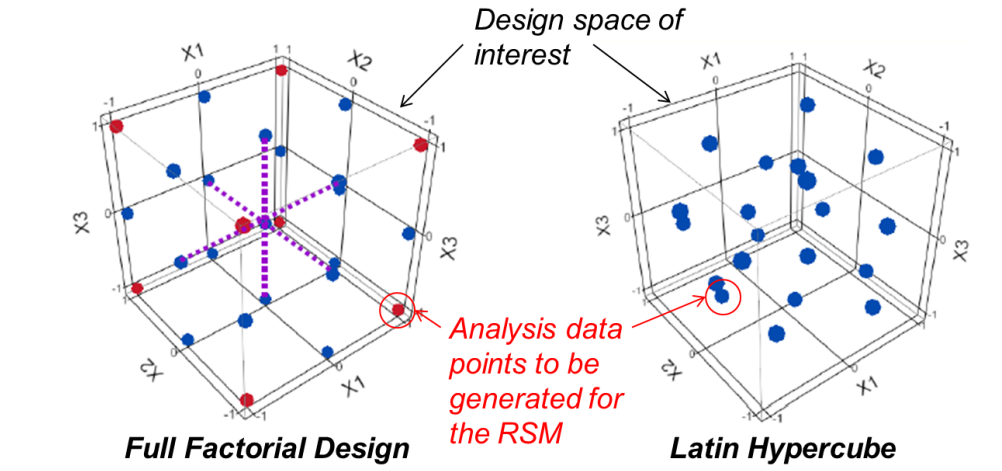

Figure 36: Two common factorial DOE design used within RSM: full factorials and Latin hypercubes..

Using the input/output data provided by the DOE, regression methods can be

used to determine an "approximating function", also referred to as a response surface equation (RSE). Equation (25) shows the typical form of an RSE, where the regression coefficients $\boldsymbol{\beta}$ have been estimated in such a way as to minimize the fit error ε.

$$y = \beta_0 + \sum_{i=1}^{k} \beta_i x_i + \sum_{i=1}^{k} \sum_{j=1}^{k} \beta_{ij} x_i x_j + \varepsilon \tag{25}$$

This is an enabler to RDS methodology, because typically RSE evaluation is much faster than evaluation of the original true system, which is often computationally expensive to run [194]. RSM is flexible in that it enables the rapid evaluation of both system performance and feasibility, as multiple RSEs can be generated for an arbitrary number of objective functions and constraints. RSM is not without drawbacks, however, as there are three main challenges that minimize the effectiveness of RSM for use in large-scale RDO applications when the number of design variables N is large:

- **Model complexity** – in the case of a fully quadratic response surface, $\mathcal{O}(N^2)$ parameters need to be estimated from $\mathcal{O}(N^2)$ function evaluations, which can become prohibitively large when considering large-scale simulation models. Latin hypercube sampling, fractional factorial DOEs, and screening tests only alleviate these issues.

- **Approximation error** – a quadratic response surface only serves as an approximation of the original simulation models, and therefore robust and optimal solutions are approximations. However, unlike Newton strategies for optimization, the meta-model region of approximation is not allowed to shrink arbitrarily as it still has to consider uncertainties.

- **Data uncertainties** – propagate into parameter uncertainties, which implies that the regression analysis should be regarded as a RDO problem itself (*i.e.* a robust response surface) [281].

6.2.3 Step 4: Monte Carlo Analysis

Using the RSEs as stand-in meta-models for the sizing and synthesis environment, the goal of this step is to create an RSE that predicts the probability of achieving (or surpassing) a target value for the system objective function. To identify a robust solution, one must identify those control variables that minimize the influence of noise variables, and shift the mean of the objective towards the target. Once this is done a second DOE is run over the control variables, and for each case in the control-variable DOE, a Monte Carlo (MC) simulation is executed with respect to the noise variables. Because the RSEs can be rapidly evaluated in comparison to the original sizing and synthesis environment, a large number of random samples can be taken to estimate the measures of robustness defined in Section 6.1.2.1. In the case of aircraft design, these MC simulations often require at least 5000 function calls to determine objective function mean and variance to statistical accuracy.

6.2.4 Step 5: Obtain a Robust Solution

Once the probabilistic RSE has been determined, a robust solution can now be obtained by maximizing $P(Y \leq T)$, while satisfying all imposed design and environmental constraints. In addition, relationships between control variables, constraints, and target probabilities can quickly be evaluated, as probabilistic RSE has essentially reduced the RDO problem to an algebraic problem.

6.3 Observations

RDS is a nondeterministic process with the intended end result of aiding informative decision making in systems design [194]. RDS is enabled by RSM, which is used to generate RSEs parameterized by both control and noise variables. RSE generation is, in turn, enabled by the use of DOEs to generate statistically informative data which can be used to perform a regression analysis to generate the RSEs. While not

Table 8: Summary of robust design optimization approaches.

	RDO Approaches	
	Deterministic	**Nondeterministic**
Accuracy	*Asymptotically Accurate*	*Statistically Accurate*
Number of Function Evaluations	*One*	*As many as required for statistical accuracy*
Number of Higher-Order Sensitivities	*As many as required for asymptotic accuracy*	*None*
Enablers	• *Automated sensitivity analysis* • *Taylor series expansins* • *Multivariate polynomial operations*	• *Response Surface Methodology* • *Uncertainty through variability* • *Factorial Design of Experiments*

being specifically tailored for dynamic experiments, this methodology is attractive for several reasons: (i) it is designed to address all the criteria stated in Section 3.3 for designing for knowledge growth to enable decision making early in the acquisition process, (ii) it has been demonstrated on large-scale complex systems, and (iii) it is relatively straightforward to implement.

Where nondeterministic techniques fall short, the deterministic techniques excel in that statistical robustness metrics can be evaluated using a single function evaluation but with higher-order information. Table 8 summarizes useful attributes of both deterministic and nondeterministic RDO approaches. Experience has dictated that calculation of higher-order gradients is not an easy task; however, because at least first-order sensitivity time-profiles are needed to construct the Fisher information matrix, methods to automatically generate this information for models will be considered in the next chapter. To this end, the following observation is made.

Observation: *Sensitivity analysis will play a critical part in enabling RDO for dynamic system identification experiments.*

Provided that higher-order sensitivities exist and are able to be computed in an accurate and timely manner, the following research questions are posed with respect to using this higher-order gradient information to conduct RDO for dynamic system identification experiments.

RQ #6.1: *Can a higher-order sensitivity analysis be used to enable a deterministic approach to robust design optimal control problems for dynamic system identification experiments?*

RQ #6.2: *Can a higher-order sensitivity analysis be used to enable a nondeterministic approach to robust optimal control problems by generating time-profile surrogate models that are parameterized by control parameters and sources of uncertainty (*i.e. *uncertainty in model parameters)?*

The consequences of the first research question imply that the Fisher information expected value and variance can be used, which is similar to the ED-optimality criterion. The R-optimality is also of interest to pursue and to that effect an alternate strategy to RDO would require the optimization of the worst-case scenario of the parameters.

This implies an exploration of the parameter space to find this worst-case scenario. This observation has led to the following additional question, **RQ #6.2**, which could enable a feasible approach to design R-optimal experiments. The consequences of the second research question would be the following: after the up-front effort to compute the higher-order sensitivities, these sensitivities can be used to compute series expansions which can be used to search the parameter uncertainty space. Therefore the computational overhead of evaluating robust information criteria is reduced by requiring a relatively few number of OCPs to be solved across the parameter space.

PART III

Proposed Approach

The last few chapters have been devoted to identifying the limitations of the system identification process and the design of dynamic experiments. To this end, *the circulatory problem* was identified. Solving this problem using a brute-force approach has proven to be intractable for large-scale engineering type problems, which can be formulated as a mixed parameter optimization/optimal control problem. Further, it was observed that a robust-optimal approach is necessary in order to design dynamic experiments efficiently and accurately in the presence of model parameter uncertainties.

The following chapters are devoted to outlining a proposed approach to enable the robust-optimal design of dynamic experiments for model identification. From a theoretical perspective, this approach will be outlined in sufficient detail with the intention of aiding the flight test designer and controls system engineer in the development of information-dense flight test designs for model-identification.

CHAPTER 7

VARIATIONAL ASYMPTOTIC EXPANSIONS

In the last chapter, it was concluded that a new modeling capability is needed for the computation of higher-order state-to-parameter sensitivities for dynamic systems to enable the robust-optimal design of a dynamic system identification experiments. Recall that, in general, this problem is formulated as a mixed optimization/optimal control problem with metrics of performance that are composed of potentially higher-order information. As a suitable starting point towards obtaining this new desired capability, a review of approximation methods is first conducted, followed by a supporting rationale for the proposed use variational asymptotic expansions in dynamic experiment design problems. The remainder of the chapter is devoted to the description of what variational asymptotic expansions are, and it will be shown that this approach can be used to obtain the required capability.

7.1 A Review of Approximation Methods

In literature there are a plethora of techniques to approximate complex models with simple functions. These techniques, known as approximation methods [177], can be broadly classified as (i) regression techniques, (ii) interpolation techniques, and (iii) expansion techniques. Applications of approximation methods have been used in diverse ways within engineering and scientific communities and are well established.

7.1.1 Regression Methods

Regression analysis is a statistical process for estimating the relations among variables and includes many techniques, such as maximum likelihood methods, Bayesian methods, and nonparametric regression methods, just to name a few [170]. Perhaps

the most common technique is linear least squares estimation [219], which operates on a given set of N number of samples from the actual model in a point-value form, $(x_1, y_1), ..., (x_N, y_N)$ which are contaminated by sources of noise ε (e.g. measurement error, human error, etc.). Assuming that the actual process is linear and that the errors are gaussian, the following equation is sought, where the error ε is considered as a random variable.

$$y = \theta x + \varepsilon \tag{26}$$

The goal of linear least squares estimation is to find parameters $\hat{\theta}$ to the linear approximating function below, which results in the minimum-variance, unbiased estimation of the conditional expectation of y given x, $E[y \mid x]$.

$$\hat{y} = \hat{\theta} x \tag{27}$$

It can be readily shown that the best choice of $\hat{\theta}$ is the one that minimizes the sum-of-squares error between the actual measured output y and the predicted output $\hat{y}$, which results in the following well-known result.

$$\hat{\theta} = \left(X^T X\right)^{-1} X^T y \tag{28}$$

The above example highlights several of the advantages and disadvantages of regression techniques. First, it is advantageous to leverage statistical estimation theory to account for the presence of noise, which is commonly present in practice. Next, regression methods provide quantifiable uncertainty bounds on $E[y \mid x]$, which allows the variation of y around the approximating function of Equation (27) to be described by a probability density function. These attributes make regression techniques an attractive approach for experimental methods; however, there are several unattractive features as well. First, application of regression methods often require *a priori* knowledge about the assumed model structure (Equation (26) from the previous example), which is often not readily known. Secondly, the performance of regression techniques

is adversely affected by signal-to-noise content and limited quantities of data and by non-gaussian noise. Recall, from the case study of Chapter 2 that flight experiments of hypersonic vehicles posses many of these problems, as they are excessively conservative and short temporal experiments.

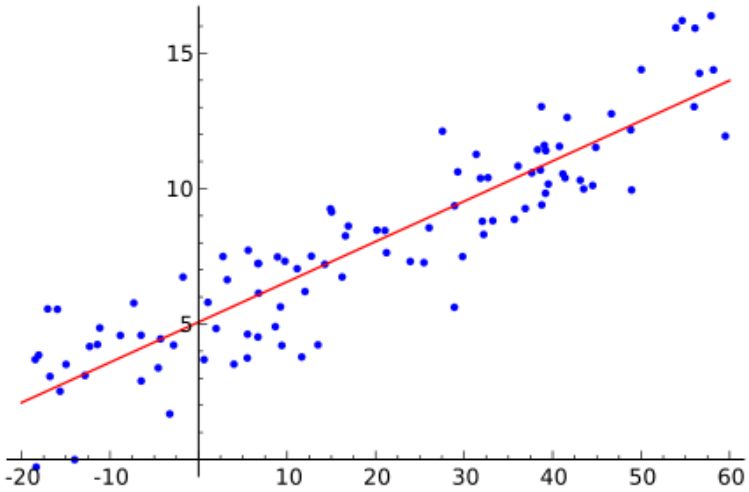

Figure 37: Illustration of linear regression analysis on a data set (blue) and the Least Squares solution (red).

7.1.2 Interpolation Methods

Situations in statistical and scientific analysis arise where the function $y = f(x)$ is available only at $N+1$ tabulated points $(x_1, y_1), ..., (x_N, y_N)$, and a method is needed to approximate $f(x)$ at nontabulated abscissas [191]. If there is a significant amount of error in the tabulated values, then regression methods should be employed; however, if these points are known to a high degree of accuracy then interpolation is preferred. Interpolation can be thought of as an approximation method for the construction of new data points within the range of the known tabulated points $(x_1, y_1), ..., (x_N, y_N)$, which are contained within some interval $a \leq x \leq b$ and are commonly obtained through sampling or experimentation. The topic of interpolation encompasses many techniques [132, 191], including: piecewise constant interpolation, linear interpolation, spline interpolation, etc. Even the evaluation of an approximating function obtained

from a regression analysis can be considered as interpolation. If evaluation points are selected that are outside of the bounded interval, then this is alternatively called "extrapolation". Extrapolation is usually undesired, as it is known that the error between the extrapolation value and the true value can grow significantly for values that are even close to the bounds of the tabulated points; however, there are methods that attempt to alleviate these issues, such as the inclusion of higher-order derivative information at tabulated values [272].

Polynomial interpolation methods are a common approach for approximating complicated functions to a high degree of accuracy and low computational expense. Equation (29) is a common example of an approximation polynomial, known as Lagrange polynomials [191].

$$f(x) = \sum_{k=0}^{N} y_k \left[\prod_{l \neq k}^{N} \frac{x - x_1}{x_k - x_0} \right] \tag{29}$$

When evaluated at the equally-spaced tabulated values, the Lagrange polynomial of equation (29) coincides with the tabulated points. Beyond providing an efficient approach to approximate complex functions, this approach also provides easy access to roots, derivatives, etc. Of course, when a simple function is used to estimate data points from the original, interpolation errors are usually present. This has led to the implementation of other polynomial approximations, such as Chebyshev and Legendre approximations, and different sampling strategies, such as Chebyshev nodes.

In general, interpolation methods are not very practical for implementation with experimental methods. This is primarily due to the existence of noise in the sampling of the tabulated values. This can be overcome by a high amount of repetitive experiments. Another limitation is the inaccuracies of extrapolation. In light of these deficiencies, if/when possible, a polynomial approximation to a more complex model should be obtained, as they enable cheap access to evaluations, derivatives, roots, etc. which is increasingly valuable for model complexity increases.

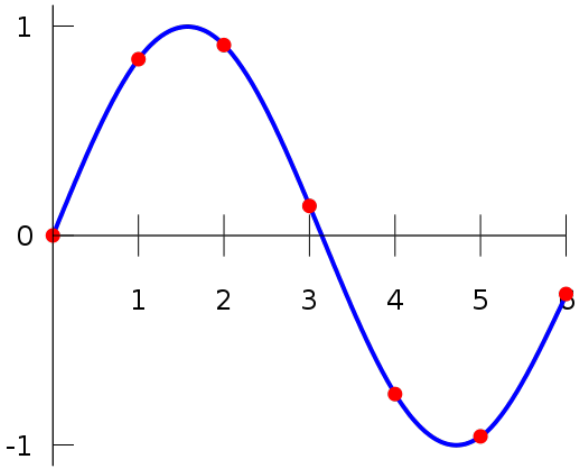

Figure 38: Plot of the sampled data from $\sin(x)$ with spline interpolation applied.

7.1.3 Expansion Methods

In mathematics, a Taylor series is a representation of a function as an infinite sum of terms that are calculated from the values of the function's derivatives at a single point. It is common practice to approximate a function by using a finite number of terms of its Taylor series, which is called a Taylor polynomial. Equation (30) shows the well known form of a N^{th}-order Taylor series expansion, centered at x_0, and an error term $E_N(x)$, which is included to enforce the equality with $f(x)$.

$$f(x) = \sum_{k=0}^{N} \frac{f^{(k)}(x_0)}{k!} (x - x_0)^k + E_N(x) \tag{30}$$

Here it is observed that if the function $f(x)$ is differentiable up to order N at a point x_0, then the expansion of Equation (30) can be constructed to provide a local approximation $f(x)$ in a local region x_0. This means that the approximation of $f(x)$ using the Taylor series expansion at values of x which are farther and farther away from x_0 will be less accurate as the error term $E_N(x)$ grows. A useful aspect of Taylor series expansions is that this error growth can be quantified with the use the $(N+1)$-order derivative of $f(x)$, as shown below.

$$E_N(x) = \frac{f^{(N+1)}(c)}{(N+1)!}(x - x_0)^{N+1} \tag{31}$$

Here, $f^{(N+1)}(x)$ is evaluated at some value $c = c(x)$, which lies between x and x_0, in such a way as to determine the upper bound of the error.

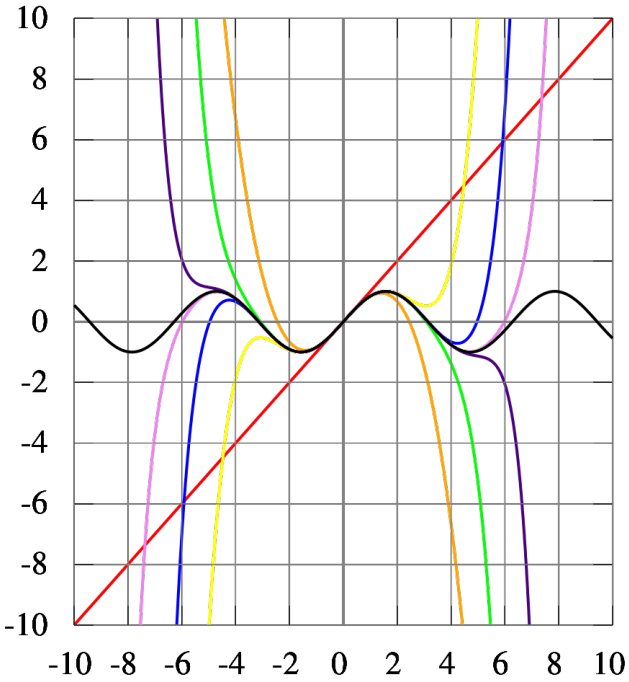

Figure 39: As the degree of the Taylor polynomial rises, it approaches the correct function. This image shows $\sin(x)$ (black) and its Taylor approximations, polynomials of degree 1 (red), 3 (orange), 5 (yellow), 7 (green), 9 (blue), 11 (purple) and 13 (pink).

As approximating functions, Taylor series expansions have the potential to provide an arbitrarily high degree of accuracy in a local region of arbitrarily large size with quantifiable error bounds. Thus, it can be deduced that rapid evaluation of any function $f(x)$ is possible if a Taylor series expansion is constructed using a suitably high number of terms to (i) control the error growth and (ii) expand the region of approximation. There are, however, a number of shortcomings that have limited the use of expansions in practice. First, the determination of higher-order derivative information is often difficult in practical applications, as symbolic differentiation and

finite differences quickly become intractable. Secondly, numerical precision becomes a significant issue if the numerical conditioning of coefficients degrades with increasing number of terms. Thus, as increasing accuracy is desired and more terms are included, numerical precision can have an increasingly adverse effect on accuracy. Finally, these series are not always guaranteed to converge for all values of x. This has been observed for even simple functions, where an asymptotic limit of convergence, called the radius of convergence, is often encountered. Approaches to mitigate these issues will be elaborated upon in subsequent discussion.

7.1.4 Observations

Regression, interpolation, and expansion techniques are all capable of providing a mathematical relations between the input(s) and output(s) of the determined model. Each of these approaches has advantages and disadvantages, but the expansion approach to building approximations, only requires a single "data point" and the associated higher-order gradient information at that point. In practice these expansions must be truncated at a certain point when higher-order terms are determined to be negligible. In this case, the resulting approximation is a polynomial called an **asymptotic expansion** (AE). Of course, in the larger context of dynamic experiment design, a "data point" is analogous to a solution of a dynamic system, but the idea still applies and in this case it is called a **variational asymptotic expansion** (VAE), as will be discussed in the next chapter. In past examples, expansion methods have proven a useful tool to the construction of models, such as a Taylor series expansion to approximate trigonometric functions. In most of these cases gradient information was provided by Taylor series identities that were readily available through theory; however, if higher-order gradient information can be obtained then the following question is posed.

Research Question: *Is it practical to utilize higher-order gradient information to generate effective and accurate surrogate models from asymptotic expansions, which can be used for the design of robust-optimal dynamic experiments for system identification?*

In the past, certain limitations have lead engineers and scientists to answer the above question as "no"; however, certain recent mathematical and computational advancements might lead to a different answer. These advancements will be discussed in the following chapters.

Figure 40 illustrates the potential benefit using VAEs to form a mixed multi-function, multi-variate surrogate model. In essence, the construction of a surrogate model using a regression analysis enabled by a DOE, consisting of a factorial number of experiments, can potentially be replaced by a single experiment, which uses higher-order gradient information to construct a model using an asymptotic expansion. Indeed this could prove to be a beneficial and desirable approach in situations where experiments are costly to run (e.g. solving OCPs using high-fidelity models), or it is difficult to evaluate a certain portion of a design space (e.g. flight envelope expansion, unstable vehicle concepts, etc.).

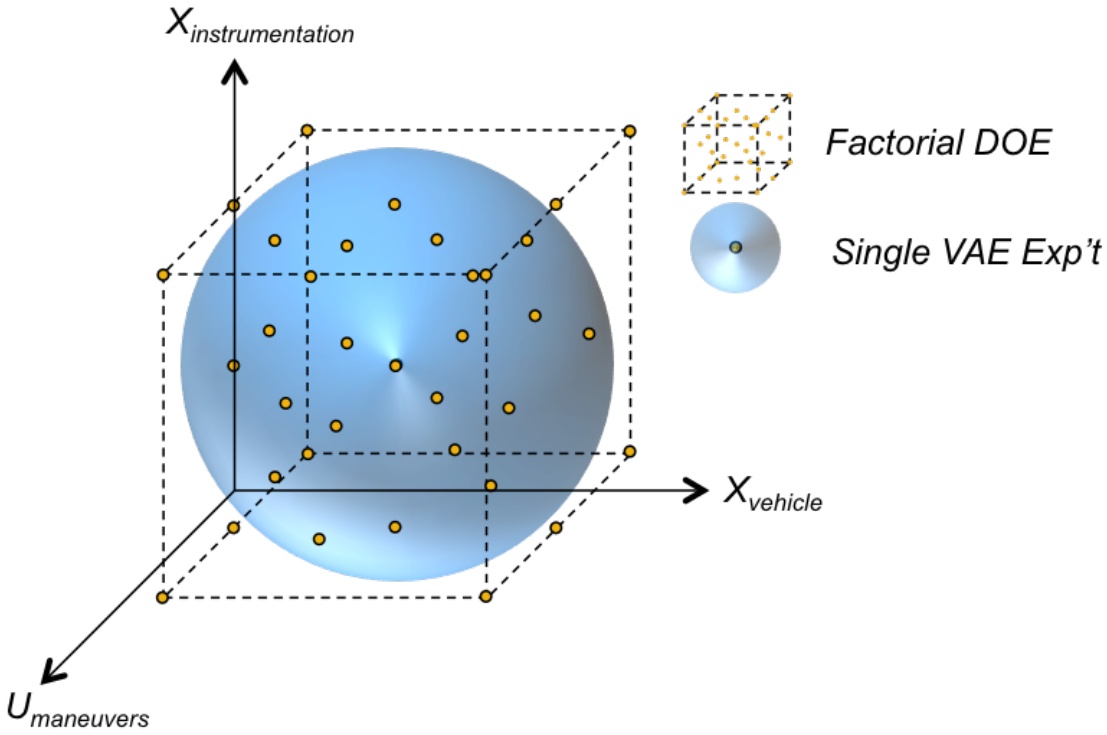

Figure 40: An illustration of the potential for VAE surrogates to be generated from higher-order gradient information of a single experiment, which can be parameterize by design variables (e.g. vehicle design and instrumentation system design) and design functions (e.g. maneuver design).

7.2 Perturbation Methods & Asymptotic Analysis

Asymptotic expansions are used within the area of perturbation methods to generate approximations to solutions of problems that arise from physics. These methods belong to a branch of applied mathematics, which is typically considered a separate analytical approach to implementing numerical methods [139, 142]. Perturbation methods and numerical methods are not, however, in competition but are rather complementary of one another (to be discussed further in later sections).

In practice perturbation methods are applied more often than is typically realized, including power series solutions of differential equations [173], linearization analysis [98, 99], and algorithmic (automatic) differentiation [122]. A relevant example is the linearization of aircraft dynamic models. Based on small perturbations about an operating point such as the conditions for steady-level flight, a linearized dynamic model can be constructed. These linearization techniques have proven useful in aircraft stability analysis and the design of flight controllers; however, this process is often tedious and requires a manual derivation using the equations of motion and simplifying assumptions. Further, the accuracy of aircraft linearization techniques degrades significantly as an aircraft moves away from the considered operating point. This means that if the entire flight envelope of an aircraft is desired to be considered, then multiple linear models must be constructed and analyzed. This is often an intractable approach.

One advantage of employing perturbation methods is that they can be utilized on a diverse set of mathematically formulated problems, including the solution of quadratic equations, eigenvalue problems, integrals and derivatives, and ordinary and partial differential equations. In all these applications, a solution is obtained using an asymptotic expansion that is parameterized with respect to a set of operating parameters of interest. The result is a parameterized family of solutions, providing for rapid access to how problem solutions vary with respect to parameters of interest

without the need to re-solve the problem. This is an especially attractive feature in the advent of large problems, where obtaining a solution can require much time and effort.

7.2.1 A Notional Example

As a notional example to illustrate how asymptotic expansions work, consider the algebraic problem of root-finding.

$$f(x, \varepsilon) = 0 \tag{32}$$

Here the variable x is the unknown scalar variable of interest, ε is a scalar parameter of the equation, and f is a known function (model). The objective here is of course to find the value x^*, which solves the equation; however, it is common in physical systems to not know the true value of the system parameters. Thus, it is typically desired to understand how the solution behaves as a function of the unknown parameter ε in which case $x^*(\varepsilon)$ is desired. Usually the parameter is assumed some *a priori* nominal value ε_0 and uncertainty bounds $\varepsilon_l \leq \varepsilon \leq \varepsilon_h$. To begin, an asymptotic expansion is postulated out to some desired number of expansions N, using an assumed set of basis functions $(\phi_n(\varepsilon) \,\forall\, n = 0, 1, ..., N)$. A convenient choice is often to select the monomial basis for the asymptotic expansion $(1, \varepsilon, \varepsilon^2, ..., \varepsilon^N)$. Equation (33) is an asymptotic expansion.

$$x(\varepsilon, \varepsilon_0) \approx \sum_{n=0}^{N} a_n \phi_n(\varepsilon) = a_0 + a_1\varepsilon + a_2\varepsilon^2 + \ldots + a_N\varepsilon^N \tag{33}$$

Next, the asymptotic expansion is substituted into $f(x, \varepsilon)$ and powers of like-terms are collected, which produces a system of equations to solve for the unknown coefficients $(a_0, a_1, a_2, \ldots, a_N)$.

$$f(x(\varepsilon), \varepsilon_0) = f_0 + f_1\varepsilon + f_2\varepsilon^2 + \ldots + f_N\varepsilon^N = 0 \tag{34}$$

$$f_0(a_0, a_1, \ldots, a_N) = 0 \tag{35}$$

$$f_1(a_0, a_1, \ldots, a_N) = 0 \tag{36}$$

$$\vdots \tag{37}$$

$$f_N(a_0, a_1, \ldots, a_N) = 0 \tag{38}$$

Solving these equations for the unknown coefficients and substituting them back into the asymptotic expansion of Equation (33) results in the desired behavior $x^*(\varepsilon)$.

$$x^*(\varepsilon, \varepsilon_0) \approx a_0 + a_1\varepsilon + a_2\varepsilon^2 + \ldots + a_N\varepsilon^N \tag{39}$$

This solution is centered about the nominal parameter ε_0, meaning that the approximation is accurate to a specified tolerance only for values of ε that are suitably close to ε_0. In theory, using an asymptotic expansion with a higher number of terms N can expand the region of accuracy to an arbitrary size. This idea of controlling accuracy with the number of expansion terms will be discussed in more detail in Chapter 9.

7.2.2 An Important Connection to Calculus

Asymptotic expansions have a remarkable connection to calculus, which as been computationally exploited in recent years (discussed in the next section). As a starting point, observe that the asymptotic expansions of Equations (33) and (39) bear a similar resemblance to Maclaurin series expansions [57, 173] (*i.e.* Taylor series expansions for $\varepsilon_0 = 0$). Indeed, an asymptotic expansion can easily be converted to the form of a Taylor series expansion by equating coefficients.

$$x^*(\varepsilon) \approx \sum_{n=0}^{N} a_n\varepsilon^n = \sum_{n=0}^{N} \frac{x^{(n)}(\varepsilon)}{n!} \tag{40}$$

$$x(0) = a_0 \tag{41}$$

$$\frac{dx(0)}{d\varepsilon} = a_1 \cdot 1! \tag{42}$$

$$\frac{d^2x(0)}{d\varepsilon^2} = a_2 \cdot 2! \tag{43}$$

$$\vdots \tag{44}$$

$$\frac{dx^N(0)}{d\varepsilon^N} = a_N \cdot N! \tag{45}$$

Algebraic manipulation of asymptotic expansions with each other is nothing more than an implementation of*the chain rule of calculus* [263], which has a profound implication about the ability of asymptotic expansions to be used for calculating derivatives of models. Figure 41 outlines a generic process to show how asymptotic expansions can be used to calculate higher-order derivatives of a function with respect to an arbitrarily chosen parameter or variable. It can be observed here that the model structure is unaltered, but that instead of using arithmetic on variables, arithmetic operations are conducted on polynomials as expansions interact internally within the model.

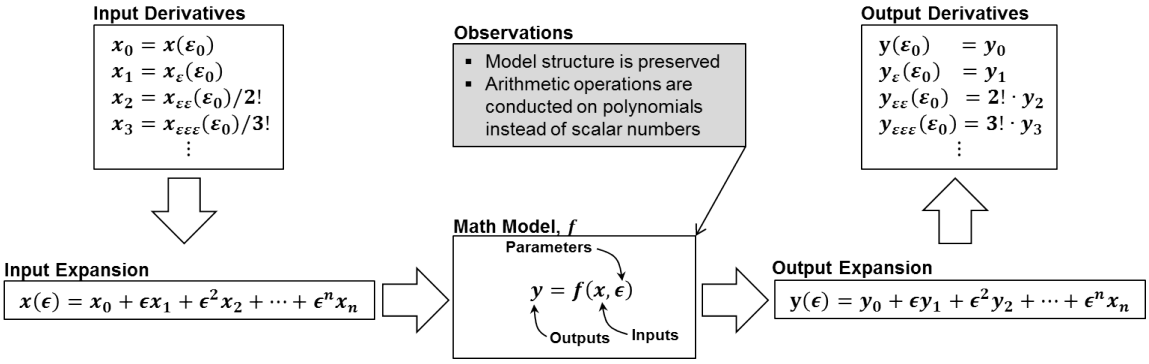

Figure 41: The relationship between asymptotic expansions and the computation of higher-order gradient information.

7.2.3 Automatic Differentiation

In recent years a computational tool known as automatic differentiation [122, 221, 234] has emerged as a systematic way of calculating gradients of a function specified by a

computer program. Indeed this is nothing more than an implementation of the process outlined in Figure 41. A brief explanation is given here to provide a foundation for potential computational implementation of asymptotic expansions in later sections.

Def. (*Automatic Differentiation*) – Using data overloading techniques, specified dependent variables are recast as N^{th}-order asymptotic expansions, enabling the chain rule to be used to compute up to N^{th}-order derives with respect to variables and parameters of interest, which are accurate to machine precision [121].

Automatic differentiation exploits the fact that computer programs, no matter how complicated, executes a sequence of elementary arithmetic operations ($+$, $-$, $\times$, $\div$, etc.) and elementary functions (exp, log, sin, cos, etc.), and by applying the chain rule repeatedly to the operations, derivatives of arbitrary order can be computed (i) automatically, (ii) accurately to working precision, and (iii) using at most a small constant factor more arithmetic operations than the original program. This is not the case when using the classical methods to calculating derivatives listed below, where the complexity of calculating higher derivatives increases exponentially.

- *Symbolic Differentiation* – a human-in-the-loop process; faces the difficulty manual developing efficient code.
- *Numerical Differentiation* – employs the method of finite differences; can introduce round-off errors in the discretization process and cancellation.

Figure 42 illustrates the differences between automatic differentiation and symbolic differentiation, which shows that only a given function $f(x)$ needs to be programmed and AD can then be invoked to compute the derivative.

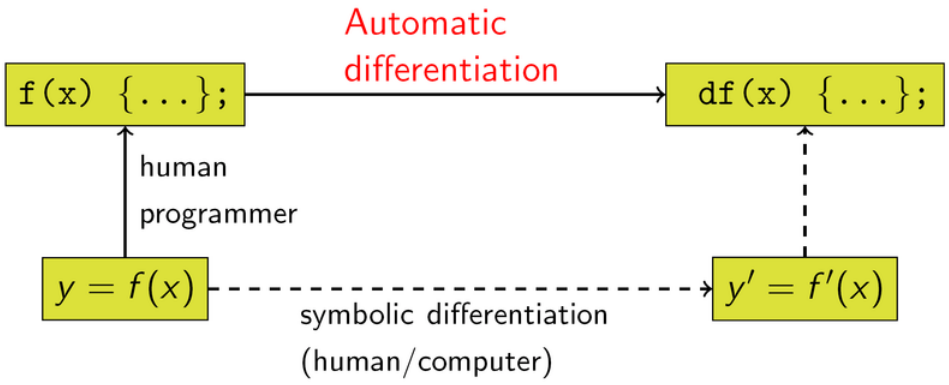

Figure 42: How automatic differentiation relates to symbolic differentiation.

Automatic differentiation has been successfully applied to scientific and engineering problems, including applications such as: numerical methods [15, 245], sensitivity analysis [60, 61, 126, 226], design optimization [39, 73, 245, 267], data assimilation, and inverse problems [15], just to name a few. One appealing aspect of automatic differentiation is that tools are readily available to be used as wrappers around code. Some of the more popular include: ADIFOR (a FORTRAN implementation) [37, 38, 40], ADOL-C (a C/C++ implementation) [121, 277, 278], and ADIMAT (a Matlab implementation) [39, 41].

7.3 Asymptotic Analysis Applied to Ordinary Differential Equations

7.3.1 Existence of Families of Solutions

Of interest to this work, is the application of perturbation methods to generate variational asymptotic expansions to approximate families of solutions to ordinary differential equations (ODEs), which are mathematically structured as follows:

$$\dot{x} = f\left(t, x, \varepsilon\right) \tag{46}$$

Recall from Equations (1)-(3) of Section 4.3.1 that this was the observed generalized model structure of aircraft dynamic models, and in Section 4.3.2 it was observed that these equations are used within an optimal control problem formulation to design

optimal inputs, which can be solved using direct methods (initial value problems (IVPs)) or indirect methods (boundary value problems (BVPs)). Figure 43 illustrates how each of these problem types operate on system of ODEs. As can be observed, the two different formulations to solving ordinary differential equations both result in unique solutions; however, parameterizations of families of solutions differ.

- **Initial Value Problems** – families of solutions are unique to values of initial time t_0, initial conditions of state variables x_0, and system parameters ε.
- **Boundary Value Problems** – families of solutions are unique to values of boundary conditions (t_0, t_F, x_0, x_F) and system parameters ε. Usually for this problem formulation, only a subset of the boundary conditions are known and the others are solved for when a solution is obtained.

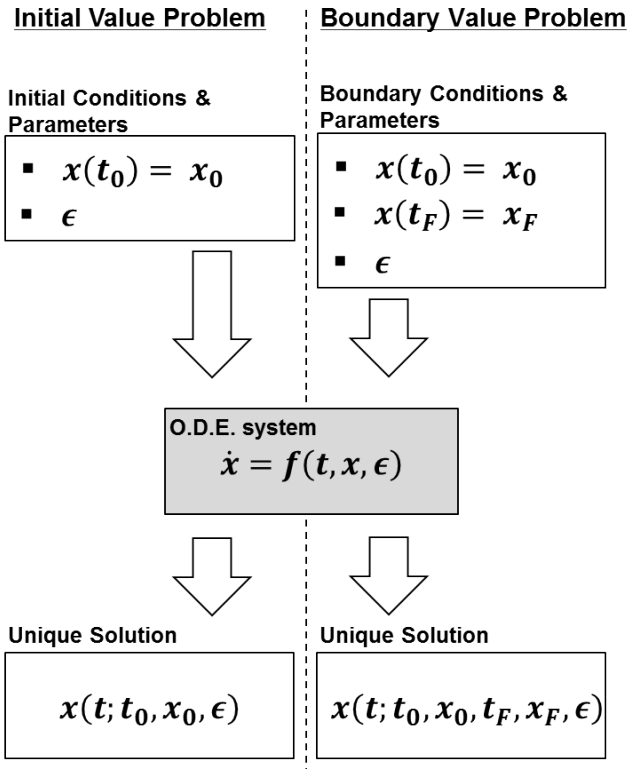

Figure 43: Two different formulations to solving ordinary differential equations both result in unique solutions but parameterizations of families of solutions differ.

In the general sense the existence and uniqueness of solutions to ODEs is not guaranteed; however, the theorem below provides the necessary and sufficient conditions for this to be the case. Usually flight dynamic models for aircraft motion satisfy this theorem, and therefore for purposes of this thesis, existence and uniqueness will be assumed for the original dynamic system.

Thm.#1 (*Existence and Uniqueness*) – If $f(x(t), \varepsilon; t)$ is analytic (*i.e.* well-behaved; smooth and bounded), then $x(t_0, x_0, \varepsilon; t)$ exists and is a deterministically repeatable solution given the values (t_0, x_0, ε) [138, 71, 127].

From the theory of equations of variation (*i.e.* variational calculus), it is known that families of solutions can be represented as a *variational series expansions* [96, 113, 120]. The concept is useful to describe the incremental changes in functions due to various sources of perturbations.

$$x(t) + \Delta x(t) = x(t) + \delta x(t) + \delta^2 x(t) + \text{H.O.T.} \tag{47}$$

Here, the term $\Delta x(t)$ is a perturbation term, which can be also represented as a variational expansion $\delta x(t) + \delta^2 x(t) + \text{H.O.T.}$ The variational expansion is a summation of terms, where each one represents the perturbative effects of a certain order. Each of these terms is a time-varying entity of designated order. Using an application of the chain rule, these terms can be represented as the multiplication of a solution to an equation of variation and a scalar perturbation variable. Equation (48) shows an example of a *variational asymptotic expansion* for an IVP-type problem, where the perturbative effects of parameters and initial conditions are considered up to the 2^{nd}-order.

$$
\begin{aligned}
x(t) + \Delta x(t) = x(t) & \\
& + \left(\frac{\partial x(t)}{\partial x_0} \delta x_0 + \frac{\partial x(t)}{\partial \varepsilon} \delta \varepsilon \right) \\
& + \frac{1}{2!} \left(\frac{\partial^2 x(t)}{\partial x_0 \partial \varepsilon} \delta x_0 \delta \varepsilon + \frac{\partial^2 x(t)}{\partial x_0^2} \delta^2 x_0 + \frac{\partial^2 x(t)}{\partial \varepsilon^2} \delta^2 \varepsilon \right) \\
& + \text{H.O.T.}
\end{aligned} \tag{48}
$$

7.3.2 Solutions to Higher-Order Equations of Variation

Using expressions for variational asymptotic expansions like the one in Equation (48), it is possible to construct a parameterized model to approximate families of solutions, but this requires the sensitivity time-histories (*i.e.* $\partial x(t)/\partial x_0$, $\partial x(t)/\partial \varepsilon$, $\partial^2 x(t)/\partial x_0 \partial \varepsilon$, etc.) to be determined. Recall that it was observed in Section 5.3.4 that the parameter-output sensitivity time-histories could be calculated from Equations (12) and (13). These equations are again in the form of system of ODEs, which were obtained through differentiation of the original dynamic system (Equations (1)-(3)) with respect to the system parameters. Therefore it can be shown that calculation of higher-order sensitivities can be done by solving higher-order systems of ODEs, which can be derived from the original system.

In the area of ordinary differential equations, the idea of differentiating systems of ODEs to obtain higher-order systems has been considered thoroughly [69, 71, 127, 138]. There are a number of supporting theorems that suggest the existence and uniqueness of these higher-order equations, called *equations of variation*. As a starting place, consider the 1$^{\text{st}}$ equation of variation, where it is desired to obtain 1$^{\text{st}}$-order sensitivity time-histories. Given that **Thm.#1** holds true for the original system, the following theorem can be applied to determine the existence and uniqueness of the first equation of variations. This simply states that if the original system is able to be differentiated, then a unique solution to the resulting system exists.

Thm.#2 (*Continuous Dependence*) – If $f(t, x, \varepsilon)$ is C^1 with respect to (t, x, ε) (*i.e.* has continuous first derivatives), then solutions to first order linear equations of variation exist and are unique.

Since the general dynamic system $f(t, x, \varepsilon)$ depends continuously on the initial time t_0, initial states x_0 and parameters ε, resulting in the unique existence of 1^{st}-order systems with respect to each of these parameters. Outlined below, are the 1^{st}-order equations of variation for an IVP-type problem. Note: the associated initial condition expression must also satisfy **Thm.#2** [127].

- 1^{st}-order continuous dependence on parameters:

$$\begin{aligned} &\frac{d}{dt}\left(\frac{\partial x}{\partial \varepsilon}\right) = \frac{\partial f}{\partial x}\frac{\partial x}{\partial \varepsilon} + \frac{\partial f}{\partial \varepsilon} \\ &\frac{\partial x\,(t_0)}{\partial x_0} = 0 \end{aligned} \tag{49}$$

- 1^{st}-order continuous dependence on initial conditions:

$$\begin{aligned} &\frac{d}{dt}\left(\frac{\partial x}{\partial x_0}\right) = \frac{\partial f}{\partial x}\frac{\partial x}{\partial x_0} \\ &\frac{\partial x\,(t_0)}{\partial x_0} = 1 \end{aligned} \tag{50}$$

- 1^{st}-order continuous dependence on initial time:

$$\frac{\partial x}{\partial t_0} = -\frac{\partial x}{\partial x_0} f(t_0, x_0, \varepsilon) \tag{51}$$

And indeed, using **Thm.#2**, it has been shown that the solutions of Equations (49)-(51) can be used to construct a linear approximation for the family of solutions to the original system, which can also be viewed as a 1^{st}-order variational asymptotic expansion for some operating point described by (t_0,x_0,ε).

$$x(t) + \Delta x(t) \approx x(t) + \frac{\partial x(t)}{\partial t_0}\delta t_0 + \frac{\partial x(t)}{\partial x_0}\delta x_0 + \frac{\partial x(t)}{\partial \varepsilon}\delta\varepsilon \tag{52}$$

Continuous dependence on parameters can be extended to higher-order if it can be shown that higher-order derivatives of the original system exist with respect to t_0,x_0,ε).

Lemma (*Extension to Thm.#2*) – If $f(t, x, \varepsilon)$ is C^n for all $n = 0, 1, 2, \ldots, N$, then higher-order (up to n^{th} order) equations of variation exist and are unique.

Figure 41 illustrates how variables and parameters can be substituted for with asymptotic expansions, which interact algebraically with each other as polynomials, preserving the overall algebraic structure of a dynamic system. Indeed, this concept also applies to the ODE model structure of Equation (46), when considering the state derivative $\dot{x}$ as simply the output of $f(t, x, \varepsilon)$. Figure 44 illustrates the effect of substituting asymptotic expansions into a scalar ODE to generate higher-order state-parameter sensitivity state derivatives. Of course, these sensitivity state derivatives are mathematically equivalent to their corresponding equations of variation and can be numerically integrated using standard numerical techniques.

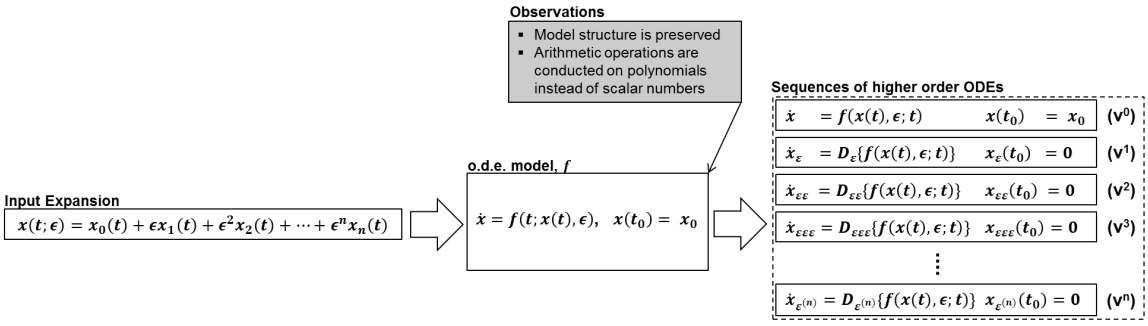

Figure 44: The relationship between asymptotic expansions and the computation of higher-order state-parameter sensitivity derivatives. As a result of **Thm.#2**, all higher-order sensitivity initial conditions are zero.

7.4 Summary

In this chapter it was shown that it is theoretically possible to construct VAEs to parameterize families of solutions for ODE systems; however, at this point the extent to which this is able to be practically implemented from a computational standpoint is still uncertain. For example, if it is desired to accommodate multiple parameters, then VAEs can be constructed that are equivalent to multivariate Taylor-series expansions, which are known to scale very poorly for increasingly higher orders and large dimensions. Discussion of this and other issues are the topic of following chapters, which are focused on illuminating any potential inhibiting factors to the practical implementation and feasible computation of VAEs.

CHAPTER 8

TEMPUS: A DYNAMIC EXPERIMENT DESIGN METHODOLOGY

The focus of this chapter is the presentation of the TEMPUS methodology for the concurrent design of information-dense dynamic experiments which are robust, or insensitive, to sources of modeling uncertainties. The proposed methodology is called TEMPUS, which stands for **T**ime-dynamic **E**xperiment design using a **M**odel-based approach to **P**ropagate **U**ncertainty for **S**ystem identification. Since this is a model-based approach, assumed parameters and models that make-up a given physics-based integrated environment will lead to inaccurate estimation of the expected information yield in a given conducted experiment. This problem was identified in Section 5.2 as *the circulatory problem* and will now be directly addressed within the TEMPUS integrated design methodology to design dynamic experiments by utilizing VAEs to quantify robustness measures.

The objective of the TEMPUS methodology is to provide the flight test designer and control systems engineer with the capability to automatically and accurately assess the information quality of simulated dynamic experiments (i.e. flight test designs), implementing flight dynamic models in a business-as-usual fashion – meaning that higher-order *equations of variation* are not derived and directly implemented by the programmer but are instead computed at runtime from the original system via the automatic differentiation approach discussed in the previous chapter.

8.1 Integrated Design Methodology

Using the top-down design decision support process within the Georgia Tech **I**ntegrated **P**roduct/**P**rocess **D**evelopment methodology (GT-IPPD) [193], TEMPUS fuses elements from two existing experiment design methodologies (previously discussed) to enable an integrated design approach to the development of large-scale dynamic system identification experiments.

- Dynamic Robust-Optimal Experiment Design (R-OED) by Asprey and Macchietto [17] – a flexible methodology for the model-based design of dynamic model-identification experiments, being used for sequential, Bayesian, and minimax design approaches; discussed previously in Section 5.3.

- Robust Design Simulation (RDS) by Mavris [194] – has been extensively applied to aerospace systems design problems, incorporating a nondeterministic approach that is enabled by response surface methodology; discussed previously in Section 6.2.

Figure 45 shows the high-level mapping of the TEMPUS methodology to the top-down design decision support process with the application of hypersonic flight testing in mind. The generation of feasible design alternatives is achieved via a sizing and synthesis method, providing for the concurrent design of measurement system parameters, control system architecture and parameters, probabilistic uncertainty models, aero-thermal-fluids models, design constraints, and even vehicle geometry and mission-level parameters. To assess the performance of a given experiment design, a variety of different information quality metrics are able to be calculated from a dynamic high-order sensitivity analysis, providing for an *a priori* estimate of expected goodness-of-fit quality in the *a posteriori* parameter estimators. To evaluate feasible alternatives, a virtual experimentation strategy is utilized to assess information performance metrics of a given alternative via nondeterministic Monte Carlo techniques.

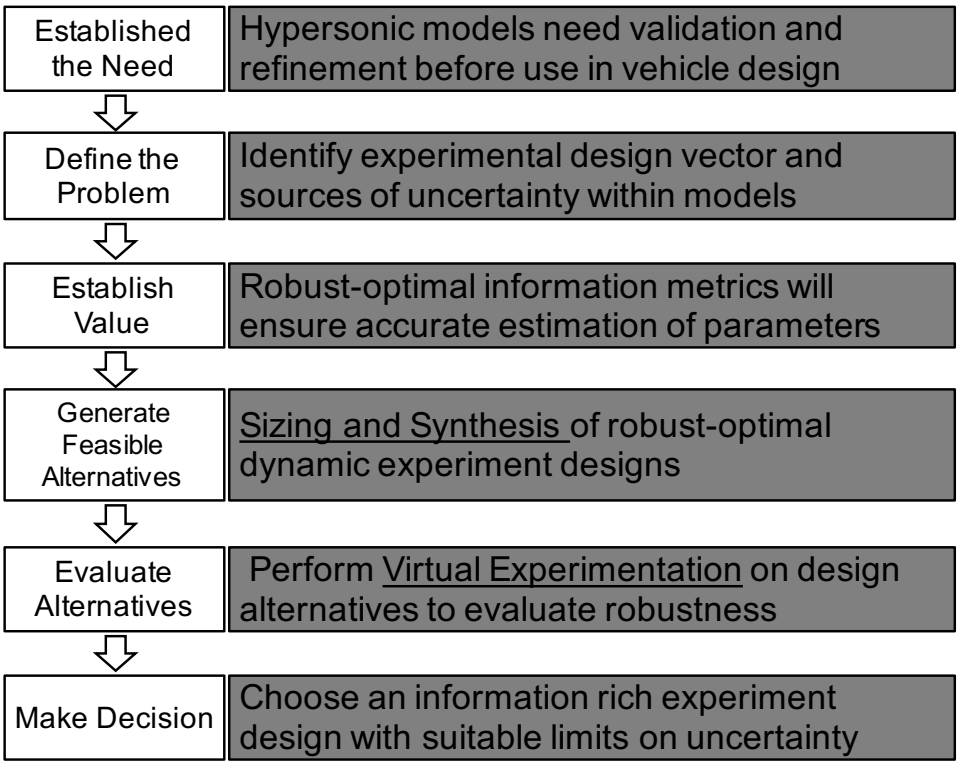

Figure 45: The TEMPUS methodology, derived from the top-down design decision support process of the the GT-IPPD [193] for the design of high information dynamic experiments which are robust with respect to sources of model parameter uncertainty.

8.2 Sizing and Synthesis of Optimal Information Experiments

Using elements of the R-OED methodology proposed by Asprey and Macchietto [17], TEMPUS utilizes the sizing and synthesis method shown below in Figure 46 to generate robust-optimal information experiments. In contrast to R-OED, this routine does not evaluate the robustness of the experiments using brute-force or nondeterministic approaches, but instead utilizes automatic differentiation to compute robust-optimal information metrics using a flexible approach, evaluating VAEs either deterministically or nondeterministically. As discussed in Section 5.2, in order to properly size a dynamic information experiment, several forms of data must be gathered, including: (i) initial guesses for instrumentation system parameters and time-dynamic maneuvers, (ii) baseline vehicle and mission profile data, (iii) statistical information on a priori model parameters, such as PDFs or crisp sets *i.e.* (min-max bounds), and (iv) constraints. These constraints include flight dynamic constraints, such as maximum angle of attack or bounds on dynamic pressure, and actuator constraints, such as limits on maximum frequency and range of motion. Essentially, the actuator constraints place limits on maneuvers. This will be discussed further in Section 9.7.2.

It must be noted that this sizing and synthesis algorithm is independent of (i) the dynamic model, (ii) the selected approach to the dynamic sensitivity analysis, and (iii) the selected approach to solving the mixed parameter optimization / optimal control problem. Recall, from equations (1)-(3) of Section 4.3.1 that flight dynamic models can be generally posed in the form of a state-space system with measured outputs. As physics-based models with higher fidelity are implemented, these equations grow more complex and the resulting the sensitivity analysis will become increasingly complex. As a result, calculation of dynamic output-parameter sensitivities from Section 5.3.4 using finite differencing or symbolic differentiation becomes less practical and automatic differentiation (see Section 7.2.3) becomes more attractive.

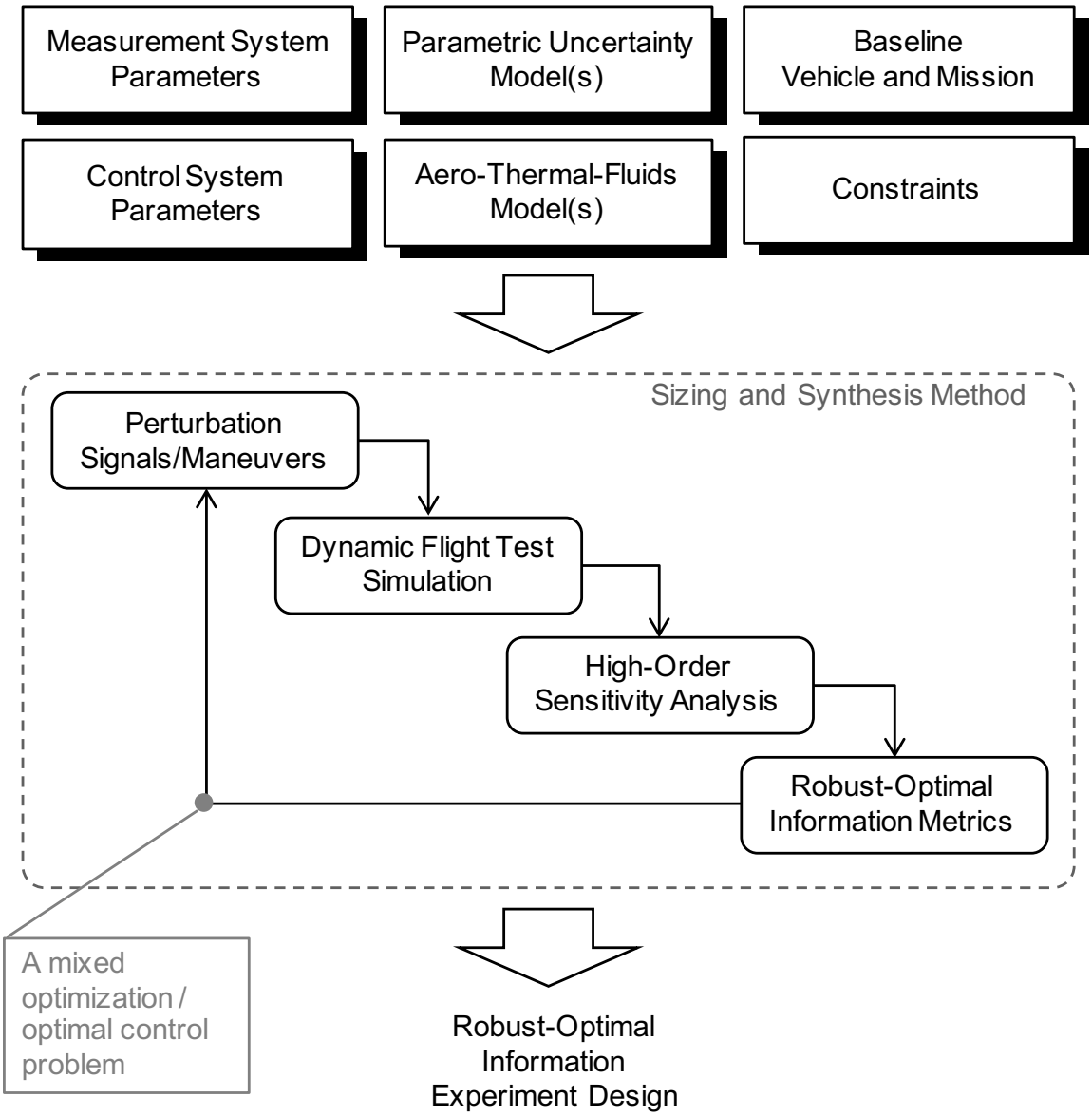

Figure 46: An illustration of the TEMPUS sizing and synthesis algorithm for high information dynamic experiment design.

As experiment designs with ever-increasing information density are desired to wring out every last drop of information possible, numerical accuracy will become an increasingly important consideration so as to eliminate sources of "computational uncertainty". Among other things, this implies that optimal information maneuvers will be investigated using a variety of parameter optimization and optimal control methods, which is represented by a feedback loop within a sizing and synthesis code. Recall from Section 5.3.5 that in contrast to direct methods, indirect methods often have convergence problems which make them difficult to automate; however, if an optimal control solution is found then the necessary conditions for optimality are satisfied.

8.3 Summary

In this chapter, the TEMPUS methodology was proposed, which draws from elements of two other methodologies: Robust-Optimal Experiment Design by Asprey and Macchietto and Robust Design Simulation by Mavris. The successful implementation of the TEMPUS methodology depends on the streamlined approach to perform a high-order dynamic sensitivity analysis in a fashion that is automatable and easily implementable by the flight test designer and the control systems engineer, all the while without introducing computational uncertainty. This methodology is intended to be flexible with respect to the different approaches for evaluating robustness by using variational asymptotic expansions. For the nondeterministic approach, a large number of evaluations can be quickly performed, considering a variational asymptotic expansion as a surrogate model, to statistically approximate information robustness metrics. These variational asymptotic expansion surrogate models can also be used to enable a deterministic approach to evaluate robustness via the formulas from Section 6.1.2.1, to asymptotically approximate information robustness metrics.

PART IV

Research Formulation

The last two chapters were devoted to introducing the TEMPUS methodology for the robust-optimal design of dynamic system identification experiments. It was observed that a critical enabler to this methodology is the ability to perform an automated and accurate high-order dynamic state-to-parameter sensitivity analysis. It was observed that the computation of variational asymptotic expansions via automatic differentiation is able to accomplish this task, minimizing the potential cumbersome derivation and implementation task by the computer programmer.

In the next chapter, a set of research questions are formulated to identify the potential limits, merits, and alternative approaches involved in utilizing variational asymptotic expansions as surrogate models to compute higher-order information metrics for the design robust-optimal dynamic experiment designs.

CHAPTER 9

RESEARCH QUESTIONS

The last two chapters were devoted to the proposition of a new approach towards the model-based design of dynamic experiments for system identification, where it was proposed to merge existing methodologies for RODE and RDS using VAEs to generate surrogate models. In Chapter 7 the following was concluded:

1. higher-order sensitivity information can be calculated using asymptotic expansions, and

2. families of solutions to ODE systems can be parameterized by parameters, initial conditions, etc. by using the sensitivity information to construct VAEs.

From the above observations, it might be deduced that implementation of VAEs for the construction of surrogate models can be readily applied; however, there are several complications that could potentially inhibit such an implementation. This statement is a not surprising one. For example, in the case of surrogate model construction via regression there are certain conditions that can minimize the effectiveness of this approach as well. In fact, many of the same issues found in regression analysis are also potential sticking points in the case of VAEs, such as (i) scaling issues with increasing dimensionality, (ii) potential diminishing returns on accuracy with increasing order, and (iii) convergence issues, just to name a few. The focus of the this chapter is to explore any potential issues that could limit the implementation and effectiveness of VAEs and pose these issues as research questions in a way that leads to a set of testable hypotheses.

9.1 The Curse of Dimensionality

As higher and higher-order equations of variation are desired, a phenomenon known as the curse of dimensionality is manifested. Figure 47 shows this effect for an original ODE system consisting of n number of state variables and m number of parameters, where 1st and2nd-order equations of variation with respect to the system parameters are desired to be computed. Note that these formulations are independent of how the equations of variation are computed (*i.e.* symbolic, finite differencing, auto-differentiation) and generically reflect how the dimensionality scales with system order. For the 1st-order equations of variation, the original system is differentiated with respect to the parameters ε, which leads to an application of the chain rule. The resulting Jacobian matrices [173] with respect to state variables, f_x, and parameters, f_ε, are $n \times n$ dimensional and $n \times m$ dimensional matrices, respectively. Therefore the 1st-order state-parameter sensitivities, x_ε, results in a $n \times m$ matrix system of equations, which must be solved along with the original system.

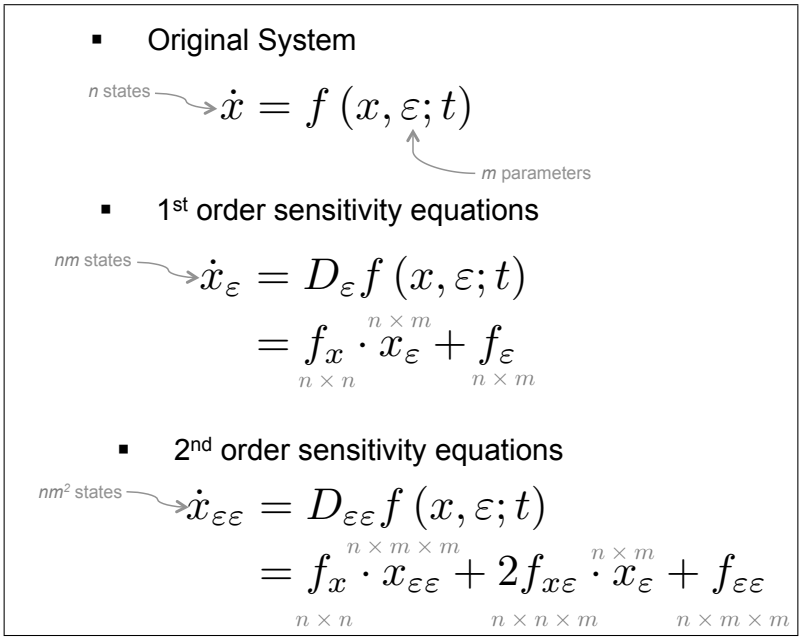

Figure 47: An illustration showing the exponential growth in the number of state variables as the system order increases.

Repeating the differentiation exercise for the 2nd-order equations of variation results in the "Jacobin-of-Jacobians" [156] $f_{x\varepsilon}$ and $f_{\varepsilon\varepsilon}$, which are respectively $n \times n \times n$ and $n \times m \times m$ dimensional matrix cubes, or 3-tensors [77]. Therefore the 2nd-order state-parameter sensitivities, $x_{\varepsilon\varepsilon}$, results in a nm^2 additional states, which must be solved along with the original n states and the nm states of the 1st-order equations of variation. Now the exponential growth in how the number of state variables scales with order can be observed, where the d^{th}-order equations requires nm^{d-1} state variables.

Returning to the implementation of VAEs to computing higher-order sensitivities can somewhat alleviate memory scaling issues. If it is desired to accommodate multiple parameters, then VAEs can be constructed that are equivalent to multivariate Taylor-series expansions, where the derivative information is stored as coefficients. Table 9 illustrates the scaling issues of a single state variable ($n = 1$), due to the curse of dimensionality with respect to parameters m and polynomial degree d (polynomial size $s = d + 1$).

Table 9: The scaling of the number of polynomial coefficients ($c = m^{d-1}$) for a single state variable with m parameters and d higher-order information.

dimension, *m* \ size, *s*	1	2	3	4	5	6	7	8	9	10
1	1	2	3	4	5	6	7	8	9	1.0E+01
2	1	4	9	16	25	36	49	64	81	1.0E+02
3	1	8	27	64	125	216	343	512	729	1.0E+03
4	1	16	81	256	625	1296	2401	4096	6561	1.0E+04
5	1	32	243	1024	3125	7776	16807	32768	59049	1.0E+05
6	1	64	729	4096	15625	46656	117649	262144	531441	1.0E+06
7	1	128	2187	16384	78125	279936	823543	2097152	4782969	1.0E+07
8	1	256	6561	65536	390625	1679616	5764801	16777216	43046721	1.0E+08
9	1	512	19683	262144	1953125	10077696	4.04E+07	1.34E+08	3.87E+08	1.0E+09
10	1	1024	59049	1048576	9765625	60466176	2.82E+08	1.07E+09	3.49E+09	1.0E+10

Due to progress in computing and memory storage, this amount of information can be accommodated for; however, many practical engineering design problems require many more parameters, commonly on the order of 50-100 parameters. Therefore

even if a sufficient amount of computational memory is available for a problem of significant size, memory management may is important. This is summarized in the following observation.

Observation – As higher-order systems are generated, the dimensionality of the subsequent systems increases exponentially, and therefore memory management will be an important aspect of computational implementation.

In light of this observation, the following research question is posed, which will be addressed in detail in Chapter 10, where a strategy for the implementation of variational asymptotic expansions is proposed.

RQ. #1 – How to practically implement VAEs so that they can be used to create useful surrogate models for suitable engineering problems (e.g. numerical simulation of aerospace vehicle dynamics)?

9.2 Asymptotic Error Control of Parametric Uncertainty

From Oberkampf [224], computational simulation results which are intended to mimic physical experimental results contain both physical uncertainty and numerical error. If comparisons are to be precisely drawn between the two then it is generally desirable to eliminate sources of numerical error to isolate the physical uncertainty of the model.

Recall from Figure 44 that asymptotic expansions applied to an ODE system generates higher-order state-parameter sensitivity derivatives, which can be numerically

integrated. Thus, numerical integration error is a source of numerical uncertainty that must be minimized. To this end stable numerical integration routines are desired where smaller time steps reduce the effects of numerical truncation error. Ultimately, shrinking the time step reaches a point where the numerical precisions of the machine are reached and any further reductions in time step result in an increase in roundoff error. This roundoff error is related to the numerical precision of the computer This numerical precision can be minimized by using higher numerical precision libraries, which effectively increase the number bits used to represent a number.

A natural way to think about the power series representation of a function is to view the expansion as the limiting case of polynomials of increasing degree. As discussed in Section 7.1.3, there is a formal connection between the numbers of terms used and the approximation accuracy to the function being approximated $f(x)$, which can be quantified according to equation (31). If an error tolerance is specified, then this equation can quantify the error growth over a region parameterized by x.

Observation: The accuracy of a VAE can be controlled through (i) minimizing the numerical integration routine error, (ii) using higher numerical precision libraries, and (iii) constructing VAEs using more higher-order gradient information.

9.3 Diminishing Returns on Accuracy

As it was mentioned in Chapter 7, the accuracy, and equivalently the region of approximation, is observed to increase as order increases. Through experience there are many limitations which cause increasingly complex VAE approximations to experience diminishing returns. This is formally stated in the following observation.

Observation: Calculating higher and higher order expansions can increase accuracy and the region of approximation, but with perceived diminishing returns.

Discussion of these diminishing returns is the topic of this section and involves consideration from different perspectives of both mathematics and computer algorithmic analysis. The following question must be answered if it is to be determined that VAEs can be used to enable a robust design approach to the sizing of optimal information experiments for system identification.

RQ. #2: To what extent can VAE approximations be practically useful, and what are the available options that can be leveraged to enhance VAE performance?

9.3.1 Using Alternative Basis Functions

One possible implication of these diminishing returns is that a substantially high-order VAE approximates only a relatively small region of parameter space. If this is the case, then the utility of using VAEs for parameter exploration of families of ODEs is limited. To this effect, the following question is posed.

RQ. #2.1: How to boost the region of approximation (radius of convergence) and accuracy (*i.e.* increasing number of expansions, basis function selection, stitching VAE surrogates, numerical precision, etc.)?

In many applications, approximations using Taylor series expansions have been found to converge only within a finite radius of convergence as order complexity increases to infinity. In several of these cases, the implementation of an asymptotic expansion using a different basis has remedied the problem. Equation (53) shows the generic form of an asymptotic expansion, which is a linear combination of coefficients and basis functions.

$$f(x) = \sum_{n=0}^{N} a_n \phi_n(x) = a_0\phi_0(x) + a_1\phi_1(x) + \ldots + a_N\phi_N(x) \tag{53}$$

There are many choices for the selection of an appropriate basis functions. Depending on the application, one basis function might be more efficient than others by exploiting the geometry of specific problem at hand. Equations (54)-(56) show three expansions to the same function $f(x)$, using different choices for basis functions – Taylor basis functions, Chebyshev basis functions, and Legendre basis functions.

$$f(x) = \sum_{n=0}^{N} a_n \left(\frac{x^n}{n!}\right) \quad \text{(Taylor Basis)} \tag{54}$$

$$f(x) = \sum_{n=0}^{N} a_n T_n(x) \quad \text{(Chebyshev Basis)} \tag{55}$$

$$f(x) = \sum_{n=0}^{N} a_n P_n(x) \quad \text{(Legendre Basis)} \tag{56}$$

Table 10 shows the mathematical form of the basis functions for the Taylor, Chebyshev, and Legendre bases. It can be seen here that the Taylor basis is very similar to the monomial (standard) basis. Advantages of this basis are (i) derivatives are directly obtained from the coefficients and (ii) arithmetic operations using this basis are relatively simple. The disadvantages of this basis include (i) non-orthogonality between basis functions and (ii) poor numerical conditioning (*i.e.* condition number of the monomial basis is 7244.534). Figure 48 shows these basis functions for the interval $-1 \leq x \leq 1$. Because of the disadvantages of the Taylor (and also the monomial) basis functions, the Chebyshev and Legendre bases are of interest. Both of these are

Table 10: Three example of different basis functions which can be used for approximation of functions using asymptotic expansions.

Taylor Basis	**Chebyshev Basis**	**Legendre Basis**
$S_0 = 1$	$T_0 = 1$	$P_0 = 1$
$S_1 = x/1!$	$T_1 = x$	$P_0 = x$
$S_2 = x^2/2!$	$T_2 = 2x^2 - 1$	$P_2 = \frac{1}{2}(3x^2 - 1)$
$S_3 = x^3/3!$	$T_3 = 4x^3 - 3x$	$P_3 = \frac{1}{2}(5x^3 - 3x)$
$S_4 = x^4/4!$	$T_4 = 8x^4 - 8x^2 + 1$	$P_4 = \frac{1}{8}(35x^4 - 30x^2 + 3)$
$\vdots$	$\vdots$	$\vdots$
$S_N = x^N/N!$	$T_N = 2xT_N - T_{N-1}$	$P_N = \frac{1}{N}((2N-1)xP_{N-1} - (N-1)P_{N-2})$

example of basis functions with good orthogonally properties and good numerical conditioning (*i.e.* condition number of the Chebyshev and normalize Legendre bases are 4.006 and 1.000, respectively); however, this comes at the price of increased complexity within arithmetic operations (to be discussed soon). Figures 49 and 50 shows these basis functions for the interval $-1 \leq x \leq 1$. Of course there are other polynomial basis functions that can be of interest, such as Bernstein polynomials, Padé approximations, and Grobner bases, but recently Chebyshev polynomials have received the most attention. This is because with a simple transformation Chebyshev polynomials can be shown to be equivalent to Fourier series, which have proven to be immensely useful in engineering, scientific, and mathematical applications [14, 16, 56, 132, 173].

In light of the discussion concerning the effects of basis function selection the following hypothesis is proposed to address **RQ #2.1**.

HYP. #2.1.1: Based on the geometry of the problem, intelligent selection of basis functions can increase the region of approximation, and hence accuracy, without experiencing the degree of diminishing returns that are observed when employing expansion approximations using Taylor basis functions.

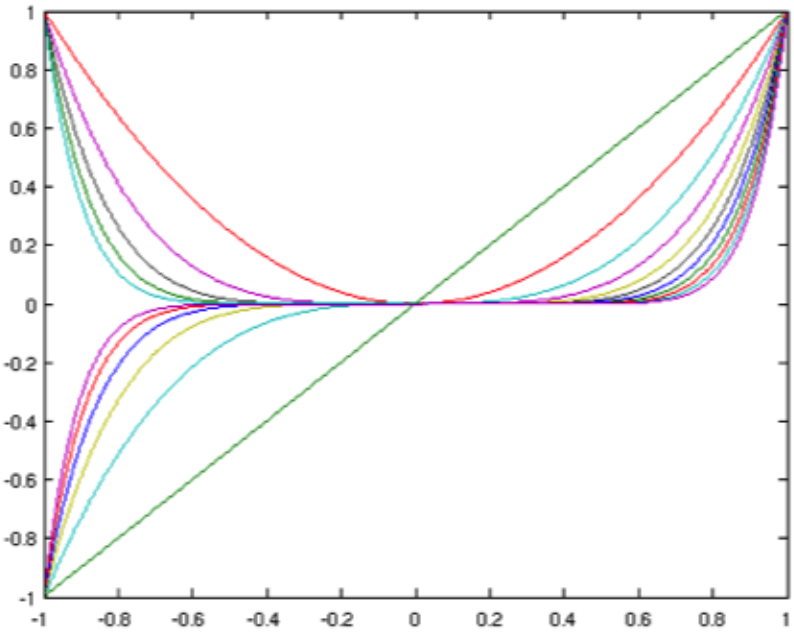

Figure 48: Monomial basis functions (condition number = 7244.534).

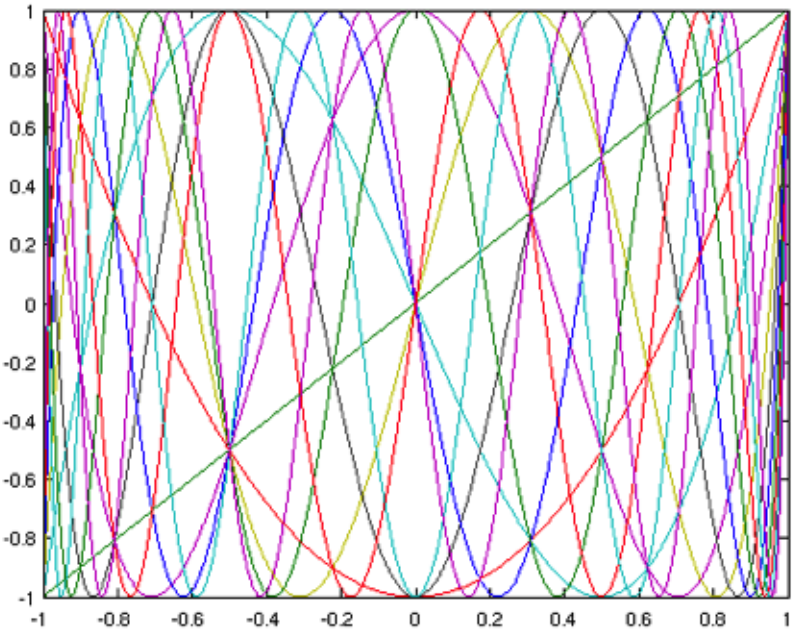

Figure 49: Chebyshev basis functions (condition number = 4.006).

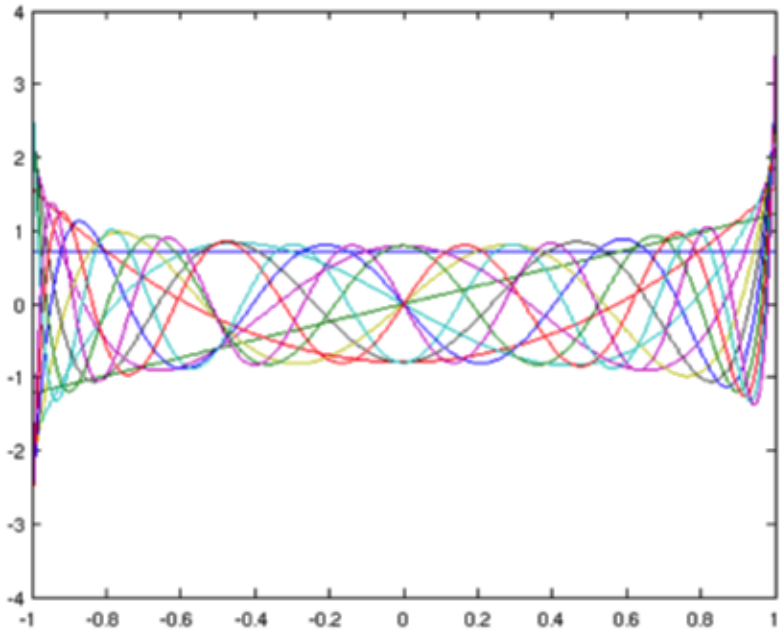

Figure 50: Normalized Legendre basis functions (condition number = 1.000).

If proven true, **HYP. #2.1.1** will imply that design space exploration will potentially be feasible using asymptotic expansions of only a single experiment! Figure 51 illustrates this, showing the expected behavior of asymptotic expansions with Chebyshev basis functions outperforming monomial expansions.

9.3.2 Numerical Precision

Returning to the issue of accuracy, there is still a cause for concern to be had regarding the proposition of using higher-order gradient information to parameterize families of solutions to ODE systems. It has previously been stated that the numerical conditioning of asymptotic expansions using the monomial basis is extremely poor. This is because the numerical contribution of the $N+1$ order term is smaller than the N order term in a local neighborhood. Considering the N^{th} term, $a_N \left(\frac{x^N}{N!}\right)$, because $x << 1$ and N is a positive integer then the expression $\left(\frac{x^N}{N!}\right) << 1$. Often time this means that the coefficient $a_N >> 1$, even to the point of exceeding the numerical precision

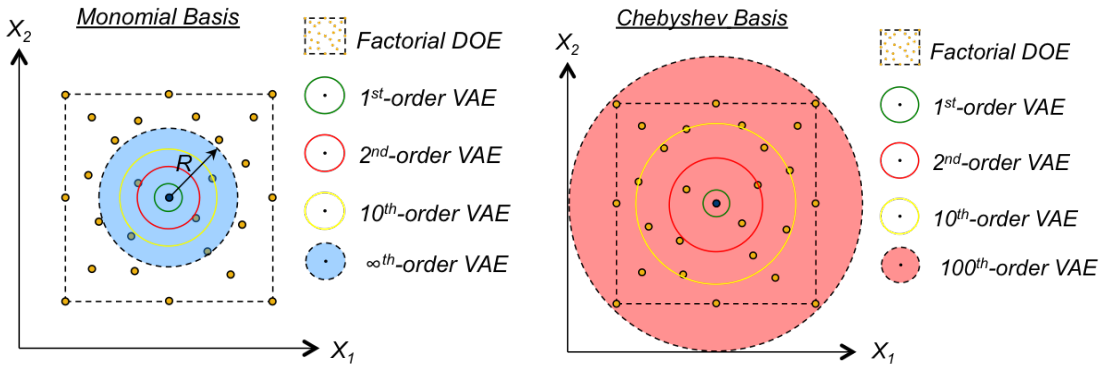

Figure 51: Monomial basis (condition number = 7244.534).

of the computer. This means that as x is chosen to be evaluated at points significantly far away from x_0 the calculation of the term $a_N\left(\frac{x^N}{N!}\right)$ contains increasingly more numerical error. Therefore even for VAEs which do converge for large regions of approximation, numerical implementation can adversely affect the accuracy of these approximations, giving the appearance that the region of approximation is smaller than it really is. It was stated that other basis functions contain better numerical conditioning properties, but it is uncertain whether these conditioning properties will ensure that all higher order coefficients will remain within the limits of numerical precisions. Therefore the following observation is stated.

Observation: Regardless of what basis is chosen to generate VAEs, numerical precision will need to be controlled using higher precision libraries and scaling approaches.

9.4 Propagation of Parameter Uncertainty Using VAEs

In the field of uncertainty analysis, discussed previously in Section 6.1.1 for dynamic systems, a common and rigorous way to propagate uncertainties forward is via the

local expansion-based method [192], which use 1^{st}-order Taylor (linear) series expansions to propagate uncertainty. These methods are very similar to what is proposed in this work; however, these methods are limited to small parameter perturbations and/or to problems with linear variation in uncertainty, due to the fact that they only utilized 1^{st}-order gradient information. *Uncertainty propagation* is the quantification of uncertainties in system output(s) propagated from uncertain inputs [192]. It focuses on the influence on the outputs from the parametric variability listed in the sources of uncertainty. The targets of uncertainty propagation analysis can be [180]:

- To evaluate low-order moments of the outputs (*i.e.* mean and variance).
- To evaluate the reliability of the outputs. This is especially useful in reliability engineering where outputs of a system are usually closely related to the performance of the system.
- To assess the complete probability distributions of the outputs. The is useful in the scenario of utility optimization where the complete distribution is used to calculate the utility.

Due to the continuous dependence of ODE solutions on parameters, initial conditions, etc. (refer back to Section 7.3.2), a neighboring perturbed solution can be approximated by evaluating a baseline VAE with the perturbed values. It logically follows that if the perturbed parameters are assigned probabilistic distributions then these distributions can be sampled and the VAE's can be used as a surrogate to propagate parameter distributions (*i.e.* parameter uncertainties), generating probabilistic solutions that are asymptotically accurate. Therefore the following hypothesis is stated.

HYP. #2.1.2: The utilization of higher-order VAE's can enable higher-order local expansion-based methods for the propagation of uncertainty through dynamic systems, where nonlinear effects and larger perturbations on parameters can be approximated to asymptotic accuracy.

9.5 The Effects of Increasing Complexity

From subject of algorithm analysis [21, 252], complexity reflects the level of difficulty that is required for implementation of a given algorithm in terms of required memory and computation time. In the case of VAEs complexity is affected by the following:

- **Order** (Number of orders, d) – the highest order derivative used to construct an expansion approximation; analogous to the highest degree of the polynomial
- **Dimension** (Number of parameters, m) – the number of independent variables used within the multivariate expansion approximation
- **States** (Number of states, n) – the number of required separate expansion approximations (one for each state variable); reflects the size of an ODE system
- **System** (Number of operations, o) – the number of operations within $f(x, \varepsilon; t)$ that are needed to compute $\dot{x}$.

Poor scaling with any of these complexities can directly lead to impractical computation of VAEs, where excessive memory is required and computation time is very large. Therefore, it is of interest to investigate the practicality of using VAEs to parameterize larger, more complex problems, which are commonly observed in engineering preliminary and detailed design problems. To this end, the following research question is posed.

RQ. #2.2: Is the numerical implementation of VAE's to large-scale problems (*e.g.* high-dimensional (number of parameters), high-order (number of derivatives)), such as robust-optimal dynamic experiment design problems, a feasible endeavor and to what extent can these complexity effects (*i.e.* time complexity, memory complexity, etc.) be monitored, controlled, or mitigated?

As previously mentioned in Figure 44 (Section 7.3.2), computing VAEs requires polynomial arithmetic operations instead of scalar variables. These polynomial operations include elementary arithmetic operations ($+$,$-$, $\times$, $\div$, etc.) and elementary functions (exp, log, sin, cos, etc.). As discussed in Chapter 10, polynomial operations can be implemented as libraries of algorithms using data overloading techniques. For example, addition/subtraction of two polynomials is a simple coefficient-wise addition/subtraction. The computational complexity of any given polynomial algorithm is dependent on the number of coefficients that are used to represent an asymptotic expansion (*i.e.* order and number of parameters). This leads to the following observation concerning complexity.

Observation: Computational complexities are directly traceable back to simple algorithms within a polynomial engine, which can be analyzed systematically using algorithm analysis.

In light of this observation it is hypothesized that the use of parallel/vectorization strategies is of paramount importance to enable the design of dynamic experiment design problems for large-scale aerospace vehicle problems, such as hypersonic SCRAM-jets.

HYP. #2.2: Parallelization/vectorization strategies to alleviate computational expense will play a critical role in the robust-optimal design of dynamic experiments of aerospace systems (*e.g.* flight-dynamic simulation and control of hypersonic SCRAM-jet vehicles).

9.5.1 Multiplication of Dense Polynomials

It is known that multiplication of dense polynomials is a bottleneck in terms of computation time and remains an active area of research [28, 204, 205, 206]. In dense polynomial multiplication, all coefficients of two multiplying polynomials are required in order to correctly compute the product. For Taylor polynomials, neglecting small terms is the same as eliminating the higher-order terms, which reduces to dense multiplication with smaller polynomials and therefore sparse polynomial multiplication strategies are not applicable here.

There are a number of techniques for multiplying polynomials, the more popular include: (i) the classical "Schoolbook" method [57, 217], (ii) the Karasuba's approach [115, 283], and (iii) the fast Fourier transform (FFT) methods [5, 217]. The traditional Schoolbook approach is easy to implement; however, its computation time scales very poorly as larger degree polynomials are multiplied. Alternatively, the FFT approach scales very well for polynomials of increasing size. The current problem with these "fast" methods is that they tend to be computationally impractical, in that the degree at which they start being better than the classical method is fairly high. In fact, the break-even point tends to be so high that they are larger than most commonly encountered problems. FFT approaches can overcome this by taking advantage of vector/parallelization strategies – something that is not possible within

the Schoolbook algorithm. Figure 52 compares the overall time complexities for polynomial multiplication using both the Schoolbook approach and the FFT approach. The Schoolbook method scales as $\mathcal{O}(n^2)$ for polynomial order, which suggests poor computational performance as the polynomial degree increases. Polynomial multiplication using the FFT approach is more complicated. This process is achieved by (i) computing a "forward" FFT in $\mathcal{O}(n \log n)$ time, converting both $a(x)$ and $b(x)$ into point-value form, (ii) performing a point-wise multiplication (Hadamard product) in $\mathcal{O}(n)$, and finally (iii) computing an "inverse" FFT in $\mathcal{O}(n \log n)$ to convert back into coefficient form. The total asymptotic time complexity for the FFT approach is $\mathcal{O}(n \log n)$. Thus regardless of the outcome of **RQ.#2.2**, the following observation is made.

Observation: For use in efficiently computing higher-order VAEs, there are a number of alternative approaches to implementing high-cost polynomial operations, which can be investigate for application in dynamic experiment design problems, if it is determined to be necessary.

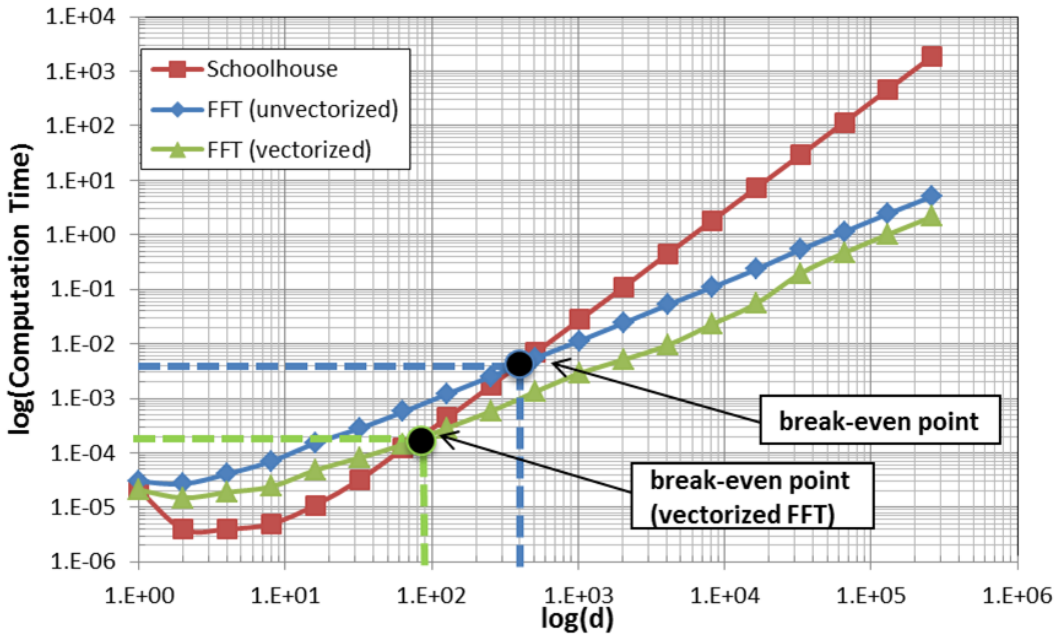

Figure 52: Computation time of d^{th}-order univariate polynomial multiplication Schoolhouse vs. FFT (vectorized and unvectorized) algorithms.

9.6 Flexibility in VAE Problem Formulation

In Chapter 8 it was mentioned that ODE systems can be posed as either IVP or BVP problems. Indeed in physical application both of these are common occurrences in engineering. For example, in Chapter 7 the design of effective flight testing strategies was shown to consist of an optimal control problem (OCP) formulation to develop time-dynamic maneuver signals to create data with high information density leading to highly accurate system identification. Here it was discussed that there are two approaches to solving OCPs (*i.e.* direct methods and indirect methods), which essentially solve ODE systems using an IVP or BVP formulation.

RQ. #2.3: Can VAE surrogates be generated to for the solution of OCPs using both a direct and indirect method approach?

Direct methods involve transcribing $u(t)$ (*i.e.* approximating $u(t)$ as a finite dimensional array $\{u(1), u(2), \ldots, u(n)\}$) and solving the result IVP. The solution of VAE-IVPs is addressed in Section 10.1.3. The discussion here focuses on approaches to solve OCPs, using a VAE-BVP approach. Consider the general OCP formulation.

$$\begin{aligned} \min_{u \in \mathscr{U}_{adm}} J[u] &= \int_{t_0}^{t_f} L(x(t), u(t), t) dx \\ \text{s.t.: } \dot{x} &= f(x(t), u(t), t) \;\; x(t_0) = x_0 \end{aligned} \tag{57}$$

From variational calculus, it is useful to construct the Hamiltonian.

$$\mathcal{H}(x(t), u(t), \lambda(t), t) = L(x(t), u(t), t) + \lambda^T(t) f(x(t), u(t), t) \tag{58}$$

Here, $\lambda(t)$ is referred to as the co-state vector and can be considered as a transient Lagrange multiplier vector. The optimal control law can be directly upon differentiation of the Hamiltonian with respect to $u(t)$ as follows.

$$\frac{\partial}{\partial u} \mathcal{H}(x(t), u(t), \lambda(t), t) = 0 \tag{59}$$

Solving this equation for $u(t)$ reveals the optimal control, which is in general a function of the states $x(t)$, co-states $\lambda(t)$, and time t. The transient response of $\lambda(t)$ can be characterized by differentiating the Hamiltonian with respect to $x(t)$, resulting in the following two-point BVP system.

$$\begin{aligned} \dot{x} &= f(x(t), u(t), t), & x(t_0) &= x_0 \\ \dot{\lambda} &= \frac{\partial}{\partial x} \mathcal{H}(x(t), u(t), \lambda(t), t), & \lambda(t_f) &= 0 \end{aligned} \tag{60}$$

To solve (60) using VAEs, the following hypothesis is states.

HYP. #2.3: Higher-order gradients can be used to generate high-accuracy VAE surrogates to OCPs, which will enable point solutions from computationally expensive OCP solvers to be utilized for parametric exploration.

9.7 Enabling Design of Dynamic Robust-Optimal SysID Experiments

As mentioned in Section 5.2 an optimal experiment for system identification is an experiment that maximizes the squared sensitivity between the measured outputs with respect to the parameters. In Section 5.3 this was shown to be mathematically formulated as a mixed optimization/optimal control problem using the design vector $\boldsymbol{\varphi} = \{\mathbf{u}(t), \bar{\mathbf{w}}, \mathbf{x}_0, \mathbf{t}_{sp}, \tau\}$ as follows:

$$\begin{aligned} \min_{\boldsymbol{\varphi}} J\left[\boldsymbol{\varphi}\right] &= \int_0^{\tau} \mathscr{I}_x(\mathbf{y}(t), \mathbf{u}(t), \boldsymbol{\theta}) dt \\ \text{s.t.: } \dot{\mathbf{x}}(t) &= f\left(\mathbf{x}(t), \mathbf{u}(t), \boldsymbol{\theta}\right), \quad \mathbf{x}(t_0) = \mathbf{x_0} \\ \mathbf{y}(t) &= g\left(\mathbf{x}(t), \mathbf{u}(t), \boldsymbol{\theta}\right) \\ \Sigma_{j=1}^{m} \mathbf{h}\left(\boldsymbol{\varphi}\right) &= 0 \\ \Sigma_{j=1}^{m'} \mathbf{g}\left(\boldsymbol{\varphi}\right) &\leq 0 \end{aligned} \tag{61}$$

Here $\mathscr{I}_x(\mathbf{y}(t), \mathbf{u}(t), \boldsymbol{\theta})$ represents a selected information metric, summarized in Table 11, which can be computed from the expression of Equation (8). The expressions $\Sigma_{j=1}^{m} \mathbf{h}\left(\boldsymbol{\varphi}\right) = 0$ and $\Sigma_{j=1}^{m'} \mathbf{g}\left(\boldsymbol{\varphi}\right) \leq 0$ represent equality and inequality constraint vectors on the design vector, which include admissible bounds on states/control inputs, bounds on initial conditions, constraints on sampling strategies, bounds on test durations, etc.

In Section 5.2 the circulatory problem was discussed, which implies that solutions to Equation (61) will yield inaccurate/sub-optimal results in the presence of parametric uncertainty, as the accurate calculation of the Fisher information matrix depends, *inter alia*, on the true values of the system parameters. Therefore *a priori* parameter values must instead be used as a best guess, leading to the inaccurate predictions. In response to this, robust-optimal information metrics have been proposed and discussed in Chapter 6; however, evaluation of these criteria is often computationally infeasible. In light of this, the following research question is posed.

Table 11: Diagram of the interdisciplinary nature of robust-optimal design for dynamic experiments.

	Information Criteria	Expression	Description
Nominal Information Criteria	A-optimality (trace)	$\mathscr{I}_a \triangleq \mathrm{tr}\left[\bar{\mathscr{M}}\left(\boldsymbol{\theta},\boldsymbol{\varphi}\right)^{-1}\right]$	• Seeks to minimize the inverse trace of the information matrix • Results in minimizing the average variance of the estimates of the regression coefficients
	L-optimality (weighted trace)	$\mathscr{I}_l \triangleq \mathrm{tr}\left[\mathbf{W}\bar{\mathscr{M}}\left(\boldsymbol{\theta},\boldsymbol{\varphi}\right)^{-1}\right]$	• Seeks to minimize the weighted inverse trace of the information matrix • Results in minimizing the weighted average variance of the estimates of the regression coefficients
	C-optimality	--	• Seeks to minimize the variance of the best linear unbiased estimator of a predetermined linear combination of model parameters
	D-optimality (determinant)	$\mathscr{I}_d \triangleq \det\left[\bar{\mathscr{M}}\left(\boldsymbol{\theta},\boldsymbol{\varphi}\right)\right]^{-1}$	• Seeks to maximize the determinant of the information matrix of the design • Results in maximizing the differential Shannon information content of the parameter estimates
	E-optimality (eigenvalue)	$\mathscr{I}_e \triangleq \lambda_{\min}\left[\bar{\mathscr{M}}\left(\boldsymbol{\theta},\boldsymbol{\varphi}\right)\right]$	• Seeks to maximize the minimum eigenvalue of the information matrix
	T-optimality (trace)	$\mathscr{I}_t \triangleq \mathrm{tr}\left[\bar{\mathscr{M}}\left(\boldsymbol{\theta},\boldsymbol{\varphi}\right)\right]$	• Seeks to maximize the trace of the information matrix
Robust-Optimal Criteria	R-optimality (minimax)	$\mathscr{I}_r \triangleq \sup_{\boldsymbol{\theta}\in\boldsymbol{\Theta}} \mathscr{I}_*\left(\bar{\mathscr{M}}\left(\boldsymbol{\theta},\boldsymbol{\varphi}\right),\boldsymbol{\theta}\right)$	• A worst-case approach that aims to determine the experiment designs that optimize the worst possible performance for any values of the parameters • The parameter information is limited only to the knowledge of the admissible domain (i.e. no information on the distribution is necessary)
	ED-optimality (Expected determinant])	$\mathscr{I}_{ed} \triangleq \mathrm{E}\left[\mathscr{I}_d\middle\vert\boldsymbol{\theta}\right]$	• Seeks to maximize the expected value of the determinant of the information matrix • The parameter distribution is known
	RC-optimality (Robust Control)	$\mathscr{I}_{rc} \triangleq \sup_{\boldsymbol{\omega}} g\left(\boldsymbol{\theta},\boldsymbol{\omega}\right)\bar{\mathscr{M}}\left(\boldsymbol{\theta},\boldsymbol{\varphi}\right)^{-1} g\left(\boldsymbol{\theta},\boldsymbol{\omega}\right)$	• Seeks to guarantee robust stability using an $\mathcal{H}_\infty$ approach • The function *g* is a frequency dependent vector related to the *v*-gap
Variance of predictions Criteria	G-optimality	$\mathscr{I}_g \triangleq \max\left[\mathrm{diag}\left[\hat{\mathscr{M}}\left(\boldsymbol{\theta},\boldsymbol{\varphi}\right)\right]^{-1}\right]$	• Seeks to minimize the maximum entry in the diagonal of the projected information matrix • Results in minimizing the maximum variance of the predicted values
	I,(V)-optimality (Integrated)	$\mathscr{I}_i \triangleq \frac{\int_{\mathbb{R}} \mathrm{Var}\left(\boldsymbol{\theta}\right)\mathrm{d}\boldsymbol{\theta}}{\int_{\mathbb{R}}\mathrm{d}\boldsymbol{\theta}}$	• Seeks to minimize the average prediction variance over the design space • Focused on prediction
Distance-based Criteria	U-optimality	$\mathscr{I}_u \triangleq \sum_{\mathbf{x}\in\mathscr{C}} \left\|\mathbf{x}-\mathbf{y}\right\|$	• Seeks to minimize the sum of the distances from each candidate point to the design • Defines a clustering of the candidate set (i.e. cluster analysis)
	S-optimality	$\mathscr{I}_s \triangleq N_D\left[\sum_{y\in\mathscr{D}}\left[\mathrm{d}\left(y,\mathscr{D}-y\right)\right]^{-1}\right]^{-1}$	• Seeks to maximize the harmonic mean distance from each design point to all the other points in the design

RQ. #3: In the context of complex dynamic systems with high degrees of uncertainty, what is the most effective approach to numerically determine robust-optimal dynamic information experiment designs?

9.7.1 Development of Robust-Optimal Information Metrics

In Section 6.1.2, RDO techniques were reviewed, in order to gain direction in how to approach robust-optimal dynamic experiment design. It was shown that these techniques can be divided into two classifications: nondeterministic RDO and deterministic RDO. Table 8 provided a summary of the attributes of both, where it was observed that nondeterministic methods require a large number of function calls and deterministic methods require access to gradient information, which is often a computationally cumbersome effort. However, given that the Fisher information matrix is constructed using 1^{st}-order gradient information, the deterministic techniques will actually need 2^{nd}-order gradient information ignored to evaluate robustness. This is where higher-order sensitivities and VAEs can provide support, and hence, the following hypothesis is stated.

HYP. #3: If the automated, generalized computation of higher-order gradient information can be made computationally feasible, then a flexible approach to robust-optimal dynamic experiment design, utilizing VAE's to automatically and accurately compute higher-order dynamic state-to-parameter sensitivities, will yield superior designs that are robust to parameter uncertainties.

The implications of this hypotheses mean several things. First, if higher-order VAE surrogates can be constructed, which accurately model the information content response with respect to uncertainty, then nondeterministic RDO methods, such as the aircraft systems engineering RDS methodology [194], can be used which already accommodate large, complex systems design problems. In this case a VAE surrogate can be used in place of an RSE for use in the rapid evaluation of Monte Carlo cases to determine robustness. Secondly, deterministic RDO approaches to dynamic experiment design can be enabled using sophisticated OCP software to numerically generate high-fidelity solutions with respect to control input excitation. This is possible because high-order sensitivity information can be used to deterministically evaluate statistical moments of Fisher information metrics (*e.g.* expected value, variance, etc.) and therefore convert a robust-optimal (control) problem into an equivalent optimization (optimal control) problem.

9.7.2 Development of Effective Constraints

The consideration of constraints is problem specific to the system under consideration. In the context of flight dynamic aircraft system identification experiment design for air-breathing hypersonic vehicles, the following question is posed.

RQ. #4: What types of constraints should be present in aircraft system identification flight experiments for air-breathing hypersonic vehicles, and how should they numerically incorporated into the numerical sizing and synthesis of high information dynamic experiments?

For the mixed parameter optimization / optimal control problem formulation of equation (61) from Section 9.7 applied to air-breathing hypersonci vehicles, formulation of appropriate constraints is still an open-ended issue. For example, frequency

constraints on control inputs is not readily incorporated into the time-domain representation of equation (61), suggesting that a frequency-based design formulation is necessary but is beyond the scope of this work [170]. An incomplete list of relevant flight test design constraints include the following.

- Amplitude constraints on aircraft response variables for model structure validity to stay close to the operation condition of the local models structures (*i.e.* linear lift approximation)
- Input amplitude are limited by mechanical stops, flight control software limiters, or model structure validity.
- length of individual maneuvers (*e.g.* subscale model test and flight conditions that cannot be sustained for a long period of time (*e.g.* high angles of attack or hypersonic flight))
- Bandwidth limitations on frequencies due to instrument dynamic response, reduced dynamic system response to high-frequency inputs, high-frequent limitations of the pilot and control system, and structural resonant frequencies. Low frequency inputs can cause the aircraft to drift away from operating conditions
- Implementation distortion of the intended input frequency and the actual frequency that is imposed on the aircraft
- limits on rates of change of input amplitudes (*e.g.* sharp-edge square wave)

PART V

Experimental Results

In the following chapters, experimental results will be presented in three parts to address the previously discussed research questions with respect to: (i) the practical aspects of the implementation of a reliable automatic differentiation tool to compute higher-order variational assymptotics for dynamic systems; (ii) the implementation and demonstration of the previously discussed TEMPUS methodology for the robust-optimal design of information-dense experiments (to be implemented first on a simple spring-mass-damper dynamic system); and (iii) overall effectiveness of a systems design methodology which utilizes variational asymptotic expansions to aid in the design of flight-dynamic experiments to robust-optimal system identification of aero-propulsive-elastic parameters that model the forces and moments exerted on air-breathing hypersonic vehicles during operational flight.

CHAPTER 10

COMPUTATION OF VARIATIONAL ASYMPTOTICS FOR DYNAMIC SYSTEMS

The focus of this chapter is first to address **RQ.#1**, which investigates how contemporary programming techniques can be utilized to generate high-order VAEs that parameterize, locally, families of solutions to dynamic systems. Next **RQ.#2** and the associated sub-questions are addressed, involving computational experimentation to determine VAE assessment in terms of numerical accuracy and computational feasibility for large-scale design problems. Figure 53 shows a taxonomy of proposed experiments and represent the structured work of this chapter.

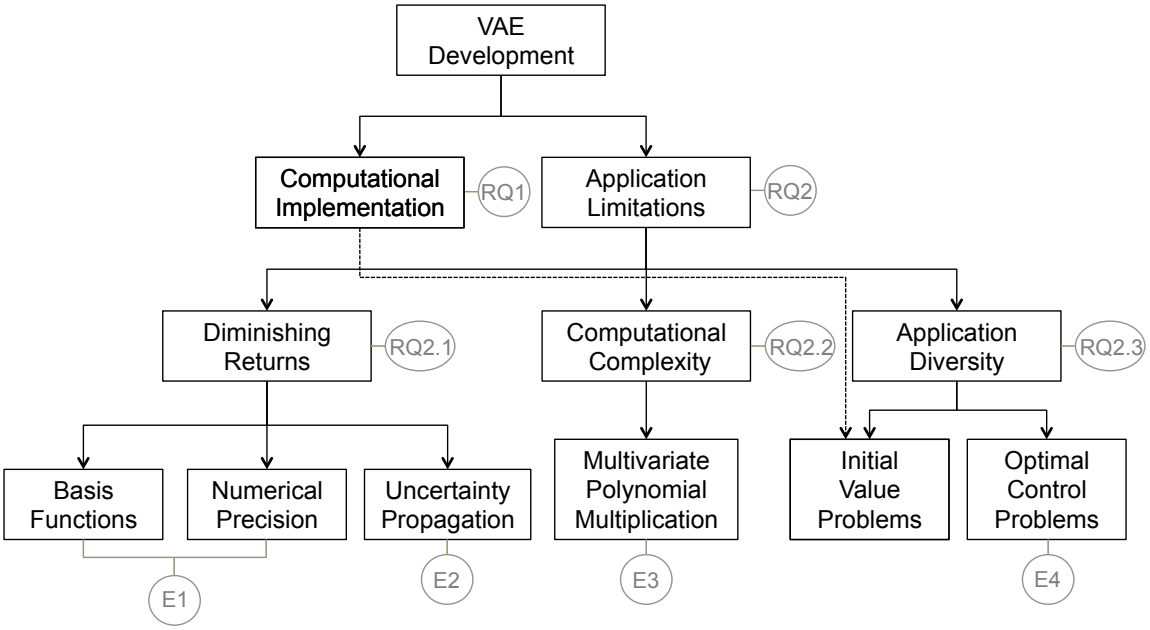

Figure 53: Experimental taxonomy of the VAE developmental portion of the proposed experimental plan.

After **RQ.#1** is addressed in Section 10.1, the group of experiments **E1**, **E2**, **E3**, and **E4** are focused on exploring the extent to which higher-order sensitivities can be practically computed and used to construct time-profile asymptotic expansions (*i.e.* VAEs). As mentioned in Chapter 9, there are a number of factors that can inhibit the feasible computation of VAEs for dynamic systems, such as: computational implementation, the curse of dimensionality, and diminishing returns on accuracy. Computational implementation is addressed in Section 10.1.3 and demonstrated on the Van der Pol oscillator, and therefore the focus of these experiments will address the hypotheses aimed at addressing issues identified as potential factors limiting application (*i.e.* **RQ #2**): diminishing returns, computational complexity, and problem diversity.

Description of each experiment set is itemized and briefly described below:

E1: (*Section 10.2*) These experiments address the discussion from Section 9.3.1, where **Hyp2.1.1** was stated in response to **RQ2.1**. The experimental objective here is to explore the potential gains in approximation accuracy and convergence rate performance by generating a VAE to a problem using different basis functions (*e.g.* Chebyshev polynomials).

E2: (*Section 10.3*) These experiments address the discussion from Section 9.4, where **Hyp2.1.2** was stated in response to **RQ2.1**. The experimental objective here is to investigate the asymptotic probabilistic convergence of trajectory distributions and to observe if the asymptotic approximations of these distributions converges differently for different parameter perturbation distributions (*e.g.* gaussian, uniform, etc.).

E3: (*Section 10.4*) These experiments address the discussion from Section 9.5, where **Hyp2.2** was stated in response to **RQ2.2**. The experimental objective of this experiment set is to investigate how the curse of dimensionality is manifested in

terms of computational effort. Here, these effects are studied for the dense multiplication of multivariate polynomials, which is a known bottle-neck algorithm in applications in computer science.

E4: (*Section 10.5*) These experiments address the discussion from Section 9.6, where **Hyp2.3** was stated in response to **RQ2.3**. The purpose of this study is a proof-of-concept demonstration following two proposed formulations as to how implement VAEs to generate higher-order in optimal control problems. The implications of this experiment are that a traditionally off-line analysis could potentially be used for design space exploration and uncertainty propagation analyses, which would enable new systems engineering capabilities.

10.1 Computational Implementation

10.1.1 Polynomial Library Construction

Within the last 50 years, the advent of computers has made it feasible to implement and manipulate large, dense polynomials. General-purpose computer algebra system (CAS) software (*i.e.* Mathematica, Maple, MathCad, Maxima, Sage, etc.) can be used to perform symbolic computations and has spurred work in algorithms over mathematical objects such as polynomial theory, as well as number theory, group theory, etc. [58, 79, 260]. For use in implementation within perturbation methods, these general-purpose CAS software options have not been found particularly useful, as these tools were not designed with implementation of asymptotic expansions to dynamic systems in mind. As a result, attempts to adapt these tools for the said purpose has resulted in algorithms (*e.g.* see Knuth [172]) with poor computational expense and effort.

In nearly all algorithms involving computations with polynomials, the polynomials are represented and stored as arrays of numbers in one of two ways: coefficient form and point-value form. Consider the univariate polynomial below in Equation (62).

$$P(x) = c_0 + c_1 x + c_2 x^2 + \ldots + c_N x^N \tag{62}$$

Coefficient form is an indexed array of the polynomial coefficients, $(c_0, c_1, c_2, \ldots, c_N)$, where the indexing of a $1 \times N$ array corresponds to the order of the coefficients. Point-value form requires twice as much memory to store a $2 \times N$ array of numbers, $((x_0, P(x_0)), (x_1, P(x_1)), (x_2, P(x_2)), \ldots, (x_N, P(x_N)))$, which can be generated by successive evaluations of $P(x)$. Polynomial interpolation techniques such as Lagrange polynomials can be used to transform point-value form back into coefficient form. In general most polynomial implementations represent polynomials in coefficient form, as this representation is often straightforward to implement and requires half as much memory. The appeal for point-value representation that computational time complexity can be significantly improved as discussed detail in Section 9.5.

An existing multivariate polynomial library that is specialized for use in generation of VAEs is not readily found in literature, but limited polynomial libraries do exist, such as the Python Polynomial Module [72]. This library was constructed from a small collection of simple algorithms for polynomials represented in coefficient form and with a monomial basis.

- **Polynomial Basics**
  - polyval – evaluate a polynomial at point x; $y = P(x)$
  - polyroots – compute roots of a polynomial; $P(x) = 0$
- **Polynomial Arithmetic**
  - polyadd – add one polynomial to another; $P(x) = W(x) + V(x)$
  - polysub – subtract one polynomial from another; $P(x) = W(x) - V(x)$
  - polymul – multiply one polynomial with another; $P(x) = W(x) \times V(x)$
  - polydiv – divide one polynomial with another; $P(x) = W(x) \div V(x)$

- polypow – raise a polynomial to a power; $P(x) = V(x)^e$

- **Polynomial Calculus**

  - polyderiv – differentiate a polynomial; $D(x) = \frac{d}{dx}P(x)$
  - polyint – integrate a polynomial; $I(x) = \int P(x)dx$

While the Python Polynomial Library is a step in the right direction, this is not a very expansive collection of polynomial routines. For example, in applications of modeling and simulation of aerospace vehicles often require the use of trigonometric functions (*i.e.* sine and cosine) for calculation of Euler and aerodynamic angles, as well as the use of hyperbolic functions (*i.e.* sinh and cosh) for guidance commands. These routines and more often simple algorithms but are scattered across the literature. A great place to start accumulating these routines is to refer to Knuth [172] and Mathews [191]. Table 12 below shows the result of a literature survey to accumulate a more extensive univariate polynomial library, which was implemented in C++ using data overloading techniques. This was done for the standard monomial (power series) basis functions, but similar routines exist for more exotic basis function types, such as Chebyshev, Bernstein, Legendre, etc. Pseudo-code for the algorithms are listed in Appendix A, and similar routines for other basis functions can be found in literature.

Table 12: Library of useful univariate polynomial routines for computation of variational asymptotic expansions to systems of ordinary differential equations (see Appendix A for more details).

	Polynomial Routines	Operation/Function	Description	Algorithm Source
Algebra	Assignment	$R(x) = P(x)$	Set one polynomial equal to another	N/A
	Add/Subtract	$R(x) = P(x) \pm Q(x)$	Add/subtract one polynomial to/from another	(Brown, 1963)
	Multiply	$R(x) = P(x) \times Q(x)$	Multiply one polynomial with another	(Knuth, 1972) (Kunis, 2003) (Giorgi, 20012)
	Divide	$R(x) = P(x) \div Q(x)$	Divide one polynomial by another	(Knuth, 1972)
	Power	$R(x) = P(x)^e$	Raise a polynomial to a power	(Knuth, 1972)
	Inversion	$R(x) = P(x)^{-1} = 1/P(x)$	Compute the reciprocal of a polynomial	(Knuth, 1972)
Calculus	Differentiate	$D(x) = \frac{\mathrm{d}}{\mathrm{d}x} P(x)$	Differentiate a polynomial	(Mathews, 1999) (Numerical Recipes, 2002)
	Integrate	$I(x) = \int P(x)\,\mathrm{d}x$	Integrate a polynomial	(Mathews, 1999) (Numerical Recipes, 2002)
Elementary Functions	Exponential/ Logarithmic	$R(x) = \exp(P(x), [b])$ $P(x) = \log(R(x), [b])$	Compute the exponential/logarithm of a polynomial, including: *exp*, *ln*, exp_2, log_2, exp_{10}, log_{10}, exp_b, log_b (*b* is arbritrary base)	Derived from (Knuth, 1972)
	Trigonometric	$V(x) = \sin(P(x))$ $W(x) = \cos(P(x))$	Compute the trigonometric function of a polynomial, including: *sin*, *cos*, *tan*, *csc*, *sec*, *cot*	Derived from (Knuth, 1972)
	Hyperbolic	$V(x) = \sinh(P(x))$ $W(x) = \cosh(P(x))$	Compute the hyperbolic function of a polynomial, including: *sinh*, *cosh*, *tanh*, *csch*, *sech*, *coth*	Derived from (Knuth, 1972)
Miscellaneous	Evaluate	$y = P(x)$	Evaluate a polynomial at *x*	(Knuth, 1972)
	Roots	x^*: $P(x^*) = 0$	Compute the roots of a polynomial	(Knuth, 1972)
	Radix shift	$P(x) \to P(x - x_0)$	Shift the polynomial center from *0* to x_0	(Knuth, 1972)
	Reversion	$y = P(x) \leftrightarrow x = P(y)$	Invert a polynomial to be parameterized by the independent variable	(Brent, 1978) (Knuth, 1972)
	Composition	$R(x) = P(Q(x))$	Evaluate a polynomial with another polynomial	Derived from (Knuth, 1972)
	Trim	$P(x) \to \tilde{P}(x)$	Remove "small trailing" coefficients from a polynomial	N/A

10.1.2 A Solution Algorithm Using an Object-Oriented Approach

Using a recursive approach, the univariate polynomial algorithms of Table 12 can be implemented on multivariate polynomials by using data overloading techniques [80, 172]. To illustrate this, consider the trivariate 2^{nd}-order polynomial below in Equation (63), which is expanded explicitly as a function of x by the 1×3 array of coefficients (a_0, a_1, a_2).

$$P(x, y, z) = a_0(y, z) + a_1(y, z)x + a_2(y, z)x^2 \tag{63}$$

Each of the coefficients a_0, a_1, a_2 can be expanded as integers, rational numbers, or polynomials that are explicitly a function of y by the 1×3^2 array of coefficients $(b_0, b_1, \ldots, b_8)$, as shown in Equation (64).

$$\begin{aligned} P(x, y, z) = &\left[b_0(z) + b_1(z)y + b_2(z)y^2\right] + \left[b_3(z) + b_4(z)y + b_5(z)y^2\right] x \\ &+ \left[b_6(z) + b_7(z)y + b_8(z)y^2\right] x^2 \end{aligned} \tag{64}$$

Again, each of the coefficients $b_0, b_1, \ldots, b_8$ can be expanded as more polynomials that are explicitly a function of z by the 1×3^3 array of coefficients $(c_0, c_1, \ldots, c_{26})$, as shown in Equation (65).

$$\begin{aligned} P(x, y, z) = &[(c_0 + c_1 z + c_2 z^2) + (c_3 + c_4 z + c_5 z^2)y + (c_6 + c_7 z + c_8 z^2)y^2] \\ &+ [(c_9 + c_{10} z + c_{11} z^2) + (c_{12} + c_{13} z + c_{14} z^2)y + (c_{15} + c_{16} z + c_{17} z^2)y^2]x \\ &+ [(c_{18} + c_1 9z + c_{20} z^2) + (c_{21} + c_{22} z + c_{23} z^2)y + (c_{24} + c_{25} z + c_{26} z^2)y^2]x^2 \end{aligned} \tag{65}$$

This approach to representing polynomials provides for a memory efficient representation of an m-dimensional polynomials and enables the univariate polynomial library of Table 12 to be implemented in a recursive fashion. It was chosen to implement this recursive approach to enable the manipulation of multivariate polynomials in C++ due to (i) a high degree of control for memory management and (ii) the ability to represent a multivariate polynomial as a k, d-array tree [80]. This is equivalently what is summarized in Equations (63)-(65), where each coefficient represents

a node of the tree and the corresponding expansion represent subsequent connecting nodes. For example, Figure 55 shows a k, d-array tree implementation of the trivariate 2^{nd}-order polynomial of Equations (63)-(65). Using k, d-array notation, each node is connected to $k = 3$ subsequent nodes and there are $d = 3$ layers of this tree. The head-node is representative of an entire multivariate polynomial and is allowed to interact with the head-nodes of other polynomials (*e.g.* addition of two polynomials together).

What enables the construction of the k, d-array trees to represent polynomials are the object-oriented programming concepts: *inheritance* and *polymorphism*, which allow for the classification of a hierarchy of polynomial variables types. In essence this allows the two fundamental Poly elements of the tree to be considered as building blocks that can be linked together as desired. Figure 54 illustrates this polymorphic hierarchy of a Poly element, which can be either type UPoly for specifying an array of numbers or MPoly for specifying an array of type Poly. In Figure 55 it can now be seen that each node is of type Poly and connected only to other Poly type nodes, but that internally these nodes are recast as either type Mpoly or Upoly.

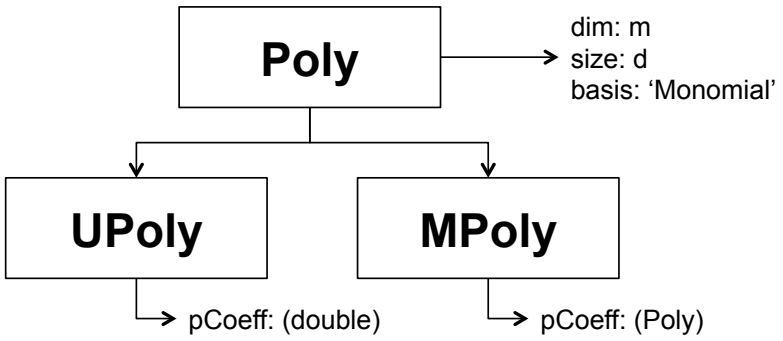

Figure 54: Polymorphic structure to be used to define the fundamental building blocks to be used in the construction of k, d-array trees for the representation of multivariate polynomials.

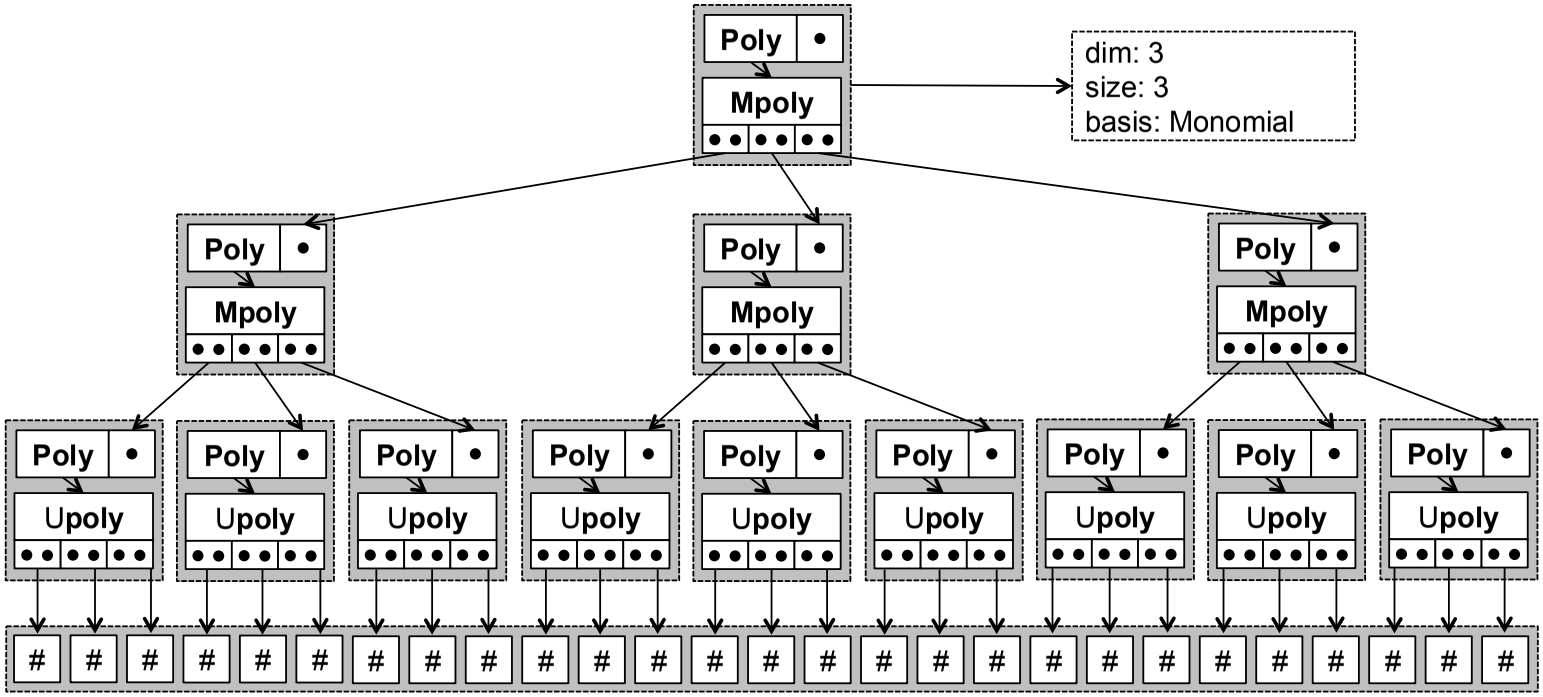

Figure 55: Recursive representation of a multivariate polynomial using a k,d-array tree for $k = d = 3$ in this case.

10.1.3 Demonstration of VAEs to Solve IVPs

*10.1.3.1 Test Problem #1: 1-State/1-Parameter System (*e.g. *Univariate Polynomial Arithmetic)*

As a simple demonstration, consider the 1st-order ODE with a single perturbation parameter s, shown below.

$$\frac{dy}{dt} = y^2 + 2s/t,\ y(1) = -1 \tag{66}$$

Figure 56 shows numerically generated results, which demonstrate the ability of higher-order VAEs to asymptotically approximate a neighboring solution by computing up to 20 higher-order derivatives at a baseline solution. The dashed black trajectory represents a baseline solution ($s = 0$), while the solid black line represents a perturbed solution ($s = 0.5$) Here it can be observed that as approximation order is increased, the VAE accuracy improves.

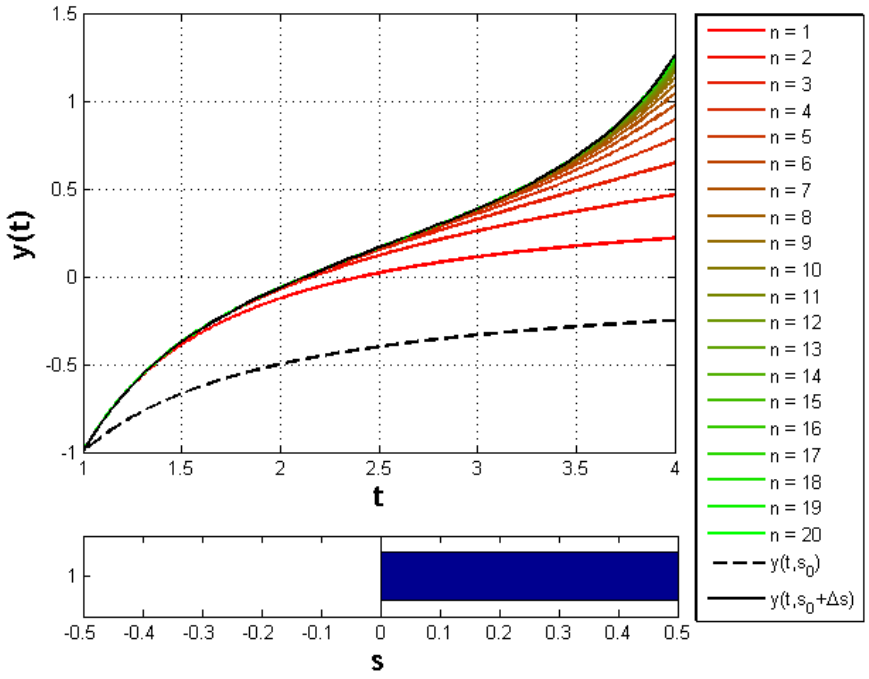

Figure 56: Comparison of increasing order-n VAE models for a simple 1-state, 1-parameter ODE. The dashed black trajectory represents a baseline solution ($s = s_0 = 0$), while the solid black line represents a perturbed solution ($s = s_0 + \delta s = 0.5$).

Figure 57 directly shows the performance of higher-order VAEs by comparing the approximation accuracy to the analytical solution for varying parameter s away from the baseline solution for $t = 4.0$. Here different color lines represent different order VAE approximations. It can be seen that as order n increases from 0 to 20 the approximation error can be improved for increasing s, however, with perceived diminishing returns as a the approximation error inevitably begins to degrade for increasing s.

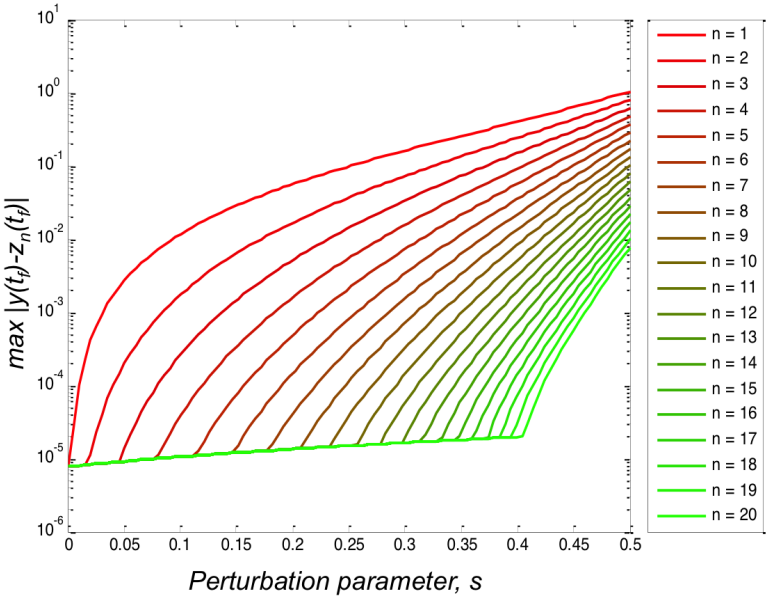

Figure 57: Increasing approximation accuracy of $y(t_f)$ for increasing order-n VAE models, $z_n(t_f)$ of an arbitrary 1-state, 1-parameter ODE ($\dot{y} = y^2 + 2s/t$, $y(1) = -1$).

*10.1.3.2 Test Problem #2: 2-State/3-Parameter System (*e.g. *Multivariate Polynomial Arithmetic)*

As an additional more involved demonstration to further highlight the capabilities of this implementation, consider the unforced Van der Pol oscillator system [254, 264]. In dynamics, the Van der Pol oscillator is a non-conservative oscillator with non-linear

damping. It evolves in time according to the second-order differential equation:

$$\frac{d^2x}{dt^2} - \mu(1 - x^2)\frac{dx}{dt} + x = 0. \tag{67}$$

Of course, this can be equivalently formulated as a system of 1st-order equations by using the transformation $v = \dot{x}$, according to the *principle of superposition*.

$$\begin{aligned} \dot{x} &= v \\ \dot{v} &= \mu\left(1 - x^2\right)v - x \end{aligned} \tag{68}$$

Suppose a response surface is desired for a family of solutions to Equation (68), parameterized by the initial conditions (x_0, y_0) and the orbit parameter μ and accurate to $E_{\text{tol}} := 1.0 \times 10^{-7}$. Table 13 shows the baseline simulation parameters and the desired range for the region of approximation. Here a Runge-Kutta-Fieldburg 5th/6th-order (RKF-56) numerical integration algorithm is used to adaptively control the simulation timestep to keep the numerical calculation of the higher-order sensitivities within the accuracy E_{tol} [132, 177, 191]. It was determined that using a maximum order of 10 was sufficient to parameterize the family of solutions within the region of approximation to sufficient accuracy to $t_f = 15$ (sec).

Figure 58 shows simulation results for two separate simulations, where the second simulation is approximated using the higher-order state-parameter sensitivities of the first. This clearly shows that the expansion is able to approximate the results of the second simulation. Figures 59 and 60 show the baseline results for the 1st and 2nd-order sensitivities, respectively. In Figure 61 the Fisher information time history was computed for the baseline results using the 1st-order sensitivities using Equation (8) at each tilmestep.

Figures 63 and 64 show hyper surfaces of families of solutions to the original 2-state system and the 1st-order 6-state sensitivity system, respectively. In all of these plots, the red line represents the baseline trajectory time history. The curse of dimensionality can be seen for just these two systems as the original system consisting

Table 13: VAE van der Pol oscillator simulation perturbation parameter descriptions.

Symbol	Parameter	Baseline	Range
x_0	Initial x-coordinate	0.5	[0.2,0.8]
v_0	Initial v-coordinate	0.5	[0.2,0.8]
μ	Orbit shape parameter	0.4	[0.1,0.7]

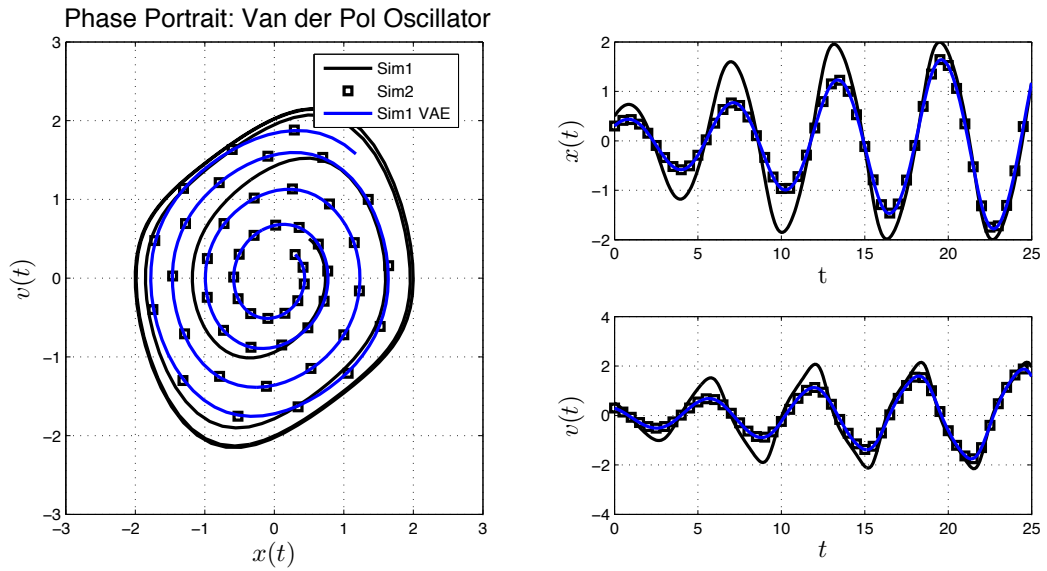

Figure 58: VAE van der Pol oscillator simulation results using the baseline values of the original system with respect to (x_0, v_0, μ).

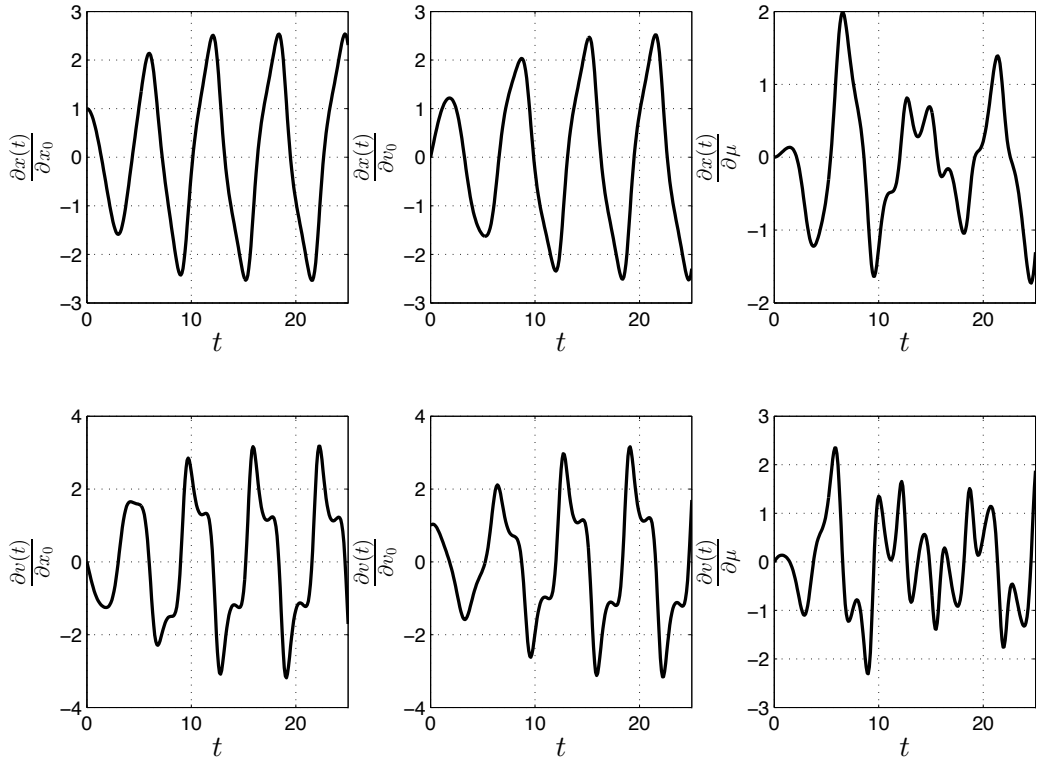

Figure 59: Simulation results of 1st-order sensitivities with respect to (x_0, v_0, μ) using the baseline values.

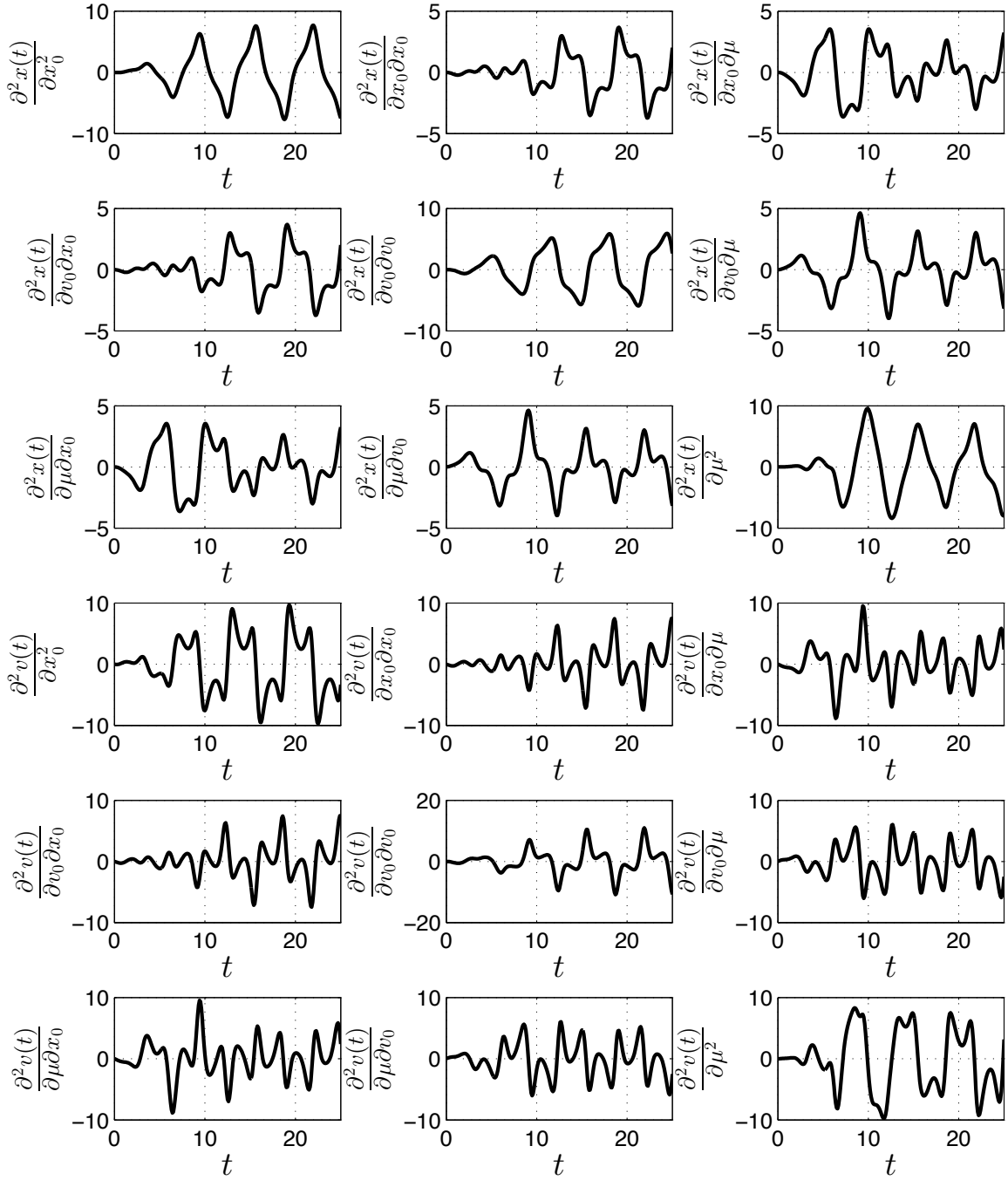

Figure 60: Simulation results of 2[nd]-order sensitivities with respect to (x_0, v_0, μ) using the baseline values.

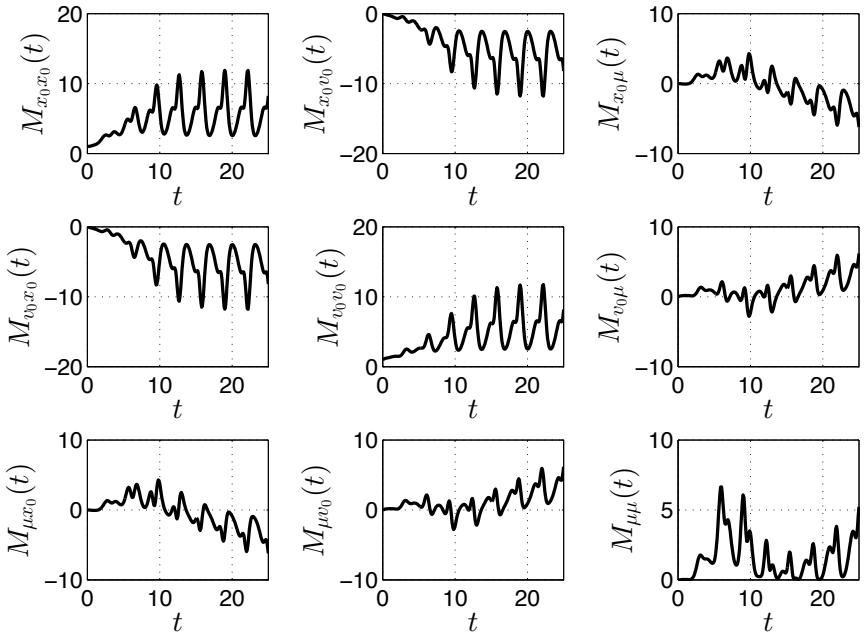

Figure 61: Simulation results of Fisher information time history, which was computed from the 1st-order state-parameter sensitivities using Equation (8) with respect to (x_0, v_0, μ) using the baseline values.

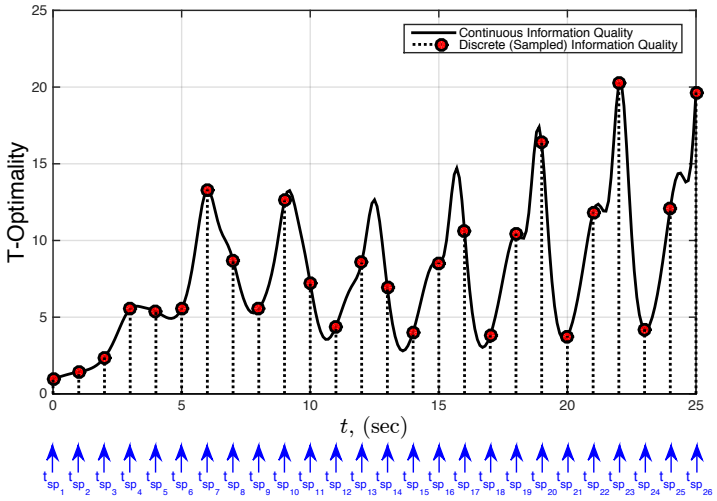

Figure 62: Illustration of sample T-Opt information quality metrics calculation using the Fisher information states from Figures 61, Equation (8) and a sampling frequency of 1 [Hz].

of 2 states and 3 parameters results in 6 hypersurfaces, and correspondingly, the 1st-order sensitivity system results in 18 hypersurfaces. It has quickly become not practical to show a single composite plot of the 2nd-order sensitivities, which would require 54 hypersurfaces.

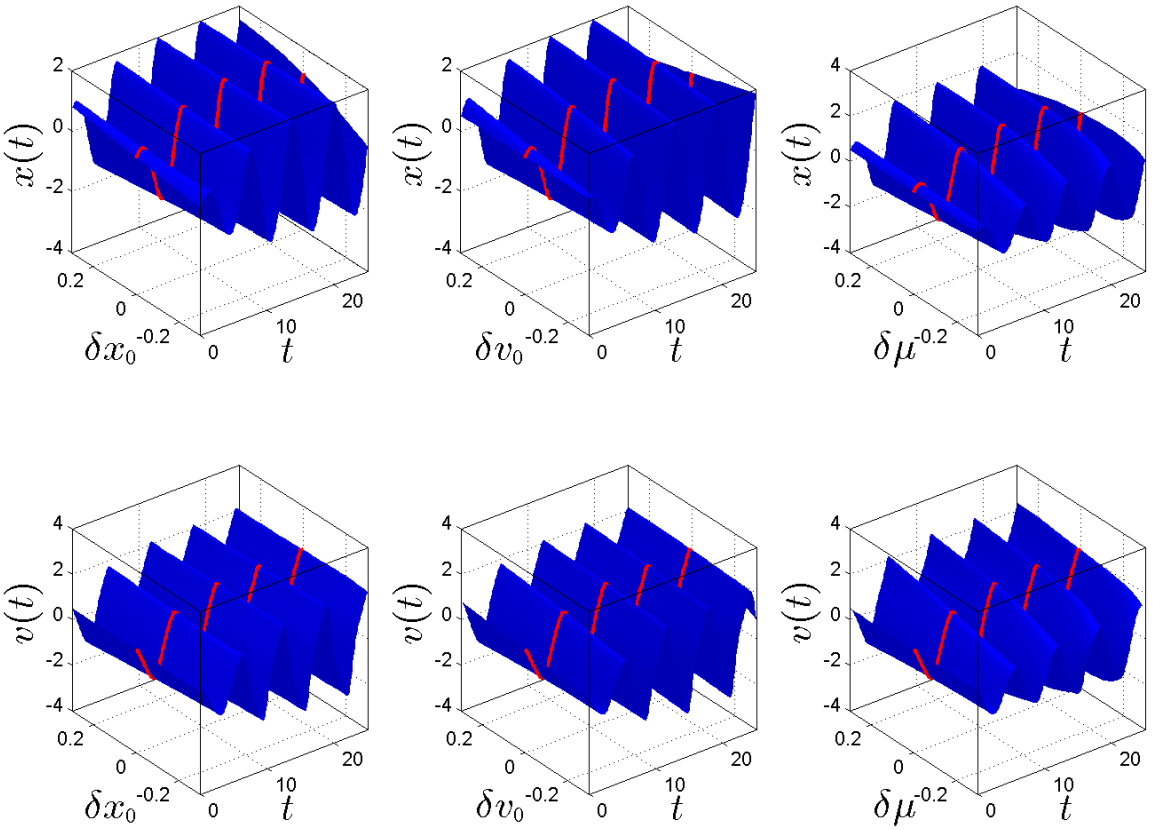

Figure 63: Hypersurfaces of families of solutions to the Van der Pol system, which are parameterized by three perturbation parameters: the initial conditions $(\delta x_0, \delta y_0)$ and the orbit shape parameter $\delta\mu$.

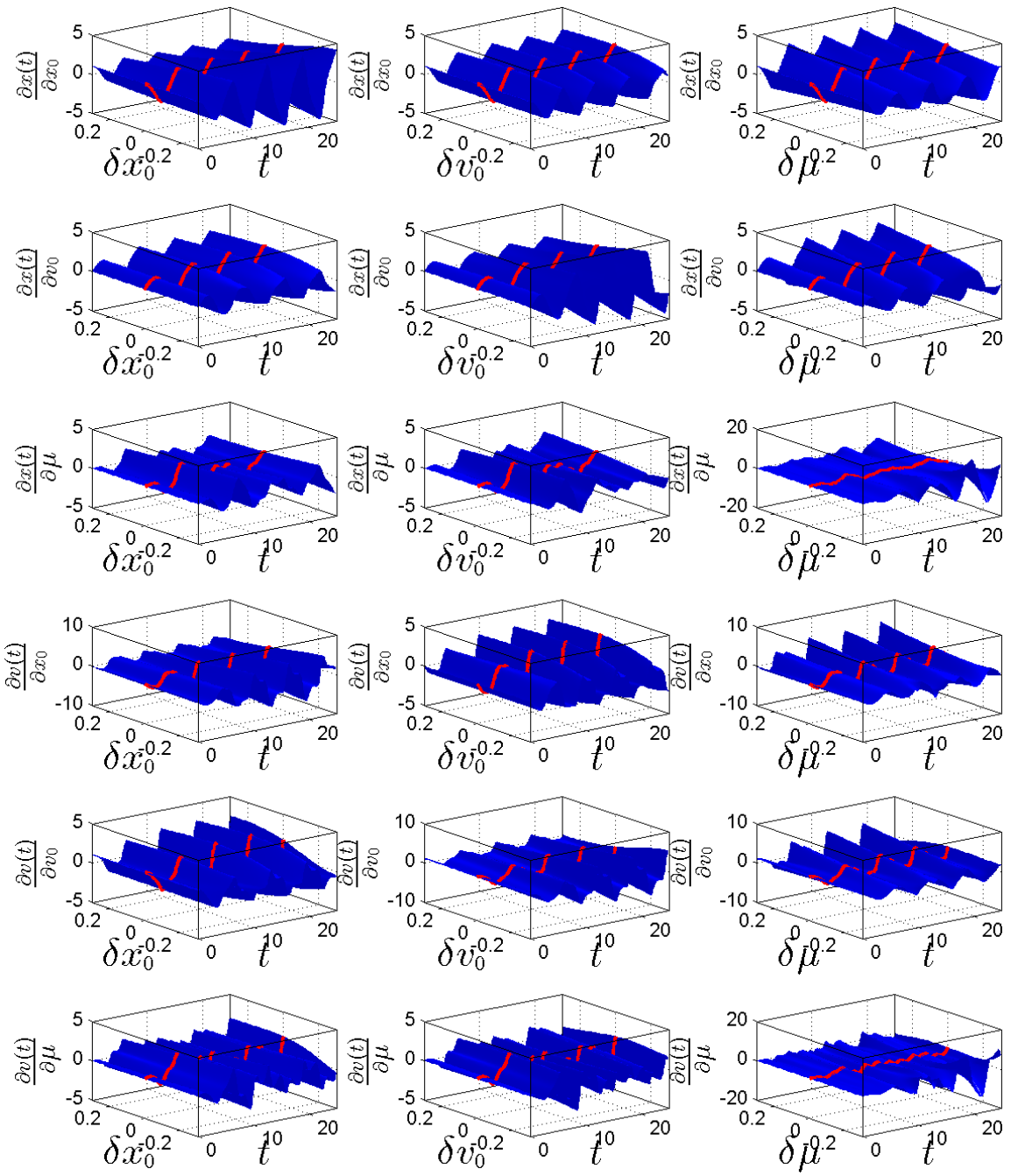

Figure 64: Hypersurfaces of families of solutions to the 2nd-order sensitivities of the Van der Pol system, which are parameterized by three perturbation parameters: the initial conditions $(\delta x_0, \delta y_0)$ and the orbit shape parameter $\delta\mu$.

In this section it has been shown that implementation of VAEs to surrogate parameterized families of solutions is possible. For the van der Pol oscillator, it was shown that by constructing a VAE solution using up to 10^{th}-order sensitivities, any trajectory within the ranges given in Table 13 can be approximated to arbitrarily sufficient accuracy. This analysis was enabled by several advances in computer science, such as polymorphism and data overloading techniques, which were used to enable the development of a multivariate polynomial engine – the core functionality required for the computation of higher-order sensitivities of dynamic systems.

10.2 Exp't #1 – Basis Function Selection

In Section 9.3.1 it was discussed that the utility of computing higher-order gradient information using Taylor (monomial) basis functions can potentially have limited effectiveness. One of the most significant limitations, is a phenomena known as the finite radius of convergence, which implies that expanding the region of approximation beyond a certain point is impossible or impractical for certain problems. To address this, **RQ.#2.1** was posed to determine if the selection of a different basis function can address this limitation in some applications, and alternate candidate basis functions of current interest in the academic community were enumerated, including: Chebyshev polynomials, Legendre polynomials, Bernstein polynomials, etc. As such, the following hypothesis was proposed.

HYP. #2.1.1: Based on the problem, intelligent selection of basis functions can increase the region of approximation as well as the rate of convergence without experiencing the degree of diminishing returns that are observed when employing expansion approximations using Taylor basis functions.

10.2.1 Experimental Procedure

To test **HYP. #2.1.1**, a standard comparative performance assessment of several numerical integration methods will be conducted on several basic test problems, where two of the numerical integrators leverage the use of automatic differentiation to compute higher-order time-derivative information. The experimental procedure for this experiment is as follows: (i) collect and implement the Chebyshev polynomial operations of Table 14; (ii) implement the four numerical integration schemes on the test problems shown in Table 16 – two of which require the computation of VAEs to construct high-accuracy numerical solutions; and (iii) compare numerical integration results from different integrators with respect to analytically derived or computationally expensive solutions to quantify numerical performances (*e.g.* numerical errors, timestep magnitude, asymptotic expansion order, etc.).

10.2.2 Chebyshev Polynomial Library Construction

If any desired polynomial basis is to be used for generation of VAEs, then analogous polynomial operations and elementary functions to the algorithms presented in Table 12 will need to be collected, derived, and then implemented. Prior to testing **HYP. #2.1.1**, an effort was made to collect and implement as many relevant polynomial operations as possible for the Chebyshev basis. Similar to the effort to collect polynomial operations in the monomial (Taylor) basis of Table 12, these algorithms are scattered across the literature. Also, there are many Chebyshev polynomial/series routines that currently have yet to be derived (*e.g.* trigonometric evaluation on a Chebyshev series), and therefore the findings of this study provide discerning evidence for continued research in this area. Table 14 summarizes the implemented algorithms for this work.

Implementation of Chebyshev operations into the recursive coefficient approach for multivariate capabilities is less straightforward with respect the the same exercise

Table 14: Library of useful univariate polynomial routines in the Chebyshev basis for computation of variational asymptotic expansions to systems of ordinary differential equations.

	Polynomial Routines	Operation/Function	Description	Algorithm Source
Algebra	Assignment	$R(x) = P(x)$	Set one Chebyshev polynomial equal to another	N/A
	Add/Subtract	$R(x) = P(x) \pm Q(x)$	Add/subtract one Chebyshev polynomial to/from another	(Brown, 1963)
	Multiply	$R(x) = P(x) \times Q(x)$	Multiply one Chebyshev polynomial with another	(Rayes, 2005) (NumPy, 2015) (Giorgi, 2013)
	Divide	$R(x) = P(x) \div Q(x)$	Divide one Chebyshev polynomial by another	(Knuth, 1972)
Calculus	Differentiate	$D(x) = \frac{\mathrm{d}}{\mathrm{d}x} P(x)$	Differentiate a polynomial	(NumPy, 2015) (Numerical Recipes, 2002)
	Integrate	$I(x) = \int P(x)\,\mathrm{d}x$	Integrate a Chebyshev polynomial	(NumPy, 2015) (Numerical Recipes, 2002)
Misc.	Evaluate	$y = P(x)$	Evaluate a Chebyshev polynomial at *x*	(Numerical Recipes, 2002)

with the Taylor basis algorithms, as most of these operations are more complex in comparison the the Taylor basis equivalent. For example, multivariate Chebyshev division involves recursively solving linear systems, which is both cumbersome to implement and time consuming to compute, as opposed to the division of Taylor basis polynomials, which has the same complexity as Taylor polynomial multiplication.

10.2.3 Numerical Integration Schemes

The four numerical integration schemes used in this study are: (i) the standard forward-Euler routine, (ii) the standard 4^{th}-order Runge-Kutta routine method, (iii) Taylor integration method, and (iv) the Taylor integration method implemented in the Chebyshev basis. Details on the first three of these integrators can be found in common numerical texts [132, 177, 191]. Both the forward Euler and 4^{th}-order Runge-Kutta methods are very common methods that are easily implemented. Table 15 shows the general method for implementing the Taylor method, which has found use applications in celestial mechanics where high-accuracy orbits that span large time scales is desired. Mathews [191] provides numerical examples that illustrate

that while the Taylor method is a superior numerical integration method it is often not practical to implement even on small problems, due to the required manual effort to analytically derive higher-order time-derivatives. Recently, the Taylor integration has seen a resurgence in use, due to the advent of automatic differentiation to enable compile-time higher-order time-derivative information to be computed at relative little computational effort and to high accuracy on a traditionally formulated dynamic system [159].

Table 15: The Taylor method numerical integration algorithm for high accuracy numerical simulation of ODE systems of the form $\dot{x} = f(t, x)$, where automatic differentiation is utilized to compute step 2(a) to an arbitrarily high-'order time-derivative.

Taylor Method Algorithm

1. **Specify**: t_0, t_n, x_0, h ((x_0,y_0) Initial conditions, t_n point where the solution is required, h the step length to be used in the marching process)
2. **Iterate**: from initial time t_0 to final time t_n
   (a) **Compute**: $f(t_i, y_i)$, $f'(t_i, x_i)$, $f"(t_i, x_i)$,...
   (b) **Compute**: $x(t_i + h) = x(t_i) + f(t_i, x_i)h + f'(t_i, x_i)h^2/2 + h^3 f"(t_i, x_i)h^2/3! + ...$
   (c) **Compute**: $t_i = t_i + h$
3. **Terminate Criterion**: $t_i = t_n$

10.2.4 Test Problem Descriptions

The test problems selected for these experiments were selected such that (i) the limited library of Table 14 was able to be implemented, (ii) numerical implementation is relatively straightforward, and (iii) the characteristics of each problem are distinct, so as to provide a level of contrast between results. The table below summarizes the selected test problems.

Table 16: Summary of test problems for comparison of VAEs in both the Taylor and Chebyshev bases.

Name	**Dynamic Model**	**Parameter Values**	**Initial Conditions**	**Description**
Spring-Mass System	$\dot{x} = v$ $\dot{v} = -(kx)/m$	$k = 3.5$ $m = 0.10$	$x_0 = 1.0$ $v_0 = 0.0$	• *conservative oscillator* • *2^{nd}-order system*
van der Pol Oscillator	$\dot{x} = v$ $\dot{v} = \mu(1 - x^2)v - x$	$\mu = 0.4$	$x_0 = 0.5$ $v_0 = 0.5$	• *non-conservative oscillator* • *limit cycle*
Lorenz Attractor	$\dot{x} = \sigma(y - x)$ $\dot{y} = x(\rho - z) - y$ $\dot{z} = xy - \beta z$	$\sigma = 10$ $\beta = 8/3$ $\rho = 28$	$x_0 = 1.0$ $y_0 = 1.0$ $z_0 = 1.0$	• *chaotic system (strange attractor)* • *sensitive dependence on initial conditions and parameters*

10.2.5 Results and Discussion

Figures 65 and 66 show simulation and residual error results for the spring-mass system described in Table 16, where the analytic (exact) solution is known to be $x(t) = \cos(\omega t)$ and $v(t) = -\omega \sin(\omega t)$ and $\omega = \sqrt{\frac{k}{m}}$. Here it is observed that only the Forward-Euler integration does a poor job of numerically approximating the exact solution, even though it has the smallest timestep of the four methods at $h = 0.05$ (sec). This is an expected result, especially when simulating systems where energy is conserved. Both the 12^{th}-order Taylor and the 30^{th}-order Chebyshev integrators are superior to the RK4 integrator, in that, they approximate the exact solution with lower numerical error and require fewer integration evaluations (*i.e.* they can take larger timesteps). Hence, while the number of derivative function evaluations at a given timestep is more expensive for the generic n^{th}-order Taylor or Chebyshev method with respect to the RK4 method, the total number of integration function evaluations can be substantially reduced while also maintaining superior numerical accuracy. This is indeed the case here where the 30^{th}-order Chebyshev integrator (only requiring 150 function calls at a timestep of $h = 3$ (sec)) is superior to the 12^{th}-order Taylor integrator (requiring 180 function calls at a timestep of $h = 1$ (sec)) while also possessing superior error performance.

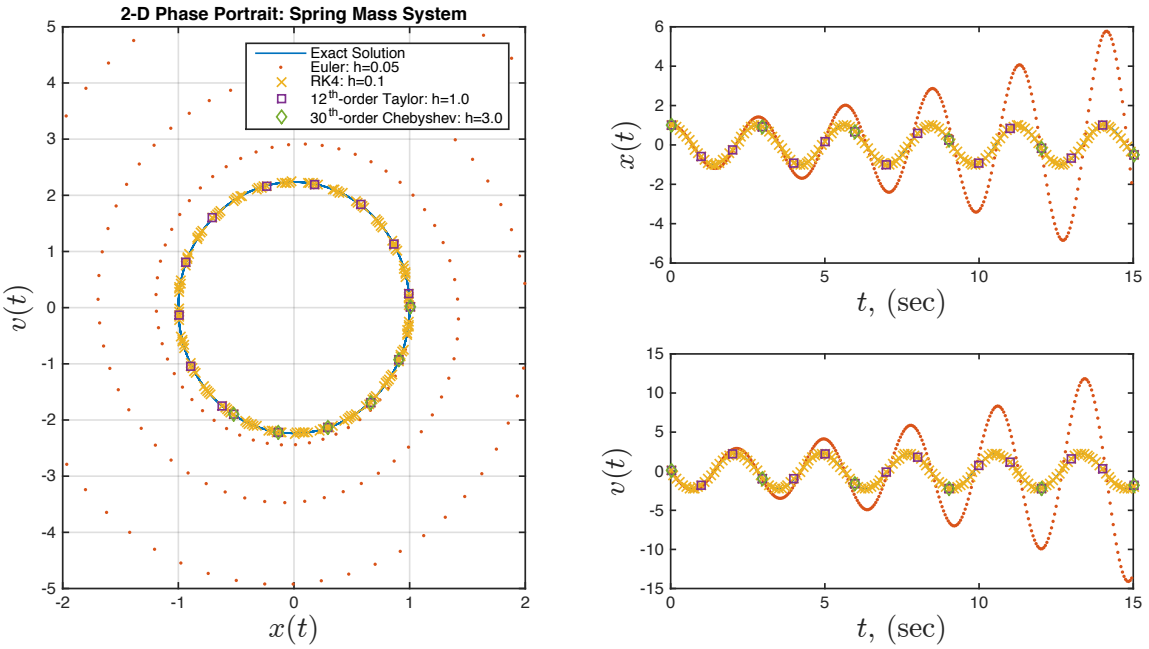

Figure 65: Spring-mass system simulation results comparing performance of traditional integrators to high-accuracy Taylor integrators in both monomial and Chebyshev basis.

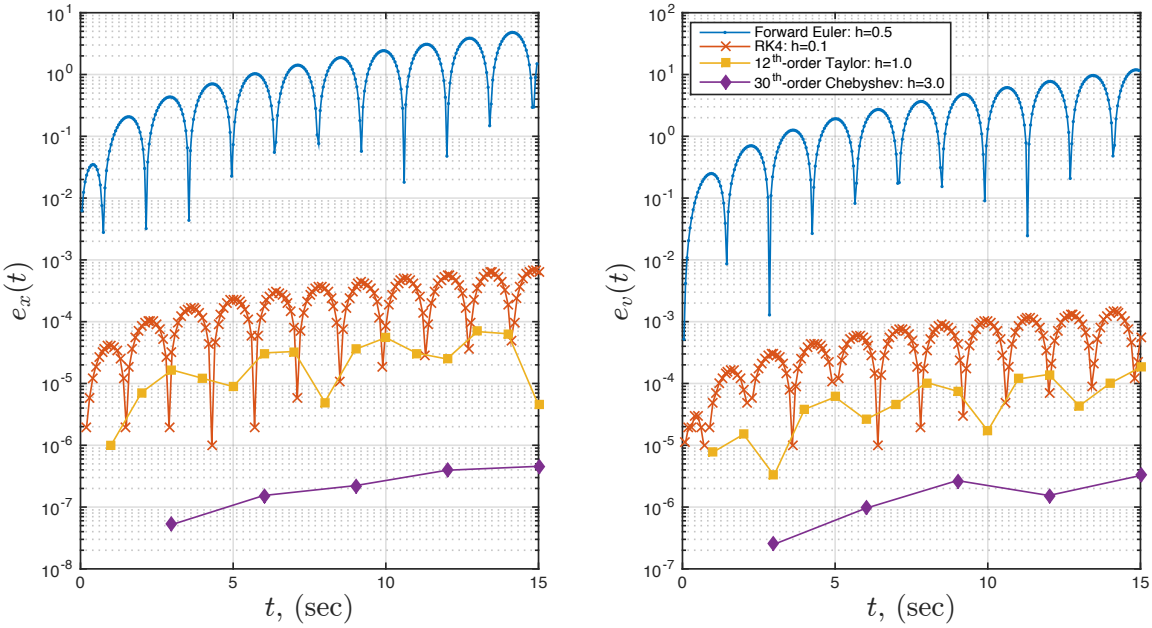

Figure 66: Spring-mass system error analysis comparing accuracy of traditional integrators to high-accuracy Taylor integrators in both monomial and Chebyshev basis.

While the results of Figures 65 and 66 illustrate the idea that higher-order expansions can generate numerically superior results, these results do not yet address **HYP#2.1.1**, because they do not directly compare the performance of the Taylor and Chebyshev integrators, because the Chebyshev integration, in this instance uses a significantly higher-order expansion than the Taylor integrator. Therefore, Table 17 and Figure 67 directly compare Taylor and Chebyshev temporal asymptotic expansions for the spring-mass system at simulation time $t_{\text{sim}} = 14.0$ (sec) for two asymptotic expansions up to 12^{th}-order. It is common knowledge that the truncation error of an asymptotic expansion can be estimated by examining the magnitude of the highest order coefficient [191, 132]. Hence, upon inspection of Table 17, it can be readily observed that the 8^{th}-order Chebyshev expansion has nearly the same approximation error at $E_{\text{approx}} \approx 10^{-5}$ as the 11^{th}-order Taylor expansion, which implies that for the same order and timestep the Chebyshev integrator requires less computational expense to generate the same accuracy performance.

Table 17: Spring-mass system 12^{th}-order temporal Taylor and Chebyshev asymptotic expansions at $v(t = 14\ (\text{sec}))$.

$\mathbf{a_n}$	**Taylor**	**Chebyshev**
c_0	1.5955	0.144242
c_1	3.50268	1.72492
c_2	-3.98874	-1.28295
c_3	-2.9189	-0.5283
c_4	1.66198	0.160911
c_5	0.729726	0.0369104
c_6	-0.276996	-0.00722556
c_7	-0.0868721	-0.00116002
c_8	0.0247318	0.000168059
c_9	0.00603279	2.06E-05
c_{10}	-0.00137399	-2.38E-06
c_{11}	-0.000274218	-2.68E-07
c_{12}	5.20E-05	2.54E-08

The information of Table 17 can also be used to obtain estimations on the radius and rate of convergence of each asymptotic expansion, using the analysis of Domb and Sykes to evaluate the following limit [88, 139].

$$\frac{1}{r} = \lim_{n\to\infty} \frac{c_n}{c_{n-1}} \tag{69}$$

An approximation of this limit can be made by fitting the data of $\frac{c_{n-1}}{c_n}$ vs. $\frac{1}{n}$ to a linear model ($\lim_{n\to\infty} \frac{c_{n-1}}{c_n} \approx \frac{1}{\epsilon_0} - \frac{1+\alpha}{\epsilon_0}\left(\frac{1}{n}\right)$), which is the so-called Domb-Sykes plot. Here the radius of convergence is approximated via extrapolation by $r \approx \epsilon_0$ and α is a parameter related to the rate of convergence. The linear regressions in Figure 67 were generated using the final five points, as it is known that for low values of n the ratio $\frac{c_{n-1}}{c_n}$ is a poor estimator. As can bee seen here, both the Taylor and Chebyshev expansions have the same radius of convergence of approximately ∞ in this case; however, the Chebyshev expansion has a fast rate of convergence, as the inverse of the regressed slope is higher. Therefore the Chebyshev expansion converges faster.

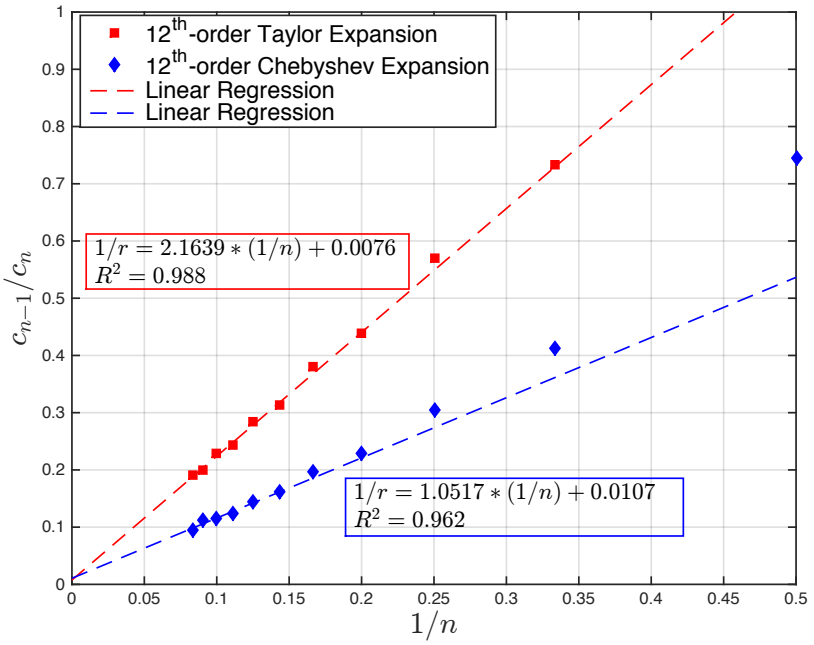

Figure 67: Domb-Sykes plot of spring-mass system comparing rate of convergence of high-accuracy Taylor integrators in both monomial and Chebyshev basis for the spring-mass system.

Figures 68 and 69 show simulation and residual error results for the van der Pol oscillator system described in Table 16, where the expensive solution was obtain by using a RKF56 (*i.e.* adaptive timestep) integrator to control the tolerance approximation error to be on order $E_{\text{tol}} \approx 10^{-8}$. For this problem, both the Taylor and Chebyshev integrators use up to 15^{th}-order approximations, and while both integrators have similar error performance, the Chebyshev integrator used a timestep that was twice as large as the Taylor integrator. Hence, the Chebyshev integrator has better performance than the Taylor integrator because it has half as many integration evaluations. Notice that the Forward-Euler method does not perform as poorly for the van der Pol oscillator as it does for the spring-mass system, which is again an anticipated result, due to the attractive nature of the limit cycle in this system.

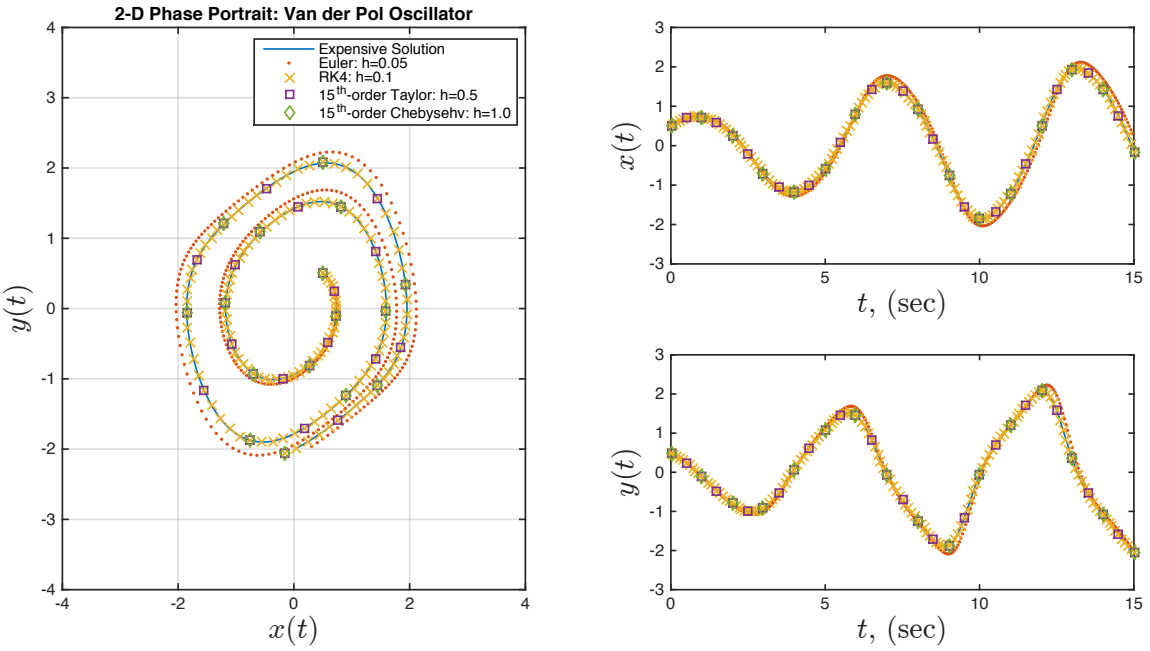

Figure 68: Van der Pol oscillator simulation results comparing performance of traditional integrators to high-accuracy Taylor and Chebyshev integrators.

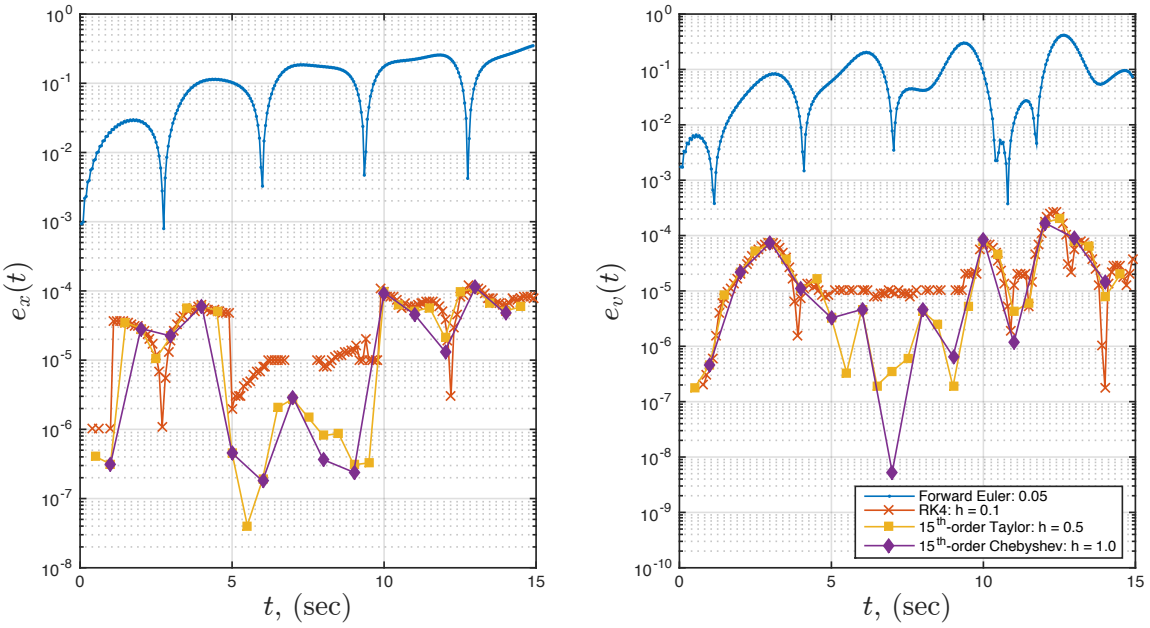

Figure 69: Van der Pol oscillator error analysis comparing accuracy of traditional integrators to high-accuracy Taylor and Chebyshev integrators.

Figures 68 and 69 show simulation results for the Lorenz system described in Table 16. This system is known for its chaotic nature, and has proven to yield interesting results in basic research [264]. Originally developed as a simplified model for atmospheric convection, a known attribute of this system is its sensitive dependence on initial conditions. This implies that regardless how close the solutions of two simulations are initially, as time progresses, eventually the two responses will drastically diverge. In the plots below, an RK4 ($h = 1 \times 10^{-4}$) is compared to a 10^{th}-order Taylor method ($h = 1 \times 10^{-3}$), which show that as integration error accumulates in the two integrators eventually the two simulations will indeed yields drastically dissimilar responses. Therefore, the Taylor integration method has the ability to control numerical integration error by (i) increasing VAE order and (ii) simply reducing the integration timestep h to smaller and smaller values.

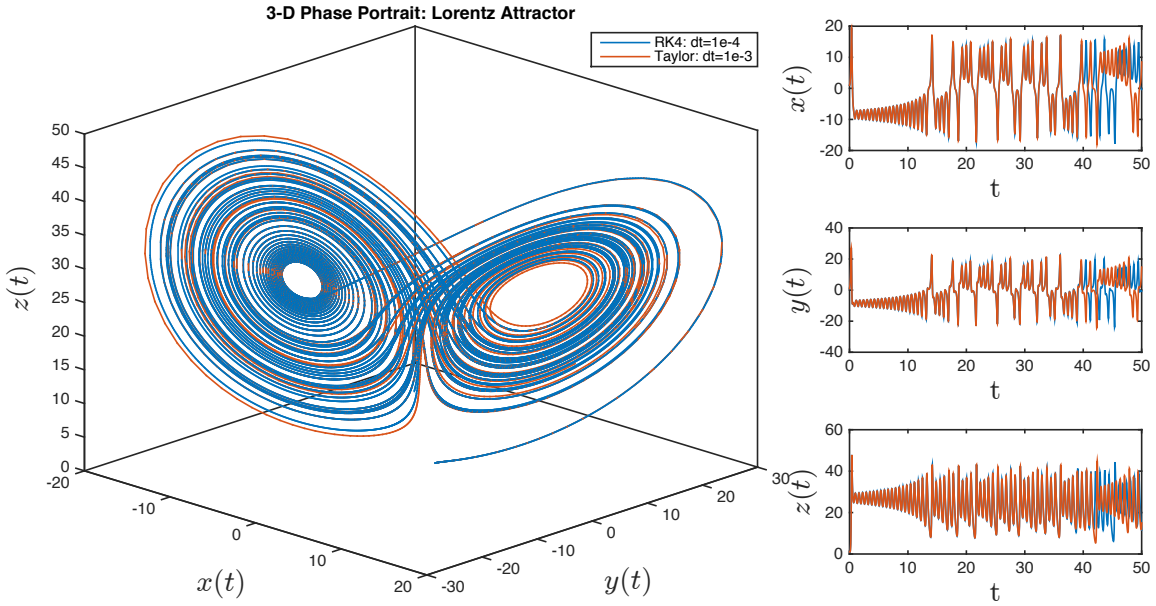

Figure 70: Lorenz system simulation results comparing the traditional RK4 ($h = 1 \times 10^{-4}$) integrator to the high-accuracy Taylor integrator ($h = 1 \times 10^{-3}$). Each integrator accumulates error differently, and for systems that demonstrate a high sensitivity to dependence on parameters, the numerical integration accuracy can have a significant effect on simulation results.

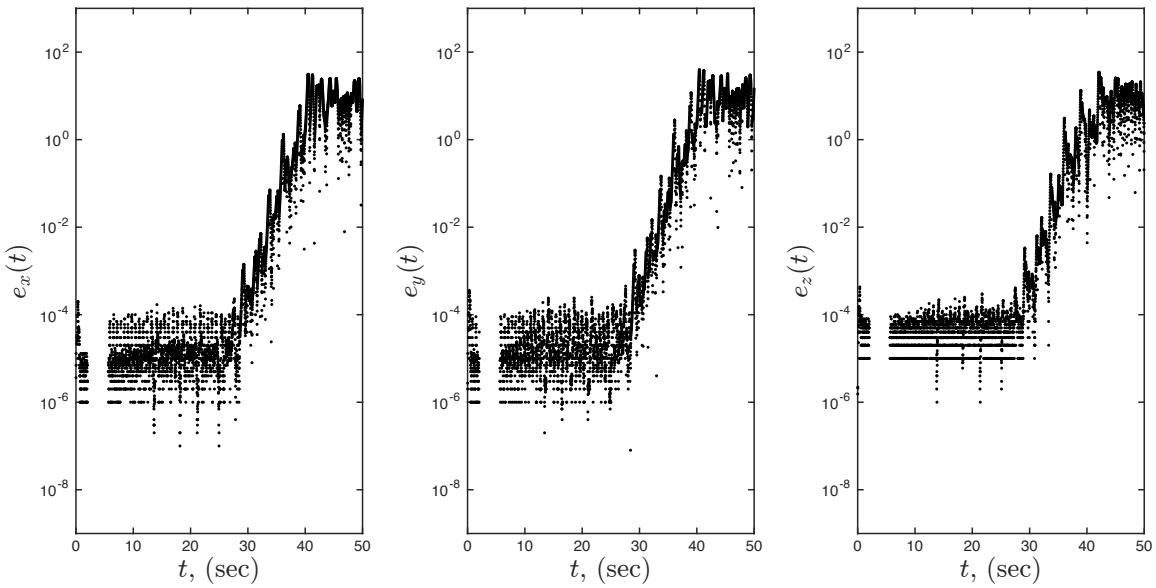

Figure 71: Relative logarithmic error between RK4 and 10^{th}-order Taylor integration results, showing the inevitable divergence of the two simulations for the same initial conditions.

10.2.6 Exp't #1 Observations

The findings of this study suggest that implementing polynomial elementary operations and functions in separate basis functions can help to generate better VAE models in terms of more computational accuracy (*i.e.* larger approximation regions) with potentially fewer high-order terms being required. Therefore **HYP#2.1.1** is accepted, and it is concluded that the results above provide strong evidence and motivation to further pursue the construction and implementation of polynomial libraries for elementary operations and functions in separate basis functions. If this effort is eventually realized, it will enhance the capabilities summarized in Table 12 to provide the STEM communities with an additional tool/method to accurately build solutions to potentially many numerical problems.

10.3 Exp't #2 – Use of VAEs for High-Accuracy Uncertainty Propagation

The purpose of this experiment is to investigate **HYP. #2.1.2** from Section 9.4, which is concerned with studying the effectiveness of how VAEs enable the propagation of parameter uncertainty with asymptotic accuracy control for dynamic systems. The potential for this capability is for utilization in robust-optimal dynamic experiment design for industrial aerospace applications.

10.3.1 Experimental Procedure

The experimental procedure for this series of experiments is as follows: (i) a simple dynamic system will be selected to serve as a test apparatus; (ii) higher-order VAEs will be generated for this system and convergence characteristics will be investigated for increasing order; (iii) Gaussian and Uniform probabilistic distributions will be selected to represent uncertainty quantification of parameter perturbations; and (iv) probabilistic convergence analyses will be performed and compared for the different distribution types to the convergence results of the VAEs for increasing order. The

expected outcome of these experiments is to observe if VAEs with slower, oscillatory convergence rates will significantly affect the feasibility of high-accuracy uncertainty propagation.

10.3.2 Test Problem Description

The test problem is a simple spring-mass-damper under non-homogeneous forcing. This system was selected because it is sufficiently simple, so that the effects of increasing complexity due to the curse of dimensionality can be mitigated for purposes of this study. Also, it is common to approximate aircraft dynamic systems using simple linearized systems, which can be shown to be equivalent to spring-mass-damper systems - therefore providing intuitive results (*e.g.* Lancaster approximation to Phugoid and short-period stability modes and response) [98, 99].

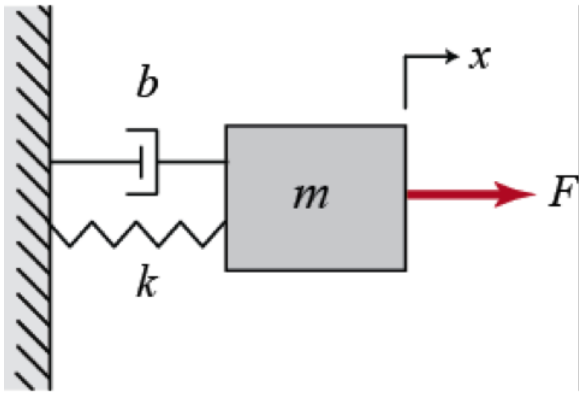

Figure 72: Diagram of spring-mass-damper problem with external forcing.

To provide further similarity with aircraft flight testing applications, the forcing function $F(t)$ was selected to be a 3-2-1-1 step input sequence to keep the system excited. This is a relevant excitation signal because it is used for SysID of fixed-winged aircraft during flight testing [170]. The mathematical model for the equation of motion for this damped 2^{nd}-order system is described below:

$$\ddot{x} = \left(-kx - c\dot{x} + F\left(t\right)\right)/m \tag{70}$$

where $F(t)$ is a 3-2-1-1 step input sequence starting at $T_{sw,0} = 2.0$ (sec).

$$F(t) = \begin{cases} \frac{1}{3} & , 2.0 \leq t < 5.0 \text{ (sec)} \\ -\frac{1}{3} & , 5.0 \leq t < 7.0 \text{ (sec)} \\ 1 & , 7.0 \leq t < 8.0 \text{ (sec)} \\ -1 & , 8.0 \leq t < 9.0 \text{ (sec)} \end{cases} \tag{71}$$

The nominal parameter values and probabilistic uncertainty models for this study are provided in Table 18.

Table 18: Spring-mass-damper parameter uncertainty models for uniform $\mathcal{U}(a, b)$ and gaussian $\mathcal{N}(\mu, \sigma^2)$ distribution parameters.

Parameter	**Nominal Value**	$\mathcal{U}(a,b)$		$\mathcal{N}(\mu,\sigma^2)$	
		a	b	μ	σ^2
k	3.50	2.80	4.20	3.50	$0.2\bar{3}$
m	0.10	0.08	0.12	0.10	$6.6\bar{6} \times 10^{-3}$
c	0.15	0.12	0.18	0.15	1.00×10^{-2}

10.3.3 Results and Discussion

Similar to what was demonstrated in Section 10.1.3 for the van der Pol oscillator, Figure 73 shows the VAE hypersurfaces (*i.e.* response surrogates) for the spring-mass-damper with non-zero initial conditions and under a forced 3-2-1-1 step input sequence. VAE parametric hypersurfaces using 0^{th}-order up to 10^{th}-order gradient information, where generated for a 10 (sec) simulation and evaluated in the perturbation parameters $\delta\theta = (\delta k, \delta m, \delta c)$ with ranges given from the bounds on uncertainty used in the uniform distributions of Table 18.

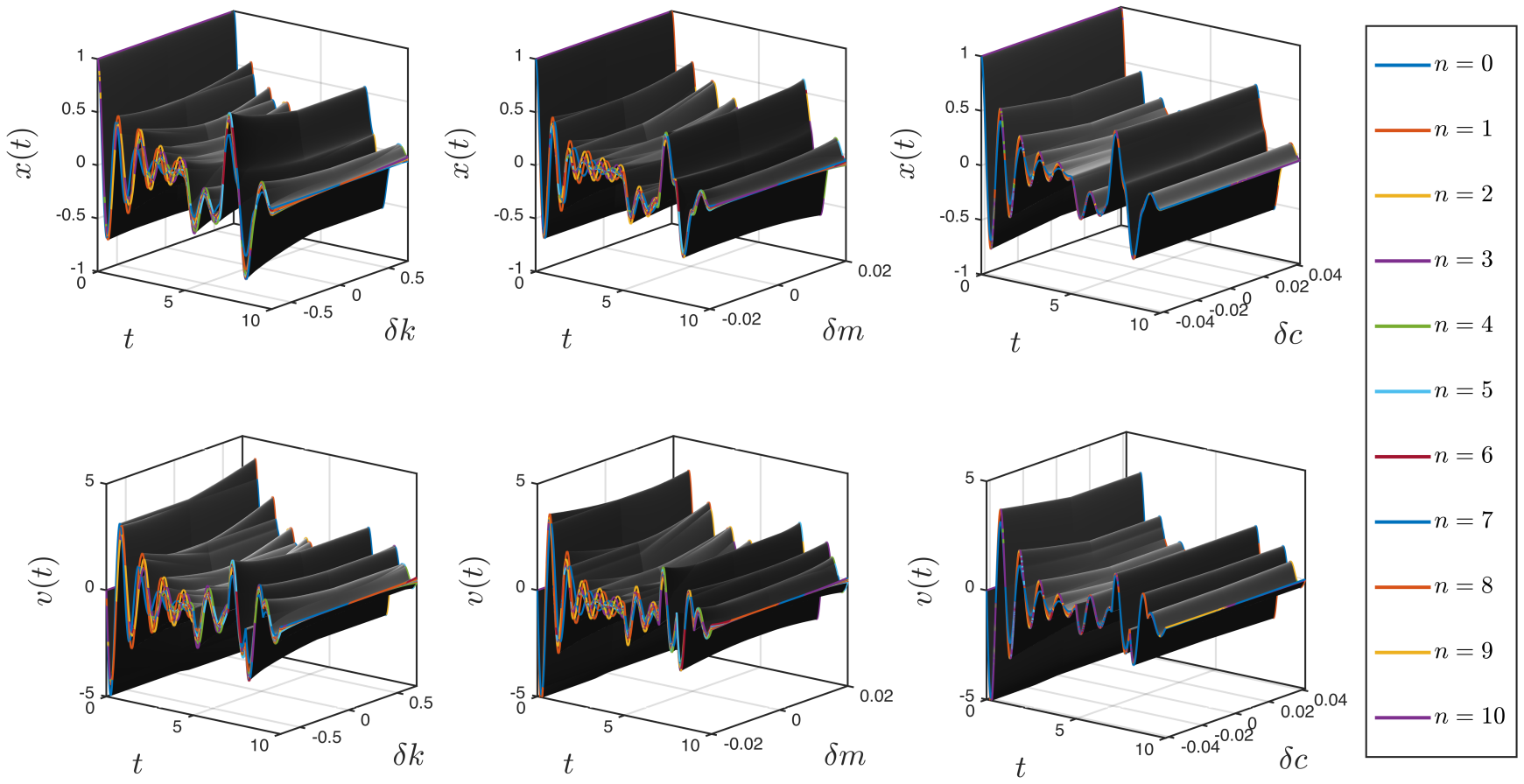

Figure 73: Spring-mass-damper numerical simulation over-layed VAE hypersurfaces using 0^{th}-order up to 10^{th}-order gradient information and parameter perturbations $\delta\theta = (\delta k, \delta m, \delta c)$.

10.3.3.1 VAE Asymptotic Convergence Analysis

From Figure 73 it is difficult to observe the convergence characteristics as VAE approximation order is increased. A global convergence analysis was performed (see Appendix B) by computing the difference between the i^{th} and $(i-1)^{\text{th}}$-order surfaces to observe relative error. Figures 139-144 in Appendix B show global relative convergence contoured results for increasing order. In these results it can be observed that relative error is well-behaved for the majority of the time-perturbation space; however, for larger perturbations, there are oscillatory regions where accuracy degrades. Figure 74 show convergence results corresponding to all the VAE-to-parameter hypersurfaces from Figure 73, where the worst-case error value was used at each order (*i.e.* the infinity norm $||\cdot||_\infty$). Observe that while all VAEs exponentially converge for increasing order that they do so at different rates.

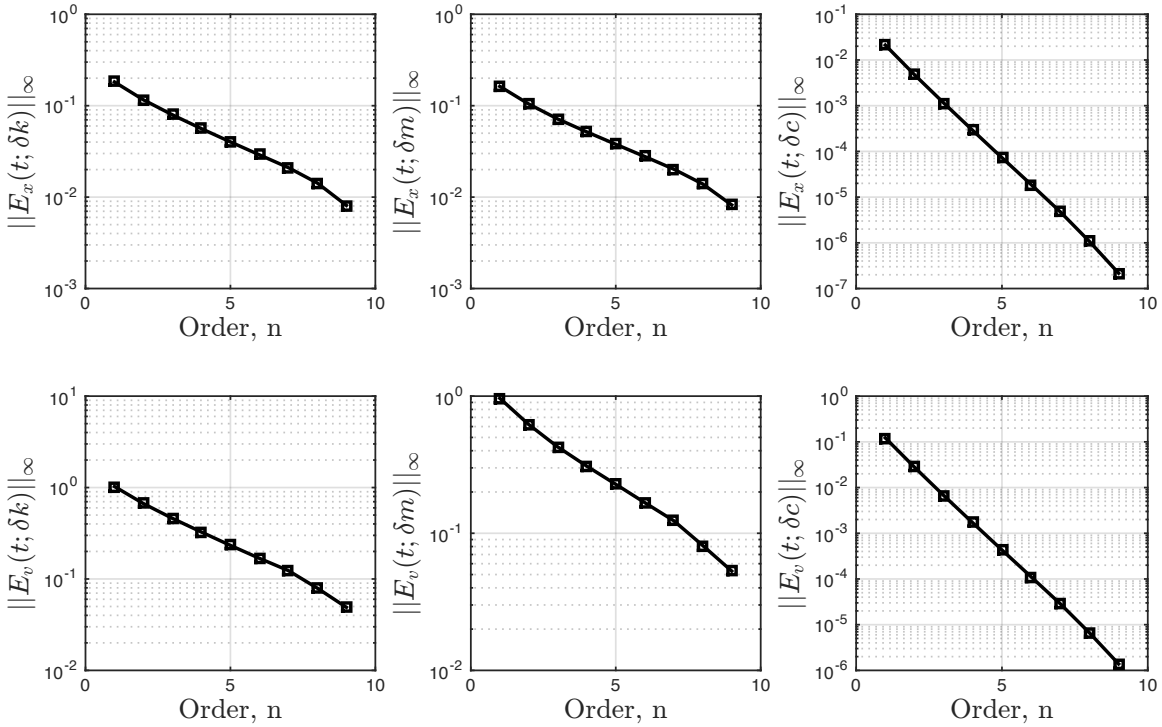

Figure 74: Global VAE asymptotic convergence analysis of the 3-2-1-1 step forced spring-mass-damper system for relative error using the infinity norm (*i.e.* max error).

It is observed in Figures 139-144 in Appendix B that for a single VAE simulation the convergence characteristic may temporally vary, as well as spatially. Figure 75 shows two sampled asymptotic expansions from the velocity state VAE parameterized by mass perturbation $v(t;\delta m)$ at $t = 3.5$ (sec) and $t = 7.25$ (sec). Here it is observed that the $t = 3.5$ (sec) asymptotic expansion converges to the true solution, which is highly nonlinear. As such first-order asymptotic expansion, which represents the local-expansion method approach to the propagation of uncertainty, performs very poorly and the region of approximate for this expansion is very small relative to the higher-order expansions. For the $t = 7.25$ (sec) asymptotic expansion, convergence is again observed; however, it does not converge as quickly as the $t = 3.5$ (sec) asymptotic expansion, requiring more higher-order information to achieve an accurate approximation. Also, oscillatory error is observed for this case, which is an undesirable effect. Here it is expected that while the $t = 7.25$ (sec) asymptotic expansion does well approximating the true solution for $\delta m < 0$, the $n = 3$ and $n = 5$ show significant approximation error for large positive values of δm. In the context of accurate uncertainty propagation, this case will need to be investigated further to confirm that response distributions are accurately approximated given the distributions on parameters from Table 18.

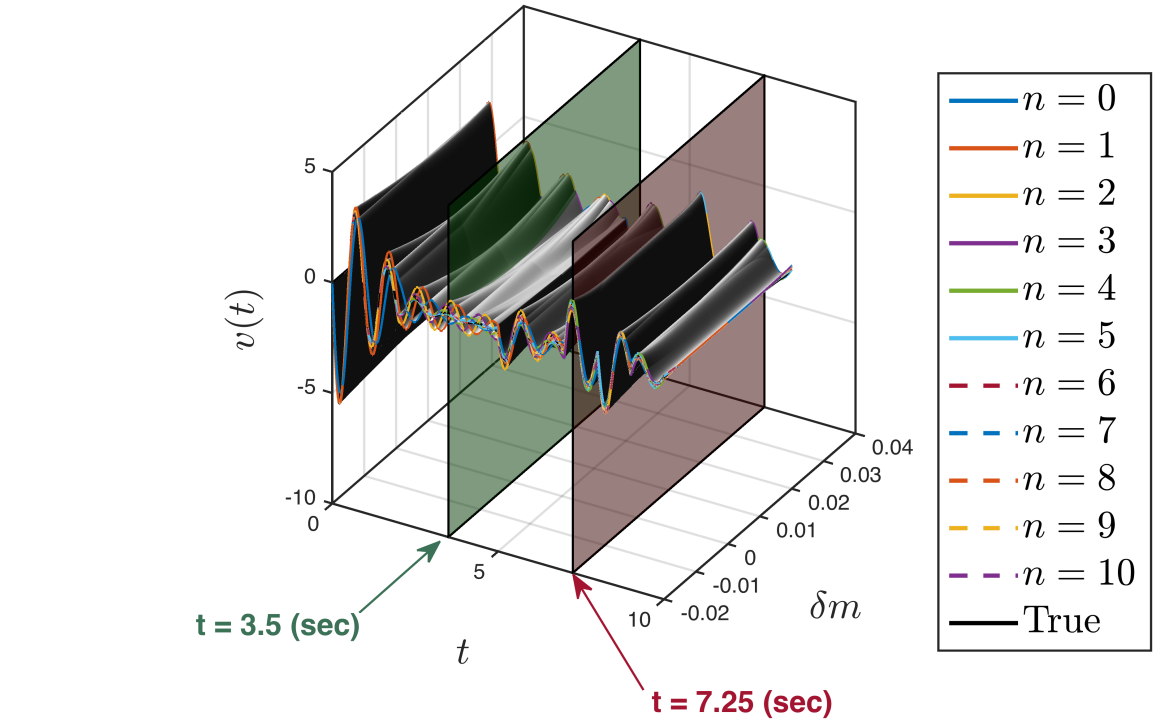

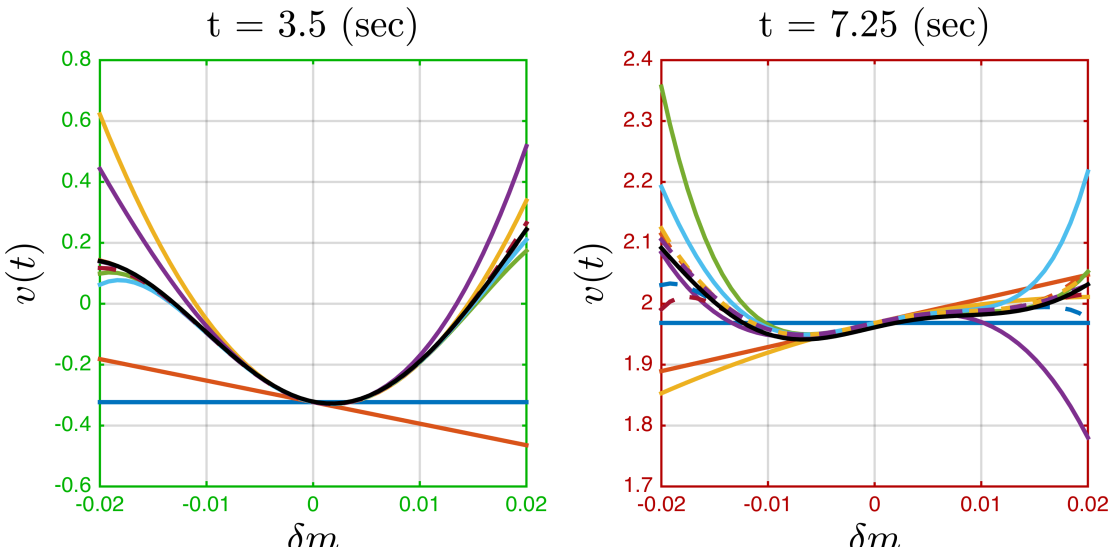

Figure 75: Asymptotic convergence analysis of $v(t; \delta m)$ VAE hypersurface for $t = 3.5$ (sec) and $t = 7.25$ (sec), which highlight that throughout simulation time of a single simulation not all VAE convergences are so well behaved.

10.3.3.2 VAE Probabilistic Convergence Analysis

In light of the results from the previous study, it is desired to repeat this analysis, using the results of Figure 73, to investigate the probabilistic asymptotic convergence of trajectory residual distributions. In the context of dynamic experiment design, the accuracy of these trajectory residual distributions and the impact of using different perturbation distributions on rate of convergence is critical for accurate calculation of robust-optimal information metrics.

Two 1000-case Monte Carlo analyses were conducted (one for each of the parameter perturbation distributions of Table 18) based on the results of the single VAE simulation. Recall, each Monte Carlo case can rapidly evaluate the VAE models of Figure 73 (*i.e.* without having to perform multiple simulations), which can be considered from the perspective of an asymptotically accurate surrogate model. The results are shown in Figure 76 as probabilistic trajectories or alternatively in Figure 77, which show just the residual uncertainty in the trajectory response. Each perturbed trajectory in these results is shown in transparent gray or black to give a qualitative sense of high-density temporal locations and represent regions with low state-to-parameter sensitivity. Here it is also observed that the trajectory residual uncertainties vary temporally, where triangular, skewed (Weibull-like), and Gaussian-like histograms are observed across a single simulation.

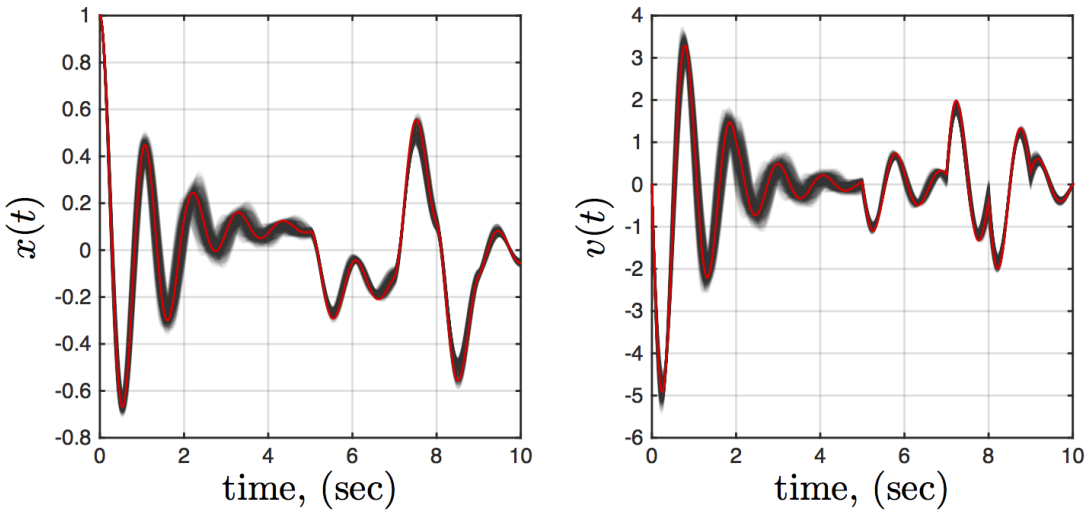

(a) Uniform parameter distributions.

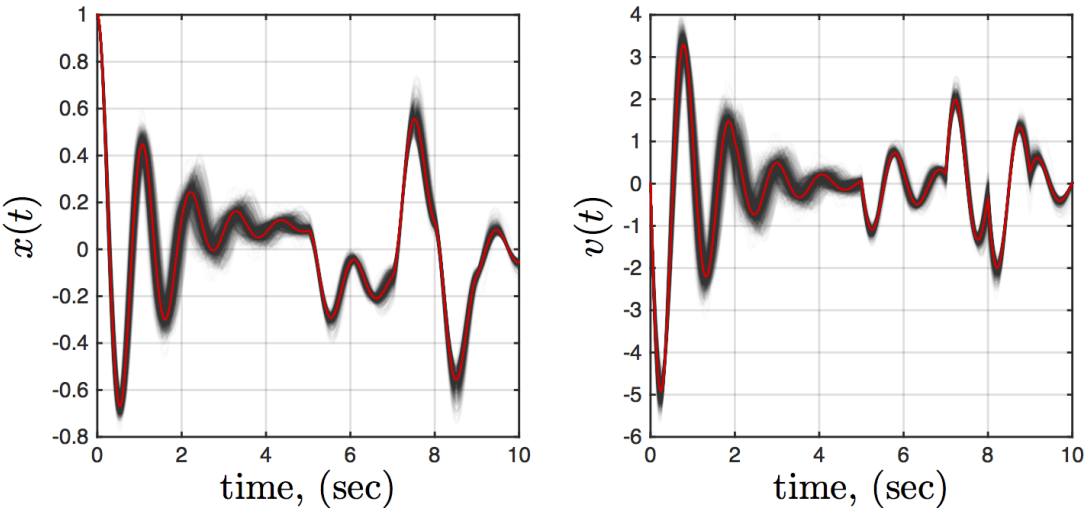

(b) Gaussian parameter distributions.

Figure 76: 10^{th}-order accuracy probabilistic (fuzzy) trajectory solutions using parameter perturbation models from Table 18. The baseline trajectory is shown in red and the perturbed trajectories are shown in transparent gray.

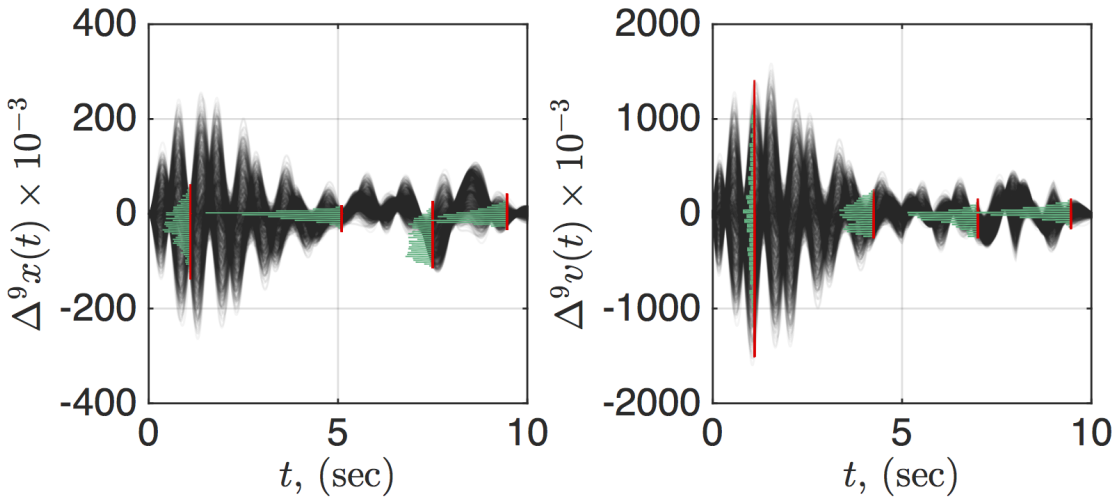

(a) Uniform parameter distributions.

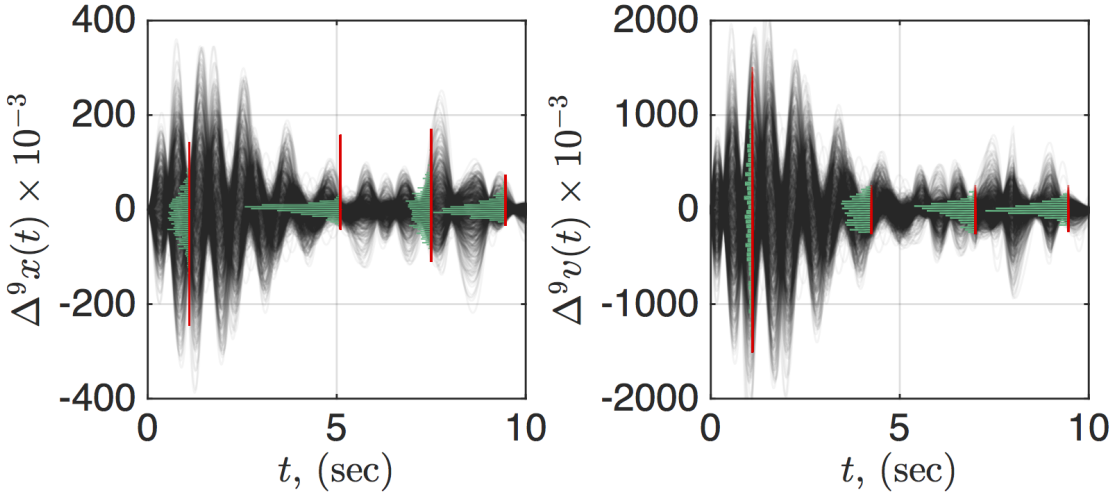

(b) Gaussian parameter distributions.

Figure 77: Trajectory residual uncertainties with superimposed snapshots of residual uncertainty distributions to illustrate the diversity in observed distributions.

To investigate probabilistic convergence, the two asymptotic expansions samples from Figure 75 were investigated for convergence of trajectory residual uncertainty distributions, given the parameter perturbation distributions from Table 18. Using the same Monte Carlo cases as before, the $t = 3.5$ (sec) and $t = 7.25$ (sec) asymptotic expansions were evaluated for increasing order for both uniform and Gaussian distributions. The results of these analyses are shown in Figures 78 and 79, respectively. Figure 80, moreover, provides for a more clear comparison of probabilistic convergence rates by comparing the n^{th}-order asymptotic trajectory residual uncertainty distributions to the exact distributions. These exact distributions were computed by the traditional Monte Carlo analysis (again for the same 1000 MC cases) by computing individual trajectory simulations and then sampling these trajectories at $t = 3.5$ (sec) and $t = 7.25$ (sec). As can be seen, the 1^{st}-order residual uncertainties yield approximations with significant bias present. This is an expected result, where forward uncertainty propagation using local-expansion methods is known to have this characteristic. Also, it can be clearly seen that the results for the $t = 7.25$ (sec) case generated by uniformly distributed parameter perturbations show significantly slower convergence rates when compared to the gaussian equivalent. Recall, that this case from Figure 75 showed slower, oscillatory convergence, and it appears that this adverse affect has led to distributions with over-prediction in multimodality even in relatively higher-order approximations (*e.g.* n=6).

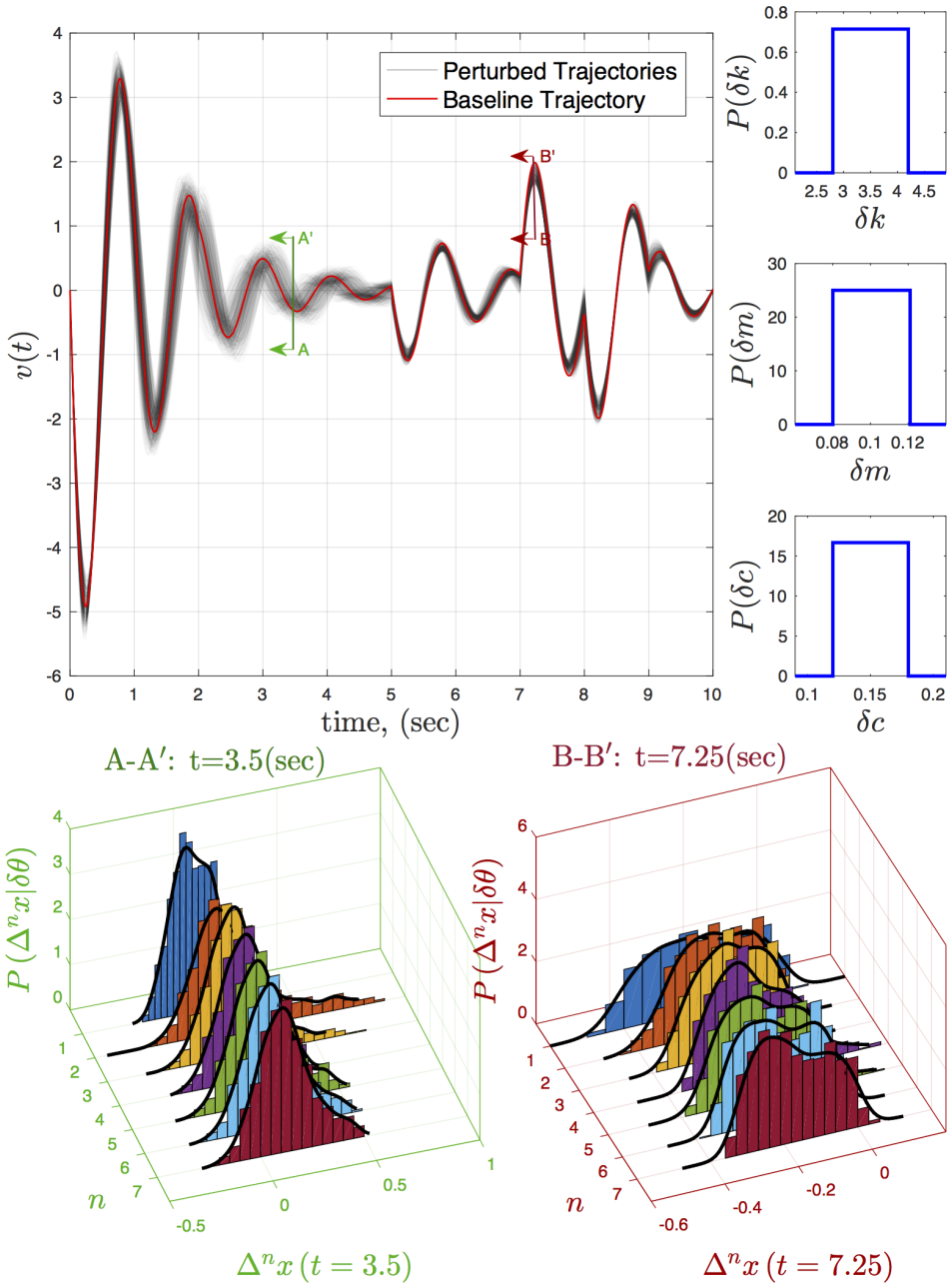

Figure 78: Asymptotic probabilistic convergence analysis of $v(t;\delta m)$ VAE hypersurface for $t = 3.5$ (sec) and $t = 7.25$ (sec) for parameter perturbations that are uniformly distributed according the Table 18.

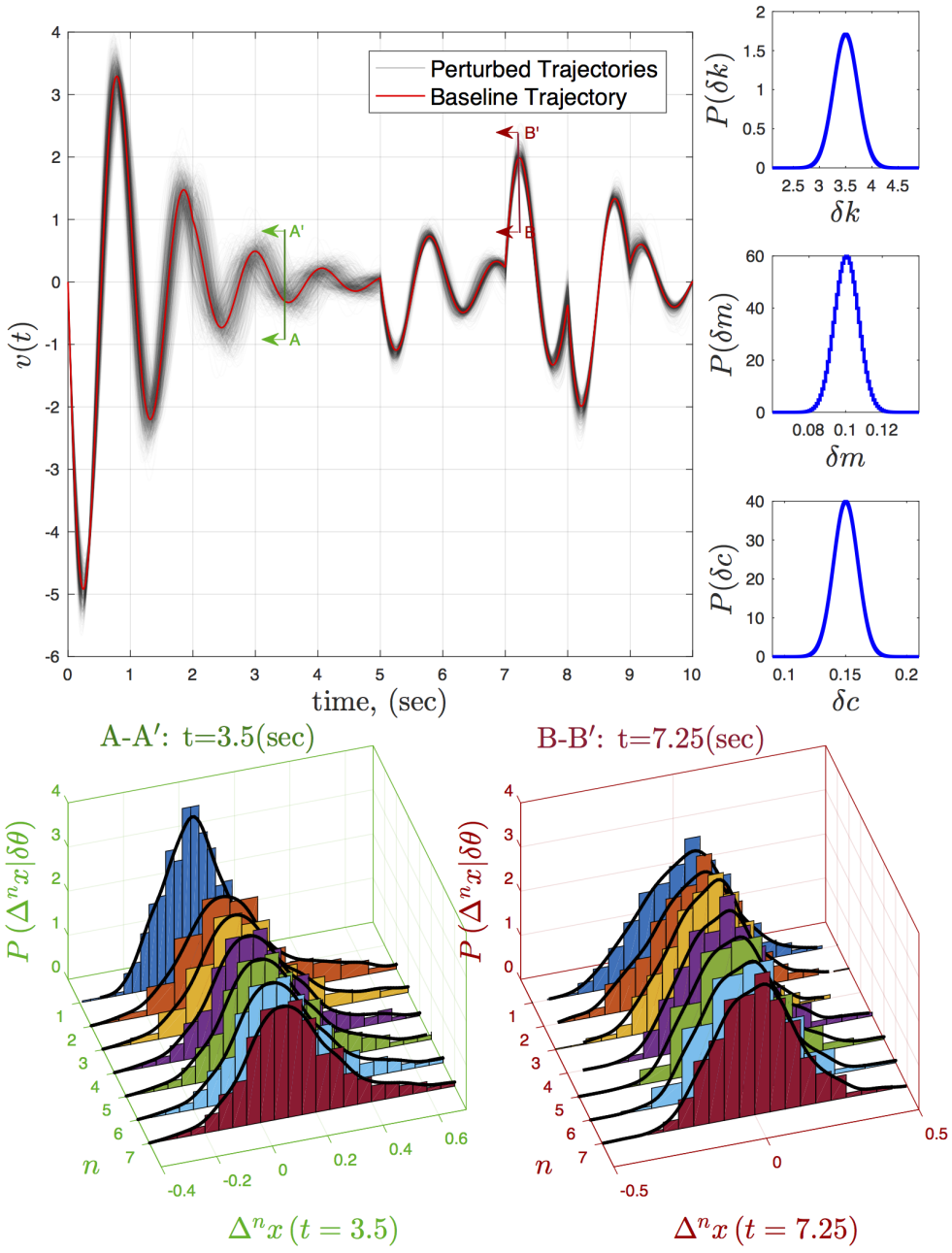

Figure 79: Asymptotic probabilistic convergence analysis of $v(t;\delta m)$ VAE hypersurface for $t = 3.5$ (sec) and $t = 7.25$ (sec) for parameter perturbations that are normally distributed according the Table 18.

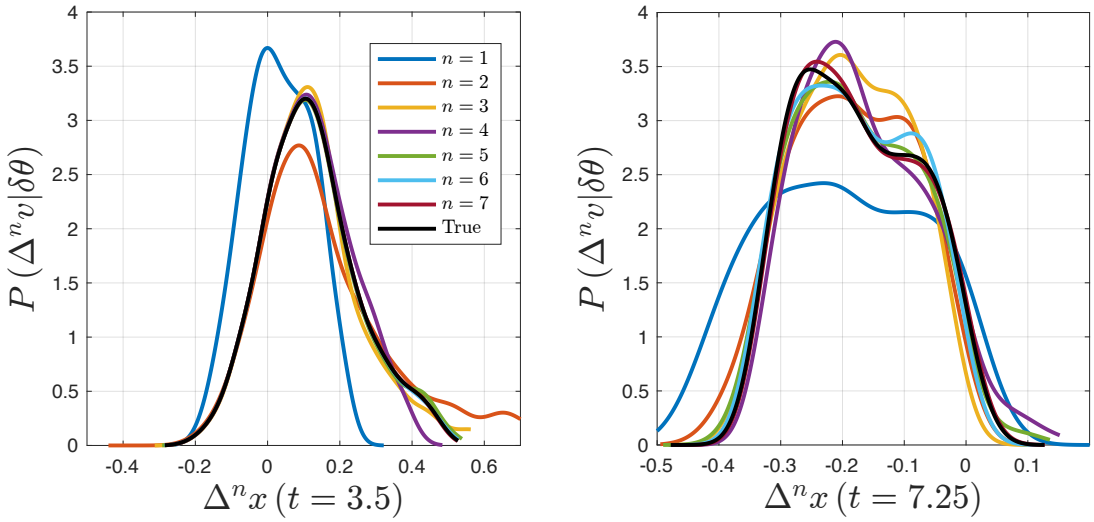

(a) Uniform perturbation parameter distributions.

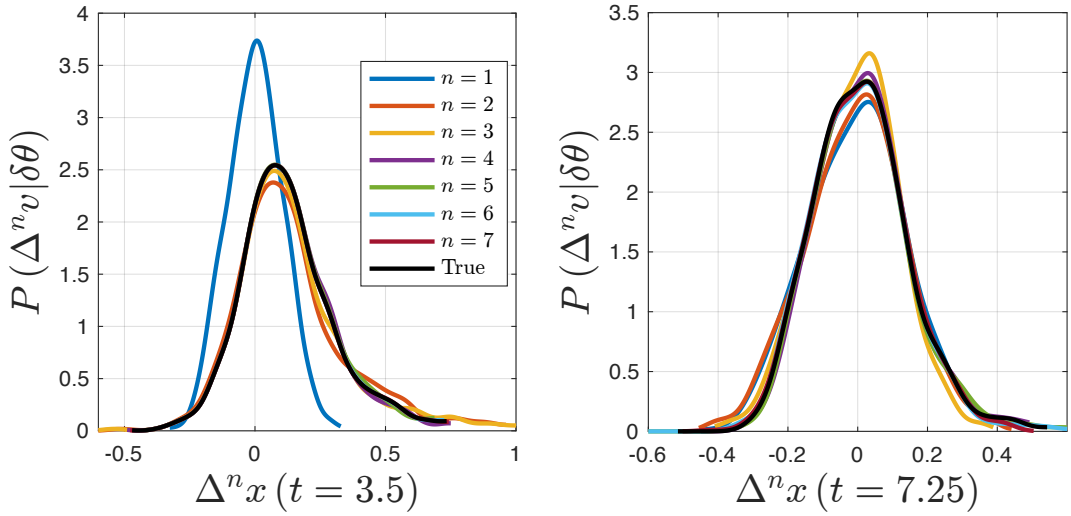

(b) Gaussian perturbation parameter distributions.

Figure 80: Time-sampled snapshots of parameter residual uncertainty distributions at $t = 3.5$ (sec) and $t = 7.25$ (sec), generated by a 1000-case Monte Carlo analysis and fit using kernel (Gaussian) density functions.

10.3.4 Exp't #2 Observations

The findings of this study suggest that the use of higher-order VAEs for the propagation of parametric uncertainties in dynamic systems is able to produce excellent results, where nonlinear effects are able to be easily captured. As a result, **HYP#2.1.2** is accepted. However, it has been observed that: (i) regions exist where poor/slow asymptotic convergence rates of state VAEs and state residual uncertainty distributions, requiring higher-order VAEs (relative to other regions where better asymptotic convergence is observed) to obtain satisfactory accuracy; and (ii) the asymptotic accuracy of state residual uncertainty distributions is also affected by perturbation parameter distribution type. This later observation is due to potential perturbation sampling in a region where convergence of the VAE region of approximation is slow. In these cases, it is possible that the necessary higher-order information required for satisfactory approximation may be impractically large. In response to this, the following observation is made.

Observation: For some problems and for some parameter uncertainty distributions, diminishing returns on accuracy in uncertainty propagation models could potentially lead to undesirable behaviors, such as artificial multimodality in probabilistic trajectory distributions.

In the context of robust-optimization design problems where probabilistic metrics are sought to be utilized, the implication of this observation is that optimized solutions may lead to sub-optimal results, regardless of how much higher-order information is used. Therefore brute-force stochastic simulation (*i.e.* Monte Carlo analysis) maybe be necessary to confirm robust-optimal results through virtual experimentation.

10.4 Exp't #3 – Computational Complexity Analysis of Multivariate Polynomial Multiplication

As discussed in Section 9.5, the curse of dimensionality is manifested in computational time and memory growth, where algorithms exhibit poor scaling as the amount of desired derivative information for a given system is increased; however, these complexities can be traced back to the polynomial library routines and can be evaluated for time and memory-complexities using existing computational techniques (*i.e.* Landau "Big-O" notation). It is commonly known that fast polynomial multiplication is a computational bottleneck and currently remains an active area of research [204, 205, 206, 28]. As such, it is expected that this operation will dominate the scaling of the complexities of computing VAEs as problem size and complexity are increased. In regards to the specific implementation proposed in Section 10.1 for multivariate polynomial multiplication, the following hypothesis is stated in response to the need to quantify the various types of complexities and for the different basis functions proposed in Section 9.3.1.

HYP. #2.2: Parallelization and vectorization strategies to alleviate computational expense will play a critical role in the robust-optimal design of dynamic experiments of aerospace systems (*e.g.* flight-dynamic simulation and control of hypersonic SCRAM-jet vehicles).

10.4.1 Experimental Procedure

The procedure for this experiment set is as follows: (i) multivariate polynomial multiplication has been identified as an operation which could dominate the scaling of computational expense; (ii) using Landau "Big-O" notation, quantify the asymptotic

scaling performances for (a) increasing polynomial order and (b) increasing polynomial dimension. This procedure will be conducted for several studies. The first study will investigate an alternate implementation of the recursive coefficient approach, by computationally representing multivariate polynomials which additionally employ degree control to more effectively manage memory usage. The expected outcome of this experiment is that the use of degree control will improve the speed-up of dense multivariate polynomial multiplication; however, it will not fundamentally alter the computational time complexity, which are still assumed to scale as polynomial complexity $\mathcal{O}(n^c)$. The next two studies will investigate the complexities of (i) high-order/low-dimension polynomial multiplication and (ii) low-order/high-dimension polynomial multiplication using recursive coefficient polynomials with degree control. The outcome of these experiments will be to observe how each case scales for the sake of gaining increased intuition on the feasibility of implementing large-scale dynamic experiment design problems with potentially many variables and derivatives.

10.4.2 Experimental Apparatus

Computation time is measured in *wall clock time* from the system-wide realtime clock using the C++ <chrono> library, which is accurate to the nearest nanosecond. Approximate quantification of required memory is determined by counting the required number of polynomial coefficients for an (N_d,N_e)-polynomial, where N_d is the polynomial dimension and N_e is the polynomial order. All cases were performed on the same system, described by the following specifications:

- **OS** – Linux: CentOS 6.6 Final
- **Processor** – 8x Intel Core i7-2600 CPU @ 3.4 GHz
- **Memory** – 16.00 GB 1333 MHz DDR3
- **Compiler** – gcc version 4.9.2 (GCC), thread model: posix

10.4.3 Investigation into the Impact of Employing Degree Control to Improve the Recursive Coefficient Approach

10.4.3.1 Recursive Implementation of Degree Control

In Section 10.1.2, the recursive coefficient approach was demonstrated on the mathematical representation of a 3-dimensional, 2^{nd}-order polynomial. The resulting polynomial, as shown in Equation (65), can be computationally represented with a k,d-array tree, consisting of a total of 27 coefficients, which was illustrated in Figure 55. While this approach is straightforward to computationally implement, it is obvious that it included terms with excessive order (*i.e.* $c_{26} = x^2y^2z^2$ is clearly a 6^{th}-order effect and therefore should not be included in a 2^{nd}-order polynomial). To eliminate these undesired higher-order terms, degree control was implemented within the recursive coefficient approach. While the addition of degree control increases complexity in terms of code readability, it is anticipated that substantial computational complexities overall will be reduced due to reductions in the required number of coefficients.

Figure 81 provides some examples to illustrate the expected gains in storage performance for the two approaches. Figure 81a compares the two approaches for a 3-dim,3-deg (quadratic) polynomial, where it can be seen that using degree control requires nearly a third less coefficients. The second case, shown in Figure 81b, increments the degree of the first case by one, where now the degree control requires nearly 69% less memory. The final case shows the most promise, where this case increments the dimension of the first case by one. As can be seen in Figure 81c, the degree control now uses almost 81% less memory than the original implementation. These results provide evidence that high-dimensional VAEs will scale very well in terms of memory growth, and this will translate into less computation time. Therefore it is hopeful that large-scale dynamic experiment design problems such as hypersonic SCRAMjet flight test design is computationally feasible.

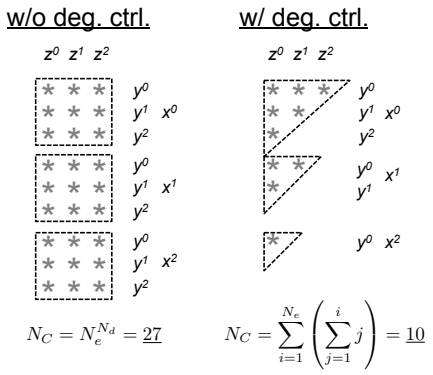

(a) Poly($N_d = 3$, $N_e = 3$)

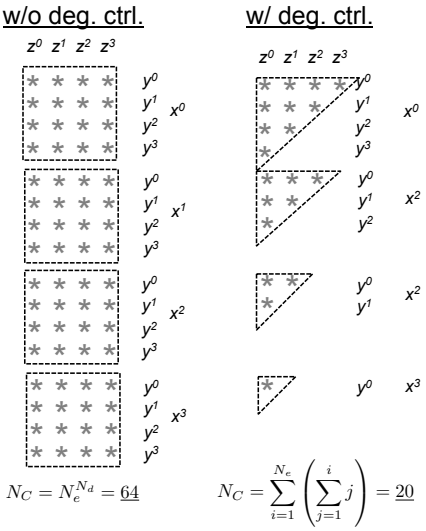

(b) Poly($N_d = 3$, $N_e = 4$)

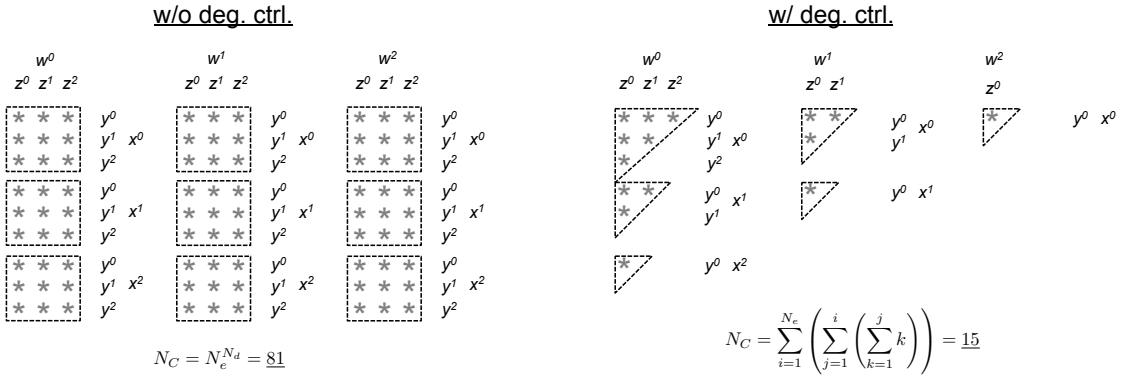

(c) Poly($N_d = 4$, $N_e = 3$)

Figure 81: Examples of polynomial storage encoding with and without degree control, where the symbol '$*$' represents a single coefficient: (a) 3-dimensional, 3^{rd}-order polynomial $P(x, y, z)$, (b) 3-dimensional, 4^{th}-order polynomial $P(x, y, z, w)$, and (c) 4-dimensional, 3^{rd}-order polynomial $P(x, y, z, w)$.

10.4.3.2 Computational Complexity Results

Figure 82 showsis comparative results of computational time and memory for recursive coefficient approaches to implement multivariate polynomials with and without degree control. Tables 19 and 20 show regressed exponential coefficients c, which were obtained via a Least-Squares regression analysis on the results of Figure 82 assuming the model structure $y = an^c$, to estimate $\mathcal{O}(n^c)$ performance. These results clearly demonstrate that employing the use of degree control yields a significant improvement in computational performance; however, as the number of dimension increases, the complexity of both approaches still degrades quickly.

Table 19: Computation time complexity regression results comparing exponential scaling (*i.e.* $\mathcal{O}(n^c)$) with and without degree control.

	w/o Degree Control		**w/ Degree Control**	
N_d	c	R^2	c	R^2
1	1.0000	1.0000	1.0000	1.0000
2	2.0000	1.0000	1.7539	0.9988
4	4.0000	1.0000	2.896	0.9942
6	6.0000	1.0000	3.7637	0.9899
8	8.0000	1.0000	4.4679	0.9862
10	10.000	1.0000	5.0619	0.9832

Table 20: Computation memory complexity regression results comparing exponential scaling (*i.e.* $\mathcal{O}(n^c)$) with and without degree control.

	w/o Degree Control		**w/ Degree Control**	
N_d	c	R^2	c	R^2
1	0.5428	0.9082	0.5428	0.9082
2	2.1168	0.9928	1.4017	0.9522
4	5.1510	0.9962	3.3611	0.9751
6	8.1900	0.9947	4.8191	0.9682
8	10.543	0.9973	6.0756	0.9618
10	12.797	0.9988	7.1587	0.9567

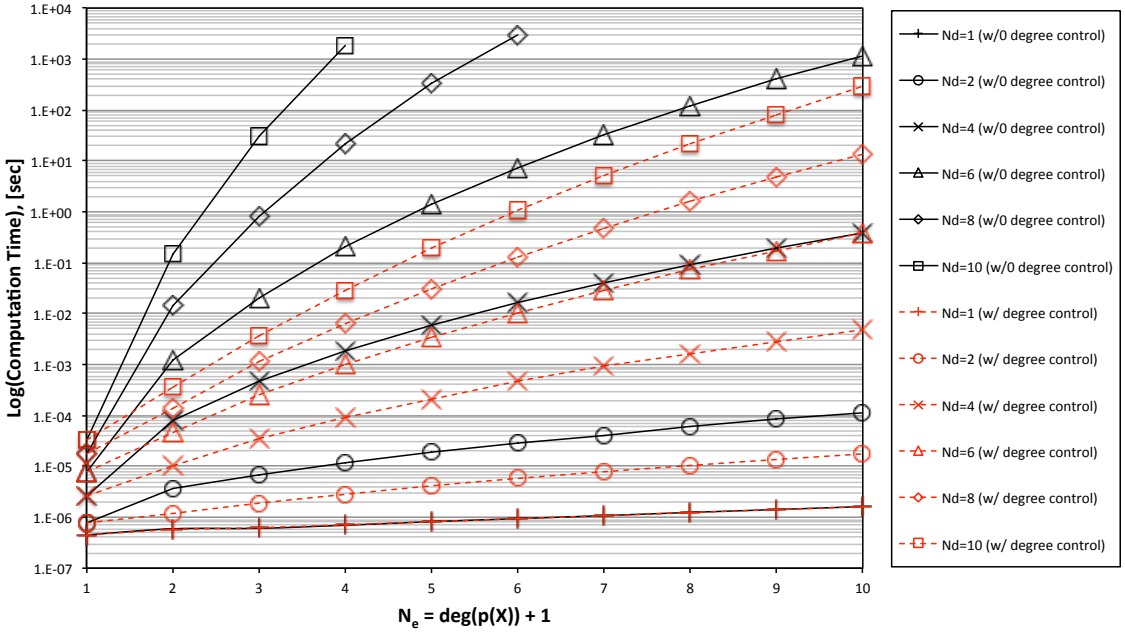

(a) Time Complexity Analysis

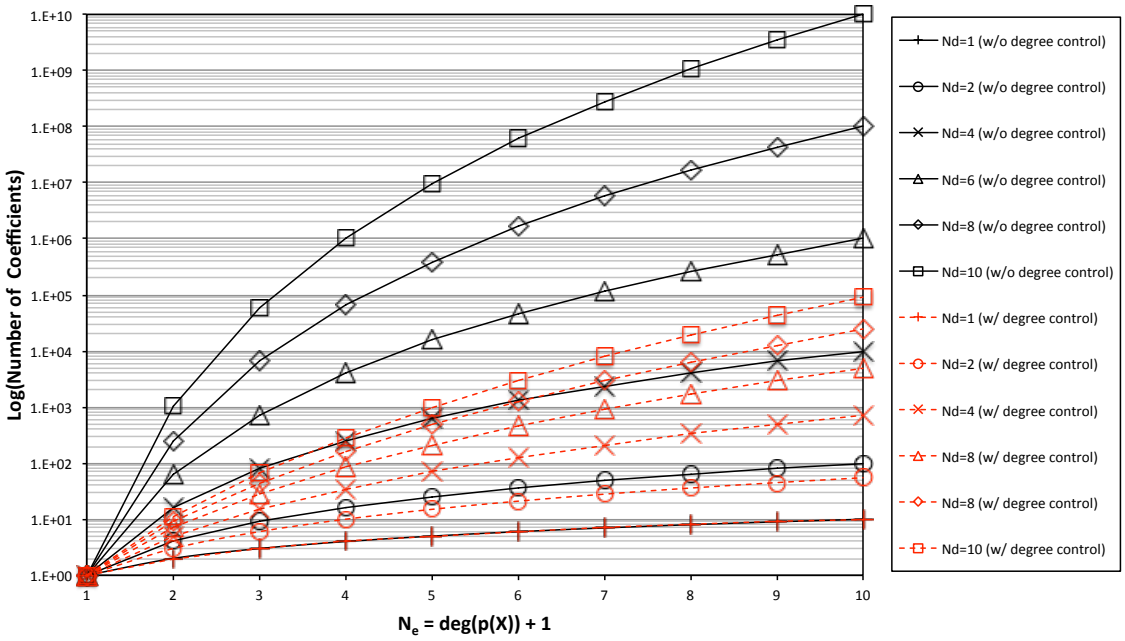

(b) Memory Complexity Analysis

Figure 82: Polynomial multiplication complexity analysis monomial basis polynomials comparing implementations of the recursive coefficient approach with and without degree control.

10.4.4 Investigation of Complexity Scaling for Multiplication of Large Polynomials

The objective of this study is to obtain the asymptotic complexity performance for large values of N_e and N_d. This will help determine to what extent that high-dimensional/high-order VAEs can be applied to industrial-sized system design problems. In order to do this, trade studies were run at the edges of the polynomial size-space, because making both N_e and N_d large simultaneously is computationally infeasible. Figure 83 demonstrates required computation time for multiplying dense multivariate polynomials using the recursive coefficient approach with degree control. Here it can be seen that computation time rapidly becomes large as both N_e and N_d are increased, but the effect is less pronounced if either N_e or N_d are increased while the other is kept relatively small.

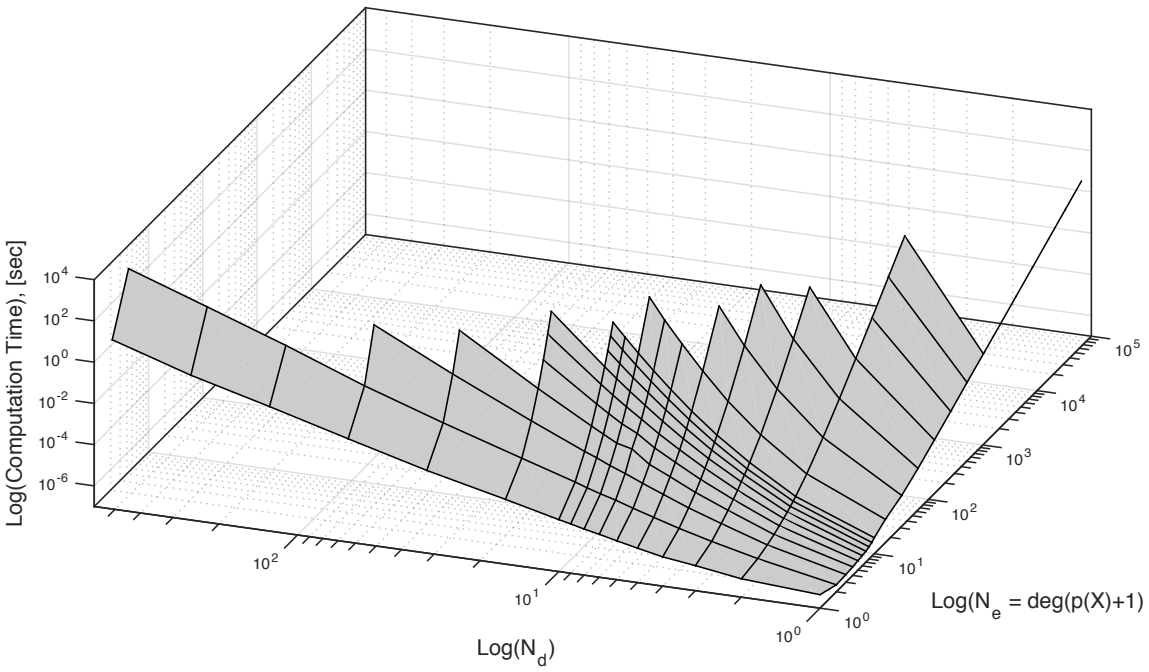

Figure 83: Dense multivariate polynomial multiplication (w/ degree control) computational time results showing additional cases, where N_d and N_e are individually increased.

10.4.4.1 Complexity Analysis the Multiplication of High-Order/Low-Dimension Polynomials

Figure 84 shows the results of fixing N_d to relatively small values, while N_e is allowed to vary over a wide range. This type of multiplication is analogous to multiplying polynomials with relatively low numbers of independent variables, where arbitrarily high-degree of derivative information, or equivalently, high-order, high-accuracy expansion surrogates are desired. Table 21 shows the asymptotic polynomial complexity using Landau notation, which was obtained by computing the log-log slopes. As can be seen, for increasing N_d, the polynomial complexity increases exponentially, where the exponent $c \approx 2N_d$. This result is consistent with the analysis by Moenick [204, 205, 206] (*i.e.* $\mathcal{O}\left(N_e^{2N_d}\right)$) and marginally improves with respect to this result as N_d increases.

10.4.4.2 Complexity Analysis the Multiplication of Low-Order/High-Dimension Polynomials

Figure 85 shows the results of fixing N_e to relatively small values, while N_d is allowed to vary over a wide range. This type of multiplication is analogous to multiplying polynomials with relatively low orders of derivative information and large numbers of independent parameters, or equivalently, high-dimension surrogates is desired. Table 22 shows the asymptotic polynomial complexity using Landau notation, which was obtained by again computing the log-log slopes, according to relation $y = ax^c$, where $x = N_d$. As can be seen in Figure 85b, for $N_e = 1$ (*i.e.* 0^{th}-order polynomials) the number of coefficients remains constant at a value of 1, but the computation time for this case still increases with N_d. This is due to the computational implementation of the recursive coefficient approach, where the memory overhead has not been accounted for when computing the number of coefficients. As N_e increases, the asymptotic complexities of computation time and number of coefficients (*a.k.a.* time and memory requirements) becoming increasingly demanding.

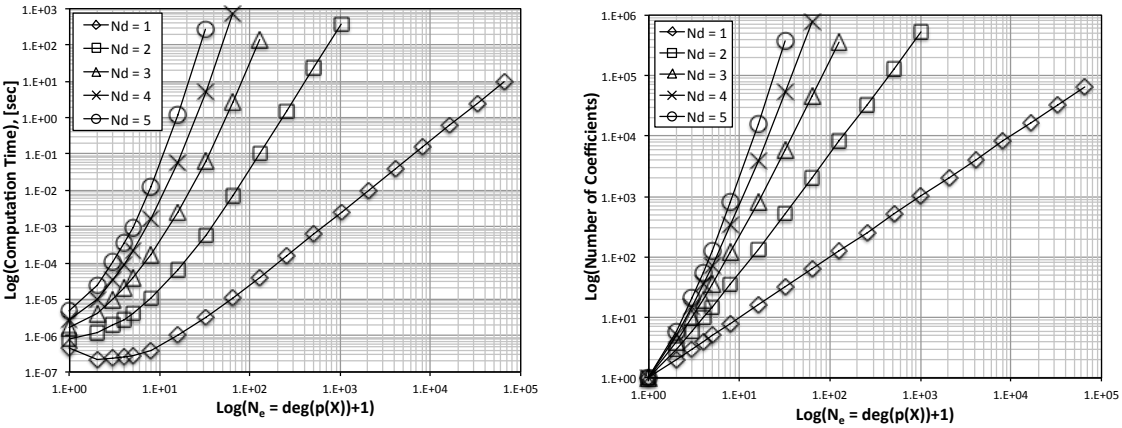

(a) Time Complexity (b) Memory Complexity

Figure 84: Polynomial multiplication complexity analysis for high-degree, low-dimension polynomials.

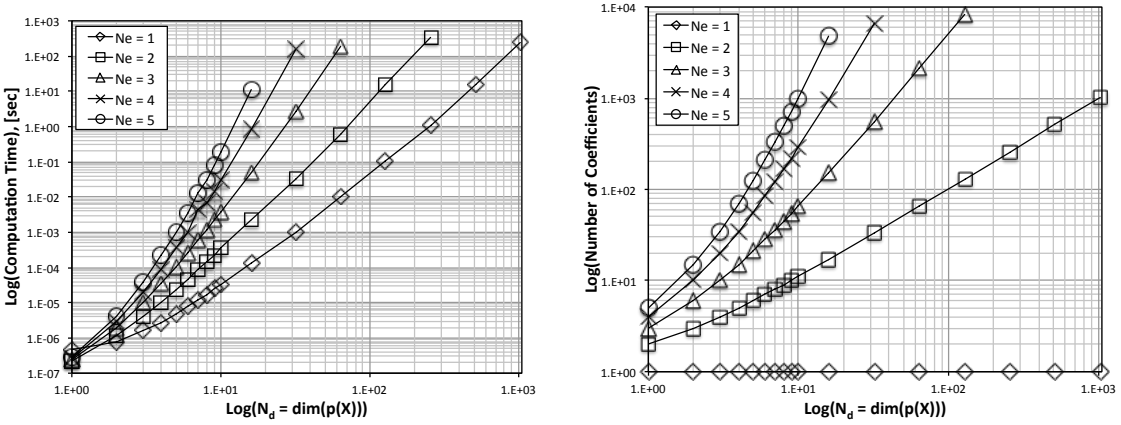

(a) Time Complexity (b) Memory Complexity

Figure 85: Polynomial multiplication complexity analysis for high-dimension, low-degree polynomials.

Table 21: Summary of asymptotic complexity analysis of high-degree, low-dimensional polynomial multiplication in the monomial basis.

N_d	**Complexity**	
	Computation Time	Number of Coefficients
1	$\mathcal{O}\left(N_e^{2.00}\right)$	$\mathcal{O}\left(N_e\right)$
2	$\mathcal{O}\left(N_e^{3.98}\right)$	$\mathcal{O}\left(N_e^{2.00}\right)$
3	$\mathcal{O}\left(N_e^{5.72}\right)$	$\mathcal{O}\left(N_e^{2.97}\right)$
4	$\mathcal{O}\left(N_e^{7.16}\right)$	$\mathcal{O}\left(N_e^{3.87}\right)$
5	$\mathcal{O}\left(N_e^{7.81}\right)$	$\mathcal{O}\left(N_e^{4.60}\right)$
6	$\mathcal{O}\left(N_e^{7.96}\right)$	$\mathcal{O}\left(N_e^{4.98}\right)$
7	$\mathcal{O}\left(N_e^{9.09}\right)$	$\mathcal{O}\left(N_e^{5.63}\right)$

Table 22: Summary of asymptotic complexity analysis of high-dimensional, low-degree polynomial multiplication in the monomial basis.

N_e	**Complexity**	
	Computation Time	Number of Coefficients
1	$\mathcal{O}\left(N_d^{3.94}\right)$	$\mathcal{O}\left(1\right)$
2	$\mathcal{O}\left(N_d^{4.44}\right)$	$\mathcal{O}\left(N_d\right)$
3	$\mathcal{O}\left(N_d^{6.15}\right)$	$\mathcal{O}\left(N_d^{1.97}\right)$
4	$\mathcal{O}\left(N_d^{7.61}\right)$	$\mathcal{O}\left(N_d^{2.76}\right)$
5	$\mathcal{O}\left(N_d^{8.69}\right)$	$\mathcal{O}\left(N_d^{3.36}\right)$
8	$\mathcal{O}\left(N_d^{11.87}\right)$	$\mathcal{O}\left(N_d^{5.04}\right)$

10.4.5 Exp't #3 Observations

Comparison of the polynomial multiplication computation time complexity results from Tables 21 and 22 show that complexity scales better for the high-order, low-dimension polynomials than for the high-dimension, low-order polynomials, but that the curse of dimensionality is ever present as dimension and order are increased. This implies that implementing problems where high accuracy is desired for VAEs that are parameterized by few perturbation variables (*i.e.* high-accuracy response surrogates) is likely a more computationally feasible endeavor than implementing problems where VAEs that are parameterized by a large number of perturbation variables with to relatively low order (*i.e.* design problems).

The scaling of the memory complexity shows similar performance between high-degree, low-dimensional polynomials and low-degree, high-dimensional polynomial. This is misleading, since the actual computation memory required includes pointer-variable overheads, as well as other types of class memory overheads. Therefore it expected that, again high-dimensional design problems will not scale as well as high-accuracy, low-dimensional problems.

In light of these observations, the results of Figure 82 show that the relatively minor addition of recursively implementing degree control has yielded a substantial improvement to the computational time by reducing the required memory. This has alleviated the adverse effects of the curse of dimensionality somewhat; however, the only way to determine if a large-scale dynamic experiment design problem is computationally feasible is simply to implement one and find out. Still, hope exists, because high-performance polynomial multiplication algorithms exist that utilize high-powered Fast Fourier transforms, and the work above is non-exhaustive. Therefore **HYP #2.2** is accepted for the current implementation, and parallel/vectorization strategies are identified as a necessary component to implement the TEMPUS methodology; however, the feasibility of this methodology must and will be assessed further.

10.5 Exp't #4 – Problem Diversity: Implementation of VAEs to Solve Optimal Control Problems

In Section 5.3.5 it was stated that the design of dynamic experiments consists of both design variables and design functions. Also, numerical techniques to solve optimal information dynamic experiments were discussed, which can be generally categorized as either direct methods or indirect methods. Here, it was discussed that there are certain cases when it might be advantageous to employ one approach over the other. To this end the following hypothesis was stated in response to **RQ. #2.3**.

HYP. #2.3: Higher-order gradients can be used to generate high-accuracy VAE surrogates to OCPs, where point solutions generated by a computationally expensive OCPs can be utilized for parametric localized approximations to families of solutions.

10.5.1 Experimental Procedure

The procedure for addressing this hypothesis is to (1) formulate higher-order OCP mathematical formulations, (2) implement these formulations on a simple example problem, and (3) evaluate the numerically generated asymptotic expansions, comparing numerical results to analytically derived solutions.

10.5.2 VAE-OCP Mathematical Formulations

Two types asymptotic OCP problems have been formulated below, where parameters θ generically include: (i) boundary conditions on states, (ii) dynamic system parameters (*e.g.* uncertainty parameters, mass/inertia parameters, aerodynamic coefficients, spring-mass-damper parameters, etc.), (iii) cost function weights, (iv) initial/final simulation time horizons, and (v) constraint boundaries on states and control inputs.

1. **VAE-OCP Formulation #1** (only higher-order states, parameterized by perturbations $\delta\theta$):

$$\min_{u\in U} J[u] = \int_{t_0}^{t_f} \mathcal{L}(x,u,\theta)\,dt$$

subject to:

$$\begin{aligned}
&(\mathbf{v}^0) && \dot{x} = f(x,u,\theta) && , x(t_0) = x_0 \\
&(\mathbf{v}^1) && \dot{x}_\theta = f_x x_\theta + f_\theta = f^1(x,x_\theta,u,\theta), && x_\theta(t_0) = 0 \\
&(\mathbf{v}^2) && \dot{x}_{\theta\theta} = f_x x_{\theta\theta} + f^1_\theta && , x_{\theta\theta}(t_0) = 0 \\
& && \vdots && \\
&(\mathbf{v}^n) && \dot{x}_{\theta^{(n)}} = f_x x_{\theta^{(n)}} + f^{n-1}_\theta && , x_{\theta^{(n)}}(t_0) = 0
\end{aligned} \tag{72}$$

Formulation #1 solves a single OCP, while including higher-order dynamic constraints and yields a solution structure as shown below in Equation (73), where the optimal trajectory $x^*(t)$ is parameterized by $\delta\theta$ but not the optimal control inputs $u^*(t)$. Each system of dynamic constraints is designated according to it's order as $(\mathbf{v}^0)$-original dynamic system constraints, $(\mathbf{v}^1)$-1st equations of variation dynamic constraints, $(\mathbf{v}^2)$-2nd equations of variation dynamic constraints, etc.

$$\begin{aligned}
x^*(t;\theta) &= x^*(t;\theta_0) + x^*_\theta(t;\theta_0)\cdot\delta\theta + \frac{x^*_{\theta\theta}(t;\theta_0)}{2!}\cdot\delta\theta^2 + \ldots + \frac{x^*_{\theta^{(n)}}(t;\theta_0)}{n!}\cdot\delta\theta^n \\
u^*(t;\theta) &= u^*(t;\theta_0)
\end{aligned} \tag{73}$$

This type of formulation is useful when, after solving an OCP, a subsequent uncertainty propagation analysis is desired to study how uncertainty models in $\delta\theta$ affect the cost about an optimal solution $(x^*(t;\theta), u^*(t;\theta))$. Note that since

$u^*(t)$ is not parameterized by $\delta\theta$ that the resulting cost distributions would reflect neighboring sub-optimal solutions.

2. **VAE-OCP Formulation #2** – (both higher-order states and control inputs, parameterized by perturbations $\delta\theta$):

$$
\begin{aligned}
\textbf{(OCP}^0\textbf{)} \qquad & \min_{u\in U} J\left[u\right] = \int_{t_0}^{t_f} \mathcal{L}\left(x,u,\theta\right) dt \\
& \text{s.t.:}\;\; \dot{x} = f\left(x,u,\theta\right) \qquad\qquad , \; x\left(t_0\right) = x_0 \\
\\
\textbf{(OCP}^1\textbf{)} \qquad & \min_{u_\theta\in U} J^1\left[u_\theta\right] = \int_{t_0}^{t_f} \mathcal{L}^1\left(x^*, x_\theta, u^*, u_\theta, \theta\right) dt \\
& \text{s.t.:}\;\; \dot{x}_\theta = f_x x_\theta + f_\theta, \qquad\qquad , \; x_\theta\left(t_0\right) = 0 \\
& \qquad\qquad \vdots \\
\textbf{(OCP}^n\textbf{)} \qquad & \min_{u_{\theta^{(n)}}\in U} J^n\left[u_{\theta^{(n)}}\right] = \int_{t_0}^{t_f} \mathcal{L}^n\left(x^*, \ldots, x_{\theta^{(n)}}, u^*, \ldots, u_{\theta^{(n)}}, \theta\right) dt \\
& \text{s.t.:}\;\; \dot{x}_{\theta^{(n)}} = f_x^{n-1} x_{\theta^{(n)}} + f_\theta^{n-1}, \; x_{\theta^{(n)}}\left(t_0\right) = 0
\end{aligned}
\tag{74}
$$

Formulation #2 solves a single OCP, while including higher-order dynamic constraints and yields a solution structure as shown below in Equation (75), where both the optimal trajectory $x^*\left(t\right)$ and the optimal control inputs $u^*\left(t\right)$ are parameterized by $\delta\theta$. In contrast to formulation #1, this formulation involves sequentially solving the next higher-order OCP, where $\textbf{(OCP}^0\textbf{)}$ is the original (*i.e.* 0^{th}-order) problem, $\textbf{(OCP}^1\textbf{)}$ is the 1^{st}-problem of variation, etc.

$$
\begin{aligned}
x^*\left(t;\theta\right) &= x^*\left(t;\theta_0\right) + x^*_\theta\left(t;\theta_0\right)\cdot\delta\theta + \frac{x^*_{\theta\theta}\left(t;\theta_0\right)}{2!}\cdot\delta\theta^2 + \ldots + \frac{x^*_{\theta^{(n)}}\left(t;\theta_0\right)}{n!}\cdot\delta\theta^n \\
u^*\left(t;\theta\right) &= u^*\left(t;\theta_0\right) + u^*_\theta\left(t;\theta_0\right)\cdot\delta\theta + \frac{u^*_{\theta\theta}\left(t;\theta_0\right)}{2!}\cdot\delta\theta^2 + \ldots + \frac{u^*_{\theta^{(n)}}\left(t;\theta_0\right)}{n!}\cdot\delta\theta^n
\end{aligned}
\tag{75}
$$

This type of formulation is useful when, after solving an OCP, a subsequent uncertainty propagation analysis is desired to study how uncertainty models in $\delta\theta$ affect the

cost about an optimal solution $(x^*(t;\theta), u^*(t;\theta))$. Note that since $u^*(t)$ is parameterized by $\delta\theta$ that the resulting cost distributions reflect neighboring optimal solutions. If perturbation parameters represented $\delta\theta$ a set of design variables, centered about a baseline design, then this formulation could also be useful for enabling traditional design space exploration techniques to investigate neighboring design candidates across the space of optimal trajectories.

10.5.3 Numerical Implementation

The numerical integrator implemented in this study is a collocation method (implemented as a direct-method optimization problem) using a family of symplectic-partitioned Runge-Kutta (spRK) high-order variational integrator using Lobatto IIIA-IIIB quadrature rules for $s = \{2, 3, 4, 5\}$ [153, 62]. Shown below in Equation (77), these types of integrators are known to be especially well-suited for solving higher-order systems of differential equations, because (i) they provide a unique discretization which numerically preserves the *symplectic* geometry for a Hamiltonian system and (ii) they *partition* the state vector x_h into position q_h and momentum p_h states, enhancing numerical stability, as discussed by Campos [62].

$$\min_{q_h, p_h, u_h} J_d(q_h, p_h, u_h) \tag{77}$$

subject to:

$$q_{k+1} = q_k + h\sum_{j=1}^{s} b_j f\left(Q_j^k, P_j^k\right) \qquad p_{k+1} = p_k + h\sum_{j=1}^{s} \bar{b}_j g\left(Q_j^k, P_j^k, U_j^k\right) \tag{77a}$$

$$Q_i^k = q_k + h\sum_{j=1}^{s} a_{ij} f\left(Q_j^k, P_j^k\right) \qquad P_i^k = p_k + h\sum_{j=1}^{s} \bar{a}_{ij} g\left(Q_j^k, P_j^k, U_j^k\right) \tag{77b}$$

$$(q_0, p_0) = \left(q^0, p^0\right) \tag{77c}$$

$$U_i^k = \mathcal{U}_{adm} \tag{77d}$$

Here the integral and differential constraint coefficients obey the symplectic relations $b_i\bar{a}_{ij} + b_j a_{ji} = b_i\bar{b}_j$ for $k = 0, \ldots, N-1$ and $i = 1, \ldots, s$. Tables 23 and 24 shows Butcher tableu's for state-2 ($s = 2$) and state-3 ($s = 3$) Lobatto IIIA-IIIB quadrature rules. Equations (77a-77d) are the integral, differential, initial conditions on states, and side constraints on controls, respectively. The design variables here are: (1) position states $q_h = \{\{q_k, Q_i^k\}_{i=1,\ldots,s}^{k=0,\ldots,N-1}, \ldots, q_N\}$, (2) momentum states $p_h = \{\{p_k, P_i^k\}_{i=1,\ldots,s}^{k=0,\ldots,N-1}, \ldots, p_N\}$, and (3) control inputs $u_h = \{\{u_k, U_i^k\}_{i=1,\ldots,s}^{k=0,\ldots,N-1}, \ldots, u_N\}$. The functions $f(q,p)$ and $g(q,p,u)$ are the partitioned governing equations of motion for an arbitrary Lagrangian system.

Table 23: Coefficients of the 2-stage Lobatto IIIA-IIIB method of order 2.

IIIA

0	0	0
1	1/2	1/2
	1/2	1/2

IIIB

0	1/2	0
1	1/2	0
	1/2	1/2

Table 24: Coefficients of the 3-stage Lobatto IIIA-IIIB method of order 4.

IIIA

0	0	0	0
1/2	5/24	1/3	-1/24
1	1/6	2/3	1/6
	1/6	2/3	1/6

IIIB

0	1/6	-1/6	0
1/2	1/6	1/3	0
1	1/6	5/6	0
	1/6	2/3	1/6

For this study, the minimization of Equations (77) is performed by the numerical optimizer ipopt [274], which is a common choice to solve the sparsely constrained type of problems commonly encountered in optimal control formulations. Ipopt is an open-source nonlinear interior-point optimizer that is natively written in C++, used frequently, and is easily integratable into Python, which allows for easy integration with the VAE polynomial library previously discussed in Table 12 of Section 10.1.2.

10.5.4 Test Problem Description

The test problem used for this study was taken from from Campos [62], because it has already been used on the proposed spRK DMOC implementation of Equation (77) and unique analytical solutions are readily obtained. The problem statement is shown below, which describes a simple optimal control problem with a linear dynamical constraint and a quadratic cost function.

$$\begin{aligned} \min_{u} J[u] &= \int_0^1 \left(\dot{q}^2 + u^2\right) dt \\ \text{s.t.: } \ddot{q} &= 1 + u, \quad (q(0), p(0)) = (q_0, p_0) \end{aligned} \tag{78}$$

From Equation (78), the Lagrangian function is $L(q, \dot{q}) = \frac{1}{2}\dot{q}^2 + q$ and the control force is $F(q, \dot{q}, u) = u$. The density cost function is $C(q, \dot{q}, u) = \dot{q}^2 + u^2$. For implementation with higher-order VAEs which are parameterized by perturbations $\delta\theta$, the parameters θ were selected to be the two initial condition values (q_0, p_0). To test and assess the ability of the VAE solutions to accurately approximate neighboring solutions, the following test cases were selected, where **Case 1** is the original problem analytically solved by Campos, et al. [62]. **Case 2** was selected to compare numerical results generated by **VAE-OCP Formulation #1** to a neighboring suboptimal problem. **Case 3** was selected to compare numerical results generation by **VAE-OCP Formulation #2** to a neighboring optimal problem.

Case 1: $(q_0, p_0) = (0, 0)$: a baseline solution

Case 2: $(q_0, p_0) = (q_0 = 2.0, p_0 = 1.5))$ given $u^*(t)$ from **Case 1**: a neighboring suboptimal solution

Case 3: $(q_0, p_0) = (q_0 = 0.5, p_0 = 0)$: a neighboring optimal solution

Analytical solutions for each of the test cases have been manually derived using *Pontryagin's Maximum Principle* [164, 59, 30], which involves construction a Hamiltonian expression and then solving for an extremum solution. Details on the derivation

and the analytical solutions themselves are found in Appendix C.

10.5.5 Numerical Results and Discussion

Figure 86 summarizes the results of numerically implementing **VAE-OCP Formulation #1** on the Problem of Equation (78), using up to ($\mathbf{v}^1$) variational dynamic state constraints to compare **Cases 1 & 2**. Due to the excellent performance of the DMOC optimization method using a spRK4 ($s = 4$) variational integration scheme, the numerical formulation was able to be significantly reduced in complexity, only requiring $N = 5$ nodes. The solid black and dashed red lines represent the analytical solutions for **Cases 1 & 2**, respectively. The black diamond and square markers represent the baseline numerical solution to **Case 1** and the VAE approximation (using the 1^{st}-order equation-of-variation state solutions from **Case 1**) to asymptoticly approximate the analytical result of **Case 2**. Here it is seen in all plots that the numerically generated VAE solution has excellent capabilities to approximate neighboring sub-optimal solutions. Again, note that the optimal control $u^*(t)$ remains un-perturbed in these results from it's baseline solution. In Figure 86b the comparison of the 1^{st}-order dynamic state constraints to the analytical solutions again is seen to be accurate to within the numerical tolerance of the nonlinear interior-point numerical optimizer.

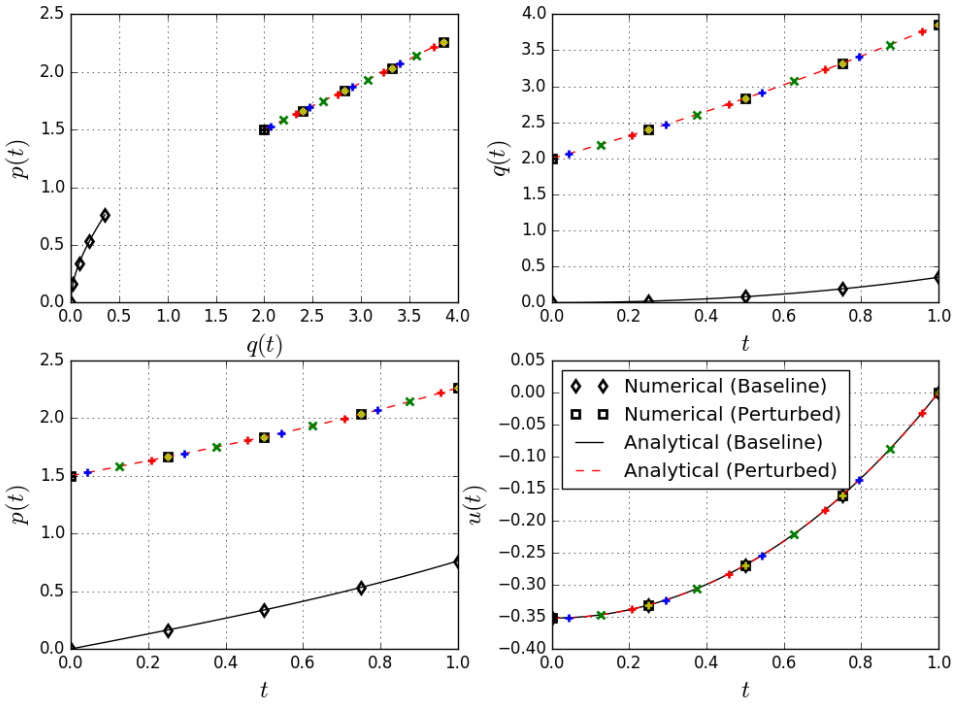

(a) Perturbed and baseline 0^{st}-order state and control solutions.

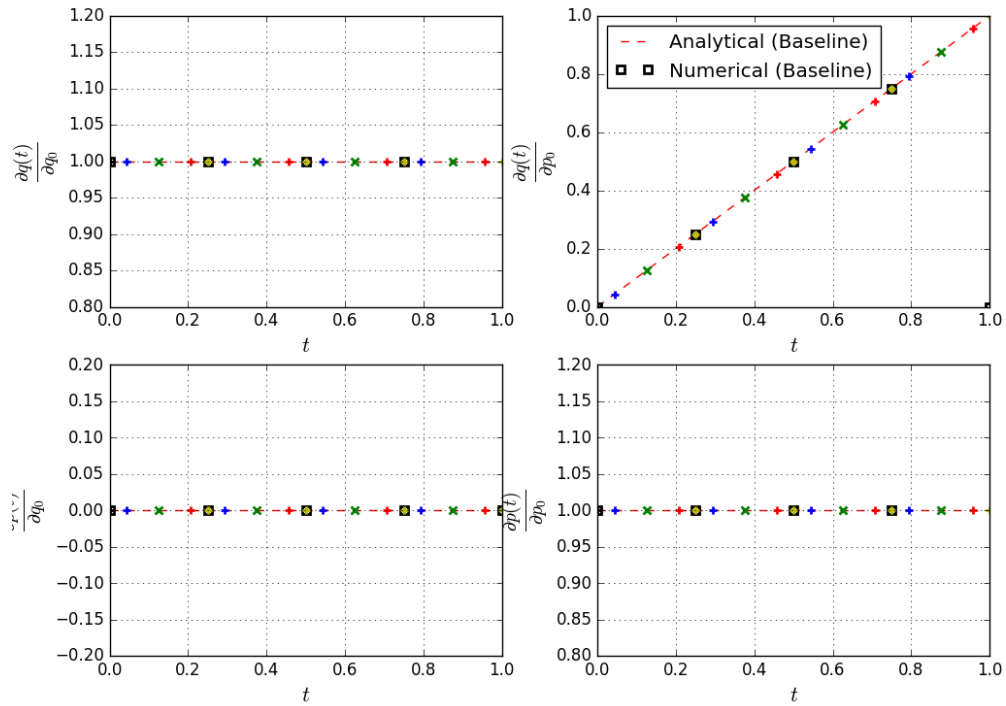

(b) 1^{st}-order state and control solutions.

Figure 86: Comparison of numerically generated VAE solutions by **VAE-OCP Formulation #1** to analytical solutions for **Case 1** and **Case 2**. These results were generated using an spRK4 variational integrator with time discretized using $N = 5$ nodes and optimization tolerances $\approx 1.0 \times 10^{-8}$.

In this special example equations of variation vanish for 2^{nd}-order and above, and the VAE hypersurfaces are numerically equivalent to the general (global) solution for all values of $(\delta q_0, \delta p_0)$. Figure 87 demonstrates this by again comparing the numerically generated VAE OCP solution to the analytical generation solution over an arbitrary range of $-2.0 \leq \delta q_0 \leq 2.0$ and $-1.5 \leq \delta p_0 \leq 1.5$. Here the red trajectories represent the 0^{th}-order (*i.e.* baseline) OCP solution and the black mesh and blue surface represent the analytical and numerical solutions, respectively, evaluated over the ranges of $\delta\theta = (\delta q_0, \delta p_0)$. Again, note that this range was arbitrarily chosen to visualize the results, and for this problem the region of approximation is actually $\pm\infty$ in both p_0 and q_0..

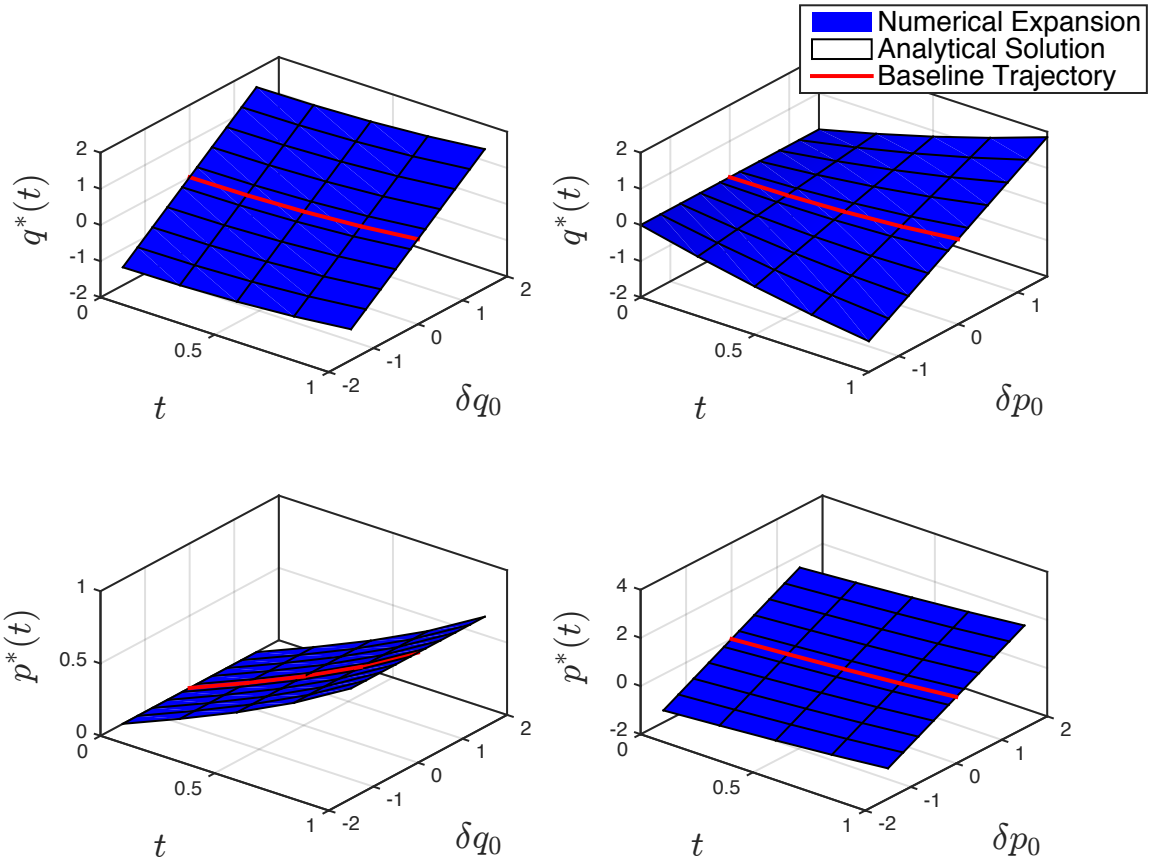

Figure 87: **VAE-OCP Formulation #1** comparison of the numerical asymptotic expansion to the analytically derived solution.

Implementation of **VAE-OCP Formulation #2** is considerably more complicated in that it now requires the sequential optimization of a family of VAE-OCPs. Using the VAE polynomial library of Section 10.1, this added complexity is easily accommodated in implementation, where evaluation of cost and constraint functions are achieved by using polynomial arithmetic with lower-order coefficients being constant parameters of previously solved lower-order VAE-OCPs and higher-order coefficients being design variables under the current-order VAE-OCP.

Figure 88 summarize the results of numerically implementing **VAE-OCP Formulation #2** on the Problem of Equation (78), using up to ($\mathbf{v}^1$) variational dynamic state constraints to compare **Cases 1 & 3**. These results were generated using the same optimization parameters as used in the previous study of: $s = 4$, $N = 5$, and $E_{\text{tol}} = 1.0 \times 10^{-8}$. For simplicity, VAE-OCP solutions are only parameterized with respect to a single perturbation parameter δq_0. Here it can be seen in all plots that the numerically generated VAE solution attempt to approximate the perturbed analytical solution, but error is present in all perturbed optimal solutions. Note that the baseline OCP solution (*i.e.* the 0^{th}-order solution) shows excellent correlation with the the baseline analytic solution for **Case 1**. Also, as time progresses, error in the perturbed position and momentum states grows; however, this is not the case with the perturbed optimal control input, which has nearly constant error throughout time. The same trends can be observed in the comparison of the 1^{st}-order optimal state and control solutions to the analytical solutions of Figure 86b. One interesting observation is that the colored markers (which indicate interior grid points used by the variational integrator) in the 1^{st}-order optimal control solution $\partial u^*/\partial q_0(t)$ exhibited distinctly different perturbed oscillatory trends, which suggests the presence of numerical oscillatory errors.

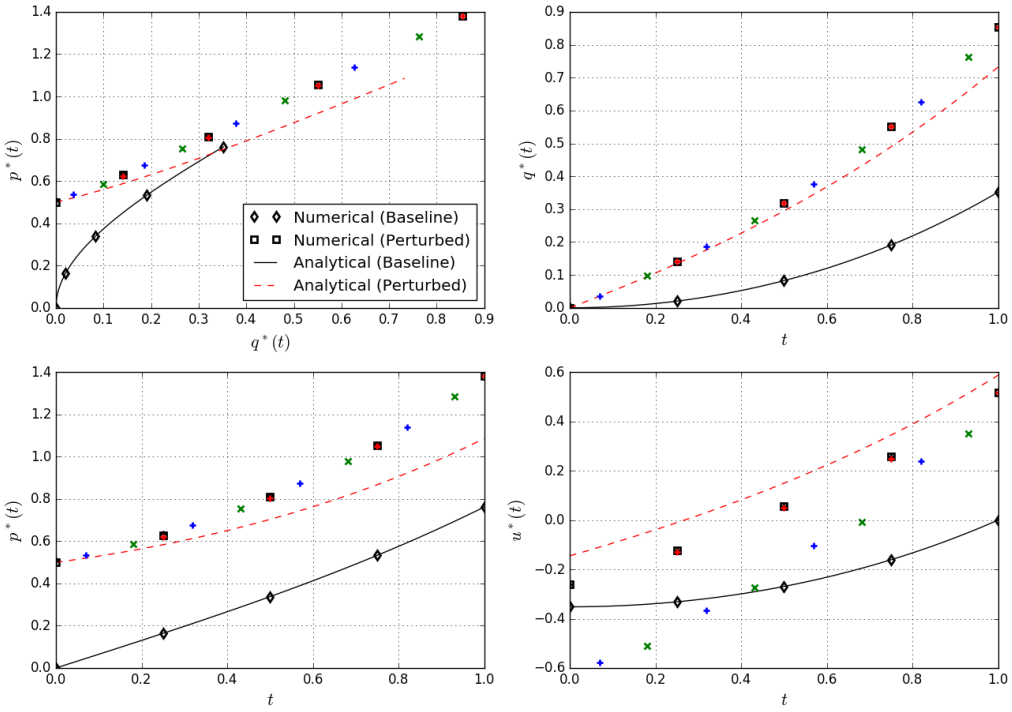

Figure 88: Comparison 0^{th}-order of numerically generated VAE solutions by **VAE-OCP Formulation #2** to analytical solutions for **Cases 1 & 3**. These results were generated using an $(s = 4)$ spRK variational integrator with time discretized using $N = 5$ nodes. Interior-point optimization tolerances $\approx 1.0 \times 10^{-8}$.

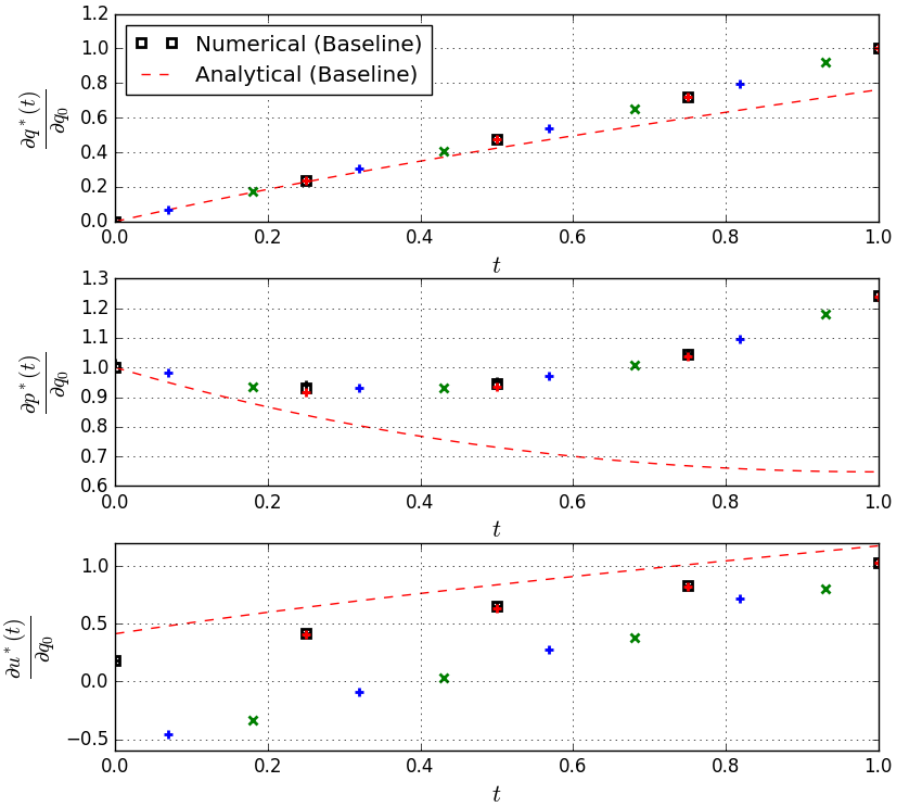

Figure 89: Comparison of the numerical and analytical 1st equation of variation optimal state and control (baseline) solutions.

To further investigate this effect, next the same analysis of Figures 88 and 89 was conducted, but this time using $N = 15$ nodes as opposed to $N = 5$ nodes. Figures 90 and 91 show these results and reveal that for increasing number of nodes that there is a perceived convergence in perturbed optimal position and momentum states but not in perturbed optimal control inputs, where the oscillatory error has been observed to increase. Further, the oscillatory error now affects the perturbed optimal control input nodes individually and not merely as an aggregate affect.

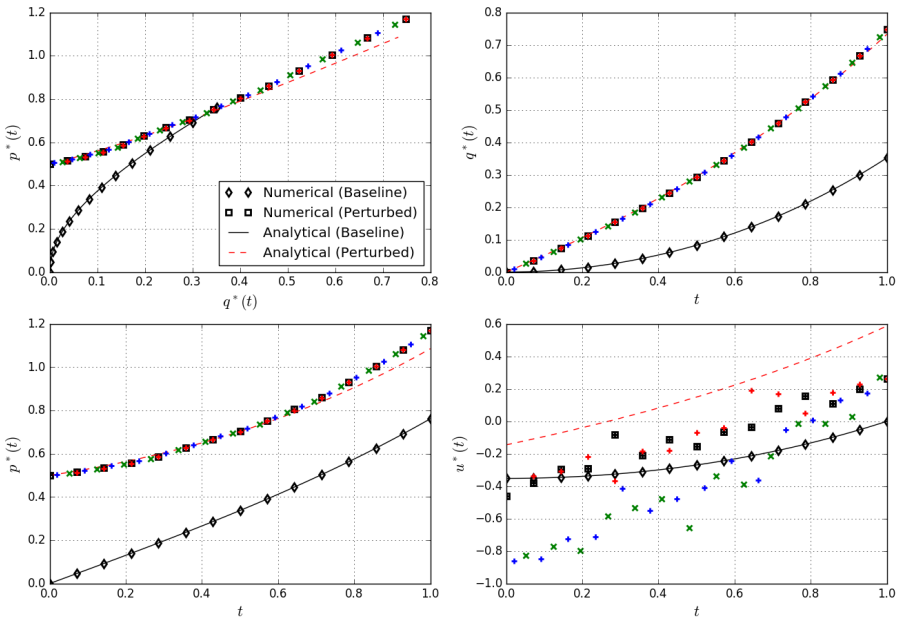

Figure 90: Comparison 0^{th}-order of numerically generated VAE solutions by **VAE-OCP Formulation #2** to analytical solutions for **Cases 1 & 3**. These results were generated using an $(s = 4)$ spRK variational integrator with time discretized using $N = 15$ nodes. Interior-point optimization tolerances $\approx 1.0 \times 10^{-8}$.

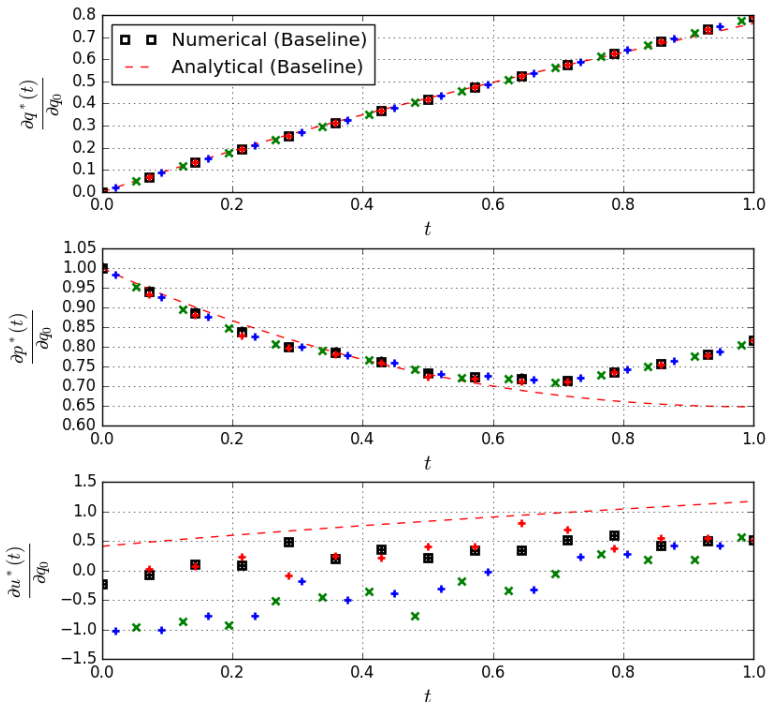

Figure 91: Comparison of the numerical and analytical 1st equation of variation optimal state and control (baseline) solutions.

The results of implementing **VAE-OCP Formulation #2** indicate that, while some error is present, the resulting VAE solution is able to approximate neighboring OCP solutions using perturbed VAE-OCP solutions; however, further work is needed to increase the numerical convergence for industrial use in large-scale problems (*e.g.* design problems). Potential issues include (i) faulty implementation (*i.e.* programming errors in the polynomial operation, numerical integration, optimization cost/constraint evaluation), (ii) numerical instability/errors (*i.e.* integrator quadrature method accuracy, nonlinear interior-point optimizer convergence, etc.) in the optimization formulation, and (iii) faulty theoretical formulation (*i.e.* limitations of variational integrators for higher-order systems, inaccurately formulation VAE-OCP formulations). Because effective demonstration of the polynomial operations have previously been shown and the 0^{th}-order OCP solutions agree with analytical predictions, this is likely not to the issue.

To briefly investigate further, analytical solutions were evaluated within the numerical optimization framework to confirm if the numerical constraint conditions for the 1^{st}-order OCP systems of both formulations was in agreement with analytical predictions. If both formulations yield constraint evaluations near zero, then issue (ii) (numerical instabilities/errors) is the likely culprit; however, if numerical constraints are not satisfied then further efforts should be focused on theoretical formulation of VAE-OCPs and higher-order variational integrators. To summarize this thought experiment, the following procedure is outlined:

1. Plug analytical solutions (both 0^{th} and 1^{st}-order) into the optimization frameworks for **VAE-OCP Formulations #1 & #2** to verify that numerical evaluations of constraints are near zero.

2. Take a closer look at the momentum integral constraint for $k = 0$, $h = 0.25$, and $s = 4$ (Lobatto IIIA-IIIB) for the Campos problem with $\theta = q_0$.

Tables 25 and 26 summarize the results of this investigation for the experimental procedure outlined above for the first two nodes of a $N = 5$ node discretization. Table 25 shows that for **VAE-OCP Formulation #1** the $(\mathbf{v}^0)$ and $(\mathbf{v}^1)$ constraints both are both satisfied; however, this is not the case for the second formulation, where Table 26 shows that $\partial \dot{P}_{jk}/\partial\theta$ are now non-zero terms, as expected, but their effects do not cancel when the constraints are numerically evaluated.

Table 25: Computed collocation spRK4 values using analytical solutions $(q^*(t),\, p^*(t))$, etc. for **Case #2**.

j	c_j	$\bar{b}_j$	$t_k + hc_j$	$\dot{P}_{jk}$	$\partial\dot{P}_{jk}/\partial\theta$	$p^*(t_k)$	$\partial p^*(t_k)/\partial\theta$
1	0	1/12	0.0000	0.6481	0.000	0.000	1.000
2	$1/2 + \sqrt{5}/10$	5/12	0.0691	0.6496	0.000	–	–
3	$1/2 + \sqrt{5}/10$	5/12	0.1809	0.6587	0.000	–	–
4	1	1/12	0.2500	0.6684	0.000	0.1636	1.000
(v^0) at $k=0$: $0 = p_{k+1} - \left(p_k + h\sum_j \bar{b}_j \dot{P}_{jk}\right) \approx -1.0649e-04$ ✓							
(v^1) at $k=0$: $0 = \frac{\partial}{\partial\theta}p_{k+1} - \left(\frac{\partial}{\partial\theta}p_k + h\sum_j \bar{b}_j \frac{\partial}{\partial\theta}\dot{P}_{jk}\right) \approx 0.0000$ ✓							

Table 26: Computed collocation spRK4 values using analytical solutions $(q^*(t),\, p^*(t))$, etc. for **Case #3**.

j	c_j	$\bar{b}_j$	$t_k + hc_j$	$\dot{P}_{jk}$	$\partial\dot{P}_{jk}/\partial\theta$	$p^*(t_k)$	$\partial p^*(t_k)/\partial\theta$
1	0	1/12	0.0000	0.6481	0.4136	0.000	0.000
2	$1/2 + \sqrt{5}/10$	5/12	0.0691	0.6496	0.4809	–	–
3	$1/2 + \sqrt{5}/10$	5/12	0.1809	0.6587	0.5836	–	–
4	1	1/12	0.2500	0.6684	0.6423	0.1636	0.8390
(v^0) at $k=0$: $0 = p_{k+1} - \left(p_k + h\sum_j \bar{b}_j \dot{P}_{jk}\right) \approx -1.0649e-04$ ✓							
(v^1) at $k=0$: $0 = \frac{\partial}{\partial\theta}p_{k+1} - \left(\frac{\partial}{\partial\theta}p_k + h\sum_j \bar{b}_j \frac{\partial}{\partial\theta}\dot{P}_{jk}\right) \approx -0.2938$ ✗							

10.5.6 Exp't #4 Observations

In Section 9.6 the following hypothesis was stated in response to **RQ. #2.3**, concerning the feasibility of VAEs to generate higher-order solutions to OCPs. From a design perspective, this is interesting because this added capability would allow for design space exploration, as well as uncertainty analysis, to be conducted on a class of problems, which has historically proven to be difficult simultaneously automate and stabilize the accurate computation of solutions.

HYP. #2.3: Higher-order gradients can be used to generate high-accuracy VAE surrogates to OCPs, which will enable point solutions from computationally expensive OCP solvers to be utilized for parametric exploration.

The findings of this study show that implementation of VAEs to generate solutions to higher-order OCPs shows promising results, and that is is indeed possible to generate higher-order OCP solutions. However, in terms of dynamic experiment design for potentially large and complex systems this still needs more work before it can be useful for design space exploration. The use of variational integrators allows for the direct optimization of OCPs while still guaranteeing that the indirect optimality criterion for the 0^{th}-order OCP system is satisfied [62]; however, subsequent investigation is need to ensure that this is also the case for higher-order OCP solutions. Also, additional VAE-OCP formulations might prove useful.

The implications of proposed capability from a vehicle systems design perspective would allow for the optimal controls expert to contribute to the systems engineering design problem in a significant way (*e.g.* the manual simulation of a higher-order VAE baseline vehicle along an optimal trajectory, which could then potentially be rapidly evaluated for alternative designs along the space of optimal mission profiles).

10.6 Summary of Observations and Conclusions

In this chapter a solution implementation algorithm for computing higher-order VAEs was proposed and demonstrated to simulate initial value problems in Section 10.1.2. Next, four experimental studies were conducted to explore the feasibility of implementing VAEs for subsequent implementation in the TEMPUS design methodology, outlined in Chapter 8.

- **Exp't #1** was designed to address **HYP#2.1.1** by investigating if the use of alternative basis functions for generating VAEs will yield expansions with faster convergence characteristics and larger regions of approximation. For the Chebyshev basis, this was indeed observed and therefore the implementation of polynomial libraries for alternate basis functions is a worthy pursuit for future efforts.

- **Exp't #2** was designed to address **HYP#2.1.2**, which is concerned with studying the effectiveness of how VAEs enable high-accuracy propagation of parameter uncertainties for nonlinear dynamic systems. The findings of this study suggest that the use of higher-order VAEs for the uncertainty propagation in nonlinear dynamic systems do produce probabilistic models that are asymptotically accurate; however, for some problems, adverse numerical effects, such diminishing returns on accuracy and oscillatory, slow convergence rates, could lead to artificial multimodality in probabilistic trajectories. In the context of robust-optimization design problems, addressed by the TEMPUS methodology, this implies that robust-optimal information metrics may lead to sub-optimal experiment designs, regardless of how much higher-order information is utilized. Therefore it may be necessary to employ a brute-force Monte Carlo analysis on virtual experiments for verification of robust-optimality.

- **Exp't #3** was designed to address **HYP #2.2**, by investigating how the adverse effects of the curse of dimensionality affect the scaling of computational complexities (*i.e.* computational time, memory allocation) in both increasing dimension and increasing order. Here dense multiplication of multivariate polynomials was selected because it is a known bottle-neck algorithm in polynomial algorithm, and therefore it's asymptotic scaling for the recursive-coefficient implementation of Section 10.1.2 should be dominated by this algorithm (or comparable algorithms). The findings of this study do confirm **HYP #2.2**, in that despite the substantial improvements observed by implementing degree control, adverse complexity growth for high-dimension/low-order polynomials is still significant. Therefore parallel/vectorization strategies most likely must be utilized when designing dynamic experiments for large-scale aerospace problems. Final confirmation of implementation of VAEs to solve these types of problems will be investigated further in Chapter 11.2, when flight test design for hypersonic SCRAMjets is addressed.

- **Exp't #4** was designed to address **HYP #2.3**, which is concerned with investigating the potential application of VAEs to solve higher-order OCPs. The findings of this study show that implementation of VAEs to generate solutions to higher-order OCPs shows promising results, and that it is indeed possible to generate higher-order OCP solutions. However, in terms of dynamic experiment design for potentially large and complex systems this still needs more work before it can be useful for design space exploration. The implications of proposed capability from a vehicle systems design perspective would allow for the optimal controls expert to contribute to the systems engineering design problem in a significant way (*e.g.* the manual simulation of a higher-order VAE baseline vehicle along an optimal trajectory, which could then potentially be rapidly evaluated for alternative designs along the space of optimal mission profiles).

CHAPTER 11

ROBUST-OPTIMAL DESIGN OF DYNAMIC SYSTEM IDENTIFICATION EXPERIMENTS

This chapter is focused on the demonstration of the TEMPUS methodology which includes an investigation into possible approaches to RDO implementation on dynamic system identification experiments, as outlined in Chapter 9. Using the VAE capability demonstrated in the previous chapter, higher-order VAEs will be used in this chapter to automatically construct Fisher information quality metrics, aiding in the investigation of possible ways to enable and improve RDO experiment design methods. These methods include (i) the potential implementation of VAE surrogates for parametric uncertainty space exploration, (ii) the deterministic construction of statistical performance metrics, and (iii) alternative approaches to design space exploration. To evaluate potential experiment designs, a virtual experimentation (VX) strategy will be outlined and utilized for performance evaluation of alternative designs.

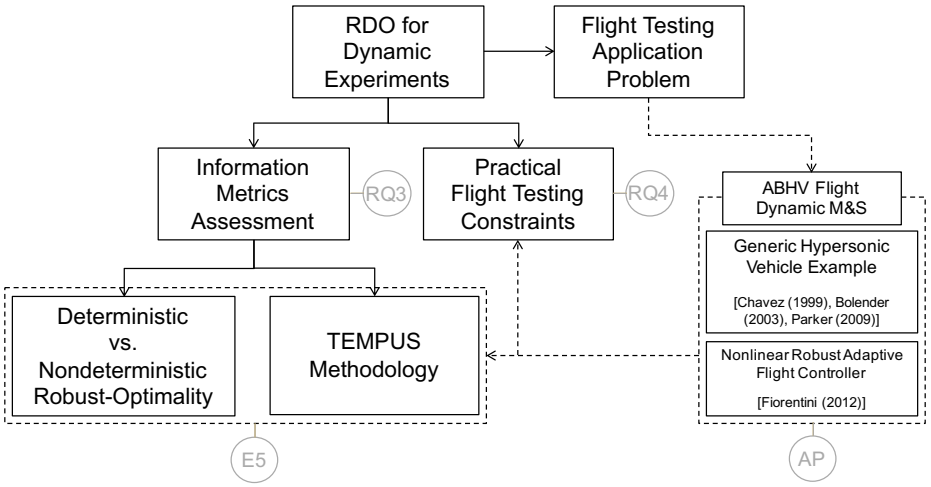

Figure 92: Experimental taxonomy of the experiments for applying VAEs to dynamic experiment design.

Summarized below, two test problems are considered for implementation of TEMPUS: (i) a simple spring-mass-damper system with non-homogenous forcing; (ii) a complex flight dynamic SCRAMjet model to simulate flight tests.

1. **Spring-Mass-Damper undergoing Forced Oscillation** – A simple 2-state/3-parameter dynamic system is first considered (i) to investigate any potential implementation issues in regards to the TEMPUS sizing and synthesis approach of Figure 8.2 (outlined in Section 46) and (ii) to explore a diverse array of robust-optimality information metrics, demonstrated using both factorial experiment design and multi-disciplinary design optimization approaches.

2. **Air-Breathing Hypersonic Vehicle Flight Test Design** – A complex flight dynamic SCRAMjet model consisting of 45-states and 8-parameters is implemented for the simulation of hypersonic flight tests, and the TEMPUS methodology is again be demonstrated, requiring the computation of VAE dynamic state-to-parameter sensitivities, parameterized by aero-propulsive-elastic coefficient values for a reference flight condition. In addition to the larger industrial size of this problem, the added challenge of dynamic instabilities requires the implementation of a sophisticated nonlinear robust-adaptive flight controller to ensure robustness in stability and control effectiveness.

From the outcome of the previous group of experiments of Chapter 10, automated computation of higher-order VAEs of dynamic systems was demonstrated, where diminishing returns and adverse complexity effects (*i.e.* due the curse of dimensionality) were observed for certain cases. In the following experiments, **HYP. #3** is now be tested (using virtual experimentation) to determine if the presence of potential adverse effects will hinder the implementation of experiment design problems that utilize VAEs to compute information quality metrics.

11.1 Exp't #5– Design of Robust-Optimal System Identification Dynamic Experiments

In Section 9.7, it was discussed that if VAEs could be used to automatically compute higher-order state-to-parameter dynamic sensitivities, then the computation of Fisher information metrics summarized in Table 11 could be used for the robust-optimization of dynamic system identification experiments. In this context, the phrase 'robust-optimization' specifically refers to the insensitivity of a given design to changes in model parameter uncertainties. Designs that are found to be robust-optimal designs are expected to directly alleviate the adverse implications of *the circulatory problem*, discussed in Section 5.2, but in contrast to the methodology proposed by Asprey and Macchietto [18], there is no need to run large amounts of cases or to compute cumbersome multi-dimensional integrals to evaluate measures of robustness. To this end, the following hypothesis was previously stated in response to **RQ. #3**.

HYP. #3: If the automated, generalized computation of higher-order gradient information can be made computationally feasible, then a flexible approach to robust-optimal dynamic experiment design utilizing VAEs to automatically and accurately compute higher-order dynamic state-to-parameter sensitivities will yield superior designs that are robust to parameter uncertainties.

11.1.1 Experimental Procedure

The experimental procedure for this experiment emulates the thought experiment of Asprey and Macchietto [18] and is implemented on both test problems, described previously. As shown in Table 27, this procedure consists of designing an experiment and then simulating that experiment design for different perturbed values of model

parameters. Here the assumption is made that the model structure is *a priori* correct, as this just adds the additional complexity of repeating this processes over a set of potential candidate models and is not considered in this work.

Table 27: Expt#5 experimental procedure to implement TEMPUS for dynamic experiment system and use virtual experimentation for performance evaluation.

Assume: model structure is correct (this can just be repeated for all model structures (NP-hard problem))

1. **Select**: model structures and nominal parameter values (reflecting the current state of knowledge) $\boldsymbol{\theta}_0$
2. **Quantify**: bounds or statistical distributions of model parameter uncertainties
3. **Iterate**: for different Fisher information metrics
   (a) **Design**: a dynamic experiment for a given information metric using the TEMPUS sizing and synthesis approach
   (b) **Evaluate**: compute the *a priori* Fisher information criterion using the design vector and the *a priori* parameters
   (c) **Iterate**: for a Monte Carlo analysis on parameter uncertainties
      i. **Test**: simulate a virtual physical experiment using the (robust)-optimized experiment design vector, the real parameter values, and measurement noise
      ii. **Estimate**: using experimental results, determine *a posteriori* parameters using a maximum likelihood function
      iii. **Evaluate**: compute the *a posteriori* Fisher information criterion using the design vector and the *a posteriori* parameters
4. **Repeat**: return to 3
5. **Compare**: all experiment designs to see which one provides best *a posteriori* joint parameter confidence regions (*i.e.* robust-optimal Fisher metrics should outperform the rest)

The numerical results of these experiments are of the same format as those described by Asprey and Macchietto [18], which include tabulated lists of design vectors, statistical confidence intervals in estimated parameters, and *a posteriori* Fisher information metrics numerical values. Shown below in Equation (79) and Figure 93 are some of the results presented in the work by Asprey and Macchietto [18] for a simple 2-state/4-parameter batch-fed bioreactor problem, where three designs were compared against each other – D-Opt, ED-Opt, and RD-Opt designs. In this study, it was observed that evaluation of the D-Optimality for each design for the identical set of perturbed parameter suggests that the RD-Opt (*i.e.* minimax or worst-case scenario) experiment design yielded the best resulting information quality.

$$\begin{aligned} \det\left[\mathscr{M}\left(\boldsymbol{\theta}^*, \boldsymbol{\varphi}_R\right)\right] &\propto 1 \times 10^{10} \\ \det\left[\mathscr{M}\left(\boldsymbol{\theta}^*, \boldsymbol{\varphi}_{ED}\right)\right] &\propto 1 \times 10^{9} \\ \det\left[\mathscr{M}\left(\boldsymbol{\theta}^*, \boldsymbol{\varphi}_D\right)\right] &\propto 1 \times 10^{8} \end{aligned} \tag{79}$$

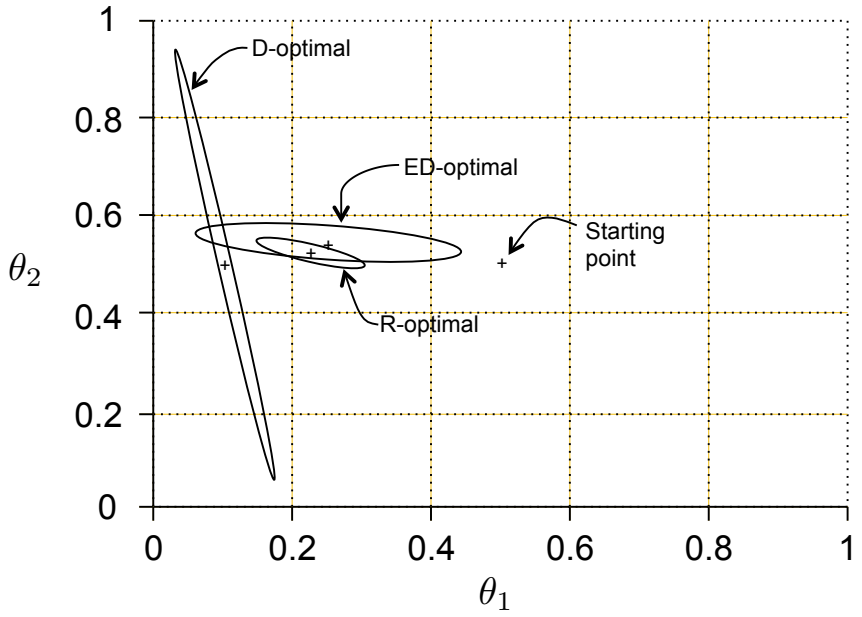

Figure 93: Joint 90%-confidence regions for parameters θ_1 and θ_2 for the small engineering design example discussed by Asprey and Macchietto [18].

11.1.2 Spring-Mass-Damper Virtual Experimentation Examples

In this section, the computational simulation of actual physical experiments is conducted, generating representative experimental data for subsequent use in SysID parameter estimation softwares. Realistic assessment of physical experiments through computational analysis, requires additional information regarding the measurement system parameters. Table 28 summarizes four different notional sensor types: SensorType:=1 (slow sampling/low accuracy), SensorType:=2 (fast sampling/low accuracy), SensorType:=3 (slow sampling/high accuracy), and SensorType:=4 (fast sampling/high accuracy). According to the experimental procedure of Table 27, two sets of model parameters are utilized: (i) a nominal set to be used in experiment design, which represents the current state of knowledge about a physical model, and (ii) a perturbed set to be used to perform a virtual experiment by simulating the effects of the circulatory dependence of information quality on true parameter values, as discussed in Section 5.2.

Table 28: Summary of sensors used for dynamic experiment design and virtual experimentation of the spring-mass-damper system described in Section 10.3.2.

		Sampling Frequency, (Hz)	
		10	25
Displacement rms measurement error, (mm)	2.5	SensorType 1	SensorType 2
	0.1	SensorType 3	SensorType 4

Table 29: SMD VX nominal parameter values ($\mathbf{p}_0$) and perturbed parameter values ($\mathbf{p}_0 + \boldsymbol{\delta}\mathbf{p}$).

	k	m	c
$\mathbf{p}_0$	3.50	0.10	0.15
$\boldsymbol{\delta}\mathbf{p}$	-0.2439	0.0037	0.0182

Figures 94 and 95 show virtual experimentation input/output results for four different experiment designs, employing (a) linear frequency sweep, (b) 3211 step, (c) sinusoidal, and (d) multi-sine input signals, respectively. In the general, any admissible functional form can be used to perturb the system response; the four input signal forms below are common functional candidates for experiment design, which are easily described by a small set of input design parameters. Here, the red dots represent measured input data, which is assumed here to be known exactly by sampling of the continuous signal shown in blue (*i.e.* perfectly accurate sensors for sampling input signals).

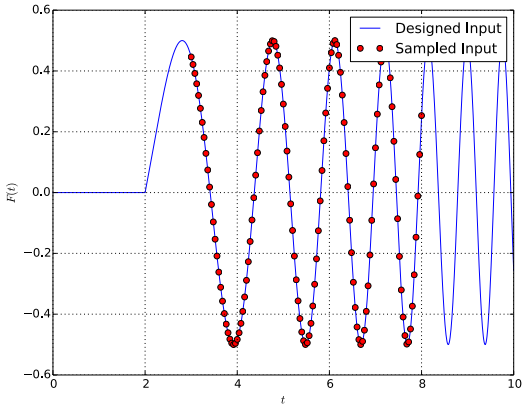

(a) Frequency Sweep

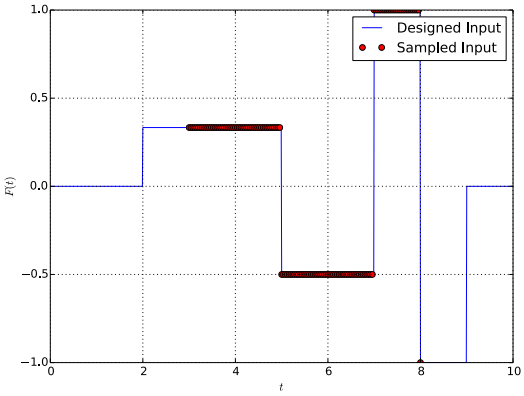

(b) 3211 Step

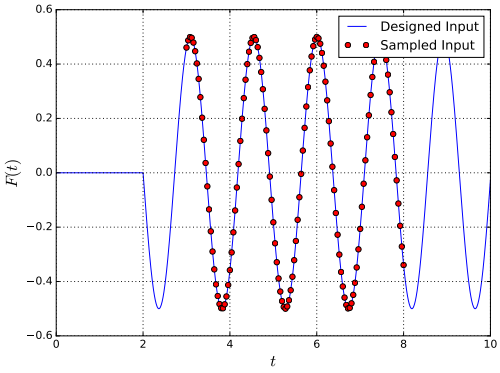

(c) Sinusoidal.

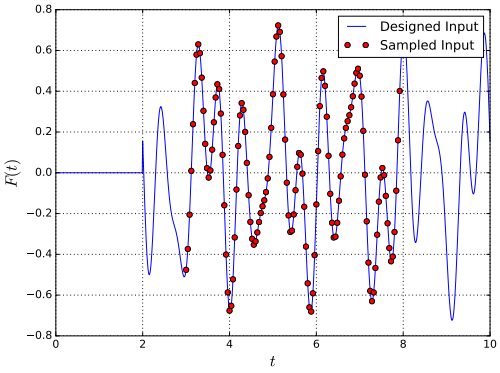

(d) Multisine.

Figure 94: Simulation results for prescribed input signals (blue) and sampled data (red dots): (a) frequency sweep, (b) 3211 step input sequence, (c) sinusoidal forcing, and (d) multi-sine forcing.

Here, the output is taken to be the measurement of displacement only, which is representative of the fact that, in general, not all states are observable and/or measurable quantities and therefore often limited data is available. As can be seen below, each input design affects the system response differently. Here each "designed" experiment was simulated using the nominal parameter values of Table 29 and the virtual experiment represents a separate simulation, using the perturbed parameters. In this study, measured data is sampled from the virtual experiment using Sensor #4 from Table 28 for a 5 second window between $3 \leq t_{\text{sim}} \leq 8$ (sec).

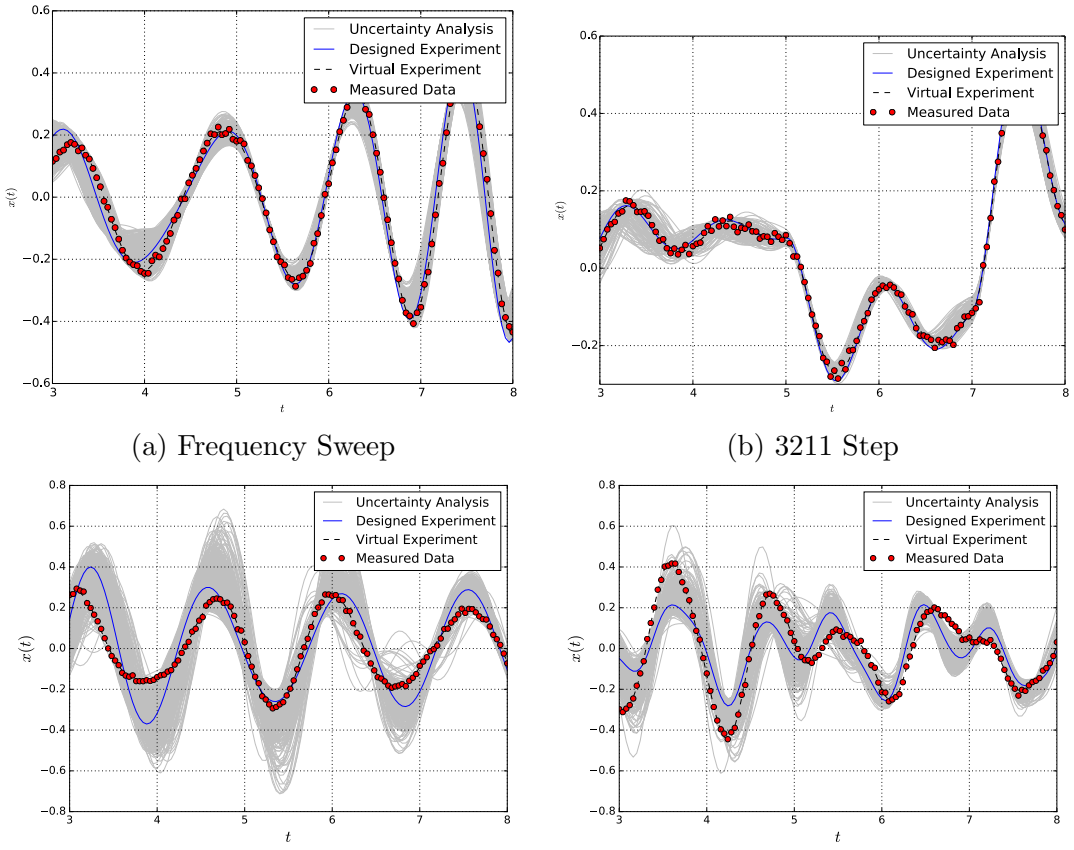

(a) Frequency Sweep

(b) 3211 Step

(c) Sinusoidal Input.

(d) Multisine.

Figure 95: Simulation results for designed (baseline) output history (blue), parametric uncertainty analysis (grey), virtual (perturbed) experiment (dashed black), and sampled data (red dots) for experiment designs under: (a) frequency sweep, (b) 3211 step input sequence, (c) sinusoidal forcing, and (d) multi-sine forcing.

System Identification of the 3211 Step Input Experiment. The following analysis is a small demonstration of a system identification method for the purpose of observing estimator performance and comparison of goodness-of-fit metrics to estimated trajectories and parameters, building a level of intuition for results of subsequent sections. Given the data set generated by a virtual experiment from the 3211 step input case, the output-error method, from the system identification software package SIDPAC [170], was used estimate the model parameters (k, m, c). The output-error method within SIDPAC employs a dual optimization scheme of first minimization using a modified Newton-Raphson and a simplex method to enforce numerical stability.

Using the raw input/output data shown in Figure 96, the output-error method was allowed to run 20 iterations, with final results shown in Table 30 and Figures 96–98. Figure 97 shows the comparison between the measured output data and the estimated displacement response, which is observed to be an excellent fit in spring-mass-damper displacement dynamic response. From Table 30 it can be observed that the largest percent error is 10.1% for estimating the value of displacement at $t_{\text{sim}} = 3$ (sec), but that all other parameters are approximately 5% error or less. The correlation matrix shows a mixture of parameter correlations that are moderately high and low.

While these results do appear to show good estimator performance, especially in terms of output-error in dynamic response, Figure 98 shows that both the estimated parameters and associated parameter estimation covariance matrix posses a level of bias when compared to the true parameter values from Table 29. As can be seen, the result of the parameter estimates lie within the associated 95% confidence ellipses with the exception of the parameter c. This error is due to the insensitivity of the measured response to the value of c, which causes degraded convergence in the parameter estimation. This behavior is unsatisfactory for experiments seeking to obtain accurate estimates of both parameters and parameter confidence intervals.

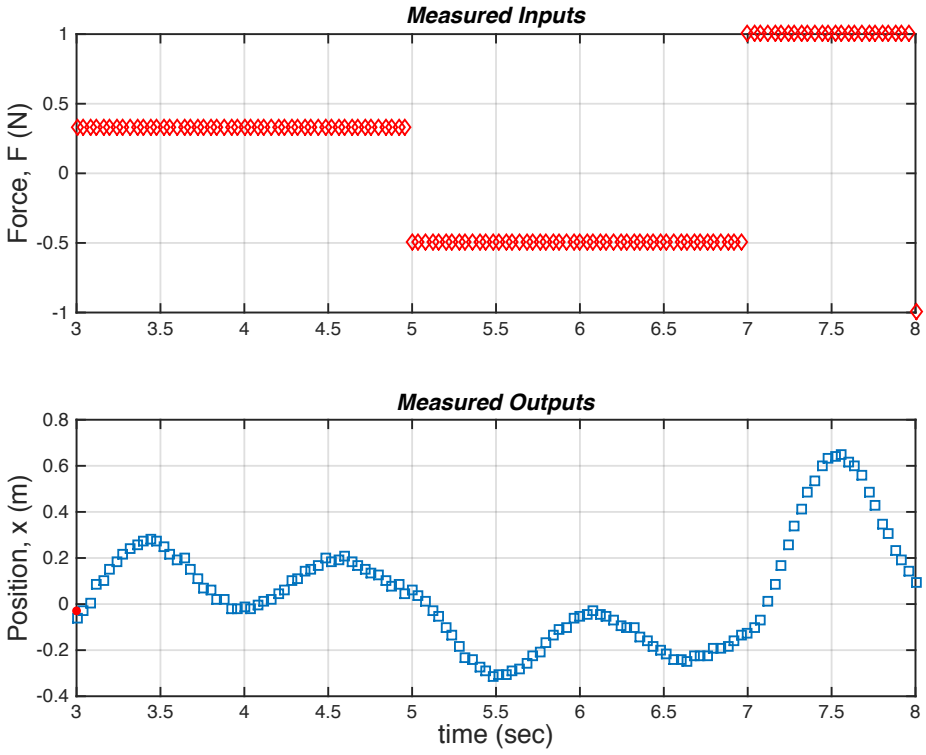

Figure 96: Virtual eXperiment: raw measured input-output data.

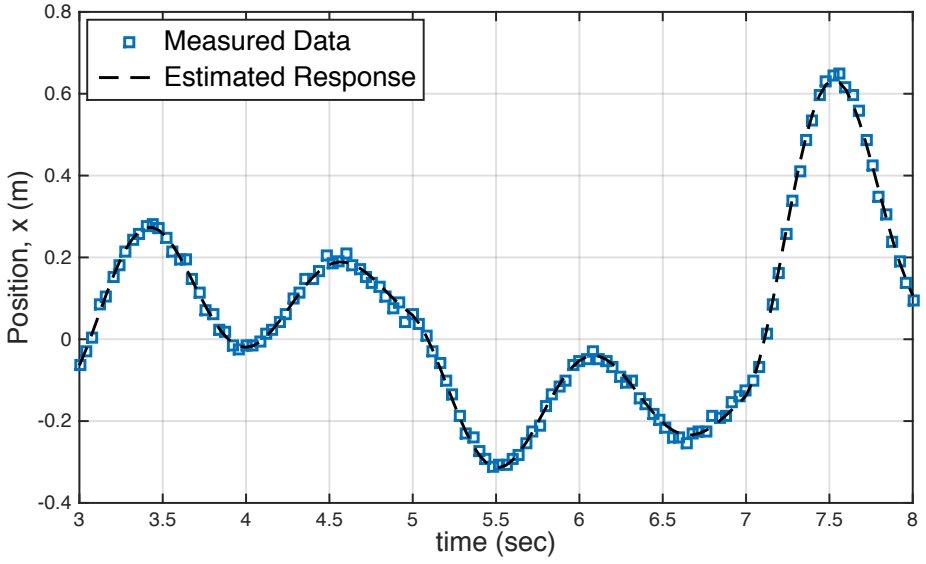

Figure 97: Output-error regressed model comparison with measurement data.

Table 30: System identification output-error estimator goodness-of-fit results for 20 iterations.

Parameters	Nominal Value	Standard Error	Percent Error	95% C.I.	Correlation Matrix				
					k	m	c	x_0	v_0
k	3.2570	2.81e-2	0.9	[3.200 , 3.313]	1.0				
m	0.1075	2.42e-3	2.3	[0.103 , 0.112]	0.84	1.0			
c	0.1276	6.48e-3	5.1	[0.115 , 0.141]	-0.028	0.464	1.0		
x_0	-0.0638	6.85e-3	10.7	[-0.077 ,-0.050]	0.59	0.78	0.41	1.0	
v_0	0.9026	4.18e-2	4.6	[0.819 , 0.986]	-0.14	0.22	0.73	0.09	1.0

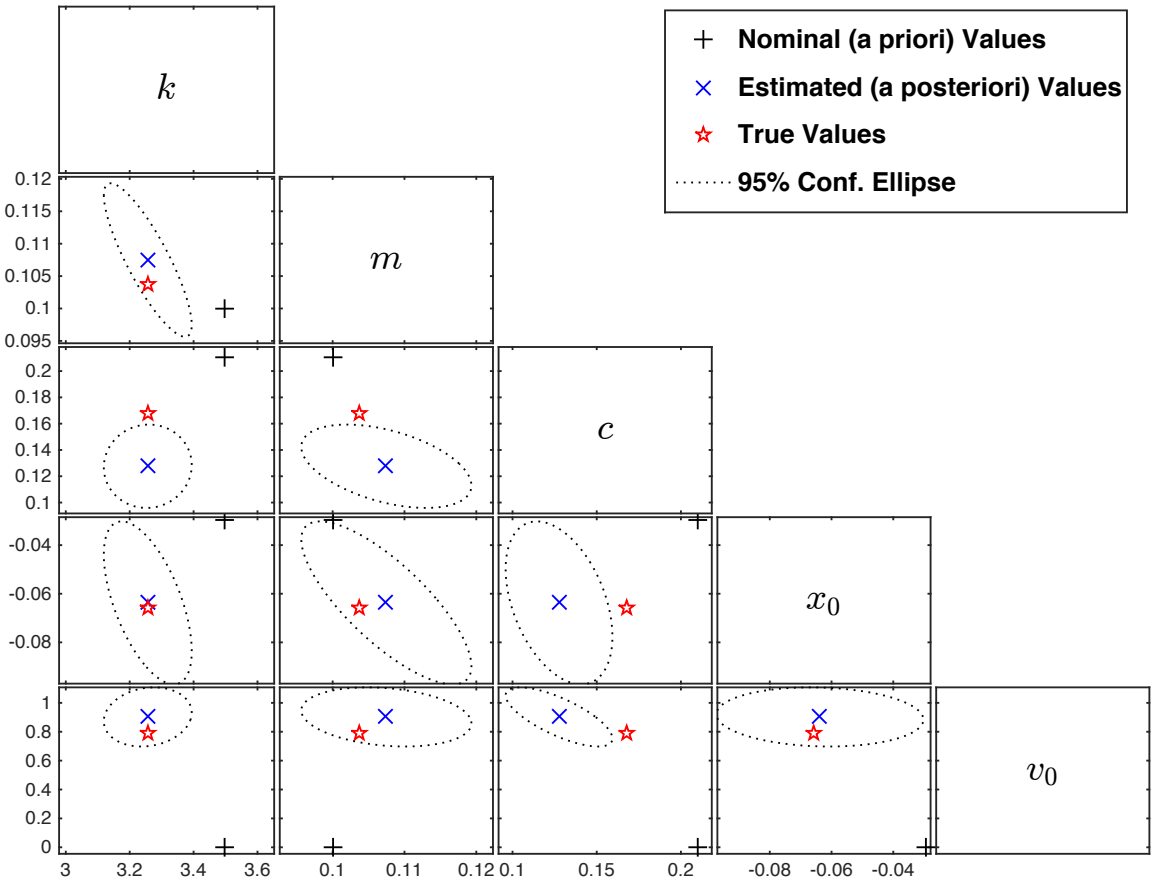

Figure 98: Multivariate plots showing output-error model estimation of nominal *a priori* values (black +), estimated *a posteriori* values (blue ×), true values (red ⋆), and 2D projections of the parameter covariance matrix.

11.1.3 SMD Design of Experiments

In the following sections, techniques for the design of robust-optimal dynamic system identification experiments are explored for the spring-mass-damper system undergoing a sinusoidal forcing function, as described in Table 31 of Section 11.1.4.

Comparison of Nominal Information Metrics. Figure 99 shows the DOE results for the nominal (D,T,A,E)-Optimality information metrics along with the information matrix condition number as a multivariate scatter plot. Only results where the matrix condition number is less than 500 are shown, and base-10 logarithmic transformations are used here to scale information metrics. Strong linear correlations between the different information metrics are observed. As can be seen, the experiments with higher information content increases as SensorType increases from a slow sampling, low accuracy sensor up to a fast sampling, high accuracy sensor, which is an intuitive result.

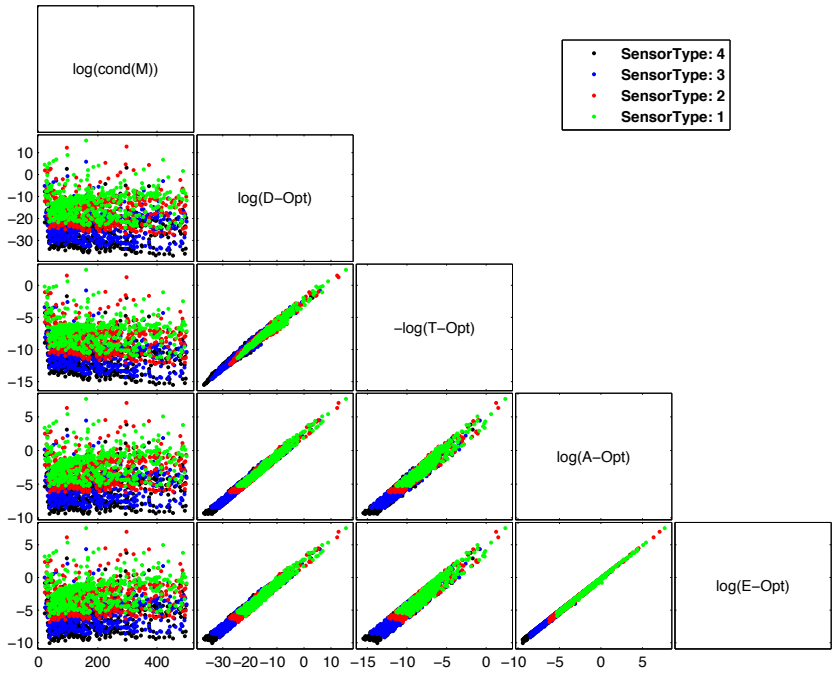

Figure 99: Multivariate scatter plot results for design of experiment results for nominal (D,T,A,E)-Optimality information metrics.

Figure 100 shows the experiment design vector for the top 100 performing experiments (top 25 for each (D,T,A,E)-Optimality information metric) in a parallel coordinate plot. To standardize the results for comparative purposed, each design variable is normalized: maximum test duration – $T_{\text{sp,max}} = 10$ (sec); maximum excitation frequency – $f_{\text{max}} = 50$ (Hz); maximum excitation duration – $T_{\text{sw,max}} = 10$ (sec). Here intuitive trends are observed in test duration, excitation frequency, excitation duration and sensor type, implying that high information quality is achieved by experiment designs which (i) sample and excite the system early in the simulation; (ii) excite the system near the natural frequency; (iii) sample the system frequently and accurately. For the initial condition variables, no significant trend is observed, where the clustering at large excitation conditions is marginally perceived.

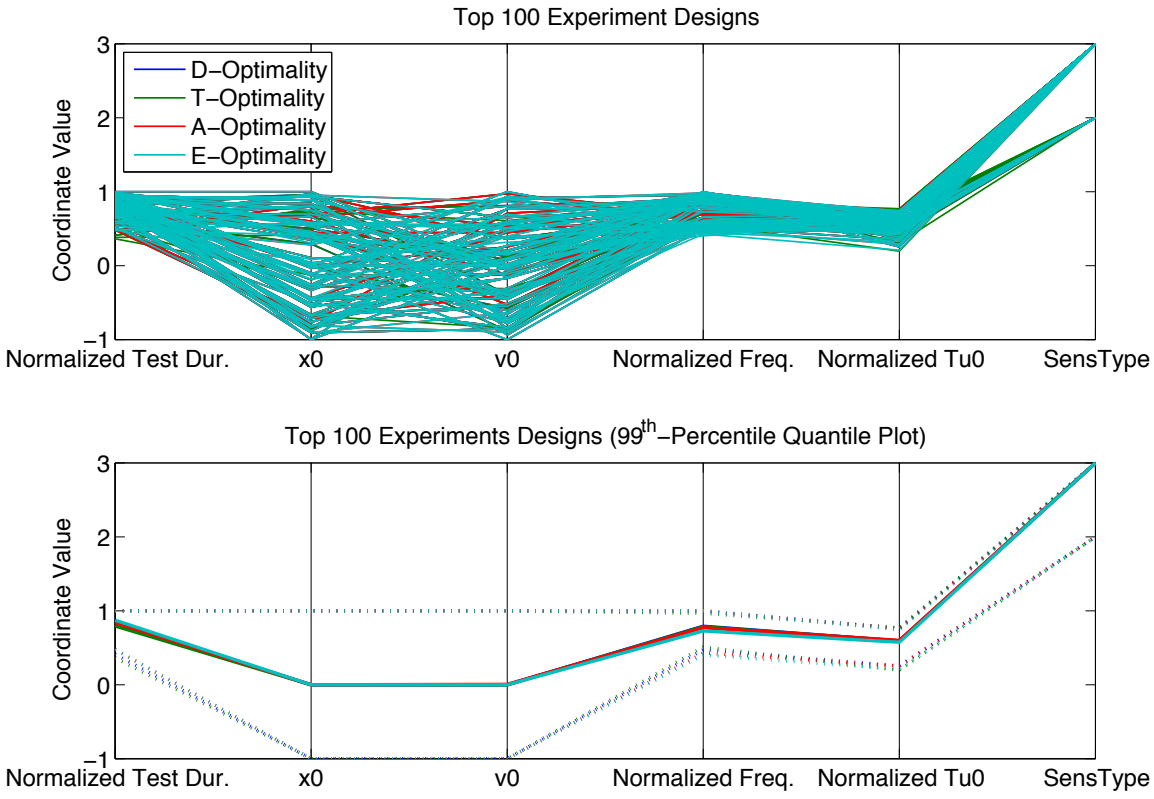

Figure 100: Parallel coordinates plot results for the top 100 performing experiment design vectors for nominal (D,T,A,E)-Optimality information metrics.

Comparison of Robust D-Optimality Information Metrics. Figure 101 shows the DOE results for the robust family of D-Opt information metrics along with the information matrix condition number as a multivariate scatter plot. For equivalent comparison between metrics computed via the nondeterministic (RD,BD,ED,VD)-Opt and deterministic (SR-ED,SR-VD)-Opt metrics, 3$^{\text{rd}}$-order state-to-parameter VAEs were computed. Only results where the matrix condition number is less than 500 are shown, and base-10 logarithmic transformations are used here to scale information metrics. Strong linear correlations between the different information metrics are observed. As can be seen, the experiments with higher information content increase as SensorType increases from a slow sampling, low accuracy sensor up to a fast sampling, high accuracy sensor.

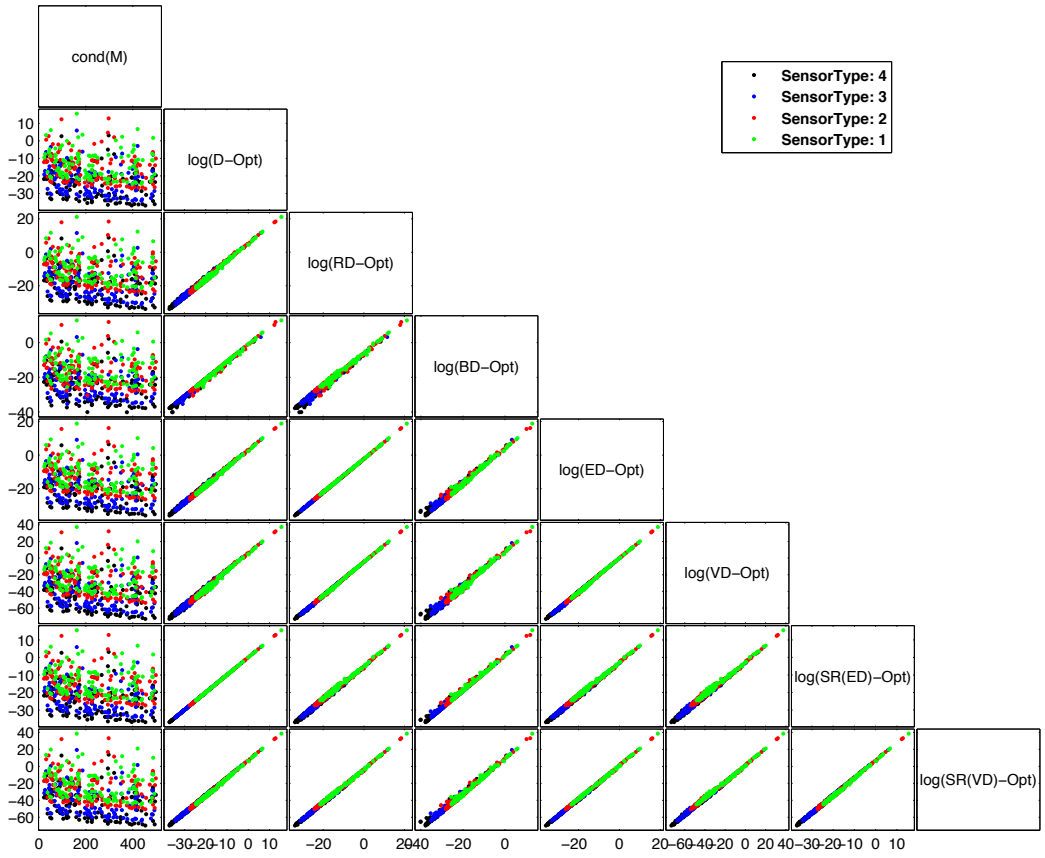

Figure 101: Multivariate scatter plot results for design of experiment results for nominal (D,RD,BD,ED,VD,SR-ED,SR-VD)-Optimality information metrics.

Investigation of Variation in Fisher Information Matrix Elements. Figure 102 shows results for the symmetric Fisher information matrix (lower-diagonal) elements for four 500-case (Latin Hypercube) DOEs, one conducted per each SensorType from Table 28. Here it can be seen that for every matrix element that very small changes are observed for SensorTypes 1 and 2, which correspond to the two lowest quality sensors in terms of rms measurement error. It appears that only a slight increase in variability can be seen for increasing sampling frequency from 10 (Hz) to 25 (Hz) in the low-accuracy sensors. For the two higher-accuracy sensors, significantly more variability is observed, where correlations between different elements is observed (*e.g.* M12 *vs.* M33, M11 *vs.* M12, M11 *vs.* M33, M22 *vs.* M33).

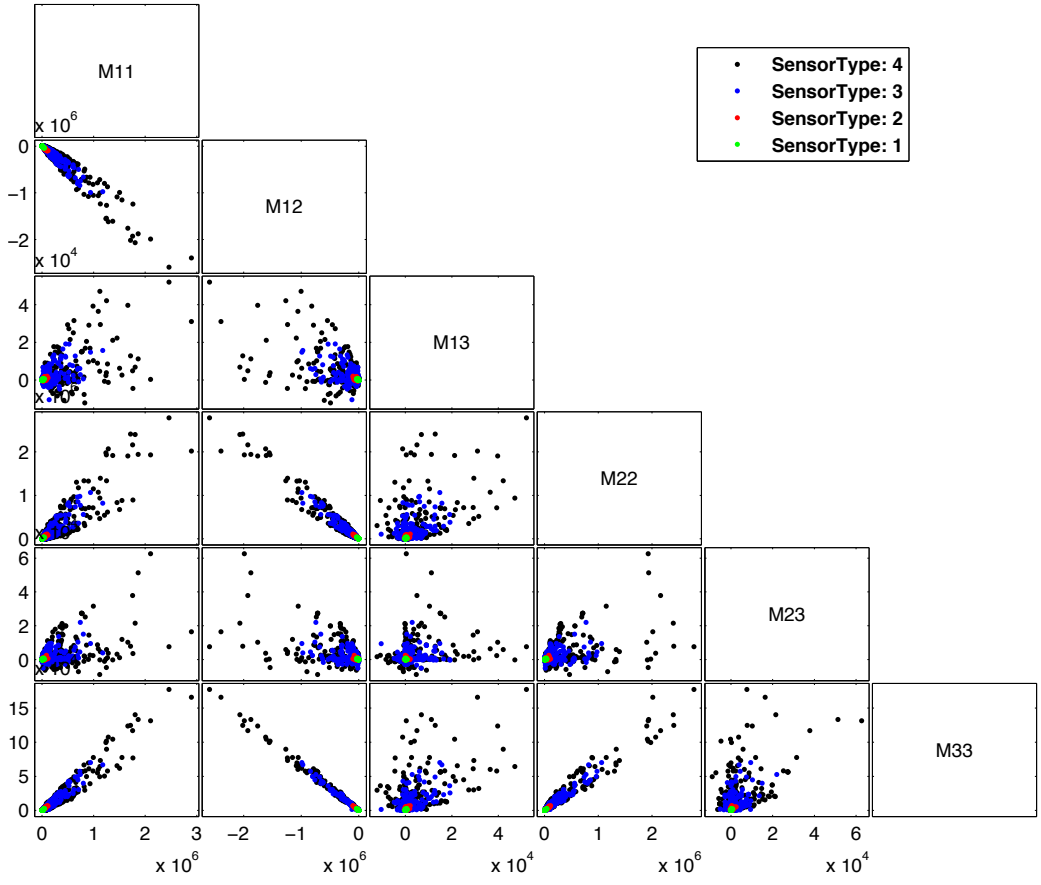

Figure 102: Multivariate scatter plot results for design of experiment results for lower-diagonal Fisher information matrix elements.

11.1.4 MDO of Robust-Optimal Dynamic Information Experiments

This section summarizes the design of robust-optimal dynamic system identification experiments for the spring-mass-damper system, from the perspective of the MDO problem formulation (shown in Equation (61) of Section 9.7) and the subsequent evaluation of design alternatives using Monte Carlo virtual experimentation, as discussed in the experimental procedure of Table 27. Here, the parametric integrated environment (PIE) simply refers to the collection and synthesis of the spring-mass-damper dynamic equations of motion from Section 10.3.2, the sensor models of Table 28 from Section 11.1.2, the parametric statistical uncertainty models of Table 18 from Section 10.3.2, and a parametric sinusoidal forcing function: $F(t) = \sin(2\pi f(t - T_{sw,0}))$.

The experiment design vector for these MDO problems is summarized below in Table 31, along with associated constraints on bounds. (Robust)-optimal information metrics were computed using VAEs with $N_e = 3$ for equivalent comparison between deterministic and nondeterministic robust design approaches, which include: (D,T,A,E)-Opt (nominal information metrics) and (E($\cdot$),R($\cdot$),SR-($\cdot$))-Opt robust-optimal information metrics. Global stochastic optimization was performed via differential evolution using the software package PyGMO, which easily accommodates mixed integer-type problems and seamlessly leverages computational resources for parallel computation. Implementation details can be found in Appendix D.

Table 31: Summary of the SMD mixed-integer experiment design vector $\boldsymbol{\varphi} = [\ x_0,\ v_0,\ f,\ T_{sw,0},\ T_{sp,0},$ SensorType] and associated bound-constraints.

Name	**Symbol**	**Bounds**	**Units**
Initial Position	x_0	[-1,1]	(m)
Initial Velocity	V_0	[-1,1]	(m/s)
Sinusoidal Forcing Frequency	f	[1,50]	(Hz)
Initial Sampling Time	$T_{sp,0}$	[0,10]	(sec)
Initial Excitation Time	$T_{sw,0}$	[0,10]	(sec)
Sensor Type	SensorType	$\{, 1, 2, 3, 4\}$	–

Table 32 summarizes all optimized designs for the spring-mass-damper problem under sinusoidal forcing. Each problem required 2-4 hrs of computation time, evaluating approximately 16,000 cases per problem. Although each design vector is different, there are some intuitive trends between the designs. First, each design utilized SensorType 4, for maximum sampling frequency and sampling accuracy. Secondly, both times $T_{sp,0}$ and $T_{sw,0}$ occur very early on in the experiments. Thirdly, with the exception of a few designs the initial conditions of the experiments are highly perturbed away from the system equilibrium point of (0,0). Finally, and perhaps most significantly, values of f are very nearly equal to the nominal natural and damping frequencies of the system of 37.172 (Hz) and 36.872 (Hz), respectively, for all designs. These observations imply that the high-performance experiments for SysID of (k,m,c) is maximized by: (i) taking high-quality measurements; (ii) sampling and exciting the system early in the experiment where initial perturbation is large; and (iii) exciting the system close to the expected resonance frequency of the system.

Table 32: Summary of all SMD robust-optimal experiment designs.

	Design Type	**Cost**	**Design Vector, X**					
			x_0	v_0	f	$T_{sw,0}$	$T_{sp,0}$	SensorType
Nominal Metrics	**D-Opt**	1.70E-16	0.89	0.13	38.33	0.30	0.95	4
	T-Opt	-7.39E+06	0.99	0.89	36.70	0.03	1.76	4
	A-Opt	3.99E-15	1.00	-0.87	36.76	0.55	0.93	4
	E-Opt	2.00E-05	-1.00	-0.86	36.32	0.04	0.57	4
Bayesian Metrics	**ED-Opt**	4.47E-15	-1.00	0.82	33.32	0.24	0.63	4
	ET-Opt	–	–	–	–	–	–	–
	EA-Opt	1.42E-03	-0.23	0.55	37.83	3.81	3.01	4
	EE-Opt	3.42E-05	-0.73	-0.29	33.25	3.74	1.83	4
Min-max Metrics	**RD-Opt**	1.43E-14	-0.95	-0.22	34.25	0.18	0.69	4
	RT-Opt	–	–	–	–	–	–	–
	RA-Opt	1.48E-03	0.75	-0.39	36.89	2.17	1.09	4
	RE-Opt	2.33E-05	-0.88	-0.80	36.31	0.03	0.32	4
Sensitivity-Robustness Metrics ($\beta = 0.5$)	**SR-D-Opt**	8.19E-17	-0.94	-0.92	34.67	0.31	0.24	4
	SR-T-Opt	–	–	–	–	–	–	–
	SR-A-Opt	2.00E-05	1.00	-0.49	36.77	0.55	0.98	4
	SR-E-Opt	1.10E-05	0.99	–0.70	36.33	0.53	0.98	4

To address **Hyp. #3**, the alternative (robust)-optimal experiment designs of Table 32 are evaluated for information performance and robustness by using the experimental procedure outlined in Table 27. To execution of this procedure implies a series of 1000-case Monte Carlo studies for each design under consideration, which were generated by sampling the uniform parameter perturbation distributions outlined previously in Table 18 of Section 10.3. For a fixed random seed, the Monte Carlo cases are identical so as to isolate the performance of the different designs. Four comparative analyses were conducted, described below:

- **Analysis#1** (*Comparison of Nominal Optimal Experiment Designs*) – Dynamic simulation and pre/post-experiment estimator performance is shown for a single virtual experiment, providing a detailed look into how each experiment design excites the spring-mass-damper system and how the data information content of each experiment affects the parameter estimation accuracy. For each Monte Carlo case, all four nominal information metrics (D-Opt, T-Opt, A-Opt, E-Opt) are computed for intended comparison amongst each of the experiment designs (D-Opt, T-Opt, A-Opt, E-Opt) for on/off-design conditions. Statistical results are presented in both graphical and tabular form to investigate if each information metric yields the intuitive geometrical results, according to the discussion from Section 5.3.4, specifically in reference to Figure 31.

- **Analysis#2** (*Comparison of D-Optimality Robust-Optimal Experiment Designs*) – Here pre/post-experiment estimator performances are shown for the identical virtual experiment of **Analysis#1**, again providing a detailed look into how each experiment design affects the parameter estimation accuracy. For each Monte Carlo case, all four nominal information metrics (D-Opt, T-Opt, A-Opt, E-Opt) are computed for intended comparison amongst each of the experiment designs (D-Opt, ED-Opt, RD-Opt, SR-D-Opt) for on/off-design conditions. Statistical results are presented in both graphical and tabular form to

determine if robust-optimal experiment designs are in fact robust with respect to parameter uncertainties.

- **Analysis#3** (*Comparison of A-Optimality Robust-Optimal Experiment Designs*) – For each Monte Carlo case, all four nominal information metrics (D-Opt, T-Opt, A-Opt, E-Opt) are computed for intended comparison amongst each of the experiment designs (A-Opt, EA-Opt (*i.e.* Bayesian/Expected-value), RA-Opt (*i.e.* minimax/worst-case scenario), SR-A-Opt) for both on/off-design conditions. Statistical results are presented in both graphical and tabular form to investigate of robust-optimal experiment designs are in fact robust with respect to parameter uncertainties.

- **Analysis#4** (*Comparison of E-Optimality Robust-Optimal Experiment Designs*) – For each Monte Carlo case, all four nominal information metrics (D-Opt, T-Opt, A-Opt, E-Opt) are computed for intended comparison amongst each of the experiment designs (E-Opt, EE-Opt, RE-Opt, SR-E-Opt) for on/off-design conditions. Statistical results are presented in both graphical and tabular form to investigate of robust-optimal experiment designs are in fact robust with respect to parameter uncertainties.

11.1.4.1 Comparison of D,T,A,E-Opt (Nominal) Designs.

Figures 103, 104, and 105 show simulation results of nominal (D,T,A,E)-Optimal experiment designs from Table 32, including baseline experiment design (solid blue), parameter uncertainty analysis of state trajectories (solid grey), virtual experiment simulation (dashed black), and sampled input/output data (red dots), for the inputs signals, state trajectories, and output (experiment window), respectively. As seen, all input signals are very similar, differing only slightly in starting actuation time, $T_{sw,0}$. The state/output responses for the (A,E)-optimal experiments are very similar, where a cancelling effect in displacement amplitude is observed between $t = 1$ (sec) and $t = 4$ (sec) followed by a growth in amplitude of the virtual experiment but not the designed (nominal) experiment.

As discussed in Section 11.1.2, computation of the sampled Fisher information matrix of Equation (8) of Section 5.2 can be used to visualize the limiting parameter estimator performances, using both *a priori* and *a posteriori* parameter sets. Tables 33 and 34 show best estimator performances for (D,T,A,E)-optimal experiment designs using the two sets of parameter values Table 29 for *a priori* and *a posteriori* cases, respectively, and Figures 106a and 106b show the 3D 95% confidence ellipse for both the *a priori* and *a posteriori* cases as multivariate 2D planar projections, respectively. In these results, it can be observed that the T-Opt experiment design has the lowest performance in terms of estimation accuracy for both *a priori* and *a posteriori* cases, with a percent error which is approximately 400% higher when compared to the other designs. As observed in the simulated virtual experiments, both the (A,E)-Opt designs show very similar estimation performances. Comparison of the correlation matrices for these two designs in both *a priori* and *a posteriori* cases reveals that the correlation terms involving damping coefficient c are nearly twice as small than the same terms for the D-Opt design; however, the confidence interval for the D-Opt design is smaller then the (A,E)-Opt designs.

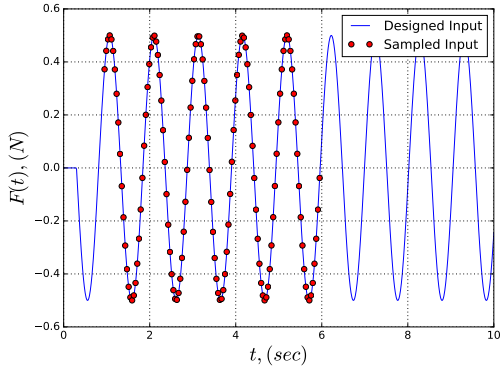

(a) D-Optimal Design.

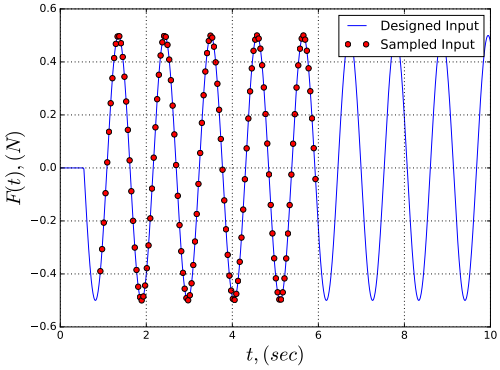

(b) T-Optimal Design.

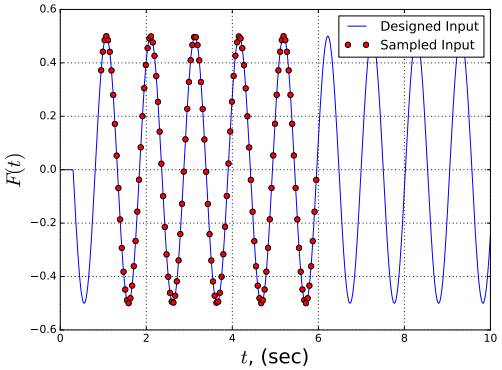

(c) A-Optimal Design.

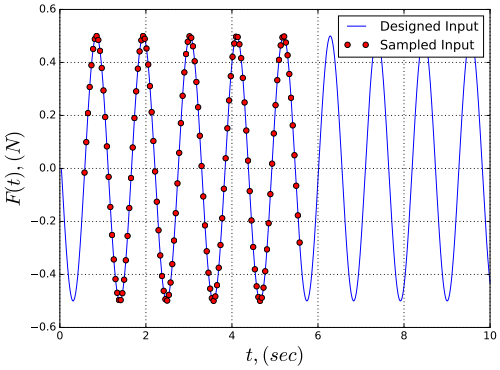

(d) E-Optimal Design.

Figure 103: Simulation results for designed input signals (blue) and sampled data (red dots) for (D,T,A,E)-Optimal nominal information experiment designs.

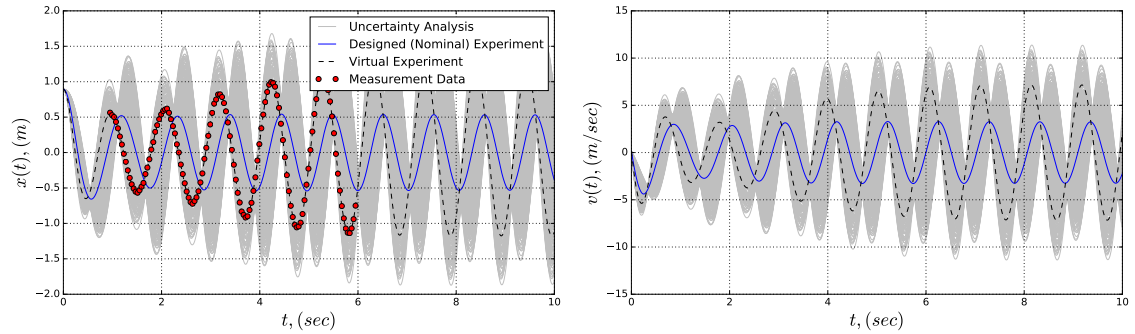

(a) D-Optimal Design.

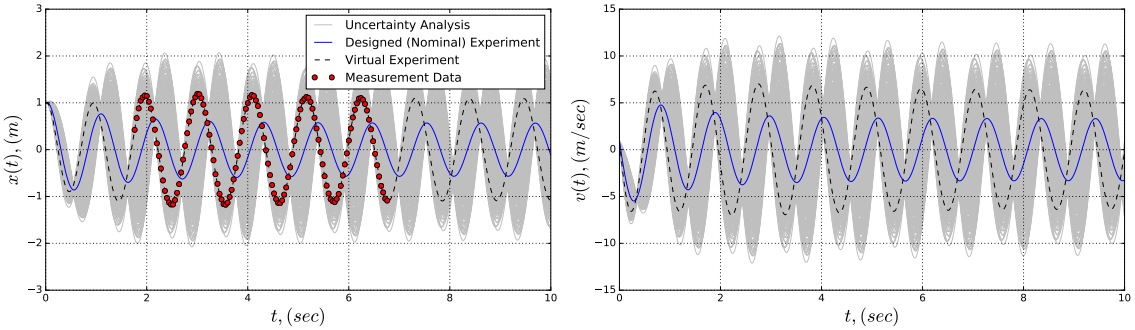

(b) T-Optimal Design.

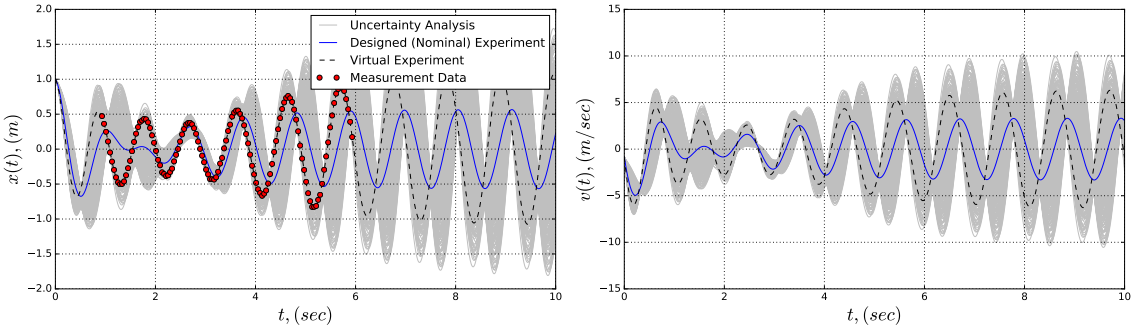

(c) A-Optimal Design.

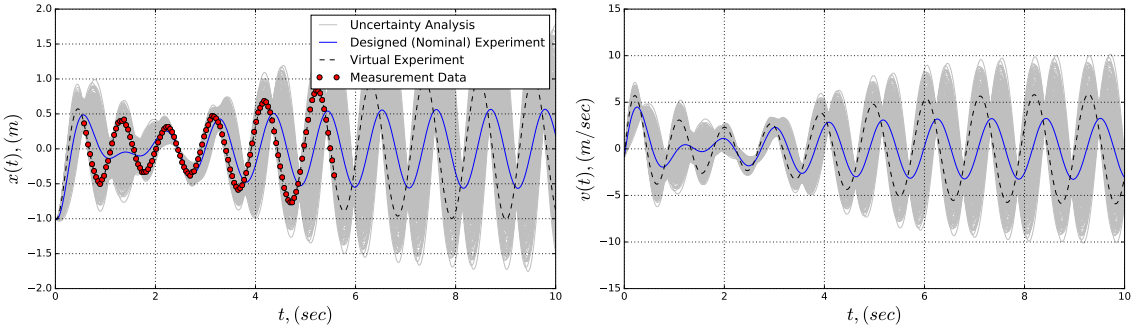

(d) E-Optimal Design.

Figure 104: Simulation results for designed (baseline) state history (blue), parametric uncertainty trajectories (grey), virtual (perturbed) experiment (dashed black), and sampled data (red dots) for (D,T,A,E)-Optimal nominal information experiment designs.

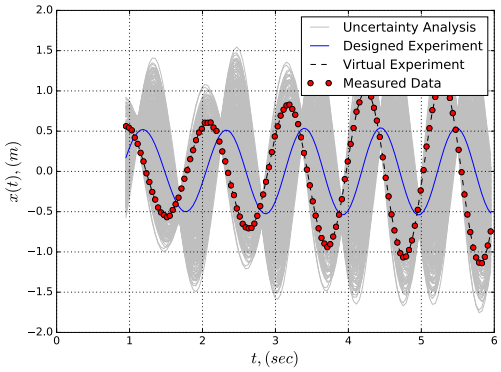

(a) D-Optimal Design.

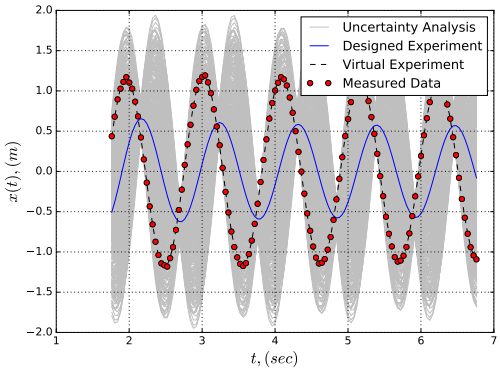

(b) T-Optimal Design.

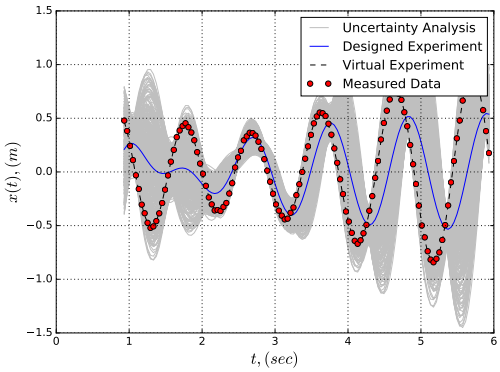

(c) A-Optimal Design

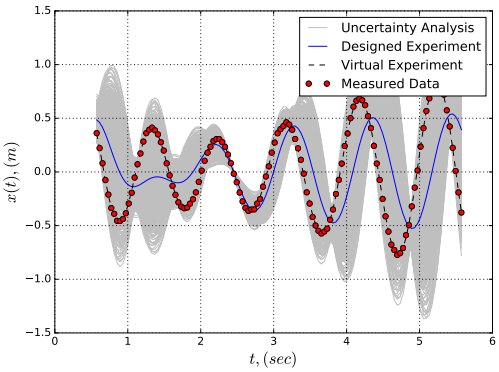

(d) E-Optimal Design

Figure 105: Simulation results for designed (baseline) output history (blue), parametric uncertainty outputs (grey), virtual (perturbed) experiment (dashed black), and sampled data (red dots) for (D,T,A,E)-Optimal nominal information experiment designs.

Table 33: *A priori* best estimator performance comparison for (D,T,A,E)-Opt dynamic experiment designs.

Design Type	**Parameters**		**Standard Error**	**Percent Error**	**95% C.I.**	**Correlation Matrix**		
	Symbol	Value				k	m	c
D-Opt	k	3.50	0.023	0.663	[3.454 , 3.546]	1.0		
	m	0.10	0.001	0.710	[0.990 , 0.101]	0.995	1.0	
	c	0.15	0.000	0.283	[0.149 , 0.151]	0.222	0.218	1.0
T-Opt	k	3.50	0.103	2.932	[3.295 , 3.705]	1.0		
	m	0.10	0.003	2.991	[0.094 , 0.106]	1.000	1.0	
	c	0.15	0.001	0.405	[0.149 , 0.151]	0.848	0.848	1.0
A-Opt	k	3.50	0.011	0.328	[3.477 , 3.523]	1.0		
	m	0.10	0.000	0.330	[0.099 , 0.101]	0.939	1.0	
	c	0.15	0.001	0.427	[0.149 , 0.151]	0.075	0.056	1.0
E-Opt	k	3.50	0.011	0.315	[3.478 , 3.522]	1.0		
	m	0.10	0.000	0.327	[0.099 , 0.101]	0.930	1.0	
	c	0.15	0.001	0.458	[0.149 , 0.151]	0.008	0.008	1.0

Table 34: *A posteriori* best estimator performance comparison for (D,T,A,E)-Opt dynamic experiment designs.

Design Type	**Parameters**		**Standard Error**	**Percent Error**	**95% C.I.**	**Correlation Matrix**		
	Symbol	Value				k	m	c
D-Opt	k	3.32	0.024	0.687	[3.452 , 3.548]	1.0		
	m	0.08	0.001	0.713	[0.990 , 0.101]	0.989	1.0	
	c	0.17	0.001	0.397	[0.149 , 0.151]	0.154	0.151	1.0
T-Opt	k	3.32	0.070	1.995	[3.360 , 3.640]	1.0		
	m	0.08	0.002	2.015	[0.096 , 0.104]	0.999	1.0	
	c	0.17	0.001	0.481	[0.149 , 0.151]	0.727	0.726	1.0
A-Opt	k	3.32	0.015	0.418	[3.471 , 3.529]	1.0		
	m	0.08	0.000	0.377	[0.099 , 0.101]	0.952	1.0	
	c	0.17	0.001	0.460	[0.149 , 0.151]	0.088	0.094	1.0
E-Opt	k	3.32	0.014	0.387	[3.473 , 3.527]	1.0		
	m	0.08	0.000	0.357	[0.099 , 0.101]	0.943	1.0	
	c	0.17	0.001	0.505	[0.148 , 0.152]	0.073	0.077	1.0

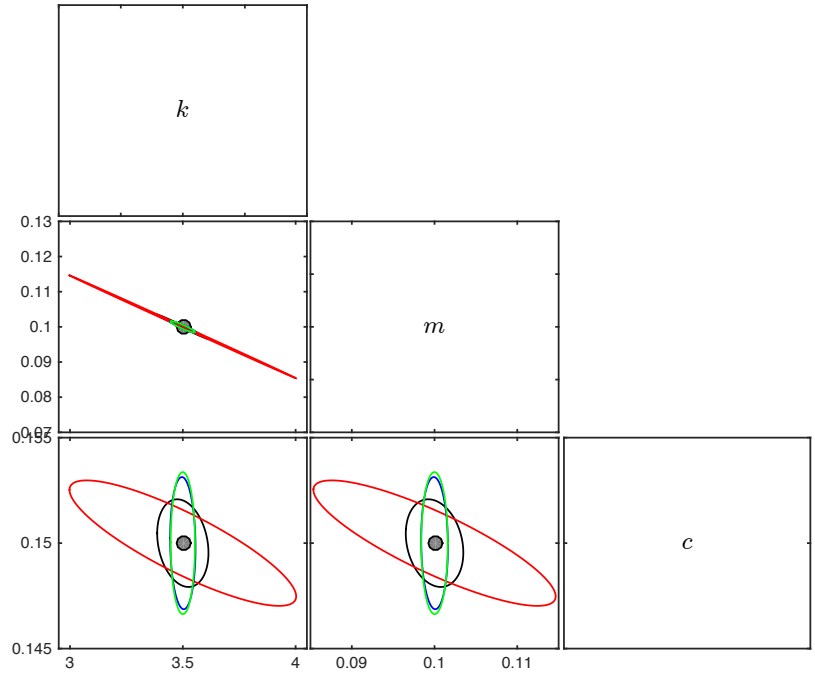

(a) *A priori* Estimator Performance.

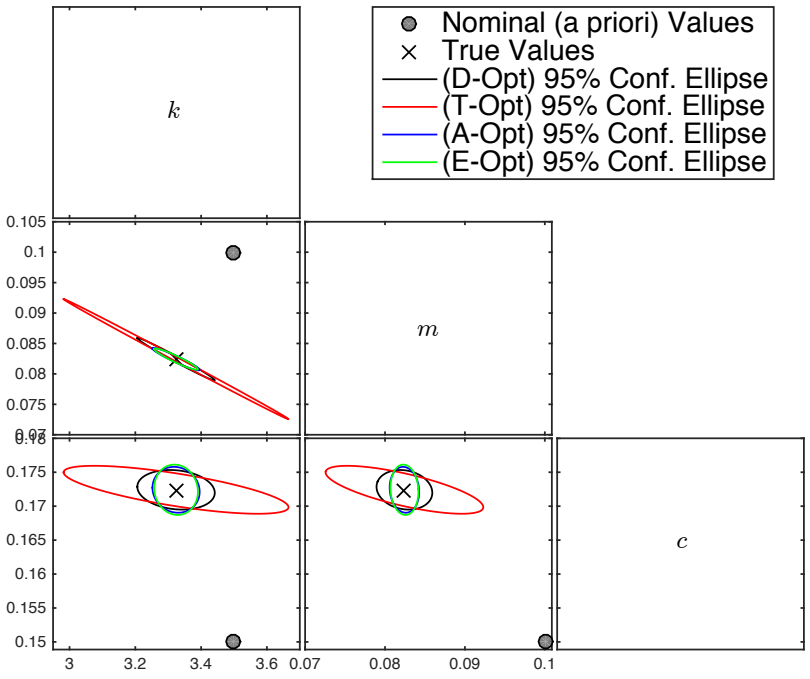

(b) *A posteriori* Estimator Performance

Figure 106: Comparison of limiting output-error estimator performances for the four nominal information metrics experiment designs.

Figure 107 and Table 35 show statistical results of the 1000-case Monte Carlo virtual experimentation analysis. Each subplot represents the statistical histogram of an information metric and the nominal (baseline) design metric (red line) for a given design (shown above each subplot). Each row of subplots represents all the statistical information distributions (D,T,A,E)-Opt for a single design, allowing for a row-wise comparison of the four designs across a single metric.

In the far left column, the (D,T,A,E)-Opt experiment designs are all compared with respect to D-Optimality. As can be seen the D-Opt design has the lowest baseline value (shown in Table 32); however, the statistical measures for the distributions of each design show that the E,A-Opt experiment designs poses superior robust-optimality in regards to D-Optimality, where statistical means for these designs are comparable to the D-Opt design, but the variances are approximately three times as small. While the D-Opt design does potentially produce an inferior information experiment with respect to the (A,E)-Opt designs, there is also a strong possibility that the D-Opt design can produce a vastly superior information experiment as the D-Opt VX distribution is skewed towards more information dense experiments and has a best-case scenario which is superior to all other designs. Note that the T-Opt experiment design is an inferior design, both, with respect to the nominal value in red (optimality) and the statistical measures (robustness).

In the middle left column, the (D,T,A,E)-Opt experiment designs are all compared with respect to the T-Opt information metric. Here, the T-Opt experiment design does poses the lowest nominal (design) value, due to the fact that this design was optimized with respect to this metric; however, this distribution has the largest variance when compared to the other designs. Again, the (A,E)-Opt designs are statistically similar and have the smallest variances. Thus, with respect to T-Optimality, the T-Opt design possess the least amount of information quality robustness, potentially

yielding a result which could be far superior/inferior than the equivalent virtual experiment with (A,E)-Opt designs, depending on which end of the T-Opt VX distribution that the VX sample falls in.

The middle and far right columns of Figure 107 show nearly identical row-wise statistical results when comparing all experiment designs in terms of (A,E)-Optimality. Here the T-Opt design is inferior to all other designs, both in terms of optimality and robustness, while the inverse is true for both the (A,E)-Opt designs. The D-Opt design possess similar robustness (in terms of statistical variance) with respect to the (A,E)-Opt designs, and while the optimality of the D-Opt is inferior with respect to the other two designs, there is a nearly 50% chance that the D-Opt design will yield better information quality than the anticipated (designed) value, as this value is nearly identical to the mean value of the VX distribution and is observed to be nearly symmetric. Both the (A,E)-Opt designs have VX distributions that are skewed towards inferior information quality, having a higher chance of producing results with information quality that is slightly less than what was designed for. Even so, comparison between the D-Opt design VX distribution with the (A,E)-Opt design VX distributions show that there is very little overlap between the best-case D-Opt and worst-case (A,E)-Opt results, and thus, while (D,A,E)-Opt designs have similar robustness with respect to (A,E)-Optimality, the (A,E)-Opt designs possess statistically superior performance.

To summarize, the (A,E)-Opt designs are the best all-around performing designs in terms of robust-optimality, where the smallest variances are observed across all VX distributions of information metrics. While each experiment design possess superior optimality with respect to the information metric that was used for optimization, both the (D,T)-Opt designs do not possess good statistical robustness large relative variances in VX distributions. The T-Opt design is the most inferior design of the four considered here, where a row-wise comparison with respect to any information

metric (column) shows inferior robust-optimality for all information metrics.

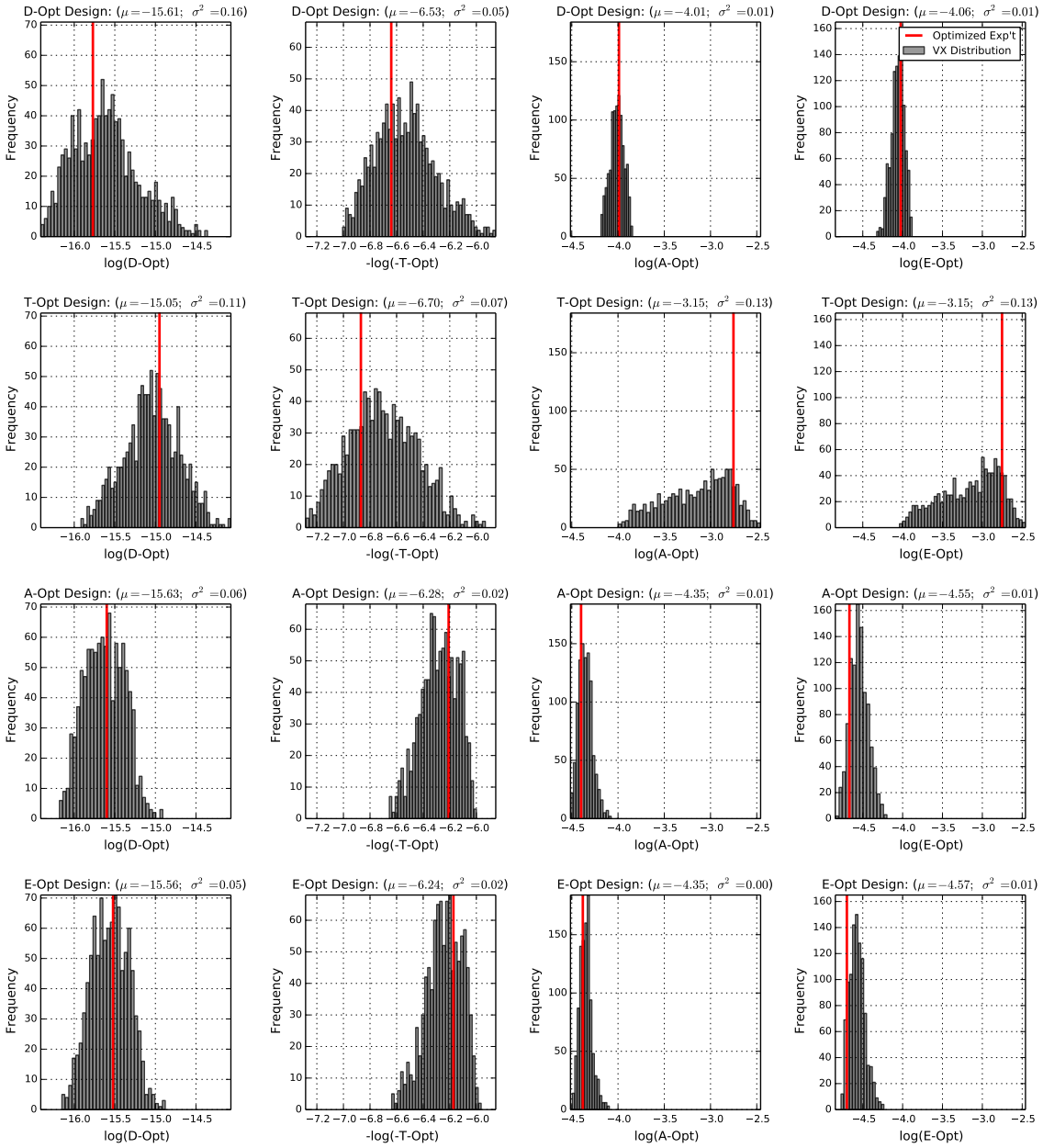

Figure 107: Comparison of distributions of (D,T,A,E)-Optimal experiment designs using uniform parameters distributions of Monte Carlo of 1000 virtual experiments according to Table 35. Horizontal rows represent a single optimal experiment design, vertical columns represent a single nominal performance metric, and red lines represent the anticipated *a priori* performance (statically optimized) values.

Table 35: Nominal experiment designs Monte Carlo distribution statistical measures.

Designs	Metrics	Statistical Measures				
		mean	**var.**	**med.**	**min.**	**max.**
log(D-Opt)	log(D-Opt)	-15.61	0.16	-15.64	-16.41	-14.35
	− log(−T-Opt)	-15.05	0.11	-15.05	-15.92	-14.07
	log(A-Opt)	-15.63	0.06	-15.63	-16.19	-14.91
	log(E-Opt)	-15.56	0.05	-15.56	-16.16	-14.87
− log(−T-Opt)	log(D-Opt)	-6.53	0.05	-6.54	-7.01	-5.85
	− log(−T-Opt)	-6.70	0.07	-6.72	-7.28	-5.93
	log(A-Opt)	-6.28	0.02	-6.28	-6.66	-6.00
	log(E-Opt)	-6.24	0.02	-6.24	-6.64	-5.96
log(A-Opt)	log(D-Opt)	-4.01	0.01	-4.01	-4.19	-3.84
	− log(−T-Opt)	-3.15	0.13	-3.09	-4.00	-2.46
	log(A-Opt)	-4.35	0.01	-4.36	-4.51	-4.07
	log(E-Opt)	-4.35	0.00	-4.35	-4.50	-4.09
log(E-Opt)	log(D-Opt)	-4.06	0.01	-4.06	-4.33	-3.88
	− log(−T-Opt)	-3.15	0.13	-3.09	-4.04	-2.46
	log(A-Opt)	-4.55	0.01	-4.55	-4.84	-4.19
	log(E-Opt)	-4.57	0.01	-4.57	-4.78	-4.23

11.1.4.2 Comparison of D-Optimality Robust-Optimal Experiment Designs.

This section presents the comparative results for the D-Optimality robust-optimal information metrics, first for a single virtual experiment and then for the Monte Carlo analysis of virtual experiments. Table 36 and 37 show best estimator performances for (D,ED,RD,SR-D)-Opt experiment designs using the two sets of parameter values Table 29 for *a priori* and *a posteriori* cases, respectively, and Figures 108a and 108b show the 3D 95% confidence ellipse for both the *a priori* and *a posteriori* cases as multivariate 2D planar projections, respectively. In these results, it is be observed that all designs have very similar estimator performance characteristics. The *a posteriori* 95% confidence ellipses for the robust-optimal designs (ED,RD,SR-D)-Opt are nearly identical in geometric shape, with a marginal improvement with respect to the nominal D-Opt design. All *a priori* and *a posteriori* percent errors are less than 1% for all designs. Comparison of the correlation matrix off-diagonal terms for all designs for both *a priori* and *a posteriori* cases show that only the correlation between k and m estimation is larger and all other terms are relatively low.

Figure 109 and Table 38 show the statistical results of the 1000-case Monte Carlo virtual experimentation analysis for (D,ED,RD,SR-D)-Opt experiment designs. Each subplot represents the statistical histogram of an information metric and the nominal (baseline) design metric (red line) for a given design (shown above each subplot). Each row of subplots represents all the statistical information distributions (D,T,A,E)-Opt for a single design, allowing for a row-wise comparison of the four designs across a single metric. For this study, the effect of all designs is to manipulate the D-Optimality VX distributions (*i.e.* the left-most column). The top row again presents the Monte Carlo VX results previously shown; however, the x-axis of all plots have been rescaled for common relative comparison.

The ED-Opt design of the second row shows that the D-Optimality VX distribution has a mean that is equal to the *a priori* anticipated design value. This is

intuitive for this design, where ED-Optimality (*i.e.* Bayesian expectation) implies that the expectation or mean value of the information matrix determinant was minimized, and therefore, the VX distribution confirms was approximated using 3^{rd}-order VAE's during optimization. The implications of this experiment design are that, while the expected experimental outcome has been designed to be minimized, this experiment design is more conservative.

The RD-Opt experiment design has a slightly less *a priori* anticipated D-Optimality than the D-Opt design; however, the variance of the RD-Opt D-Optimality VX distribution is nearly three times smaller than the D-Opt design, implying three times greater robustness. While robustness has been improved, this result is not entirely intuitive, in that, the *a priori* anticipated information quality was expected to be a lesser and more conservative value, since this design represents a minimax design (*e.g.* worst-case scenario). This result does however agree with the results of Asprey and Macchietto [18], where D,ED,RD-Opt designs were conducted on a simple 2-state, 4-parameter batch-fed bioreactor problem.

The SR-D-Opt design of the fourth row posses *a priori* anticipated information quality that is very similar to the nominal D-Opt design, and marginal improvements to robustness. Relative to the D-Opt design, the worst-case D-Optimality scenario of the SR-D-Opt has been improved to a relatively similar value of the RD-Opt design. The best-case D-Optimality, however, is superior to the other designs, which suggests that the SR-D-Opt design has the best statistical up-side. For A,E-Optimality the RD-Opt design shows superior robust-optimality, while the SR-D-Opt design again shows marginal improvement.

To summarize, the D-Optimality robust-optimization designs were observed to contribute towards increasing robustness of the D-Opt dynamic experiment. For this problem, (RD,SR-D)-Opt designs provided comparable optimality relative to the D-Opt design, while providing increased robustness with respect to information quality.

Table 36: *a priori* best estimator performance comparison for (D,ED,RD,SR-D)-Opt exp't designs.

Design Type	Parameters		Standard Error	Percent Error	95% C.I.	Correlation Matrix		
	Symbol	Value				k	m	c
D-Opt	k	3.50	0.023	0.663	[3.454 , 3.546]	1.0		
	m	0.10	0.001	0.710	[0.990 , 0.101]	0.995	1.0	
	c	0.15	0.000	0.283	[0.149 , 0.151]	0.222	0.218	1.0
ED-Opt	k	3.50	0.019	0.552	[3.461 , 3.539]	1.0		
	m	0.10	0.001	0.561	[0.099 , 0.101]	0.992	1.0	
	c	0.15	0.000	0.293	[0.149 , 0.151]	0.328	0.327	1.0
RD-Opt	k	3.50	0.017	0.494	[3.456 , 3.544]	1.0		
	m	0.10	0.000	0.479	[0.099 , 0.101]	0.987	1.0	
	c	0.15	0.000	0.318	[0.149 , 0.151]	0.133	0.124	1.0
SR-D-Opt	k	3.50	0.022	0.663	[3.456 , 3.544]	1.0		
	m	0.10	0.001	0.710	[0.099 , 0.101]	0.993	1.0	
	c	0.15	0.000	0.283	[0.149 , 0.151]	0.347	0.339	1.0

Table 37: *a posteriori* best estimator performance comparison for (D,ED,RD,SR-D)-Opt exp't designs.

Design Type	Parameters		Standard Error	Percent Error	95% C.I.	Correlation Matrix		
	Symbol	Value				k	m	c
D-Opt	k	3.32	0.024	0.687	[3.452 , 3.548]	1.0		
	m	0.08	0.001	0.713	[0.990 , 0.101]	0.989	1.0	
	c	0.17	0.001	0.397	[0.149 , 0.151]	0.154	0.151	1.0
ED-Opt	k	3.32	0.019	0.536	[3.462 , 3.538]	1.0		
	m	0.08	0.001	0.516	[0.099 , 0.101]	0.982	1.0	
	c	0.17	0.001	0.435	[0.149 , 0.151]	0.418	0.412	1.0
RD-Opt	k	3.32	0.018	0.523	[3.463 , 3.537]	1.0		
	m	0.08	0.000	0.486	[0.099 , 0.101]	0.978	1.0	
	c	0.17	0.001	0.424	[0.149 , 0.151]	0.277	0.267	1.0
SR-D-Opt	k	3.32	0.022	0.687	[3.458 , 3.542]	1.0		
	m	0.08	0.001	0.713	[0.099 , 0.101]	0.986	1.0	
	c	0.17	0.000	0.397	[0.148 , 0.152]	0.459	0.449	1.0

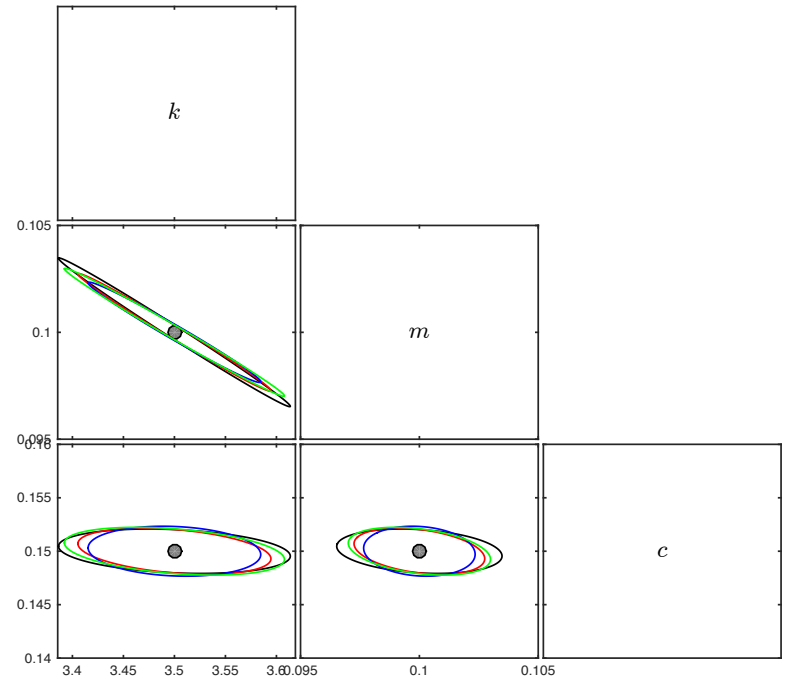

(a) *a priori* Estimator Performance.

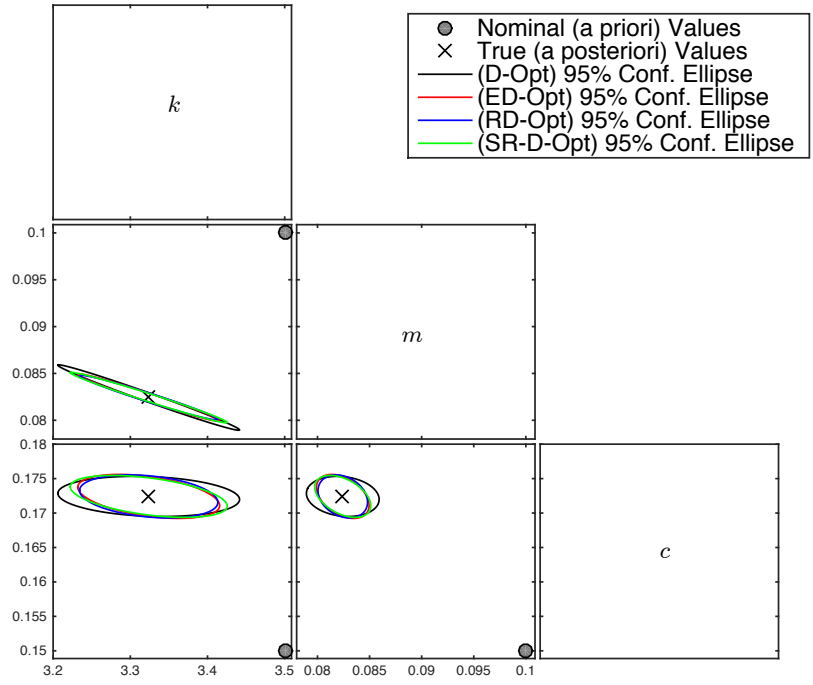

(b) *a posteriori* Estimator Performance

Figure 108: Comparison of limiting output-error estimator performances for the four robust D-optimal experiments designs.

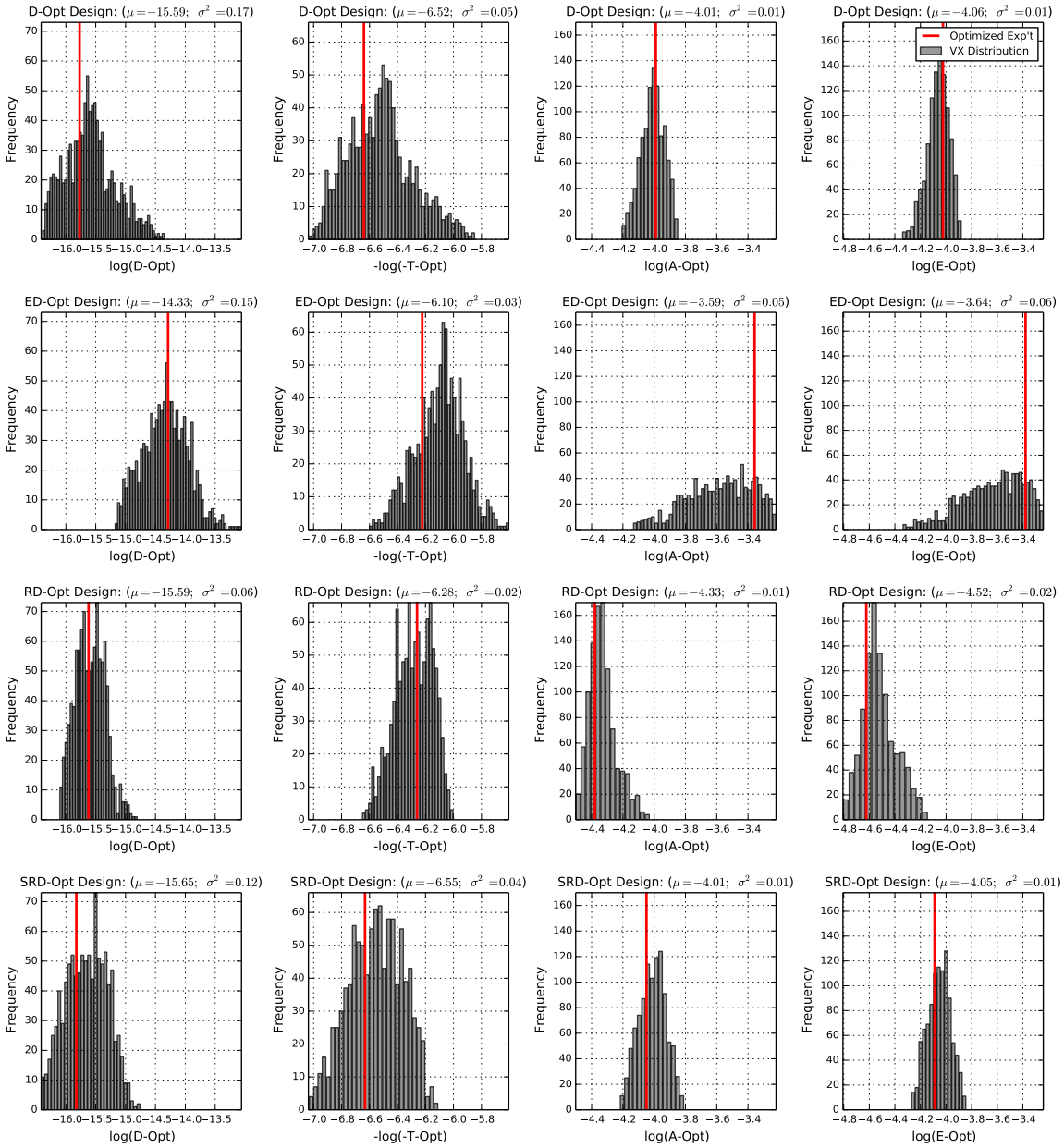

Figure 109: Comparison of distributions of information metrics for (D,ED,RD,SRD)-Opt experiment designs using uniform parameters distributions of Monte Carlo of 1000 virtual experiments according to Table 38. Horizontal rows represent a single optimal experiment design, vertical columns represent a single nominal performance metric, and red lines represent the anticipated *a priori* performance (statically optimized) values.

Table 38: D-Optimality robust-optimal experiment design comparisons Monte Carlo distribution statistical measures.

Designs	Metrics	Statistical Measures				
		mean	**var.**	**med.**	**min.**	**max.**
log(D-Opt)	log(D-Opt)	-15.59	0.17	-15.62	-16.39	-14.35
	log(ED-Opt)	-14.33	0.15	-14.33	-15.18	-13.06
	log(RD-Opt)	-15.59	0.06	-15.60	-16.10	-14.80
	log(SR-D-Opt)	-15.65	0.12	-15.64	-16.41	-14.76
$-\log(-$T-Opt)	log(D-Opt)	-6.52	0.05	-6.53	-7.04	-5.85
	log(ED-Opt)	-6.10	0.03	-6.09	-6.60	-5.60
	log(RD-Opt)	6.28	0.02	-6.28	-6.65	-6.00
	log(SR-D-Opt)	-6.55	0.04	-6.55	-7.03	-6.11
log(A-Opt)	log(D-Opt)	-4.01	0.01	-4.01	-4.21	-3.85
	log(ED-Opt)	-3.59	0.05	-3.57	-4.13	-3.22
	log(RD-Opt)	-4.33	0.01	-4.34	-4.50	-4.03
	log(SR-D-Opt)	-4.01	0.01	-4.01	-4.22	-3.81
log(E-Opt)	log(D-Opt)	-4.06	0.01	-4.06	-4.34	-3.88
	log(ED-Opt)	-3.64	0.06	-3.61	-4.34	-3.24
	log(RD-Opt)	-4.52	0.02	-4.54	-4.81	-4.14
	log(SR-D-Opt)	-4.05	0.01	-4.05	-4.27	-3.84

11.1.4.3 Comparison of A-Optimality Robust-Optimal Experiment Designs.

This section presents the comparative results for the A-Optimality robust-optimal experiment designs of Table 32 for the 1000-case Monte Carlo analysis of virtual experiments, outlined in Table 27. Figure 110 and Table 39 show the statistical results of the 1000-case Monte Carlo VX analysis for (A,EA,RA,SR-A)-Opt experiment designs. Each subplot represents the statistical histogram of an information metric and the nominal (baseline) design metric (red line) for a given design (shown above each subplot). Each row of subplots represents all the statistical information distributions (D,T,A,E)-Opt for a single design, allowing for a row-wise comparison of the four designs across a single metric. For this study, the effect of all designs is to manipulate the A-Optimality VX distributions (*i.e.* the middle right column). The top row again presents the Monte Carlo VX results previously shown; however, the x-axis of all plots have been rescaled for common relative comparison.

Similar to the results of the previous study on D-Optimality, the EA-Opt experiment design does accurately predict the expected A-Optimality information measure, and again, the experiment design is significantly more conservative than the nominal A-Opt design. The EA-Opt VX distribution is skewed towards improved performance.

In contrast to the results of the previous study on D-Optimality, the RA-Opt experiment design provides for a significantly more conservative *a priori* experiment than the nominal design; however, the VX distribution suggests that better information quality in regards to the anticipated result is statistically expected.

Finally, the SR-A-Opt experiment design is observed to be statistically identical to the nominal A-Opt design. This observation suggests that the A-Opt design does possess robustness to the variance in predicted A-Optimality.

To summarize, the (A,SR-A)-Opt designs yield statistically identical results in terms of expected information quality, while the (EA,RA)-Opt designs offer relatively conservative approaches.

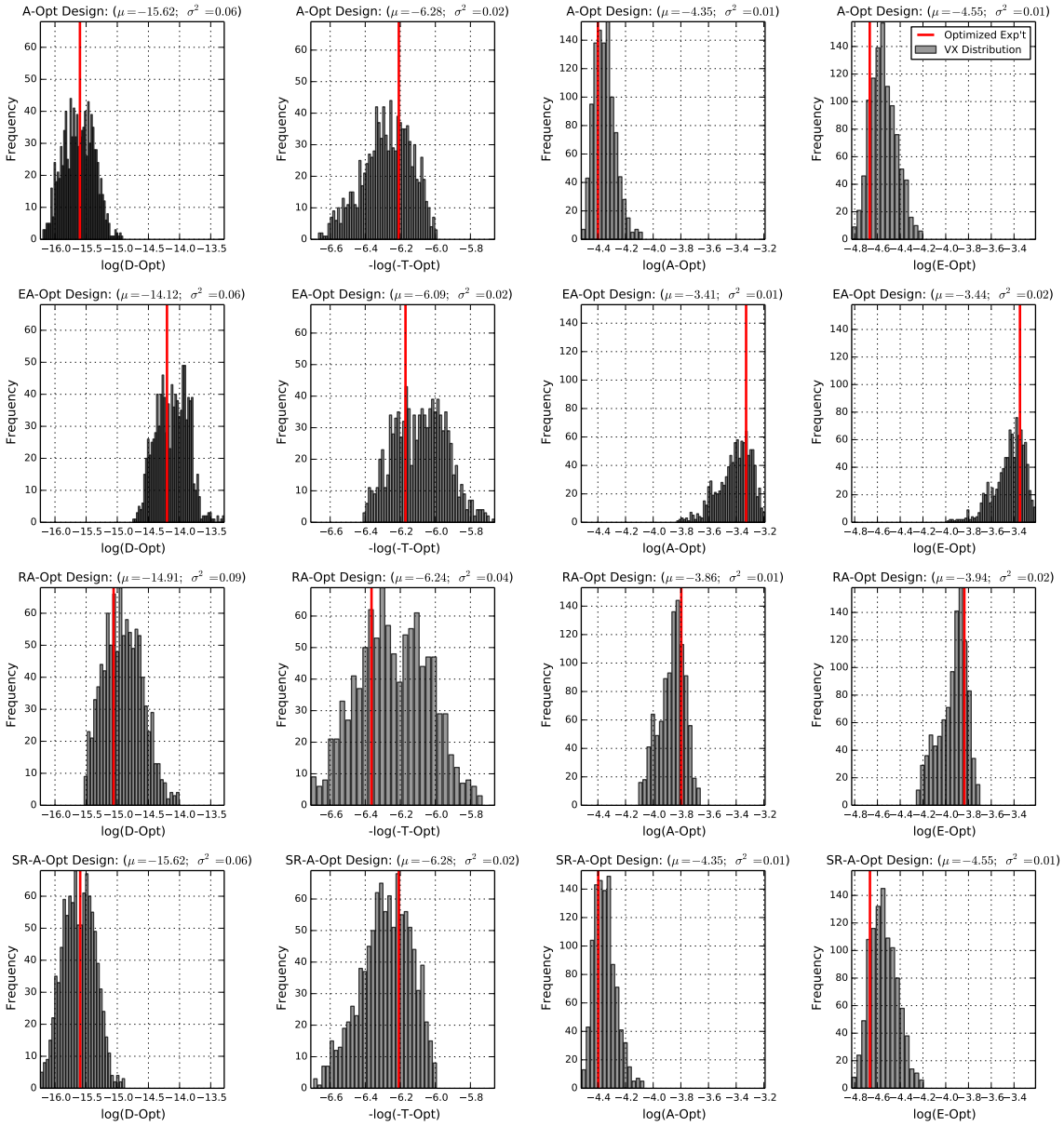

Figure 110: Comparison of distributions of nominal and robust-optimal (A,EA,RA,SR-A)-Opt experiment designs using uniform parameters distributions of Monte Carlo of 1000 virtual experiments according to Table 39. Horizontal rows represent a single optimal experiment design, vertical columns represent a single nominal performance metric, and red lines represent the anticipated *a priori* performance (statically optimized) values.

Table 39: A-Optimality robust-optimal experiment design comparisons Monte Carlo distribution statistical measures.

Designs	Metrics	Statistical Measures				
		mean	**var.**	**med.**	**min.**	**max.**
log(D-Opt)	log(A-Opt)	-15.62	0.06	-15.62	-16.20	-14.91
	log(EA-Opt)	-14.12	0.06	-14.11	-14.75	-13.28
	log(RA-Opt)	-14.91	0.09	-14.92	-15.54	-14.00
	log(SR-A-Opt)	-15.62	0.06	-15.62	-16.23	-14.88
$-\log(-$T-Opt)	log(A-Opt)	-6.28	0.02	-6.27	-6.67	-5.99
	log(EA-Opt)	-6.09	0.02	-6.08	-6.41	-5.66
	log(RA-Opt)	-6.24	0.04	-6.25	-6.71	-5.73
	log(SR-A-Opt)	-6.28	0.02	-6.27	-6.70	-5.99
log(A-Opt)	log(A-Opt)	-4.35	0.01	-4.36	-4.52	-4.08
	log(EA-Opt)	-3.41	0.01	-3.39	-3.83	-3.19
	log(RA-Opt)	-3.86	0.01	-3.85	-4.11	-3.66
	log(SR-A-Opt)	-4.35	0.01	-4.35	-4.52	-4.06
log(E-Opt)	log(A-Opt)	-4.55	0.01	-4.55	-4.82	-4.20
	log(EA-Opt)	-3.44	0.02	-3.42	-3.99	-3.21
	log(RA-Opt)	-3.94	0.02	-3.91	-4.26	-3.70
	log(SR-A-Opt)	-4.55	0.01	-4.56	-4.83	-4.19

11.1.4.4 Comparison of E-Optimality Robust-Optimal Experiment Designs.

This section presents the comparative results for the E-Optimality robust-optimal experiment designs of Table 32 for the 1000-case Monte Carlo analysis of virtual experiments, outlined in Table 27. Figure 111 and Table 40 show the statistical results of the 1000-case Monte Carlo VX analysis for (E,EE,RE,SR-E)-Opt experiment designs. Each subplot represents the statistical histogram of an information metric and the nominal (baseline) design metric (red line) for a given design (shown above each subplot). Each row of subplots represents all the statistical information distributions (D,T,A,E)-Opt for a single design, allowing for a row-wise comparison of the four designs across a single metric. For this study, the effect of all designs is to manipulate the E-Optimality VX distributions (*i.e.* the right-most column). The top row again presents the Monte Carlo VX results previously shown in Section **??**; however, the x-axis of all plots have been rescaled for common relative comparison.

As discussed in Section 5.3.4, E-Optimal designs yield results which are better numerical conditioned. The results shown below reveal statically identical *a priori* designs and VX distributions for (E,RE,SR-E)-Opt experiment designs, suggesting that the E-Opt design already possess a level of robust-optimality. Here, the E-Optimality of these three designs reveal distributions that are nearly lower-bounded by the *a priori* anticipated outcome and are skewed towards decreasing information quality but with statistically small variance. Again, the EE-Opt (Bayesian) design provides for a more conservative design that has an expected statistical outcome nearly equal to the *a priori* anticipated outcome.

To summarize, the E-Opt experiment design is observed to be a robust-optimal design, being statistically equivalent to the (RE,SR-E)-Opt designs, but the expected result is marginally inferior to the *a priori* anticipated result. Again, the Bayesian experiment is a conservative design.

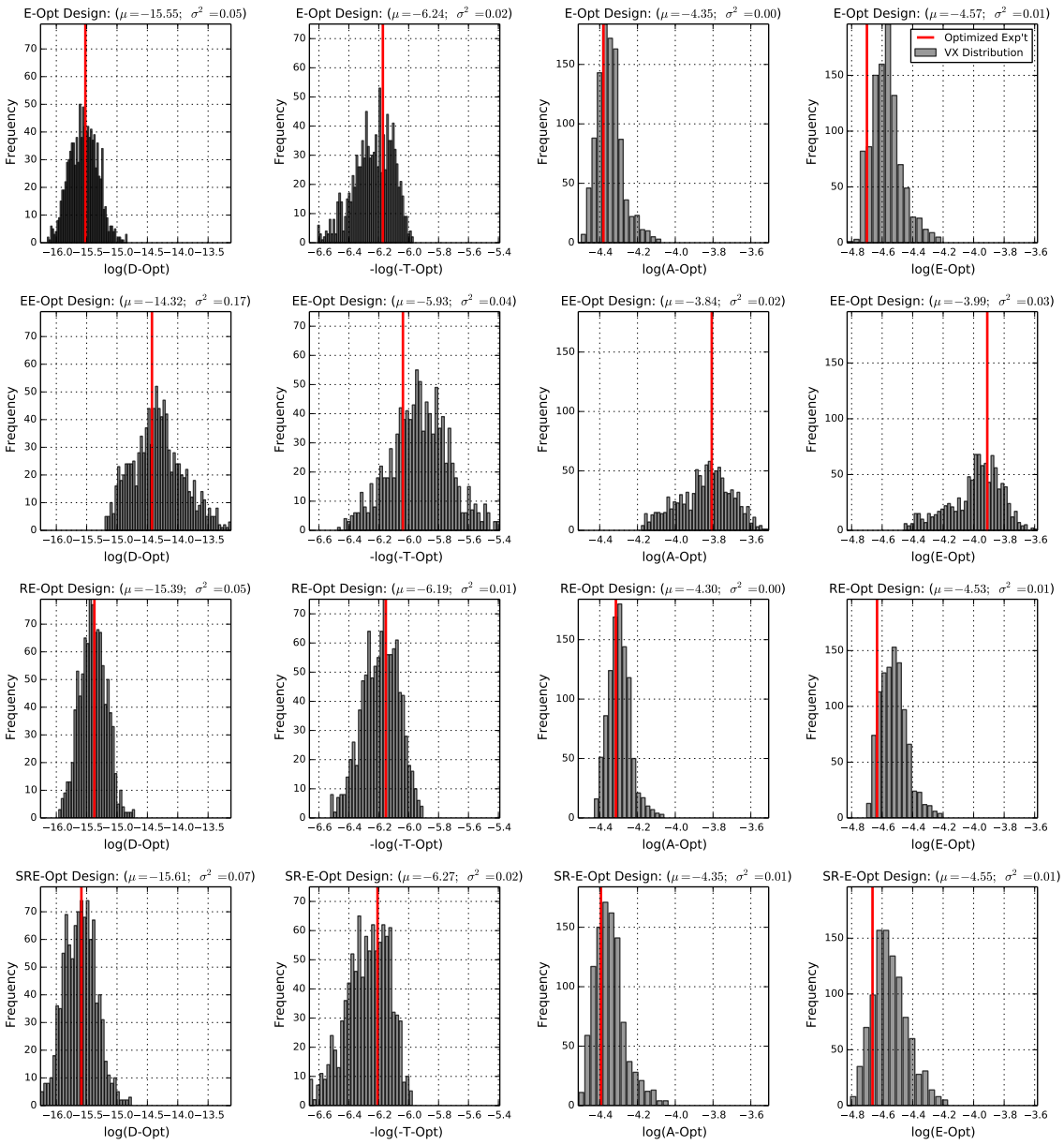

Figure 111: Comparison of distributions of nominal and robust-optimal (E,EE,RE,SR-E)-Opt experiment designs using uniform parameters distributions of Monte Carlo of 1000 virtual experiments according to Table 40. Horizontal rows represent a single optimal experiment design, vertical columns represent a single nominal performance metric, and red lines represent the anticipated *a priori* performance (statically optimized) values.

Table 40: E-Optimality robust-optimal experiment design comparisons Monte Carlo distribution statistical measures.

Designs	Metrics	Statistical Measures				
		mean	**var.**	**med.**	**min.**	**max.**
log(D-Opt)	log(E-Opt)	-15.55	0.05	-15.55	-16.15	-14.83
	log(EE-Opt)	-14.32	0.17	-14.34	-15.20	-13.12
	log(RE-Opt)	-15.39	0.05	-15.40	-15.96	-14.71
	log(SR-E-Opt)	-15.61	0.07	-15.61	-16.26	-14.76
$-\log(-$T-Opt$)$	log(E-Opt)	-6.24	0.02	-6.23	-6.61	-5.97
	log(EE-Opt)	-5.93	0.04	-5.93	-6.48	-5.39
	log(RE-Opt)	-6.19	0.01	-6.18	-6.52	-5.90
	log(SR-E-Opt)	-6.27	0.02	-6.27	-6.66	-5.97
log(A-Opt)	log(E-Opt)	-4.35	0.00	-4.35	-4.50	-4.07
	log(EE-Opt)	-3.84	0.02	-3.83	-4.18	-3.51
	log(RE-Opt)	-4.30	0.00	-4.30	-4.43	-4.06
	log(SR-E-Opt)	-4.35	0.01	-4.36	-4.51	-4.03
log(E-Opt)	log(E-Opt)	-4.57	0.01	-4.58	-4.83	-4.21
	log(EE-Opt)	-3.99	0.03	-3.96	-4.46	-3.58
	log(RE-Opt)	-4.53	0.01	-4.53	-4.20	-4.70
	log(SR-E-Opt)	-4.55	0.01	-4.56	-4.81	-4.17

11.1.5 Exp't #5 Observations

Exp't #5 was designed to address **HYP#3** by investigating the robust-optimality of the robust-optimal information metrics, which were constructed using higher-order VAEs. To do this a simple spring-mass-damper system was implemented within TEMPUS for the sizing and synthesis of robust-optimal information-dense dynamic experiment designs. Through a Monte Carlo virtual experimentation investigation, it was observed that these higher-order information metrics do provide various levels of robustness; however, it was observed that not all information metrics, computed form the Fisher information matrix are created equal. For example, the T-Opt (information matrix trace) frequently yielded inferior designs in terms of both robustness and optimality, where conversely the A-Optimal (inverse information matrix trace) provided for some of the best designs. Therefore **HYP. #3** is accepted, and the utilization of VAEs to compute higher-order information quality metrics for robust-optimal dynamic experiment design has been successfully demonstrated for the spring-mass-damper system.

11.2 *Application Problem– Robust-Optimal Flight Test Design for Air-Breathing Hypersonic Vehicles*

Morelli [212, 170] proposed the use of and design of multi-sine inputs for characterizing stability and control derivatives of the X-43A Hyper-X vehicle during the descent portion of the flight test. The idea was to excite the vehicle using inputs with wideband frequency content near the expected vehicle harmonics, while satisfying practical constraints (*e.g.* limited test duration, input amplitude bounds, stable flight, etc.). As discussed in Section 2.3.3, flight testing strategy here consisted of a 3-phase procedure, as shown below in Figure 112: (1) ascent phase – the Hyper-X is boosted to (h,V) conditions using a modified Pegasus rocket booster; (2) SCRAMjet operation phase – the propulsion system was operated for approximately 11 seconds at Mach 10 [229, 230]; and (3) descent phase – the engine cowl door is closed and a series of multi-sine inputs maneuvers were executed for aerodynamic parameter estimation, as the vehicle descended and Mach number decreased between $3 \leq Ma \leq 8$. Despite leveraging minimal *a priori* information in design, the multi-sine perturbation maneuvers allowed for successful aerodynamic parameter estimation during the unpowered (descent) portion of the flight test. However, the same cannot be concluded for the powered phase of the flight test, where a conservative robust control strategy was used to ensure proper SCRAMjet operation.

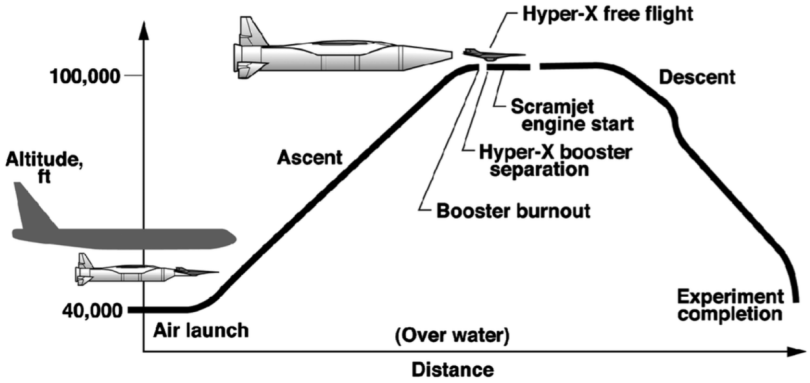

Figure 112: Hyper-X mission profile [212].

11.2.1 Description of Notional Flight Testing Procedure

The generic experimental procedure outlined in Table 27 is again followed for the design of SCRAMjet-powered hypersonic flight tests. This section is an implementation of the TEMPUS sizing and synthesis approach for the design of flight tests followed by a Monte Carlo analysis of virtual experiments to evaluate these designs for robust-optimality with respect to uncertainties in aero-propulsive-elastic thrust coefficients. Recall in Section 2.3.2 that due to deficiencies in hypersonic ground testing facilities that high-confidence models and parameters related to SCRAMjet propulsion operation are very difficult to obtain, requiring flight test data to construct dynamic models via aircraft system identification tecniques [25, 26, 183].

Morelli [170, 212] proposed the use of multi-sine perturbative excitation inputs to be designed for characterizing stability and control derivatives of the Hyper-X vehicle during the descent portion of the flight test. The work here also incorporates the use of multi-sines; however, in contrast to the work by Morelli [212], a model-based approach is proposed that leverages *a priori* information on aero-propulsive-elastic forces and moments models to design SCRAMjet-powered flight phase (phase 2) of the Hyper-X test plan shown above in Figure 112. Hence, for purposes of this dissertation, a SCRAMjet flight test for propulsion systems identification is defined as free, guided flight at a defined steady-level cruise condition.

11.2.2 Description of Multi-sine Perturbative Excitation Signals

In addition to reducing infinite-dimensional input signals into finite-dimensional vectors, the multi-sine approach to designing perturbative excitation maneuvers provides several advantages for flight testing of hypersonic vehicles, where small test duration windows constrain abundant data collection.

- *Multiple simultaneous inputs*: For maximum flight-test efficiency and to ensure that the vehicle response in all axes is recorded at approximately a constant flight conditions, all control surfaces on the vehicle should be moved simultaneously, as opposed to the conventional approach of moving one control surface at a time in sequence.

- *Orthogonal inputs*: Inputs can be designed that are mutually orthogonal in both frequency and time domains. Referring back to Section 4.3.6, this helps the parameter estimation by completely decorrelating the inputs, which improves accuracy of control effectiveness estimates.

- *Wideband frequency content*: Very little information about the dynamic system is required to design inputs (*i.e.* omit frequencies where dynamic resonance is expected). Frequency content can be chosen over a broad range to excite vehicle response at or near rigid body modal frequencies.

- *Flexibility in inputs*: Because each input has wideband frequency content, a single input design can be applied at various flight conditions which simplifies the flight test and requires a small amount of onboard memory.

- *Small excursions*: Because of the various frequencies and phase angles, and the small amplitudes of the input perturbations, applying these inputs simultaneously to the vehicle produces a dynamic response similar to what might be seen

in flight through light to moderate turbulence. Consequently, the vehicle stays near its nominal trajectory with small perturbative excursions.

Shown below is the functional form of a multi-sine input excitation signal for the j^{th} frequency component input, where each input is a sum of sinusoids with unique frequencies that cover a specified frequency band of interest (similar to frequency sweeps [170]).

$$u_j = \sum_{k\in\{1,2,\ldots,\mathrm{M}\}} A_k \sin\left(\frac{2\pi k\mathbf{t}}{T} + \phi_k\right) \quad j = 1, 2, \ldots, M \tag{80}$$

Here, M is the total number of available harmonically related frequencies, T is the time length of the excitation, and A_k is the amplitude for the k^{th} sinusoidal component. The variable $\mathbf{t}$ represents a vector of N discrete time points, $\mathbf{t} = [t(0)\ t(1)\ \ldots\ t(N-1)]^T$, and $\mathbf{u}_j$ represents the vector of corresponding amplitudes for the j^{th} input, $\mathbf{u}_j = [u_j(0)\ u_j(1)\ \ldots\ u_j(N-1)]^T$. Each of the m inputs is composed of selected components from the group of M sinusoids with frequencies $\omega_k = 2\pi k/T,\ k = 1, 2, \ldots, M$.

As previously discussed, the Hyper-X experiments [212] did not conduct a model-based design, leveraging *a priori* information on existing developed models. Instead, the amplitudes A_k were chosen to achieve a specific power distribution, and the phase angles ϕ_k of the selected harmonic components are chosen to minimize the *relative peak factor* (RPF) [170, 212].

$$\mathrm{RPF}(\mathbf{u}_j) = \frac{[\max(\mathbf{u}_j) - \min(\mathbf{u}_j)]/2}{\sqrt{2(\mathbf{u}_j^T\mathbf{u}_j)/N}} = \frac{[\max(\mathbf{u}_j) - \min(\mathbf{u}_j)]}{2\sqrt{2}\mathrm{rms}(\mathbf{u}_j)} \tag{81}$$

Equation (81) is a measure of the efficiency of an input for parameter estimation purposes, in terms of the amplitude range of the input divided by a measure of the input energy. Note that RPF is not directly dependent on the aircraft model structure or parameters. Figure 113 shows an example of a multi-sine input (*i.e.* elevator, aileron, and rudder) for the Hyper-X flight experiment.

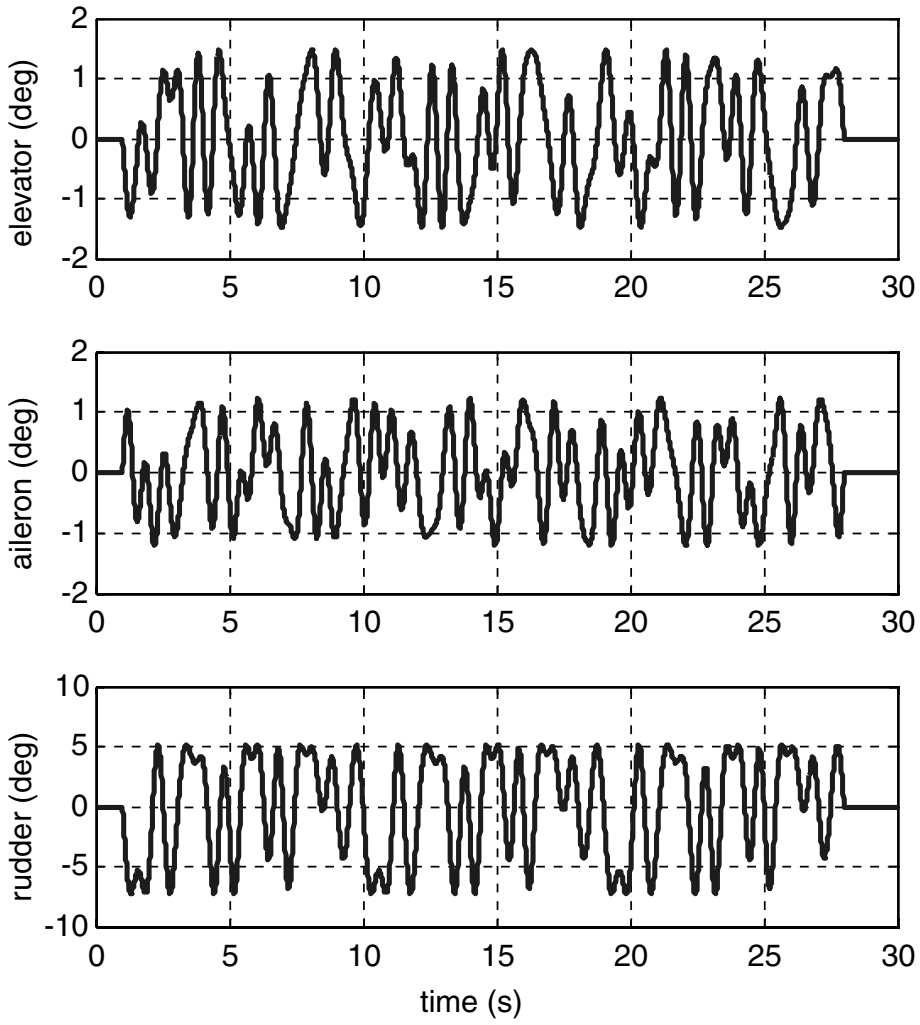

Figure 113: Multiple orthogonal phase-optimized multisine input design for the X-43A stability and control derivatives estimation flight experiment at Mach 6 (post-scramjet demonstration experiment) [212].

11.2.3 The Generic Hypersonic Vehicle (GHV) Model

In this section the approach to modeling and simulation of SCRAMjet flight dynamics is discussed, highlighting key assumptions and important physical phenomena when necessary. Known as the Generic Hypersonic Vehicle (GHV), this collection of models was first proposed by Chavez and Schmidt [65] and later revised by Bolender and Doman [45] and Groves et al. [123]. The GHV model captures the nonlinear coupling between aero-propulsive-elastic effects, both implicitly within the forces and moments and explicitly through inertial-elastic (heave) coupling, while also being suitable for use in control-oriented modeling and vehicle design. Because of this, the GHV model has been extensively considered in literature with a focus on applications in flight dynamics as well as stability and controls [45, 65, 66, 104, 225, 228]. However, due to the strong inertial-elastic couplings and nonlinearities, control-oriented modeling of this vehicle is challenging, where unstable, non-affine, and non-minimum phase behavior is observed in the open-loop system response, shown by Parker, et al. [228].

11.2.3.1 Vehicle Description

Figure 114 shows an operational schematic of the GHV geometric model used in this work under notional steady-level flight. The vehicle is 100 ft long with weight (density) 6,139 lb per foot of depth and has a bending mode at about 20 rad/sec. The controls include: (i) elevator deflection angle δ_e, (ii) stoichiometrically normalized fuel equivalency ratio Φ, (iii) diffuser area ratio $\bar{A}_D$ (not used in this study), and (iv) canard deflection angle δ_c. The nominal model parameter values for this vehicle are provided below in Table 41, and additional details about the model may be found in the following references [45, 66, 104].

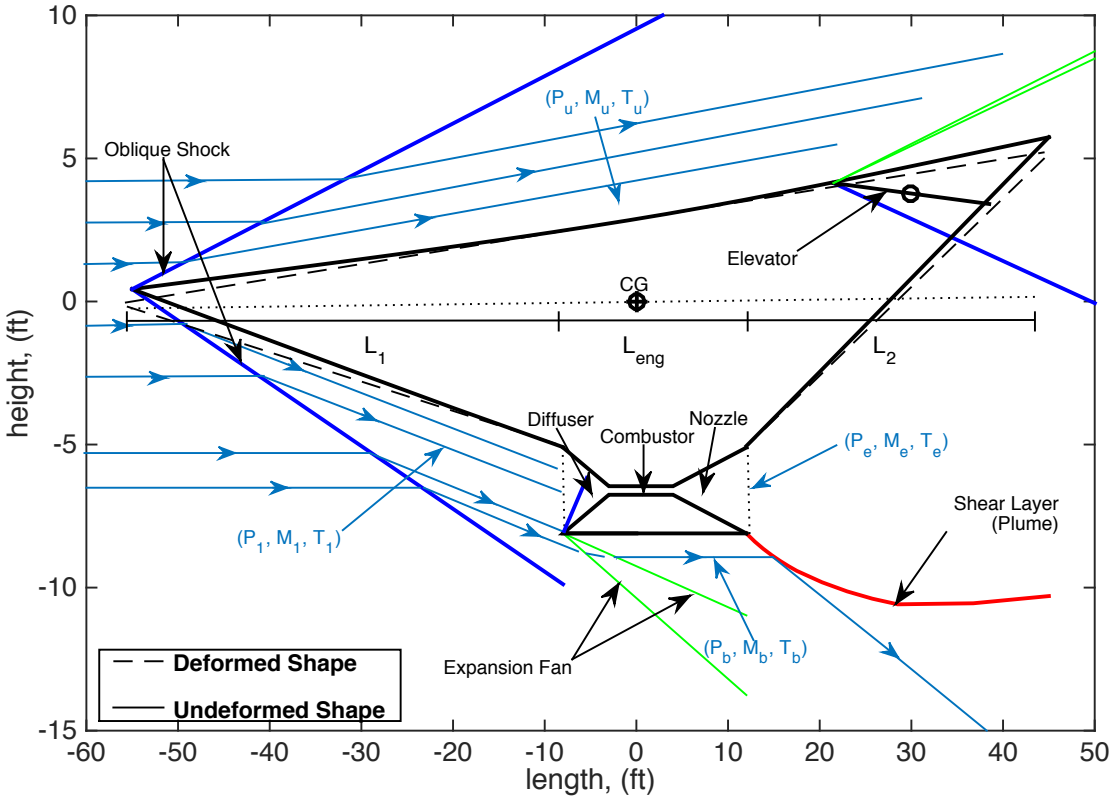

Figure 114: Operational schematic of the GHV SCRAMjet during a notional steadlevel flight condition at $h = 85,000$ (ft), $\bar{q} = 2000$ (psi), and $\alpha = 2$ (deg), annotated with thermal-fluidic flow properties along streamlines.

Table 41: Summary of GHV vehicle nominal parameter values [45, 104, 258].

Parameter	**Nominal Value**	**Parameter**	**Nominal Value**
Total Length (L)	100 ft	Nacelle Length (L_{eng})	20 ft
Forebody Length (L_1)	47 ft	Aftbody Length (L_2)	33 ft
Elevator Position (Δr_{el})	(-30,-3.5) ft	Elevator Area (S_{el})	17 ft^2
Canard Position (Δr_{ca})	(40, 0.0) ft	Canard Area (S_{ca})	17 ft^2
Engine Inlet Height (h_i)	3 ft	Engine Exhaust Height (h_e)	3 ft
Diffuser Area Ratio ($\bar{A}_D$)	0.1	Nozzle Area Ratio ($\bar{A}_E$)	10
Upper Forebody Angle ($\tau_{1,U}$)	3.0^o	Lower Forebody Angle ($\tau_{1,L}$)	6.2^o
Tail Angle (τ_2)	14.342^o	Mean Elasticity Modulus (E)	8.65$\times$10^7 psi
Center Of Gravity (Δr_{cg})	(-55, 0) ft	Weight Per Unit Width (W/w)	6.14 $\times$10^3 lbs/ft
Titanium Thickness (t_{TI})	9.6 in	Moment Of Inertia (I_{yy})	8.67 $\times$10^4 slugs-ft^2/ft
First Flex Mode (ω_1)	19.76 rad/sec	Second Flex Mode (ω_2)	47.84 rad/sec
Third Flex Mode (ω_3)	94.91 rad/sec	Flex Mode Damping (ζ)	0.02

11.2.3.2 Nonlinear Longitudinal Dynamics with Heave Coupling

The vehicle dynamics are derived from an Euler-Lagrangian approach, modeling the longitudinal motion of both rigid body and elastic states. The dynamic system state vector $\vec{x} \in \mathbb{R}^9$ consists of five rigid body states (altitude – h, velocity – V, angle of attack – α, pitch angle – θ, and pitch rate – Q), and four flexible states – (η_f, η_f, $\dot{\eta}_f$, $\dot{\eta}_a$) to model each bending mode of fore/aft-body as fixed-free beams, using Euler-Bernoulli beam theory [45]. Typically, only the first three bending modes are considered in GHV modeling. The equations of motion are given below.

$$\dot{h} = V \sin(\theta - \alpha) \tag{82}$$

$$m\dot{V} = (T\cos(\alpha) - D) - mg\sin(\theta - \alpha) \tag{83}$$

$$mV\dot{\alpha} = -(T\sin(\alpha) + L) + mQV + mg\cos(\theta - \alpha) \tag{84}$$

$$\dot{\theta} = Q \tag{85}$$

$$I_{yy}\dot{Q} - \tilde{\psi}_f\ddot{\eta}_f - \tilde{\psi}_a\ddot{\eta}_a = M \tag{86}$$

$$\ddot{\eta}_f + \frac{\tilde{\psi}_f\tilde{\psi}_a}{I_{yy}}\ddot{\eta}_a = -2\zeta\omega_f\dot{\eta}_f - \omega_f^2\eta_f + N_f - \tilde{\psi}_f\frac{M}{I_{yy}} \tag{87}$$

$$\frac{\tilde{\psi}_f\tilde{\psi}_a}{I_{yy}}\ddot{\eta}_f + \ddot{\eta}_a = -2\zeta\omega_a\dot{\eta}_a - \omega_a^2\eta_a + N_a - \tilde{\psi}_a\frac{M}{I_{yy}} \tag{88}$$

Here (L, D, T, M) denote lift, drag, engine thrust, and pitching moment, respectively, and (N_f, N_a) denote the generalized forces for the fore/aft-body beams. The inertial properties of the vehicle are described by (m and I_{yy}), which are the vehicle total mass and moment of inertia. The elastic properties of the vehicle can be described by (ω_f, ω_a, ζ_f, ζ_a, $\tilde{\psi}_f$, $\tilde{\psi}_a$), which are the natural frequencies, damping ratios, and inertial-elastic coupling parameters for the fore/aft-body beams, respectively. The controls (δ_c, δ_e, $\bar{A}_D$, Φ) do not appear explicitly in the equations of motion but instead enter through the forces and moment terms. In the subsequent discussion on modeling aero-propulsive-elastic forces and moments, these dependencies are more extensively discussed.

Table 42: GHV state vector summary.

#	Symbol	Description	Units
1	h	altitude	ft
2	V	speed	ft/sec
3	α	angle of attack	deg
4	θ	pitch angle	deg
5	Q	pitch rate	deg/sec
6	$\eta_{f,i}$	forebody i^{th} flex mode	–
7	$\dot{\eta}_{f,i}$	forebody i^{th} flex mode rate	–
8	$\eta_{a,i}$	aftbody i^{th} flex mode	–
9	$\dot{\eta}_{a,i}$	aftbody i^{th} flex mode rate	–

Table 43: GHV control vector summary.

#	Symbol	Description	Units
1	Φ	stoichiometrically normalized fuel equivalence ratio	–
2	δ_c	canard deflection angle	deg
3	δ_e	elevator deflection angle	deg
4	$\bar{A}_D$	cowl door deflection; diffuser area ratio	–

11.2.3.3 Aero-Propulsive-Elastic Forces and Moments

Two distinct models of the aero-propulsive-elastic forces and moments are considered, as categorized by Fiorentini, et al. [104]: (i) a physics-based truth model (TM), used exclusively for physically accurate determination forces and moments; (ii) a reduced-complexity, statistics-based control-oriented model (COM), employed for control design and a quantitative stability analysis of the closed-loop system. Apart from differences in the actual model structures, the COM is similar to the so-called curve-fitted model (CFM) in Parker, et al. [228]. However, in that study the control design was performed on the basis of a further simplified control-oriented model obtained by removing the flexible states, the altitude dynamics, and a set of weak couplings from the CFM, whereas here, and in work by Fiorentini [104], these effects have been retained in the model for use in the controller design.

GHV Truth Model (TM). To calculate aero-propulsive-elastic forces and moments, the models developed by Chaves and Schmidt [65] (and later by Bolender and Doman [45]), utilize panel methods (*i.e.* piston theory and finite-area methods) to determine aero-thermal-fluidic properties about the surface of the vehicle (*i.e.* pressure, velocity, and temperature distributions), given aero-thermal-fluidic states, elastic states, and vehicle control inputs (see Figure 115). Different inviscid compressible flow theories are employed depending on the region of applicability. Assuming that air is a calorically perfect gas (*i.e.* constant specific heats and specific heat ratio: $\gamma = \frac{c_p}{c_v} = 1.4$), these theories include: shock theories (*i.e.* normal and oblique), Prandtl-Meyer expansion theory, Newtonian impact theories, internal compressible flow theories (*i.e.* isentropic area change, constant-area heat addition (*i.e.* Rayleigh-line flow), etc.) [6, 7, 10]. Two fixed-free Euler-Bernoulli beams are used to model forced transverse vibrational motion, where the first three bending moments are calculated via the pressure distributions, as discussed by Meirovitch [201] (see Figure 116). The scramjet used for this model is similar to that used by Chavez and Schmidt [65], which as been used extensively in literature and models effects such as mass spillage, engine inlet turning forces, isentropic inefficiencies, and even diffuser/thermal choking. An exhaust plume analysis on the lower aftbody surface of the vehicle calculates distributions of aero-thermal property by determining the shape of a shear layer between internal and external flows by balancing the pressure difference at each node, moving aftwards from the nozzle exit plane to the tail.

An example output of the TM can be seen in Figure 117, where scaled aero-thermal distributions are shown for the configuration shown in Figure 114. The pressure distributions are used to calculate component forces/moments and velocity distributions are used in total thrust calculations. Appendix F provides a more detailed discussion on the modeling approaches used in each element of the TM.

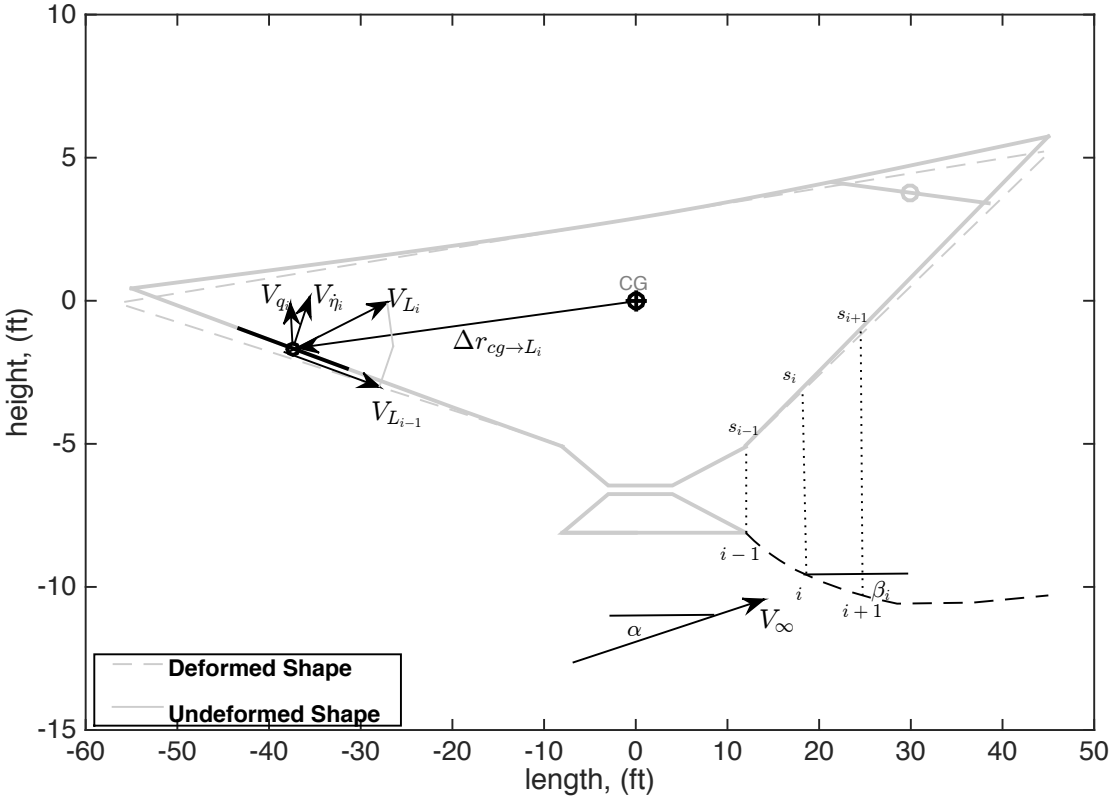

Figure 115: Illustration of panel methods for modeling aero-thermal properties on (i) external surfaces: lower forebody, upper-surface, control surfaces, and lower engine cowl/nacelle and (ii) the lower aftbody exhaust (plume).

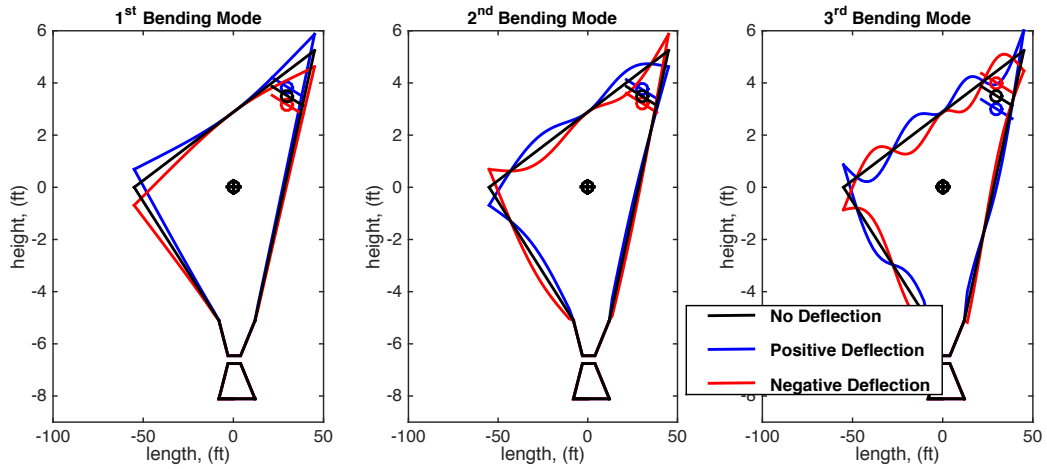

Figure 116: GHV transverse bending deflections (scaled) modes 1-3 using two fixed-free Euler-Bernoulli beams for the fore/aftbodies.

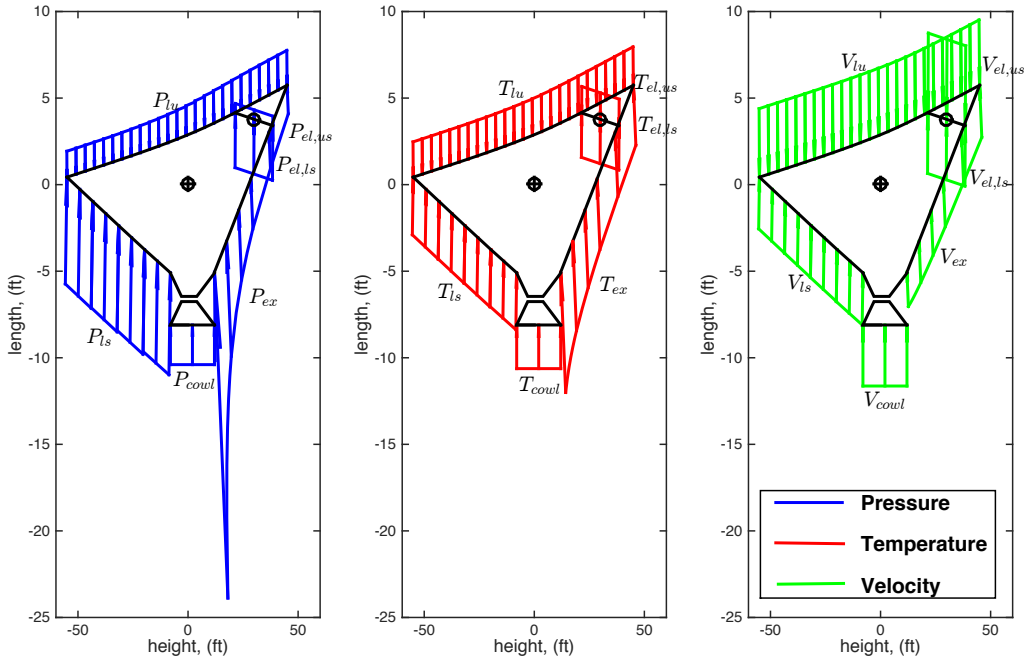

Figure 117: Scaled aero-thermal properties for the GHV geometry and flight condition of Figure 114, $h = 85,000$ (ft) and $\bar{q} = 2000$ (psi).

GHV Control-Oriented Model (COM). The cause/effect relationships between forces/moments and states/controls in the TM do not admit a closed-form representation. Following work by Parker, et al. [228] and Fiorentini [104], a reduced-complexity control-oriented model has been developed for control design and stability analysis. The COM model structure is presented below, where numerical data is generated for the COM by using response surface methodology (RSM) to perform a regression analysis on data generated from the TM (see Appendix F for the numerical results used in this work) [228, 219].

$$
\begin{aligned}
T &\approx \bar{q}S\left[C_{T,\Phi}(\alpha)\Phi + C_T(\alpha) + C_T^{\boldsymbol{\eta}}\boldsymbol{\eta}\right] \\
L &\approx \bar{q}SC_L\left(\alpha, \boldsymbol{\delta}, \boldsymbol{\eta}\right) \\
D &\approx \bar{q}SC_D\left(\alpha, \boldsymbol{\delta}, \boldsymbol{\eta}\right) \\
M &\approx z_T T + \bar{q}\bar{c}SC_M\left(\alpha, \boldsymbol{\delta}, \boldsymbol{\eta}\right) \\
N_{f,i} &\approx \bar{q}S\left[N_{f,i}^{\alpha^2}\alpha^2 + N_{f,i}^{\alpha}\alpha + N_{f,i}^{\boldsymbol{\delta}}\boldsymbol{\delta} + N_{f,i}^{0} + N_{f,i}^{\boldsymbol{\eta}}\boldsymbol{\eta}\right] \\
N_{a,i} &\approx \bar{q}S\left[N_{a,i}^{\alpha^2}\alpha^2 + N_{a,i}^{\alpha}\alpha + N_{a,i}^{\boldsymbol{\delta}}\boldsymbol{\delta} + N_{a,i}^{0} + N_{a,i}^{\boldsymbol{\eta}}\boldsymbol{\eta}\right] \\
&\quad i = 1, 2, 3
\end{aligned}
\tag{89}
$$

Here, $\boldsymbol{\delta} = [\delta_c, \delta_e]^T$, $\boldsymbol{\eta}_i = [\eta_{f,i}, \eta_{a,i}]^T$, and

$$
\begin{aligned}
C_{T,\Phi}(\alpha) &= C_T^{\Phi\alpha^3}\alpha^3 + C_T^{\Phi\alpha^2}\alpha^2 + C_T^{\Phi\alpha}\alpha + C_T^{\Phi} \\
C_T(\alpha) &= C_T^{\alpha^3}\alpha^3 + C_T^{\alpha^2}\alpha^2 + C_T^{\alpha}\alpha + C_T^{0} \\
C_M\left(\alpha, \boldsymbol{\delta}, \boldsymbol{\eta}\right) &= C_M^{\alpha^2}\alpha^2 + C_M^{\alpha}\alpha + C_M^{\boldsymbol{\delta}}\boldsymbol{\delta} + C_M^{0} + C_M^{\boldsymbol{\eta}}\boldsymbol{\eta} \\
C_L\left(\alpha, \boldsymbol{\delta}, \boldsymbol{\eta}\right) &= C_L^{\alpha}\alpha + C_L^{\boldsymbol{\delta}}\boldsymbol{\delta} + C_L^{0} + C_L^{\boldsymbol{\eta}}\boldsymbol{\eta} \\
C_D\left(\alpha, \boldsymbol{\delta}, \boldsymbol{\eta}\right) &= C_D^{\alpha^2}\alpha^2 + C_D^{\boldsymbol{\delta}^2}\boldsymbol{\delta}^2 + C_D^{\alpha}\alpha + C_D^{\boldsymbol{\delta}}\boldsymbol{\delta} + C_D^{0} + C_D^{\boldsymbol{\eta}}\boldsymbol{\eta} \\
C_j^{\eta_f} &= \left[C_j^{\eta_{f,1}}, 0, C_j^{\eta_{f,2}}, 0, C_j^{\eta_{f,3}}, 0\right] \\
C_j^{\eta_a} &= \left[C_j^{\eta_{a,1}}, 0, C_j^{\eta_{a,2}}, 0, C_j^{\eta_{a,3}}, 0\right], \quad j = T, L, D, M \\
N_{f,i}^{\eta_f} &= \left[N_{f,i}^{\eta_{f,1}}, 0, N_{f,i}^{\eta_{f,2}}, 0, N_{f,i}^{\eta_{f,3}}, 0\right] \\
N_{a,i}^{\eta_a} &= \left[N_{a,i}^{\eta_{a,1}}, 0, N_{a,i}^{\eta_{a,2}}, 0, N_{a,i}^{\eta_{a,3}}, 0\right], \quad i = 1, 2, 3.
\end{aligned}
\tag{90}
$$

Here the regression parameters, including $C_T^{\Phi\alpha^3}$, $C_T^{\Phi\alpha^2}$, $C_T^{\Phi\alpha}$, C_T^{Φ}, $C_T^{\alpha^3}$, $C_T^{\alpha^2}$, C_T^{α}, C_T^0, $C_T^{\boldsymbol{\eta}}$, $C_M^{\alpha^2}$, C_M^{α}, $C_M^{\boldsymbol{\delta}}$, C_M^0, $C_M^{\boldsymbol{\eta}}$, C_L^{α}, $C_L^{\boldsymbol{\delta}}$, C_L^0 etc., are collectively referred to as the stability and control (SnC) coefficients and are referenced to a given vehicle operating condition (*e.g.* altitude and velocity). The nonlinear model structure, albeit still quite complex, offers the advantage of being analytically tractable, while retaining the relevant dynamical features of the simulation model. In contrast to the model structure proposed by Parker, et al. [228], the thrust, lift, drag, and moment coefficient structures of the COM proposed by Fiorentini [104] depend explicitly on the elastic modes. Also, the COM by Fiorentini [104] includes lift due to the elevator and the effect of the thrust on the pitching moment. The COM model structures shown in Equations (89) and (90) differ from the COM proposed by Fiorentini [104], where here two fixed-free beam models are used to capture heave-coupling effects. The implications of including this is discussed subsequently in Section 11.2.3.4, where the nonlinear robust-adaptive flight controller is addressed.

Observe that within the COM of Equations (89) and (90), the effects of states and control inputs are explicitly stated and suitably captured with the omission of two states: h and V (or equivalently $\bar{q}$). This was done because accurate approximation of h and V via Taylor expansions was observed to produce excessively high order terms, greatly increasing the model structure complexity. To capture the added effects of velocity and altitude, SnC coefficients are computed over a grid of sufficient resolution and tabulated accordingly. As a result, accurate computation of GHV SnC coefficients during simulation will require a 2D interpolation technique as h and V evolve through simulation time.

Unmodeled Phenomena/Effects. All models possess fundamental limitations. Realizing model limitations is crucial in order to avoid model misuse. Given this, a (somewhat complete) list of phenomena/effects that are not captured within the above non-linear model is summarized below, as discussed by Sridharan [258]. (For reference purposes, flow physics effects and modeling requirements for the X-43A are summarized within [70].)

- *Dynamics.* The above model does not capture longitudinal-lateral coupling in dynamics [54] associated with 6DOF effects. Secondary dynamic effects such as mass/inertial changes associated with fuel burn (*i.e.* dynamically changing mass/inertia parameters), fuel slosh, rotating/spherical earth effects, aero-servo-elasticity, and higher-order heaving coupling terms are also neglected [36].

- *Aerodynamics.* Aerodynamic phenomena/effects not captured in the model include the following: boundary layer growth, displacement thickness, viscous interaction, entropy and vorticity effects, laminar versus turbulent flow, flow separation, high temperature and real gas effects (*e.g.* caloric imperfection, electronic excitation, thermal imperfection, chemical reactions such as 0_2 dissociation) [7], non-standard atmosphere (*e.g.* troposphere, stratosphere), unsteady atmospheric effects (*e.g.* wind gusting) [78], 3D effects, aerodynamic load limits. Many of these effects will be most severe along the aftbody of the vehicle [6].

- *Propulsion.* Propulsion phenomena/effects not captured in the model include the following: cowl door dynamics, forebody boundary layer transition and turbulent flow to inlet diffuser losses[32, 33], internal shock effects, diffuser-combustor interactions, fuel injection and mixing, flame holding, engine ignition via pyrophoric silane [69] (requires finite-rate chemistry; cannot be predicted

via equilibrium methods [259]), finite-rate chemistry and the associated thrust-AoA-Mach-FER sensitivity effects [271], internal and external nozzle losses, 2D and 3D thermal choking induced phenomena, engine unstart dynamics, combined cycle issues [135], etc. Within [271], a higher fidelity propulsion model is presented which addresses internal shock effects, diffuser-combustor interaction, finite-rate chemistry and the associated thrust-AoA-Mach-FER sensitivity effects. While the nominal Rayleigh-based model (considered here) exhibits increasing thrust-AOA sensitivity with increasing AoA, the more complex model in [271] exhibits reduced thrust-AoA sensitivity with increasing AoA - a behavior attributed to finite-chemistry effects. Future work will examine the impact of internal engine losses, and high temperature gas dynamics effects.

- *Structures.* Structural phenomena not captured in the model include the following: out of plane and torsional effects, internal structural layout, unsteady thermo-elastic heating effects, aerodynamic heating due to shock impingement, distinct material properties [116], and aero-servo-elasticity [22, 181], etc.

- *Heating-Flexibility Issues.* Finally, it should be noted that Bolender and Doman have addressed a variety of effects in their publications. For example, within [44, 279] the authors address the impact of heating on (longitudinal) structural mode frequencies and mode shapes. Comprehensive heating-mass-flexibility-control studies are beyond the scope of this work.

11.2.3.4 Nonlinear Robust-Adaptive Controller

As previously mentioned, due to the strong inertial-elastic couplings and nonlinearities, control-oriented flight dynamic modeling of the SCRAMjet vehicles is challenging, where unstable, non-affine, and non-minimum phase behavior is commonly observed in the open-loop system response (refer to Parker, et al. [228]). This behavior is further exacerbated by the presence of parametric uncertainties in vehicle

mass/inertia and aero-propulsive-elastic parameters, which drive increasing requirements for stability and control of SCRAMjets. The following discussion addresses these challenges. The viable controller approach used in this work is described below.

Parametric Uncertainty Models. In developing the controller and assessing its closed-loop behavior, it is assumed that all of the coefficients of the COM are subject to uncertainty, apart from obvious parameters corresponding to physically measurable quantities or known constants. The vector of all uncertain parameters, denoted by $\mathbf{p} \in \mathbb{R}^m$, includes in general the vehicle inertial parameters and the aero-propulsive-elastic coefficients that appear in the force and moment approximations (that is: $C_T^{(\cdot)}$, $C_M^{(\cdot)}$, etc.). For purposes of this study, only uncertainty in the aero-propulsive-elastic coefficients are considered. The nominal TM values of $\mathbf{p}$ are denoted by $\mathbf{p_0}$ and the perturbed values relative to $\mathbf{p_0}$ are denoted by $\delta\mathbf{p}$. It is assumed that $\mathbf{p} \in \mathcal{P}$,where $\mathcal{P}$ is a compact convex set that represents the admissible range of variation of $\mathbf{p}$ such that $\mathbf{p_0}$ lies in its interior. For example, a maximum uniform variation within 40% of the nominal value can be considered, yielding the admissible parameter set $\mathcal{P} = \{\mathbf{p} \in \mathbb{R}^m | 0.6p_i^0 \leq 1.4p_i^0|,\ i = 1, \ldots, m\}$.

The natural frequencies, ω_i, of the flexible dynamics depend on the mass of the vehicle, which decreases as fuel is consumed. Because this variation occurs on a slower time scale than the speed of the references to be tracked, the mass is considered constant for the purpose of control design during each tracking maneuver. However, both the vehicle mass and the natural frequencies of the flexible dynamics are considered as uncertain parameters ranging within the intervals given in Table 1 of Sigthorsson, et al. [253] corresponding to a 100% variation in fuel level. Note that these values remain within the assumed 40% of the vector of nominal values.

Controller Design. Due to the presence of parametric uncertainties, a control formulation is required that has the ability to adapt to evolving parameter estimates,

while still adequately tracking a commanded reference model. Mathematically, a controller of the form shown below is desired, where the state vector is now augmented with an adaptive state vector.

$$\dot{\hat{\boldsymbol{\theta}}} = \mathbf{F}\left(\hat{\boldsymbol{\theta}}, \mathbf{x}, \mathbf{y}_{\text{ref}}\right), \quad \hat{\boldsymbol{\theta}} \in \mathbb{R}^{\nu} \qquad \mathbf{u} = \mathbf{H}\left(\hat{\boldsymbol{\theta}}, \mathbf{x}, \mathbf{y}_{\text{ref}}\right) \tag{91}$$

Here $\mathbf{x} = [h, V, \gamma, \alpha, Q]^T$ are the state variable feedback (rigid-body states only), $\mathbf{y}_{\text{ref}} = [h_{\text{ref}}, V_{\text{ref}}]^T$ are reference trajectories (*e.g.* providing smooth transition from one trim state to another, etc.), $\mathbf{u} = [\Phi, \delta_e, \delta_c]^T$ are the active control inputs, $\boldsymbol{\theta}$ are true values of adaptive parameters (*i.e.* aero-propulsive-elastic parameters), and $\hat{\boldsymbol{\theta}}$ are the estimated values of adaptive parameters, which vary dynamically.

The controller architecture implemented here is a modification of the GHV flight controller developed by Fiorentini [104] for cruise/climb-cruise type trajectories and is therefore not applicable for ascent/reentry-type vehicles. Nonlinear dynamic inversion (geometric feedback) [254] was used to develop three separate dynamic adaptive subsystems, which are integrated together using sequential loop closure (*i.e.* backstepping) [174]: (1) the horizontal translational dynamics (the V-subsystem); (2) the vertical translation dynamics (the (h,γ)-subsystem); and (3) the rotational dynamics (the (α,Q)-subsystem). Each subsystem is controlled separately using the available inputs (Φ,δ_c,δ_e) and intermediate virtual control commands (γ_{cmd},α_{cmd},Q_{cmd}), as shown in Figure 118. Because the control authority of the canard on the flight-path angle dynamics is significantly smaller than the one of the angle of attack, the main control action will be performed through the command α_{cmd}. Thus, the role of the canard is to adaptively decouple lift from elevator commands (thus rendering the system as minimum phase), to enforce the equilibrium at the desired trim condition, and to provide a supplementary stabilizing action.

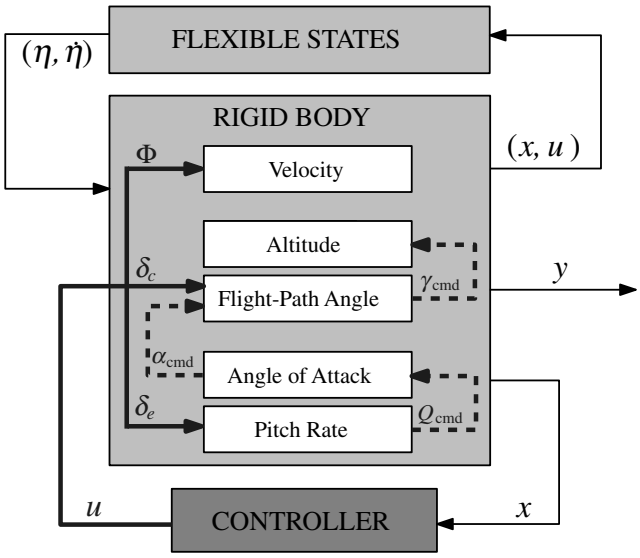

Figure 118: Block diagram of the control architecture showing direct control inputs Φ, δ_c, and δ_e (bold solid lines) and virtual control inputs γ_{cmd}, α_{cmd}, and Q_{cmd} (dashed lines) [104].

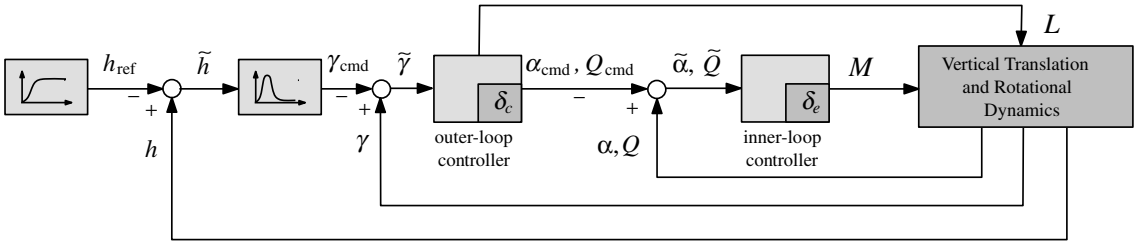

Figure 119: Control of the vertical translation and rotational dynamics using sequential loop closure (*i.e.* back-stepping) [104].

Table 44: Summary of GHV nonlinear robust-adaptive flight control laws [104].

	Control Laws:	Adaptive Parameters:
(V)-Subsystem	$\dot{\hat{\theta}}_1 = \mathrm{Proj}_{\hat{\theta}_1 \in \Theta_1}\left\{\tilde{V}\Gamma_1\left[\mathbf{B}_1(x)\Phi - \mathbf{\Psi}_1(\mathbf{x},\mathbf{u},\mathbf{y}_{\mathrm{ref}})\right]\right\}$ $\mathbf{\Phi} = \dfrac{1}{\hat{\theta}_1^T \mathbf{B}_1(\mathbf{x})}\left[-k_1\tilde{V} + \mathbf{\Psi}_1\left(\mathbf{x},\mathbf{u},\mathbf{y}_{\mathrm{ref}}\right)\right]$	$\theta_1 = [C_T^{\Phi\alpha^3}, C_T^{\Phi\alpha^2}, C_T^{\Phi\alpha}, C_T^{\Phi}, C_T^{\alpha^3}, C_T^{\alpha^2}, C_T^{\alpha},$ $\left(C_T^0 + C_T^\eta \eta^*\right), C_D^{\alpha^2}, C_D^{\alpha}, C_D^{\delta_e^2}, C_D^{\delta_e}, C_D^{\delta_c^2}, C_D^{\delta_c},$ $\left(C_D^0 + C_D^\eta \eta^*\right), m]$
(h,fpa)-Subsystem	$\dot{\hat{\theta}}_2 = \mathrm{Proj}_{\hat{\theta}_2 \in \Theta_2}\left\{-\dfrac{\bar{q}\tilde{\gamma}}{V}\Gamma_2 \mathbf{\Psi}_2\left(\mathbf{x},\mathbf{u},\mathbf{y}_{\mathrm{ref}}\right)\right\}$ $\delta_c = \mathbf{\Psi}_2\left(\mathbf{x},\mathbf{u},\mathbf{y}_{\mathrm{ref}}\right)^T \hat{\theta}_2 - k_3\tilde{\gamma}$	$\theta_2 = \left[\dfrac{C_L^{\delta_e}}{C_L^{\delta_c}}, \dfrac{C_L^0 + \mathbf{C}_L^\eta \eta^* + c_1(\alpha^*)}{C_L^{\delta_c}}, \dfrac{c_2(\alpha^*)}{C_L^{\delta_c}}, \dfrac{m}{sC_L^{\delta_c}}\right]$
(AoA,Q)-Subsystem	$\dot{\hat{\theta}}_3 = \mathrm{Proj}_{\hat{\theta}_3 \in \Theta_3}\left\{\Gamma_3\left[\mathbf{B}_3(x)\delta_e - \mathbf{\Psi}_3(\mathbf{x},\mathbf{u},\mathbf{y}_{\mathrm{ref}})\right]\tilde{Q}\right\}$ $\delta_e = \dfrac{1}{\hat{\theta}_3^T \mathbf{B}_3(\mathbf{x})}\left[\mathbf{\Psi}_3\left(\mathbf{x},\mathbf{u},\mathbf{y}_{\mathrm{ref}}\right)^T \hat{\theta}_3 - k_5\tilde{Q}\right]$	$\theta_3 = (S/I_{yy})[\bar{c}C_M^{\delta_e}, \bar{c}C_M^{\delta_c}, z_T C_T^{\Phi\alpha^3}, z_T C_T^{\Phi\alpha^2}, z_T C_T^{\Phi\alpha},$ $z_T C_T^{\Phi}, z_T C_T^{\alpha^3}, \left(z_T C_T^{\alpha^2} + \bar{c}C_M^{\alpha^2}\right), \left(z_T C_T^{\alpha} + \bar{c}C_M^{\alpha}\right),$ $\left(z_T C_T^0 + \bar{c}C_M^0\right) + \left(z_T \mathbf{C}_T^\eta + \bar{c}\mathbf{C}_M^\eta\right)\eta^*, I_{yy}/S]$

The robust-adaptive controllers for each subsystem are displayed in Table 44, where expressions ($\mathbf{\Psi}_1(\mathbf{x})$,$\mathbf{\Psi}_2(\mathbf{x})$,$\mathbf{\Psi}_3(\mathbf{x})$) and ($\mathbf{B}_1(\mathbf{x})$,$\mathbf{B}_3(\mathbf{x})$) are called regressor and input matrices, respectively, [104] and $\mathrm{Proj}_{\hat{\boldsymbol{\theta}} \in \boldsymbol{\Theta}}(\cdot)$ is a smooth parameter projection operator [174]. For each subsystem, a control Lyapunov function candidate is selected and a robust-adaptive control law is designed to ensure that the closed-loop stability of rigid-body dynamics, where a complete characterization of the internal (zero) dynamics includes the structural dynamics. The resulting control gains (k_1, k_2, k_3, k_4, k_5, k_6) and adaptive gain matrices ($\Gamma_1 \in \mathbb{R}^{16\times16}$, $\Gamma_2 \in \mathbb{R}^{4\times4}$, $\Gamma_3 \in \mathbb{R}^{11\times11}$) can then be tuned to achieve the desired performance tracking of reference trajectories (h_{ref},V_{ref}) and intermediate state commands (γ_{cmd},α_{cmd},Q_{cmd}). Prior to simulation, the reference and command trajectories are defined such that the asymptotic values yield the desired trim condition of the rigid-body state, $x^* = [V^*, h^*, 0, \alpha^*, 0]^T$, that is, $\lim_{t\to\infty} V_{\mathrm{ref}}(t) = V^*$, $\lim_{t\to\infty} h_{\mathrm{ref}}(t) = h^*$, and $\lim_{t\to\infty} \alpha_{\mathrm{cmd}}(t) = \alpha^*$, whereas $\lim_{t\to\infty} \gamma_{\mathrm{cmd}}(t) = 0$ and $\lim_{t\to\infty} Q_{\mathrm{cmd}}(t) = 0$. Therefore, the tracking error to be regulated to zero is defined as $\tilde{x} = \left[\tilde{V}, \tilde{h}, \tilde{\gamma}, \tilde{\alpha}, \tilde{Q}\right]^T := [V - V_{\mathrm{ref}}, h - h_{\mathrm{ref}}, \gamma - \gamma_{\mathrm{cmd}}, \alpha - \alpha_{\mathrm{cmd}}, Q - Q_{\mathrm{cmd}}]^T$.

11.2.3.5 Actuator Dynamics

Simple first and second order actuator models (contained within the original model) were used in each of the control channels: canard (δ_c) - $\frac{0.01}{0.01s^2+0.95s+25}$ elevator (δ_e) - $\frac{0.01}{0.01s^2+0.95s+25}$, fuel-equivalence-ratio (Φ) - $\frac{20}{s+20}$, (Note: $\bar{A}_D$ not used in this work). Elevator position and rate saturation become very important given the vehicle's (open loop) unstable dynamics [86]. The effects of the actuator dynamics were not considered during controller design.

11.2.3.6 Region of Admissible State and Control Action

As mentioned previously, the GHV nonlinear robust-adaptive flight controller utilized in this work takes into account only cruise trajectories and does not consider the ascent or reentry vehicle-type trajectories. As a consequence, the velocity and altitude references and the set point for the angle of attack are generated to satisfy the bounds shown in Table 45, which determine the flight envelope, together with the admissible range for the control inputs. Herein, $\mathcal{A} \in \mathbb{R}^8$ is denoted as the admissible region for all variables in Table 45.

Table 45: Admissible regions, $\mathcal{A}$, for states, inputs, dynamic pressure, and Mach number.

Symbol	**Lower bound**	**Upper bound**
h	85,000 (ft)	135,000 (ft)
α	-5 (deg)	15 deg
Q	-10 (deg/sec)	10 (deg/sec)
Φ	0.05	1.2
δ_c	-20 (deg)	20 (deg)
δ_e	-20 (deg)	20 (deg)
$\bar{q}$	500 (lbf/ft^2)	2,000 (lbf/ft^2)
M_∞	5	12

11.2.4 Simulation of Notional SCRAMjet-Powered Flight Test

This section is dedicated to the demonstration of the notional SCRAMjet flight, described previously in Section 11.2, for stead-level flight at $h = 99,826.00$ (ft), $V = 10,797.03$ (ft/sec), and $\alpha = 3.5$ (deg). Prior to dynamic simulation a trim analysis, followed by a controller gains Monte Carlo tuning exercise were conducted to ensure sustained steady-level flight at the desired conditions. The procedures for these analyses is found in Appendix G and Appendix H, respectively. Numerical results for these analyses are shown below in Tables 46 and 47. The GHV flight dynamic simulation is partitioned into three sequential control phases over a simulation time of $t_{\text{sim}} = 20$ (sec): (i) $t_{\text{sim}} = [0, 2]$ (sec) – transient stabilizing flight, (ii) $t_{\text{sim}} = (2, 18]$ (sec) – multi-sine excitation; (iii) $t_{\text{sim}} = (18, 20]$ (sec) transient stabilizing flight. In these simulations the numerical RK4 integrator, described in Section 10.2.3, was used here with the time step $h = 1 \times 10^{-3}$ (sec). At every timestep, the controller was called to compute new command inputs, making the implementation here a digital (zero-order-hold) controller with sampling frequency $T_s = 1 \times 10^{-3}$ (sec).

Table 46: Trim analysis results from the analysis described in Appendix G for steady-level flight at $h = 99,826.0$ (ft), $V = 10,797.0323$ (ft/sec), and $\alpha = 3.5$ (deg).

Symbol	η_f	η_a	Φ	δ_c	δ_e
Value	2.7891	1.3179	0.2288	-0.1073	0.061465

Table 47: Summary of tuned controller gains using Monte Carlo analysis described in Appendix H to evaluate stability success percentage as an assessment for robustness.

Gain	**Value**	**Gain Matrix**	**Values**
k_1	100	$\text{diag}(\Gamma_1)$	1e-4 × [1e5,1e4,100,1,1e4,100,1,1,1e4,1,1000,10,10,10,1,1]
k_2	1×10^{-4}	$\text{diag}(\Gamma_2)$	1e4 × [40,1,0.1,1000]
k_3	100	$\text{diag}(\Gamma_3)$	1e3 × [10,10,1000,100,1e4,1000,100,1e4,1e4,1000,1,10]
k_4	3		
k_5	3		

Figure 120 describes the design of a notional multi-sine perturbative excitation signal. The normalized power spectra provides for the intuitive inspection of how much energy that each frequency component contains. Given fixed amplitude and frequency parameters, the effect of the phase angles is to essentially define the signal shape, which can be chosen or designed as desired. Within the nonlinear robust-adaptive flight controller, the reference models are used to determine both control inputs (Φ, δ_c, δ_e) and virtual commands (γ_{cmd}, α_{cmd}, Q_{cmd}) and requires higher-order reference models to be computed, as discussed in the work by Fiorentini [104]. For the multi-sines functional form of Equation (80), the computation of derivatives, term by term, is not an analytically difficult task. Figure 121 shows the resulting higher-order reference models. Notice here that the power spectra of the higher-order reference models increases significantly for increasing order as indicated by the increases in composition signal amplitudes.

Figures 122 – 126 show the numerical simulation results for the GHV rigid-body, flexible, control input, output, and adaptive parameter state responses. For verification of model correctness, the notional GHV simulation was implemented twice: (i) first in MATLAB (because prototyping and debugging is easier) and then in C++ (to enable the computation of higher-order VAEs). As seen below, both of these implementations yield identical results.

Initial conditions for states, inputs, and outputs were set to the trimmed values, but for the adaptive states the nominal *a priori* aero-propulsive-elastic coefficients (see Appendix F) were used to compute the initial conditions of ($\boldsymbol{\theta}_1$, $\boldsymbol{\theta}_2$, $\boldsymbol{\theta}_3$) according to Table 44. Figure 127 shows the state feedback error signals that are regulated by the nonlinear robust-adaptive light controller with asymptotic stability. Notice that for the first phase of flight some of the error signals diverge from the initial conditions (trim state), but that after the multi-sine excitation signal has ended, these error signals quickly decay with reducing in magnitude.

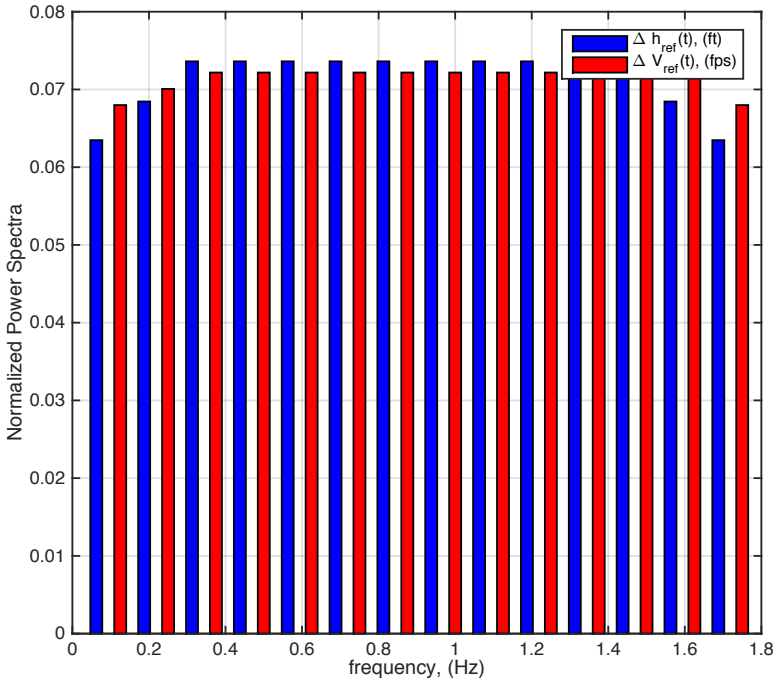

(a) $A_k + k$

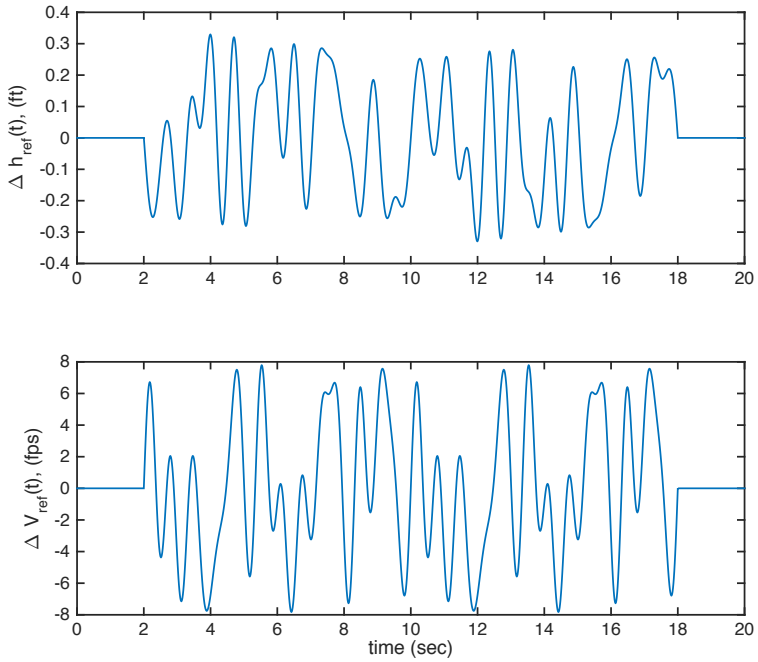

(b) $A_k + k + \phi_k$

Figure 120: Example (baseline) multi-sine perturbative inputs for perturbing nonlinear adaptive controller reference models: (a) amplitude/frequency power spectra, (b) altitude and velocity multi-sine transient responses ($h_{\text{ref}}(t)$ and $V_{\text{ref}}(t)$).

Table 48: Multi-Sine baseline input design for the SCRAMjet-powered stead-level flight testing at $h = 99,826.00$ (ft), $V = 10,797.03$ (ft/sec), and $\alpha = 3.5$ (deg) with $T = 20.0$ (sec).

Input	A_k, (deg)	k	ϕ_k, (rad)	RPF
h_{ref}	0.0650	1	0.1356	1.4274
	0.0675	3	2.7368	
	0.0700	5	-0.3800	
	0.0700	7	-0.3101	
	0.0700	9	1.2786	
	0.0700	11	3.1393	
	0.0700	13	-1.2020	
	0.0700	15	-1.5385	
	0.0700	17	2.7439	
	0.0700	19	-0.1261	
	0.0700	21	2.6789	
	0.0700	23	2.4822	
	0.0675	25	0.8446	
	0.0650	27	-1.2219	
V_{ref}	1.6475	2	3.1024	1.3807
	1.6725	4	-0.0255	
	1.6975	6	0.7765	
	1.6975	8	-0.9669	
	1.6975	10	-1.0068	
	1.6975	12	0.9306	
	1.6975	14	-0.0231	
	1.6975	16	-1.3301	
	1.6975	18	0.4577	
	1.6975	20	0.8148	
	1.6975	22	1.8706	
	1.6975	24	0.2096	
	1.6975	26	-1.4572	
	1.6475	28	-0.1935	

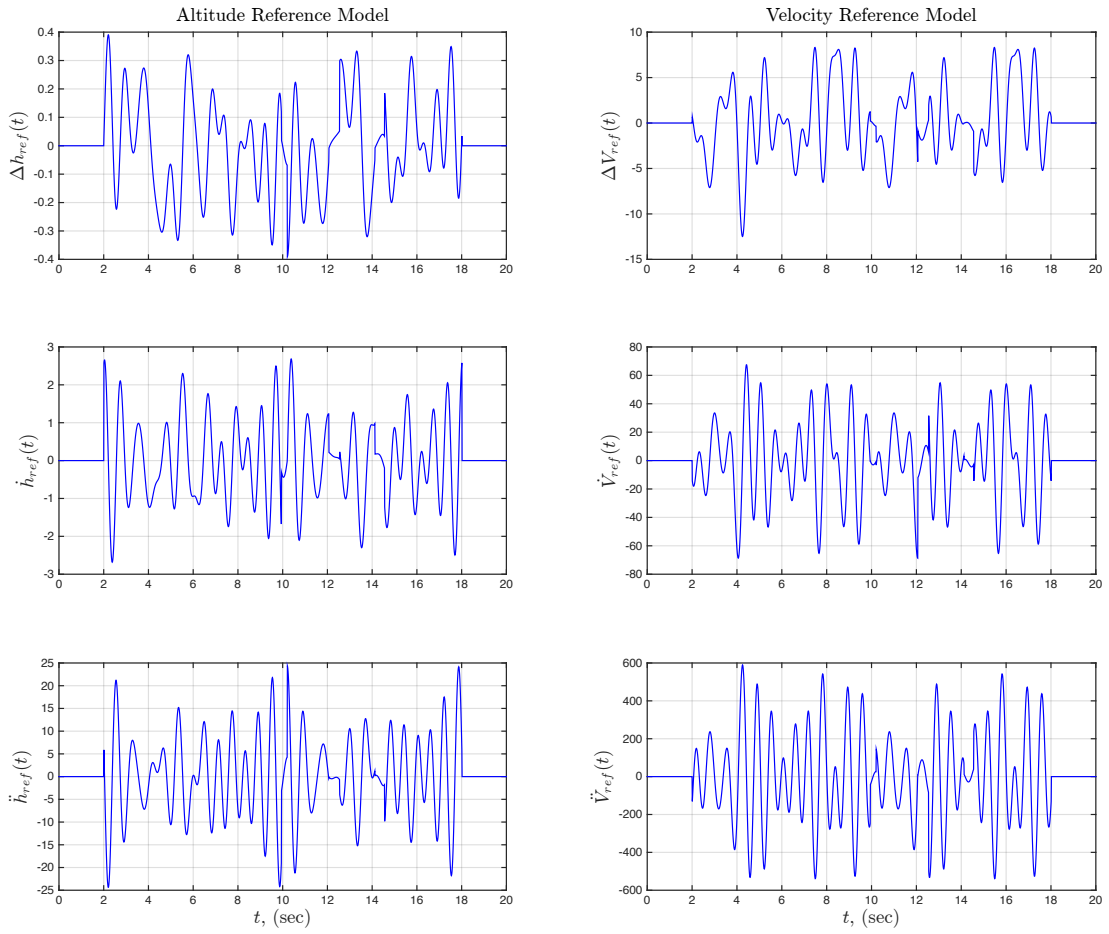

Figure 121: GHV multisine reference models and higher-order reference models for virtual commands within the nonlinear robust-adaptive flight controller.

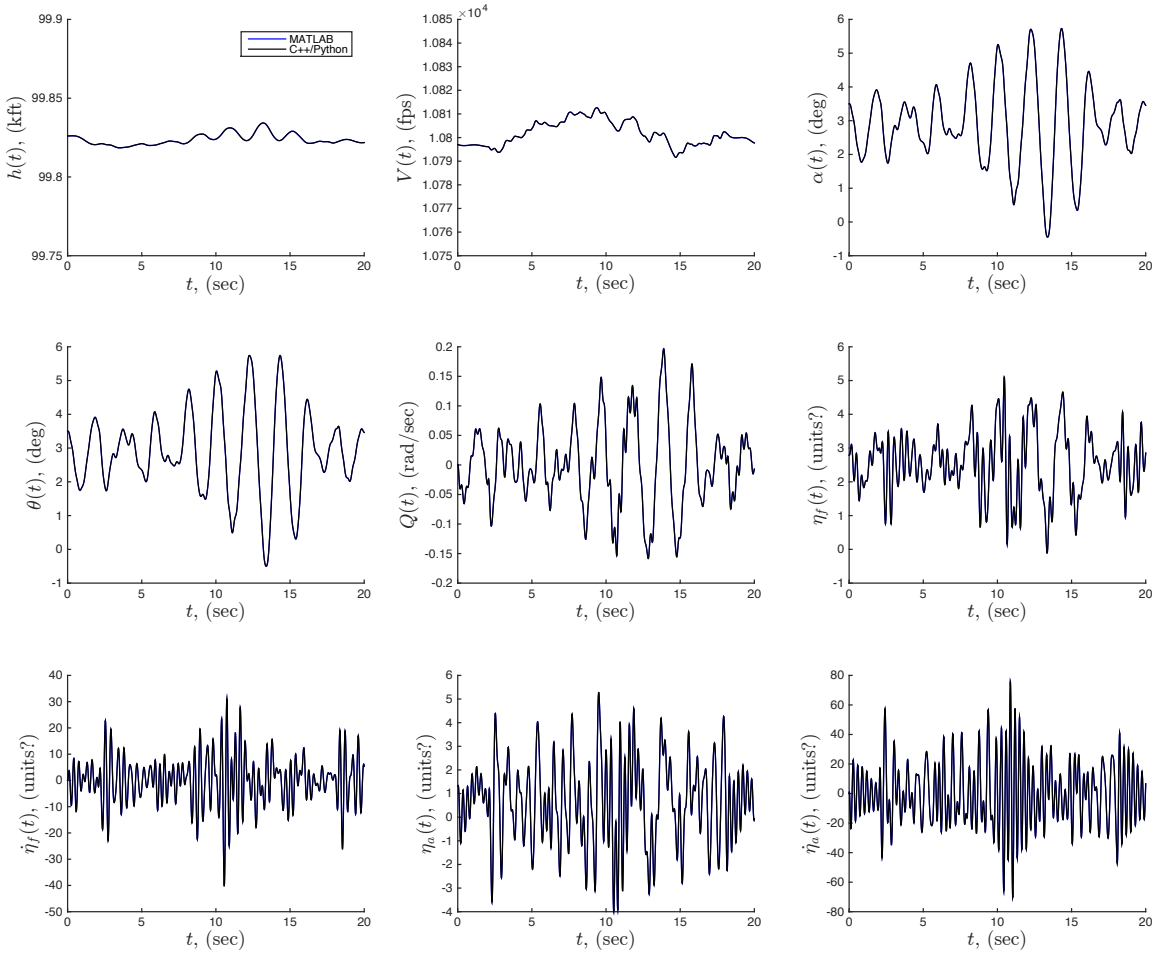

Figure 122: GHV controlled rigid-body and elastic coordinate state trajectories, implemented in both C++ (solid black) and MATLAB (solid blue).

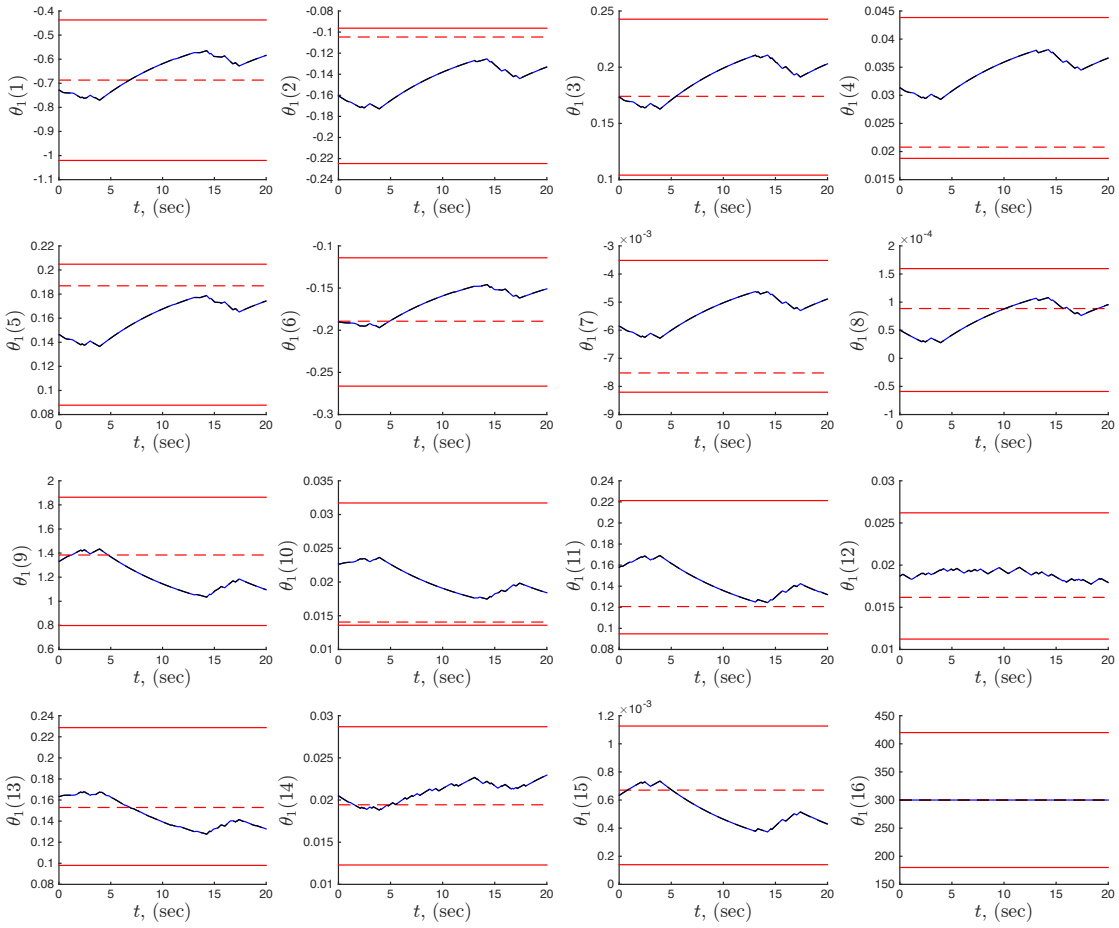

Figure 123: Simulation results of the (V)-subsystem adaptive state evolution, implemented in C++ (dashed black) and MATLAB (solid blue), where the dashed red lines represent the *a priori* values of $\boldsymbol{\theta}_1$ and the solid red lines represent bounds on the admissible region $\boldsymbol{\Theta}_1$.

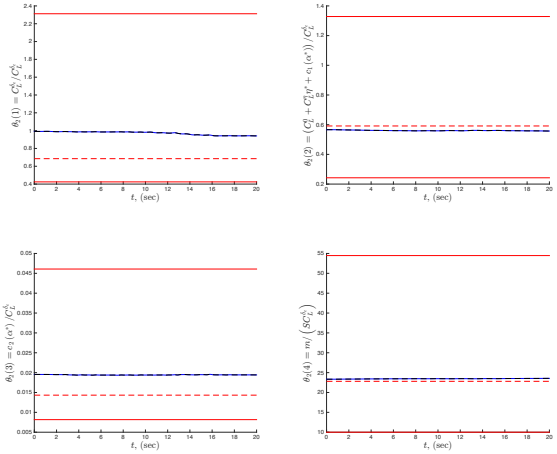

Figure 124: Simulation results of the (h,γ)-subsystem adaptive state evolution, implemented in C++ (dashed black) and MATLAB (solid blue), where the dashed red lines represent the *a priori* values of $\boldsymbol{\theta}_2$ and the solid red lines represent bounds on the admissible region $\boldsymbol{\Theta}_2$.

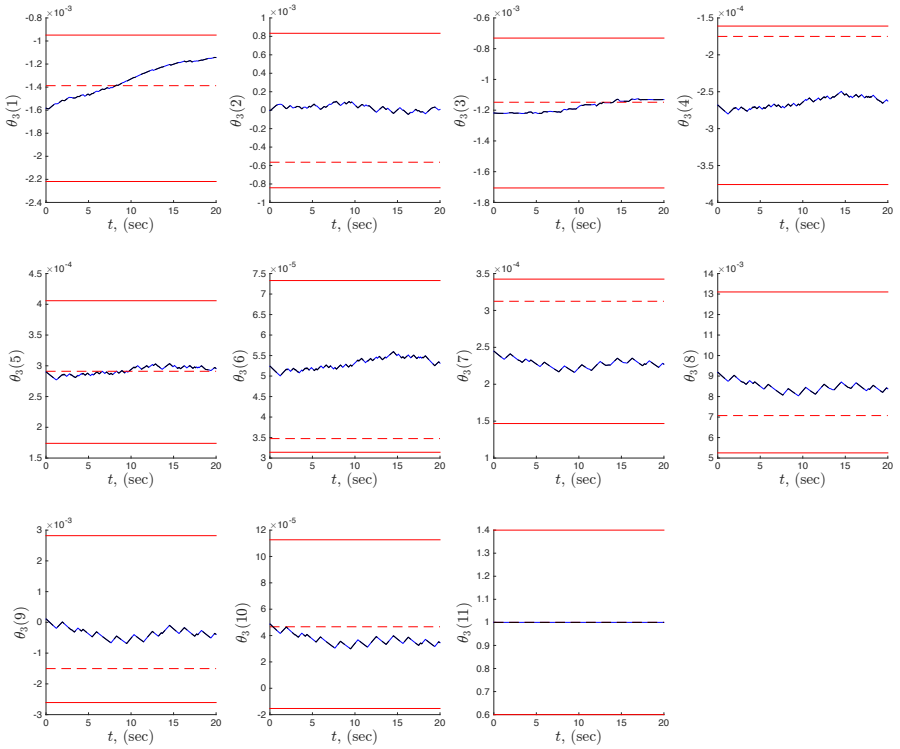

Figure 125: Simulation results of the (α,Q)-subsystem adaptive state evolution, implemented in C++ (dashed black) and MATLAB (solid blue), where the dashed red lines represent the *a priori* values of $\boldsymbol{\theta}_3$ and the solid red lines represent bounds on the admissible region $\boldsymbol{\Theta}_3$.

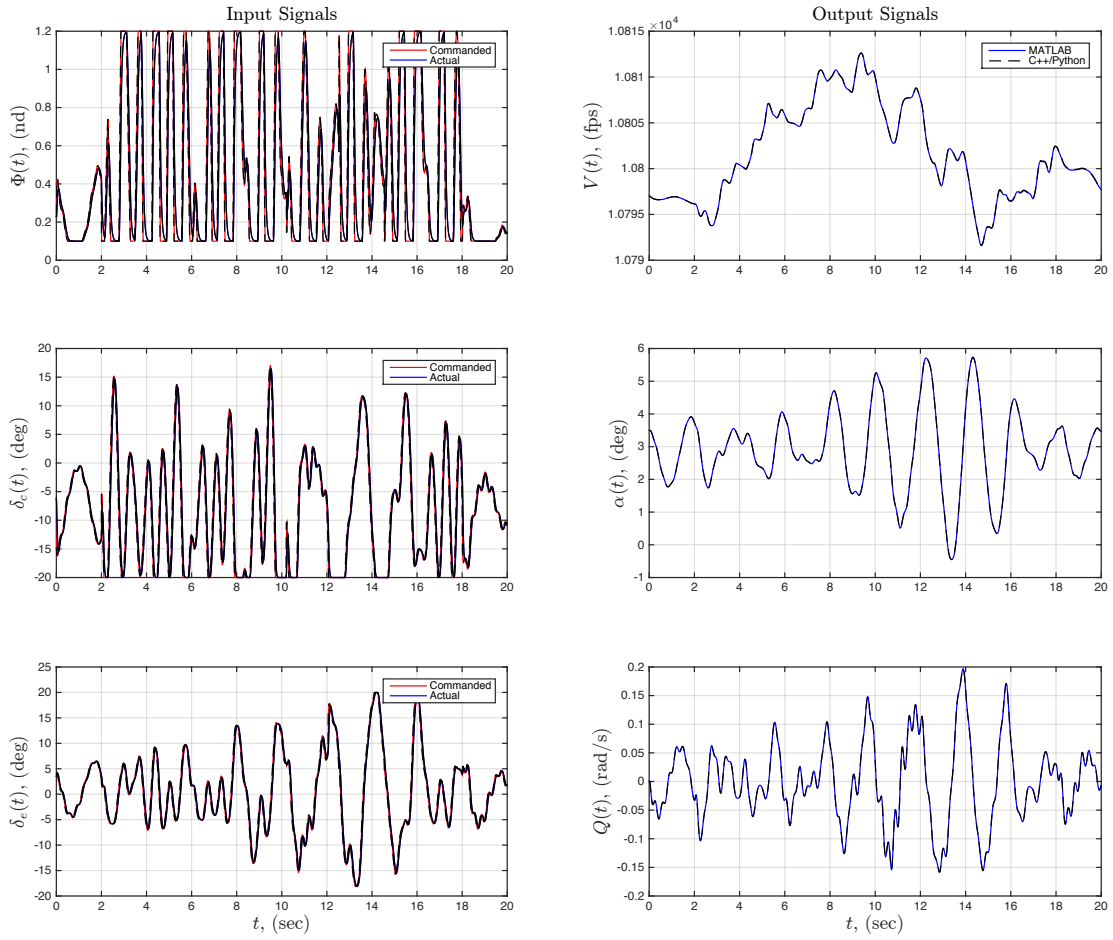

Figure 126: GHV input/output signals, implemented in both C++ (dashed black) and MATLAB (solid blue), shown for the output signals. For the input signals, the commanded control signals (solid red) and actual signals (solid blue) illustrate the effects of actuator lag.

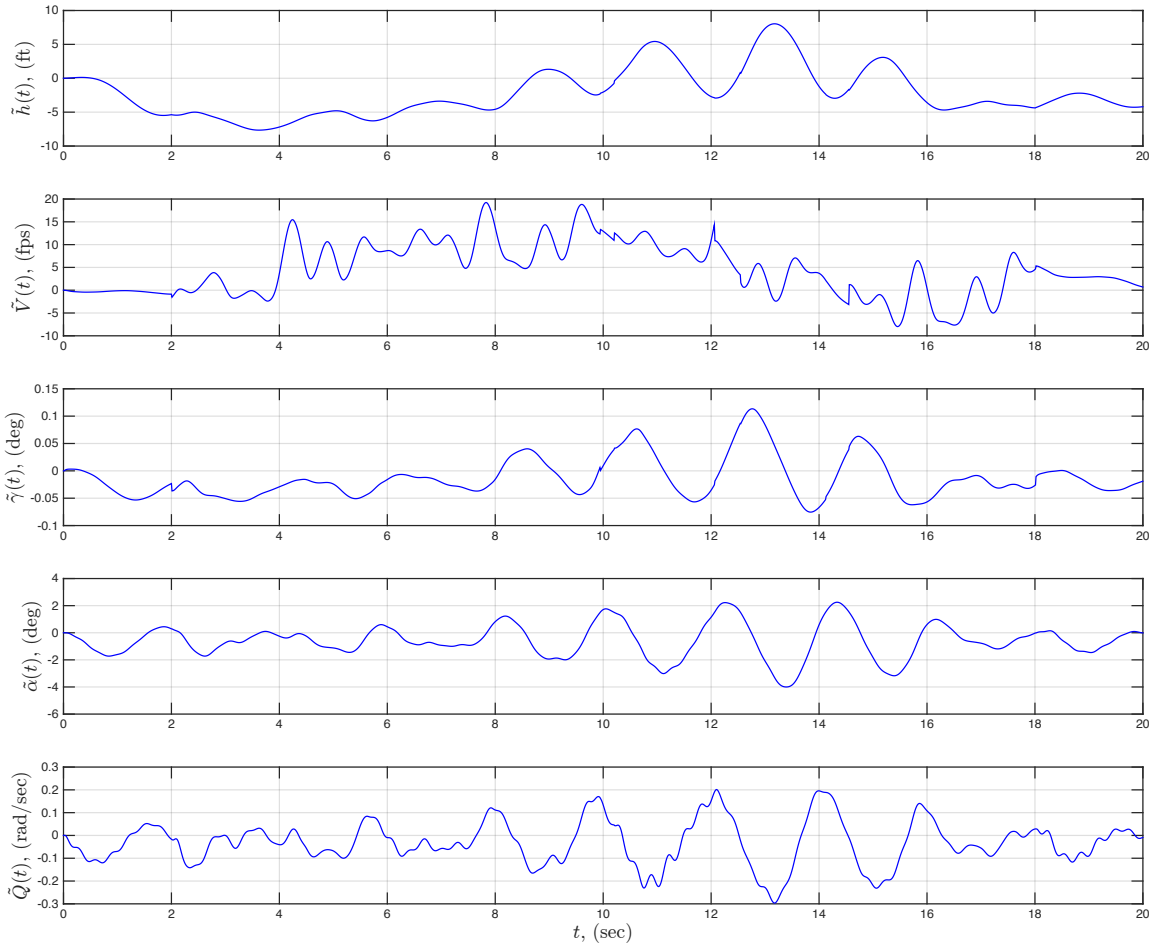

Figure 127: GHV nonlinear robust-adaptive flight controller state feedback error signal trajectories (altitude error – $\tilde{h}(t)$, velocity error – $\tilde{V}(t)$, flight path angle error – $\tilde{\gamma}(t)$, aerodynamic angle of attack error – $\tilde{\alpha}(t)$, and pitch rate error $\tilde{Q}(t)$).

11.2.5 Exp't #2: VAE-GHV Feasibility Assessment

The focus of this section is to revisit **HYP. #2.2** to investigate the computational complexity of implementing VAE's to compute solutions to higher-order equations of variation for the GHV flight dynamic model, previously discussed in Section 11.2.3. Recall that in Section 9.5 that **HYP. #2.2** was posed in response to **RQ. #2.2**, which concerns the feasibility of VAE implementation for large industrial-sized aerospace flight dynamic systems from a computational complexity perspective. **Exp't #3** partially addressed this issue in Section 10.4 by observing that fast, dense multivariate polynomial multiplication is a known computational bottleneck and then investigating the computational complexities on the implementation approach outlined in Section 10.1.2. Here it is observed that there are several mechanisms that serve as future work to the current implementation to improve complexities, but that the confirmation of **HYP. #2.2** ultimately requires the implementation of VAE's on a large flight dynamic model such as the GHV model outline in Section 11.2.3

Table 49 summarized computer specifications for three machines used in this study, which involved implementation of the codes on three separate operating systems: (i) Linux (CentOS, (ii) Windows 7, and (iii) mac OS X (El Capitan). Figure 128 summarizes the results of this analysis for $1 \leq N_e \leq 5$, where simulation time is again measured, as described in Section 10.4. Recall, that the VAE's implemented in this problem are 8-dimensional (*i.e.* $\delta\boldsymbol{\theta} = \left[\delta C_T^{\alpha^3\Phi}, \delta C_T^{\alpha^2\Phi}, \delta C_T^{\alpha\Phi}, \delta C_T^{\Phi}, \delta C_T^{\alpha^3}, \delta C_T^{\alpha^2}, \delta C_T^{\alpha}, \delta C_T^{0}\right]^T$). As shown, the computational time complexity for increasing order N_e scales exponentially for all three machines, where **Computer 1** has the best performance but still requires 548.61 minutes (9.14 hours) to compute numerical solutions to up to 4^{th}-order equations of variation. As cumbersome as this seems, the GHV system consists of 5 rigid-body, 4 flexible, 5 actuator, and 31 adaptive states for a total of 45 states, and for $N_e = 5$ and $N_d = 8$ each state (polynomial) has 495 coefficients, which means this simulation actually consists of $45 \times 495 = 22,275$ state variables.

Table 49: Summary of computer specifications used to generate the simulation time results shown in Figure 128.

	Computer 1	Computer 2	Computer 3
operating system:	*Linux: CentOS 6.6 Final*	*Windows 7 Enterprise (Service Pack 1)*	*OS X 10.11.4 (El Capitan)*
processor:	*8 x Intel Core i7-2600 CPU @ 3.40 GHz*	*Intel® Core™ i7-2600 CPU @ 3.40GHz 3.40 GHz*	*2.6 GHz Intel Core i5*
memory:	*16.00 GB 1333 MHz DDR3*	*8.00 GB (4x)*	*8.00 GB 1600 MHz DDR3*
compiler:	*gcc version 4.9.2 (GCC), thread model: posix*	*gcc version 4.5.2 (GCC), thread model: win32*	*Apple LLVM version 7.3.0 (clang-703.0.29)*

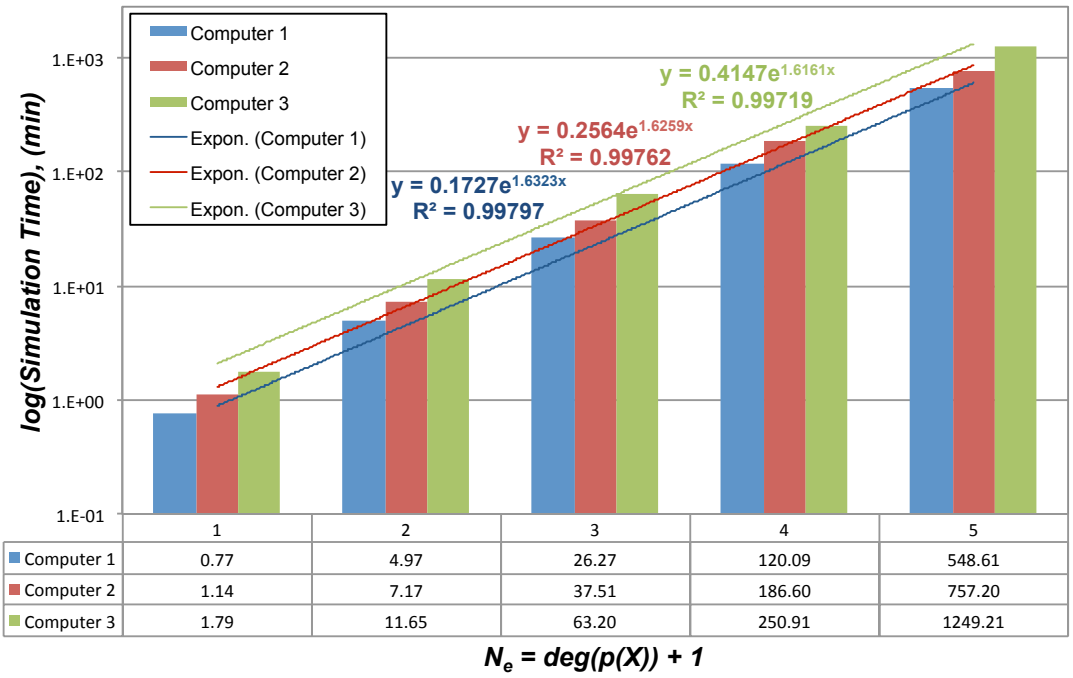

Figure 128: Computational time complexity scaling results for increasing order N_e on the GHV simulation example described in Section 11.2.4.

11.2.6 GHV Example Virtual Experiment

In this section, the notional SCRAMjet flight test described in the previous section is now simulated as a virtual experiment (VX), generating representative experimental data for the subsequent evaluation of information quality. Table 50 summarizes a hypothetical instrumentation and measurement suite (IMS) implemented in this dissertation. Table 51 shows the two sets of model parameters that were utilized: (1) a nominal set to be used in experiment design, which represents the current state of knowledge about a physical model, and (2) a perturbed set to be used to perform a virtual experiment by simulating the effects of the *circulatory problem*, as discussed in Section 5.2. Figure 129 shows simulation results for an uncertainty propagation analysis using $N_e = 5$ VAEs. The VX inputs and outputs are shown in Figures 130 and 131, respectively.

Table 50: Instrumentation characteristics (notional) used for the GHV flight testing virtual experimentation.

Measured	**Transducer Quantity**	**Resolution**	**RMS Measurement Error**	**Measurement Bias**
h, (m)	Altimeter	10.00 (0.05 millibars)	2.7500	0.0000
V, (m/s)	Pressure transducer	0.0370	0.8900	0.0000
α, (deg)	Flow vane	0.0290	0.0270	0.0000
θ, (deg)	Vertical gyro	0.0980	0.0920	0.0000
Q, (deg/s)	Rate gyro	0.0320	0.1900	0.0000
a_x, (g)	Accelerometer	0.0010	0.0046	0.0000
δ_c, (deg)	Potentiometer	0.0100	0.0037	0.0000
δ_e, (deg)	Potentiometer	0.0100	0.0061	0.0000

Table 51: GHV VX: C_T COM model SnC coefficient nominal parameter and perturbed values.

	C_T^0	C_T^α	$C_T^{\alpha^2}$	$C_T^{\alpha^3}$	C_T^Φ	$C_T^{\Phi\alpha}$	$C_T^{\Phi\alpha^2}$	$C_T^{\Phi\alpha^3}$
$\mathbf{p}_0$	1.06e-04	-8.77e-03	-1.44e-01	9.01e-02	2.55e-02	1.92e-01	-1.09e-01	-7.21e-01
$\boldsymbol{\delta}\mathbf{p}$	1.75e-05	2.31e-03	-5.39e-04	-3.59e-02	-1.56e-02	5.4e-02	-1.74e-02	2.82e-01

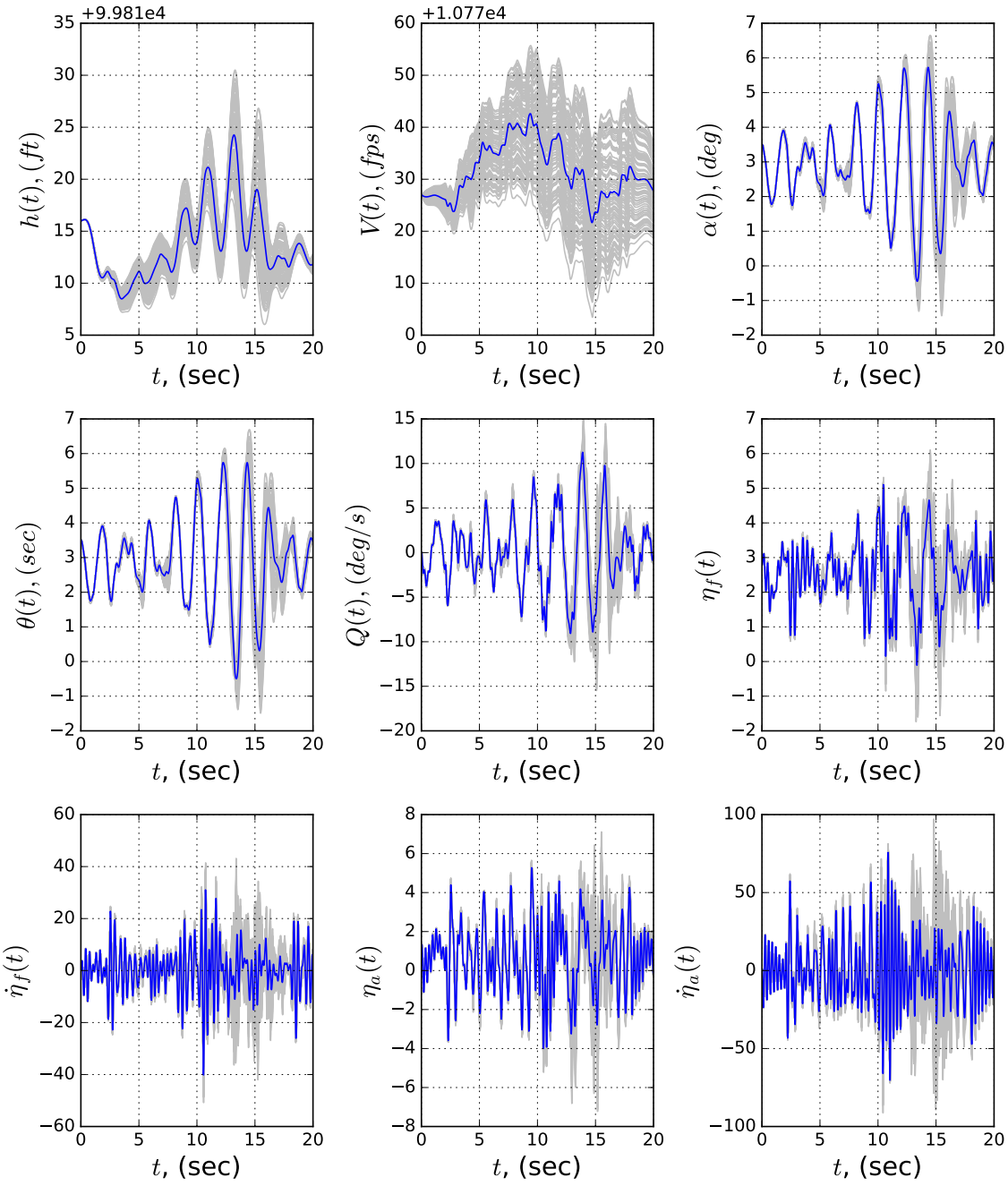

Figure 129: GHV baseline states (blue) and parametric uncertainty propagation analysis (grey), generated with $N_e = 5$ VAEs.

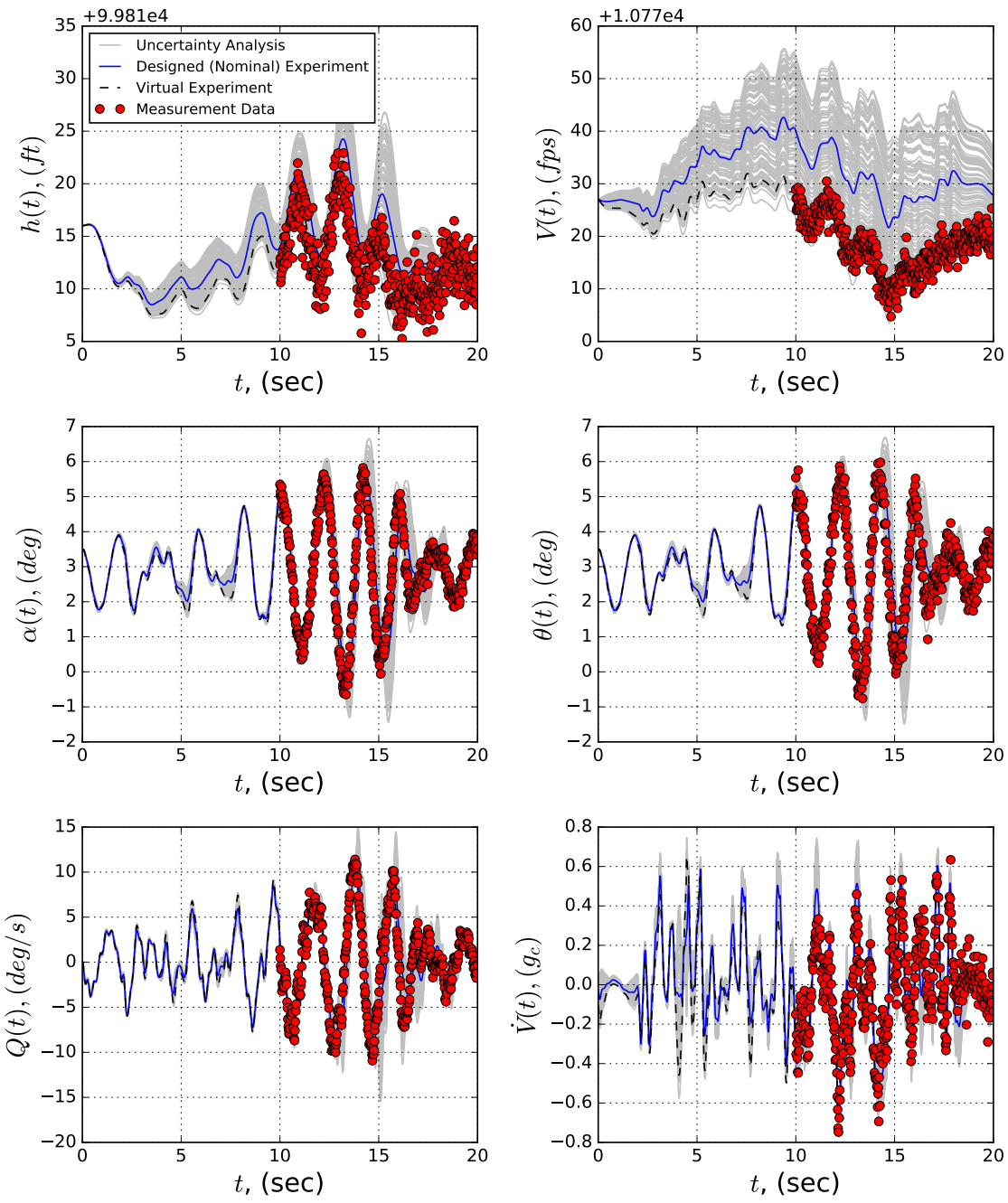

Figure 130: GHV virtual experiment output responses: design (nominal) experiment (solid blue), VAE uncertainty propagation analysis (grey), perturbed virtual experiment (dashed black), and virtual experiment measurement data (red dots).

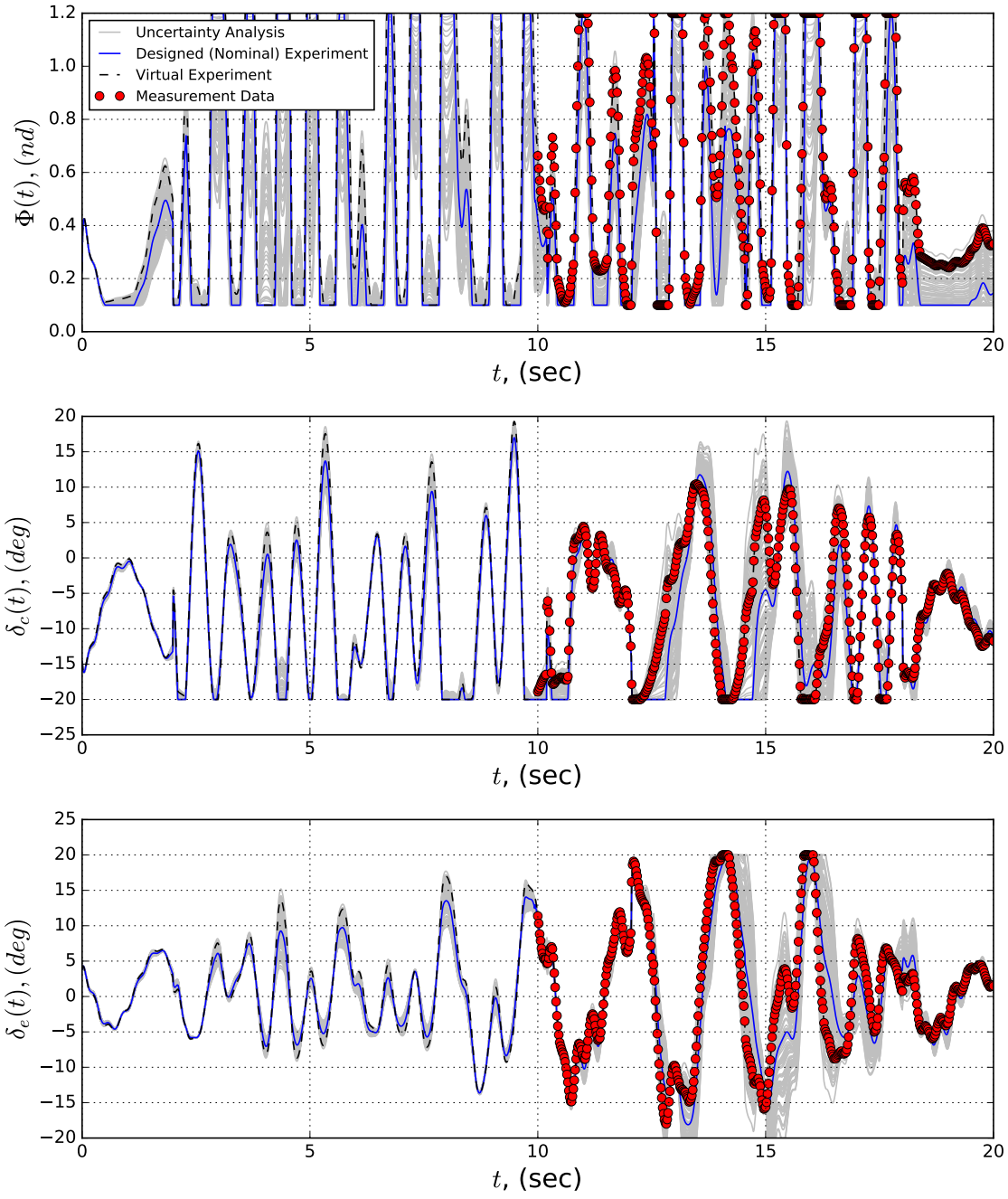

Figure 131: GHV virtual experiment input responses: design (nominal) experiment (solid blue), VAE uncertainty propagation analysis (grey), perturbed virtual experiment (dashed black), and virtual experiment measurement data (red dots).

Figure 132 shows associated *a posteriori* information metrics for the VX results above, where $N_e = 5$. It is important to recall that the computation of these metrics is now automated, as opposed to the traditional approach, involving symbolic derivation to derive the necessary 1^{st}-order expressions and is no small task to manually develop for this result. Any of these metrics can be used within an optimization framework for dynamic experiment design, and perhaps multiple metrics can be used for multi-objective experiment design, since the information matrix is in fact a symmetric matrix. For the remainder of this chapter, the experimental procedure of Table 27 will again be conducted for the design of GHV flight tests to determine robust-optimality of information metrics.

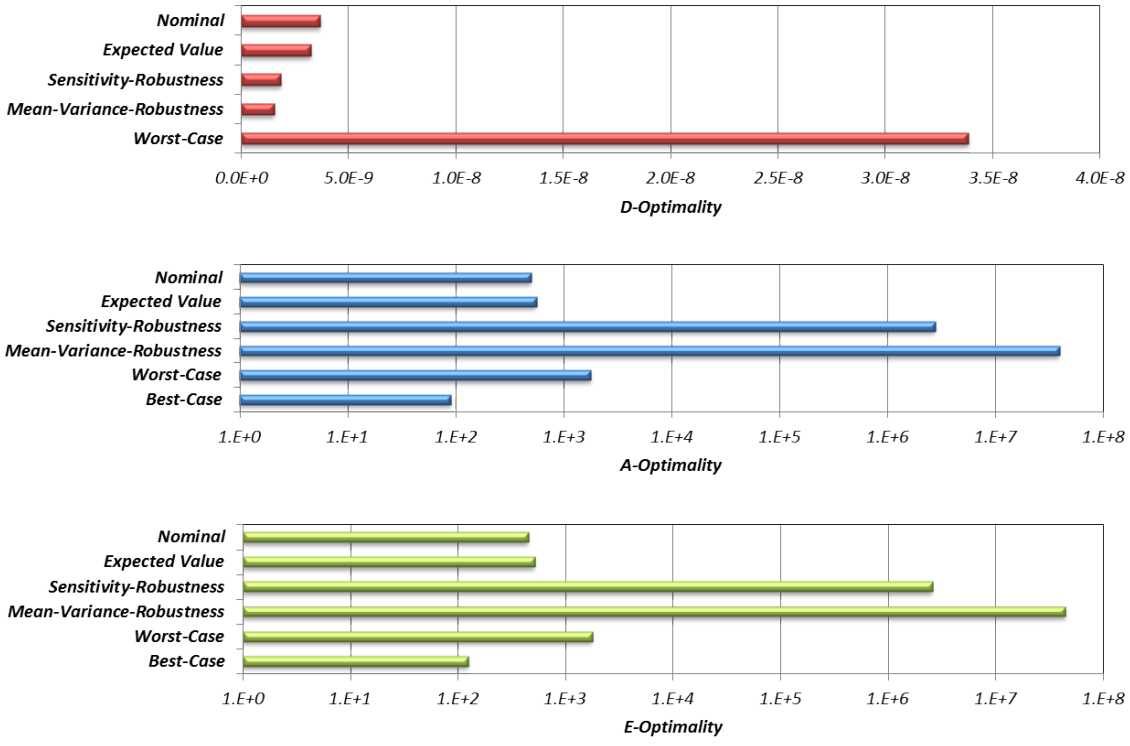

Figure 132: GHV virtual experiment information metrics, computed from the VX input/output measurement data of Figures 130 and 131.

Table 52 and Figure 133 show numerical predictions of best-estimator performance for system identification using the VX flight test data from Figures 130 and 131. Clearly, this flight test data has poor information quality for estimation of $C_{T_\alpha^3}$ and $C_{T_{\Phi\alpha^3}}$, since Table 52 represents the best estimator performance possible. As can be seen here, percent error in all parameters is very high, but especially for the $C_{T_\alpha^3}$ and $C_{T_{\Phi\alpha^3}}$ parameters, which is 2765% and 850%, respectively. The cause for this adverse performance is the relatively sparse amount of high-AoA data, and thus, the cause/effect relationship between high-AoA flight on propulsive SCRAMjet thrust forces is difficult to estimate from this test data. The *a posteriori* correlation matrix for these results suggest significant correlation in between most parameters.

An alternate way to view the best estimator performance (and perhaps a more informative way) is via a multivariate tile plot of 2D projections of the covariance hyper-ellipse of the best-estimator performance, as shown in Figure 132. All subplots have been scaled to ± 50 in both x,y-axes for relative comparison of 2D ellipse projections between each parameter. Again, $C_{T_\alpha^3}$ and $C_{T_{\Phi\alpha^3}}$ have poor information quality in this data, which translate to large 95% confidence ellipses (*i.e.* low confidence in predictions of values for these parameters). Here it is observed that the confidence intervals with respect to $C_{T_\alpha^3}$ and $C_{T_{\Phi\alpha^3}}$ is so high that the inspect of the confidence intervals of the other parameters is visually difficult to ascertain from the plots of Figure 132.

Table 52: Theoretical best-estimator performance for the GHV example VX.

Parameters	Nominal Value	Standard Error	Percent Error	95% C.I.	Correlation Matrix							
					C_{T_0}	C_{T_α}	$C_{T_{\alpha^2}}$	$C_{T_{\alpha^3}}$	C_{T_Φ}	$C_{T_{\Phi\alpha}}$	$C_{T_{\Phi\alpha^2}}$	$C_{T_{\Phi\alpha^3}}$
C_{T_0}	0.0001	2.0e-4	136.49	±2.0e-4	1.0							
C_{T_α}	-0.0063	0.02	243.75	±1.5e-2	-0.62	1.0						
$C_{T_{\alpha^2}}$	-0.1668	0.43	257.28	±0.43	0.34	-0.94	1.0					
$C_{T_{\alpha^3}}$	-0.1186	3.28	2765.26	±3.28	-0.21	0.86	-0.94	1.0				
C_{T_Φ}	0.0417	3.0e-3	0.83	±3.0e-4	-0.76	0.59	-0.42	0.33	1.0			
$C_{T_{\Phi\alpha}}$	0.1622	0.04	22.21	±3.6e-2	0.37	-0.74	0.73	-0.70	-0.77	1.0		
$C_{T_{\Phi\alpha^2}}$	-0.1657	0.94	566.98	±0.94	-0.20	0.72	-0.80	0.80	0.61	-0.97	1.0	
$C_{T_{\Phi\alpha^3}}$	-0.7920	6.73	850.17	±6.73	-0.11	-0.68	0.81	0.84	-0.51	0.91	-0.98	1.00

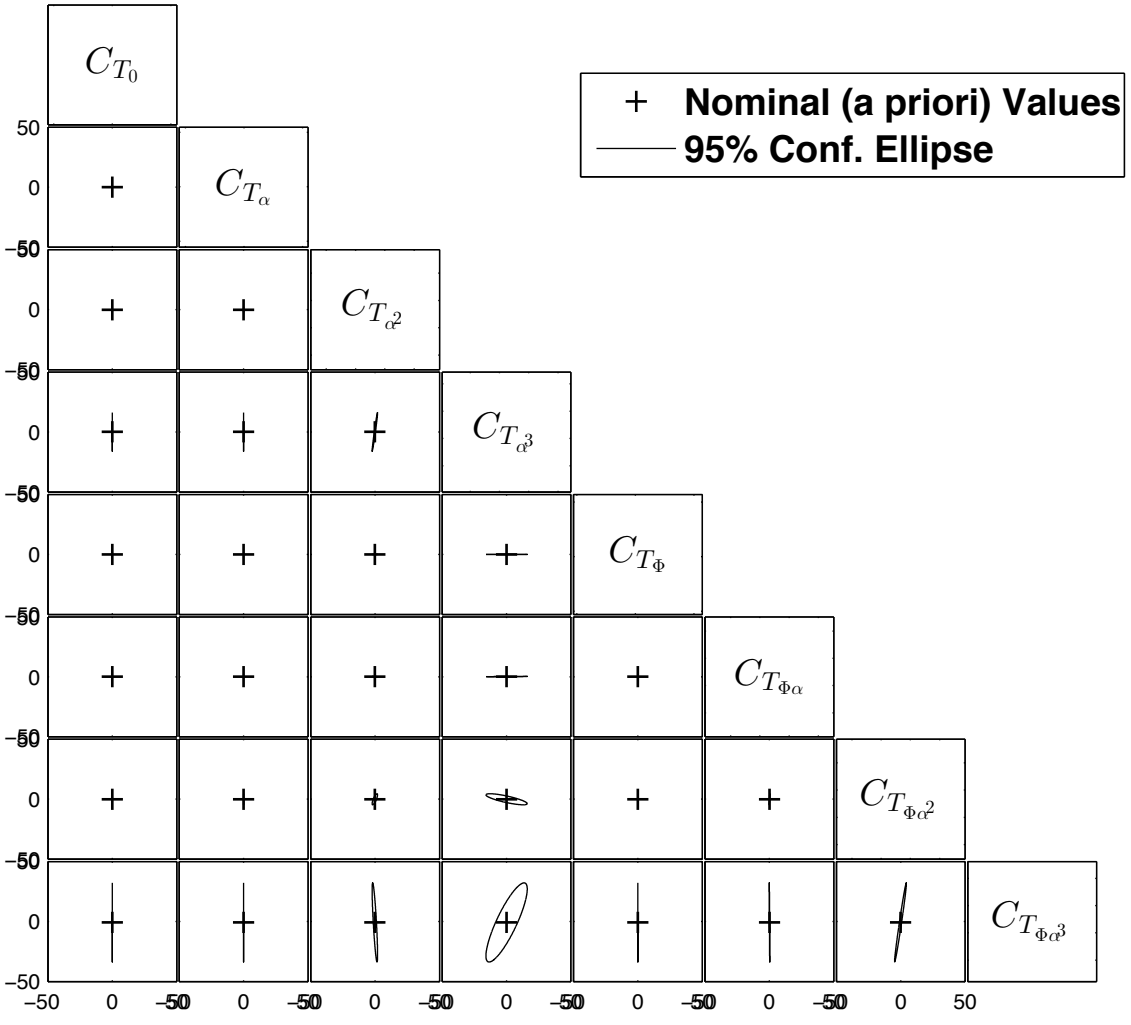

Figure 133: GHV virtual experiment *a posteriori* best-estimator parameter covariance Cramer-Ráo lower-bound (*i.e.* limiting case).

11.2.7 GHV Design of Experiments

In the following sections, techniques for the design of robust-optimal dynamic system identification experiments are explored for the GHV system, as described in the previous sections. The design vector described in Section 11.2.8 is used in the following 1000-case (Latin Hypercube) DOE studies.

Comparison of Nominal Information Metrics. Figure 134 shows the DOE results for the nominal (D,T,A,E)-Optimality information metrics. Base-10 logarithmic transformations are used here to scale information metrics. For the majority of points, strong correlation between the information metrics is observed with the exception of T-Optimality metrics. The best performing designs are highlighted as colored markers, where the (D,T)-Opt best designs are the same design. Note: (1) that the E-Opt best-case has the lowest (best) condition number of the four best-case designs, and (2) that all the best-case design fall in regions with little to no correlation.

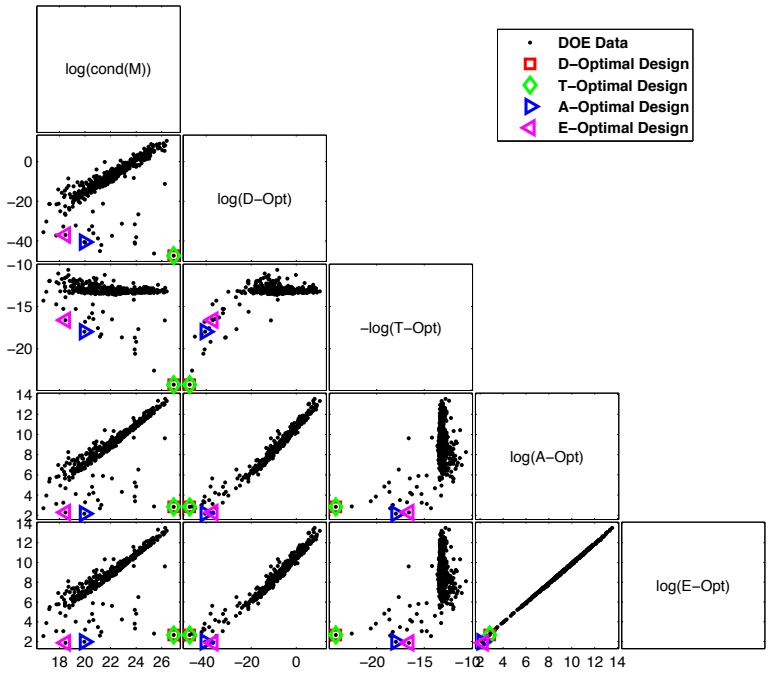

Figure 134: Multivariate scatter plot results for design of experiment results for nominal (D,T,A,E)-Optimality information metrics.

Figure 135 shows the experiment design vector for the top 20 performing experiments from Figure 134 (top 5 for each (D,T,A,E)-Optimality information metric) as a parallel coordinate plot. Here no apparent trends in the design vector are perceived as the phase angles arbitrarily change between [-π,π], which could potentially imply a multimodal design space.

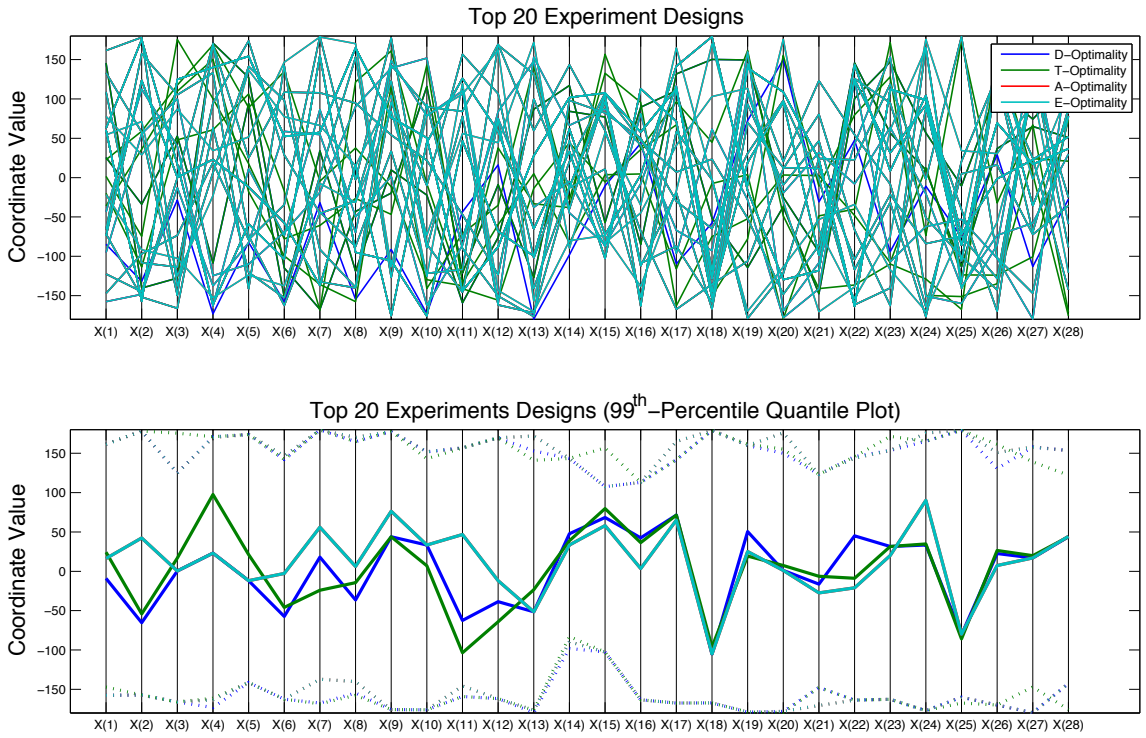

Figure 135: Parallel coordinates plot results for the top 20 performing experiment design vectors for nominal (D,T,A,E)-Optimality information metrics.

Comparison of Robust D-Optimality Information Metrics. Figure 136 shows the DOE results for the nominal (D,RD,ED,SR-D)-Optimality information metrics along with the information matrix condition number. For equivalent comparison between metrics computed via the nondeterministic (RD,ED) and deterministic (SR-D) metrics, 3rd-order state-to-parameter VAEs were used. Again base-10 logarithmic transformations are used here to scale information metrics. Strong correlations between the different information metrics are observed; however, there is a distinct bend in the SR-D-Opt comparison plots. The same design (highlighted as a red marker) is the best-case design for all four robust-optimality information metrics; however, this point is very poorly conditioned. In fact, it is the worst-conditioned experiment design of the entire set, which suggests that this design has very good information content for low-AoA SnC coefficients but also very poor information content for high-AoA SnC coefficients. As discussed in Section 5.3.4, this is a common deficiency of D-Optimal experiments.

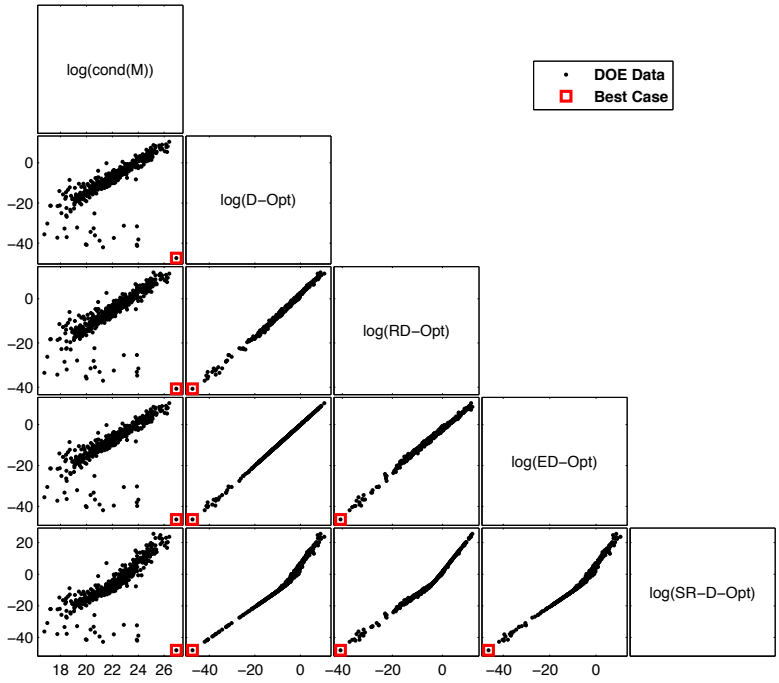

Figure 136: Multivariate scatter plot results for design of experiment results for nominal (D,ED,RD,SR-D)-Optimality information metrics.

Comparison of Robust A-Optimality Information Metrics. Figure 137 shows the DOE results for the nominal (A,RA,EA,SR-A)-Optimality information metrics along with the information matrix condition number. For equivalence comparison between metrics computed via the nondeterministic (RA,EA) and deterministic (SR-A) metrics, 3rd-order state-to-parameter sensitivities were computed. Again base-10 logarithmic transformations are used here to scale information metrics. Moderately strong to moderately weak correlations between the different information metrics are observed. The best performing designs are highlighted as colored markers, where the (RA,SR-A)-Opt best-case designs are the same design. Note: the (EA,RA,SR-A)-Opt best-case designs all have approximately the same condition number, while the A-Opt best-case design is a relatively better conditioned experiment.

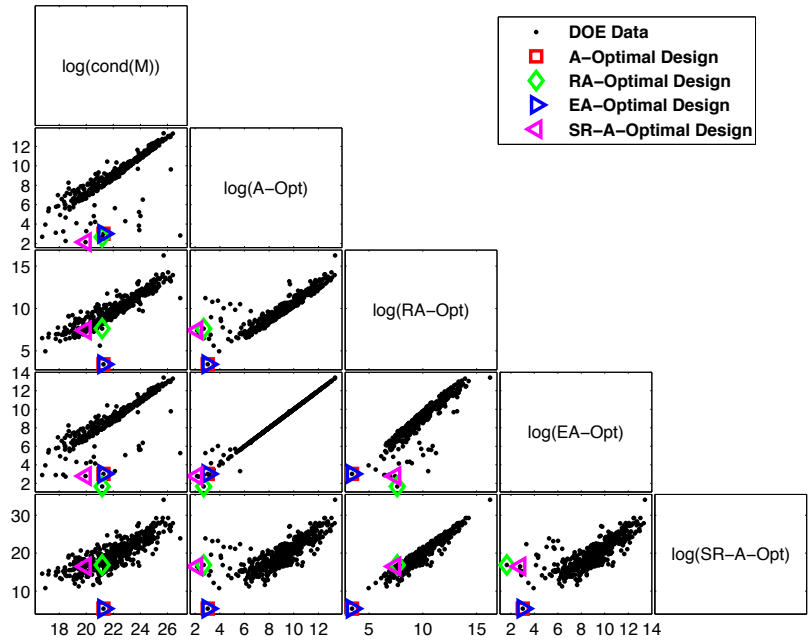

Figure 137: Multivariate scatter plot results for design of experiment results for nominal (A,EA,RA,SR-A)-Optimality information metrics.

Comparison of Robust E-Optimality Information Metrics. Figure 138 shows the DOE results for the nominal (E,RE,EE,SR-E)-Optimality information metrics along with the information matrix condition number. For equivalence comparison between metrics computed via the nondeterministic (RE,EE) and deterministic (SR-E) metrics, 3rd-order state-to-parameter sensitivities were computed. Again base-10 logarithmic transformations are used here to scale information metrics. Strong to moderately weak correlations between the different information metrics are observed. The best performing designs are highlighted as colored markers, where the (RE,SR-E)-Opt best-case designs are the same design. Note: the (EE,RE,SR-E)-Opt best-case designs all have approximately the same condition number, while the E-Opt best-case design is a relatively better conditioned experiment.

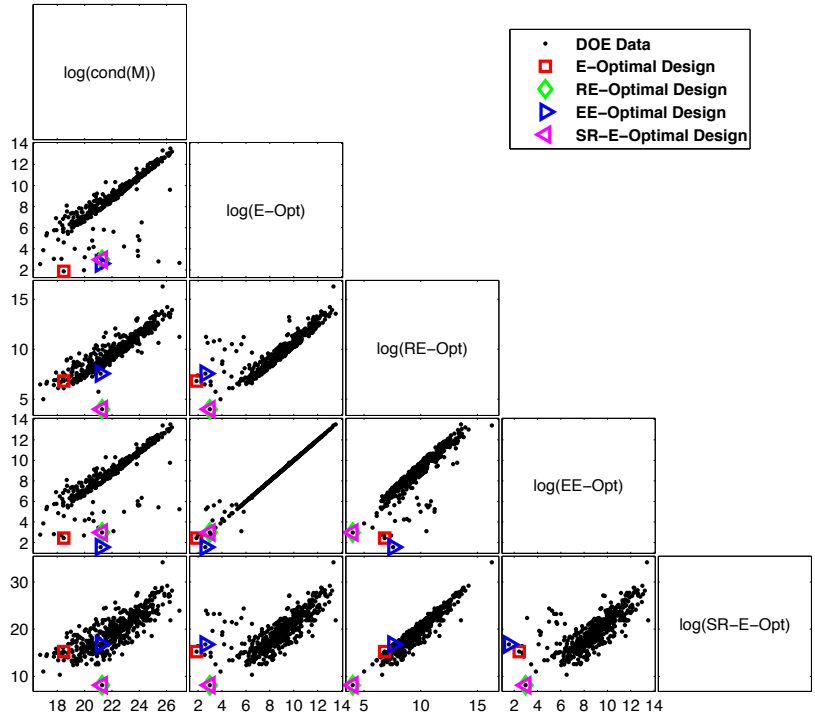

Figure 138: Multivariate scatter plot results for design of experiment results for nominal (E,EE,RE,SR-E)-Optimality information metrics.

11.2.8 GHV Robust-Optimal Flight Test Design

This section summarizes the design of robust-optimal dynamic system identification SCRAMjet-powered flight tests, from the perspective of a MDO problem formulation (shown in Equation (61) of Section 9.7), and the subsequent evaluation of design alternatives using Monte Carlo virtual experimentation, as discussed in the experimental procedure of Table 27. Here, the parametric integrated environment (PIE) refers to the collection and synthesis of the GHV physics-based models from Section 11.2.3, the sensor models of Table 50 from Section 11.2.6, the parametric statistical uncertainty models from Section 11.2.3.4, and parametric multi-sine perturbation signals from Section 11.2.2.

The experiment design vector for these MDO problems is chosen to be the phase angles ϕ_k of the multi-sine (baseline) design of Table 48, which are constrained to be bounded by $\pm\pi$. The amplitude and frequency parameters are fixed to the values in Table 48. (Robust)-optimal information metrics were computed using VAEs with $N_e = 3$ for equivalent comparison between deterministic and nondeterministic robust design approaches, which include: (D,T,A,E)-Opt (nominal information metrics) and (E($\cdot$),R($\cdot$),SR-($\cdot$))-Opt robust-optimal information metrics. Global stochastic optimization was performed via differential evolution using the software package PyGMO, which seamlessly leverages computational resources for parallel computation. Implementation details can be found in Appendix D.

Table 53 summarizes all optimized designs for the GHV SCRAMjet problem under multi-sine perturbative excitation. Each problem required 1-2 weeks of computation time, evaluating approximately 16,000 cases per problem. Here each flight test design is uniquely different, potentially suggesting multimodal design spaces.

Table 53: Summary of all GHV SCRAMjet-powered robust-optimal flight test designs.

		Nominal Designs				Minimax Designs		Sens.-Robust Designs	
		D-Opt	T-Opt	A-Opt	E-Opt	RD-Opt	RE-Opt	SR-D-Opt	SR-E-Opt
	Log(F(X))	-42.72	-97.78	-0.79	-1.07	-38.53	1.61	-43.61	-5.30
Design Vector, X	X(1)	2.61	1.31	-3.05	-0.55	0.36	-1.61	2.61	-2.99
	X(2)	0.36	-1.83	-2.45	-1.72	1.16	0.51	0.36	0.25
	X(3)	-2.50	1.62	2.33	-0.76	-1.91	-0.55	-2.50	1.11
	X(4)	1.17	-1.45	-2.84	-3.06	-0.74	0.27	1.17	1.18
	X(5)	1.07	-1.87	-2.85	1.87	-2.31	-2.61	1.07	-2.28
	X(6)	2.92	1.53	-2.29	-1.45	1.78	0.81	2.92	-1.73
	X(7)	-3.05	-0.61	0.75	0.52	0.89	1.43	-3.05	2.88
	X(8)	1.60	0.24	2.76	-2.98	3.10	2.56	1.60	-0.20
	X(9)	-0.30	-2.12	0.02	1.02	-1.83	-3.11	-0.30	-1.62
	X(10)	1.75	-0.45	-2.39	-0.71	-0.79	0.66	1.75	-0.46
	X(11)	-0.37	-1.46	0.90	-0.02	-2.10	-0.06	-0.37	-0.34
	X(12)	-1.49	-0.11	-3.13	-0.53	2.41	-2.22	-1.49	-1.42
	X(13)	2.73	0.19	1.77	-0.94	0.65	2.85	2.73	-2.41
	X(14)	-2.90	-0.18	2.29	0.32	0.76	-2.88	-2.90	-0.93
	X(15)	2.15	-2.60	1.98	2.97	0.86	1.93	2.15	-2.07
	X(16)	-0.26	2.00	0.75	-2.43	2.08	-2.75	-0.26	2.52
	X(17)	-2.45	2.78	-1.10	-1.17	-2.39	-0.64	-2.45	1.29
	X(18)	-0.54	2.86	0.09	-2.88	-1.65	-1.69	-0.54	-1.62
	X(19)	0.04	-1.26	-1.63	1.50	1.80	0.47	0.04	0.48
	X(20)	-1.96	-2.75	0.66	-0.69	2.74	1.08	-1.96	2.72
	X(21)	-1.21	0.16	-1.19	0.85	-0.22	1.07	-1.21	0.90
	X(22)	0.91	1.72	-2.48	-0.52	-2.75	-1.05	0.91	2.65
	X(23)	2.95	2.39	-0.76	0.90	0.67	-0.60	2.95	2.40
	X(24)	-0.51	2.19	2.12	1.01	-2.40	0.33	-0.51	1.84
	X(25)	2.37	0.66	-2.85	-2.07	-0.11	-2.32	2.37	2.90
	X(26)	1.80	-3.08	-0.58	1.49	-1.50	-1.20	1.80	-0.49
	X(27)	-0.87	0.81	-2.76	2.45	-2.46	2.98	-0.87	1.00
	X(28)	2.31	1.59	-1.34	1.80	3.01	0.60	2.31	2.72
Info Metrics	D-Opt	1.92E-43	1.83E-15	4.90E-43	7.51E-42	2.22E-48	1.07E-17	4.90E-44	1.43E-12
	T-Opt	-1.75E+19	-5.38E+05	-1.13E+18	-4.40E+15	-8.73E+18	-1.24E+07	-1.58E+19	-6.27E+05
	A-Opt	0.29	10.55	0.16	0.11	0.13	23.97	0.19	52.03
	E-Opt	0.18	7.42	0.13	0.09	0.11	22.77	0.14	47.82

11.3 Summary of Observations and Conclusions

In this chapter, the TEMPUS methodology was demonstrated using higher-order VAEs to design robust-optimal information-dense dynamic experiments on two test problems: (i) a simple spring-mass-damper system with non-homogenous forcing; and (ii) a complex flight dynamic SCRAMjet model to simulate SCRAMjet-powered flight tests.

- **Exp't #5** was designed to address **HYP.#3** by investigating the robust-optimality of the robust-optimal information metrics, which were constructed using higher-order VAEs. To do this, a simple spring-mass-damper system was implemented within TEMPUS for the sizing and synthesis of robust-optimal information-dense dynamic experiment designs. Through a Monte Carlo virtual experimentation investigation, it was observed that these higher-order information metrics do provide various levels of robustness; however, it was observed that not all information metrics, computed form the Fisher information matrix are created equal. For example the T-Optimal (information matrix trace) frequently yielded inferior designs in terms of both robustness and optimality, where conversely the A-Optimal (inverse information matrix trace) provided for some of the best designs.

- **Application Problem** again implemented the TEMPUS methodology but now for an industrial-sized hypersonic SCRAMjet flight dynamic model. Here the experimental procedure of **Exp't #5** was again implemented to test **HYP.#3**; however, this time for a system where a sophisticated control system is required to regulate stability in the presence of parametric uncertainties. Additionally, **Exp't #2** was revisited to investigate the computation time complexity on an industrial-sized problem. Here it was observed that the computation of VAEs up to 4^{th}-order was computationally feasible for implementing optimal dynamic

experiment design problems, but that parallel/vectorization computing strategies are necessary for the timely solution of these design problems. Through simulation it was observed that the matrix conditioning of the Fisher information for the GHV aero-propulsive-elastic SnC coefficients of the SCRAMjet thrust force model is significantly poor for high-AoA coefficients ($C_T^{\Phi\alpha^3}$, $C_T^{\Phi\alpha^2}$, $C_T^{\alpha^3}$). This is due to the combination of the adaptive control architecture and multi-sine excitation maneuvers, where adaptation is known to have a canceling effect on the open-loop dynamics, and therefore, making it difficult to excite the system enough to generate sufficient amounts of the high angle of attack data for improving the information content of the high-order coefficients $C_T^{\Phi\alpha^3}$ and $C_T^{\alpha^3}$. This observation is consistent with the discussion by Ljung [182] for performing closed-loop experiments. It is hypothesized that alternative control strategies, employing machine learning for real-time estimation of open-loop natural frequencies, may improve the information quality, but implementation of this is beyond the scope of this work. Nevertheless, TEMPUS does allow for the robust-optimal assessment of information quality for alternative flight test designs (by using the computation of variational asymptotic expansions to overcome the deficiencies of the circulatory problem), implying that trade-offs between alternative controls architectures, measurement systems, etc. is now an available capability to the flight test designer and controls system engineer.

PART VI

Concluding Remarks

In the following chapter, the findings of this research are summarized following a restatement of the research objective. Next, summarizing remarks are made, and a summary of contributions is outlined. Finally, a discussion on directions for future work are be presented.

CHAPTER 12

SUMMARY AND CONCLUSIONS

12.1 Summary of Thesis Objectives

The development of appropriate flight tests has proven to be a critical piece in the design process of revolutionary next-generation aerospace vehicles. In the case of air-breathing hypersonic SCRAMjets, large physics-based computational tools exist that are capable of designing high-performance integrated vehicles. These tools require extensive validation and calibration to establish a suitable level of confidence in their predictive abilities, before subsequent use in systems design problems. Due to the challenges caused by ground testing limitations, high model uncertainties, and highly integrated systems, the design of flight testing strategies is vitally important to jump-start the capabilities of hypersonic computational modeling and design, expanding the hypersonic database. In the case of hypersonic SCRAMjets, this has proven to be a formidable challenge, where excessive complexity, high costs, long development times, and rampant uncertainties often lead to flight tests which are conservative, risk-averse endeavors, yielding little gain in knowledge and understanding of aero-propulsive-elastic modeling elements. The research objective, restated below, is given in response to these limitations.

Research Objective: From the consideration that a flight test is an integrated system, the research objective of this thesis is to develop a methodology to enable intelligent design of these time-dynamic experiments, which can efficiently and accurately extract information in the presence of uncertainty.

Proposed in this work, a dynamic experiment design methodology to size robust-optimal dynamic system identification experiments is developed – TEMPUS (**T**ime-dynamic **E**xperiment design using a **M**odel-based approach to **P**ropagate **U**certainty for **S**ystem Identification). To enable this methodology, it has been hypothesized that the use of higher-order sensitivity information is a key enabler, allowing for: (i) surrogate model construction and higher-order state-to-parameter sensitivity computation without the need to run many experiments, and (ii) flexible model-based robust-optimal design of dynamic system identification experiments, involving a design vector that consists of a mixed set of variables and functions (*i.e.* control input maneuvers). The surrogate model of (i) can be constructed using the higher-order sensitivity information using variational asymptotic expansions over the entire time-profile of a numerical solution to a dynamic simulation. This expansion can be parameterized by sources of uncertainty and design variables, essentially, enabling the exploration of the entire dynamic system response using a set of perturbation parameters. The flexible approach to robust-optimal design from (ii) implies that the higher-order sensitivity information can be used to deterministically evaluate the related statistical parameters of robustness to a given information quality metric. This essentially means that a robust-optimization problem can be reduced to an optimization problem, which would drastically reduce computational effort. Also, in the case of dynamic experiment design for system identification, the Fisher information matrix usually chosen as a basis for optimization. This matrix is a function of output-parameter sensitivities and therefore requires at least a first-order sensitivity analysis to evaluate this metric. The circulatory dependence of this metric of on the "true parameter values" of the system suggests that a robust approach to design experiment design was necessary in the first place to overcome model parameter uncertainty.

12.2 Research Summary

Several research questions were developed in Chapter 9 to guide the process of meeting the research objective. The first research question **RQ.#1** was stated in Section 9.1, which is concerned with how contemporary programming techniques can be utilized to implement the high-order, multivariate VAE capability described in Chapter 7. The resulting implementation strategy, which was described and demonstrated in Section 10.1, motivates the next research question **RQ.#2**, which essentially asks to what extent can be VAE approximations be practically useful, and what are the available options that can leveraged to enhance VAE performance and effectiveness in limiting situations. From **RQ.#2**, a number of sub-questions were posed to address this more specifically. **RQ.#2.1** was posed to investigate how to combat the potentially adverse effects of diminishing returns on accuracy. In response to this, the first testable hypothesis was formulated, as restated below.

HYP. #2.1.1: Based on the geometry of the problem, intelligent selection of basis functions can increase the region of approximation, and hence accuracy, without experiencing the degree of diminishing returns that are observed when employing expansion approximations using Taylor basis functions.

Exp't #1 was designed to address **HYP#2.1.1** by investigating if the use of alternative basis functions for generating VAEs will yield expansions with faster convergence characteristics and larger regions of approximation. For the Chebyshev basis, this was indeed observed and therefore the implementation of polynomial libraries for alternate basis functions is a worthy pursuit.

The second testable hypothesis was formulated to investigate how diminishing returns on accuracy could impact uncertainty propagation through dynamic systems and is restated below.

HYP. #2.1.2: The utilization of higher-order variational asymptotic expansions can enable higher-order local expansion-based methods for the propagation of uncertainty through dynamic systems, where nonlinear effects and larger perturbations on parameters can be approximated to asymptotic accuracy.

Exp't #2 was designed to address **HYP#2.1.2**, which is concerned with studying the effectiveness of how VAEs enable high-accuracy propagation of parameter uncertainties for nonlinear dynamic systems. The findings of this study suggest that the use of higher-order VAEs for the uncertainty propagation in nonlinear dynamic systems do produce probabilistic models that are asymptotically accurate; however, for some problems, adverse numerical effects, such diminishing returns on accuracy and oscillatory, slow convergence rates, could lead to artificial multimodality in probabilistic trajectories. In the context of robust-optimization designs problems (addressed by the TEMPUS methodology) this implies that robust-optimal information metrics may lead to sub-optimal experiment designs, regardless of how much higher-order information is utilized. Therefore it is necessary to employ a Monte Carlo analysis to conduct virtual experiments for verification of robust optimality.

Next, **RQ.#2.2** was posed to investigate the potential adverse effects that the curse of dimensionality might pose to hinder the practical computation of VAEs for large industrial-sized problems (*e.g.* aerospace multi-disciplinary design and optimization problems) from a computational perspective. As a result, the second testable hypothesis was formulated, as restated below.

HYP. #2.2: Parallelization/vectorization strategies to alleviate computational expense will play a critical role in the robust-optimal design of dynamic experiments of aerospace systems (*e.g.* flight-dynamic simulation and control of hypersonic SCRAMjet vehicles).

Exp't #3 was designed to address **HYP #2.2**, by investigating how the adverse effects of the curse of dimensionality affect the scaling of computational complexities (*i.e.* computational time, memory allocation) in both increasing dimension and increasing order. Here dense multiplication of multivariate polynomials was selected because it is a known bottle-neck algorithm in polynomial algorithm, and therefore it's asymptotic scaling for the recursive-coefficient implementation of Section 10.1.2 should be dominated by this algorithm, or comparable algorithms. The findings of this study do confirm **HYP #2.2**, in that despite the substantial improvements observed by implementing degree control, adverse complexity growth for high-dimension/low-order polynomials still significant, and therefore parallel/vectorization strategies most likely must be utilized when design dynamic experiment designs for large-scale aerospace problems. Final confirmation of implementation of VAEs to solve these types of problems was investigated further during flight test design for hypersonic SCRAMjets and is addressed below when the application problem is discussed.

The next research question, **RQ.#2.3**, was developed to investigate the potential implementation of VAEs to solve for solutions of *higher-order optimal control problems of variation*. Among other things, this capability has potential implications on future approaches to dynamic experiment design, where a VAE to a single optimal point solution can be used to explore neighboring designs across a design space consisting

of design variables and functions. In response, the following hypothesis is restated.

HYP. #2.3: Higher-order gradients can be used to generate high-accuracy VAE surrogates to OCPs, which will enable point solutions from computationally expensive OCP solvers to be utilized for parametric exploration.

Exp't #4 was designed to address **HYP #2.3**, which was concerned with investigating the potential application of VAEs to solve higher-order OCPs. The findings of this study show that implementation of VAEs to generate solutions to higher-order OCPs shows promising results, and that is is indeed possible to generate higher-order OCP solutions. However, in terms of dynamic experiment design for potentially large and complex systems this still needs more work before it can be useful for design space exploration. The implications of proposed capability from a vehicle systems design perspective would allow for the optimal controls expert to contribute to the systems engineering design problem in a significant way (*e.g.* the manual simulation of a higher-order VAE baseline vehicle along an optimal trajectory, which could then potentially be rapidly evaluated for alternative designs along the space of optimal mission profiles).

Finally, **RQ.#3** was posed, which also represents the overarching research question of this work and addresses the potential as an enabler that the computation of VAEs can have on the robust-optimal design of dynamic experiments for system identification. The following hypothesis is restated, which also represents the overarching hypothesis of the entire thesis.

HYP. #3: If the automated, generalized computation of higher-order gradient information can be made computationally feasible, then a flexible approach to robust-optimal dynamic experiment design, utilizing VAE's to automatically and accurately compute higher-order dynamic state-to-parameter sensitivities, will yield superior designs that are robust to parameter uncertainties.

Exp't #5 was designed to address **HYP#3** by investigating the robust-optimality of the robust-optimal information metrics, which were constructed using higher-order VAEs. To do this a simple spring-mass-damper system was implemented within TEMPUS for the sizing and synthesis of robust-optimal information-dense dynamic experiment designs. Through a Monte Carlo virtual experimentation investigation, it was observed that these higher-order information metrics do provide various levels of robustness; however, it was observed that not all information metrics, computed form the Fisher information matrix are equally effective. For example the T-Optimal (information matrix trace) frequently yielded inferior designs in terms of both robustness and optimality, where conversely the A-Optimal (inverse information matrix trace) provided for some of the best designs.

The **Application Problem** again implemented the TEMPUS methodology but now for an industrial-sized hypersonic SCRAMjet flight dynamic model. Here the experimental procedure of **Exp't #5** was again implemented to test **HYP#3**, however this time for a system where a sophisticated control system is required to regulate stability in the presence of parametric uncertainties. Additionally, **Exp't #2** was revisited to investigate the computation time complexity on an industrial-sized problem. Here it was observed that the computation of VAEs up to 4^{th}-order was computationally feasible for implementing optimal dynamic experiment design problems, but

that parallel/vectorization computing strategies are necessary for the timely solution of these design problems. Through simulation it was observed that the matrix conditioning of the Fisher information for the GHV aero-propulsive-elastic SnC coefficients of the SCRAMjet thrust force model is significantly poor for high-AoA coefficients ($C_T^{\Phi\alpha^3}$, $C_T^{\Phi\alpha^2}$, $C_T^{\alpha^3}$). The use of multi-sine perturbative excitation signals, which were designed only by changing phase angles, was observed to be only a marginally effective approach for improving the information matrix conditioning, because large quantities of sampled high-AoA data is difficult to obtain. For further improvements, control logic to adaptively tune multi-sine frequency/amplitude parameters may be required so as to excite the open-loop GHV dynamics as much as possible, while still ensuring safe operation, but this is a topic for future work.

12.3 Summary of Contributions

The contributions of this effort all stem from the ability of a generalized higher-order sensitivity analysis software to be applied to dynamic systems. The application of choice here is dynamic experiment design, and as a result, there are three primary areas of contribution: (i) the development of the VAE analysis tool itself (*i.e.* automatic differentiation tool for dynamic systems), (ii) the TEMPUS design methodology for the sizing of robust-optimal high information dynamic experiments, and (iii) the engineering application of this methodology to ABHV flight testing strategies. The choice of ABHVs for an application problem was selected because nearly every challenging aspect facing engineering design is present in this class of vehicles and therefore if effective flight test strategies can be designed, then it will serve as a litmus test for the capability of the proposed methodology.

1. **A new tool/capability** – a generalized tool for the generation of higher-order gradient information; it can be used for:

    - *A new surrogate modeling approach*: automated construction VAEs for generic ODE systems using the automatic differentiation capability of Section 10.1.
    - *Implementation of VAEs in the Chebyshev basis*: many elementary operations and functions were implemented to create an equivalent capability in the Chebyshev basis. Future work is need to boost this capability to be equivalent to the monomial/Taylor basis.
    - *Implementation of VAEs in optimal control problems*: two VAE-OCP formulations were proposed and implemented on a simple OCP where analytical solutions are readily available. Results were promising, where larger engineering-type problems should be implemented next.

- *Implementation of VAEs for higher-order uncertainty propagation*: VAEs were demonstrated on perturbation variables which were sampled from distributions. Results were determined to possess numerically superior accuracy relative to the local expansion methods of forward uncertainty propagation, which only utilize 1^{st}-order gradient information.
- *Using Fisher information criteria*: the automated construction of the Fisher information-based criteria requires output-parameter sensitivities to the simulation of generic ODE system and implies a RDO approach to experiment design in light of the circulatory problem.
- *Flexibility approaches to dynamic experiment design*: taking a deterministic approach to RDO by enabling asymptotic construction of the expected value and variance metrics of an objective function.

2. **A new methodology** – dynamic experiment design methodology for system identification in the context of designing robust-optimal information dynamic experiment designs which can be used for estimation of expected flight test results.

   - *A sizing and synthesis routine*: considering dynamic experiment design as an integrated system with a design vector consisting of vehicle design, flight conditions, estimation models, input maneuvers, and instrument system parameters.
   - *A systems engineering methodology*: systematically design high-information-density experiments while accounting for uncertainties in model parameters, environmental conditions, and variations in the instrumentation and measurement system.

3. **A new application problem** – demonstrate the approach to taking the existing, current state of an multi-disciplinary, computational integrated environment for vehicle design and use this to design a dynamic flight testing strategy which will result in a high degree of refinement in the models, hence improving the level of confidence in the predictive capabilities.

    - *The Generic Hypersonic Vehicle (GHV) Model* – a nonlinear longitudinal dynamic model, incorporating aero-propulsive-elastic effects in hypersonic forces and moments and heave coupling inertial aeroelastic effect for fore,aft-body Euler-Bernoulli beams under transverse deflections [36, 45, 65, 103, 246]. A nonlinear robust-adaptive flight control is necessary for stability and control of the GHV vehicle, which is known to possess non-minimum phase, unstable open-loop dynamics [104].
    - *Robust-Optimal Flight Test Design for Dynamic System Identification* – Expanded on the work of Morelli [212] to the robust-optimal design of dynamic experiments using multi-sines perturbative excitation signals for SysID of aero-propulsive-elastic SnC coefficients for the SCRAMjet thrust model during powered SCRAMjet operation at steady-level flight.
    - Tested robust-optimality of dynamic experiment designs using a Monte Carlo virtual experimentation to statistically observe information quality robustness.

12.4 Recommendations for Future Work

There are several avenues of future research that can expand upon the work presented in this thesis. These avenues are elaborated upon in following discussions and references are provided for the interested reader.

- **Computation of Variational Asymptotics for Dynamic Systems**
  - *Construction of polynomial libraries in other basis functions* – In Section 10.2.2 several of the polynomial library routines implemented in Section 10.1 were expanded to the Chebyshev basis; however, many algorithms have yet to be derived or implemented. In addition to the Chebyshev basis, there are a number of other basis functions which are commonly employed in numerical analysis and are of interest to this work, including: Legendre polynomials, Hermite polynomials, Laguerre polynomials, and Bernstein polynomials. The Numpy Polynomials module is an open source reference for many of these algorithms as univariate polynomials [72]. Also, derivation of many of these algorithms is very simple, using the approach discussed by Knuth [172].
  - *Fast algorithms for dense multivariate polynomials* – In Section 10.4 a complexity analysis was conducted on the implementation of Section 10.1, which utilizes a recursive coefficient approach to construct multivariate polynomials. While in Section 11.2.5 it was concluded that this implementation was sufficient for the purposes of this dissertation, the eventual implementation of high-performance polynomial multiplication algorithms that utilize fast Fourier transforms is expected to substantially increase the performance of the current capability. In addition, the potential utilization of cryptographic techniques is also another avenue of potentially substantial improvement to the current capability, allowing for compact

computational representations (encodings) of polynomials.

  - *Implementation of VAE-OCP problems* – In Section 10.5 two VAE-OCP formulations were presented and implemented for a simple OCP, where analytical solutions are readily available. Future work in this area potentially leads to an unlimited number of applications where implementation of a diverse problem set can be crossed with implementation of various numerical methods to solve optimal control with the addition of VAEs to generate higher-order solutions (*e.g.* Belman's Dynamic Programming [164]). In the context of aerospace systems design, VAE-OCP solutions could provide for a model-based approach to vehicle design, operating over the space of optimal trajectory/control solutions (*e.g.* high-performance capability-based vehicle design); however, additional motivations for implementing VAE-OCP problems extend into a more broadly into many fields within mathematics, science, and engineering.)

- **Robust-Optimal Design of Dynamic System Identification Experiments**

  - *Polynomial Basic linear Algebra Subroutine (BLAS) library* – The implemented design problems in Chapter 11 utilize a relative simple numerical linear algebra library of polynomial subroutines, which take advantage of the fact that the Fisher information matrix is expected to be a positive definitive, symmetric matrix. This allows for the polynomial overloading of the relatively simple Cholesky decomposition algorithm, decomposing the information matrix into a manageable form. This allows for capabilities such as matrix inversion, eigenvalue computation, rapid matrix determinant evaluation, and matrix condition number computation – all with matrix elements as polynomials. Beyond the obvious (*i.e.* implementing

as many BLAS-type methods as possible), one particularly attractive capability to implement for applications in experiment design would be to implement a polynomial singular-value decomposition (SVD) algorithm. Besides being a more numerically stable algorithm with respect to Cholesky decomposition, it is not limited to symmetric, positive-definite matrices. In addition, SVD provides a way to manage poorly conditioned matrices, which is a common necessity in system identification analyses.

– *Incorporation of cost and risk assessment* – The robust-optimal design of flight tests was accomplished by utilizing VAEs to accurately propagate uncertainty though dynamic simulations. One obvious extension of this capability is to incorporate cost and risk impact into the design performance.

– *Higher-order output-error method for large nonlinear dynamic systems* – The focus of this dissertation has been on the robust-optimal design of dynamic experiments for system identification; however, implementation of VAEs to system identification methods themselves could potentially allow for higher-accuracy nonlinear estimators. For example, the output-error method described by Klein and Morelli [170] implemented a truncated 2^{nd}-order Taylor series expansion to derive a sequential optimization approach, utilizing a modified Newton-Rhapson approach to determine optimality. Within this formulation, the definition of the Fisher information matrix (Equation (8)) used in this work arose. If a higher-order expansion were used here, then new (more accurate) definitions of the Fisher information matrix can be defined, depending on order, and the sequential optimization approach can be reduced to a root-finding problem (*i.e.* the squared different between measured data and simulation VAE output).

- **Miscellaneous Applications of Variational Asymptotics**

  - *Implementation of singular perturbation techniques* – The methods implemented in this dissertation fall under the very narrow umbrella of perturbation techniques for regular-type problems. In many applications, the perturbation parameters can encounter singularities for certain values. There has been much work that has been done on these types of problems, collectively referred to as singular perturbation techniques. One clear application of these techniques could be for the parametric representation of dynamic stability (*i.e.* using root-locus methods) for a system which can be made both stable and un-stable at certain values of the perturbation parameters.

  - *Implementation of VAEs on partial differential equations* – The focus of the work of this dissertation was on dynamic systems, which can be mathematically represented as ordinary differential equations. In many applications, engineering physics problems can be represented as a system of partial differential equations. Two common applications are in computational fluid dynamics and finite element analysis for thermal-fluids and structural engineering applications. Thus, an obvious extension of this work would be to implement VAEs to solve these types of engineering problems for higher-order solutions, resulting in parametric asymptotic expansions of entire vector fields of solutions (*e.g.* wing design of a low-speed commercial airliner utilizing a single VAEs in a sequential optimization approach).

APPENDIX A

AUTOMATIC GENERATION OF TAYLOR COEFFICIENTS

The polynomial routines that were enumerated upon in Table 12 of Section 10.1 are presented here. These algorithms, for computing Taylor coefficients recursively, have been known since the 60's. Commonly referenced in *automatic differentiation* literature [234], these algorithms have been employed in software packages such as ATOFMT, ADIFOR, ADOLC, etc. [37, 39, 121, 278]. A detailed description of automatic differentiation can be found in [159] (see more references therein), but here, a brief account of the idea is illustrated.

Let $f(t)$ be an analytic function and denote the i^{th} Taylor coefficient at t_0 by

$$(f)_i = \frac{f^i(t_0)}{i!},$$

where $f^i(t_0)$ is the i^{th} derivative of f at t_0. The Taylor expansion of $f(t)$ around t_0 can be conveniently expressed as

$$f(t_0 + h) = (f)_0 + (f)_1 h + (f)_2 h^2 + \ldots + (f)^n h^n \ldots$$

Using a contiguous array of coefficients, the *chain rule of calculus* can be enforced by using the following polynomial online operations to replace the traditional implementations on scalar valued numbers. Below is a non-exhaustive list of simple online algorithms for Taylor (monomial) polynomial elementary operations, calculus operations, and elementary functions, which were utilized in this work. More details on how to acquire/derive these algorithms can be found in Section 4.7 of Knuth [172].

Elementary Operations:

- **Addition/Subtraction** – $(p \pm q)_i = (p)_i \pm (q)_i$
- **Multiplication** – $(pq)_i = \sum_{r=0}^{i} (p)_r (q)_{i-r}$
- **Division** – $\left(\frac{p}{q}\right)_i = \frac{1}{q}\left\{(p)_i - \sum_{r=1}^{i} (q)_r \left(\frac{p}{q}\right)_{i-r}\right\}$
- **Power** – $(p^a)_i = \frac{1}{p}\sum_{r=0}^{i-1}\left(a - \frac{r(a+1)}{i}(p)_{i-r}(p^a)_r\right)$ where a is a real constant and $(p^a)_0 = (p_0)^a$
- **Inversion** – $(\frac{1}{p})_i = \sum_{r=0}^{i-1} (p)_i (\frac{1}{p})_{i-r}/(p)_0$ where $(\frac{1}{p})_0 = (p)_0^{-1}$

Calculus Operations:

- **Differentiation** – $\left(\frac{dp}{dx}\right)_i = (i+1)(p)_{i+1}$
- **Integration** – $\left(\int p\, dx\right)_i = \frac{(p)_{i-1}}{i}$ where $\left(\int p\, dx\right)_0 = \text{const.}$

Elementary Functions:

- **Exponential** – $(e^p)_i = \sum_{r=0}^{i-1}\left(1 - \frac{r}{i}\right)(e^p)_r\,(p)_{i-r}$ where $(e^p)_0 = e^{(p)_0}$
- **Logarithmic** – $(\ln p)_i = \frac{1}{p}\left\{(p)_i - \sum_{r=0}^{i-1}\left(1 - \frac{r}{i}\right)(p)_r\,(\ln p)_{i-r}\right\}$ where $(\ln p)_0 = \ln (p)_0$
- **Sine** – $(\sin\ p)_i = \sum_{r=0}^{i-1}\left(\frac{r+1}{i}\right)(\cos\ p)_{i-1-r}(p)_{r+1}$ where $(\sin\ p)_0 = \sin (p)_0$
- **Cosine** – $(\cos\ p)_i = -\sum_{r=0}^{i-1}\left(\frac{r+1}{i}\right)(\sin\ p)_{i-1-r}(p)_{r+1}$ where $(\cos\ p)_0 = \cos (p)_0$
- **Arctangent** – $(\tan^{-1}\ p)_i = \sum_{r=0}^{i-1}\left(1 - \frac{r}{i}\right)\left(\frac{1}{1+p^2}\right)_r (p)_{k-r}$ where $(\tan^{-1}\ p)_0 = \tan^{-1}(p)_0$
- **Hyperbolic Sine** – $(\sinh\ p)_i = \sum_{r=0}^{i-1}\left(\frac{r+1}{i}\right)(\cosh p)_{i-1-r}(p)_{r+1}$ where $(\sinh\ p)_0 = \sinh (p)_0$
- **Hyperbolic Cosine** – $(\cosh\ p)_i = \sum_{r=0}^{i-1}\left(\frac{r+1}{i}\right)(\sinh p)_{i-1-r}(p)_{r+1}$ where $(\cosh\ p)_0 = \cosh (p)_0$

APPENDIX B

VAE GLOBAL SENSITIVITY ANALYSIS – INTERMEDIATE RESULTS

For the spring-mass-damper VAE that was constructed in Section 10.3.3.1 for the investigation of **Exp't #2** (*i.e.* use of VAEs for high-accuracy uncertainty propagation), the infinity norm relative error was computed from the following Figures 139-144, where were computed by taking the relative difference between sequential orders of VAEs (*e.g.* $\Delta^i x(t;\delta) - \Delta^{i-1} x(t;\delta)$).

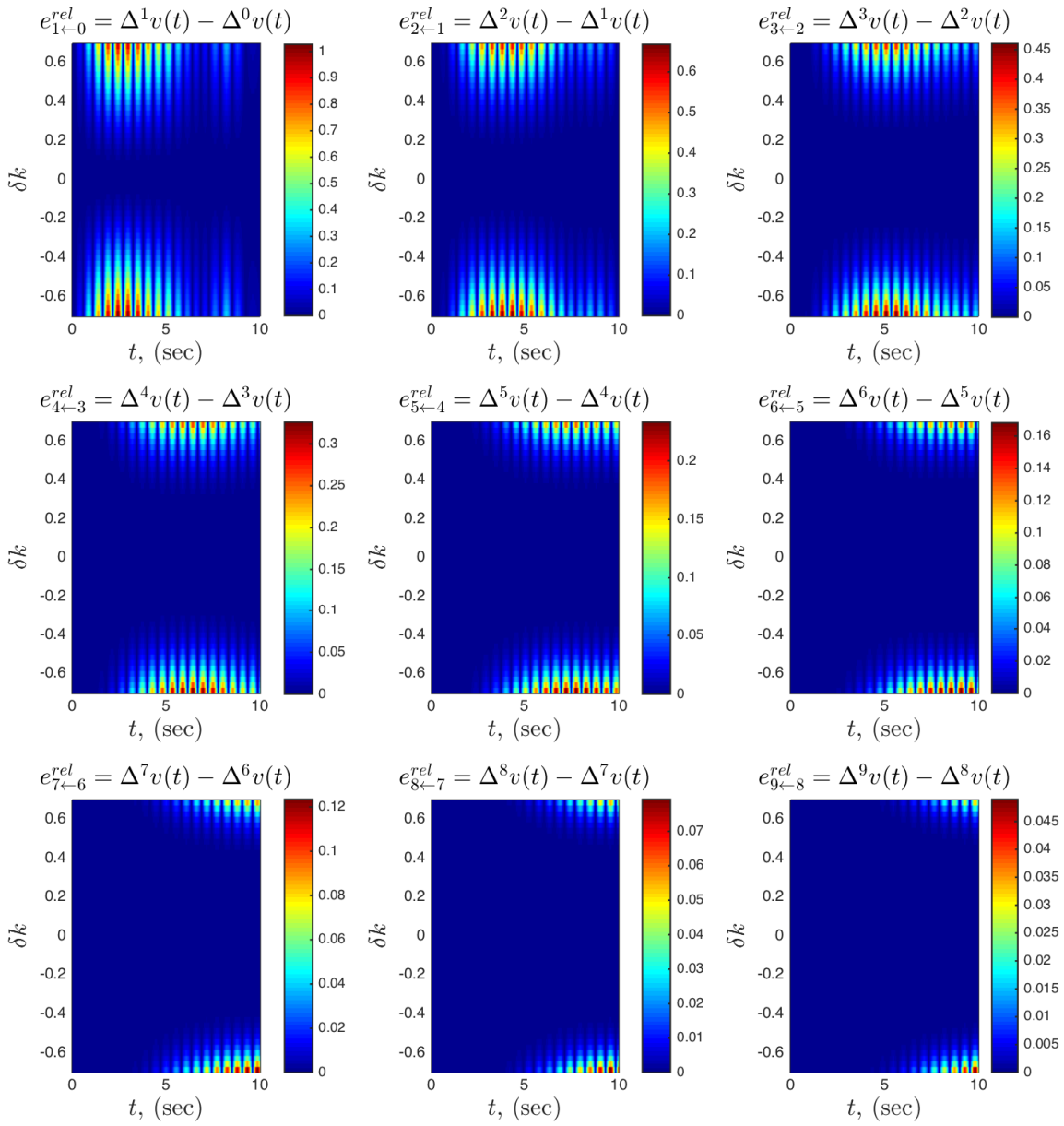

Figure 139: Asymptotic convergence analysis of the VAE for $x(t)$, comparing relative error $e^{rel}_{i+1\leftarrow i}$ for $i = 0, \ldots, 9$ parameterized by δk between $-0.2k_0 \leq \delta k \leq 0.2k_0$ for $k_0 = 3.5$.

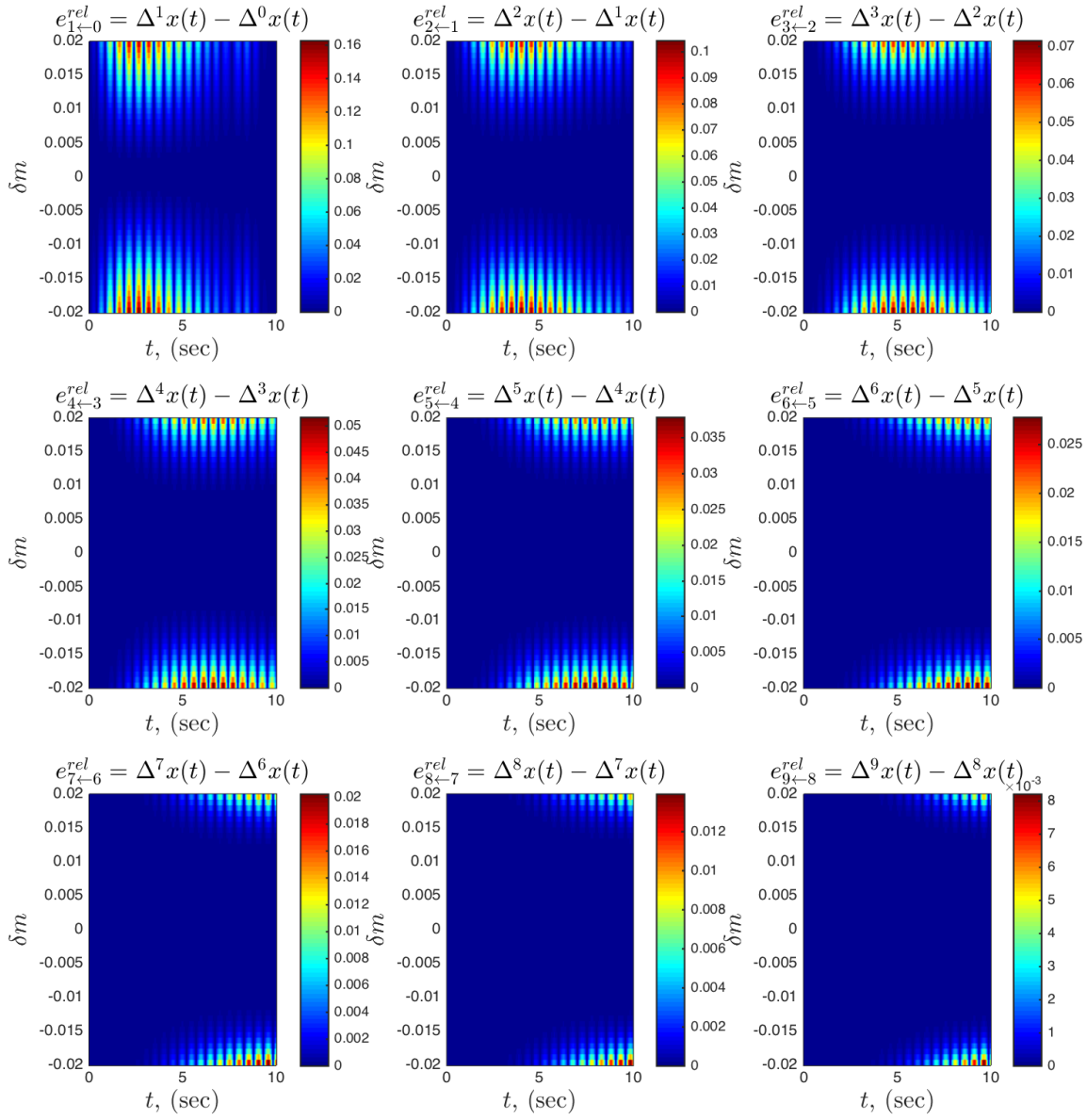

Figure 140: Asymptotic convergence analysis of the VAE for $x(t)$, comparing relative error $e^{rel}_{i+1\leftarrow i}$ for $i = 0, \ldots, 9$ parameterized by δm between $-0.2m_0 \leq \delta m \leq 0.2m_0$ for $m_0 = 0.10$.

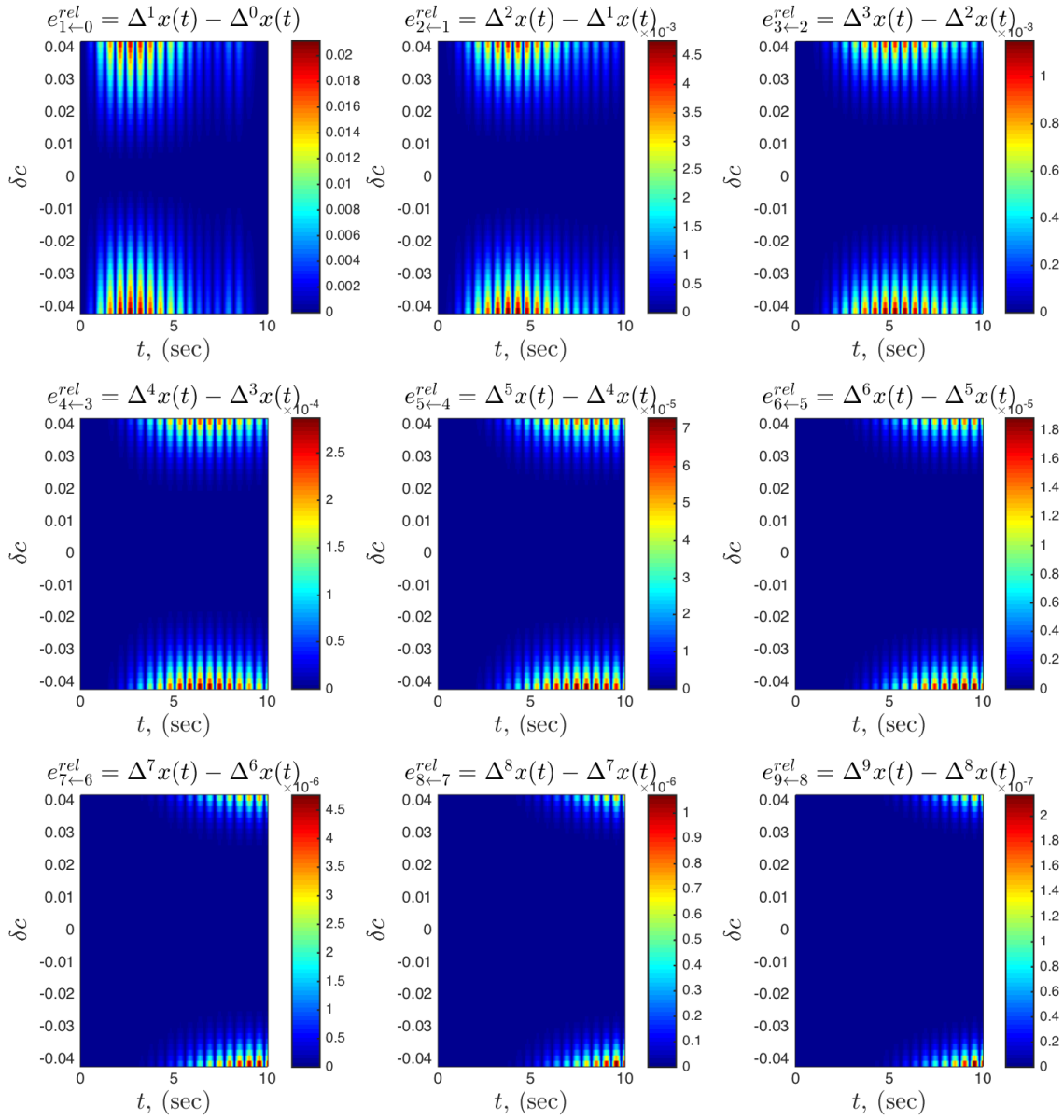

Figure 141: Asymptotic convergence analysis of the VAE for $x(t)$, comparing relative error $e^{rel}_{i+1\leftarrow i}$ for $i = 0, \ldots, 9$ parameterized by δc between $-0.28c_0 \leq \delta c \leq 0.28c_0$ for $c_0 = 0.15$.

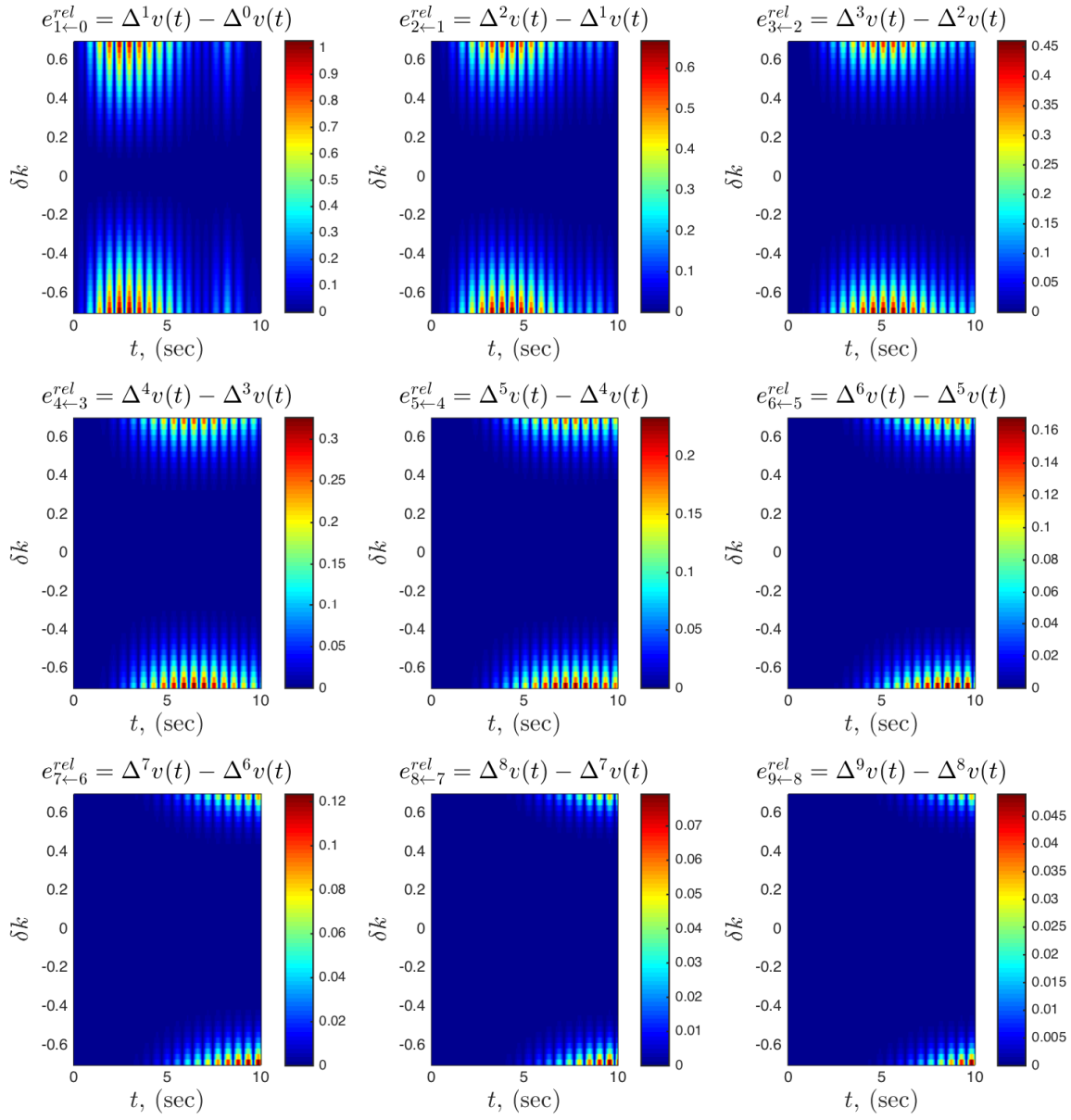

Figure 142: Asymptotic convergence analysis of the VAE for $v(t)$, comparing relative error $e^{rel}_{i+1\leftarrow i}$ for $i = 0, \ldots, 9$ parameterized by δk between $-0.2k_0 \leq \delta k \leq 0.2k_0$ for $k_0 = 3.5$.

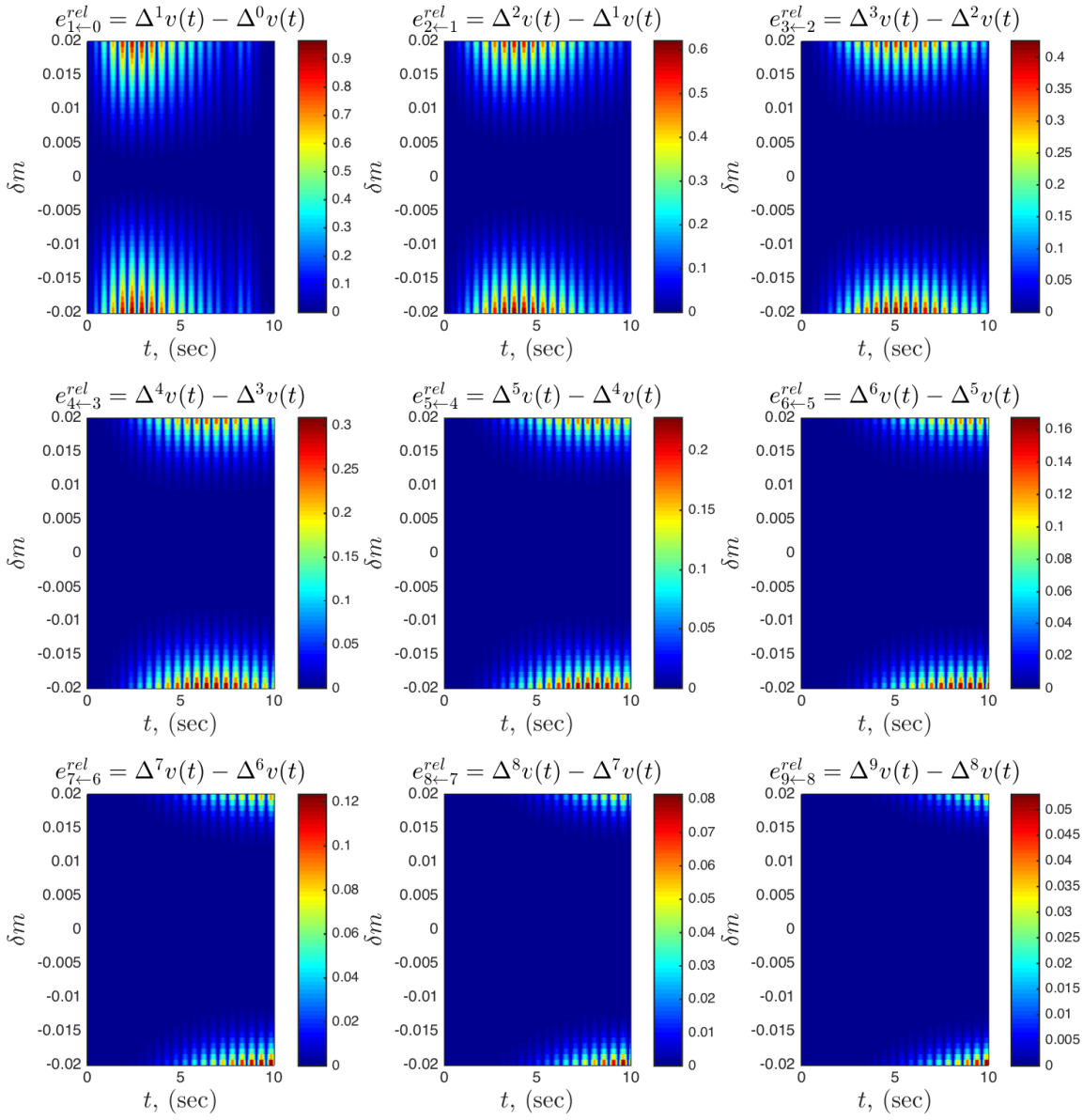

Figure 143: Asymptotic convergence analysis of the VAE for $v(t)$, comparing relative error $e^{rel}_{i+1\leftarrow i}$ for $i = 0, \ldots, 9$ parameterized by δm between $-0.2m_0 \leq \delta m \leq 0.2m_0$ for $m_0 = 0.10$.

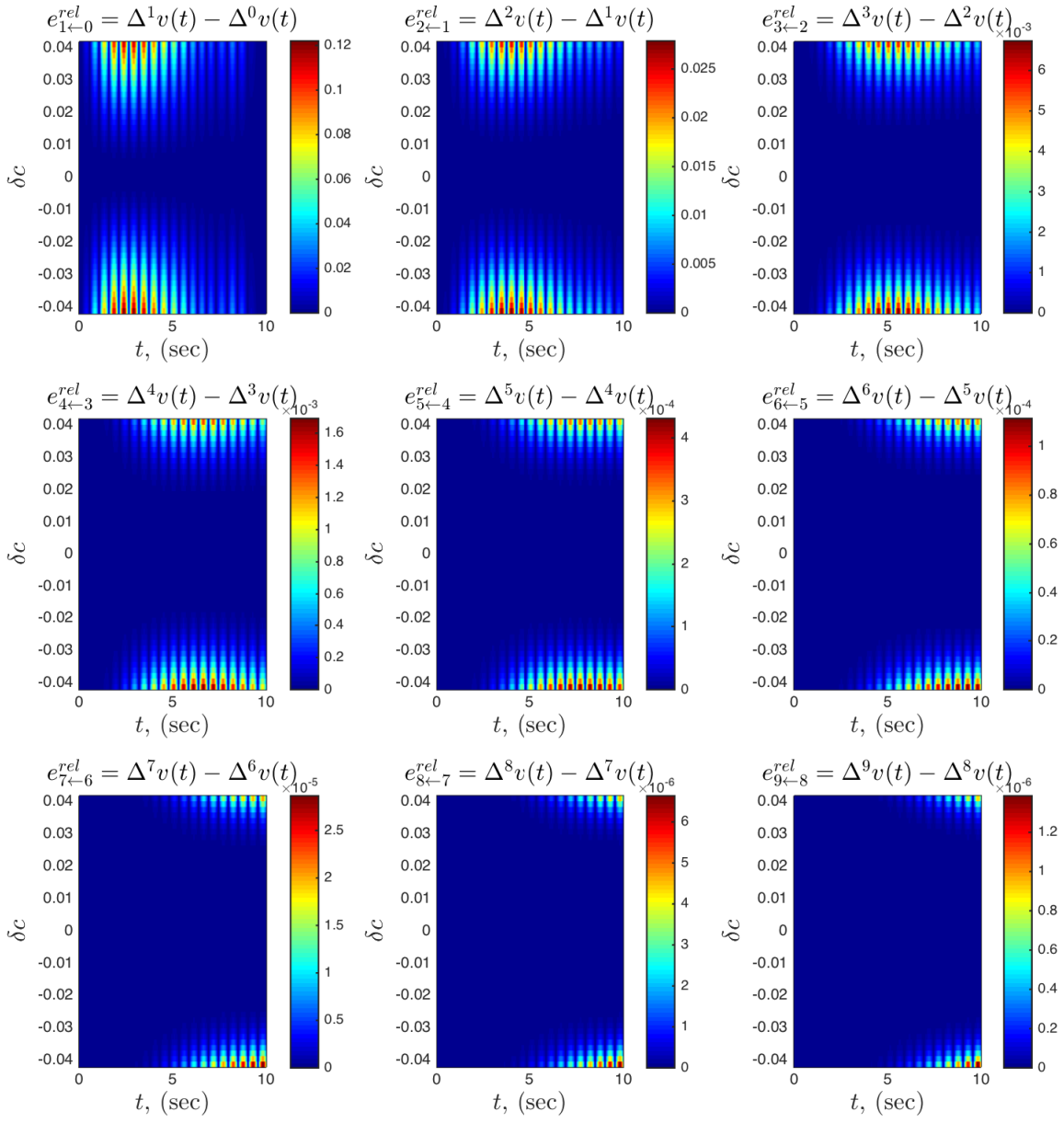

Figure 144: Asymptotic convergence analysis of the VAE for $v(t)$, comparing relative error $e^{rel}_{i+1\leftarrow i}$ for $i = 0, \ldots, 9$ parameterized by δc between $-0.28c_0 \leq \delta c \leq 0.28c_0$ for $c_0 = 0.15$.

APPENDIX C

DERIVATION OF ANALYTICAL SOLUTIONS FOR EXP'T #4

Here the analytical solutions to the Campos problem (Equation (78) from Section 10.5.4) are presented, along with a brief description of the derivation. The purpose of these solutions is to serve as validation cases for the numerical implementation of the VAE-OCP formulations presented in Section 10.5.2. As stated in Section 10.5.4 , the three cases of interest are summarized below, where the perturbations on the initial conditions (q_0, p_0) are sought to be used for parameterization of VAEs to optimal control problems (OCPs).

- Case #1: $(q_0, p_0) = (0, 0)$: the original solutions from Campos, et al. [62]; represents the baseline (unperturbed) case.
- Case #2: $(q_0, p_0) = (\delta q_0, \delta p_0)$ given $u^*(t)$ from Case #1: represents a perturbed (sub-optimal) case to the optimal solution of the baseline optimal control solution; serves to test VAEs generated by **VAE-OCP Formulation #1**.
- Case #3: $(q_0, p_0) = (\delta q_0, \delta p_0)$: represents a neighboring optimal control solution to the baseline optimal control solution; serves to test VAEs generated by **VAE-OCP Formulation #2**.

The Hamiltonian is first constructed for the problem from Equation (78) in Section 10.5.4, as shown below:

$$\mathcal{H} = p^2 + u^2 + \lambda_q p + \lambda_p (1 + u) \tag{92}$$

Here (λ_q, λ_p) are referred to as the costates and can be considered to be time-varying Lagrange multipliers.

Using the *Pontryagin's maximization principle* (PMP) from standard optimal control theory to analytically derive optimal state/control solutions [30, 59, 164], the optimal control law is $u^*(t) = -\lambda_p/2$, and the results differential-algebraic equations (DAE) are as shown below:

$$\begin{aligned} \dot{q} &= p \qquad\quad , \quad q(0) = q_0 \\ \dot{p} &= 1 - \frac{\lambda_p}{2} , \quad p(0) = p_0 \\ \dot{\lambda_q} &= 0 \qquad\quad , \quad \lambda_q(T) = 0 \\ \dot{\lambda_p} &= -2p \quad , \quad \lambda_p(T) = 0 \end{aligned} \tag{93}$$

Using standard approaches to solving systems of boundary value problems, an augmented general solution to the DAE system can be determined (*i.e.* E and F are included to account for the additional mathematical structure due to Case #2).

$$\begin{aligned} q^*(t) &= A\cosh(t) + B\sinh(t) + Et + C \\ p^*(t) &= A\sinh(t) + B\cosh(t) + F \\ \lambda_q^*(t) &= 0 \\ \lambda_p^*(t) &= -2(A\cosh(t) + B\sinh(t) + D) \end{aligned} \tag{94}$$

Also, the optimal control law is explicitly determined as shown below.

$$u*(t) = A\cosh(t) + B\sinh(t) + D \tag{95}$$

To determine the exact solution, the four unknown constants (A, B, C, D, E, F) can be found by applying the four boundary conditions and solving the resulting set of simultaneous equations. Table 54 summarizes the expressions for the three cases. Note, that for Case #2 the constants (A, B, C, D) were determined by first

computing the optimal control law by using the constants from Case #1 and then simplifying the DAE system of Equation (94) above prior to applying the non-zero (symbolic) boundary conditions.

Table 54: Summary of constants for the analytical optimal control problem solutions to the test problem of Exp't #4 which are parameterized by initial conditions on states (q_0, p_0).

	A	B	C	D	E	F
Case #1	$1/\cosh(T)$	0	$-1/\cosh(T)$	-1	0	0
Case #2	$1/\cosh(T)$	0	$q_0 - 1/\cosh(T)$	0	p_0	p_0
Case#3	$(1 - p_0 \sinh(T))/\cosh(T)$	p_0	$q_0 - (1 - p_0 \sinh(T))/\cosh(T)$	-1	0	0

Upon specifying values for δq_0 and δp_0, the numerically computed VAEs can be compared to perturbed analytical solution for each of the VAE-OCP formulations from Section 10.5.2. In addition, the analytical solutions can be symbolically differentiated with respect to the parameters q_0 and p_0, generating 1$^{\text{st}}$-order state-to-parameter time-history solutions and allowing for comparison of analytical solutions to the numerically determined 1$^{\text{st}}$-order optimal control problems of variation. For Case #1, these time-histories are trivially equal to zero for all time since there is no explicit dependence on (q_0, p_0) in (A, B, C, D, E, F). For Case #2 and Case #3, the 1$^{\text{st}}$-order state-to-parameter sensitivity OCP solutions are given below.

- Case #2

$$q^*_{q_0}(t) = 1 \qquad q^*_{p_0}(t) = t \tag{96}$$

$$p^*_{q_0}(t) = 0 \qquad p^*_{p_0}(t) = 1 \tag{97}$$

$$u^*_{q_0}(t) = 0 \qquad u^*_{p_0}(t) = 0 \tag{98}$$

- Case #3

$$q^*_{q_0}(t) = 1 \qquad q^*_{p_0}(t) = \sinh(t) - \tanh(T)(\cosh(t) - 1) \tag{99}$$

$$p^*_{q_0}(t) = 0 \qquad p^*_{p_0}(t) = \cosh(t) - \tanh(T)(\sinh(t)) \tag{100}$$

$$u^*_{q_0}(t) = 0 \qquad u^*_{p_0}(t) = \sinh(t) - \sinh(T)(\cosh(t)/\cosh(T) - 1) \tag{101}$$

An interesting observation for the test problem used in this study (Exp't #4) is that VAEs of $q^*(t)$, $p^*(t)$, and $u^*(t)$ with respect to (q_0, p_0) are expected to contain only 0^{th} and 1^{st}-order terms, since it can seen above that there is no explicit analytical dependence on (q_0, p_0) in the 1^{st}-order state-to-parameter sensitivities of all cases under consideration. Therefore for this study the numerically generated VAE hypersurfaces are exactly equivalent to the general solution to the family of solutions for all values of (q_0, p_0).

APPENDIX D

PYGMO (THE PYTHON PARALLEL GLOBAL MULTI-OBJECTIVE OPTIMIZER)

The following discussion describes the optimization strategy utilized in Sections 11.1.4 and 11.2.8 to perform an MDO analysis to generate robust-optimal information-dense dynamic experiment designs. PyGMO (the Python Parallel Global Multi-objective Optimizer) is a scientific library providing a large number of optimization problems and algorithms under the same powerful parallelization abstraction built around the generalized island-model paradigm [149, 150, 242]. Originally implemented as a C++ API (PaGMO), PyGMO is essentially python bindings that provide fast, easy implementation of natively developed stochastic optimizers (*e.g.* particle swarming, genetic algorithm, differential evolution, firefly, monotonic basin hopping, etc.), as well as provide hooks for integrating 3$^{\text{rd}}$-party optimizer packages (*i.e.* SNOPT, IPOPT, GSL, etc.) [274]. What this means to the user is that the available algorithms are all automatically parallelized (asynchronously, coarse-grained approach) thus making efficient use of the underlying multicore architecture. PyGMO can be used to solve constrained, unconstrained, single objective, multiple objective, continuous, mixed-integer optimization problems, or to perform research on novel algorithms and paradigms and easily compare them to state-of-the-art implementations of established ones. Table 55 shows the PyGMO optimization setup used to solve the dynamic experiment design problems of Table 32 from Section 11.1.4 and Table 53 from Section 11.2.8.

Table 55: Example PyGMO optimizer python script, utilizing an 8-core computer to run eight separate variants of differential evolution for five evolutions and ten generations per evolutions.

```
#*** IMPORT PYTHON MODULES ***#
from PyGMO import *
from SMDWrapper import SMD_Prob

#*** PROBLEM INIT ***#
optns = { 'Ne' : 4 ,
          'OptType' : 'A-Opt' ,
          'ctrl_type' : 'Sinusoidal' }
myprob = SMD_Prob(**optns)

#*** PyGMO OPTIMIZER INIT ***#
#(a) define optimizer parameters
NumIslands = 8 #! No. of cores per node (archipelago)
IslandPop = 10 #! No. of cases per core per generation
NumGens = 10 #! No. of generations per evolution
NumEvos = 5 #! No. of evolutions
#(b) construct list of algorithms (differential evolution variants)
algo = [ ]
for i in range(1, NumIslands+1):
    algo.append( algorithm.de(NumGens, variant = i) )
#(c) construct an archipelago with ring topology
archi = archipelago( topology = topology.ring() )
for i in range(0, NumIslands):
    archi.push_back( island(algo[i], prob, IslandPop) )

#*** SOLVE OPTIMIZATION PROBLEM ***#
#(a) start the asynchronous generalized island model.
archi.evolve( NumEvos )
#(b) wait for it to finish
archi.join( )
#(c) print out the results
print 'Champion Obj Func: ', min([isl.population.champion.f for isl in archi])
print 'Champion Design Vector: ', min([isl.population.champion.x for isl in
archi])
```

APPENDIX E

GHV AERO-PROPULSIVE-ELASTIC PHYSICAL MODELING APPROACHES

The following discussion is supplementary to Section 11.2.3 in reference to the GHV TM, summarizing the modeling approaches that have been used for the various regions and phenomena that occur around the GHV during a standard operating condition. These include: the upper and lower surfaces of the forebody, the lower aftbody (exhaust), control surfaces, the internal flow regions within the cowl, etc.

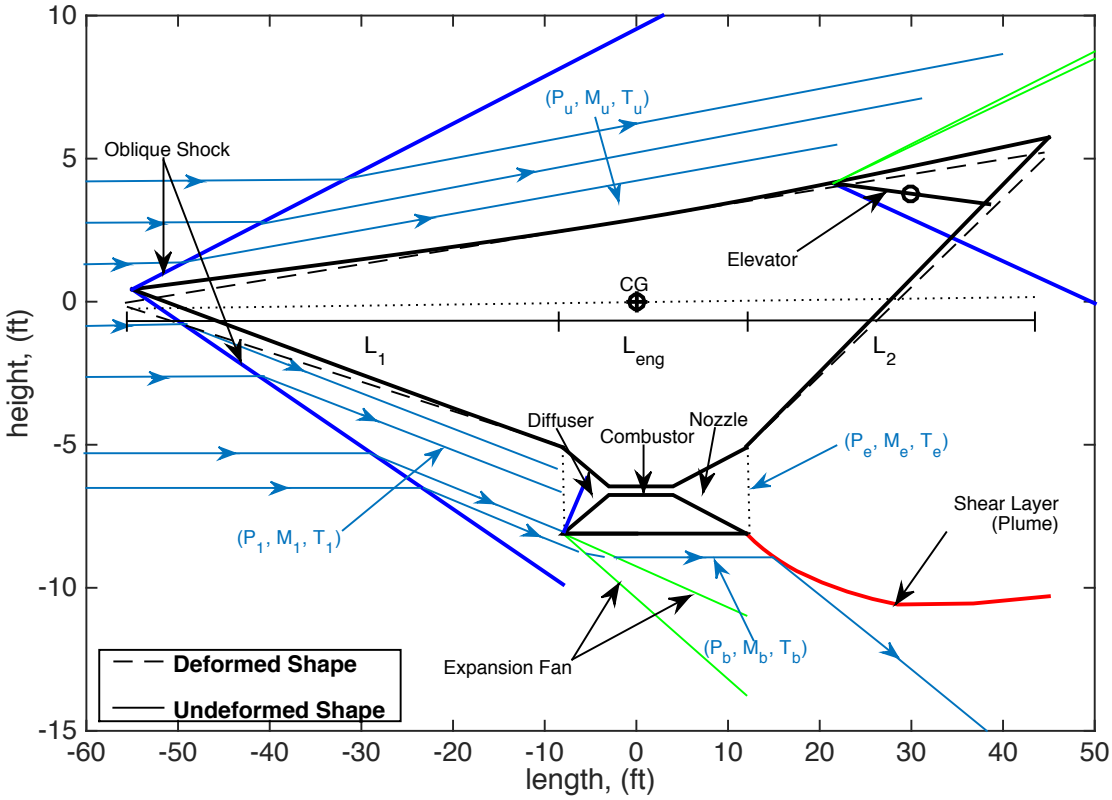

Figure 145: Operational schematic of the GHV SCRAMjet during a notional steady-level flight condition at $h = 85,000$ (ft), $\bar{q} = 2000$ (psi), and $\alpha = 2.0$ (deg), annotated with high-level thermal-fluidic flow properties.

Forebody/Upper-Surface Pressures. The pressure on the forebody is determined by either oblique shock theory or Prandtl-Meyer flow and is dependent upon the angle of attack and the amount of structural bending. When the angle of attack is greater than the forebody ramp angles, the flow behaves as if it is flowing over a concave corner; therefore, an oblique shock occurs ahead of the lower forebody. The shock angle with respect to the horizontal (in this case, taken to be the direction of the oncoming freestream flow), is a function of angle of attack and the ramp angle, $\tau_{1,L}$. On the other hand, in the cases where there is flow over a convex corner, a Prandtl-Meyer expansion fan will be manifested [10]. Prandtl-Meyer theory predicts that as $M_1 \to \infty$, the maximum angle through which the flow can be expanded is 130.4 deg. This upper bound on the expansion angle imposes limits on the angle of attack and on the control surface deflection. In the latter case, the control surface deflection limit may be less than that imposed by the actuator.

Once the downstream pressures are calculated according to either oblique shock theory or Prandtl-Meyer expansion flow theory, the aerodynamic forces acting on the vehicle can be determined via numerical integration of the pressure distributions. The aerodynamic center of the lower forebody occurs at the midpoint of the i^{th} panel, $(x_{f,i},\, z_{f,i})$, because the pressure distribution on the lower forebody is uniform behind the oblique shock wave. Likewise, the pressures on the upper-surface are determined in a similar fashion.

SCRAMjet Model. The scramjet used for this model is similar to that used by Chavez and Schmidt [66], which as been used extensively in literature. Figure 146 shows the thermal-fluidic properties within the SCRAMjet nacelle for the vehicle and operating conditions of Figure 114. The thrust is computed by the following equation.

$$\mathcal{T} = \dot{m}_a(V_e - V_\infty) + (p_e - p_\infty)A_e + (p_1 - p_\infty)A_i \tag{102}$$

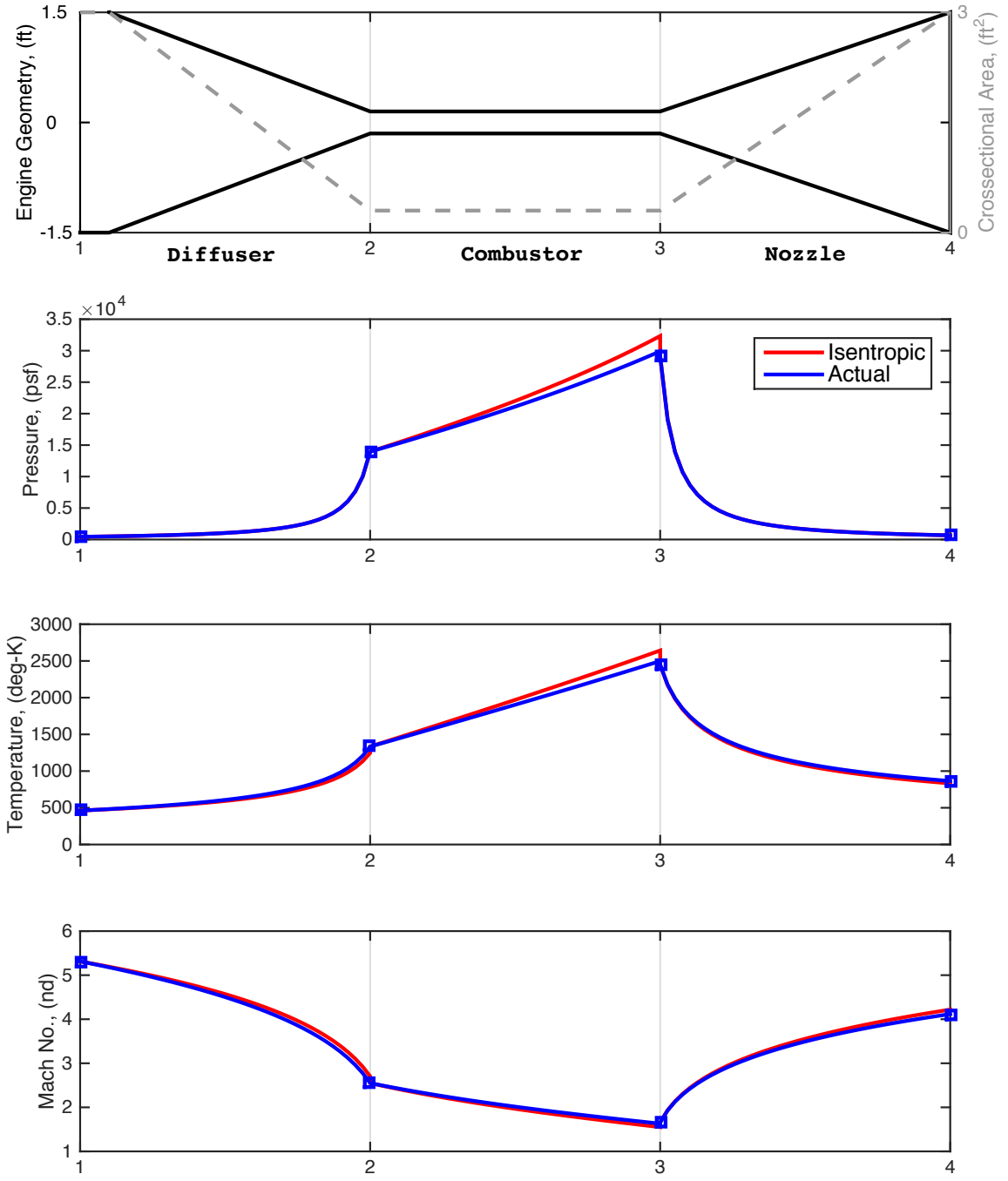

Figure 146: GHV SCRAMjet thermodynamic analysis of internal flowpath for the GHV geometry of Figure 114 flying at stead-level flight at $h = 85,000$ (ft) and $\bar{q} = 2000$ (psi).

The conditions given at the engine inlet (station 1) are primarily determined by the Mach number and angle of attack at which the aircraft is flying. These parameters determine, in part, the properties of the bow shock. The two control variables that determine the thrust setting are the diffuser area ratio $\bar{A}_D$ and the fuel equivalence ratio Φ. The equivalence ratio effectively determines the change in total temperature that results from the combustion process. Choosing Φ as a control parameter is the same as controlling the fuel flow, because how much air is captured by the propulsion system is lumped in this quantity. This avoids having to make *a priori* assumptions regarding the fuel schedule and the parameters used for scheduling. Controlling $\bar{A}_D$ allows one to modulate the Mach number and the static pressure of the air entering into the combustion chamber. Ideally, the air remains supersonic to avoid significant ram drag penalties and excessive heating. Because the air entering the combustor is supersonic, the heat release due to fuel combustion reduces the Mach number of the airstream that is passing through the engine. Care must be taken to ensure that the amount of heat added does not thermally choke the combustor flow.

1. **Diffuser.** In the diffuser, the continuity equation (conservation of mass) is used to determine the Mach number at the diffuser exit/combustor inlet (station 2) given the diffuser inlet Mach. It is assumed that the diffuser isentropic efficiency is $\eta_D = 0.85$.

2. **Combustor.** The combustor is modeled as a constant-area, frictionless duct with heat addition. The change in total temperature within the combustor is due to the burning of fuel (either liquid hydrogen (LH2) or a hydrocarbon-based fuel such as JP-8). Engine thrust is strongly dependent upon the fuel-to-air ratio ($f = \dot{m}_f/\dot{m}_a$) in the combustor. Typically, the fuel-to-air ratio is normalized by the stoichiometric fuel-to-air ratio, and the fuel equivalence ratio is used as a control input to the engine instead of the change in total temperature across

the combustor. Numerically, this approach avoids some of the scaling problems associated with using the change in temperature as a control input. The fuel equivalence ratio is defined as $\Phi = f/f_{st}$. Values of f_{st} and H_f for LH2 and the hydrocarbon-base fuel, JP-8, are given in Table 56 and are taken from Heiser and Pratt [135], whereas the values for C_p are taken from [12]. It is assumed that the combustion efficiency is $\eta_C = 0.9$. It should be noted that for this model the equivalence ratio maps linearly to the change in total temperature in the combustor, which, in turn, maps linearly to the thrust. In actuality, one expects to see a decrease in thrust for some value of Φ that is slightly above unity. Because this combustion model does not capture the finite-rate chemistry that occurs in the combustion process, the model is only physically meaningful where the thrust is a linear function of the equivalence ratio.

Table 56: Properties of common scramjet fuels [12, 135].

Fuel	f_{st}	H_f, BTU/lmb	C_p, BTU/(lbm-^{o}R)
LH2	0.0291	51,500	0.24
JP-8	0.0664	19,100	0.54

3. **Nozzle.** The flow, upon leaving the combustor, enters a diverging, nearly isentropic nozzle that will ultimately increase the exit Mach number. Again, similar to the diffuser analysis, the continuity equation (conservation of mass) is used to determine the Mach number at the nozzle exit (station 4) given the combustor exit Mach (station 3). The exit nozzle area ratio is assumed to be fixed, and It is assumed that the nozzle efficiency is $\eta_N = 0.95$.

This model captures diffuser and thermal choking, which leads to a well-known failure phenomena SCRAMjet engine un-starting. Engine un-starting has proven to be a significant issue during SCRAMjet operation (*e.g.* the X-51 program). Figures 147 and 148 show aero-thermal behavior for these choking phenomena.

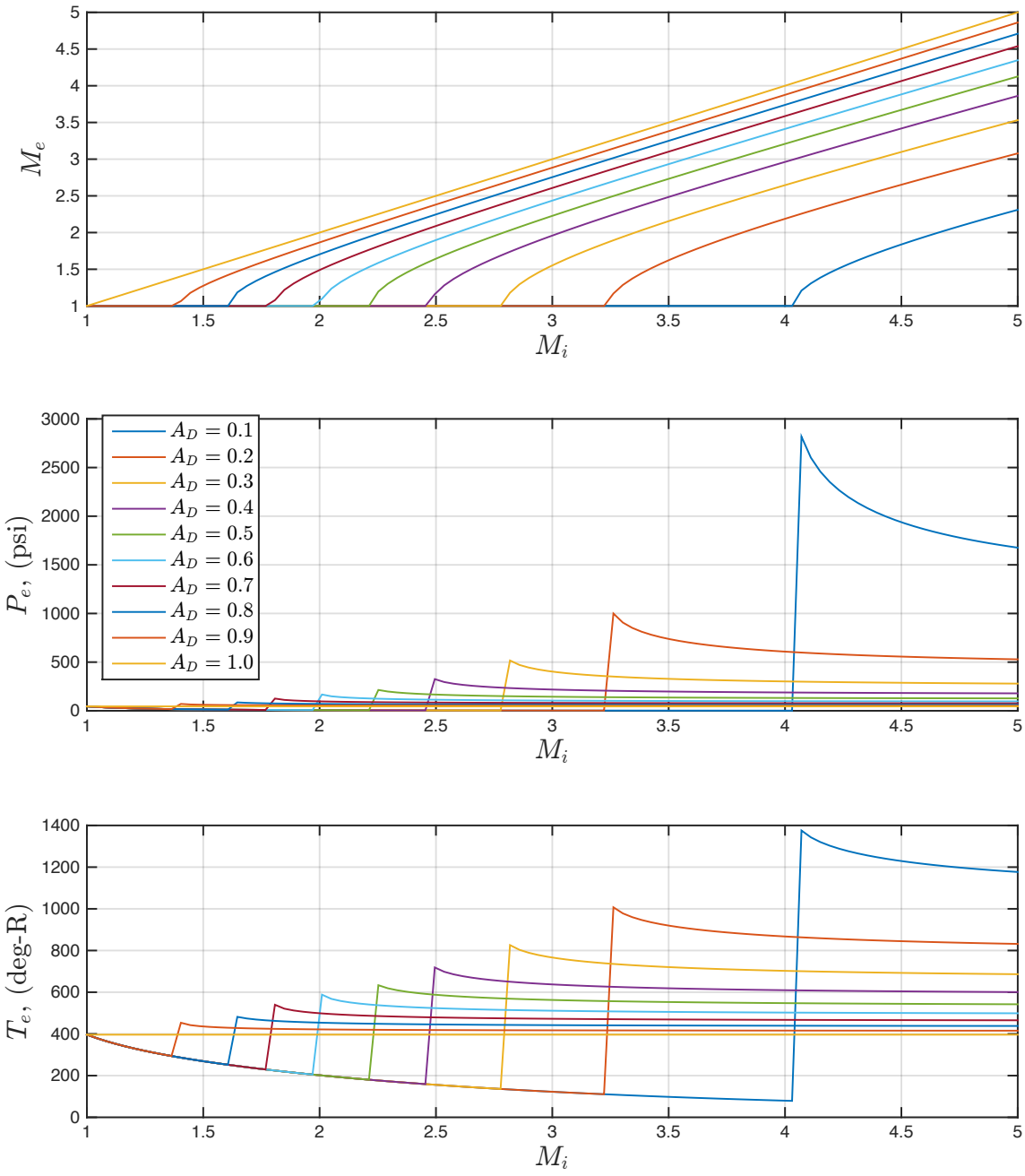

Figure 147: GHV SCRAMjet aero-thermodynamic analysis of internal diffuser for varying diffuser geometries.

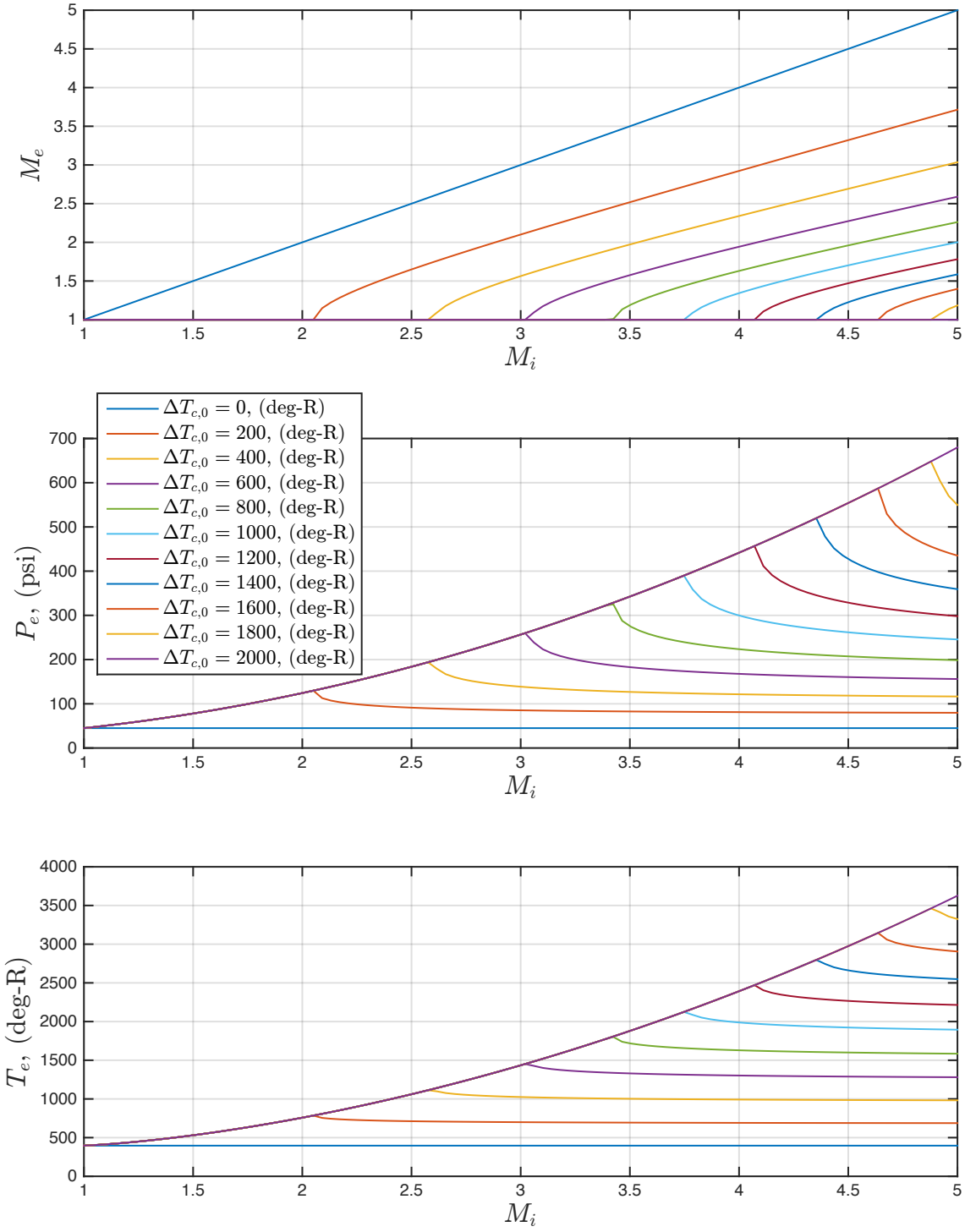

Figure 148: GHV SCRAMjet aero-thermodynamic analysis of the combustor for varying delivered stagnation temperature addition due to increasing fuel-to-air ratios.

There are a few additional aero-thermal physical effects which were included in the GHV model, as described below. Both of these phenomenon are modeled using the quasi-1D/2D flow models, previously discussed above for the aero-thermal modeling on external vehicle surfaces.

1. **Mass Flow Spillage Effects.** Deflection of the forebody due to aerodynamic forces can lead to SCRAMjet performance reduction, and even failure, if the pressure and mass flow changes that occur significantly affect the thrust, lift, and pitching moment. Furthermore, changes in the stability and control derivatives due to the structural dynamics could possibly have adverse effects on the pole and zero locations, which, in turn, could degrade the gain and phase margins of an inner-loop control system. If mass flow spillage effects are not negligible, then some sort of active control device may be necessary in order to regulate the mass flow of air into the engine.

2. **Engine Inlet Turning Forces.** The airflow, after passing through the lower-forebody oblique shock, is parallel to the forebody upon entry into the engine cowl; therefore, the flow must be turned parallel to the engine centerline. The mechanism for turning the flow axial to the engine is a second oblique shock, and there will be a resulting rise in static pressure and temperature and a decrease in Mach number as the flow crosses this shock.

Aftbody Pressure. The pressure acting on the aftbody of the vehicle is due to the external expansion of the exhaust from the scramjet engine. The aftbody forms the upper part of an aerospike nozzle, where the shear layer that results from the interaction of the exhaust plume with the freestream flow forms the lower surface, shear layer, of the aerospike nozzle. The pressure distribution along the aftbody is then a function of the position of the shear layer. The shear layer is formed where the pressure in the plume is balanced by the freestream pressure. The exact position

of the shear layer can be calculated, as shown below in Figure 149, by approximating the plume by a series of panels. Given the ambient atmospheric pressure, the exit pressure from the engine internal nozzle, and the angle of the expansion ramp, the location of the shear layer can be calculated by balancing the pressure trailing the lower-surface forebody oblique shock with the pressure internal to the exhaust plume. Schmidt has derived a simplified analytical relationship describing the external pressure distribution for ideal operation [65].

The lower-surface aftbody pressure makes a contribution to the lift and also acts to offset the drag of the forebody. The pitching moment due to these forces is assumed to act on the aftbody panel at the point where the mean value of the pressure distribution occurs.

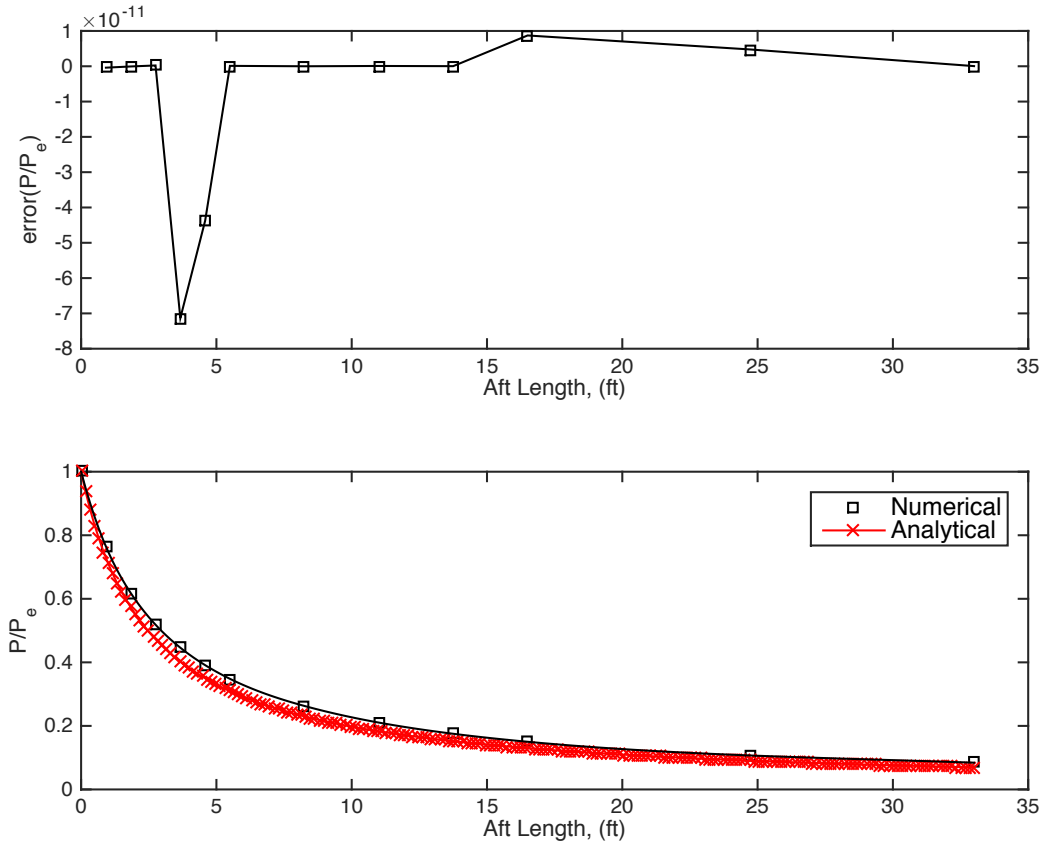

Figure 149: An illustration of a computed scaled pressure distribution given the reference flight condition of Figure 145 over the lower-surface aftbody.

Control Surface Model. As shown in Figure 114, there is a control surface available that is used to control the pitching moment acting on the aircraft. The control surface is modeled as a flat plate that is hinged at its mid-chord point so that the entire surface deflects. This is consistent with the designs of both the X-43 and NASP, where the wing tips were deflected for pitch control. The pressures on the upper and lower surfaces of the elevator are determined by the orientation of each control surface with the flow. The incidence angle is a function of the angle of attack, the deflection of the elevator with respect to the body-fixed x-axis and the slope of the fuselage's neutral axis that occurs at the hinge point. Therefore, due to aero-elastic deflection of the vehicle structure (discussed subsequently), there is a change in the turn angle of the flow, which will affect elevator effectiveness. Because flat plates are used in this model to approximate control surfaces, the pressure is easily determined by Prandtl-Meyer expansion flow on one side of the plate and by oblique shock theory on the other side.

Forced-Vibration (Dynamic Aeroelastic) Effects. For full-scale air-breathing hypersonic SCRAMjets, aero-elastic flexibility effects play an important part in the performance and reliability of the vehicle. Considering the discussion in the previous section, it is evident that the structural bending will manifest itself in the flow deflection angles and, as a result, will have an effect on the angle of the bow shock, thereby affecting the pressures downstream of that shock. For example, deflection of the forebody affects the thrust not only through changes in pressure due to the moving shock, but also through the effects of mass flow spillage. Thus, one can expect that structural vibrations will cause the engine to operate under off-design conditions most of the time, causing inlet flow pressure and mass flow spillage losses.

For flight dynamic simulation, a vibrational model of the fuselage is necessary. Hypersonic vehicles are generally tapered at the fore and aft ends, thus concentrating

the mass toward the middle of the vehicle. In this case, one would expect the elastic deflection of the fuselage at the center of mass to be much less than that at either end of the vehicle. Therefore, the fuselage is modeled as comprising of two cantilever beams, one pointing forward and one pointing aft. Each beam has one end clamped at the center of mass of the fuselage. Thus, the root of each beam will rotate and translate according to the motion of the aircraft's center of mass. As discussed by Bolender and Doman for the GHV [45], only the transverse displacements of the beams are of interest. It is assumed that the displacements are sufficiently small such that Hooke's law is valid. At the center of gravity, there will be no structural displacement or rotation of the beams, due to the assumption that they are clamped at this point.

The aeroelastic modeling approach developed here uses beam theory from Meirovitch [201], where the transverse vibration of a cantilever beam with constant EI and constant mass density $\hat{m}$ satisfies the following partial-differential equation.

$$EI\frac{\partial^4 w(x,t)}{\partial x^4} + \hat{m}\frac{\partial^2 w(x,t)}{\partial t^2} = p(x,t) + P_j(t)\boldsymbol{\delta}(x - x_j) \tag{103}$$

From the expansion theorem (*i.e.* separation of variables approach to analytically solving PDEs), the solution of Equation (103) is of the following form.

$$w(x,t) = \sum_{k=1}^{\infty} \phi_k(x)\eta_k(t) \tag{104}$$

Here, $\phi_k(x)$ are spacial solutions to the k^{th}-order bending mode, which can be analytically determined prior to dynamic simulation. $\eta_k(t)$ satisfies the differential equation below:

$$\ddot{\eta}_k + \omega_k^2\eta_k = N_k(t), \tag{105}$$

where the generalized modal force associated with the k^{th} bending mode shape is

$$N_k(t) = \int_0^L \phi_k(t) p(x,t) dx + \sum_{j=1}^{l} \phi_k(x_j) P_j(t) \tag{106}$$

In Equation (106), l is the number of concentrated forces applied to the beam (*e.g.* control surface point forces on the GHV fuselage). This equation is a key component of the equation of motion for the flexible GHV aircraft. Figure 150 shows the transverse beam deflection of both the fore/aft-body fixed-free beams for the first three bending modes, using the vehicle parameters of Table 41.

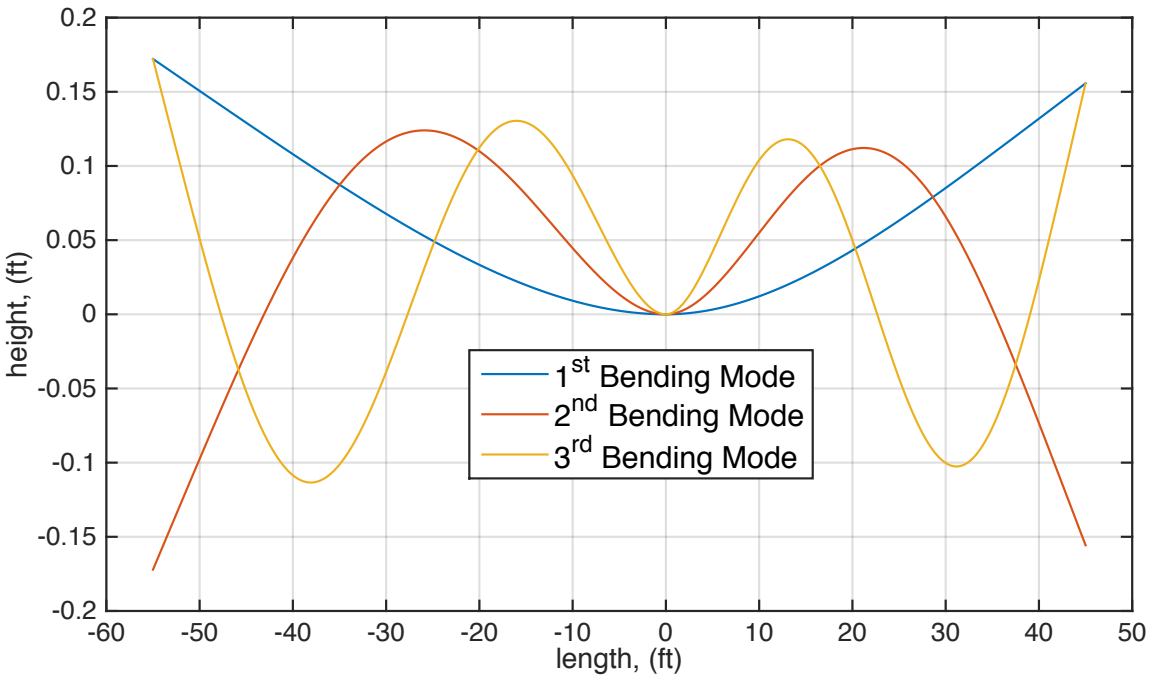

Figure 150: GHV aeroelastic Euler-Bernoulli beam deflections modes 1-3 using a separation of variables approach, as described in [45, 201].

APPENDIX F

GHV CONTROL-ORIENTED MODELING REGRESSION ANALYSES

In Section 11.2.3.3 the development of the control-oriented models (COMs) for the aero-propulsive-elastic (APE) parameters was described. A grid of design of experiments (DOEs) were run to compute tabulated coefficients of these models (also referred to as response surface equations (RSEs)) over a range of altitudes and dynamic pressures, consistent with the work by Bolender and Doman [45]. What follows is an RSE analysis of the GHV model for a single point in the gridded 2-dimensional space of altitude and dynamic pressure (or equivalently the total velocity) – $h = 99,860$ (ft) and $\bar{q} = 2000$ (psf).

Figure 151 shows a 500-case DOE over the admissible ranges of states and inputs listed in Table 45 of Section 11.2.3.6. The black points represent proper SCRAMjet engine operation, and the blue points represent cases where thermal choking occurs inside the combustor; thus, causing imminent failure of the SCRAMjet engine – a phenomenon referred to as engine unstarting. Across the range of altitude/dynamic pressure conditions, operational failures are possible even within the admissible ranges of states and inputs. In the top-left scatter plot, C_D is plotted versus C_L, resulting in a quadratic trend similar to the drag polar common for fixed-winged, rigid-body vehicles. Other comparisons show much less intuitive interactions, capturing more complicated effects between the regions of safe and unsafe operation. For example, the trends involving C_M behavior where operational failures appear to be distributed irregularly over the space. Another trend that provides interesting insight into the limits of GHV operation is the comparison C_T *vs.* N_f, which shows an irregularly

bounded envelope, where engine unstarting occurs for the upper-bounded values of N_f and for any value of C_T, large or small. This can be explained by the causation of the high values of N_f to elastically deform vehicle fore-body to high degrees of flexing, hence increasing the inlet flow turning angle across the lower-surface of the fore-body and increasing the oblique shock angle and strength. This induces a subsequent loss in aerothermal energy entering the engine, which in turn causes choking inside the combustor if too much fuel is ejected.

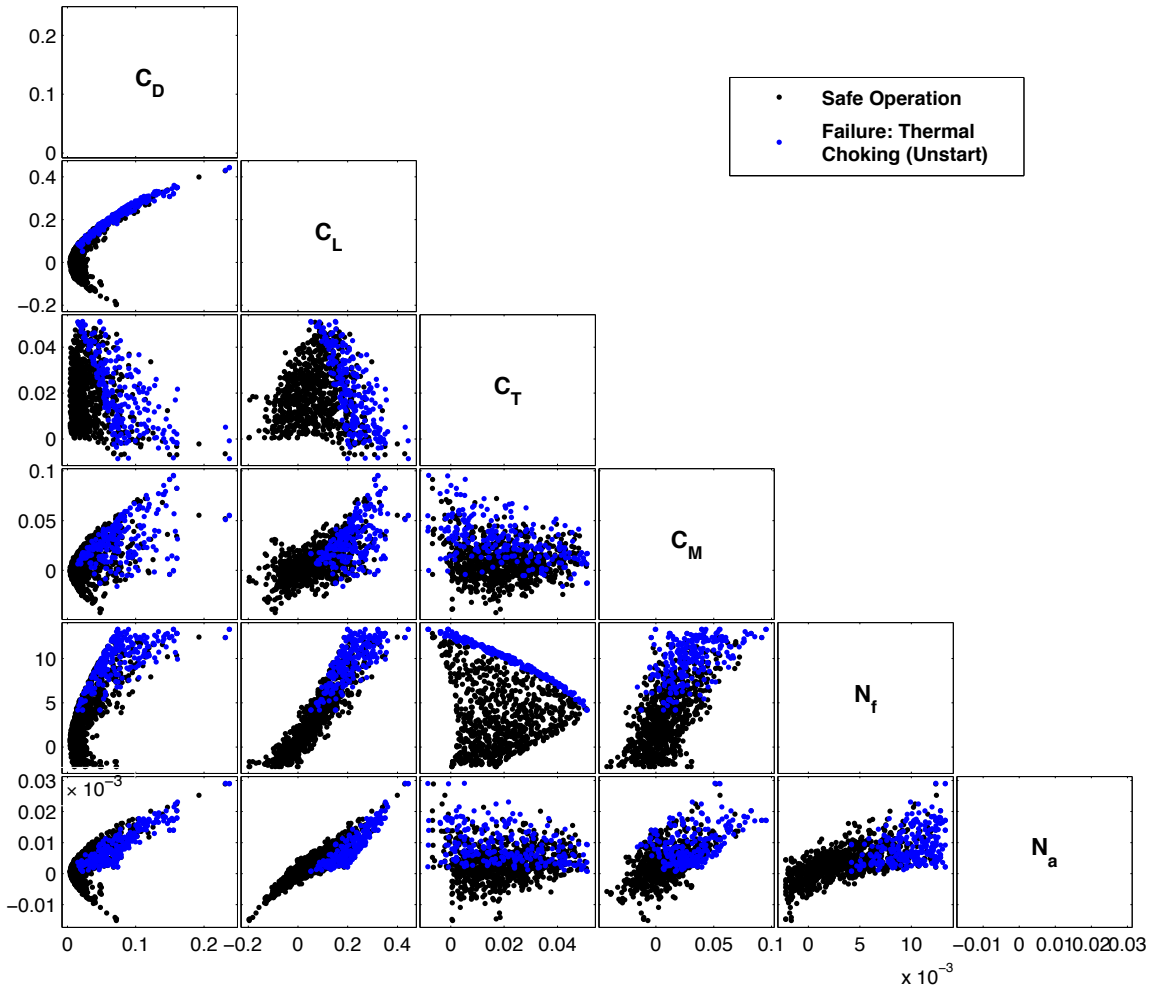

Figure 151: Multivariate scatterplot results of a 500-case DOE, comparing GHV coefficients for forces and moments (both pitch and bending moments) for $h = 99,860$ (ft) and $\bar{q} = 2000$ (psf).

F.1 Control-Oriented Model Regression Analysis

Below are the regressed COMs for the data shown above in Figure 151. The trends shown here are very similar to results presented by Parker, et al. [228], which validates the GHV aerothermal physics models developed for this work.

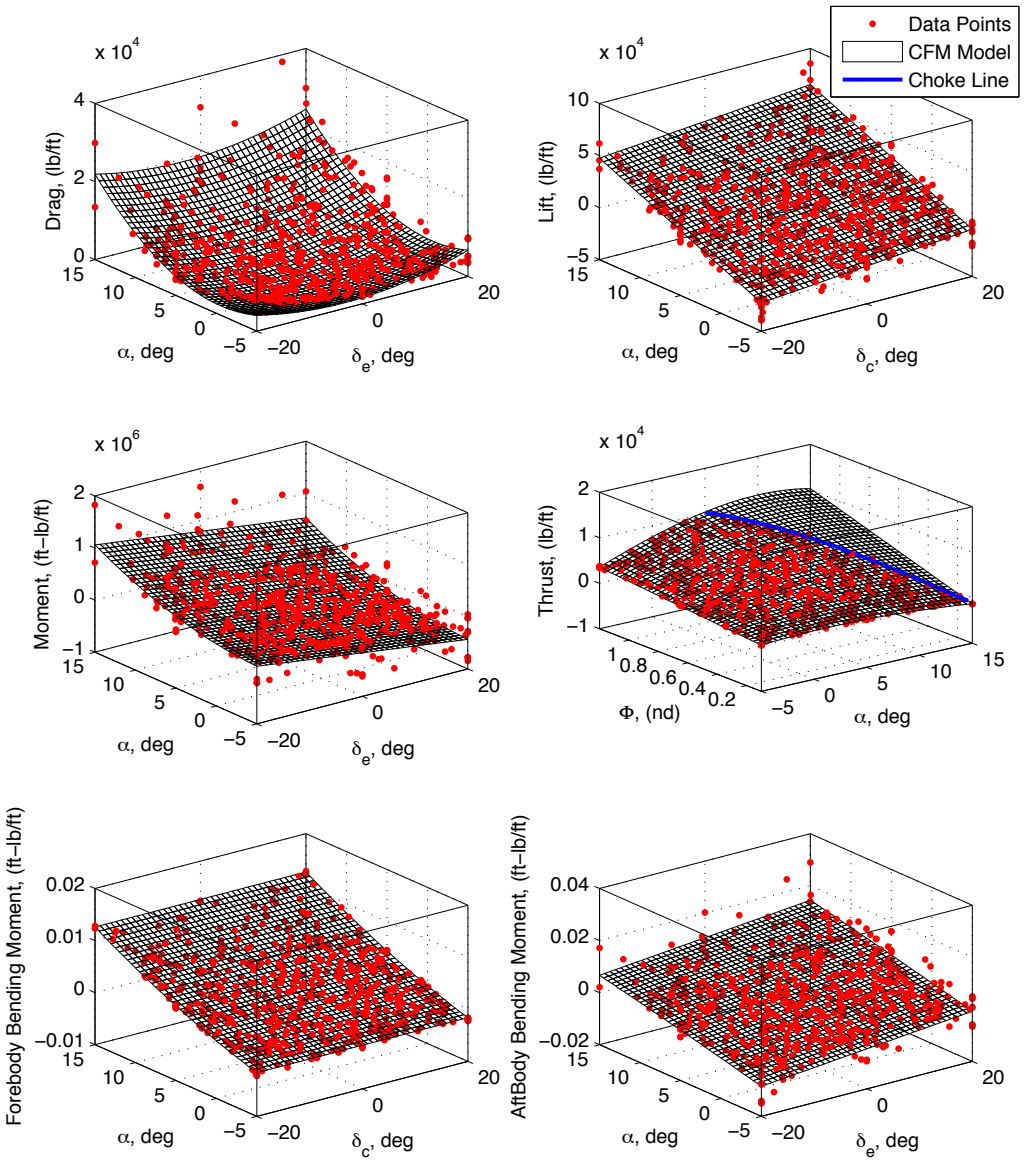

Figure 152: Control-oriented model fits at conditions: $h = 99.86$ (kft) and $\bar{q} = 2000$ (psf). These trends are validated by the results of Parker, et al. [228].

Figures 153-158 show goodness-of-fit results for the regression analysis of the COMs above. As discussed qualitatively by Parker, et al. [228], the fit for the drag COM yields a less accurate model than the other models; however, it is highly desirable to retain this familiar model structure for subsequent control systems design exercises. The regressed thrust force COM (Equation (90) from Section 11.2.3.3) on the other hand is an excellent fit; however, this model will provide complications in subsequent control systems design exercises, as this model's dependency on the cube of angle of attack as well as up to 4^{th}-order interactions between fuel-equivalence-ratio and angle of attack.

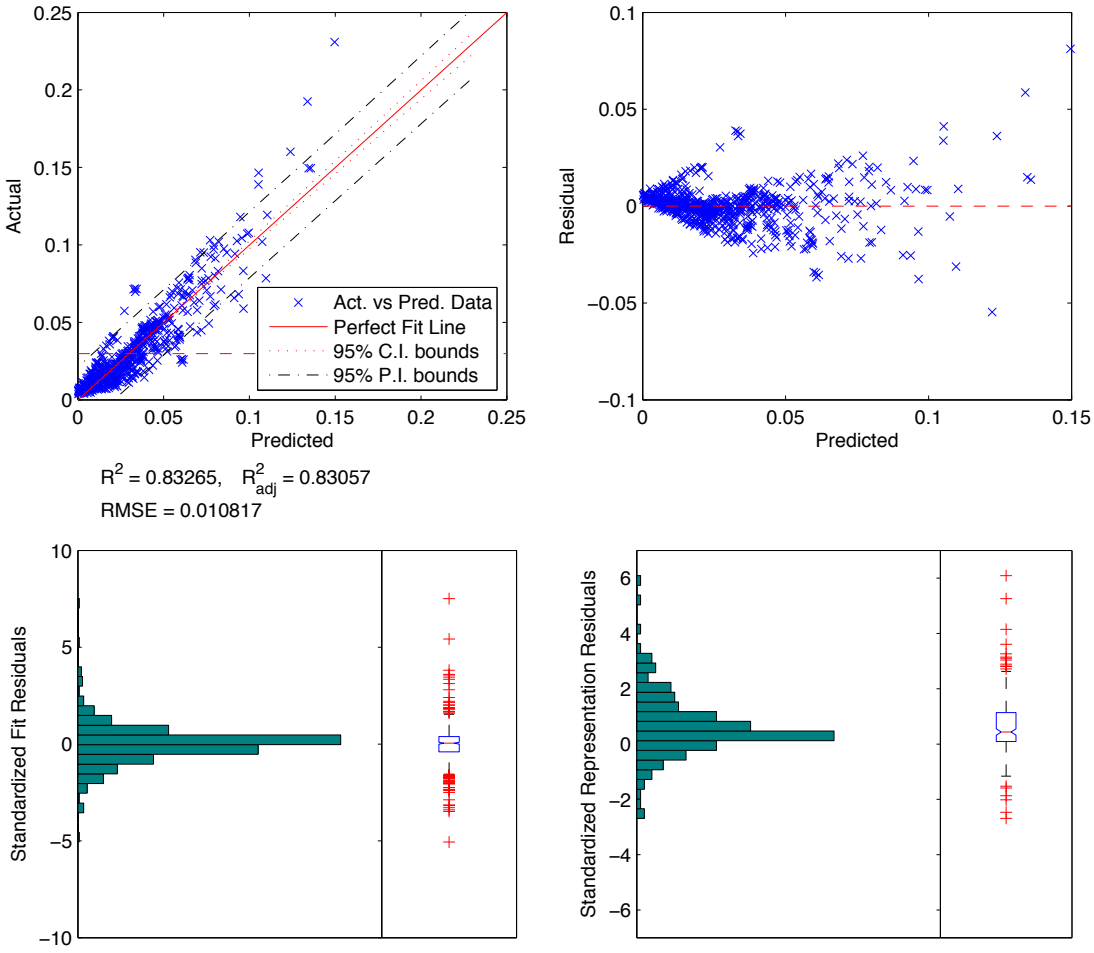

Figure 153: Control-oriented model goodness-of-fit metrics for total drag C_D coefficient model at conditions: $h = 99.86$ (kft) and $\bar{q} = 2000$ (psf).

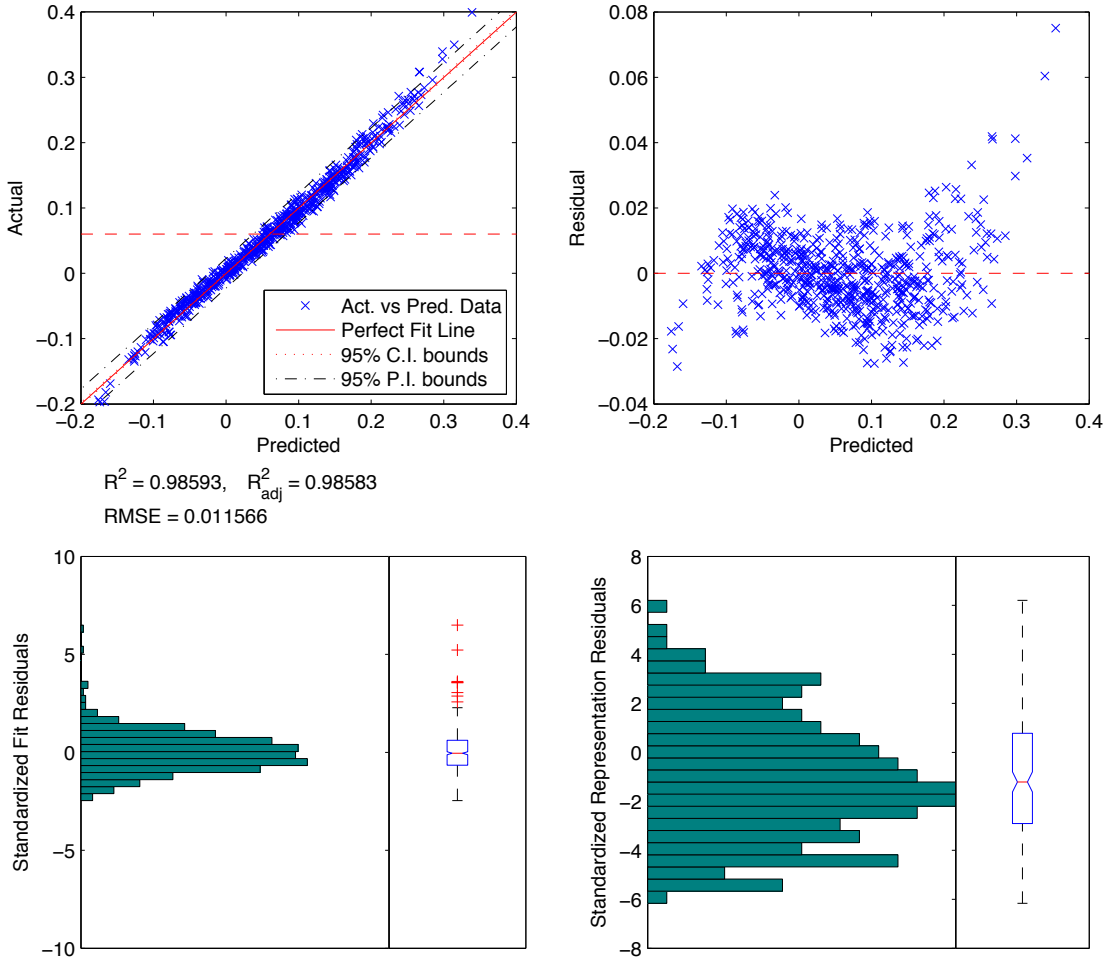

Figure 154: Control-oriented model goodness-of-fit metrics for lift coefficient model C_L at flight conditions: $h = 99.86$ (kft) and $\bar{q} = 2000$ (psf).

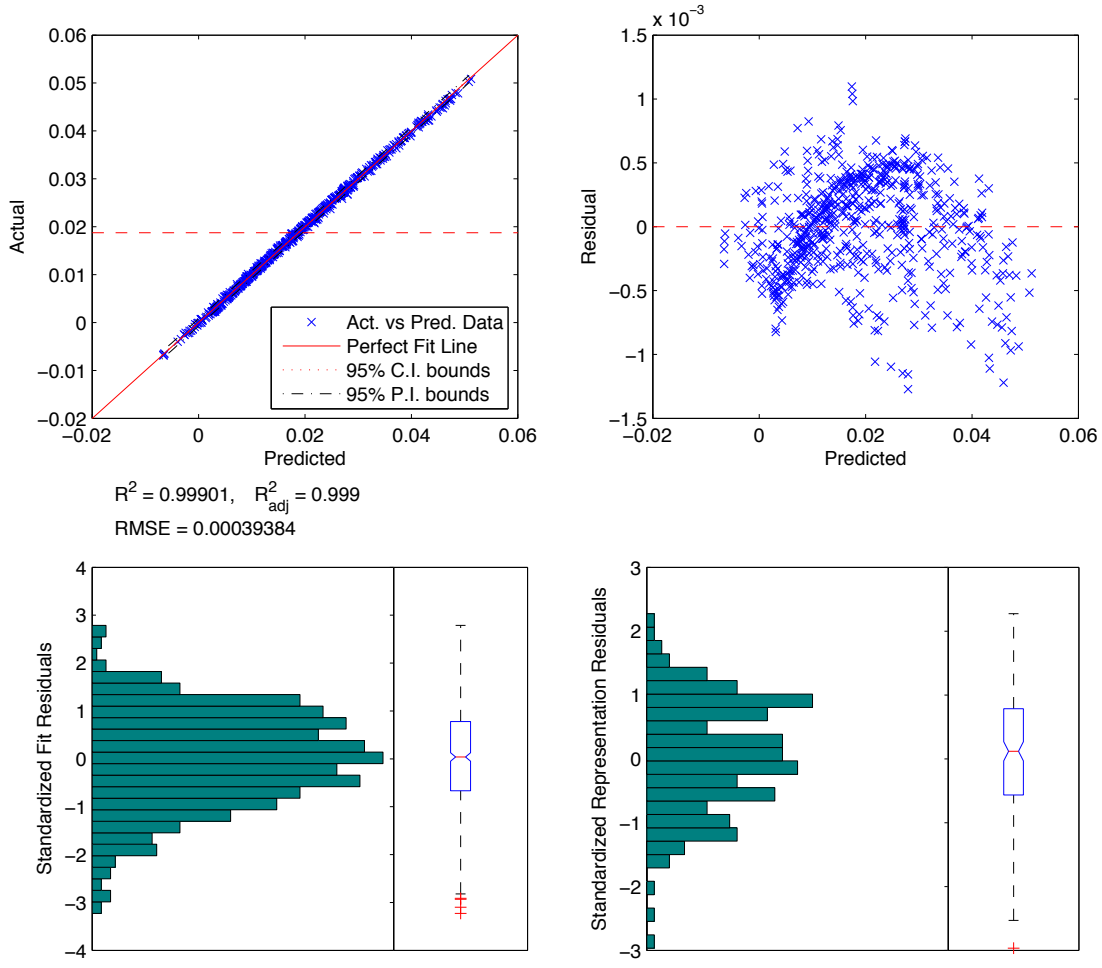

Figure 155: Control-oriented model goodness-of-fit metrics for thrust coefficient model C_T at flight conditions: $h = 99.86$ (kft) and $\bar{q} = 2000$ (psf).

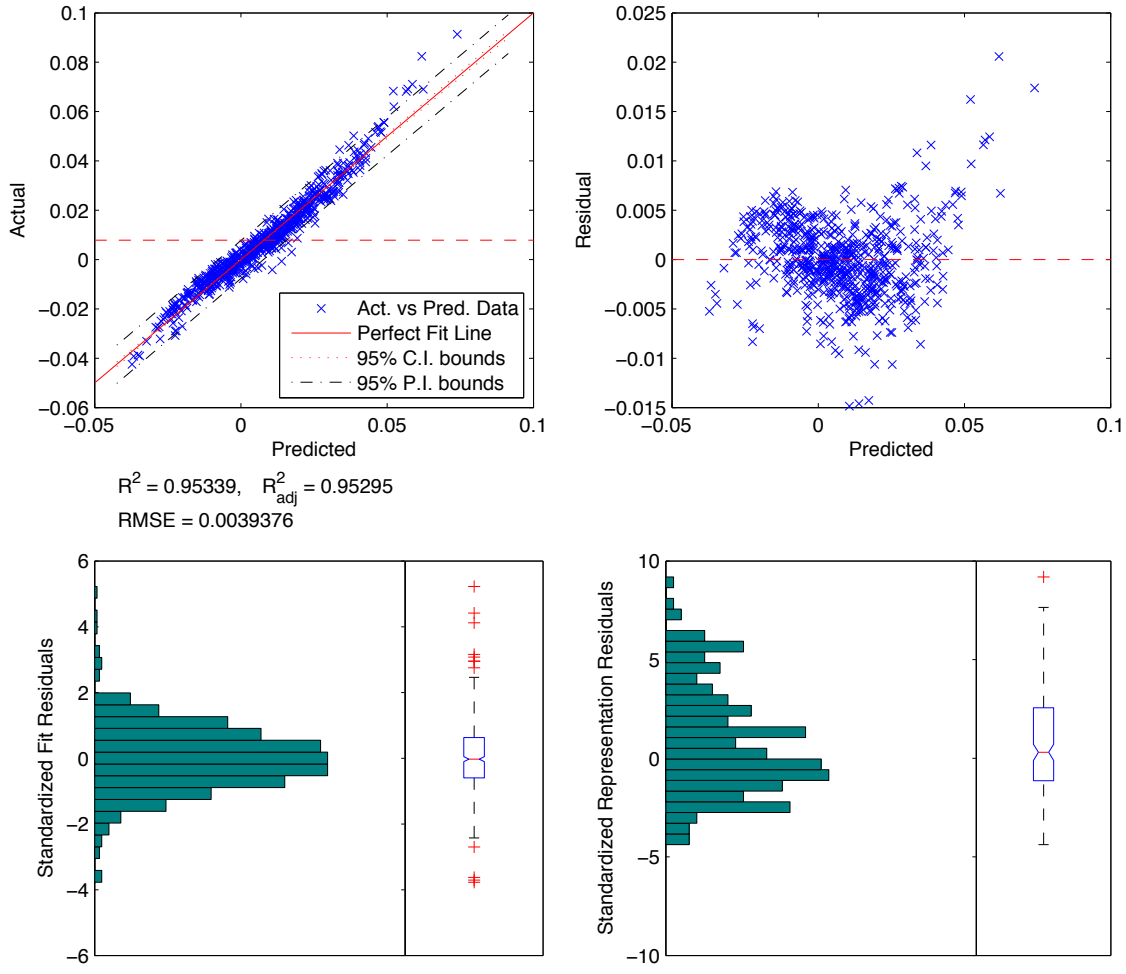

Figure 156: Control-oriented model goodness-of-fit metrics for the pitching moment coefficient model C_M (excluding the contribution due to thrust) at flight conditions: $h = 99.86$ (kft) and $\bar{q} = 2000$ (psf).

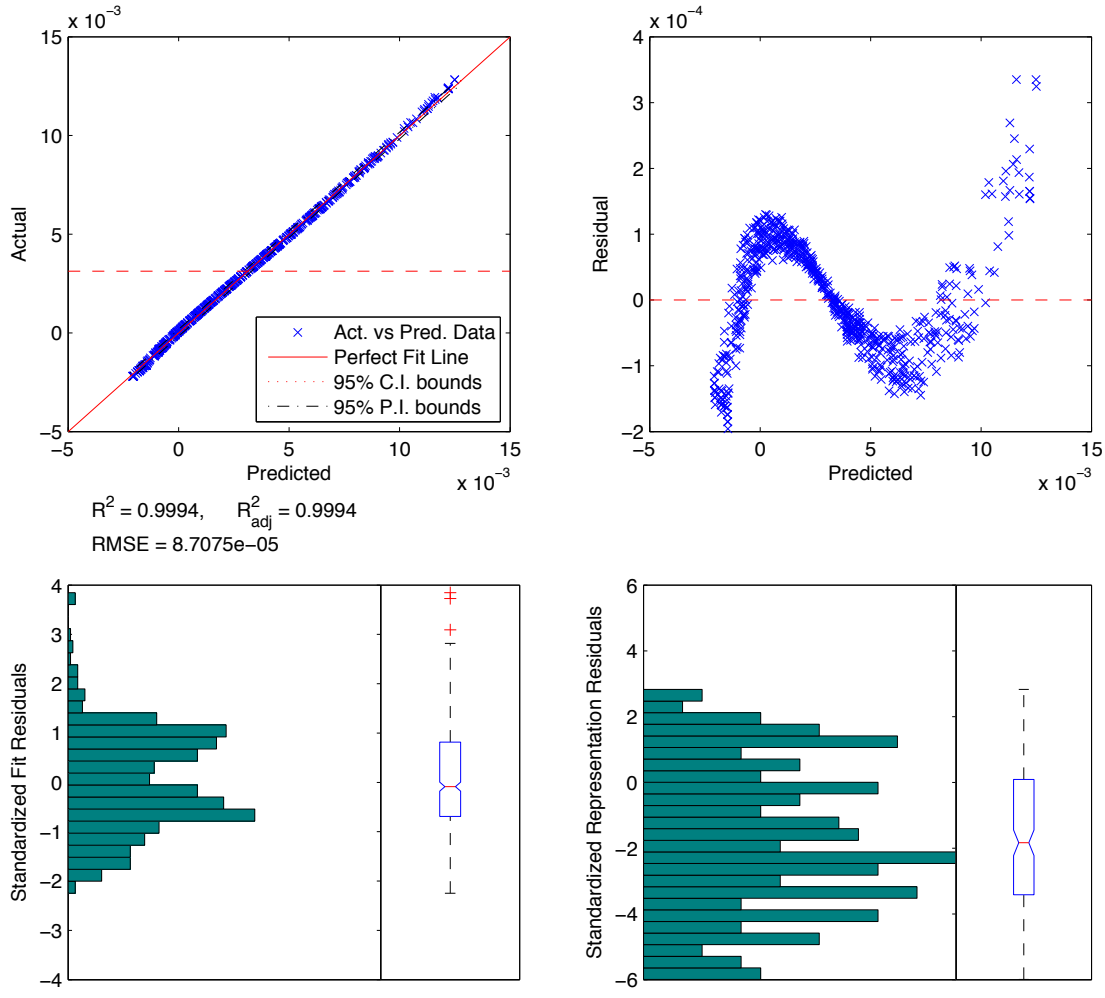

Figure 157: Control-oriented model goodness-of-fit metrics for the 1st-mode fore-body bending moment coefficient model N_f (excluding the contribution due to thrust) at flight conditions: $h = 99.86$ (kft) and $\bar{q} = 2000$ (psf).

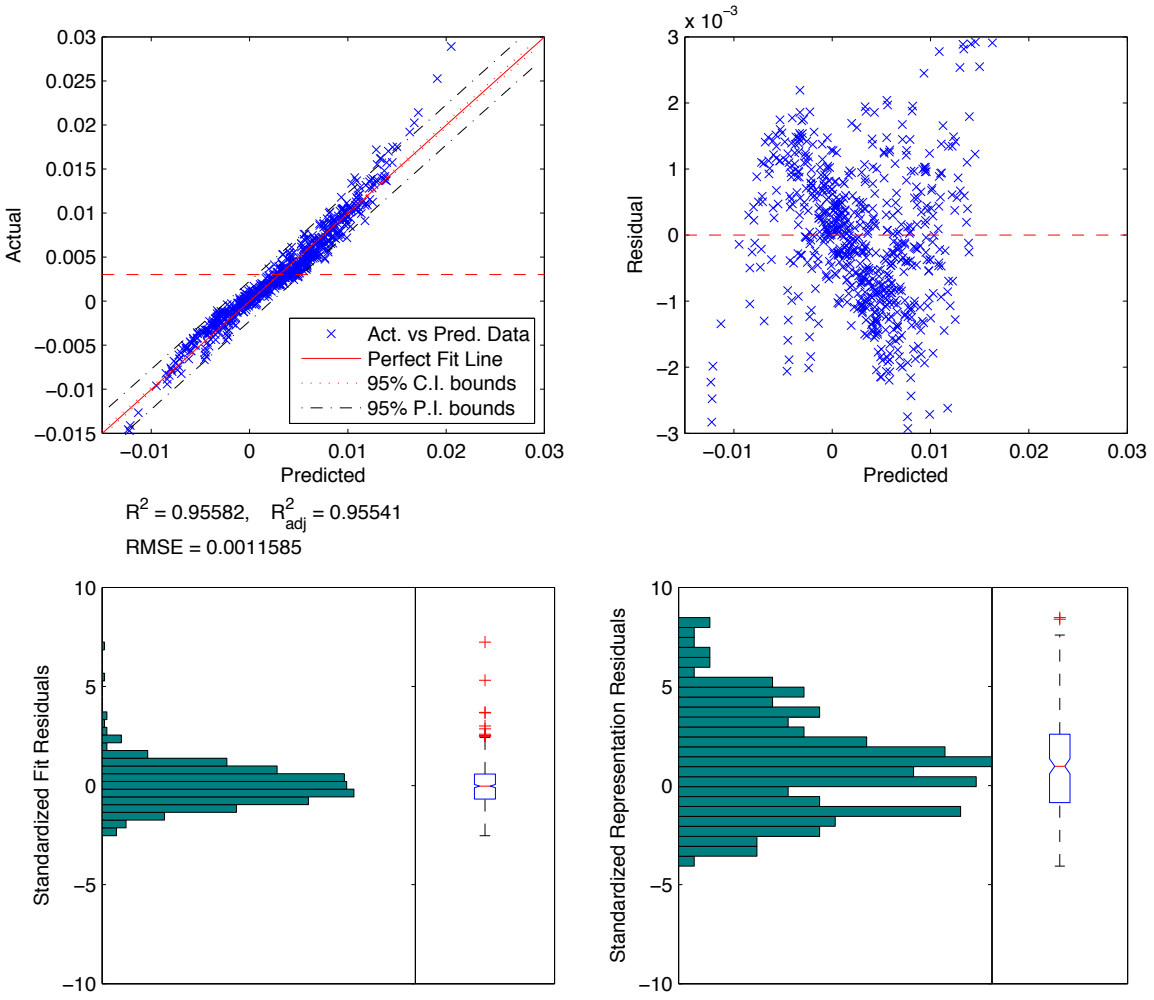

Figure 158: Control-oriented model goodness-of-fit metrics for the 1st-mode aft-body bending moment coefficient model N_a (excluding the contribution due to thrust) at flight conditions: $h = 99.86$ (kft) and $\bar{q} = 2000$ (psf).

F.2 3rd-Order Stepwise Regression Analysis

The following analysis generated stepwise regression control-oriented models (SRMs) and was conducted for two reasons: (i) to investigate the required increase in complexity with respect to the COMs when obtaining regressions with higher-accuracy; and (ii) to obtain regressions of the failure margin models, such as: choking margin in the diffuser and the combustor. These failure models are useful for controls systems design to anticipate unexpected failures.

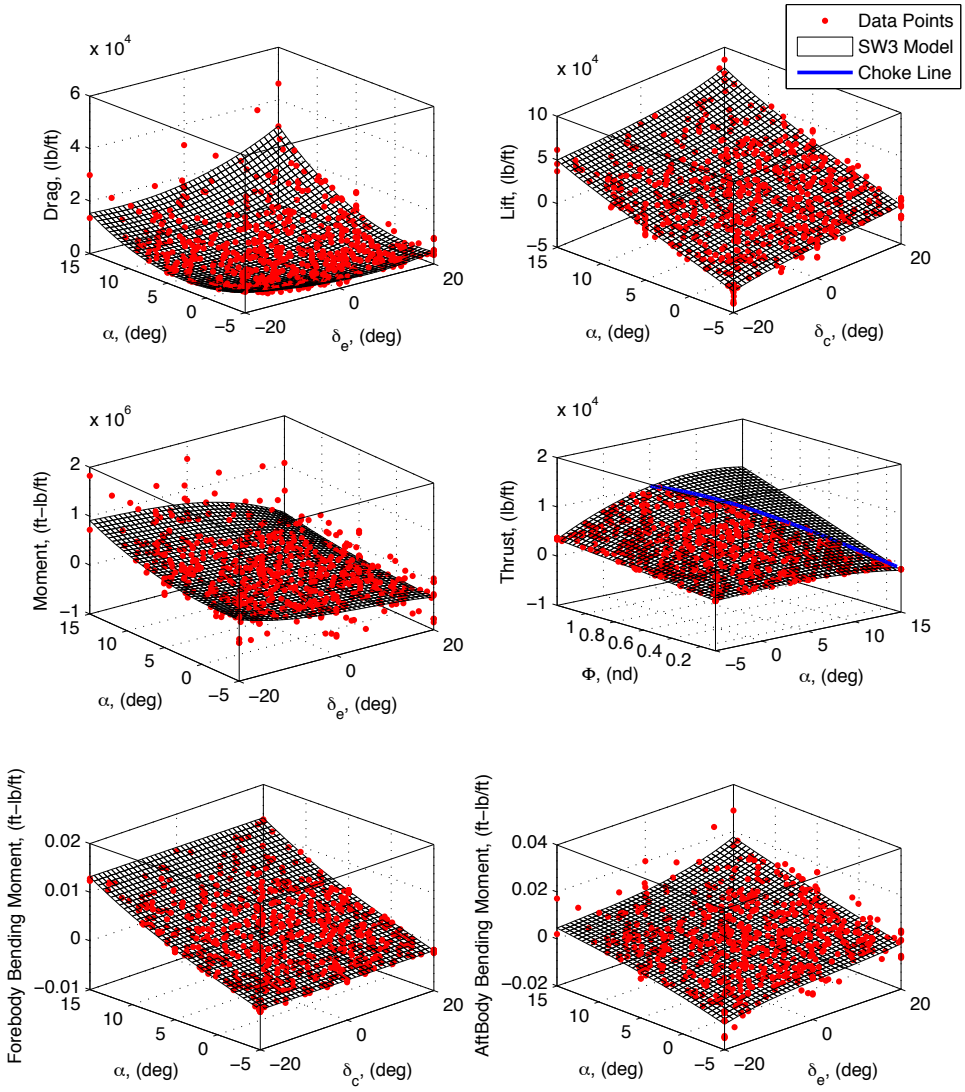

Figure 159: 3th-order SRMs for forces and moments at conditions: $h = 99.86$ (kft) and $\bar{q} = 2000$ (psf).

Figure 160 shows the regressed models for four identified failure modes that the vehicle might excite even while operating within the admissible ranges for states, controls, dynamic pressure, Mach number, etc. The failure models considered in this work are: (i) distance to diffuser choking limit (*i.e.* diffuser choking margin) – $\Delta\bar{A}_D$, (ii) distance to combustor choking limit (*i.e.* thermal choking margin) – $\Delta T_{c,0}$, (iii) maximum internal cowl pressure – $P_{\max}$, and (iv) maximum internal cowl temperature – $T_{\max}$. The blue constraint lines in Figures 152, 159, and 160 represent portions of the admissible region, where $\Delta\bar{A}_D$ and $\Delta T_{c,0}$ are positive in value, and hence, SCRAMjet engine unstarting occurs beyond this boundary.

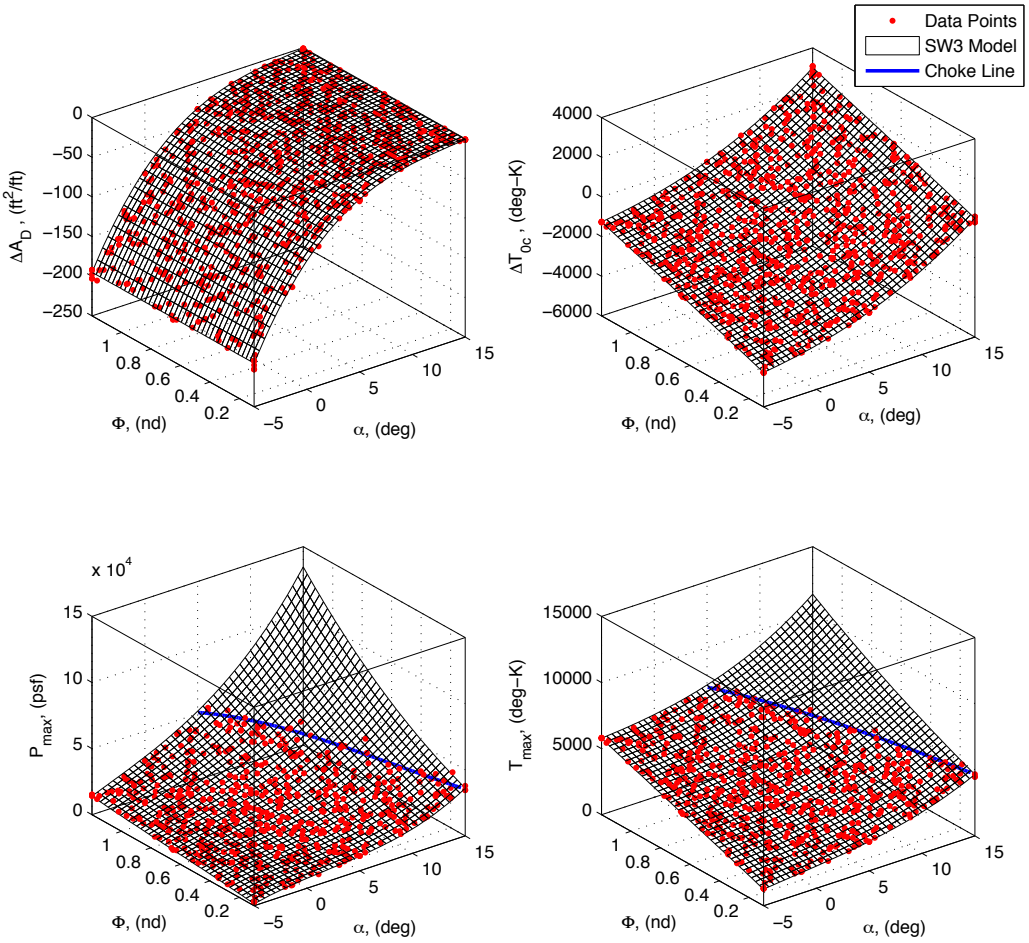

Figure 160: 3$^{\text{th}}$-order SRMs for failure modes ($\Delta\bar{A}_D$, $\Delta T_{c,0}$, $P_{\max}$, and $T_{\max}$) at conditions: $h = 99.86$ (kft) and $\bar{q} = 2000$ (psf).

The resulting model structures for the SRM failure modes are shown below. Here it can be observed that these behaviors are dominated by angle of attack and fuel equivalence ratio.

$$
\begin{aligned}
\Delta\bar{A}_D(\alpha) &= \Delta\bar{A}_D^0 + \Delta\bar{A}_D^\alpha\alpha + \Delta\bar{A}_D^{\alpha^2}\alpha^2 + \Delta\bar{A}_D^{\alpha^3}\alpha^3 \\
\Delta T_{c,0}(\alpha,\Phi) &= \Delta T_{c,0}^0 + \Delta T_{c,0}^\alpha\alpha + \Delta T_{c,0}^{\alpha^2}\alpha^2 + \Delta T_{c,0}^{\alpha^3}\alpha^3 + \Delta T_{c,0}^\Phi\Phi + \Delta T_{c,0}^{\Phi^2}\Phi^2 \\
T_{\max}(\alpha,\Phi) &= T_{\max}^0 + T_{\max}^\alpha\alpha + T_{\max}^{\alpha^2}\alpha^2 + \left(T_{\max}^\Phi + T_{\max}^{\alpha\Phi}\alpha\right)\Phi + T_{\max}^{\Phi^2}\Phi^2 \\
P_{\max}(\alpha,\Phi) &= P_{\max}^0 + P_{\max}^\alpha\alpha + P_{\max}^{\alpha^2}\alpha^2 + \left(P_{\max}^\Phi + P_{\max}^{\alpha\Phi}\alpha + P_{\max}^{\alpha^2\Phi}\alpha^2\right)\Phi \\
&\quad + \left(P_{\max}^{\Phi^2} + P_{\max}^{\alpha\Phi^2}\alpha\right)\Phi^2
\end{aligned}
\tag{107}
$$

Figures 161-166 present goodness-of-fit results for the 3$^{\text{th}}$-order stepwise regression analysis. As expected, the SRM analysis yields higher-accuracy regressions when compared to the equivalent metrics from the previous COM analysis of Appendix F.1, where the mean values of the standardized residuals are much closer to zero-mean white noise. A significant drawback of the SRMs is that the resulting model structure is not only more complicated (possessing many more higher order terms than the COMs), but also the resulting structure may vary depending on flight conditions for altitude and dynamic pressure. For example, at low altitudes and dynamics pressures, the bending moments may have a weak 3$^{\text{th}}$-order dependence on angle of attack, which may become significantly stronger as the vehicle accelerates and dynamic pressure increases. This fact will lead to significant complications in control systems design exercises for GHVs. As a consequence, a given SRM model structure may be required to be fixed to the highest order of complexity of model structure across the region of operation of interest. This will result in a more complex COM-type model structure, and linear regression techniques can be applied to across a desired range of flight conditions, where certain higher-order terms will most likely be statistically insignificant for certain conditions. Investigation of uncertainties in model structures and the resulting impacts on control systems design is a topic for future work.

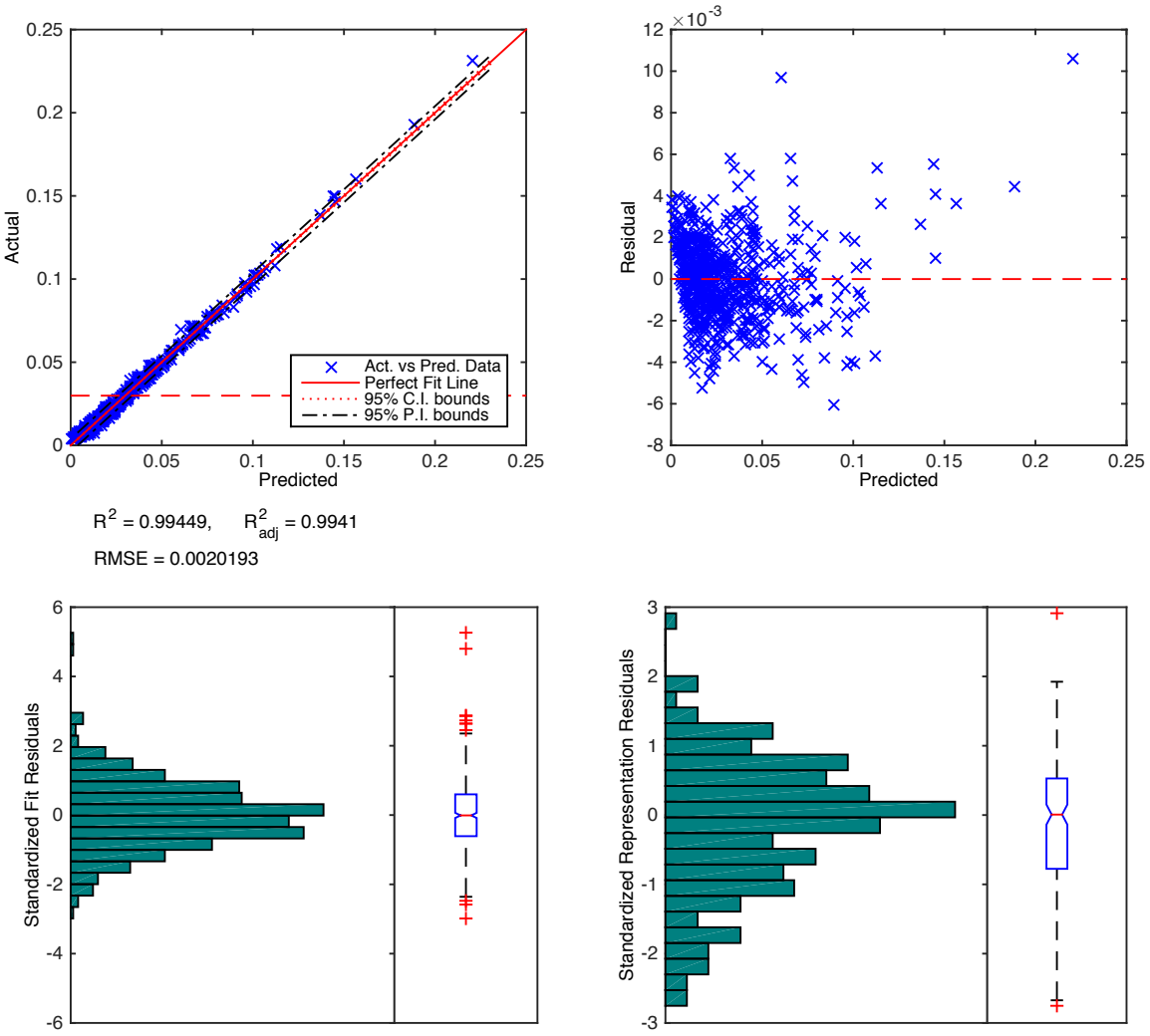

Figure 161: 3rd-order stepwise model goodness-of-fit metrics for total drag C_D coefficient model at conditions: $h = 99.86$ (kft) and $\bar{q} = 2000$ (psf).

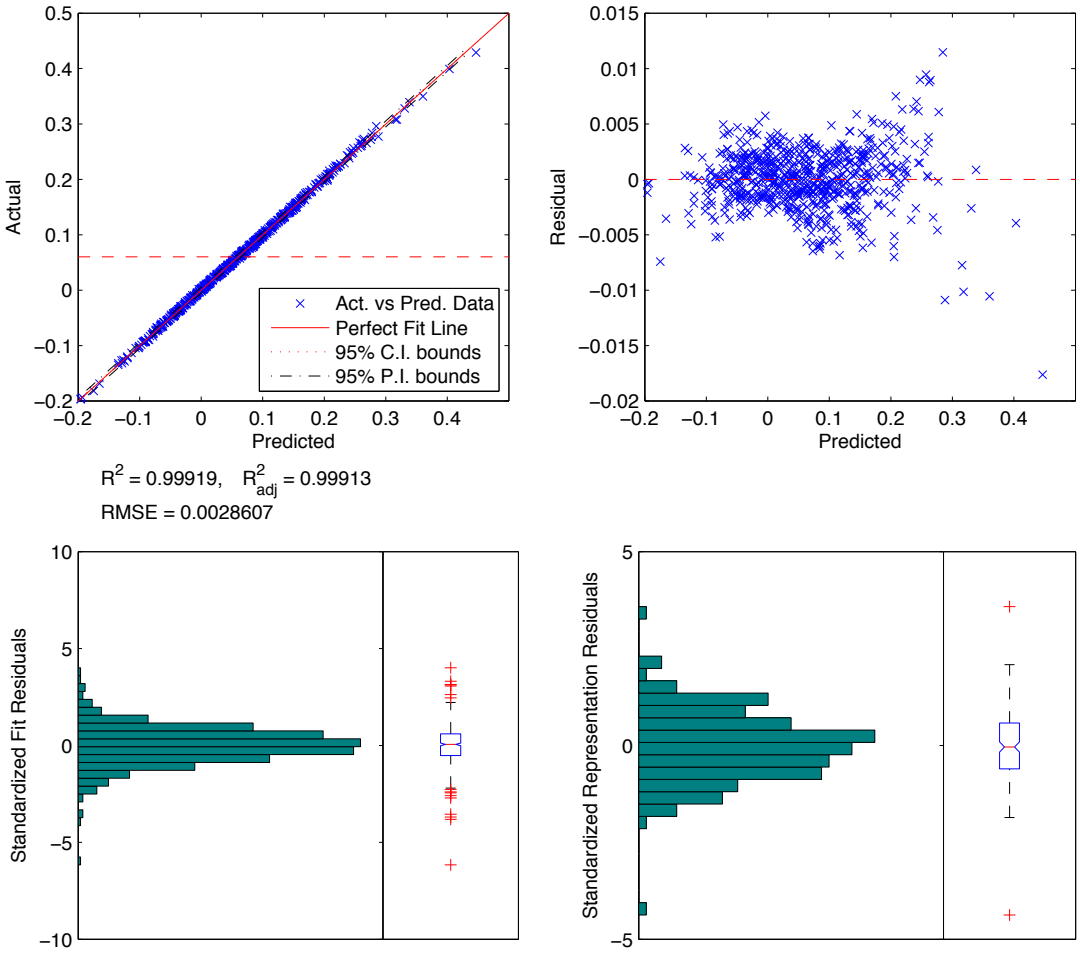

Figure 162: 3[rd]-order stepwise model goodness-of-fit metrics for lift coefficient model C_L at flight conditions: $h = 99.86$ (kft) and $\bar{q} = 2000$ (psf).

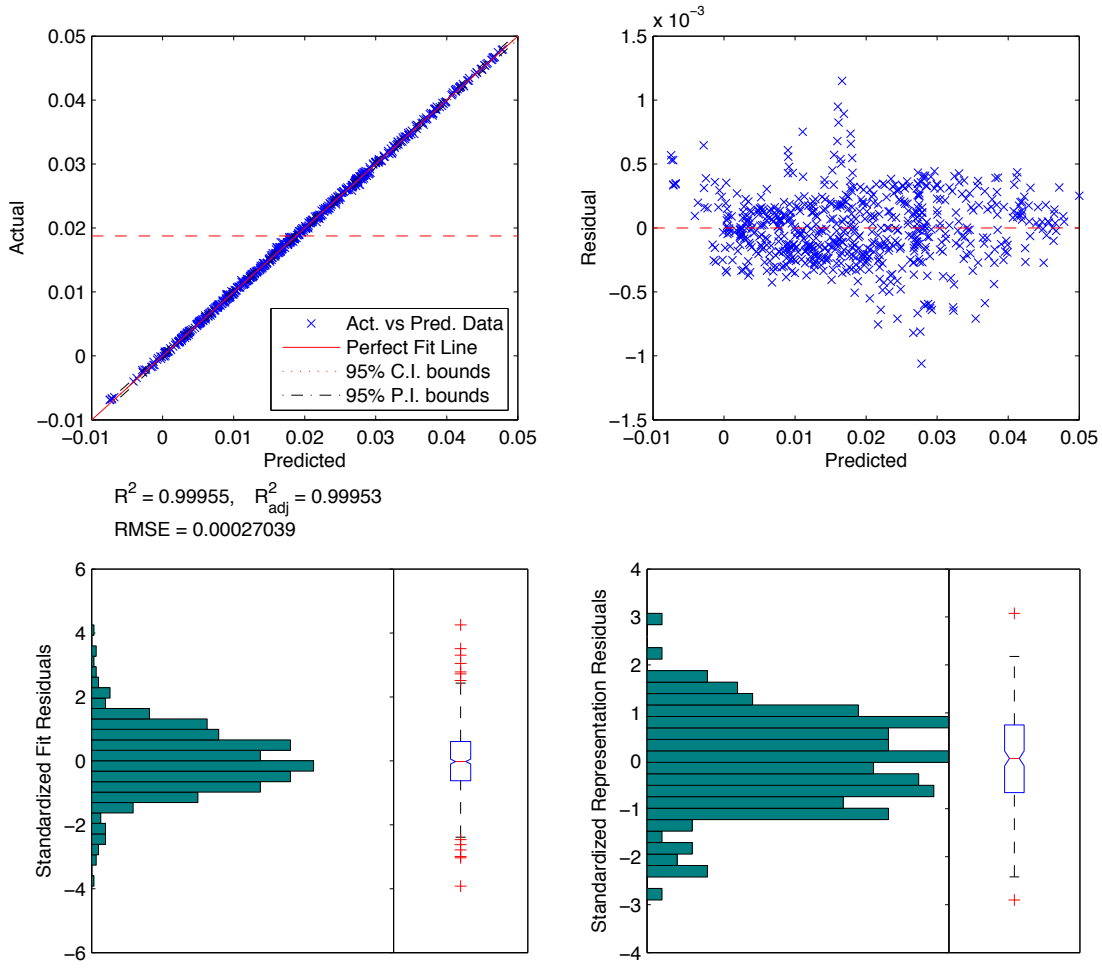

Figure 163: 3rd-order stepwise model goodness-of-fit metrics for thrust coefficient model C_T at flight conditions: $h = 99.86$ (kft) and $\bar{q} = 2000$ (psf).

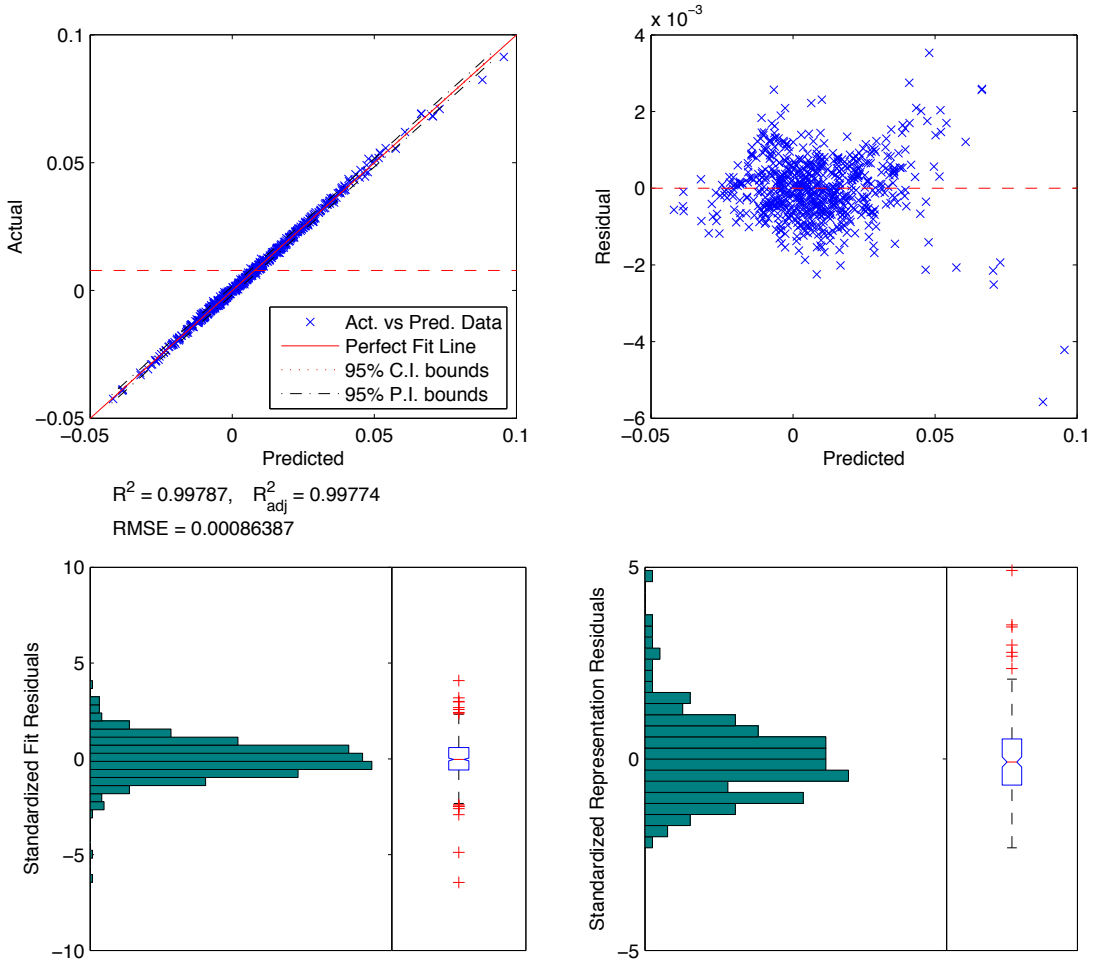

Figure 164: 3rd-order stepwise model goodness-of-fit metrics for the pitching moment coefficient model C_M (excluding the contribution due to thrust) at flight conditions: $h = 99.86$ (kft) and $\bar{q} = 2000$ (psf).

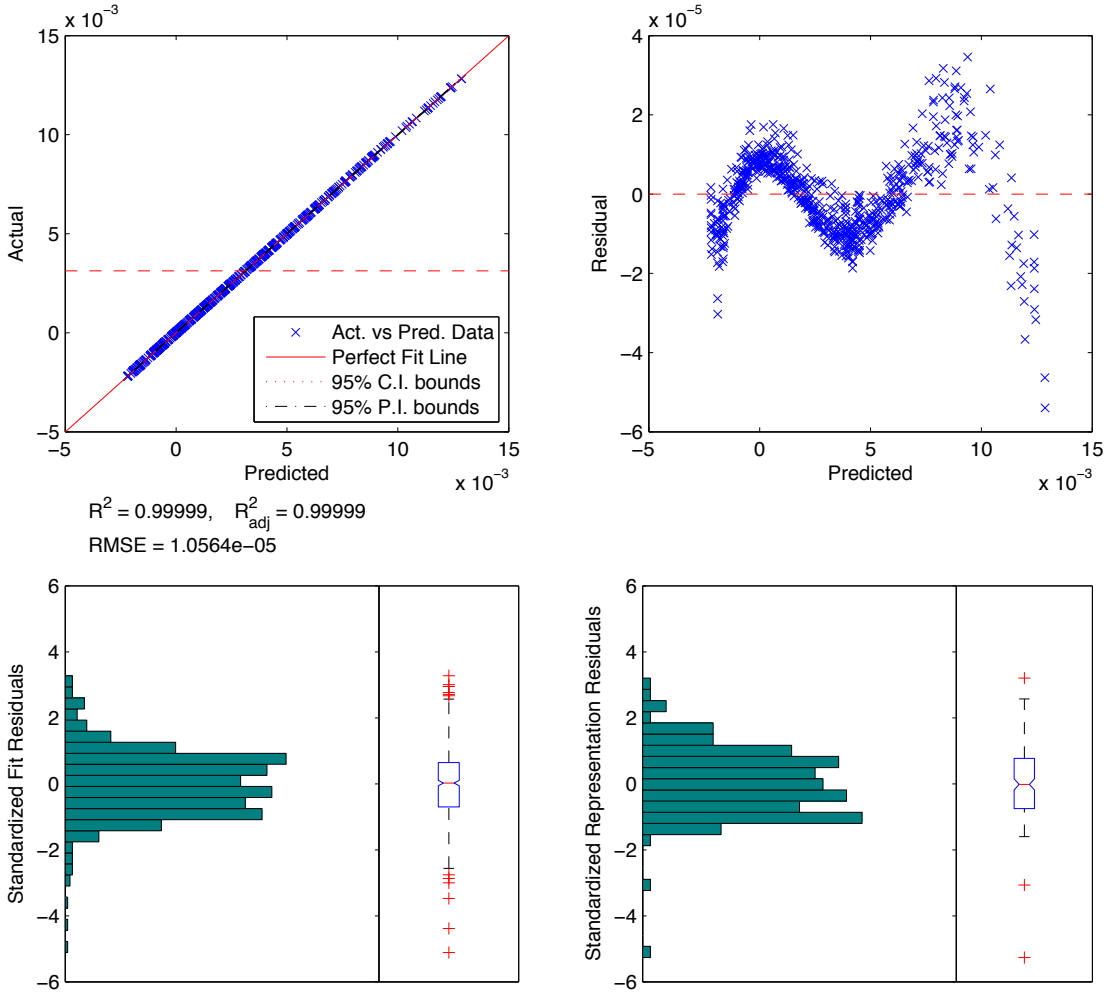

Figure 165: 3[rd]-order stepwise model goodness-of-fit metrics for the 1[st]-mode forebody bending moment coefficient model N_f (excluding the contribution due to thrust) at flight conditions: $h = 99.86$ (kft) and $\bar{q} = 2000$ (psf).

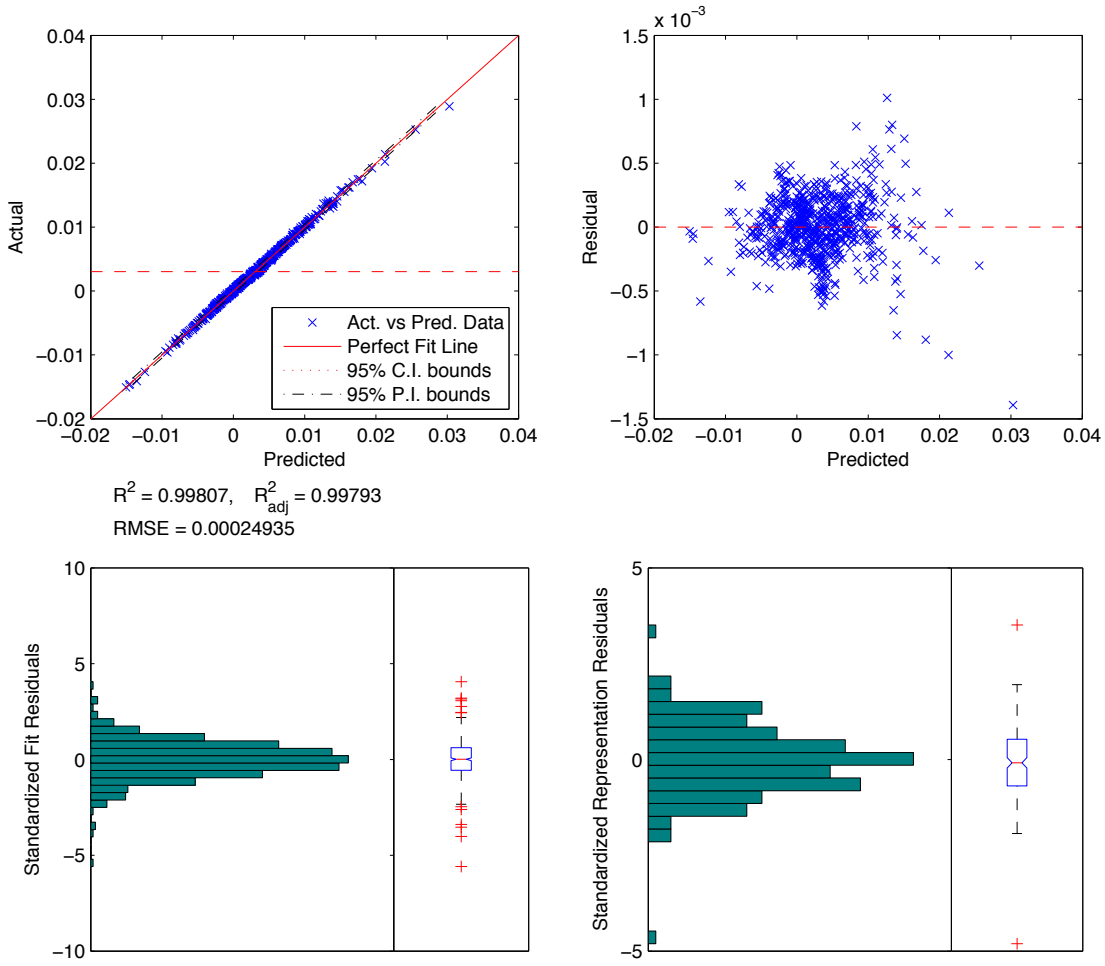

Figure 166: 3rd-order stepwise model goodness-of-fit metrics for the 1st-mode aft-body bending moment coefficient model N_a (excluding the contribution due to thrust) at flight conditions: $h = 99.86$ (kft) and $\bar{q} = 2000$ (psf).

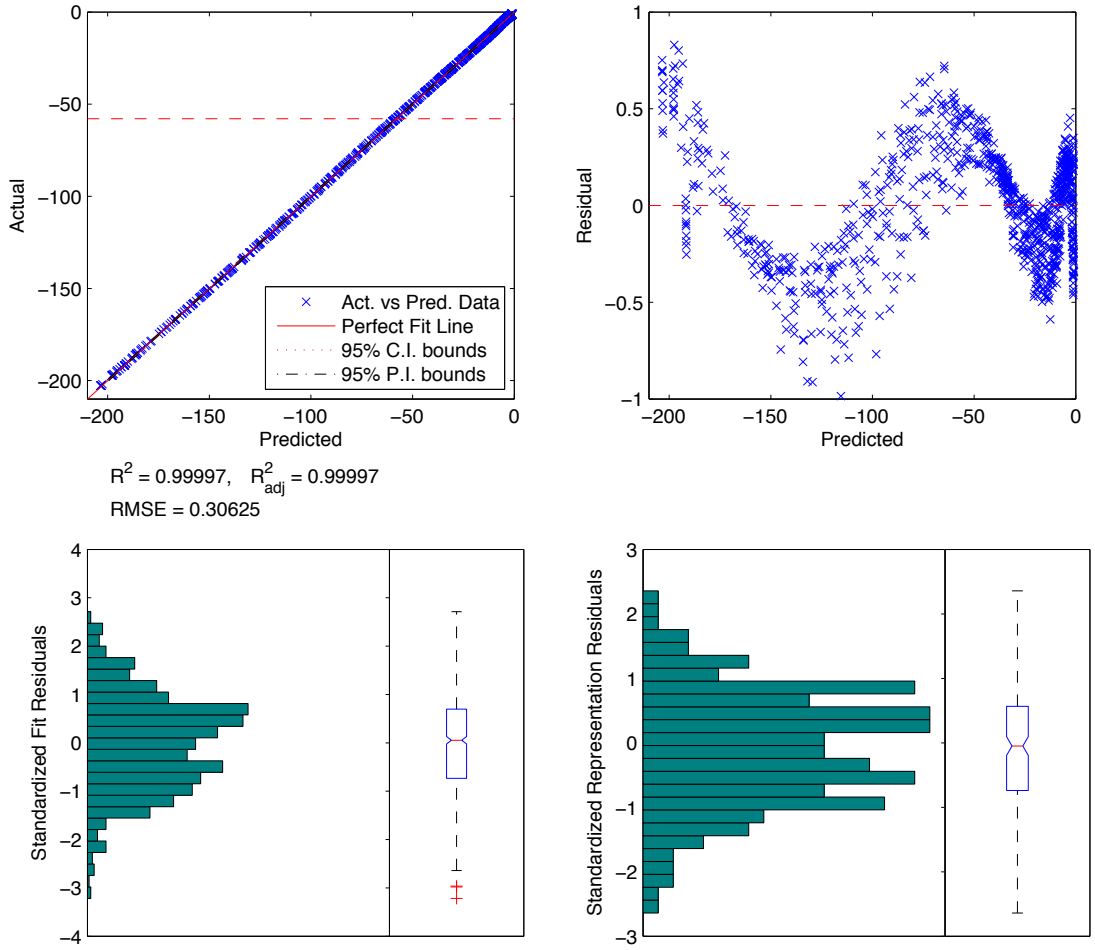

Figure 167: 3[rd]-order stepwise model goodness-of-fit metrics for the diffuser choke margin (failure mode) model $\bar{A}_D$ (excluding the contribution due to thrust) at flight conditions: $h = 99.86$ (kft) and $\bar{q} = 2000$ (psf).

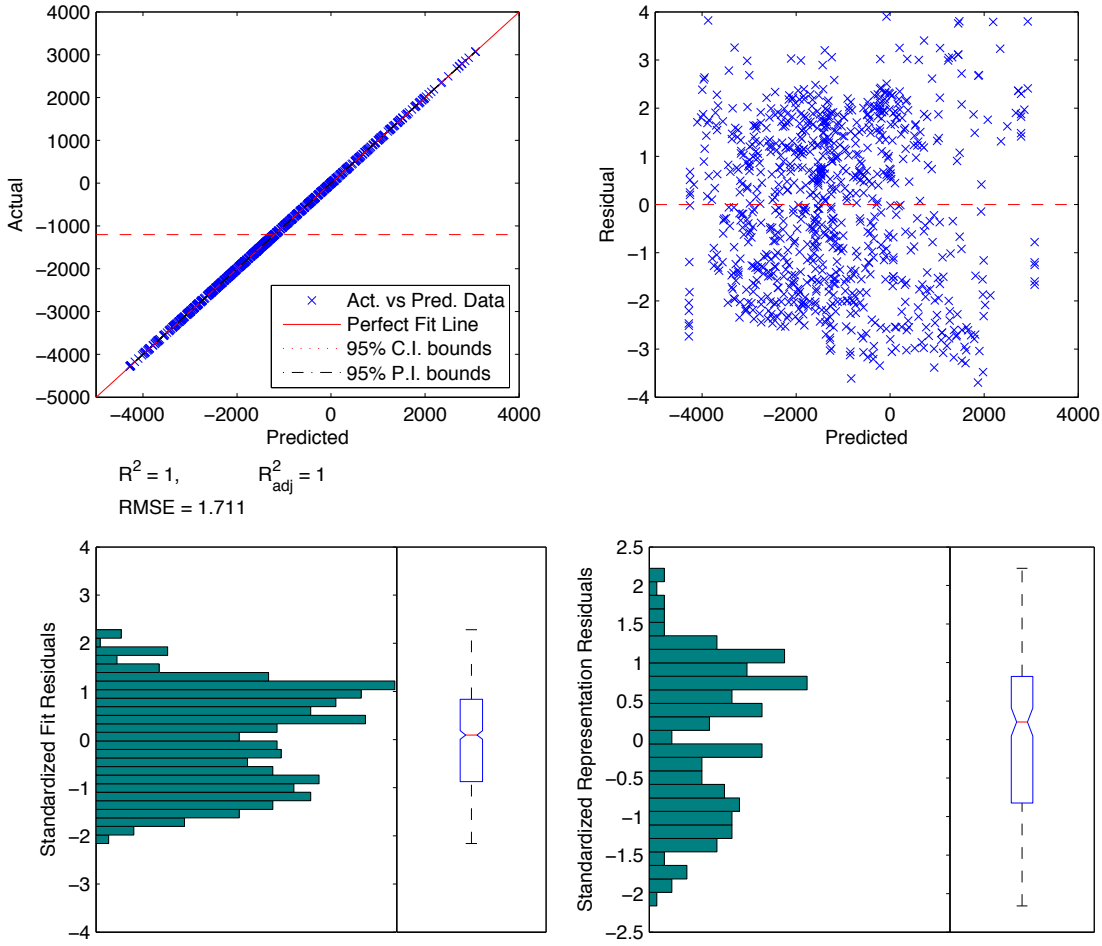

Figure 168: 3[rd]-order stepwise model goodness-of-fit metrics for the thermal choke margin (failure mode) model $\Delta T_{c,0}$ (excluding the contribution due to thrust) at flight conditions: $h = 99.86$ (kft) and $\bar{q} = 2000$ (psf).

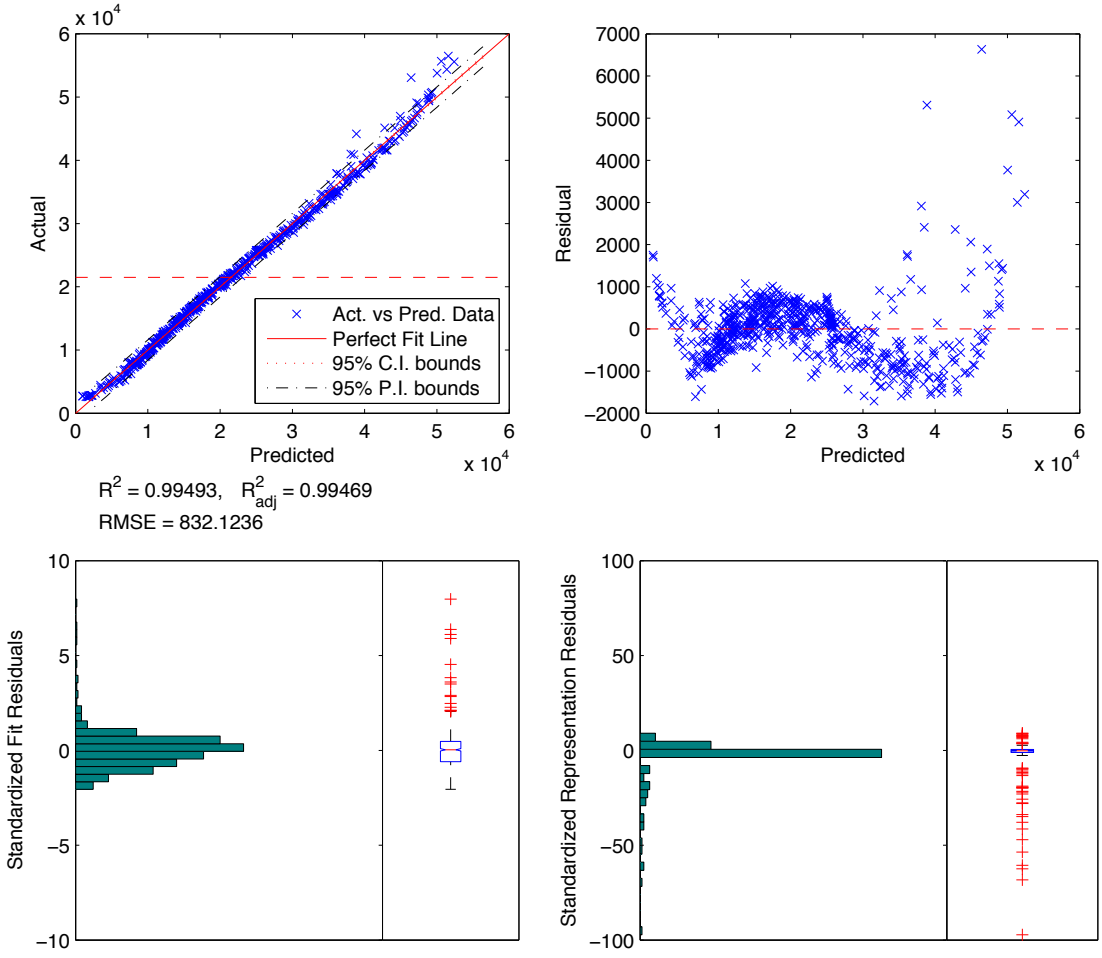

Figure 169: 3rd-order stepwise model goodness-of-fit metrics for the maximum internal pressure (failure mode) model $P_{\max}$ (excluding the contribution due to thrust) at flight conditions: $h = 99.86$ (kft) and $\bar{q} = 2000$ (psf).

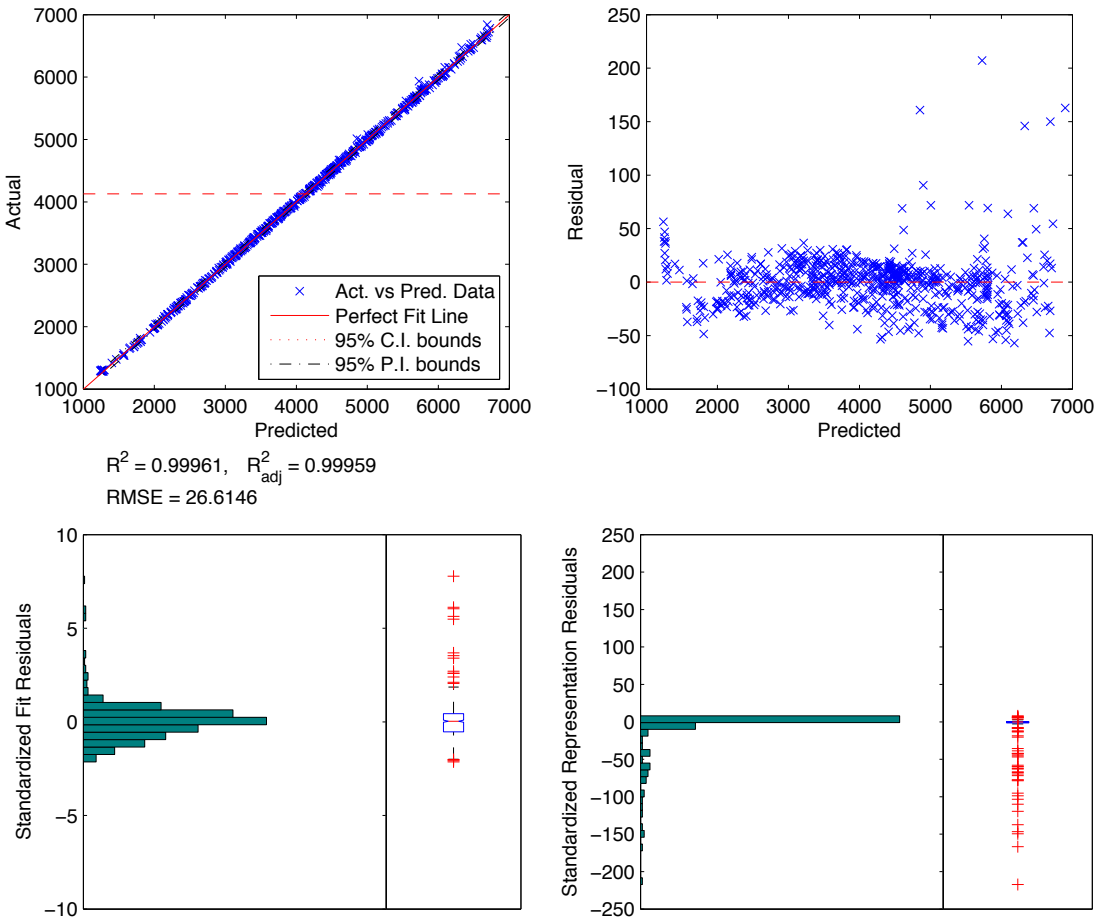

Figure 170: 3rd-order stepwise model goodness-of-fit metrics for the maximum combustor temperature (failure mode) model $T_{\max}$ (excluding the contribution due to thrust) at flight conditions: $h = 99.86$ (kft) and $\bar{q} = 2000$ (psf).

F.3 GHV Aero-Propulsive-Elastic Stability and Control Coefficients

The exercise outlined in Appendix F.1 was performed for the COM model structures of the GHV forces and moments across the operational envelope of altitude and dynamics pressures discussed at the beginning of this appendix. Additionally, the four SRM failure-mode models were also generated. Figures 171-176 show resulting tabulated data in the format of stability and control (SnC) coefficients for all the parameters of the COM model structures presented in Equations (90) from Section 11.2.3.3. As seen below, many of these plots are well behaved across the admissible region of altitude and dynamic pressure; however, many are also not as well behaved, especially at low altitudes and low speeds. Along this edge of the admissible region, many coefficients become increasingly jagged and often show distinct ridges within the surfaces, as the SCRAMjet engine begins to near choking conditions. This is undoubtedly due to discrete changes in configurations of shock and expansion waves around the vehicle, inducing phenomena such as: externally impinging oblique shocks, spillage effects, exhaust plume overexpansion, etc.

Figures 177 - 182 show the resulting goodness-of-fit metrics across the operational envelope for each of the COMs and the failure-mode SRMs. Observe that operation of the vehicle at low altitudes and low speeds is ill-advised as confidence in the model structure becomes increasingly uncertain here.

As mentioned previously, these COM SnC coefficients are utilized in control systems design, relying on a model-based approach to estimating hypersonic physics during actual operation. Often times, linearized dynamic models are incorporated where each of these SnC coefficient surfaces may be sampled at discrete points, effectively reducing tabulated data into a single set of parameters. Other more exotic control strategies often seek to mitigate this dependency, but the use of these parameters within onboard controllers is rarely ever completely eliminated.

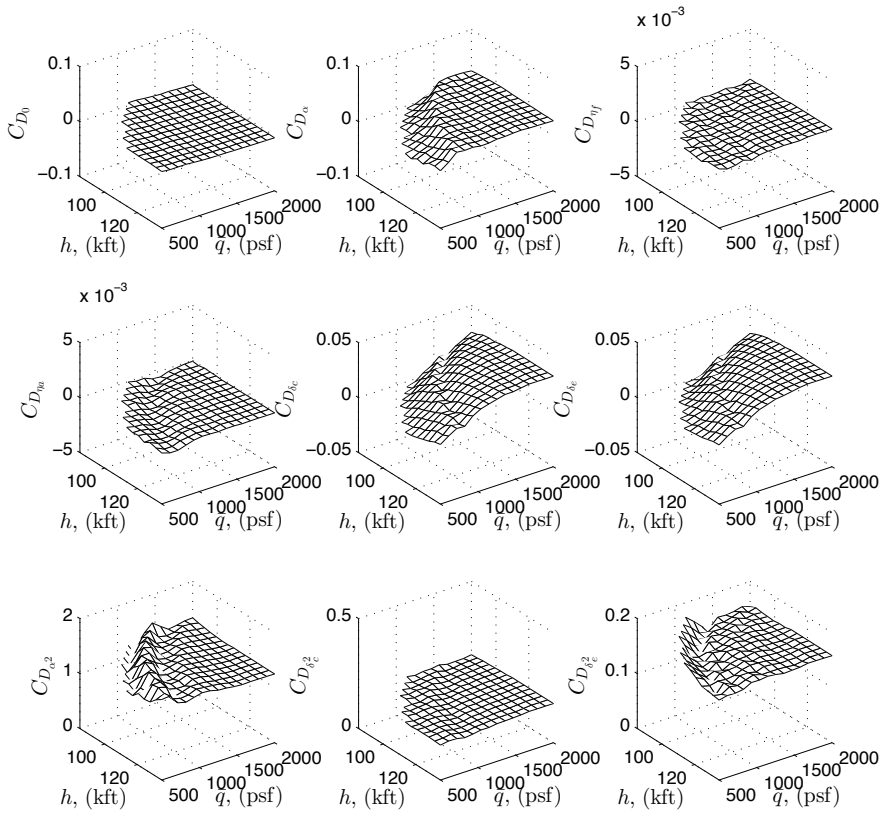

Figure 171: COM drag force stability and control coefficients.

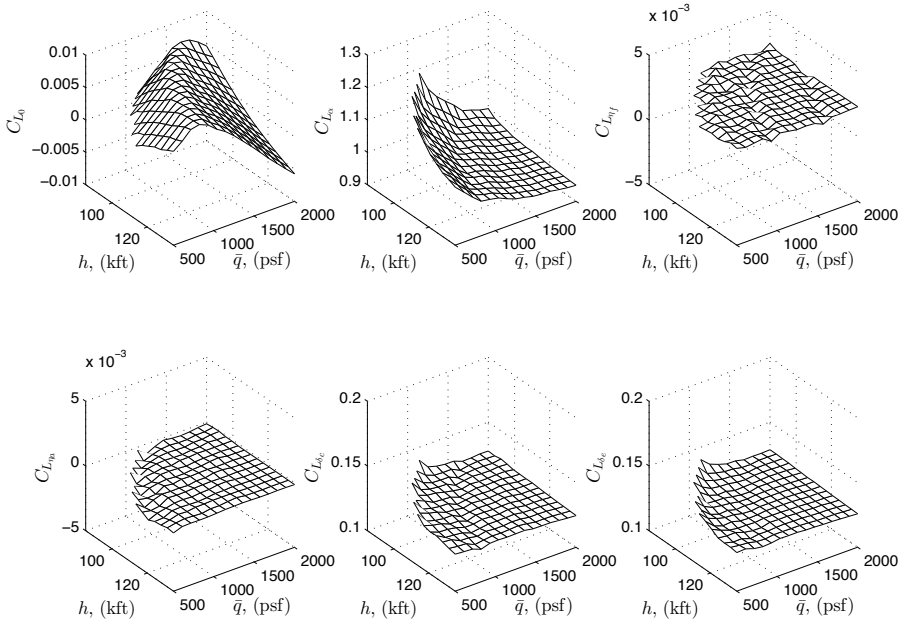

Figure 172: COM lift force stability and control coefficients.

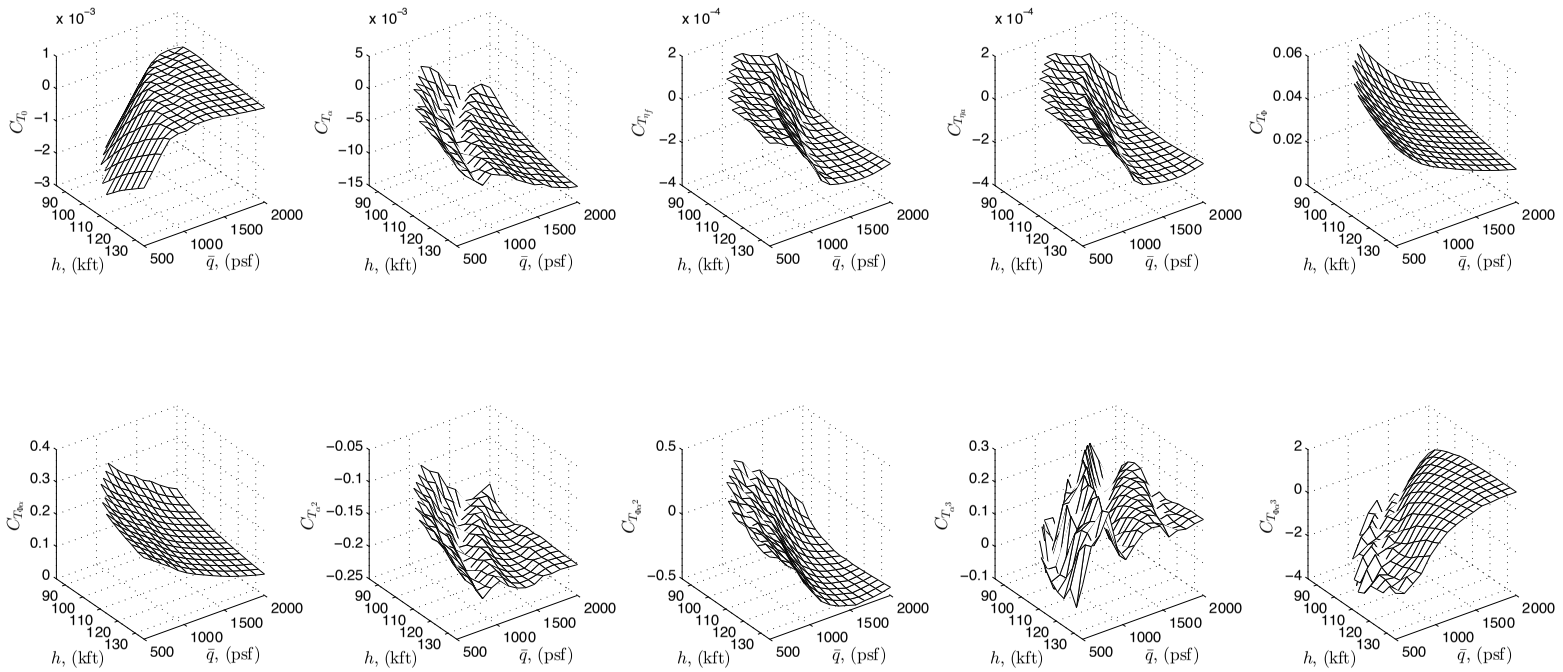

Figure 173: COM thrust force stability and control coefficients.

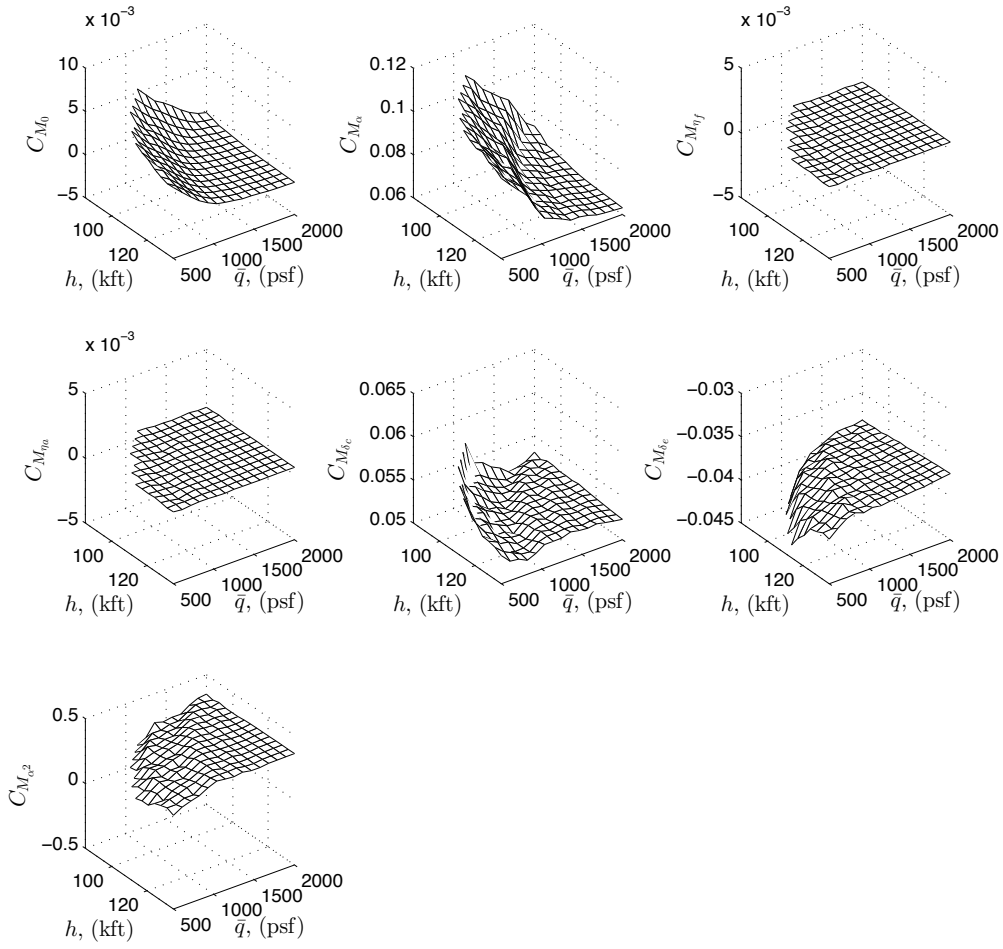

Figure 174: COM pitching moment stability and control coefficients.

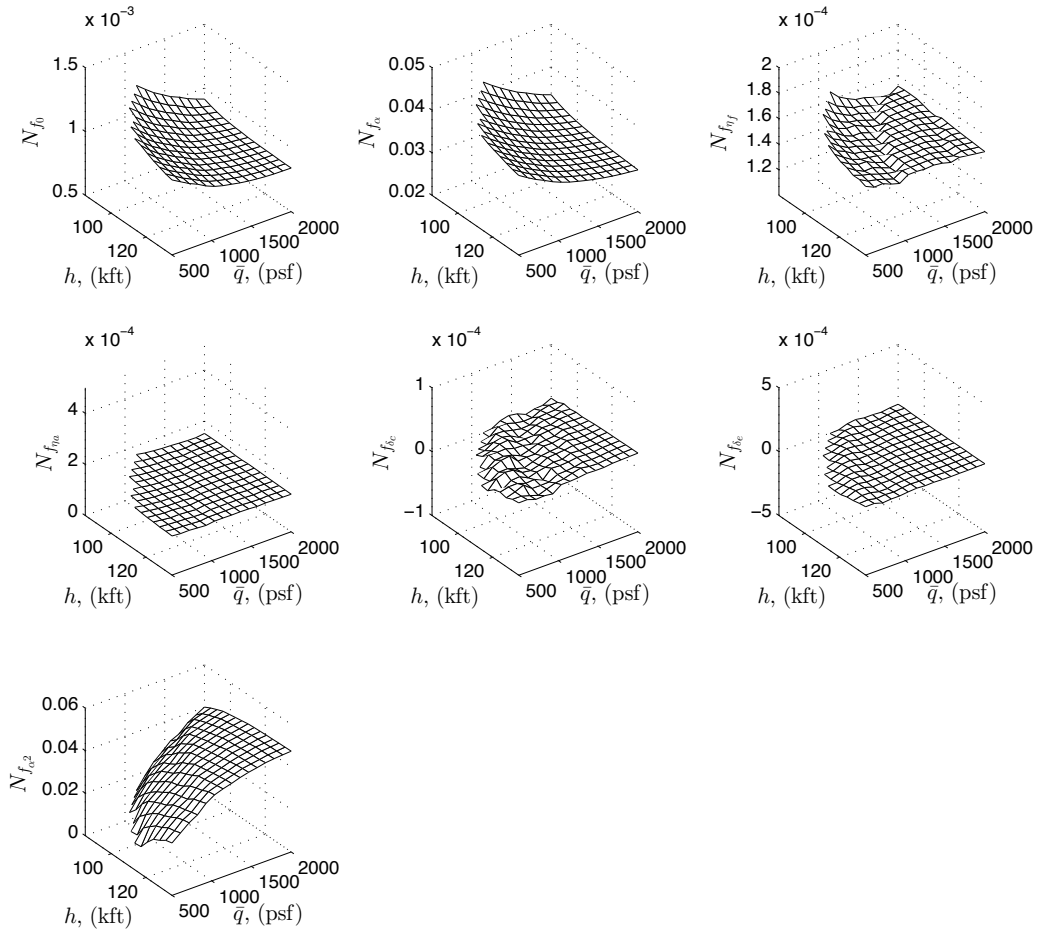

Figure 175: COM fore-body bending moment stability and control coefficients.

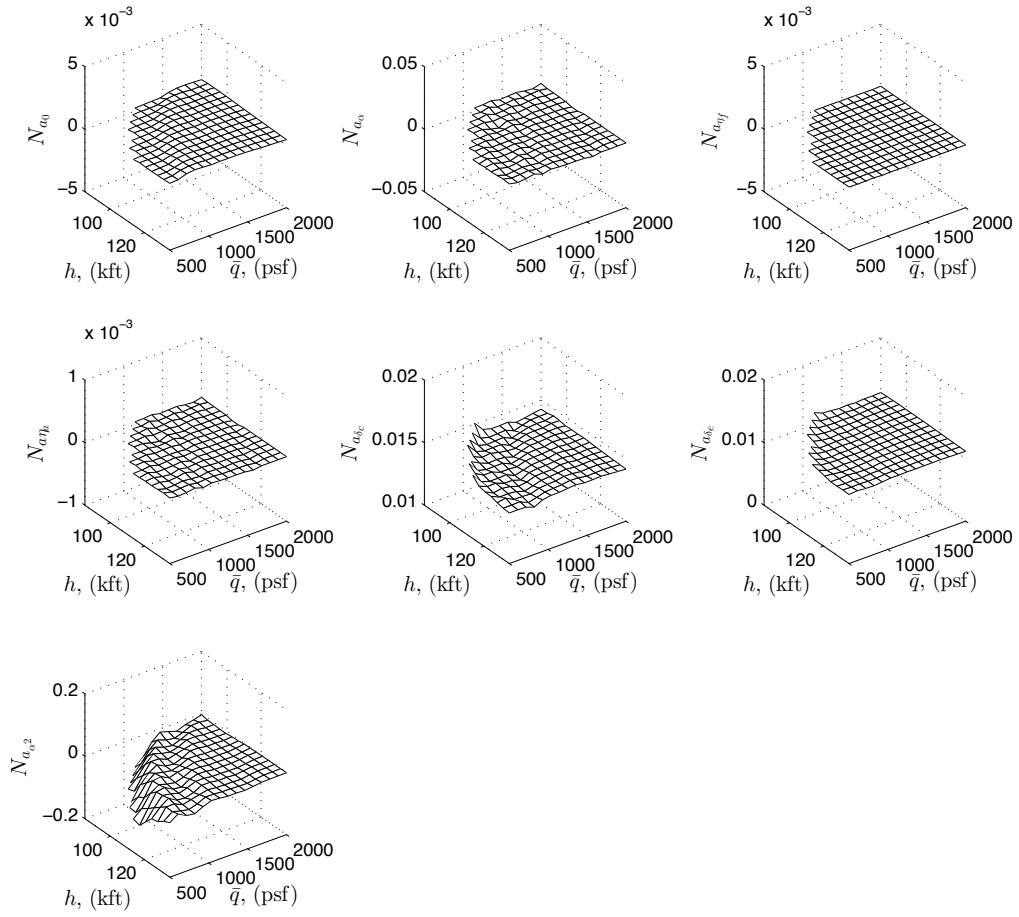

Figure 176: COM aft-body bending moment stability and control coefficients.

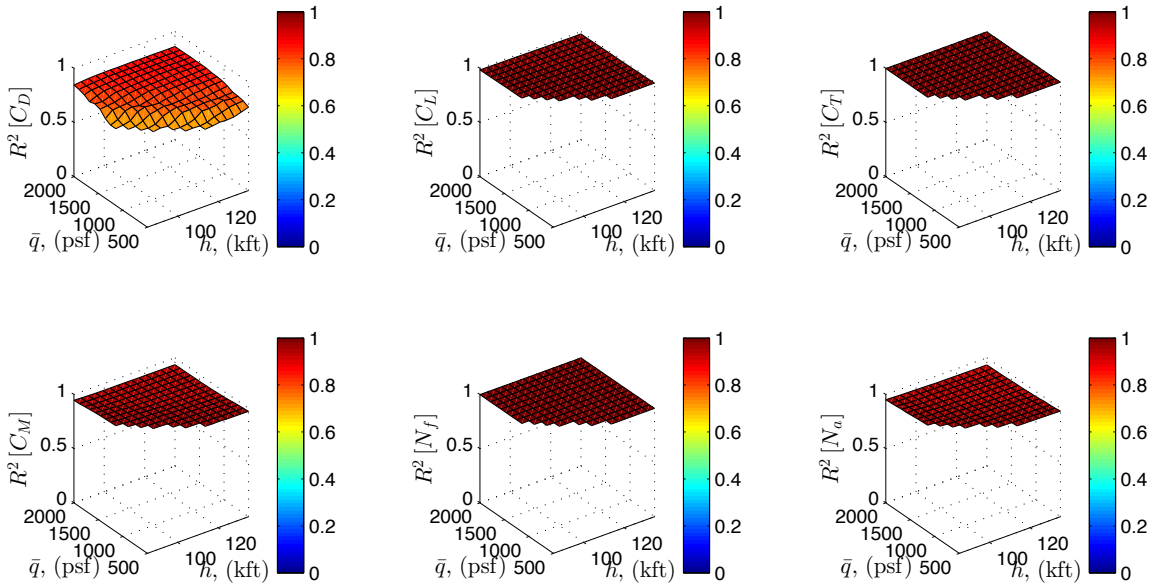

Figure 177: COM goodness-of-fit R^2 plotted across the operational envelope.

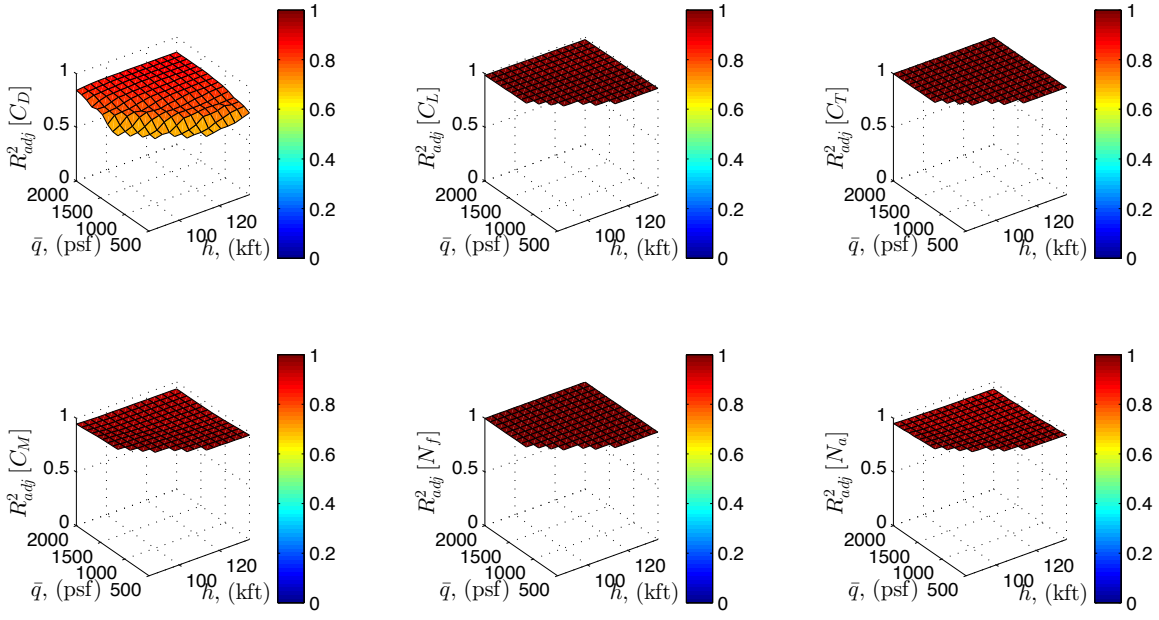

Figure 178: COM goodness-of-fit R^2_{adj} plotted across the operational envelope.

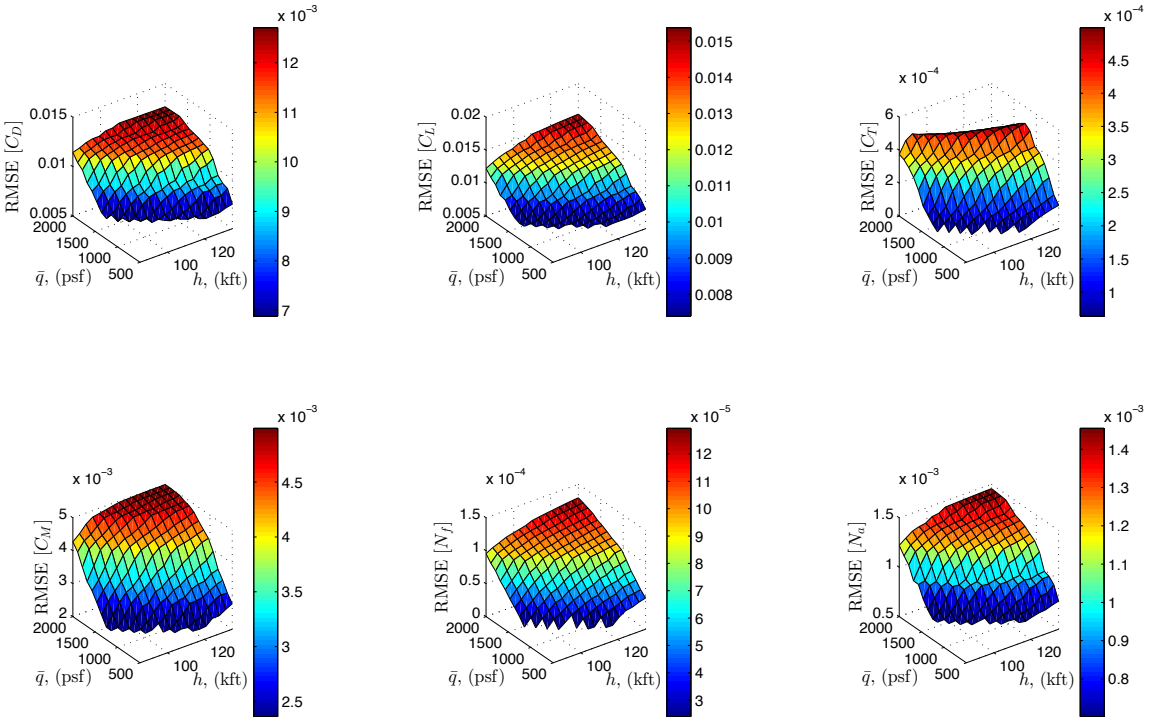

Figure 179: COM goodness-of-fit RMSE plotted across the operational envelope.

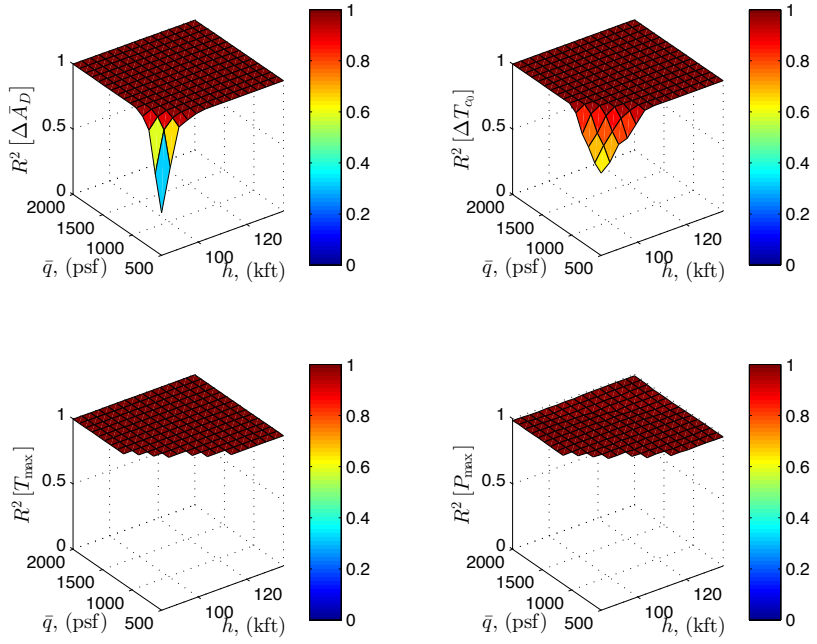

Figure 180: SRM failure mode goodness-of-fit R^2 plotted across the operational envelope.

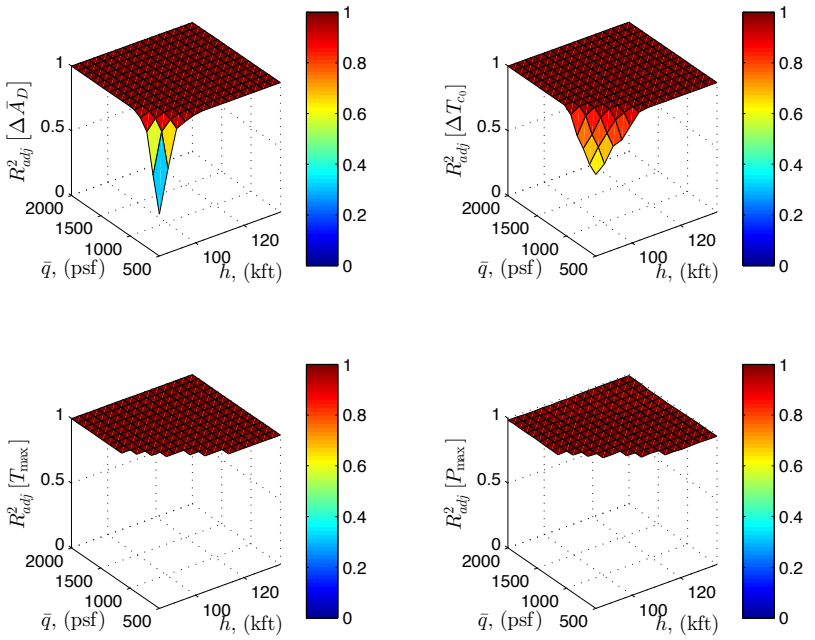

Figure 181: SRM failure mode goodness-of-fit R^2_{adj} plotted across the operational envelope.

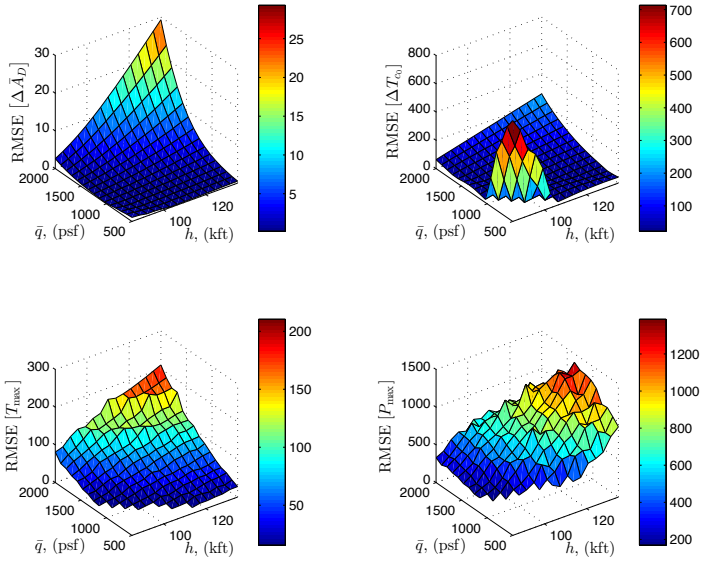

Figure 182: SRM failure mode goodness-of-fit RMSE plotted across the operational envelope.

APPENDIX G

DYNAMIC SYSTEM TRIM AND LINEARIZATION

The following discussion described the trimming and linearization procedures utilized on the GHV flight dynamic model of Section 11.2.3. Trimming the vehicle refers to finding an equilibrium point of the nonlinear model presented in Equations (82)-(88). Linearization is used to obtain a linear model (small signal approximation) to the nonlinear differential equations of the vehicle dynamics.

G.1 Trimming

The equations of motion from Equations (82)-(88) can be represented compactly in a state space representation.

$$\begin{aligned} \dot{x}(t) &= f(x(t), u(t), \theta_0), \quad x(0) = x_0 \\ y(t) &= g(x(t), u(t), \theta_0) \end{aligned} \tag{108}$$

Here $x(t)$ is the state vector, $y(t)$ is the output vector, $u(t)$ is the control input vector, and θ_0 is the *a priori* parameter vector. Assuming values for θ_0, (x_e, u_e) is an equilibrium point, or trim condition, of the nonlinear system at $t = 0$ if $f(x, u) = 0 \ \forall \ t \geq 0$. The act of *trimming* refers to finding system equilibria (*i.e.* state/control vector pairs (x_e,u_e) such that $f(x_e, u_e) = 0$. For the GHV, the trimmable (*i.e.* a sub-region of the admissible region from Table 45) region is limited by three effects: (i) structural loading due to high dynamic pressure $\bar{q} = 2000$ (psf); (ii) thermal choking with the engine; and (iii) $\Phi = 1.2$ [239]. The general procedure for trimming the vehicle is as follows.

1. Choose Mach, angle of attack, and altitude (within the admissable region).

2. Set pitch rate, flexible state derivatives to zero.

3. Set $\theta = \alpha$ (level flight or $\gamma = \theta - \alpha = 0$ (deg)).

4. Solve $f(x, u) = 0$ for flexible states and control inputs.

In order to obtain the equilibrium numerically, following optimization problem can be solved:

$$\min_{\eta,u} ||\dot{x}||_\infty \tag{109}$$

Here $\dot{x}$ is the derivatives of the rigid-body states, η is the elastic state vector, u are the controls. Once a trim solution of the nonlinear differential equation is found, vehicle dynamics can be linearized about that trimmed operating (equilibrium) point. This is examined below.

G.2 Linearization

The state space representation shown above in Equation (110) can be linearized into a linear state space form, utilizing standard finite differencing to compute numerical Jacobian matrices (A, B, C, D) about the trim condition (x_e, u_e).

$$\begin{aligned} \delta\dot{x}(t) &= A\delta x(t) + B\delta u(t), \quad \delta x(0) = \delta x_0 \\ \delta y(t) &= C\delta x(t) + D\delta u(t) \end{aligned} \tag{110}$$

where

$$A = \left[\begin{array}{ccc} \frac{\partial f_1}{\partial x_1} & \cdots & \frac{\partial f_1}{\partial x_n} \\ \vdots & \vdots & \vdots \\ \frac{\partial f_n}{\partial x_1} & \cdots & \frac{\partial f_n}{\partial x_n} \end{array}\right]_{(x_e,u_e)} \quad B = \left[\begin{array}{ccc} \frac{\partial f_1}{\partial u_1} & \cdots & \frac{\partial f_1}{\partial u_n} \\ \vdots & \vdots & \vdots \\ \frac{\partial f_n}{\partial u_1} & \cdots & \frac{\partial f_n}{\partial u_n} \end{array}\right]_{(x_e,u_e)}$$

$$C = \left[\begin{array}{ccc} \frac{\partial g_1}{\partial x_1} & \cdots & \frac{\partial g_1}{\partial x_n} \\ \vdots & \vdots & \vdots \\ \frac{\partial g_n}{\partial x_1} & \cdots & \frac{\partial g_n}{\partial x_n} \end{array}\right]_{(x_e,u_e)} \quad D = \left[\begin{array}{ccc} \frac{\partial g_1}{\partial u_1} & \cdots & \frac{\partial g_1}{\partial u_n} \\ \vdots & \vdots & \vdots \\ \frac{\partial g_n}{\partial u_1} & \cdots & \frac{\partial g_n}{\partial u_n} \end{array}\right]_{(x_e,u_e)} \tag{111}$$

$$\delta u(t) \stackrel{\text{def}}{=} y(t) - u_e \qquad \delta x(t) \stackrel{\text{def}}{=} x(t) - x_e \qquad \delta x_0 \stackrel{\text{def}}{=} x_0 - x_e$$

$$\delta y(t) \stackrel{\text{def}}{=} y(t) - y_e \qquad y_e \stackrel{\text{def}}{=} g(x_e, u_e).$$

Once a nonlinear state space dynamic system has been linearized, many analyses from *linear systems theory* can be conducted with have been highly industrialized and have a proven track record. One particularly useful analysis is the computation of open loop system pole/transmission-zeros of the linearized system. From this analysis, the assessment of system stability, harmonic frequencies, and more is readily available.

Figure 183 shows the results of a stability analysis performed using a linearized model of the GHV nonlinear model which is trimmed using the COM results of Appendix F. The left plot shows the open loop root locus poles and transmission zeros, while the right plot shows the closed loop case. Comparison of the open loop case to the results shown in Parker, et al. [228] shows that the two results are nearly identical upon inspection. In the case of the closed loop system, pole placement was used to design a feedback gain matrix that is just marginally stable by prescribing the open loop unstable poles to be equal to -0.05. This resulted in a feedback gain matrix with relatively large gains (*e.g.* $K_{\alpha\delta} = 94.57$), showing that the control effort to marginally stabilize this vehicle is very high and suggesting that the vehicle geometry should be altered to alleviate the issue of stiff controllability.

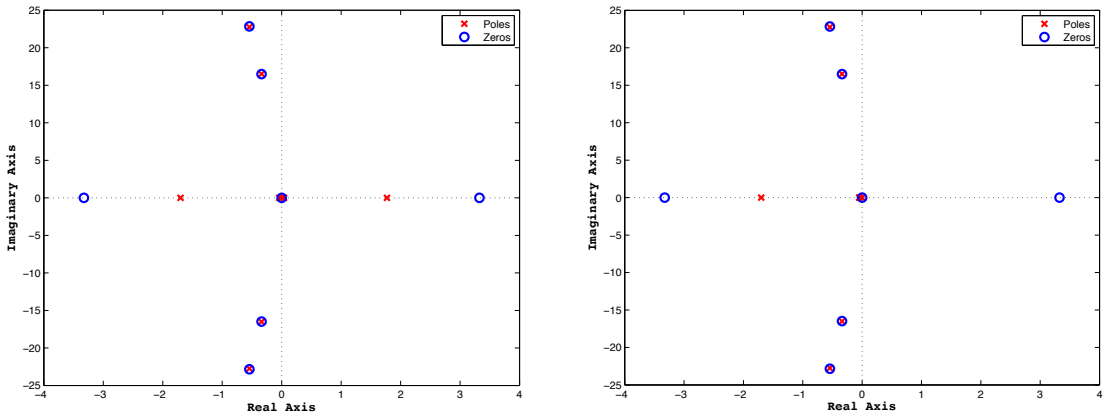

(a) Open Loop (b) Closed Loop

Figure 183: Pole/transmission zero maps of Jacobian linearization of the GHV SCRAMjet during a notional steady-level flight condition at $h = 85,000$ (ft), $\bar{q} = 2000$ (psi), and $\alpha = 2.0$ (deg).

APPENDIX H

GHV NONLINEAR ROBUST-ADAPTIVE CONTROLLER GAINS TUNING

As discussed in Section 11.2.4, the adaptive/controller gains were obtained semi-heuristically, using the values provided by Fiorentini [104] as a starting point for a 100 case Monte Carlo analysis where all aero-propulsive-elastic parameters were perturbed according to the discussion in Section 11.2.3.4 and gains were tuned until 100% success rate was observed. Figure 184 shows the results of this analysis for the error dynamics, which are all observed to dampen out initial condition perturbations and asymptotically approach a desired flight (reference) conditions.

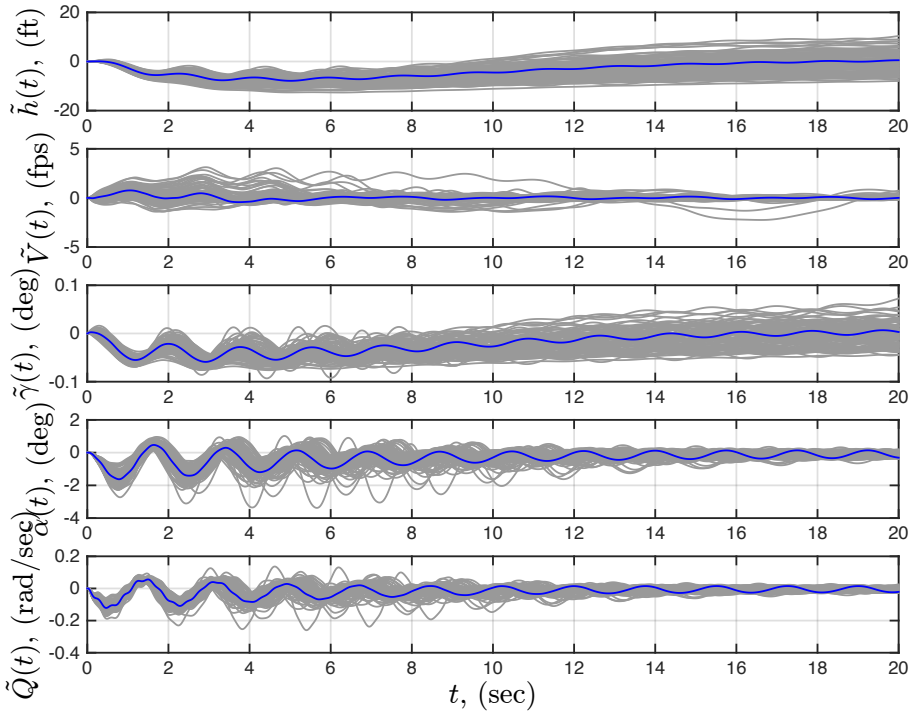

Figure 184: Feedback state error dynamic responses: dynamic responses for aero-propulsive-elastic parameter baseline values (blue), perturbed values (grey).

REFERENCES

[1] "Why and whither hypersonics research in the us air force," tech. rep., United States Air Forces Scientific Advisory Board, December 2000. SAB-TR-00-03.

[2] "Ballistic missile defense review report," tech. rep., U.S. Department of Defense, February 2010.

[3] *Journal of Aircraft*, vol. 42, no. 1, Jan.-Feb., 2005.

[4] *Journal of Aircraft*, vol. 41, no. 4, July-Aug., 2004.

[5] Alagar, V. S. and Probst, D. K., "A fast, low-space algorithm for multiplying dense multivariate polynomials," *ACM Transactions on Mathematical Software (TOMS)*, vol. 13, no. 1, pp. 35–57, 1987.

[6] Anderson, J. D., *Modern compressible flow: with historical perspective*, vol. 12. McGraw-Hill New York, 1990.

[7] Anderson, J. D., *Hypersonic and high temperature gas dynamics*. Aiaa, 2000.

[8] Anderson, J. D., *The airplane, a history of its technology*. Aiaa, 2002.

[9] Anderson, J. D., *Introduction to flight*, vol. 199. McGraw-Hill Boston, 2005.

[10] Anderson Jr, J. D., *Fundamentals of aerodynamics*. Tata McGraw-Hill Education, 1985.

[11] Andradóttir, S., "A review of simulation optimization techniques," in *Proceedings of the 30th conference on Winter simulation*, pp. 151–158, IEEE Computer Society Press, 1998.

[12] Anon, *Handbook of Aviation Fuel Properties*. CRC, Inc., Atlanta, Georgia, 1983.

[13] Antczak, J., "Nasa's scramjet, the x-43a prepares for flight," 2004.

[14] Arfken, G. and Pan, Y., "Mathematical methods for physicists," *American Journal of Physics*, vol. 39, no. 4, pp. 461–461, 1971.

[15] Arora, N. and Biegler, L. T., "A trust region sqp algorithm for equality constrained parameter estimation with simple parameter bounds," *Computational Optimization and Applications*, vol. 28, no. 1, pp. 51–86, 2004.

[16] Askey, R. and Haimo, D. T., "Similarities between fourier and power series," *American Mathematical Monthly*, pp. 297–304, 1996.

[17] Asprey, S. and Macchietto, S., "Statistical tools for optimal dynamic model building," *Computers & Chemical Engineering*, vol. 24, no. 2, pp. 1261–1267, 2000.

[18] Asprey, S. and Macchietto, S., "Designing robust optimal dynamic experiments," *Journal of Process Control*, vol. 12, no. 4, pp. 545–556, 2002.

[19] Atkinson, A. C., "Optimum experimental design," in *International Encyclopedia of Statistical Science*, pp. 1037–1039, Springer, 2011.

[20] Atkinson, A. C., Chaloner, K., Herzberg, A. M., and Juritz, J., "Optimum experimental designs for properties of a compartmental model," *Biometrics*, pp. 325–337, 1993.

[21] Baase, S., *Computer algorithms: introduction to design and analysis*. Pearson Education India, 2009.

[22] Baldelli, D. H., Lind, R., and Brenner, M., "Nonlinear aeroelastic/aeroservoelastic modeling by block-oriented identification," *Journal of guidance, control, and dynamics*, vol. 28, no. 5, pp. 1056–1064, 2005.

[23] Bar-Shalom, Y. and Li, X.-R., "Estimation and tracking- principles, techniques, and software," *Norwood, MA: Artech House, Inc, 1993.*, 1993.

[24] Bar-Shalom, Y., Li, X.-R., and Kirubarajan, T., *Estimation, Tracking and Navigation: Theory, Algorithms and Software*. Wiley, 2001.

[25] Barber, T. A., Maicke, B. A., and Majdalani, J., "Current state of high speed propulsion: Gaps, obstacles, and technological challenges in hypersonic applications," *AIAA Paper*, vol. 5118, 2009.

[26] Barber, T. A., "A survey of gaps, obstacles, and technical challenges for hypersonic applications," Master's thesis, University of Tennessee, 2012.

[27] Bard, Y., *Nonlinear parameter estimation*, vol. 1209. Academic Press New York, 1974.

[28] Baszenski, G. and Tasche, M., "Fast polynomial multiplication and convolutions related to the discrete cosine transform," *Linear algebra and its applications*, vol. 252, no. 1, pp. 1–25, 1997.

[29] Belsley, D. A., Kuh, E., and Welsch, R. E., *Regression diagnostics: Identifying influential data and sources of collinearity*, vol. 571. John Wiley & Sons, 2005.

[30] Ben-Asher, J. Z., *Optimal control theory with aerospace applications*. American institute of aeronautics and astronautics, 2010.

[31] Bermudez, J. S., *A history of ballistic missile development in the DPRK*. No. 2, Monterey Institute of International Studies, Center for Nonproliferation Studies, 1999.

[32] Berry, S., Daryabeigi, K., Wurster, K., and Bittner, R., "Boundary-layer transition on x-43a," *Journal of Spacecraft and Rockets*, vol. 47, no. 6, pp. 922–934, 2010.

[33] Berry, S. A., Auslender, A. H., Dilley, A. D., and Calleja, J. F., "Hypersonic boundary-layer trip development for hyper-x," *Journal of Spacecraft and Rockets*, vol. 38, no. 6, pp. 853–864, 2001.

[34] Bertin, J. J. and Cummings, R. M., "Fifty years of hypersonics: where we've been, where we're going," *Progress in Aerospace Sciences*, vol. 39, no. 6, pp. 511–536, 2003.

[35] Beyer, H.-G. and Sendhoff, B., "Robust optimization–a comprehensive survey," *Computer methods in applied mechanics and engineering*, vol. 196, no. 33, pp. 3190–3218, 2007.

[36] Bilimoria, K. D. and Schmidt, D. K., "Integrated development of the equations of motion for elastic hypersonic flight vehicles," *Journal of Guidance, Control, and Dynamics*, vol. 18, no. 1, pp. 73–81, 1995.

[37] Bischof, C., Carle, A., Corliss, G., Griewank, A., and Hovland, P., "Adifor–generating derivative codes from fortran programs," *Scientific Programming*, vol. 1, no. 1, pp. 11–29, 1992.

[38] Bischof, C., Carle, A., Khademi, P., Mauer, A., and Hovland, P., "Adifor 2.0 user's guide," tech. rep., Citeseer, 1995.

[39] Bischof, C., Corliss, C., Green, L., Griewank, A., Haigler, K., and Newman, P., "Automatic differentiation of advanced cfd codes for multidisciplinary design," 2003.

[40] Bischof, C., Khademi, P., Mauer, A., and Carle, A., "Adifor 2.0: Automatic differentiation of fortran 77 programs," *Computational Science & Engineering, IEEE*, vol. 3, no. 3, pp. 18–32, 1996.

[41] Bischof, C. H., Bucker, H., Lang, B., Rasch, A., and Vehreschild, A., "Combining source transformation and operator overloading techniques to compute derivatives for matlab programs," in *Source Code Analysis and Manipulation, 2002. Proceedings. Second IEEE International Workshop on*, pp. 65–72, IEEE, 2002.

[42] Boehner, P. and Brown, S. F., *Philosophical writings: a selection*. Hackett Publishing, 1990.

[43] Bogue, R. K. and Erbland, P., *Perspective on the National Aero-space Plane program instrumentation development*. National Aeronautics and Space Administration, Office of Management, Scientific and Technical Information Program, 1993.

[44] Bolender, M. and Doman, D., "Modeling unsteady heating effects on the structural dynamics of a hypersonic vehicle," *AIAA Paper*, vol. 6646, p. 2006, 2006.

[45] Bolender, M. A. and Doman, D. B., "Nonlinear longitudinal dynamical model of an air-breathing hypersonic vehicle," *Journal of Spacecraft and Rockets*, vol. 44, no. 2, pp. 374–387, 2007.

[46] Bordelon, L. L., "Design of experiments applied to flight testing," *Missions Systems Engineering, RTO-ENSCI-176*, pp. 3–1, 2006.

[47] Bowcutt, K. G., "A perspective on the future of aerospace vehicle design," *AIAA Paper*, vol. 6957, p. 2003, 2003.

[48] Bowcutt, K. G., Kuruvila, G., Grandine, T. A., Hogan, T. A., and Cramer, E. J., "Advancements in multidisciplinary design optimization applied to hypersonic vehicles to achieve closure," *American Institute of Aeronautics and Astronautics AIAA-2008-2591*, 2008.

[49] Box, G. E. and Draper, N. R., "The bayesian estimation of common parameters from several responses," *Biometrika*, vol. 52, no. 3-4, pp. 355–365, 1965.

[50] Box, G. E. and Hill, W., "Discrimination among mechanistic models," *Technometrics*, vol. 9, no. 1, pp. 57–71, 1967.

[51] Box, G. E. and Hunter, W. G., "The experimental study of physical mechanisms," *Technometrics*, vol. 7, no. 1, pp. 23–42, 1965.

[52] Box, G. E., Hunter, W. G., Hunter, J. S., and others, "Statistics for experimenters," 1978.

[53] Box, G. E. and Lucas, H., "Design of experiments in non-linear situations," *Biometrika*, pp. 77–90, 1959.

[54] Breitsamter, C., Cvrlje, T., Laschka, B., Heller, M., and Sachs, G., "Lateral-directional coupling and unsteady aerodynamic effects of hypersonic vehicles," *Journal of Spacecraft and Rockets*, vol. 38, no. 2, pp. 159–167, 2001.

[55] Brent, R. P. and Kung, H. T., "Fast algorithms for manipulating formal power series," *Journal of the ACM (JACM)*, vol. 25, no. 4, pp. 581–595, 1978.

[56] Brown, J. W. and Churchill, R. V., "Fourier series and boundary value problems," *AMC*, vol. 10, p. 12, 2012.

[57] Brown, J. W., Churchill, R. V., and Lapidus, M., *Complex variables and applications*, vol. 7. McGraw-Hill New York, 1996.

[58] Brumberg, V. A., "Analytical techniques of celestial mechanics," *Analytical Techniques of Celestial Mechanics, VIII, 236 pp. 5 figs.. Springer-Verlag Berlin Heidelberg New York*, vol. 1, 1995.

[59] Bryson, A. E. and Ho, Y.-C., "Applied optimal control: optimization, estimation, and control [m]," *Washington: Hemisphere*, 1975.

[60] Bücker, H., Lang, B., Rasch, A., and Bischof, C., "From analytic to automated derivatives: a case study of the electrostatic potential," 2001.

[61] Cacuci, D. G., "Sensitivity theory for nonlinear systems. i. nonlinear functional analysis approach," *Journal of Mathematical Physics*, vol. 22, no. 12, pp. 2794–2802, 1981.

[62] Campos, C. M., Ober-Blöbaum, S., and Trélat, E., "High order variational integrators in the optimal control of mechanical systems," *arXiv preprint arXiv:1502.00325*, 2015.

[63] Chaloner, K. and Larntz, K., "Optimal bayesian design applied to logistic regression experiments," *Journal of Statistical Planning and Inference*, vol. 21, no. 2, pp. 191–208, 1989.

[64] Chaloner, K. and Verdinelli, I., "Bayesian experimental design: A review," *Statistical Science*, pp. 273–304, 1995.

[65] Chavez, F. R. and Schmidt, D. K., "Analytical aeropropulsive-aeroelastic hypersonic-vehicle model with dynamic analysis," *Journal of Guidance, Control, and Dynamics*, vol. 17, no. 6, pp. 1308–1319, 1994.

[66] Chavez, F. R. and Schmidt, D. K., "Uncertainty modeling for multivariable-control robustness analysis of elastic high-speed vehicles," *Journal of Guidance, Control, and Dynamics*, vol. 22, no. 1, pp. 87–95, 1999.

[67] Chen, R. T., "Input design for aircraft parameter identification: Using time-optimal control formulation," *AGARD Methods for Aircraft State and Parameter Identification 15 p(SEE N 75-29997 21-01)*, 1975.

[68] Chernoff, H., "Sequential design of experiments," *The Annals of Mathematical Statistics*, pp. 755–770, 1959.

[69] Chicone, C. C., *Ordinary differential equations with applications*, vol. 1. Springer, 1999.

[70] Cockrell, C. E., Engelund, W. C., Bittner, R. D., Jentink, T. N., Dilley, A. D., and Frendi, A., "Integrated aeropropulsive computational fluid dynamics methodology for the hyper-x flight experiment," *Journal of spacecraft and rockets*, vol. 38, no. 6, pp. 836–843, 2001.

[71] Coddington, E. A. and Levinson, N., *Theory of ordinary differential equations*. Tata McGraw-Hill Education, 1955.

[72] Community, T. S., "Python: GNU Polynomial Module version 1.4.0," November.

[73] Courty, F., Dervieux, A., Koobus, B., and Hascoët, L., "Reverse automatic differentiation for optimum design: from adjoint state assembly to gradient computation," *Optimization Methods and Software*, vol. 18, no. 5, pp. 615–627, 2003.

[74] Cramér, H., *Mathematical methods of statistics*, vol. 9. Princeton university press, 1999.

[75] D'Argenio, D. and Van Guilder, M., "Design of experiments for parameter estimation involving uncertain systems, with applications to pharmacokinetics," in *Proc. 12th IMACS World Congress on Scientific Computation*, pp. 511–513, 1988.

[76] Darlington, J., Pantelides, C. C., Rustem, B., and Tanyi, B., "An algorithm for constrained nonlinear optimization under uncertainty," *Automatica*, vol. 35, no. 2, pp. 217–228, 1999.

[77] Das, A. J., *Tensors: the mathematics of relativity theory and continuum mechanics*. Springer, 2007.

[78] Davis, M. C. and White, J. T., "X-43a flight-test-determined aerodynamic force and moment characteristics at mach 7.0," *Journal of Spacecraft and Rockets*, vol. 45, no. 3, pp. 472–484, 2008.

[79] de Souza, P. N., Fateman, R. J., Moses, J., and Yapp, C., "The maxima book," *See http://maxima. sourceforge. net/docs/maximabook/maximabook-19-Sept-2004. pdf*, 2004.

[80] Deitel, P. J. and Deitel, H. M., *C: how to program*, vol. 2. Prentice Hall, 2010.

[81] DeLaurentis, D. A. and Mavris, D. N., "Uncertainty modeling and management in multidisciplinary analysis and synthesis," *AIAA paper*, vol. 422, p. 5, 2000.

[82] Der Kiureghian, A. and Ditlevsen, O., "Aleatory or epistemic? does it matter?," *Structural Safety*, vol. 31, no. 2, pp. 105–112, 2009.

[83] DeRusso, P. M., Desrochers, A. A., Roy, R. J., and Close, C. M., *State variables for engineers*. John Wiley & Sons, Inc., 1997.

[84] Dette, H. and Biedermann, S., "Robust and efficient designs for the michaelis–menten model," *Journal of the American Statistical Association*, vol. 98, no. 463, pp. 679–686, 2003.

[85] Dette, H., Melas, V. B., and Pepelyshev, A., "Optimal designs for a class of nonlinear regression models," *Annals of statistics*, pp. 2142–2167, 2004.

[86] Dickeson, J. J., Rodriguez, A. A., Sridharan, S., and Korad, A., "Elevator sizing, placement, and control-relevant tradeoffs for hypersonic vehicles," in *AIAA Guidance, Navigation, and Control Conference*, p. 8339, 2010.

[87] Dolvin, D., "Hypersonic international flight research and experimentation (hifire)," *AIAA paper*, vol. 2581, p. 2008, 2008.

[88] Domb, C. and Sykes, M., "On the susceptibility of a ferromagnetic above the curie point," in *Proceedings of the Royal Society of London A: Mathematical, Physical and Engineering Sciences*, vol. 240, pp. 214–228, The Royal Society, 1957.

[89] Draper, N. R. and Hunter, W. G., "Design of experiments for parameter estimation in multiresponse situations," *Biometrika*, vol. 53, no. 3-4, pp. 525–533, 1966.

[90] Draper, N. R. and Smith, H., "Applied regression analysis 2nd ed.," 1981.

[91] DSTO and AFRL, "Hifire program," 2015.

[92] Dutta, S. and Braun, R. D., "Cramér–rao lower-bound optimization of flush atmospheric data system sensor placement," *Journal of Spacecraft and Rockets*, pp. 1–16, 2014.

[93] Eckermann, E., "World history of the automobile," *Metallurgy*, vol. 2015, pp. 06–22, 2001.

[94] Efroymson, M., "Multiple regression analysis," *Mathematical methods for digital computers*, vol. 1, pp. 191–203, 1960.

[95] El-Gamal, M. A., McKelvey, R. D., and Palfrey, T. R., "A bayesian sequential experimental study of learning in games," *Journal of the American Statistical Association*, vol. 88, no. 422, pp. 428–435, 1993.

[96] Elsgolc, L. D., *Calculus of variations*. Courier Dover Publications, 2012.

[97] Espie, D. and Macchietto, S., "The optimal design of dynamic experiments," *AIChE Journal*, vol. 35, no. 2, pp. 223–229, 1989.

[98] Etkin, B., *Dynamics of atmospheric flight*. Courier Dover Publications, 2012.

[99] Etkin, B. and Reid, L. D., *Dynamics of flight: stability and control*. Wiley New York, 1996.

[100] Fedorov, V. V., *Theory of optimal experiments*. Elsevier, 1972.

[101] Fedorov, V., "Convex design theory 1," *Statistics: A Journal of Theoretical and Applied Statistics*, vol. 11, no. 3, pp. 403–413, 1980.

[102] Ferlemann, P. G., "Forebody and inlet design for the hifire 2 flight test," in *55th JANNAF Propulsion Meeting, Newton, MA*, 2008.

[103] Fidan, B., Mirmirani, M., and Ioannou, P. A., "Flight dynamics and control of air-breathing hypersonic vehicles: review and new directions," *AIAA paper*, vol. 7081, no. 2003, 2003.

[104] Fiorentini, L., Serrani, A., Bolender, M. A., and Doman, D. B., "Nonlinear robust adaptive control of flexible air-breathing hypersonic vehicles," *Journal of guidance, control, and dynamics*, vol. 32, no. 2, pp. 402–417, 2009.

[105] Fisher, R. A., "The design of experiments.," 1935.

[106] Ford, I. and Silvey, S., "A sequentially constructed design for estimating a nonlinear parametric function," *Biometrika*, vol. 67, no. 2, pp. 381–388, 1980.

[107] Ford, I., Titterington, D., and Wu, C., "Inference and sequential design," *Biometrika*, vol. 72, no. 3, pp. 545–551, 1985.

[108] Forrester, A., Sobester, A., and Keane, A., *Engineering design via surrogate modelling: a practical guide*. John Wiley & Sons, 2008.

[109] Franceschini, G. and Macchietto, S., "Model-based design of experiments for parameter precision: State of the art," *Chemical Engineering Science*, vol. 63, no. 19, pp. 4846–4872, 2008.

[110] Free Software Foundation, I., "The gnu mpfr library," 2014.

[111] Free Software Foundation, I., "The gnu multiple precision arithmetic library," 2014.

[112] Gainer, T. G. and Hoffman, S., "Summary of transformation equations and equations of motion used in free flight and wind tunnel data reduction and analysis," 1972.

[113] Gelfand, I. M., Gelfand, I. M., and Fomin, S., *Calculus of variations*.

[114] Gerlach, O., *The determination of stability derivatives and performance characteristics from dynamic manoeuvres*. Delft University of Technology, 1971.

[115] Giorgi, P., "On polynomial multiplication in chebyshev basis," *Computers, IEEE Transactions on*, vol. 61, no. 6, pp. 780–789, 2012.

[116] Glass, D. E., "Ceramic matrix composite (cmc) thermal protection systems (tps) and hot structures for hypersonic vehicles," in *15th AIAA space planes and hypersonic systems and technologies conference*, pp. 1–36, 2008.

[117] Goodwin, G. C. and Payne, R. L., "Dynamic system identification: experiment design and data analysis," 1977.

[118] Green, L. L., Lin, H.-Z., and Khalessi, M. R., "Probabilistic methods for uncertainty propagation applied to aircraft design," *AIAA Paper*, vol. 3140, p. 2002, 2002.

[119] Greenberg, H., *A survey of methods for determining stability parameters of an airplane from dynamic flight measurements*. National Advisory Committee for Aeronautics, 1951.

[120] Greenwood, D. T., *Classical dynamics*. Courier Dover Publications, 1997.

[121] Griewank, A., Juedes, D., and Utke, J., "Algorithm 755: Adol-c: a package for the automatic differentiation of algorithms written in c/c++," *ACM Transactions on Mathematical Software (TOMS)*, vol. 22, no. 2, pp. 131–167, 1996.

[122] Griewank, A. and Walther, A., *Evaluating derivatives: principles and techniques of algorithmic differentiation*. Siam, 2008.

[123] Groves, K. P., Sigthorsson, D. O., Serrani, A., Yurkovich, S., Bolender, M. A., and Doman, D. B., "Reference command tracking for a linearized model of an air-breathing hypersonic vehicle," *AIAA paper*, vol. 6144, 2005.

[124] Gupta, N. K. and Hall, W. E., *Input design for identification of aircraft stability and control derivatives*, vol. 2493. National Aeronautics and Space Administration, 1975.

[125] Gupta, N., "Bias and mean square error properties of general estimators," in *Decision and Control including the 15th Symposium on Adaptive Processes, 1976 IEEE Conference on*, vol. 15, pp. 624–628, IEEE, 1976.

[126] Hakami, A., Odman, M. T., and Russell, A. G., "High-order, direct sensitivity analysis of multidimensional air quality models," *Environmental science & technology*, vol. 37, no. 11, pp. 2442–2452, 2003.

[127] Hale, J. K., "Ordinary differential equations," *Pure and Applied Mathematics, John Wiley & Sons, New York*, 1969.

[128] Hallion, R. P., "The hypersonic revolution," *Volume I*, pp. 294–319, 1987.

[129] Hallion, R. P., "The history of hypersonics: or," back to the future-again and again," January 2005.

[130] Hamel, P. G. and Jategaonkar, R. V., "Evolution of flight vehicle system identification," *Journal of Aircraft*, vol. 33, no. 1, pp. 9–28, 1996.

[131] Hamel, P. and Jategaonkar, R., "The role of system identification for flight vehicle applications-revisited," in *RTO-SCI Symposium on System Identification for Integrated Aircraft Development and Flight Testing, Proceedings RTO-MP*, vol. 11, DTIC Document, 1999.

[132] Hamming, R., *Numerical methods for scientists and engineers*. Courier Dover Publications, 2012.

[133] Hank, J. M., Murphy, J. S., and Mutzman, R. C., "The x-51a scramjet engine flight demonstration program," *AIAA Paper*, vol. 2540, p. 2008, 2008.

[134] Haug, E. J. and Arora, J. S., *Applied optimal design: mechanical and structural systems*. John Wiley & Sons, 1979.

[135] Heiser, W. H. and Pratt, D. T., *Hypersonic airbreathing propulsion*. Aiaa, 1994.

[136] Hennigan, W. J., "Test flight of hypersonic x-51a ends in failure."

[137] Hicks, J. W., *Flight testing of airbreathing hypersonic vehicles*, vol. 4524. National Aeronautics and Space Administration, Office of Management, Scientific and Technical Information Program, 1993.

[138] Hille, E., "Lectures on ordinary differential equations," 1969.

[139] Hinch, E. J., *Perturbation methods*. Cambridge university press, 1991.

[140] Hjalmarsson, H., "From experiment design to closed-loop control," *Automatica*, vol. 41, no. 3, pp. 393–438, 2005.

[141] Hocking, R. R., "A biometrics invited paper. the analysis and selection of variables in linear regression," *Biometrics*, pp. 1–49, 1976.

[142] Holmes, M. H., *Introduction to perturbation methods*, vol. 20. Springer, 2012.

[143] Hui, K. and Srinivasan, R., "The inclusion of higher-order rotor dynamics to improve the dynamic model of a single rotor helicopter in hover," in *RTO SCI Symposium: System Identification For Integrated Aircraft Development And Flight Testing, RTO MP-11, Madrid, Spain*, pp. 5–7, 1998.

[144] Hutto, G., "Test for leaders: What you should know," 2004.

[145] Iliff, K. W. and Maine, R., "Bibliography for aircraft parameter estimation," 1986.

[146] Iliff, K. W., Powers, B. G., and Taylor Jr, L., "A comparison of newton-raphson and other methods for determining stability derivatives from flight data.," 1969.

[147] Iliff, K. W. and Shafer, M. F., "A comparison of hypersonic flight and prediction results," *NASA TM-104313 (1995)*, pp. 19–22, 1997.

[148] IM, K., "Development and application of the collaborative optimization architecture in a multidisciplinary design environment," 1995.

[149] Izzo, D., "Pygmo and pykep: Open source tools for massively parallel optimization in astrodynamics (the case of interplanetary trajectory optimization)," in *Proceedings of the Fifth International Conference on Astrodynamics Tools and Techniques, ICATT*, 2012.

[150] Izzo, D., Ruciński, M., and Biscani, F., "The generalized island model," in *Parallel Architectures and Bioinspired Algorithms*, pp. 151–169, Springer, 2012.

[151] Jackson, K. R., Gruber, M. R., and Buccellato, S., "Mach 6–8+ hydrocarbon-fueled scramjet flight experiment: The hifire flight 2 project," *Journal of Propulsion and Power*, vol. 31, no. 1, pp. 36–53, 2014.

[152] Jategaonkar, R. V., "Flight vehicle system identification(a time domain methodology)," *Progress in astronautics and aeronautics*, 2006.

[153] Jay, L., "Symplectic partitioned runge-kutta methods for constrained hamiltonian systems," *SIAM Journal on Numerical Analysis*, vol. 33, no. 1, pp. 368–387, 1996.

[154] Jensen, M. C., "The modern industrial revolution, exit, and the failure of internal control systems," *the Journal of Finance*, vol. 48, no. 3, pp. 831–880, 1993.

[155] Johnson, H., Alba, C., Candler, G., MacLean, M., Wadhams, T., and Holden, M., "Boundary-layer stability analysis of the hypersonic international flight research transition experiments," *Journal of Spacecraft and Rockets*, vol. 45, no. 2, pp. 228–236, 2008.

[156] Johnson, W. P., "The curious history of faà di bruno's formula," *American Mathematical Monthly*, pp. 217–234, 2002.

[157] Johnston, G. and Fowler, F. G., *The Australian Pocket Oxford Dictionary*. Oxford University Press, 1976.

[158] Jones, D. R., Schonlau, M., and Welch, W. J., "Efficient global optimization of expensive black-box functions," *Journal of Global optimization*, vol. 13, no. 4, pp. 455–492, 1998.

[159] Jorba, À. and Zou, M., "A software package for the numerical integration of odes by means of high-order taylor methods," *Experimental Mathematics*, vol. 14, no. 1, pp. 99–117, 2005.

[160] Kailiwai III, G., "The united states air force flight test center experiment in experimental design," *Air Force Flight Test Center*, 2005.

[161] Keskar, D. and Klein, V., "Determination of instrumentation errors from measured data using maximum likelihood method," 1980.

[162] Kiefer, J., "Optimum experimental designs," *Journal of the Royal Statistical Society. Series B (Methodological)*, pp. 272–319, 1959.

[163] Kimberlin, R. D., *Flight testing of fixed wing aircraft*. Aiaa, 2003.

[164] Kirk, D. E., *Optimal control theory: an introduction*. Courier Corporation, 2012.

[165] Klein, V. and MORGAN, D., "Estimation of bias errors in measured airplane responses using maximum likelihood method," 1987.

[166] Klein, V., *Determination of stability and control parameters of a light airplane from flight data using two estimation methods*, vol. 1306. National Aeronautics and Space Administration, Scientific and Technical Information Office, 1979.

[167] Klein, V., "Identification evaluation methods," *AGARD Lecture Series*, vol. 104, 1979.

[168] Klein, V., "Estimation of aircraft aerodynamic parameters from flight data," *Progress in Aerospace Sciences*, vol. 26, no. 1, pp. 1–77, 1989.

[169] Klein, V., "Application of system identification to high performance aircraft," in *Decision and Control, 1993., Proceedings of the 32nd IEEE Conference on*, pp. 2253–2259, IEEE, 1993.

[170] Klein, V. and Morelli, E. A., *Aircraft system identification: theory and practice*. American Institute of Aeronautics and Astronautics Reston, VA, USA, 2006.

[171] Klein, V. and Murphy, P. C., *Aerodynamic Parameters of High Performance aircraft estimated from wind tunnel and flight test data*. National Aeronautics and Space Administration, 1998.

[172] Knuth, D. E., *The Art of Computer Programming, Volume 2: Seminumerical Algorithms*. Addison-Wesley Professional, 2014.

[173] Kreyszig, E., *Advanced engineering mathematics*. John Wiley & Sons, 2007.

[174] Krstic, M., Kanellakopoulos, I., and Kokotovic, P. V., *Nonlinear and adaptive control design*. Wiley, 1995.

[175] Kunis, S. and Potts, D., "Fast spherical fourier algorithms," *Journal of Computational and Applied Mathematics*, vol. 161, no. 1, pp. 75–98, 2003.

[176] L Moses, P., L Rausch, V., T Nguyen, L., and R Hill, J., "Nasa hypersonic flight demonstrators?overview, status, and future plans," *Acta Astronautica*, vol. 55, no. 3, pp. 619–630, 2004.

[177] Lanczos, C., *Applied analysis*. Courier Dover Publications, 1988.

[178] Landaw, E., "Robust sampling designs for compartmental models under large prior eigenvalue uncertainties.," *MATHEMATICS AND COMPUTERS IN BIOMEDICAL APPLICATIONS., 1985,*, pp. 181–188, 1985.

[179] Lau, K. Y., Silvester, T., Alesi, H., Paull, A., Paull, R., and Dolvin, D. J., "Hifire 4: a low-cost aerodynamics, stability, and control hypersonic flight experiment," 2011.

[180] Lee, S. H. and Chen, W., "A comparative study of uncertainty propagation methods for black-box-type problems," *Structural and Multidisciplinary Optimization*, vol. 37, no. 3, pp. 239–253, 2009.

[181] Lind, R. and Brenner, M., *Robust aeroservoelastic stability analysis: Flight test applications*. Springer Science & Business Media, 2012.

[182] Ljung, L., "System identification," in *Signal Analysis and Prediction*, pp. 163–173, Springer, 1998.

[183] Lu, F. K. and Marren, D. E., *Advanced hypersonic test facilities*, vol. 198. Aiaa, 2002.

[184] Lucas, R. E., *Lectures on economic growth*. Harvard University Press, 2002.

[185] Lukasiewicz, J., *Experimental methods of hypersonics*, vol. 3. M. Dekker, 1973.

[186] Maine, R. E. and Iliff, K. W., *The theory and practice of estimating the accuracy of dynamic flight-determined coefficients*, vol. 1077. National Aeronautics and Space Administration, Scientific and Technical Information Branch, 1981.

[187] Maine, R. and Iliff, K. W., "Application of parameter estimation to aircraft stability and control: The output-error approach," 1986.

[188] Marshall, L. A., Corpening, G. P., and Sherrill, R., "A chief engineer's view of the nasa x-43a scramjet flight test," in *Proceedings of 13th AIAA/CIRA international space planes and hypersonic systems and technologies conference*, pp. 1181–200, 2005.

[189] Martin, L., "Sr72program," 2013.

[190] Marvin, J. G., "A cfd validation roadmap for hypersonic flows," *NASA STI/Recon Technical Report N*, vol. 92, p. 30982, 1992.

[191] Mathews, J. H. and Fink, K. D., *Numerical methods using MATLAB*, vol. 3. Prentice hall Upper Saddle River, NJ, 1999.

[192] Matthies, H. G., "Quantifying uncertainty: modern computational representation of probability and applications," in *Extreme man-made and natural hazards in dynamics of structures*, pp. 105–135, Springer, 2007.

[193] Mavris, D. N., Baker, A. P., and Schrage, D. P., "Ippd through robust design simulation for an affordable short haul civil tiltrotor," 1997.

[194] Mavris, D. N., Bandte, O., and DeLaurentis, D. A., "Robust design simulation: a probabilistic approach to multidisciplinary design," *Journal of Aircraft*, vol. 36, no. 1, pp. 298–307, 1999.

[195] Mavris, D. N., DeLaurentis, D. A., Bandte, O., and Hale, M. A., "A stochastic approach to multi-disciplinary aircraft analysis and design," in *36th Aerospace Sciences Meeting & Exhibit, Reno, NV*, 1998.

[196] McClinton, C. R., Rausch, V. L., Nguyen, L. T., and Sitz, J. R., "Preliminary x-43 flight test results," *Acta Astronautica*, vol. 57, no. 2, pp. 266–276, 2005.

[197] McClinton, C. R., Rausch, V. L., Sitz, J., and Reukauf, P., "Hyper-x program status," *AIAA paper*, vol. 828, p. 2001, 2001.

[198] Mehra, R. K., "Maximum likelihood identification of aircraft parameters," in *Proceedings of the Joint Atomatic Control Conference*, vol. 104, 1970.

[199] Mehra, R. K., "Optimal inputs for linear system identification," *Automatic Control, IEEE Transactions on*, vol. 19, no. 3, pp. 192–200, 1974.

[200] Mehra, R. K. and Eupta, N., "Status of input design for aircraft parameter identification," 1975.

[201] Meirovitch, L., *Analytical methods in vibration*, vol. 16. Macmillan, New York, 1967.

[202] Melas, V., "Optimal designs for exponential regression," *Statistics: A Journal of Theoretical and Applied Statistics*, vol. 9, no. 1, pp. 45–59, 1978.

[203] Milliken Jr, W. F., "Progress in dynamic stability and control research," *Journal of the Aeronautical Sciences (Institute of the Aeronautical Sciences)*, vol. 14, no. 9, 2012.

[204] Moenck, R. T., "Another polynomial homomorphism or how to make short fat polynomials look long and thin," 1975.

[205] Moenck, R. T., "Another polynomial homomorphism," *Acta Informatica*, vol. 6, no. 2, pp. 153–169, 1976.

[206] Moenck, R. T., "Practical fast polynomial multiplication," in *Proceedings of the third ACM symposium on Symbolic and algebraic computation*, pp. 136–148, ACM, 1976.

[207] Montgomery, D. C., Peck, E. A., and Vining, G. G., *Introduction to linear regression analysis*, vol. 821. John Wiley & Sons, 2012.

[208] Morelli, E. A., *Practical input optimization for aircraft parameter estimation experiments*. 1993.

[209] Morelli, E. A., "Flight test validation of optimal input design and comparison to conventional inputs," in *AIAA Atmospheric Flight Mechanics Conference*, vol. 1, pp. 11–13, 1997.

[210] Morelli, E. A., "Advances in experiment design for high performance aircraft," *Hampton, VA: NASA Langley Research Center, 1998a*, 1998.

[211] Morelli, E. A., "System identification programs for aircraft (sidpac)," in *AIAA Atmospheric Flight Mechanics Conference*, 2002.

[212] Morelli, E. A., "Flight-test experiment design for characterizing stability and control of hypersonic vehicles," *Journal of Guidance, Control, and Dynamics*, vol. 32, no. 3, pp. 949–959, 2009.

[213] Morelli, E. A., Derry, S. D., and Smith, M. S., "Aerodynamic parameter estimation for the x-43a (hyper-x) from flight data," *AIAA paper*, vol. 5921, p. 2005, 2005.

[214] Morelli, E. E. and Klein, V., *Determining the accuracy of maximum likelihood parameter estimates with colored residuals*. National Aeronautics and Space Administration, Langley Research Center, 1994.

[215] Mulder, J. A., *Design and evaluation of dynamic flight test manoeuvres*. PhD thesis, Technische Universiteit Delft, 1986.

[216] Müller, W. G. and Pötscher, B. M., *Batch sequential design for a nonlinear estimation problem*. Institute for Advanced Studies, 1989.

[217] Mulmuley, K., "A fast parallel algorithm to compute the rank of a matrix over an arbitrary field," in *Proceedings of the eighteenth annual ACM symposium on Theory of computing*, pp. 338–339, ACM, 1986.

[218] Myers, R. H., "Classical and modern regression with applications (duxbury classic)," *Duxbury Press, Pacific Grove*, 2000.

[219] Myers, W. R. and Montgomery, D. C., "Response surface methodology," *Encycl Biopharm Stat*, vol. 1, pp. 858–869, 2003.

[220] Narendra, K. S. and Parthasarathy, K., "Identification and control of dynamical systems using neural networks," *Neural Networks, IEEE Transactions on*, vol. 1, no. 1, pp. 4–27, 1990.

[221] Neidinger, R. D., "Introduction to automatic differentiation and matlab object-oriented programming," *SIAM review*, vol. 52, no. 3, pp. 545–563, 2010.

[222] Norris, G., "X-51a waverider achieves goal on final flight."

[223] Norris, G., "Son of blackbird," *Aviation Week: Science and Technology*, 2013.

[224] Oberkampf, W. L., DeLand, S. M., Rutherford, B. M., Diegert, K. V., and Alvin, K. F., "Error and uncertainty in modeling and simulation," *Reliability Engineering & System Safety*, vol. 75, no. 3, pp. 333–357, 2002.

[225] Omran, A., Newman, B., and Landman, D., "Global aircraft aeropropulsive linear parameter-varying model using design of experiments," *Aerospace Science and Technology*, vol. 22, no. 1, pp. 31–44, 2012.

[226] Oniki, H., "Comparative dynamics (sensitivity analysis) in optimal control theory," *Journal of Economic Theory*, vol. 6, no. 3, pp. 265–283, 1973.

[227] Padula, S. and Li, W., "Options for robust airfoil optimization under uncertainty," in *9th AIAA Multidisciplinary Analysis and Optimization Symposium*, pp. 4–6, 2002.

[228] Parker, J. T., Serrani, A., Yurkovich, S., Bolender, M. A., and Doman, D. B., "Control-oriented modeling of an air-breathing hypersonic vehicle," *Journal of Guidance, Control, and Dynamics*, vol. 30, no. 3, pp. 856–869, 2007.

[229] Peebles, C., *Road to Mach 10: lessons learned from the X-43A flight research program*. American Institute of Aeronautics & Astronautics, 2008.

[230] Peebles, C. and Allen, N., *Eleven Seconds Into the Unknown: A History of the Hyper-X Program*. American Institute of Aeronautics and Astronautics, 2010.

[231] Pike, J., "X-51 scramjet engine demonstrator - waverider (sed-wr)," 2013.

[232] Pronzato, L., "Optimal experimental design and some related control problems," *Automatica*, vol. 44, no. 2, pp. 303–325, 2008.

[233] Pronzato, L. and Walter, É., "Robust experiment design via maximin optimization," *Mathematical Biosciences*, vol. 89, no. 2, pp. 161–176, 1988.

[234] Rall, L. B., "Automatic differentiation: Techniques and applications," 1981.

[235] Ramnath, R. V., *Multiple scales theory and aerospace applications*. American Institute of Aeronautics and Astronautics, 2010.

[236] Rao, C. R., "Information and the accuracy attainable in the estimation of statistical parameters," in *Breakthroughs in statistics*, pp. 235–247, Springer, 1992.

[237] Rao, C. R. and Gupta, S. D., *Selected papers of CR Rao*, vol. 5. Taylor & Francis, 2001.

[238] Richman, M. S., Kenyon, J. A., and Sega, R. M., "High speed and hypersonic science and technology," *AIAA Paper*, vol. 4099, p. 2005, 2005.

[239] Rodriguez, A. A., Dickeson, J. J., Cifdaloz, O., McCullen, R., Benavides, J., Sridharan, S., Kelkar, A., Vogel, J. M., and Soloway, D., "Modeling and control of scramjet-powered hypersonic vehicles: challenges, trends, and tradeoffs," in *AIAA guidance, navigation and control conference and exhibit*, vol. 6793, 2008.

[240] Rojas, C. R., Welsh, J. S., Goodwin, G. C., and Feuer, A., "Robust optimal experiment design for system identification," *Automatica*, vol. 43, no. 6, pp. 993–1008, 2007.

[241] Roy, C. J. and Blottner, F. G., "Review and assessment of turbulence models for hypersonic flows," *Progress in Aerospace Sciences*, vol. 42, no. 7, pp. 469–530, 2006.

[242] Ruciński, M., Izzo, D., and Biscani, F., "On the impact of the migration topology on the island model," *Parallel Computing*, vol. 36, no. 10, pp. 555–571, 2010.

[243] Ryan, G. W. and Platz, S. J., "Developing aerial refueling simulation models from flight test data using alternative pid methods," *Star*, vol. 37, p. 5, 1999.

[244] Sanders, A. D., Jenista, C. G., Arrowood, R. H., Donnan, R. A., Goodman, J. M., Gordon, S. E., Maschmeyer III, T. L., Laughlin, B. P., and Mavris, D. N., "Multi-disciplinary design of a supersonic, long-range, air-superiority missile through parametric design space exploration and physics-based modeling,"

[245] Schlenkrich, S., Walther, A., Gauger, N. R., and Heinrich, R., "Differentiating fixed point iterations with adol-c: Gradient calculation for fluid dynamics," in *Modeling, Simulation and Optimization of Complex Processes*, pp. 499–508, Springer, 2008.

[246] Schmidt, D. K. and Hermann, J. A., "Use of energy-state analysis on a generic air-breathing hypersonic vehicle," *Journal of guidance, control, and dynamics*, vol. 21, no. 1, pp. 71–76, 1998.

[247] Schneider, S. P., "Development of hypersonic quiet tunnels," *Journal of Spacecraft and Rockets*, vol. 45, no. 4, pp. 641–664, 2008.

[248] Schrage, D. P., "Technology for rotorcraft affordability through integrated product/process development (ippd)," 1999.

[249] Schweppe, F. C., *Uncertain dynamic systems*, vol. 160. Prentice-Hall Englewood Cliffs, NJ, 1973.

[250] Sebastiani, P. and Wynn, H. P., "Maximum entropy sampling and optimal bayesian experimental design," *Journal of the Royal Statistical Society: Series B (Statistical Methodology)*, vol. 62, no. 1, pp. 145–157, 2000.

[251] Shirt, R. W., Harris, T. J., and Bacon, D. W., "Experimental design considerations for dynamic systems," *Industrial & engineering chemistry research*, vol. 33, no. 11, pp. 2656–2667, 1994.

[252] Shonkwiler, R. W. and Lefton, L., *An Introduction to Parallel and Vector Scientific Computation*, vol. 41. Cambridge University Press, 2006.

[253] Sigthorsson, D., Jankovsky, P., Serrani, A., Yurkovich, S., Bolender, M., and Doman, D. B., "Robust linear output feedback control of an airbreathing hypersonic vehicle," *Journal of Guidance, Control, and Dynamics*, vol. 31, no. 4, pp. 1052–1066, 2008.

[254] Slotine, J.-J. E., Li, W., and others, *Applied nonlinear control*, vol. 199. Prentice-Hall Englewood Cliffs, NJ, 1991.

[255] Smart, M. and Suraweera, M., "Hifire 7–development of a 3-d scramjet for flight testing," *AIAA Paper*, vol. 7259, p. 2009, 2009.

[256] Sobieszczanski-Sobieski, J. and Haftka, R. T., "Multidisciplinary aerospace design optimization: survey of recent developments," *Structural optimization*, vol. 14, no. 1, pp. 1–23, 1997.

[257] Sorenson, H. W., *Parameter estimation: principles and problems*. Marcel Dekker New York, 1980.

[258] Sridharan, S., *Multidisciplinary optimization for the design and control of uncertain dynamical systems*. PhD thesis, Arizona State University, 2014.

[259] Starkey, R. P., Liu, D., Baldelli, D. H., Chang, R., and Chen, P., "Rapid conceptual design and analysis of a hypersonic air-breathing missile," in *15th AIAA International Space Planes and Hypersonic Systems and Technologies Conf*, vol. 2590, p. 2008, 2008.

[260] Stein, W. and Joyner, D., "Sage: System for algebra and geometry experimentation," *ACM SIGSAM Bulletin*, vol. 39, no. 2, pp. 61–64, 2005.

[261] Stephen, E. J., Hoenisch, S. R., Riggs, C. J., Waddel, M. L., McLaughlin, T., and Bolender, M. A., "Hifire 6 unstart conditions at off-design mach numbers," January 2015.

[262] Stepner, D. E. and Mehra, R. K., *Maximum likelihood identification and optimal input design for identifying aircraft stability and control derivatives*, vol. 2200. National Aeronautics and Space Administration, 1973.

[263] Stewart, J., *Single variable calculus: early transcendentals*. Cengage Learning, 2011.

[264] Strogatz, S. H., *Nonlinear dynamics and chaos: with applications to physics, biology and chemistry*. Perseus publishing, 2001.

[265] Stueber, T. J., Le, D. K., and Vrnak, D. R., "Hypersonic vehicle propulsion system control model development roadmap and activities," tech. rep., NASA/TM?2009-215483 (January 2009), 2009.

[266] Taguchi, G., *Introduction to quality engineering: designing quality into products and processes*. 1986.

[267] Takemiya, T., *Aerodynamic design applying automatic differentiation and using robust variable fidelity optimization*. ProQuest, 2008.

[268] Tang, M. and Chase, R. L., "The quest for hypersonic flight with air-breathing propulsion," *AIAA*, vol. 2546, p. 2008, 2008.

[269] Tarantola, A., *Inverse problem theory and methods for model parameter estimation*. SIAM, 2005.

[270] Thompson, E., Henry, K., and Williams, L., "Faster than a speeding bullet: Guinness recognizes nasa scramjet," *NASA*, vol. 20, pp. 05–156, 2005.

[271] Torrez, S. M., Scholten, N. A., Micka, D. J., Driscoll, J. F., Bolender, M. A., Doman, D. B., and Oppenheimer, M. W., "A scramjet engine model including effects of precombustion shocks and dissociation," *AIAA Paper*, vol. 4619, p. 2008, 2008.

[272] Vanderplaats, G. N., *Multidiscipline design optimization*. Vanderplaats Research & Development, Incorporated, 2007.

[273] Vila, J., "New algorithmic and software tools for d-optimal design computation in nonlinear regression," in *Compstat*, pp. 409–414, Springer, 1988.

[274] Waechter, A., Laird, C., Margot, F., and Kawajir, Y., "Introduction to ipopt: A tutorial for downloading, installing, and using ipopt," 2009.

[275] Walberg, G. D., "Hypersonic flight experience," *Philosophical Transactions of the Royal Society of London. Series A: Physical and Engineering Sciences*, vol. 335, no. 1637, pp. 91–119, 1991.

[276] Walter, E. and Pronzato, L., "Identification of parametric models," *Communications and Control Engineering*, 1997.

[277] Walther, A. and Griewank, A., "Getting started with adol-c," *Combinatorial Scientific Computing*, pp. 181–202, 2012.

[278] Walther, A., Griewank, A., and Vogel, O., "Adol-c: Automatic differentiation using operator overloading in c++," *PAMM*, vol. 2, no. 1, pp. 41–44, 2003.

[279] Williams, T., Bolender, M. A., Doman, D. B., and Morataya, O., "An aerothermal flexible mode analysis of a hypersonic vehicle," *AIAA paper*, vol. 6647, p. 2006, 2006.

[280] Wujek, B., Renaud, J. E., and Batill, S., "A concurrent engineering approach for multidisciplinary design in a distributed computing environment," *Multidisciplinary Design Optimization: State of the Art*, pp. 189–208, 1997.

[281] Xu, D. and Albin, S. L., "Robust optimization of experimentally derived objective functions," *IIE Transactions*, vol. 35, no. 9, pp. 793–802, 2003.

[282] Zadeh, L. A., "From circuit theory to system theory," *Proceedings of the IRE*, vol. 50, no. 5, pp. 856–865, 1962.

[283] Zanoni, A., "Iterative karatsuba for multivariate polynomial multiplication," *Preprint*, no. 624, 2009.

[284] Zhao, K., Glover, K., and Doyle, J., "Robust and optimal control," 1995.

[285] Zipfel, P. H., *Modeling and simulation of aerospace vehicle dynamics*. Aiaa, 2000.